Diffuse interface models and adapted numerical schemes for the simulation of subcritical to supercritical flows

Milan Pelletier

NNT : 2019SACLC059

Thèse de doctorat

Diffuse interface models and adapted numerical schemes for the simulation of subcritical to supercritical flows

Thèse de doctorat de l'Université Paris-Saclay
préparée à École CentraleSupélec

Ecole doctorale n°579 Sciences, mécaniques et énergétiques, matériaux et géosciences (SMEMaG)
Spécialité de doctorat : Énergétique

Thèse présentée et soutenue à Gif-sur-Yvette, le 10/07/2019, par

MILAN PELLETIER

Composition du Jury :

Richard Saurel Professeur des Universités, Aix-Marseille Université (LMA)	Président, Rapporteur
Vincent Giovangigli Directeur de Recherche CNRS, École Polytechnique (CMAP)	Rapporteur
Vincent Moureau Chargé de Recherche CNRS, INSA Rouen (CORIA)	Examinateur
Angelo Murrone Chargé de Recherche ONERA, Centre de Châtillon	Examinateur
Sébastien Ducruix Directeur de Recherche CNRS, CentraleSupélec (EM2C)	Directeur de thèse
Adam Larat Chargé de recherche CNRS, ENSIMAG (LJK)	Co-encadrant
Thomas Schmitt Chargé de Recherche CNRS, CentraleSupélec (EM2C)	Co-encadrant

Remerciements

Je souhaite remercier tout d'abord les professeurs et chercheurs qui ont accepté de participer à mon jury de thèse. Ainsi, je remercie les professeurs Vincent Giovangigli et Richard Saurel, rapporteurs de cette thèse, dont les avis d'experts m'auront permis d'améliorer la qualité et la clarté du manuscrit. Merci également à Angelo Murrone et Vincent Moureau pour les discussions enrichissantes que nous avons pu mener pendant la soutenance, couvrant tous les aspects de ce travail. J'ai été sincèrement honoré de votre présence et de l'intérêt que vous avez porté à ces recherches.

Je tiens ensuite à témoigner ma profonde gratitude à mes encadrants, Thomas Schmitt, Adam Larat et Sébastien Ducruix, qui ont toujours été présents quand le besoin s'en faisait sentir. Au-delà de leurs expertises respectives, desquelles ils ont su me faire bénéficier, et dont j'ai énormément appris, ils ont été d'excellents compagnons de route. Sébastien, pour avoir représenté une certaine "force tranquille" qui, malgré les nombreuses sollicitations liées à son statut de directeur de laboratoire dans une période mouvementée de déménagement, aura toujours pu m'apporter des repères, et ses avis éclairés et bienveillants. Adam, pour m'avoir aussi bien appris à implémenter des méthodes RKDG qu'à faire un noeud en double de huit. Thomas, pour m'avoir appris que *faire de la belle recherche* et *être pragmatique* ne sont pas antinomiques, tout cela sur fond de métal symphonique. Il est évident que si cette expérience a été aussi riche pour moi, c'est en grande partie grâce à vous et à la confiance et l'amitié que nous avons partagées au long de ces années.

Merci également à l'équipe qui prend la relève sur les modèles multifluides au CERFACS, en premier lieu Thomas L., et aussi Simon et Julien. Merci bien sûrà Bénédicte Cuenot et Antony Misdariis qui accompagnent ce projet du côté de Toulouse et qui y apportent leur expérience. Notre collaboration aura été très enrichissante et c'est aussi important de voir que les recherches vont se poursuivre sur cette voie.

Ensuite, merci à Aymeric pour m'avoir offert l'opportunité de poursuivre quelques temps au laboratoire. J'espère que `TITAN 1.0` aura très vite toute une batterie de méthodes multifluides nouvelle génération qui tournent sur MPI-openMP-GPU dans le *cloud*. En parlant de TITAN, je remercie également Jean-Michel pour son implication et pour tous les éclairages sur les nombreux écueils rencontrés, et Victor pour ses histoires de cube-chopping et ses gouttes qui bougent.

Je voudrais également témoigner toute ma gratitude à Noï, Nathalie et Brigitte. Merci d'avoir été chaque fois réactives et diablement efficaces afin que toutes les démarches se déroulent sans encombre. C'est une véritable chance de pouvoir compter sur vous pour être dans les meilleures dispositions pour mener nos recherches. Vous êtes toujours à l'écoute, et, en plus, vous avez toujours des bonbons.

Je remercie plus généralement tous les permanents du laboratoire avec qui j'ai pu avoir des discussions fructueuses, ou simplement des échanges sympathiques autour d'un café.

Bien évidemment, je suis très reconnaissant envers tous les amis doctorants dont j'ai croisé la route. En premier lieu, merci à Davy pour m'avoir recruté, pour m'avoir mis le pied à l'étrier dans le monde des interfaces diffuses, et pour avoir été à mes côtés pendant toute la première partie de la thèse. C'était une vraie fierté d'être un Argonaute à tes côtés et j'ai pris plaisir à noircir des tableaux blancs au gré de nos discussions. Je te souhaite de boucler brillamment ta thèse, ce sur quoi je n'ai aucun doute.

Merci à mes nombreux *co-bureaux* : Robin, Augustin, Pierre, Pedro, David, Ulysse, Ciprian, Preethy,

Arnaud, Meng, Mathieu et Benjamin. J'ai passé d'excellents moments à vos côtés, que ce soit pour partager des RU ou des truffades, la discographie de Brassens, des cafés, des débats féconds sur la supériorité des combustionnistes sur les plasmiciens, des leçons sur l'utilisation de phonèmes éphel-cystiques et paragoges, des cours d'Allemand, ou même, parfois, des discussions scientifiques. Merci également à tous les autres doctorants et post-docs du labo. Les vieux pour leur sagesse légendaire: Cedric et son RC Strasbourg, Nicolas D., Kevin P., Erwan et Mélody. Le "bureau des filles" où on pouvait toujours se faire gronder pour n'importe quelle raison : Théa, Abi et Lorella, ainsi que Valentin, Léo et Quentin. Et tous ceux avec qui on a partagé des cafés et des RU : Aurélien, Thomas E., Constantin, Livia, David (Mercier), Claire, Arthur D., Guilhem, Minou, Hernando, Yacine, Karl, Kevin T., Amanda, Victorien, Corentin, Junghwa, Guillaume, Renaud, Paul, Lantao, Adrien, Giunio, Giampaolo, Suzanne, Jan, Arthur C., Sergey, Marco, et tous les autres !

Je souhaite également saluer mes amis qui ont supporté mon intermittence pendant ces années. Une mention spéciale aux Oursons, Pierre et Grégoire, pour ces moments de défoulement frénétique en studio de répétition, mais aussi pour tout le reste. Merci à tous les amis venant des alentours du Centre du Monde (i.e. Tournan-en-Brie), même à ceux qui habitent rive droite ou Bruxelles. Big up aux copains de la Ferme Électrique. Merci aux amis de Condorcet, et bon courage à ceux qui soutiennent bientôt ! Merci en particulier (et félicitations) à Mariana et Alexander pour leur invitation au Brésil juste après le rendu du manuscrit. Merci aux copains des Ponts de nous avoir accueilli dans vos diverses fêtes de Nouvel An et autres bons moments. Merci aux copains de Centrale, les jeunes mariés Bizot-Tomada et les très jeunes mariés Lavorel-Trofimoff, l'inénarrable Flavien, Arthurinho, ainsi que tous les autres qui se reconnaîtront, qu'ils soient à Londres, Rouen, Paris, au Gabon ou n'importe où ailleurs.

J'adresse un remerciement tout particulier à ma famille pour avoir toujours été attentive et m'avoir aidé mieux que j'aurai pu l'espérer. Je suis conscient de la chance de vous avoir, Papa et Maman, Lola et Louise. Vous avez construit quelque chose de très précieux, et je sais qu'on peut toujours compter les uns sur les autres, pour passer d'excellents moments mais aussi pour ceux, plus difficiles, que nous avons dû traverser au cours de ces dernières années. J'embrasse très fort papi *Peppe* et mamie *Gi'*, mamie *Mo'*, et je pense fort à papi Michel. Sans vous tous, les choses seraient infiniment moins chouettes.

Pour terminer, je remercie de tout cœur Laurène, pour m'avoir accompagné à travers cette aventure. C'était un sacré défi que de commencer nos thèses en ce même jour du 1er décembre 2015, mais nous voilà à présent tous deux docteurs et prêts à attaquer la suite à pleines dents. Merci pour ton soutien, que tu m'as apporté même quand c'était difficile pour toi aussi. Merci de me comprendre, et merci pour tout ce qui reste à venir. J'ai hâte de découvrir la suite, et surtout de le faire à tes côtés.

Contents

List of Tables

List of Figures

Chapter 1

General introduction

Motivation and research context

Liquid injection engines are extensively used in industrial and transportation systems. Indeed, storing the reactant under a liquid state provides a very compact energy source, which is particularly beneficial to transportation devices. Nonetheless, the two-phase flows involved in such liquid injection systems are highly complex, and their modeling is still a very active field of research.

Thanks to the swift development of the computing capacity, the accurate representation of two-phase flows has become a reasonable target. Yet, their modeling, and especially the representation of liquid-gas interfaces still raises many unresolved questions.

In addition to this complexity, the topology of the flow for liquid injection systems is known to be strongly impacted by the operating pressure of the chamber. At low pressure, the *capillary forces* are responsible for the surface tension, causing the liquid jet to break into smaller inclusions (ligaments, droplets) when subject to shear stress. When the pressure crosses the limit of the *critical pressure*, the capillary forces responsible for the structure of the liquid-gas interface are observed to progressively vanish. In the supercritical regime, the interface has disappeared and the injected flow has become a single-phase flow with large density variations.

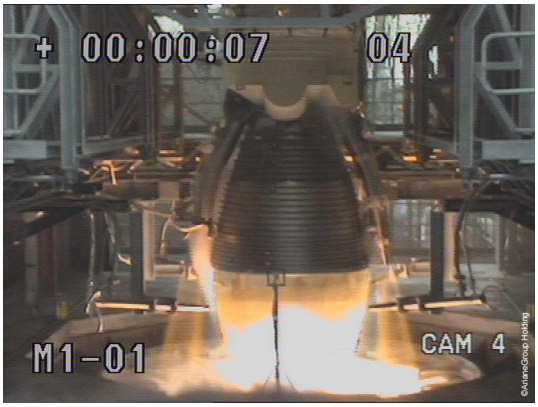

Figure 1.1: Photography of a test of Ariane VI's Vulcain engine (source: www.futura-sciences.com)

In the industry, there are multiple examples of two-phase flows that operate under a very wide range of pressure, for which the transition from subcritical to supercritical states may be encountered. In particular, at ignition, the transient regime of a liquid rocket engine typically starts at low pressure

and reaches a supercritical pressure in the steady regime. For instance, the Vulcain engine of Ariane V and Ariane VI (see figure 1.1) is ignited at atmospheric pressure and its operating pressure is typically $P_{\text{op}} = 11.5$ MPa, while the critical pressure of the injected liquid oxygen is $P^c_{O_2} = 5.043$ MPa. Similarly, during the compression phase of a Diesel engine, the pressure within a cylinder reaches about $P_{\text{cyl}} = 4$ MPa, while the critical pressure of heptane, the main constituent of Diesel fuel is $P^c_{C_{12}H_{26}} = 1.82$ MPa. In these contexts, the disappearance of the interface may be encountered – although the supercritical nature of these flows also depends on the multicomponent mixing within the chamber, so that two-phase flows may be encountered at pressures higher than the critical pressure of the pure components.

The accurate description of these injection processes is essential for the development of safe and efficient devices. A variety of physical phenomena are involved in these reactive flows, which result in a very high complexity. To quote but a few, the precise description of these flows involves non-ideal thermodynamics, phase change, compressibility effects, heat transfer, multicomponent transport, turbulence and chemical reactions. All these phenomena are very different in nature and involve various length scales, typically ranging from about one meter to a few nanometers.

Also, the mathematical nature of the models that describe these phenomena are not always compatible. In this respect, simulating an interface generally requires to use tailored numerical methods.

Different aspects of the simulation of both subcritical two-phase flows and supercritical flows are described in what follows, in order to present the research context in which the present thesis work is led.

Modeling supercritical flows

The modeling of supercritical reactive flows has been the object of very intense research efforts for about 30 years, and now benefits from a rather wide literature. Especially in the context of space propulsion devices, this modeling effort has been supported by experimental campaigns conducted by the DLR[1] and the AFRL[2] [Oschwald et al., 2006, Segal and Polikhov, 2008], and by ONERA[3] and Laboratoire EM2C [Habiballah et al., 2006, Candel et al., 2006].

The general modeling strategy that is commonly accepted relies on the use of real gas thermodynamics [Poling et al., 2001] in order to account for the non-ideal molecular interactions that occur at high pressure. In particular, cubic equations of state [Soave, 1972, Peng and Robinson, 1976] with appropriate mixing rules are widely used, as they provide good representation of the fluid properties. This allowed to evidence the consequences of supercritical injection on the flow and flame dynamics [Oefelein, 2005, Bellan, 2006, Ribert et al., 2008, Schmitt et al., 2011, Giovangigli et al., 2011, Giovangigli and Matuszewski, 2012]. For instance, results from [Schmitt, 2019] are illustrated in figure 1.2, showing an accurate prediction of the flame structure and length.

Such developments paved the way for the investigation of more complex coupled phenomena such as combustion instabilities [Urbano et al., 2016], applied to practical configurations.

In order to address the modeling of supercritical flows, the present work follows the general guidelines provided by these previous works, as they offer convincing results. In particular, cubic equations of state are chosen to address the non-ideal thermodynamics, as they provide a good trade-off between accuracy, complexity and computational cost.

It is worth underlining that despite the convincing results obtained by the community of supercritical flow modeling, some aspects can still be improved and are still studied. For example, one can evoke the question of conservative transport, which is known to generate noise when applied with cubic equations of states, which motivated the recent works of [Pantano et al., 2017] and [Lacaze et al., 2019].

[1] Deutsche Zentrum für Luft- and Raumfahrt
[2] American Air Force Research Laboratory
[3] Office National d'Études et de Recherches Aérospatiales

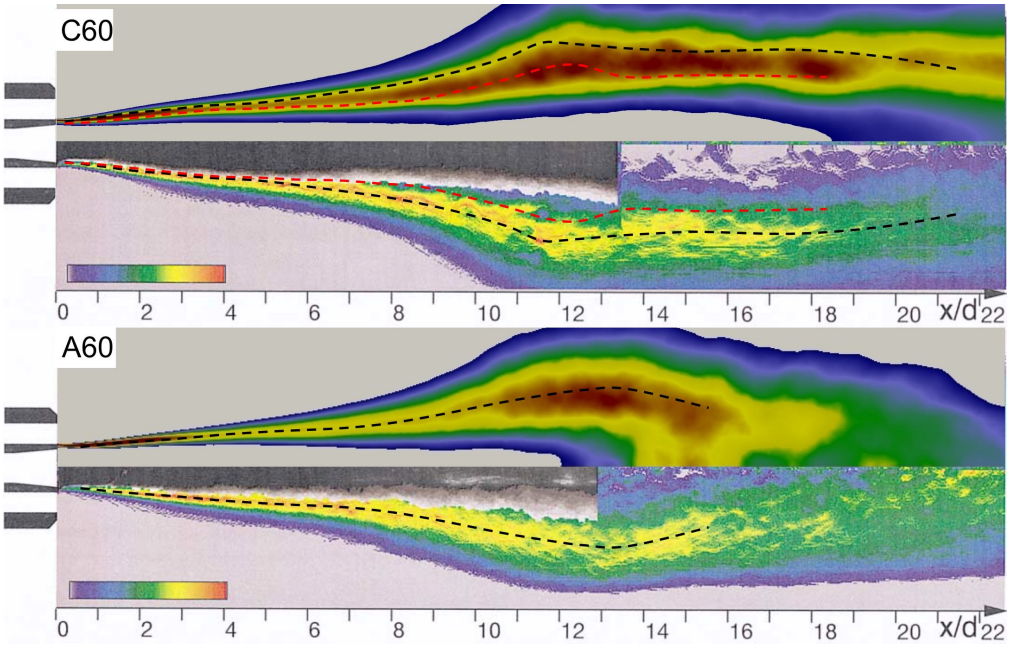

Figure 1.2: Comparison between experimental and large-eddy simulation results for supercritical combustion. Upper half: Mean OH concentration from large-eddy simulation. Lower half: Abel transform of OH* emission from experiments [Singla et al., 2005, Juniper et al., 2000]. d is the oxygen injector diameter. Dashed lines indicate the position of the flame, experimentally obtained as the zone maximum emission. The pictures are courtesy of [Schmitt, 2019].

Modeling subcritical flows

As previously said, the study of liquid injection in subcritical regimes requires to address two-phase flows and in particular to handle the liquid-gas interface. A very rich literature is available on the interface modeling methods. They rely on various approaches, representing the interface either as a sharp or a diffuse zone, and using either a Lagrangian or an Eulerian formulation to ensure the interface transport. These approaches have different range of applications. An overview of the works on liquid-gas interface modeling is the object of chapter 3 of the present manuscript.

Since reactive compressible two-phase flows are targeted by the present study, the choice of interface model has been oriented towards towards hyperbolic diffuse interface methods, and more precisely the hyperbolic multifluid methods. Indeed, such methods are well-suited to compressible applications, for which they guarantee discrete conservation of the mass, momentum and energy.

The different multifluid methods are generally referred to using the number of transport equations they involve:

- the 7-equation models [Baer and Nunziato, 1986, Saurel and Abgrall, 1999, Furfaro and Saurel, 2016] allow the phases to be in full disequilibrium, so that they can locally have different velocities, pressures, temperatures and chemical potentials.
- the 5-equation models [Kapila et al., 2001, Allaire et al., 2002, Murrone and Guillard, 2005] assume that the phases have locally identical pressure and velocity values, considering the short relaxation time that characterizes such mechanical disequilibria at the liquid-gas interface.
- the 4-equation and 3-equation models [Le Martelot et al., 2014, Chiapolino et al., 2016, Chiapolino et al., 2017] push further the equilibrium assumptions between phases. The 4-equation model considers that the phases are in velocity, pressure and temperature equilibrium, and the 3-equation model considers that they are in velocity, pressure, temperature and chemical potential equilibrium, respectively. This is particularly adapted for stiff phase change situations.

An example of a simulation result for a multifluid method is given in figure 1.3.

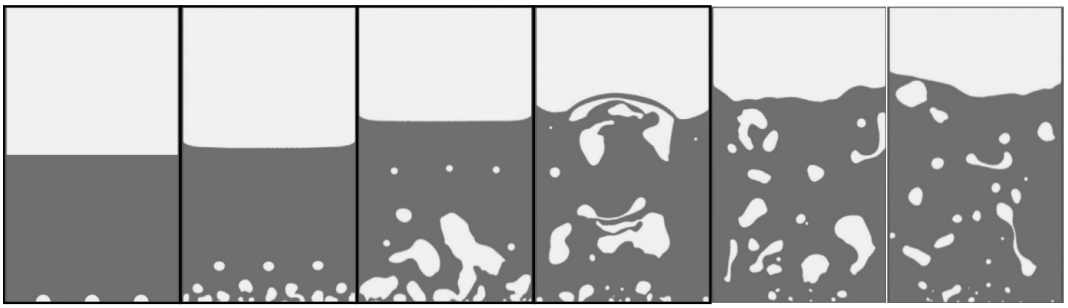

Figure 1.3: Snapshots of a simulation of boiling water using a multifluid model in [Le Martelot et al., 2014].

These models require a thermodynamic closure for each phase. Generally, the gas phase is represented by an ideal gas mixture, while the liquid phase is described by either a stiffened gas [Le Métayer et al., 2004] or a Noble-Abel stiffened gas (NASG) [Le Métayer and Saurel, 2016] equation of state. This choice of equations of state is convenient as they provide valuable convexity properties and are easily invertible. Yet, it is not naturally suited for an extension towards supercritical regimes. Indeed, there is no trivial way to define a unique equation of state for the single supercritical phase from the two equations of state used in the subcritical regime.

This motivated the idea of using a single cubic equation of state to describe liquid, vapour and supercritical states, as planned by the ANR[4] project "*Sub/Super Jet*" in which the present work takes its place. Nonetheless, the use of cubic equations of state in subcritical regimes is not straightforward, as such equations are not unconditionally convex, unlike the ideal gas, stiffened gas or NASG equations of states.

In this respect, a specific care must be taken to guarantee that the states predicted by the cubic equation of state remains in its domain of convexity. Thanks to this formulation, the developments proposed in the current work, based on the 3-equation and 4-equation models, provide a method that can cover the range of both subcritical and supercritical regimes. In a multicomponent context, the choice of this formulation requires to handle complex multicomponent real gas thermodynamic equilibrium computations [Michelsen and Mollerup, 2004].

It is worth noting that very recently, the community of Diesel injection modeling has also shown a growing interest for the simulation of subcritical to supercritical flows. Gathered around the challenge of reproducing experimental results provided by the ECN[5], the works of [Matheis and Hickel, 2018], [Ma et al., 2019] and [Yi et al., 2019] have also investigated the use of a single cubic equation of state for liquid, vapour and supercritical states.

Numerical methods

The numerical methods used with multifluid methods generally consist in finite-volume methods associated with approximate Riemann solvers [Saurel and Abgrall, 1999, Allaire et al., 2002, Murrone and Guillard, 2005]. In this context, second-order of accuracy is generally achieved by means of slope reconstruction techniques using the neighbour values (MUSCL schemes [Toro, 2013]). As liquid-gas interface problems are likely to involve stiff gradients that cause the reconstruction methods to generate spurious oscillations in the solution, the slope reconstruction process is classically associated with a slope limitation technique, allowing to guarantee positivity preservation.

[4] Agence Nationale de la Recherche
[5] Engine Combustion Network [Pickett et al., 2010]

An originality of the present thesis consists in using finite element methods, more precisely Taylor-Galerkin methods [Donea and Huerta, 2003, Colin and Rudgyard, 2000] in order to compute the numerical transport of the multifluid equations. This required to provide specific derivations on the models in order to integrate them in a Taylor-Galerkin framework. Such methods are very efficient low-dissipation methods that are particularly adapted to the large-eddy simulation of reactive flows. They are used by AVBP, a HPC[6] unstructured multicomponent LES solver, co-developed by CERFACS and IFPEN, in which the present developments have been implemented.

In addition to the integration of a multifluid method into a finite-element framework, the question of positivity preservation has been investigated. In particular, a study of finite-element methods with flux-corrected transport was conducted, based on the works of [Boris and Book, 1973, Löhner et al., 1988, Kuzmin et al., 2004, Kuzmin et al., 2012]. This study led to the proposition of a positivity preserving method based on two-step Tayor-Galerkin schemes.

Objectives of the thesis

The objective of the present Ph.D thesis is to set up a solver able to cover the range of subcritical to supercritical regimes. To achieve this, an extension to subcritical two-phase flows of the pre-existing supercritical flow solver of AVBP is provided. Subsequently, the solver is applied to multidimensional test cases to demonstrate the feasibility of such computations.

Outline of the manuscript

The present manuscript is structured as follows.

Chapter 2 introduces the non-ideal thermodynamics involved in the targeted flows. In particular, high-pressure effects are presented and the family of cubic equations of states are introduced. In addition, the theoretical description and practical computation of two-phase equilibrium, in the subcritical context, are provided. More specifically, the two-phase equilibrium is described in a single-component and a multicomponent context, and a computationally efficient approximate formulation of the two-phase equilibrium multicomponent is proposed.

Chapter 3 then details the different methods that may be used to model liquid-gas interfaces. This literature review is split into two classically admitted families: *sharp interface models* and *diffuse interface models*. Among the first family, the *volume-of-fluid* (VoF), the *level-set* and the *front-tracking* methods are presented. Then, diffuse interface methods are described, first considering the *phase-field* methods and eventually the *multifluid* methods. This chapter allows to evidence the relevance of multifluid methods according to the targeted applications.

Chapter 4 is dedicated to numerical methods. It recalls the general properties of hyperbolic conservation laws, presenting different approximate Riemann solvers that are important to handle the existing works on multifluid methods. Then, different types of numerical methods, which have been implemented and studied during this Ph.D thesis, are presented. In particular, cell-centered methods such as the Godunov-like methods and the Runge-Kutta discontinuous Galerkin methods are introduced. Then, vertex-centered methods are presented, including the Runge-Kutta-Galerkin method and Taylor-Galerkin methods. In this latter section, original developments on the finite-element methods with flux-corrected transport are presented.

Chapter 5 then summarizes the required developments for the implementation of the multifluid 3-equation and 4-equation models in AVBP. In particular, the Jacobian matrices of the flux function required by the Taylor-Galerkin methods are derived, and characteristic boundary conditions are formulated. These developments are provided for both the approximate multicomponent equilibrium

[6] high-performance computing

formulation and the exact multicomponent equilibrium. Academic numerical test cases are then provided in order to validate the implementation of the method.

Chapter 6 is dedicated to multidimensional numerical simulations. The Mascotte configuration of ONERA is studied, for which a 10 bar (subcritical) operating point is considered. First, two-dimensional computations are provided: a first one using the 3-equation model with the approximate equilibrium, a second one with the 4-equation model with the approximate equilibrium, and a third one with the 4-equation model and the exact equilibrium, in order to compare the different strategies. Then, a three-dimensional reactive case, using the 3-equation model with the simplified equilibrium, is computed and compared to experimental data. A last section is dedicated to simulations of the ECN Spray A configuration, on which the 3-equation model with simplified equilibrium is applied.

Chapter 7 focuses on the spurious pressure oscillations caused by the multifluid models which were observed in the previous chapter. In particular, elementary test cases are run considering 5-equation, 4-equation and 3-equation models in order to analyse their respective behaviour in terms of spurious pressure oscillations, as such discussion is quite original and can be extremely useful.

Chapter 8 finally investigates an hypothesis on the cause of the spurious pressure noise encountered with the 3-equation model. As the discontinuity of the speed of sound at the limit between the single-phase regime and the two-phase regime in the 3-equation model could indeed be responsible for this noise, an more regular thermodynamic closure is proposed. The set of thermodynamic properties for the regularized equation of state is derived. The continuity of the speed of sound is shown to be restored, and simple computations are provided in order to check whether this strategy reduced the spurious noise generation.

Chapter 2

Non-ideal thermodynamics and two-phase equilibrium

This chapter is dedicated to the thermodynamic developments required for the description of non-ideal two-phase flows. In particular, the family of cubic equations of state and their properties are recalled. The computation of two-phase equilibrium with such equations of state is then presented both for single-component and multi-component mixtures.

2.1 The fundamental laws of thermodynamics

The development of thermodynamics is motivated by the need for macroscopic models able to deal with systems of high complexity. Such complexity arises from the study of matter at a macroscopic scale, which cannot be viably described by studying thoroughly the dynamics of its elementary components (e.g. the molecules). Thermodynamics allow for the global description of the state of matter and its transformations through the application of two fundamental laws. In this section, these laws are briefly recalled, and the relevant thermodynamic quantities and notations are introduced.

2.1.1 The first law of thermodynamics

Let Ω be a thermodynamic system of volume $\mathcal{V}$. We denote by Ω^c the *surroundings* of Ω. The system can be characterized by the way it interacts with its surroundings, as depicted in Figure 2.1

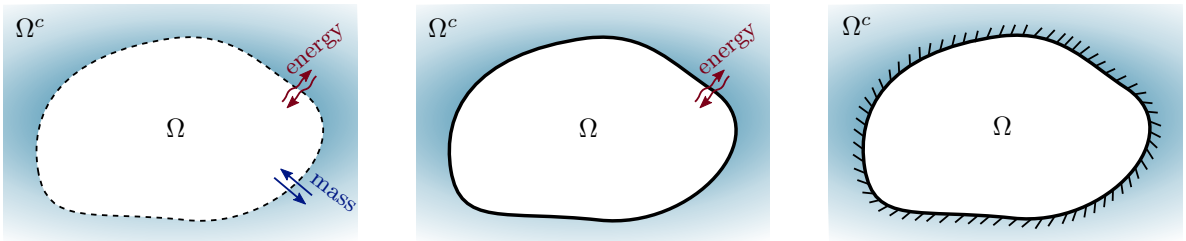

(a) Open thermodynamic system (b) Closed thermodynamic system (c) Isolated thermodynamic system

Figure 2.1: Different interactions between a thermodynamic system and its surroundings

The considered thermodynamic system is filled by a fluid, made of molecules that interact together. The amount of matter contained in Ω is denoted by $n = \sum_{i=1}^{N_s} n_i$, in moles, with total mass $m = \sum_{i=1}^{N_s} m_i$, where N_s is the number of chemical species in the mixture.

The thermodynamical energy content of the fluid is described by its *internal energy* (also called *sensible energy*), denoted $\mathcal{E}_s$, consisting in the sum of the kinetic energy of thermal motion – which excludes the advective kinetic energy – and the potential energy of interaction between the molecules [Hirschfelder et al., 1954]. The internal energy is a *state function*, meaning that it only depends on the current state of the system and not on the way this state has been obtained. The total energy of the system is then defined as the sum of its internal energy, its advective kinetic energy, and the external potential energy due to volume forces such as gravity:

$$\mathcal{E}_{\text{tot}} = \mathcal{E}_s + \mathcal{E}_c + \mathcal{E}_p. \tag{2.1.1}$$

The *first law of thermodynamics* can be expressed as follows:

The total energy of an isolated system is constant.

Equivalently, for a closed system Ω, it can be written as the following identity:

$$\mathrm{d}\mathcal{E}_{\text{tot}} = \delta Q + \delta W, \tag{2.1.2}$$

stating that the variations of the energy of a closed system are exactly equal to the amount of heat δQ and work δW exchanged with its surroundings. In other words, the total energy is a conservative quantity.

2.1.2 The second law of thermodynamics

The first law presented above is a pillar of the theory of physics, but it is insufficient to completely describe the evolution of thermodynamic systems. Indeed, some physical processes – such as the homogenization of temperature when pouring together cold and hot water – are observed to occur spontaneously in one way, but cannot spontaneously go back to their initial state, even though such transformation would not violate the first law. The asymmetry characterizing such phenomena is not addressed by the first law and requires the formulation of a second law.

The second law, as formulated by Lord Kelvin in 1851, is:

> "*It is impossible, by means of inanimate material agency, to derive mechanical effect from any portion of matter by cooling it below the temperature of the coldest of the surrounding objects.*"

An equivalent expression was published by Rudolf Clausius in 1854, as:

> "*Heat can never pass from a colder to a warmer body without some other change, connected therewith, occurring at the same time.*"

The second law can be put into a mathematical form, by postulating the existence of an extensive quantity called *entropy*, denoted $\mathcal{S}$, such that for any infinitesimal transformation of a closed system Ω, one has

$$\mathrm{d}\mathcal{S} = \frac{\delta Q}{T} + \delta\mathcal{S}_{\text{irr}} \tag{2.1.3}$$

with

$$\delta\mathcal{S}_{\text{irr}} \geq 0, \tag{2.1.4}$$

where $\mathcal{S}_{\text{irr}}$ denotes the internal and external irreversibilities caused by the transformation. Similarly to the internal energy, the entropy $\mathcal{S}$ is also a state funcion.

Entropy is interpreted in the field of theory of information and in statistical physics as a measure of disorder within the system. It can be expressed [Hirschfelder et al., 1954] as a function of the number of possible microscopic states $\#\Omega$ that correspond to the macroscopic state of the system. In the case of equiprobable microstates, it verifies $\mathcal{S} = k_B \ln(\#\Omega)$, with k_B the Boltzmann constant.

2.1.3 Important thermodynamic relations

2.1.3.1 Variance of a thermodynamic system and Euler's theorem

The *variance* ($\mathrm{Var}(\Omega)$) of a thermodynamic system Ω denotes the number of independent variables necessary to define the state of the system, i.e. the number of independent variables required to evaluate its extensive state functions, such as sensible energy or entropy. For instance, it is observed that knowing the temperature, pressure and mass of a monocomponent gas is sufficient to completely determine its thermodynamic state (in extensive variables), hence a variance $\mathrm{Var} = 3$. For a gas or a liquid consisting of N_s species, the variance increases to $\mathrm{Var} = 2 + N_s$. For example, the sensible energy of a system Ω can be expressed as a function of its entropy, volume and mass composition, so that

$$\mathcal{E}_s = f\left(\mathcal{S}, \mathcal{V}, m_1, ..., m_{N_s}\right). \tag{2.1.5}$$

Its differential thus reads

$$\mathrm{d}\mathcal{E}_s = \left.\frac{\partial \mathcal{E}_s}{\partial \mathcal{S}}\right|_{\mathcal{V}, m_j} \mathrm{d}\mathcal{S} + \left.\frac{\partial \mathcal{E}_s}{\partial \mathcal{V}}\right|_{\mathcal{S}, m_j} \mathrm{d}\mathcal{V} + \sum_{i=1}^{N_s} \left.\frac{\partial \mathcal{E}_s}{\partial m_i}\right|_{\mathcal{S}, \mathcal{V}, m_{j\neq i}} \mathrm{d}m_i. \tag{2.1.6}$$

The partial derivative of $\mathcal{E}_s$ with respect to $\mathcal{S}$ (respectively $\mathcal{V}$ and m_i) defines the *temperature* T of the system (resp. the *pressure* P and mass-specific *partial Gibbs energy* g_i) [Poling et al., 2001]. Equation (2.1.6) then writes

$$\mathrm{d}\mathcal{E}_s = T\,\mathrm{d}\mathcal{S} - P\,\mathrm{d}\mathcal{V} + \sum_{i=1}^{N_s} g_i\,\mathrm{d}m_i, \tag{2.1.7}$$

which is called the Gibbs relation. The temperature, pressure and mass-specific partial Gibbs energy are intensive properties of the system, i.e. independent of the volume $\mathcal{V}$.

From this point, it is interesting to remark that, using the extensive nature of the system sensible energy $\mathcal{E}_s$, its entropy $\mathcal{S}$ and its components masses $(m_i)_{i=1..N_s}$, the system $\lambda\Omega$ obtained by scaling system Ω by a factor $\lambda > 0$ results in equally scaling its energy $\lambda\mathcal{E}_s$, entropy $\lambda\mathcal{S}$, volume $\lambda\mathcal{V}$ and i^{th} species mass λm_i. In other words, for any factor $\lambda > 0$, one has

$$\lambda\mathcal{E}_s = f\left(\lambda\mathcal{S}, \lambda\mathcal{V}, \lambda m_1, ..., \lambda m_{N_s}\right). \tag{2.1.8}$$

Mathematically, the extensive sensible energy $\mathcal{E}_s$ is said to be a *1-homogeneous* function in the extensive variables. Indeed, a function is said to be k-homogeneous in its variables when it verifies, for a scalar λ, the relation $f\left(\lambda x_1, ..., \lambda x_n\right) = \lambda^k f\left(x_1, ..., x_n\right)$. Differentiating equation (2.1.8) with respect to the scaling factor λ then yields

$$\frac{\partial\left(\lambda\mathcal{E}_s\right)}{\partial\lambda} = T\frac{\partial\left(\lambda\mathcal{S}\right)}{\partial\lambda} - P\frac{\partial\left(\lambda\mathcal{V}\right)}{\partial\lambda} + \sum_{i=1}^{N_s} g_i \frac{\partial\left(\lambda m_i\right)}{\partial\lambda}, \tag{2.1.9}$$

which finally gives the so-called Euler's theorem:

$$\mathcal{E}_s = T\mathcal{S} - P\mathcal{V} + \sum_{i=1}^{N_s} g_i m_i. \tag{2.1.10}$$

Differentiating Euler's theorem (2.1.10) and subtracting Gibbs relation (2.1.7) provides the Gibbs-Duhem relation:

$$\sum_{i=1}^{N_s} m_i\,\mathrm{d}g_i = -\mathcal{S}\,\mathrm{d}T + \mathcal{V}\,\mathrm{d}P. \tag{2.1.11}$$

2.1.3.2 Thermodynamic potentials and Maxwell relations

2.1.3.2.1 Additional state functions

From the definition of the sensible energy, it is possible to introduce other quantities to equivalently represent the energetic contents of the system. We then note the sensible enthalpy of the system $\mathcal{H}_s$, defined as

$$\mathcal{H}_s = \mathcal{E}_s + P\mathcal{V}, \tag{2.1.12}$$

the Helmholtz energy (or free energy)

$$\mathcal{F}_s = \mathcal{E}_s - T\mathcal{S}, \tag{2.1.13}$$

and the Gibbs energy (or free enthalpy)

$$\mathcal{G} = \mathcal{E}_s + P\mathcal{V} - T\mathcal{S}. \tag{2.1.14}$$

These *thermodynamic potentials* are convenient quantities to represent the system regarding available data. Indeed, their differentials read

$$\begin{cases} \mathrm{d}\mathcal{H}_s = T\,\mathrm{d}\mathcal{S} + \mathcal{V}\,\mathrm{d}P + \displaystyle\sum_{i=1}^{N_s} g_i\,\mathrm{d}m_i, & \text{(2.1.15a)} \\ \mathrm{d}\mathcal{F}_s = -\mathcal{S}\,\mathrm{d}T - P\,\mathrm{d}\mathcal{V} + \displaystyle\sum_{i=1}^{N_s} g_i\,\mathrm{d}m_i, & \text{(2.1.15b)} \\ \mathrm{d}\mathcal{G} = -\mathcal{S}\,\mathrm{d}T + \mathcal{V}\,\mathrm{d}P + \displaystyle\sum_{i=1}^{N_s} g_i\,\mathrm{d}m_i, & \text{(2.1.15c)} \end{cases}$$

For example, enthalpy is a handy quantity to describe a system that undergoes isentropic or isobaric transformations, whereas Gibbs energy is interesting when isothermal or isobaric transformations are involved.

2.1.3.2.2 Maxwell relations

It appears from equations (2.1.7) and (2.1.15) that thermodynamic state variables can be characterized by different ways. For instance, for the pressure P, one has

$$P = -\left.\frac{\partial \mathcal{E}_s}{\partial \mathcal{V}}\right|_{\mathcal{S},m_j} = -\left.\frac{\partial \mathcal{F}_s}{\partial \mathcal{V}}\right|_{T,m_j}. \tag{2.1.16}$$

Interesting relations can also be obtained by means of Schwarz's (or Young's) theorem, when applied to the second-order derivatives of the thermodynamic potentials. For example, the sensible energy reads:

$$\left.\frac{\partial\left(\left.\frac{\partial \mathcal{E}_s}{\partial \mathcal{V}}\right|_{\mathcal{S},m_j}\right)}{\partial \mathcal{S}}\right|_{\mathcal{V},m_j} = \left.\frac{\partial\left(\left.\frac{\partial \mathcal{E}_s}{\partial \mathcal{S}}\right|_{\mathcal{V},m_j}\right)}{\partial \mathcal{V}}\right|_{\mathcal{S},m_j}, \tag{2.1.17}$$

so that

$$-\left.\frac{\partial P}{\partial \mathcal{S}}\right|_{\mathcal{V},m_j} = \left.\frac{\partial T}{\partial \mathcal{V}}\right|_{\mathcal{S},m_j}. \tag{2.1.18}$$

A whole set of relations between thermodynamic state variables differentials can then be derived this way. These relations are called *Maxwell relations*, and can be summarized as:

$$\begin{cases} -\left.\dfrac{\partial P}{\partial \mathcal{S}}\right|_{\mathcal{V},m_j} = \left.\dfrac{\partial T}{\partial \mathcal{V}}\right|_{\mathcal{S},m_j}, & \text{(2.1.19a)} \\ \left.\dfrac{\partial T}{\partial P}\right|_{\mathcal{S},m_j} = \left.\dfrac{\partial \mathcal{V}}{\partial \mathcal{S}}\right|_{P,m_j}, & \text{(2.1.19b)} \\ \left.\dfrac{\partial \mathcal{S}}{\partial \mathcal{V}}\right|_{T,m_j} = \left.\dfrac{\partial P}{\partial T}\right|_{\mathcal{V},m_j}, & \text{(2.1.19c)} \\ \left.\dfrac{\partial \mathcal{V}}{\partial T}\right|_{P,m_j} = -\left.\dfrac{\partial \mathcal{S}}{\partial P}\right|_{T,m_j}. & \text{(2.1.19d)} \end{cases}$$

Such relations will be useful for the thermodynamic derivations of the present work.

2.1.3.3 Intensive definitions of the state functions

It is possible to introduce intensive forms of the state functions, by defining their mass-specific counterparts (in $\mathrm{J \cdot kg^{-1}}$). They are noted as follows:

$$e_s = \frac{\mathcal{E}_s}{m} \quad ; \quad h_s = \frac{\mathcal{H}_s}{m} \quad ; \quad f_s = \frac{\mathcal{F}_s}{m} \quad ; \quad g = \frac{\mathcal{G}}{m}. \tag{2.1.20a}$$

The mass-specific entropy (in $\mathrm{J \cdot kg^{-1} \cdot K^{-1}}$) and the mass-specific volume (in $\mathrm{m^3 \cdot kg^{-1}}$) write

$$s = \frac{\mathcal{S}}{m} \quad ; \quad v = \frac{\mathcal{V}}{m}. \tag{2.1.20b}$$

Similarly, the notation for molar state functions (in $\mathrm{J \cdot mol^{-1}}$) is the following

$$E_s = \frac{\mathcal{E}_s}{n} \quad ; \quad H_s = \frac{\mathcal{H}_s}{n} \quad ; \quad F_s = \frac{\mathcal{F}_s}{n} \quad ; \quad G = \frac{\mathcal{G}}{n}, \tag{2.1.21a}$$

(the Gibbs energy is written G because of its identity with the *chemical potential* which is usually noted this way) and for the molar entropy (in $\mathrm{J \cdot mol^{-1} \cdot K^{-1}}$) and molar volume (in $\mathrm{m^3 \cdot mol^{-1}}$),

$$S = \frac{\mathcal{S}}{n} \quad ; \quad V = \frac{\mathcal{V}}{n}. \tag{2.1.21b}$$

Finally, the notation for volume-specific thermodynamic potentials (in $\mathrm{J \cdot m^{-3}}$) is

$$\hat{e}_s = \frac{\mathcal{E}_s}{\mathcal{V}} \quad ; \quad \hat{h}_s = \frac{\mathcal{H}_s}{\mathcal{V}} \quad ; \quad \hat{f}_s = \frac{\mathcal{F}_s}{\mathcal{V}} \quad ; \quad \hat{g} = \frac{\mathcal{G}}{\mathcal{V}}, \tag{2.1.22a}$$

and for the volume-specific entropy (in $\mathrm{J \cdot m^{-3} \cdot K^{-1}}$) and the density (in $\mathrm{kg \cdot m^{-3}}$),

$$\hat{s} = \frac{\mathcal{S}}{\mathcal{V}} \quad ; \quad \rho = \frac{m}{\mathcal{V}} = \frac{1}{v}. \tag{2.1.22b}$$

It is possible to reformulate Maxwell relations using the intensive (e.g. mass-specific) form of the

variables:

$$\begin{cases} \left.\dfrac{\partial P}{\partial s}\right|_{\rho,m_j} = \rho^2 \left.\dfrac{\partial T}{\partial \rho}\right|_{s,m_j}, & (2.1.23a) \\ \left.\dfrac{\partial \rho}{\partial s}\right|_{P,m_j} = -\rho^2 \left.\dfrac{\partial T}{\partial P}\right|_{s,m_j}, & (2.1.23b) \\ \left.\dfrac{\partial P}{\partial T}\right|_{\rho,m_j} = -\rho^2 \left.\dfrac{\partial s}{\partial \rho}\right|_{T,m_j}, & (2.1.23c) \\ \left.\dfrac{\partial \rho}{\partial T}\right|_{P,m_j} = \rho^2 \left.\dfrac{\partial s}{\partial P}\right|_{T,m_j}. & (2.1.23d) \end{cases}$$

The composition of the mixture can be described by the vector of intensive variables $\underline{\boldsymbol{Y}}$, defined as

$$Y_i = \frac{m_i}{m}. \tag{2.1.24}$$

Y_i is the *mass fraction* of species i, and one has $\sum_{i=1}^{N_s} Y_i = 1$.

Similarly, the differentials of the mass-specific thermodynamic potentials can be expressed as

$$\begin{cases} \mathrm{d}e_s = T\,\mathrm{d}s - P\,\mathrm{d}v + \sum_{i=1}^{N_s} g_i\,\mathrm{d}Y_i, \qquad (\textit{Gibbs relation}) & (2.1.25a) \\ \mathrm{d}h_s = T\,\mathrm{d}s + v\,\mathrm{d}P + \sum_{i=1}^{N_s} g_i\,\mathrm{d}Y_i, & (2.1.25b) \\ \mathrm{d}f_s = -s\,\mathrm{d}T - P\,\mathrm{d}v + \sum_{i=1}^{N_s} g_i\,\mathrm{d}Y_i, & (2.1.25c) \\ \mathrm{d}g = -s\,\mathrm{d}T + v\,\mathrm{d}P + \sum_{i=1}^{N_s} g_i\,\mathrm{d}Y_i. & (2.1.25d) \end{cases}$$

where equation (2.1.25a) is the mass-specific form of Gibbs relation (2.1.7).

It is worth mentioning that an extensive quantity is a 1-homogeneous function in its extensive parameters, and a 0-homogeneous function in its intensive parameters.

2.1.4 Closing the system

Now that the thermodynamic quantities and notations have been set, one can observe that the description of the system is incomplete. As said before, the definition of a thermodynamic system (with *extensive* variables) has a variance of $(N_s + 2)$. In other words, once that $(N_s + 2)$ variables have been set, the complete system state should be defined. Yet, describing the system with a thermodynamic potential (for instance the sensible energy $\mathcal{E}_s$ defined in equation (2.1.10)) provides *one* relation between $2(N_s + 2)$ variables, namely

$$[P, T, \mathcal{S}, \mathcal{V}, m_1, \cdots, m_{N_s}, g_1, \cdots, g_{N_s}].$$

Thus, there is so far only 1 equation for a system of $2(N_s + 2)$ unknowns with $(N_s + 2)$ degrees of freedom, which means that $(N_s + 1)$ relations are missing to close the system.

The N_s first closure relations are usually provided by defining the reference mass-specific *isochoric heat capacity* $c^0_{v,i}$ of the different species ($i = 1...N_s$):

$$c^0_{v,i} = \left.\frac{\partial e_s}{\partial T}\right|_{\rho} (T^0, P^0, Y_i = 1), \tag{2.1.26}$$

where $c^0_{v,i}$ represents the variation of sensible energy with respect to the temperature for an isochoric transformation, at the reference temperature and pressure (T^0, P^0) and for a pure component i. It is obtained by empirical relations based on experimental measurements.

The missing closure relation is provided by defining an *equation of state* of the system, which can usually be expressed as a relation between the pressure, the temperature, the density and the mixture composition $\underline{\boldsymbol{Y}} = \{Y_i\}_{i=1..N_s}$. The derivation and properties of equations of state of interest for this work are the object of the next section.

2.2 Modeling non-ideal thermodynamics

The physical description of a fluid can be addressed at different scales. The usual approach in classical thermodynamics is to gather the complexity of the microscopic phenomena that rule the system into an algebraic relation between macroscopic variables, called the *Equation of State* (EoS) of the system. In this section, the construction of theoretically important EoS are presented and related to the relevant physical phenomena they describe.

2.2.1 Towards real-gas equations of state

2.2.1.1 Ideal gases

Following the need for simple macroscopic models motivated by the intensive use of steam machines during the industrial revolution, the ideal gas model has been established in the early 19^{th} century from empirical observations, by combining Gay-Lussac's, Charles' and Avogadro's laws together. It has been stated that, for an ideal gas, its pressure P, volume $\mathcal{V}$, temperature T and amount of substance n are linked by the relation:

$$P\mathcal{V} = n\mathcal{R}T, \tag{2.2.1}$$

where $\mathcal{R} = 8.3144598\ \mathrm{J \cdot mol^{-1} \cdot K^{-1}}$ is the universal gas constant. This law can be equivalently written under the volume-specific form:

$$P(\rho, T, \underline{\boldsymbol{Y}}) = \rho \bar{r} T, \tag{2.2.2}$$

where $\bar{r} = \mathcal{R}\bar{\mathrm{W}}^{-1}$ with $\bar{\mathrm{W}}(\underline{\boldsymbol{Y}}) = \left(\sum_{i=1}^{N_s} Y_i \mathrm{W}_i^{-1}\right)^{-1}$ the molar mass of the gas mixture and W_i the molar mass of the i^{th} component. A property of the ideal gas law is that, by defining for each chemical species the *partial pressure* $P_i = Y_i \rho r_i T$ with $r_i = \mathcal{R}\mathrm{W}_i^{-1}$, one has $P_i = X_i P$ with $X_i = \frac{n_i}{n}$ the i^{th} component's mole fraction. As the mole fractions sum to unity, this yields the so-called Dalton's law, which states that

$$P = \sum_{i=1}^{N_s} P_i\left(Y_i, \rho, T\right) \tag{2.2.3}$$

for an ideal mixture. The partial pressure depends only on the mixture density and temperature, and the considered species properties. In this respect, the partial pressure of the component i is independent of the nature of the other components, which is an noteworthy feature of ideal mixtures.

It has been observed that gases at relatively low pressures satisfyingly follow this EoS. Later on, the development of the *Kinetic Theory of Gases* provided a demonstration to this law, by modeling the gas molecules as *hard spheres* only interacting together through collisions. The hard-sphere model can be expressed as an infinitely stiff interaction potential between molecules V^{HS}:

$$V^{\mathrm{HS}} = \begin{cases} 0 & \text{if } r > r_{\min} \\ +\infty & \text{if } r \leq r_{\min} \end{cases} \tag{2.2.4}$$

Unfortunately, the errors made by this very simple model become unacceptable when the molecular interactions are no longer dominated by mere collisions. In particular, this is the case when the density increases, which corresponds to a high pressure and a low temperature. The deviation from the ideal gas behaviour can be characterized by introducing the *compressibility factor* $\mathcal{Z}$, which is illustrated in Figure 2.2.

$$\mathcal{Z} = \frac{PV}{\mathcal{R}T} = \frac{P}{\rho \bar{r} T}, \tag{2.2.5}$$

with V the molar volume defined in (2.1.21b). $\mathcal{Z}$ is observed to vary relatively strongly with the

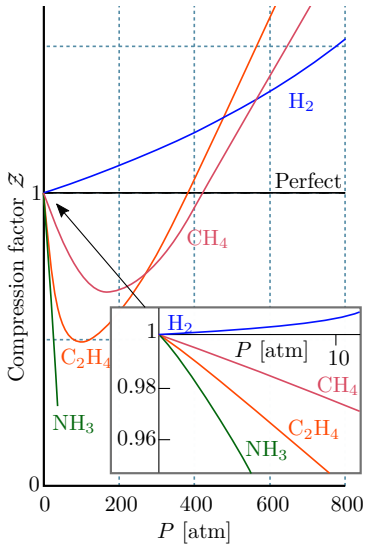

Figure 2.2: Illustration of the deviation of the compressibility factor from unity (corresponding to the ideal gas law) when varying the pressure, along 0 °C isothermal lines for different chemical species. Data for this picture is taken from [Atkins et al., 2018].

pressure. Although the compressibility factor of the different species tends to unity at low pressures, the behaviour of $\mathcal{Z}$ in the neighbourhood of $P = 0$ involves different slopes.

2.2.1.2 Non-ideal molecular interactions

In this respect, more complex molecular interactions have to be considered. Although the exhaustive description of molecules mechanics would require to address quantum effects, approximate models have been proposed to capture the overall trends. They take advantage of the statistical convergence of the quantum systems towards classical mechanics.

A rather simple representation consists in expressing the non-ideal molecular interactions as a potential well [Hirschfelder et al., 1954, Atkins et al., 2018], so that molecules repel each other at close distances

but attract each other further away. For example, such form includes Morse's potential V^{M}, or Lennard-Jones' (LJ) potential V^{LJ}. They can be formulated as:

$$V^{\mathrm{M}}(r) = V^0 \left[\exp\left(-2\ln(2)\,\frac{r - r_0}{r_0 - \sigma} \right) - 2\exp\left(-\ln(2)\,\frac{r - r_0}{r_0 - \sigma} \right) \right], \tag{2.2.6a}$$

$$V^{\mathrm{LJ}}(r) = 4V^0 \left[\left(\frac{\sigma}{r} \right)^{12} - \left(\frac{\sigma}{r} \right)^{6} \right], \tag{2.2.6b}$$

where r is the intermolecular distance. r_0, σ and V^0 are the model parameters, respectively the Morse minimal-potential distance, the zero-potential distance, and the depth of the potential well (cf. figure 2.3). It is readily seen that when the intermolecular distance is such that $r > r_0$, an attractive interaction will occur. Conversely, for $r < r_0$, the interaction will become repulsive.

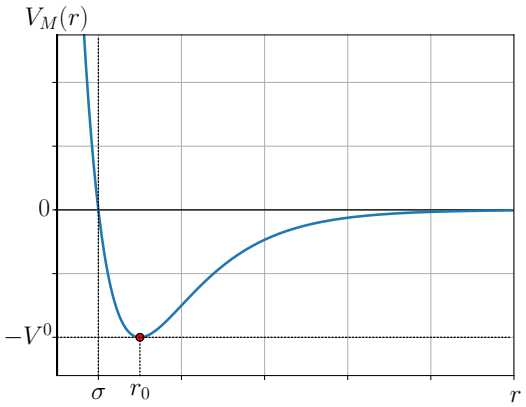

Figure 2.3: Typical shape of an attractive-repulsive molecular interaction potential. Here, the Morse potential is depicted.

At low temperatures, and high densities, the molecules are close enough and the kinetic energy of thermal motion becomes small enough for them to be trapped in the potential well. The molecules are bound together by their attractive interaction, which characterizes a liquid state.

It is important to note that the interaction parameters depend on the considered chemical species. For instance, when two molecules of different chemical nature interact, the Lennard-Jones potential becomes

$$V_{ij}^{\mathrm{LJ}}(r) = 4V_{ij}^0 \left[\left(\frac{\sigma_{ij}}{r} \right)^{12} - \left(\frac{\sigma_{ij}}{r} \right)^{6} \right] \tag{2.2.7}$$

with $V_{ij}^0 = \sqrt{V_i^0 V_j^0}$ and $\sigma_{ij} = \frac{\sigma_i + \sigma_j}{2}$. Thus, it is not possible to treat the thermodynamics of the different species independently, as for ideal gases, for example through Dalton's law, since crossed terms appear in the molecular interactions.

Pushing forward the Kinetic Theory of Gases allows to formulate an EoS that uses more detailed descriptions of the molecular interactions, considering in particular multiple molecules interaction at once. This leads to the formulation of the Virial EoS [Poling et al., 2001], which writes as a polynomial series of the inverse of the volume:

$$P = \frac{\mathcal{R}T}{\mathcal{V}} + \mathcal{R}T \sum_{k=2}^{K} \frac{B_k(T)}{\mathcal{V}^k}. \tag{2.2.8}$$

Equation (2.2.8) expresses the Virial EoS truncated at order K, in which the term of k^{th} degree expresses the non-ideal interactions between k different molecules. The coefficients $B_k(T)$ can be expressed as functions of the chosen interaction potential. Thus, they depend on the temperature and the species composition of the mixture.

Unfortunately, the coefficients of the Virial EoS are generally difficult to evaluate. The EoS is then often truncated at low-degree terms (typically 2 or 3). This limits its use to the prediction of only small deviations from the ideal gas behaviour. Nonetheless, this EoS is of major theoretical interest as it provides a description of the fluid that can be fed with conceptually any interaction potential form, and expanded to an arbitrary order.

In addition to their ability to explain the behaviour of high-pressure gases, the non-ideal molecular interactions are observed to be responsible for strong changes in the topology of matter, as they underly the existence of *liquid phases*.

2.2.1.3 Fluid phases, the liquid-vapour interface and the critical point

The state of matter of a pure component varies with the nature of the predominant molecular interactions occurring within it. Figure 2.4 displays the typical phase diagram of a pure (single-component) system. The lines correspond to thermodynamic points where two phases can coexist. The areas delimited by these lines correspond to pure-phase areas.

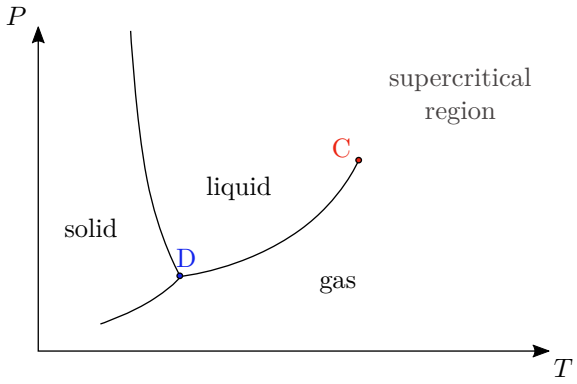

Figure 2.4: Typical phase diagram for a pure system. Point C denotes the critical point. Point D denotes the triple point, where the three phases can coexist.

In the liquid phase, the density is high enough and the kinetic energy of thermal motion small enough for the molecules to remain bound together (trapped in the potential well shown in Figure 2.3). In the gas phase, the density being lower, the short-range attractive forces are weaker and the molecules mostly interact through the repulsive forces. The simultaneous coexistence of both liquid and vapour phases introduces an anisotropy along the transition region between the two phases: the *interface*. This anisotropy results in a force called *surface tension*, which tends to minimize the surface of interaction, causing for example the break-up of liquid droplets into smaller inclusions when the interface is too deformed by the hydrodynamic constraints.

When the temperature increases, the molecules in the liquid phase acquire more and more kinetic energy of thermal motion up to a point where the potential well of attractive interaction is no longer sufficient to maintain them bound together. As the attractive forces get weaker and weaker, the anisotropy between the liquid and the gas at the interface decreases. Thus, the surface tension drops, and the thickness of the interface becomes increasingly diffuse. At the critical point (see figure 2.4), the surface tension and the liquid-gas interface have vanished and a smooth transition between variable densities is observed, similarly to what is shown in Figure 2.5.

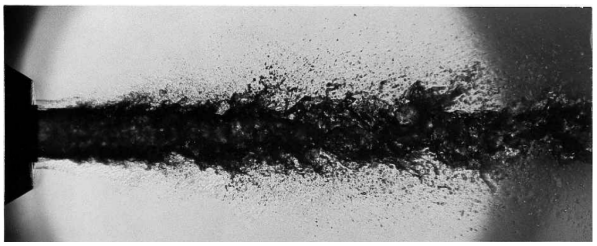

(a) Subcritical jet

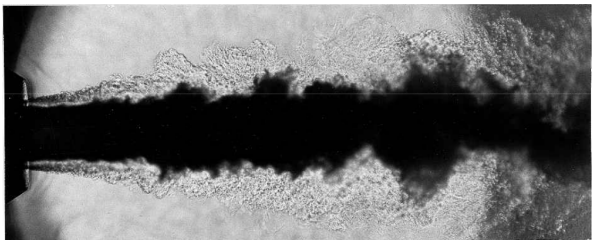

(b) Supercritical jet

Figure 2.5: Shadowgraph images of LN_2/He injection at sub- and supercritical conditions (Taken from [Mayer et al., 1998]). 2.5a displays a typical subcritical behaviour with sharp liquid-gas interface, ligaments and droplets formation. 2.5b illustrates the fading of surface tension, which results in a diffused liquid-vapour interface: the flow becomes a mere turbulent mixing of variable-density fluid.

For a single-component system, the critical point is characterized by (T_c, P_c, ρ_c), respectively the *critical temperature* T_c, *critical pressure* P_c and *critical density* ρ_c.

2.2.1.4 The corresponding states principle

The study of fluids relatively to their critical properties has been shown by van der Waals to be particularly relevant. Indeed, when plotting the compressibility factor $\mathcal{Z}$ defined in (2.2.5) with respect to the *reduced pressure* P_r, defined as

$$P_r = \frac{P}{P_c}, \tag{2.2.9}$$

at different reduced temperatures T_r, defined by

$$T_r = \frac{T}{T_c}, \tag{2.2.10}$$

and for different pure species, he has noticed that, their behaviour is strongly similar, as depicted in Figure 2.6.

This statement led van der Waals to formulate the *corresponding states principle* (CSP):

"*Real gases at a given reduced temperature and reduced pressure have the same reduced volume.*"

Naturally, this principle is a simplified model. In particular, polar or highly non-spherical molecules are known to show discrepancies with this principle. To overcome this, additional parameters, such as the *acentric factor* (see Section 2.2.1.5) can be taken into account. However, this principle is a key element for the development of the widely used cubic EoS which provide a satisfying and universal estimation of the thermodynamics of real gas mixtures with a reduced number of parameters.

2.2.1.5 The van der Waals EoS

In the late XIX^{th} century, van der Waals [van der Waals, 1873] introduced a rather simple equation of state to describe the real gas effects more accurately. Global physical considerations can be exposed

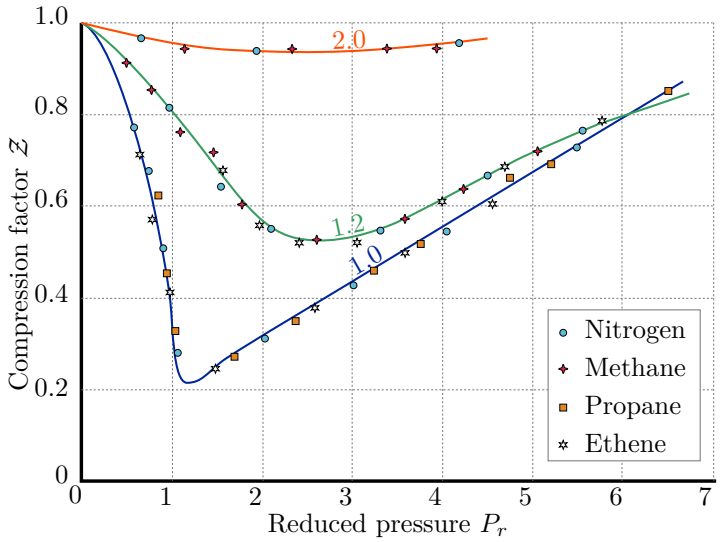

Figure 2.6: Compressibility factor $\mathcal{Z}$ with respect to the reduced pressure P_r for different values of T_r and different pure species. The data for this image is taken from [Atkins et al., 2018]

to justify the construction of this EoS. The first idea is that the volume appearing in the expression of repulsive effect in the EoS should take into account the bulk of the molecules. In this respect, the *covolume* $\bar{b}$ is added to the ideal gas law, so that the repulsive effects are now represented by $\frac{\mathcal{R}T}{V-\bar{b}^{\mathrm{m}}} = \frac{\rho\bar{r}T}{1-\bar{b}\rho}$, with $\bar{b}^{\mathrm{m}}$ being the molar counterpart of $\bar{b}$. Furthermore, attractive interactions have two joint effects on the pressure. They reduce both the strength and the frequency of the collisions on a given surface. Considering that each of these effects, taken separately, is proportional to the density (or molar concentration), the pressure is corrected by the term

$$\bar{a}\rho^2 = \frac{\bar{a}^{\mathrm{m}}}{V^2},$$

with $\bar{a}$ a proportionality coefficient and $\bar{a}^{\mathrm{m}}$ its molar counterpart. Both coefficients $\bar{a}$ and $\bar{b}$ are assumed independent of the temperature and of the density. They are properties of the chemical species involved in the mixture and then only depend on the mixture composition, described either by the species mole fractions $\underline{\boldsymbol{X}}$ (with $X_i = n_i/n$) or by the mass fractions $\underline{\boldsymbol{Y}}$.

Finally, the van der Waals EoS writes, in a molar form:

$$P(V, T, \underline{\boldsymbol{X}}) = \frac{\mathcal{R}T}{V - \bar{b}^{\mathrm{m}}V} - \frac{\bar{a}^{\mathrm{m}}}{V^2} \tag{2.2.11}$$

or also, in its mass-specific form:

$$P(\rho, T, \underline{\boldsymbol{Y}}) = \frac{\rho\bar{r}T}{1 - \bar{b}\rho} - \bar{a}\rho^2. \tag{2.2.12}$$

The global behaviour of the van der Waals EoS is depicted in Figure 2.7. One can see that, unlike for ideal gases, isothermal lines have inflexion points. Also, along an isothermal line T, up to three values of the specific-volume v (or the density ρ) can be found for the same pressure P. Mathematically, this comes from the cubic nature of the EoS, hence the name of this class of EoS. Physically, the existence of multiple positive density solutions conveys the possible simultaneous existence of liquid and gas phases. Moreover, Figure 2.7 shows that above a particular value of the temperature, the isothermal lines become monotonic: phase coexistence is no more possible. This temperature corresponds to the critical temperature T_c of the considered species.

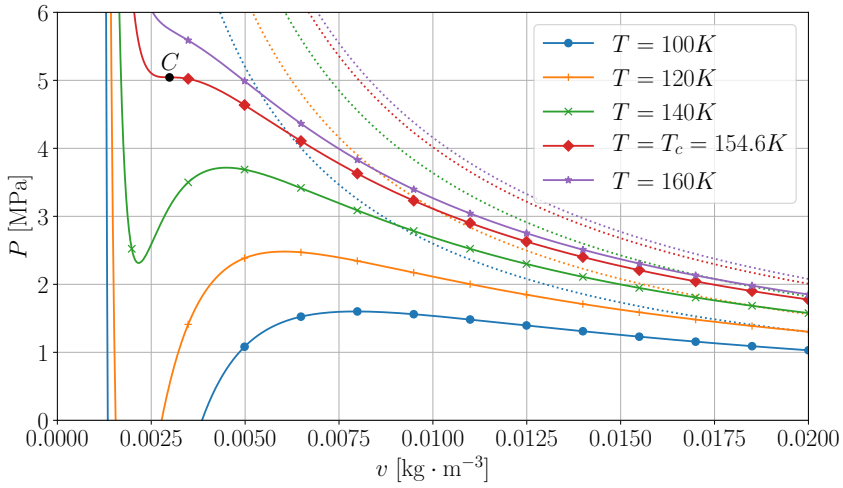

Figure 2.7: Clapeyron diagram displaying isothermal lines for the van der Waals EoS applied to pure O_2. Dashed lines indicate the corresponding isothermal lines computed with the ideal gas EoS. Point C denotes the critical point.

For a species i, the critical properties appear in the definition of the parameters a and b, which take the form:

$$a_i = \frac{27 r_i^2 T_{c,i}^2}{64 P_{c,i}}, \qquad \Longleftrightarrow \qquad a_i^{\mathrm{m}} = \frac{27 \mathcal{R}^2 T_{c,i}^2}{64 P_{c,i}} \tag{2.2.13a}$$

$$b_i = \frac{r_i T_{c,i}}{8 P_{c,i}}, \qquad \Longleftrightarrow \qquad b_i^{\mathrm{m}} = \frac{\mathcal{R} T_{c,i}}{8 P_{c,i}} \tag{2.2.13b}$$

This EoS is described by [Poling et al., 2001] as a two-parameter CSP EoS. Indeed, only two parameters, $T_{c,i}$ and $P_{c,i}$, are needed to characterize the EoS specifically for the i^{th} component.

For multicomponent mixtures, the van der Waals mixing rules [Poling et al., 2001] allow to estimate the mixture parameters $\bar{a}$ and $\bar{b}$, as

$$\bar{a}(\underline{\boldsymbol{Y}}) = \sum_{i=1}^{N_s} Y_i Y_j \left(1 - k_{ij}\right) \sqrt{a_i a_j} \qquad \Longleftrightarrow \qquad \bar{a}^{\mathrm{m}}(T) = \sum_{i=1}^{N_s} X_i X_j \left(1 - k_{ij}\right) \sqrt{a_i^{\mathrm{m}} a_j^{\mathrm{m}}} \tag{2.2.14a}$$

$$\bar{b}(\underline{\boldsymbol{Y}}) = \sum_{i=1}^{N_s} Y_i b_i, \qquad \Longleftrightarrow \qquad \bar{b}^{\mathrm{m}} = \sum_{i=1}^{N_s} X_i b_i^{\mathrm{m}} \tag{2.2.14b}$$

with $k_{ij} = k_{ji}$ being the *binary interaction coefficients*, which are specific to each pair of species.

Despite its theoretical interest and its ability to predict global tendencies of the fluid state evolution, the van der Waals EoS suffers from high discrepancies with respect to experimental data for some chemical species. Indeed, this EoS formulation assumes that molecules are spherical and non-polar. To improve the quantitative predictions of the van der Waals EoS for non-spherical molecules, a family of enhanced cubic EoS have been proposed. They are described in the next section.

2.2.2 Three-parameter CSP cubic equations of state

One century after van der Waals' pioneering work, motivated by a need for increased accuracy, a large variety of cubic equations of state have been developed [Poling et al., 2001], in particular between 1972 and 1998. Among them, two EoS are especially used for numerical simulation of real-gas flows. The

first one is an extension of the Redlich-Kwong EoS, proposed by Soave [Soave, 1972] and resulting in the so-called Soave-Redlich-Kwong (SRK) EoS. The second one was introduced a few years later by Peng and Robinson (PR) [Peng and Robinson, 1976]. This section describes these EoS in more details, as they will be used as the thermodynamic closure for the present work. All the relevant quantities needed for this work are also presented.

2.2.2.1 Equation of state formulation

The SRK and PR EoS write respectively, in a molar form:

$$P_{\text{SRK}}(\rho, T, \underline{\boldsymbol{X}}) = \frac{\mathcal{R}T}{V - \bar{b}^{\text{m}}} - \frac{\bar{a}^{\text{m}}(T)}{V^2 + \bar{b}^{\text{m}}V}, \tag{2.2.15a}$$

$$P_{\text{PR}}(\rho, T, \underline{\boldsymbol{X}}) = \frac{\mathcal{R}T}{V - \bar{b}^{\text{m}}} - \frac{\bar{a}^{\text{m}}(T)}{V^2 + 2\bar{b}^{\text{m}}V - \bar{b}^{\text{m}\,2}}, \tag{2.2.15b}$$

or, in a mass-specific form:

$$P_{\text{SRK}}(\rho, T, \underline{\boldsymbol{Y}}) = \frac{\rho\bar{r}T}{1 - \bar{b}\rho} - \frac{\bar{a}(T)\rho^2}{1 + \bar{b}\rho}, \tag{2.2.16a}$$

$$P_{\text{PR}}(\rho, T, \underline{\boldsymbol{Y}}) = \frac{\rho\bar{r}T}{1 - \bar{b}\rho} - \frac{\bar{a}(T)\rho^2}{1 + 2\bar{b}\rho - \bar{b}^2\rho^2}. \tag{2.2.16b}$$

These cubic EoS may be gathered into the following form:

$$P(\rho, T, \underline{\boldsymbol{Y}}) = \frac{\rho\bar{r}T}{1 - \bar{b}\rho} - \frac{\bar{a}(T)\rho^2}{1 + \varepsilon_1\bar{b}\rho - \varepsilon_2\bar{b}^2\rho^2} \tag{2.2.17}$$

with parameters ε_1 and ε_2 given in Table 2.1.

EoS	vdW	SRK	PR
ε_1	0	1	2
ε_2	0	0	1
ε_{12}	0	1	$2\sqrt{2}$

Table 2.1: Cubic EoS parameters for SRK and PR. ε_{12}, defined as $\varepsilon_{12} = \sqrt{\varepsilon_1^2 + 4\varepsilon_2}$, is a useful coefficient for the thermodynamic developments presented in Section 2.2.2.2.

Two major modifications are made compared to the van der Waals EoS: the attractive term is modified to include effects of the covolume, and the attractive coefficient $\bar{a}$ is now given as a function of the temperature: its formulation introduces a new parameter, the *acentric factor* ω_i [Poling et al., 2001]. This coefficient represents the deviation of the molecule from a perfectly spherical shape.

The covolume and the attractive coefficient for a species i read,

$$\begin{cases} a_i(T) = \dfrac{\Phi_{c,i}}{\mathrm{W}_i^2}\Psi_i(T)^2 & \text{or} \quad a_i^{\text{m}}(T) = \Phi_{c,i}\Psi_i(T)^2 \qquad (2.2.18a) \\ b_i = b_0\dfrac{r_i T_{c,i}}{P_{c,i}} & \text{or} \quad b_i^{\text{m}} = b_0\dfrac{\mathcal{R}T_{c,i}}{P_{c,i}} \qquad (2.2.18b) \end{cases}$$

with the following definitions:

$$\begin{cases} \Phi_{c,i} = \Phi_0 \dfrac{\mathcal{R}^2 T_{c,i}^2}{P_{c,i}}, & \text{(2.2.19a)} \\ \Psi_i(T) = 1 + \Psi_{0,i}\left(1 - \sqrt{\dfrac{T}{T_c}}\right), & \text{(2.2.19b)} \\ \Psi_{0,i} = \psi_0 + \psi_1 \omega_i + \psi_2 \omega_i^2. & \text{(2.2.19c)} \end{cases}$$

The constants $b_0, \Phi_0, \psi_0, \psi_1, \psi_2$ characterize the considered EoS. Their values are summarized in Table 2.2.

Coefficient	PR	SRK
b_0	0.427480	0.086640
Φ_0	0.457236	0.077796
ψ_0	0.37464	0.48508
ψ_1	1.54226	1.5517
ψ_2	−0.26992	−0.15613

Table 2.2: Values of PR and SRK EoS coefficients, from [Poling et al., 2001].

Given a mixture state $(T, P, \underline{\boldsymbol{Y}})$, computing the density requires to find the roots of the following cubic equation:

$$\left(1 + \varepsilon_1 \bar{b}\rho - \varepsilon_2 \bar{b}^2 \rho^2\right)\left(1 - \bar{b}\rho\right) P + \left(1 - \bar{b}\rho\right) \bar{a}\rho^2 - \left(1 + \varepsilon_1 \bar{b}\rho - \varepsilon_2 \bar{b}^2 \rho^2\right) \rho \bar{r} T = 0, \tag{2.2.20}$$

hence the name of this family of EoS. Details about its resolution using Cardano's method are provided in Appendix A.2.

2.2.2.2 Thermodynamic potentials

From the EoS definition, one can derive all the thermodynamic properties of the fluid. This is achieved by evaluating the so-called *departure values* [Poling et al., 2001]. These quantities allow to describe the evolution of a thermodynamic property ϕ of a real fluid, from a state $(P_1, T_1, \underline{\boldsymbol{Y}})$ to another $(P_2, T_2, \underline{\boldsymbol{Y}})$, as depicted in Figure 2.8.

The departure value $\underset{P}{\Delta}\phi(P, T, \underline{\boldsymbol{Y}})$, represents the difference between the real-gas value of the quantity ϕ and its ideal-gas counterpart ϕ^{IG}, evaluated at the same thermodynamic point $(P, T, \underline{\boldsymbol{Y}})$:

$$\underset{P}{\Delta}\phi(P, T, \underline{\boldsymbol{Y}}) = \phi(P, T, \underline{\boldsymbol{Y}}) - \phi^{\mathrm{IG}}(P, T, \underline{\boldsymbol{Y}}). \tag{2.2.21}$$

In Figure 2.8, the red thermodynamic path AG and the blue one $ABDEFG$ are equivalent. The path $ABDEFG$ actually consists in splitting the variations of ϕ in two parts. The first part consists in the evolution of the reference ideal-gas state, corresponding to the sub-path $BDEF$. The second one is the variation of the state function ϕ with respect to the reference ideal-gas state when including the non-ideal molecular interactions, corresponding to the sub-paths AB and FG. At this point, it is interesting to note that, as the pressure tends to zero, the non-ideal molecular interactions vanish and the real-gas state tends to the ideal-gas one, which writes:

$$\lim_{P \to 0} \left[\phi(P, T, \underline{\boldsymbol{Y}}) - \phi^{\mathrm{IG}}(P, T, \underline{\boldsymbol{Y}})\right] = 0. \tag{2.2.22}$$

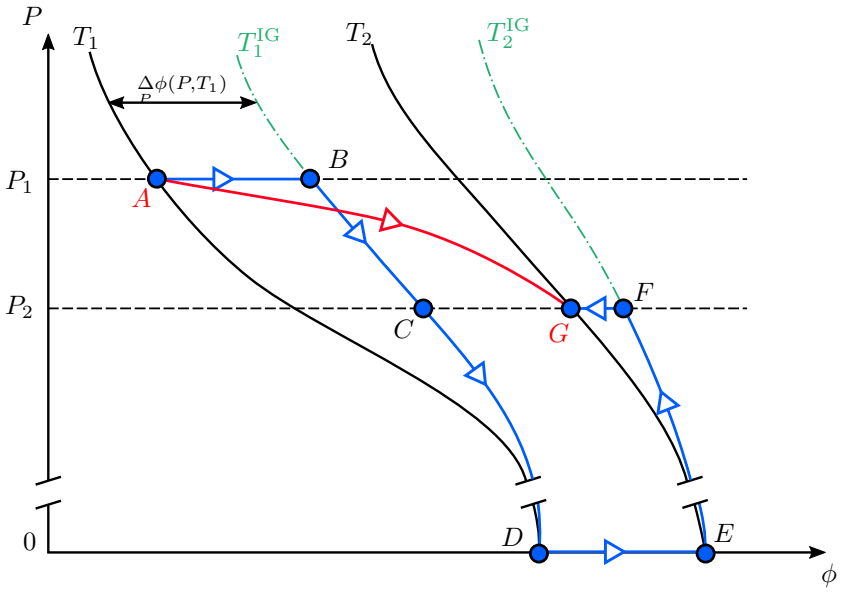

Figure 2.8: Thermodynamic path to compute variations of a thermodynamic potential for a real-gas EoS. Real-gas isothermal lines are displayed in black solid lines, while ideal-gas isothermal lines are the green dash-dotted lines. Red and blue lines with arrows denote two equivalent thermodynamic paths.

In this respect, the departure value can be evaluated by integrating the deviation of the real-gas state with the ideal-gas one from the zero-pressure limit, which reads:

$$\underset{P}{\Delta}\phi(P,T,\underline{\boldsymbol{Y}}) = \int_0^P \left(\left.\frac{\partial\phi}{\partial P}\right|_{T,\underline{\boldsymbol{Y}}} - \left.\frac{\partial\phi^{\mathrm{IG}}}{\partial P}\right|_{T,\underline{\boldsymbol{Y}}} \right) \mathrm{d}P_*. \tag{2.2.23}$$

An equivalent reasoning can be led by defining the *residual value* $\underset{\rho}{\Delta}\phi(\rho,T,\underline{\boldsymbol{Y}})$, which correspond to the difference between ϕ and ϕ^{IG} evaluated at the same temperature, composition and density [Poling et al., 2001]. Similarly to the departure values, the residual values can be computed using the fact that the non-ideal molecular interactions vanish in the zero-density limit, i.e.

$$\lim_{\rho\to 0}\left[\phi(\rho,T,\underline{\boldsymbol{Y}}) - \phi^{\mathrm{IG}}(\rho,T,\underline{\boldsymbol{Y}})\right] = 0, \tag{2.2.24}$$

so that the residual value reads

$$\underset{\rho}{\Delta}\phi(\rho,T,\underline{\boldsymbol{Y}}) = \phi(\rho,T,\underline{\boldsymbol{Y}}) - \phi^{\mathrm{IG}}(\rho,T,\underline{\boldsymbol{Y}}) = \int_0^\rho \left(\left.\frac{\partial\phi}{\partial\varrho}\right|_{T,\underline{\boldsymbol{Y}}} - \left.\frac{\partial\phi^{\mathrm{IG}}}{\partial\varrho}\right|_{T,\underline{\boldsymbol{Y}}} \right) \mathrm{d}\varrho. \tag{2.2.25}$$

In practice, it is more convenient to use the departure values. For example, a liquid and its vapour at equilibrium share the same pressure and temperature, so that their thermodynamic state evaluated with the departure values have the same reference ideal-gas state, whereas evaluating their state with residual values would involve different reference ideal-gas states, since their densities are different. Nonetheless, as the cubic EoS is defined explicitly with respect to the density, it is convenient to reformulate the departure values as a function of the temperature, the density and the composition.

This can be done by introducing $P_{\text{IG}} = \rho \bar{r} T$ and decomposing the departure value into:

$$\begin{aligned}\underset{P}{\Delta}\phi(\rho, T, \underline{\boldsymbol{Y}}) &= \phi\left(P(\rho, T, \underline{\boldsymbol{Y}}), T, \underline{\boldsymbol{Y}}\right) - \phi^{\text{IG}}\left(P(\rho, T, \underline{\boldsymbol{Y}}), T, \underline{\boldsymbol{Y}}\right), \\ &= \underbrace{\phi(P(\rho, T, \underline{\boldsymbol{Y}}), T, \underline{\boldsymbol{Y}}) - \phi^{\text{IG}}(P_{\text{IG}}, T, \underline{\boldsymbol{Y}})}_{①} + \underbrace{\phi^{\text{IG}}(P_{\text{IG}}, T, \underline{\boldsymbol{Y}}) - \phi^{\text{IG}}(P(\rho, T, \underline{\boldsymbol{Y}}), T, \underline{\boldsymbol{Y}})}_{②}.\end{aligned} \tag{2.2.26}$$

In this expression, the term denoted by ① is actually equal to the residual value $① = \underset{\rho}{\Delta}\phi\big(\rho(P, T, \underline{\boldsymbol{Y}}), T, \underline{\boldsymbol{Y}}\big)$. Introducing $\rho_{\text{IG}}(\rho, T, \underline{\boldsymbol{Y}}) = \frac{P(\rho, T, \underline{\boldsymbol{Y}})}{\bar{r}T}$, the term denoted ② can be interpreted as

$$② = \phi^{\text{IG}}\big(\rho, T, \underline{\boldsymbol{Y}}\big) - \phi^{\text{IG}}\big(\rho_{\text{IG}}, T, \underline{\boldsymbol{Y}}\big) = \int_{\rho_{\text{IG}}}^{\rho} \left.\frac{\partial \phi^{\text{IG}}}{\partial \varrho}\right|_{T} \mathrm{d}\varrho \tag{2.2.27}$$

so that the final formulation of the departure values reads:

$$\underset{P}{\Delta}\phi(\rho, T, \underline{\boldsymbol{Y}}) = \underset{\rho}{\Delta}\phi(\rho, T, \underline{\boldsymbol{Y}}) + \int_{0}^{\rho} \left.\frac{\partial \phi^{\text{IG}}}{\partial \varrho}\right|_{T, \underline{\boldsymbol{Y}}} \mathrm{d}\varrho. \tag{2.2.28}$$

Following these considerations, the departure values of different thermodynamic quantities are summarized hereafter, and their expression for SRK and PR EoS are provided.

The **sensible energy** departure value writes

$$\underset{P}{\Delta} e_s(\rho, T, \underline{\boldsymbol{Y}}) = \int_{0}^{\rho} \left(\frac{P}{\varrho^2} - \frac{T}{\varrho^2} \left.\frac{\partial P}{\partial T}\right|_{\rho, \underline{\boldsymbol{Y}}} \right) \mathrm{d}\varrho, \tag{2.2.29a}$$

since the sensible energy of an ideal gas depends only on its temperature and its composition,

$$\left.\frac{\partial e_s^{\text{IG}}}{\partial \varrho}\right|_{T, \underline{\boldsymbol{Y}}} = 0. \tag{2.2.29b}$$

This yields, for PR and SRK EoS:

$$\boxed{\underset{P}{\Delta} e_s(\rho, T, \underline{\boldsymbol{Y}}) = \frac{\bar{a} - T\bar{a}'}{\bar{b}\varepsilon_{12}} \ln\left(\frac{2 + (\varepsilon_1 - \varepsilon_{12})\rho\bar{b}}{2 + (\varepsilon_1 + \varepsilon_{12})\rho\bar{b}} \right),} \tag{2.2.29c}$$

with coefficients ε_1, ε_2 and ε_{12} defined in Table 2.1.

The **enthalpy** departure value is

$$\underset{P}{\Delta} h_s(\rho, T, \underline{\boldsymbol{Y}}) = \int_{0}^{\rho} \left(\frac{P}{\varrho^2} - \frac{T}{\varrho^2} \left.\frac{\partial P}{\partial T}\right|_{\rho, \underline{\boldsymbol{Y}}} \right) \mathrm{d}\varrho + \frac{P}{\rho} - \bar{r}T, \tag{2.2.30a}$$

yielding

$$\boxed{\underset{P}{\Delta} h_s(\rho, T, \underline{\boldsymbol{Y}}) = \frac{\bar{a} - T\bar{a}'}{\bar{b}\varepsilon_{12}} \ln\left(\frac{2 + (\varepsilon_1 - \varepsilon_{12})\rho\bar{b}}{2 + (\varepsilon_1 + \varepsilon_{12})\rho\bar{b}} \right) + \frac{P}{\rho} - \bar{r}T.} \tag{2.2.30b}$$

The departure **Helmoltz energy** is given by

$$\underset{P}{\Delta} f_s(\rho, T, \underline{\boldsymbol{Y}}) = \int_{0}^{\rho} \left(\frac{P}{\varrho^2} - \frac{\bar{r}T}{\varrho} \right) \mathrm{d}\varrho - \bar{r}T \ln\left(\frac{P}{\rho \bar{r} T} \right); \tag{2.2.31a}$$

which boils down to

$$\boxed{\underset{P}{\Delta} f_s(\rho, T, \underline{\boldsymbol{Y}}) = -\frac{\bar{a}}{\bar{b}\varepsilon_{12}} \ln\left(\frac{2+(\varepsilon_1+\varepsilon_{12})\rho\bar{b}}{2+(\varepsilon_1-\varepsilon_{12})\rho\bar{b}}\right) - \bar{r}T\ln\left(\frac{P}{\rho\bar{r}T}\right).} \tag{2.2.31b}$$

The **Gibbs energy** departure value is

$$\underset{P}{\Delta} g(\rho, T, \underline{\boldsymbol{Y}}) = \int_0^\rho \left(\frac{P}{\varrho^2} - \frac{\bar{r}T}{\varrho}\right) \mathrm{d}\varrho - \bar{r}T\ln\left(\frac{P}{\rho\bar{r}T}\right) + \frac{P}{\rho} - \bar{r}T, \tag{2.2.32a}$$

which reads

$$\boxed{\underset{P}{\Delta} g(\rho, T, \underline{\boldsymbol{Y}}) = \frac{\bar{a}}{\bar{b}\varepsilon_{12}} \ln\left(\frac{2+(\varepsilon_1-\varepsilon_{12})\rho\bar{b}}{2+(\varepsilon_1+\varepsilon_{12})\rho\bar{b}}\right) - \bar{r}T\left[1+\ln\left(\frac{P\left(1-\bar{b}\rho\right)}{\rho\bar{r}T}\right)\right] + \frac{P}{\rho},} \tag{2.2.32b}$$

and, finally, the **entropy** departure value is computed as

$$\underset{P}{\Delta} s(\rho, T, \underline{\boldsymbol{Y}}) = \int_0^\rho \left[\frac{\bar{r}}{\varrho} - \frac{1}{\varrho^2}\left.\frac{\partial P}{\partial T}\right|_{\rho,\underline{\boldsymbol{Y}}}\right] \mathrm{d}\varrho + r\ln\left(\frac{P}{\rho\bar{r}T}\right), \tag{2.2.33a}$$

which reads

$$\boxed{\underset{P}{\Delta} s(T, \rho, \underline{\boldsymbol{Y}}) = -\frac{a'}{\bar{b}\varepsilon_{12}} \ln\left(\frac{2+(\varepsilon_1-\varepsilon_{12})\,\bar{b}\rho}{2+(\varepsilon_1+\varepsilon_{12})\,\bar{b}\rho}\right) + \bar{r}\ln\left(\frac{P\left(1-\bar{b}\rho\right)}{\rho\bar{r}T}\right).} \tag{2.2.33b}$$

The expressions for the reference values that are used to compute the thermodynamic potentials, corresponding to the ideal gas law, are provided in Appendix A.1.

Finally, one can introduce the *fugacity* $\hat{f}$ (not to be mistaken with the free energy f_s), an additional thermodynamic quantity homogeneous to a pressure, which characterizes the departure Gibbs energy. It is defined as:

$$\bar{r}T\ln\left(\frac{\hat{f}}{P}\right) = \underset{P}{\Delta} g(\rho, T, \underline{\boldsymbol{Y}}) = \frac{\bar{a}}{\bar{b}\varepsilon_{12}} \ln\left(\frac{2+(\varepsilon_1-\varepsilon_{12})\rho\bar{b}}{2+(\varepsilon_1+\varepsilon_{12})\rho\bar{b}}\right) - \bar{r}T\left[1+\ln\left(\frac{P\left(1-\bar{b}\rho\right)}{\rho\bar{r}T}\right)\right] + \frac{P}{\rho} \tag{2.2.34}$$

The fugacity is homogeneous to a pressure, and one can also define the dimensionless *fugacity coefficient* φ, as

$$\varphi = \frac{\hat{f}}{P}. \tag{2.2.35}$$

Then, the fugacity coefficient writes

$$\boxed{\varphi = \frac{\rho\bar{r}T}{P\left(1-\bar{b}\rho\right)} \left(\frac{2+(\varepsilon_1-\varepsilon_{12})\rho\bar{b}}{2+(\varepsilon_1+\varepsilon_{12})\rho\bar{b}}\right)^{\left(\bar{a}/\bar{b}\varepsilon_{12}\right)} \exp\left(\frac{P}{\rho\bar{r}T} - 1\right).} \tag{2.2.36}$$

2.2.2.3 Multicomponent mixtures and partial quantities

In a multicomponent mixture, it is interesting to define the *partial* thermodynamic quantities of species, that characterize the dependence of mixture thermodynamic quantities to the amount of the considered species.

The partial quantity of a mass-specific thermodynamic potential ϕ for the i^{th} species writes:

$$\phi_i(T,P,\{m_1,...,m_{N_s}\}) = \left.\frac{\partial\left(m\phi\right)}{\partial m_i}\right|_{T,P,m_{j\neq i}}. \tag{2.2.37}$$

Using the 1-homogeneity of the extensive thermodynamic potential $m\phi(T,P,\{m_1,...,m_{N_s}\})$ with respect to the extensive variables $\{m_1,...,m_{N_s}\}$, it is obvious that the partial quantities of a mixture verify

$$\sum_{i=1}^{N_s} Y_i\phi_i(T,P,\{m_1,...,m_{N_s}\}) = \phi(T,P,\{m_1,...,m_{N_s}\}). \tag{2.2.38}$$

The partial specific volume $v_i(\rho,T,\underline{\boldsymbol{Y}})$ of the i^{th} component reads:

$$v_i(\rho,T,\underline{\boldsymbol{Y}}) = \beta\left[\frac{T}{1-\bar{b}\rho}\left(r_i+\frac{\rho\bar{r}b_i}{1-\bar{b}\rho}\right)+\frac{\rho}{1+\varepsilon_1\bar{b}\rho-\varepsilon_2\bar{b}^2\rho^2}\left(\frac{(\varepsilon_1-2\varepsilon_2\bar{b}\rho)b_i\bar{a}\rho}{1+\varepsilon_1\bar{b}\rho-\varepsilon_2\bar{b}^2\rho^2}-2\sum_{j=1}^{N_s}Y_ja_{ij}\right)\right]. \tag{2.2.39}$$

For PR and SRK EoS, the partial sensible energy obtained by differentiating its departure value (2.2.29c) and reference value (A.1.1) reads

$$\begin{aligned} e_{s,i}(\rho,T,\underline{\boldsymbol{Y}}) =& \frac{1}{\bar{b}\varepsilon_{12}}\ln\left(\frac{2+(\varepsilon_1-\varepsilon_{12})\rho\bar{b}}{2+(\varepsilon_1+\varepsilon_{12})\rho\bar{b}}\right)\left[2\sum_{k=1}Y_k(a_{ik}-Ta'_{ik})-\frac{(\bar{a}-T\bar{a}')b_i}{\bar{b}}\right] \\ &+\frac{\bar{a}-T\bar{a}'}{\bar{b}}\frac{\rho b_i-\rho^2\bar{b}v_i}{1+\varepsilon_1\rho\bar{b}-\varepsilon_2\rho^2\bar{b}^2}+e^{\text{IG}}_{s,i}(T). \end{aligned} \tag{2.2.40}$$

The partial enthalpy is then

$$\begin{aligned} h_{s,i}(\rho,T,\underline{\boldsymbol{Y}}) =& \frac{1}{\bar{b}\varepsilon_{12}}\ln\left(\frac{2+(\varepsilon_1-\varepsilon_{12})\rho\bar{b}}{2+(\varepsilon_1+\varepsilon_{12})\rho\bar{b}}\right)\left[2\sum_{k=1}Y_k(a_{ik}-Ta'_{ik})-\frac{(\bar{a}-T\bar{a}')b_i}{\bar{b}}\right] \\ &+\frac{\bar{a}-T\bar{a}'}{\bar{b}}\frac{\rho b_i-\rho^2\bar{b}v_i}{1+\varepsilon_1\rho\bar{b}-\varepsilon_2\rho^2\bar{b}^2}+Pv_i-r_iT+h^{\text{IG}}_{s,i}(T). \end{aligned} \tag{2.2.41}$$

Because the definitions of the Helmoltz and Gibbs energies involve the entropy, it is important to first introduce the notion of *entropy of mixing* within ideal mixtures. Indeed, in a mixture of ideal gases, the partial entropy of the i^{th} component is not simply given by applying (A.1.3) to species i. An additional entropy term must be considered, to take into account the fact that mixing several gases together introduces more disorder than when considering one delimited volume per species. This additional term is called the *entropy of mixing*. It can be obtained from Dalton's law. Compared to the case where each species has its own delimited volume $V_i^0 = \frac{n_i\mathcal{R}T}{P}$ at temperature and pressure (T,P), the mixed state involves instead the partial pressures $P_i = X_iP = \frac{n_i\mathcal{R}T}{V}$, with V the volume of the whole mixture. The species behave as if it had undergone an isothermal expansion from the pressure

P to the partial pressure $X_i P$. The entropy of mixing is then equivalent to the entropy change due to this expansion, and takes the following form:

$$s_i^{\text{mix}}(X_i) = -r_i \ln(X_i) \tag{2.2.42}$$

which is obviously positive in agreement with the Second Law, since $X_i \in [0,1]$.
To sum up, the partial entropy of species i is given by

$$s_i(\rho, T, \underline{\boldsymbol{Y}}) = s_i^{\text{IG}}(\rho, T, Y_i = 1) + s_i^{\text{mix}}(X_i) + \underset{P}{\Delta} s_i(\rho, T, \underline{\boldsymbol{Y}}) \tag{2.2.43}$$

which reads

$$\begin{aligned} s_i(\rho, T, \underline{\boldsymbol{Y}}) = &- \frac{1}{\bar{b}\varepsilon_{12}} \left[2\sum_{j=1}^{N_s} Y_j a'_{i,j} - \frac{\bar{a}' b_i}{\bar{b}} \right] \ln\left(\frac{2 + (\varepsilon_1 - \varepsilon_{12})\,\rho\bar{b}}{2 + (\varepsilon_1 + \varepsilon_{12})\,\rho\bar{b}} \right) \\ &+ \frac{\bar{a}'}{\bar{b}} \frac{\rho b_i - \rho^2 \bar{b} v_i}{1 + \varepsilon_1 \bar{b}\rho - \varepsilon_2 \bar{b}^2 \rho^2} + \frac{\rho\bar{r}}{1 - \bar{b}\rho}(v_i - b_i) + r_i \left[\ln\left(\frac{P(1-\bar{b}\rho)}{X_i \rho \bar{r} T} \right) - 1 \right] \\ &+ s_i^{\text{IG}}(P/(\bar{r}T), T, Y_i = 1). \end{aligned} \tag{2.2.44}$$

Finally, the partial Helmoltz and Gibbs energies can be computed, yielding:

$$\begin{aligned} f_i(\rho, T, \underline{\boldsymbol{Y}}) = &\frac{1}{\bar{b}\varepsilon_{12}} \ln\left(\frac{2 + (\varepsilon_1 + \varepsilon_{12})\rho\bar{b}}{2 + (\varepsilon_1 - \varepsilon_{12})\rho\bar{b}} \right) \left[\frac{\bar{a} b_i}{\bar{b}} - 2\sum_{k=1}^{N_s} Y_k a_{ik} \right] \\ &- \frac{\bar{a}}{\bar{b}} \frac{\rho b_i - \rho^2 \bar{b} v_i}{1 + \varepsilon_1 \rho\bar{b} - \varepsilon_2 \rho^2 \bar{b}^2} + 2\bar{r}T + r_i T \left[\ln\left(\frac{X_i \rho \bar{r} T}{P} \right) - 1 \right] \\ &- \rho\bar{r}T v_i + f_i^{\text{IG}}(P/(\bar{r}T), T, Y_i = 1), \end{aligned} \tag{2.2.45}$$

$$\begin{aligned} g_i(\rho, T, \underline{\boldsymbol{Y}}) = &\frac{1}{\bar{b}\varepsilon_{12}} \ln\left(\frac{2 + (\varepsilon_1 - \varepsilon_{12})\rho\bar{b}}{2 + (\varepsilon_1 + \varepsilon_{12})\rho\bar{b}} \right) \left[2\sum_{k=1} Y_k a_{ik} - \frac{\bar{a} b_i}{\bar{b}} \right] \\ &+ \left(\frac{P}{\rho} - \bar{r}T \right) \frac{b_i}{\bar{b}} + r_i T \ln\left(\frac{X_i \rho \bar{r} T}{P\left(1 - \bar{b}\rho\right)} \right) \\ &+ g_i^{\text{IG}}(P/(\bar{r}T), T, Y_i = 1). \end{aligned} \tag{2.2.46}$$

It is also convenient to introduce the fugacities of the species in the mixture, which are defined by

$$\bar{r}T \ln\left(\frac{\hat{f}_i(\rho, T, \underline{\boldsymbol{Y}})}{X_i P} \right) = \underset{P}{\Delta} g_i(\rho, T, \underline{\boldsymbol{Y}}). \tag{2.2.47}$$

Eventually, the fugacity coefficient of the i^{th} species is defined as

$$\varphi_i(\rho, T, \underline{\boldsymbol{Y}}) = \frac{\hat{f}_i}{X_i P}. \tag{2.2.48}$$

2.2.2.4 Other important thermodynamic quantities

The heat capacities must also be modified to account for the real gas effects. The departure *isochoric heat capacity* is given by

$$\underset{P}{\Delta} c_v(\rho, T, \underline{\boldsymbol{Y}}) = -\int_0^{\rho} \frac{T}{\varrho^2} \left.\frac{\partial^2 P}{\partial T^2}\right|_{\rho} \mathrm{d}\varrho, \tag{2.2.49a}$$

which is expressed, for SRK and PR EoS, as

$$\boxed{\underset{P}{\Delta} c_v(\rho, T, \underline{\boldsymbol{Y}}) = T \frac{\mathrm{d}^2 \bar{a}}{\mathrm{d}T^2}(T) \ln\left(\frac{2 + (\varepsilon_1 - \varepsilon_{12})\,\bar{b}\rho}{2 + (\varepsilon_1 + \varepsilon_{12})\,\bar{b}\rho}\right).} \tag{2.2.49b}$$

It is also useful to introduce the *isobaric thermal expansion coefficient* α, defined as:

$$\alpha(\rho, T, \underline{\boldsymbol{Y}}) = -\frac{1}{\rho} \left.\frac{\partial \rho}{\partial T}\right|_{P, \underline{\boldsymbol{Y}}}, \tag{2.2.50}$$

and the *isothermal compressibility coefficient* β, which reads

$$\beta(\rho, T, \underline{\boldsymbol{Y}}) = \frac{1}{\rho} \left.\frac{\partial \rho}{\partial P}\right|_{T, \underline{\boldsymbol{Y}}}. \tag{2.2.51}$$

For the cubic EoS, they respectively write

$$\begin{cases} \alpha(\rho, T, \underline{\boldsymbol{Y}}) = \beta(\rho, T, \underline{\boldsymbol{Y}}) \left.\dfrac{\partial P}{\partial T}\right|_{\rho, \underline{\boldsymbol{Y}}} = \beta(\rho, T, \underline{\boldsymbol{Y}}) \left[\dfrac{\rho \bar{r}}{1 - \bar{b}\rho} - \dfrac{\mathrm{d}\bar{a}}{\mathrm{d}T} \dfrac{\rho^2}{1 + \varepsilon_1 \bar{b}\rho - \varepsilon_2 \bar{b}^2 \rho^2}\right], & \text{(2.2.52a)} \\ \beta(\rho, T, \underline{\boldsymbol{Y}}) = \left[\dfrac{\bar{r}T}{\left(1 - \bar{b}\rho\right)^2} - \dfrac{\bar{a}\rho\left(2 + \varepsilon_1 \bar{b}\rho\right)}{\left(1 + \varepsilon_1 \bar{b}\rho - \varepsilon_2 \bar{b}^2 \rho^2\right)^2}\right]^{-1}. & \text{(2.2.52b)} \end{cases}$$

The real gas isobaric heat capacity can then be obtained as:

$$c_p(\rho, T, \underline{\boldsymbol{Y}}) = c_v + \frac{\alpha^2 T}{\rho \beta}, \tag{2.2.53}$$

in which the isochoric heat capacities includes the departure terms of equation (2.2.49).

Finally, a last quantity that is relevant for this work is the *isentropic speed of sound*, denoted c, defined by:

$$c^2(\rho, T, \underline{\boldsymbol{Y}}) = \left.\frac{\partial P}{\partial \rho}\right|_{s} = \frac{c_p}{\rho \beta c_v}. \tag{2.2.54}$$

2.2.3 Other relevant equations of state

2.2.3.1 The stiffened gas (SG) EoS

This equation of state was introduced by [Le Métayer et al., 2004] to provide a simple form able to treat liquid-vapour mixtures within a compressible framework [Le Martelot et al., 2014, Chiapolino

et al., 2016]. This EoS is presented as it is extensively used in the context of multifluid methods, e.g. in these latter references. It writes

$$P(\rho,T) = \rho\,(\gamma-1)\,c_v T - P_\infty, \tag{2.2.55}$$

This EoS involves several tuning parameters, fitted on experimental data. For liquid-vapour simulations, two sets of parameters are necessary: one for the liquid phase $(P_{\infty,\ell}, c^0_{v,\ell}, \gamma_\ell, e_{0,\ell}, s_{0,\ell})$ and one for the vapour phase $(P_{\infty,v}, c^0_{v,v}, \gamma_v, e_{0,v}, s_{0,v})$. A method for their estimation is provided in [Le Métayer et al., 2004]. Because these parameters are constant, this EoS lacks accuracy when used on a wide range of temperatures and pressures.

It is readily seen that the stiffened gas EoS consists in shifting the ideal gas law by a constant value P_∞. Naturally, for $P_\infty = 0$, this EoS degenerates to the ideal gas law. In practice, the vapour phase EoS is defined with $P_{\infty,v} = 0$, while the liquid phase has a positive value for $P_{\infty,\ell}$ [Le Martelot et al., 2014, Chiapolino et al., 2016].

Computing the thermodynamic quantities for this EoS using the departure values methodology of paragraph 2.2.2.2 yields (c^0_v being assumed constant with respect to the temperature):

$$e_s(\rho,T) = c^0_v T + \frac{P_\infty}{\rho} + e_0, \tag{2.2.56}$$

The isochoric heat capacity departure value is zero, so that $c_v(\rho,T) = c^0_v$ is a constant, as is the isobaric heat capacity $c_p(\rho,T) = c^0_p = \gamma c^0_v$.

A convenient explicit density-energy form of the SG EoS (2.2.55) is also available:

$$P(\rho,e_s) = \rho\,(\gamma-1)\,(e_s - e_0) - \gamma P_\infty. \tag{2.2.57}$$

Another advantage of this EoS is the absence of non-linear terms compared to the cubic EoS (and in particular the repulsive term), which are known to be a source of spurious pressure noise when used in a numerical simulation where the conservative quantities $(\rho, \rho\vec{u}, \rho e_\mathrm{t})$ are simply transported [Pantano et al., 2017, Lacaze et al., 2019]. Note that, nonetheless, spurious noise is encountered for the stiffened gas EoS, and even for the ideal gas law, when a multicomponent flow is considered, as studied by [Abgrall, 1996], this phenomenon being observed when a non-constant heat capacity ratio γ is considered. On the other hand, this EoS does not account for the critical point.

2.2.3.2 The Noble-Abel stiffened gas (NASG) EoS

An improvement of the stiffened gas EoS has been proposed by the same authors [Le Métayer and Saurel, 2016]. It consists in adding a covolume parameter b to the repulsive term in the same fashion as for the van der Waals EoS, in order to increase the range of validity of the SG EoS.

The Noble-Abel Stiffened Gas (NASG) EoS expresses as:

$$P(\rho,T) = \frac{\rho\,(\gamma-1)\,c_v T}{1-b\rho} - P_\infty. \tag{2.2.58}$$

Computing the sensible energy using its departure value yields

$$e_s(\rho,T) = c_v T + \frac{1-b\rho}{\rho} P_\infty + e_0. \tag{2.2.59}$$

The choice was made to present only the relevant EoS in the scope of this work. On the one hand, the different cubic EoS offer a good trade-off between simplicity and accuracy, and can be used to describe the liquid, vapour and supercritical states of a fluid. On the other hand, the SG and NASG EoS are convenient to treat liquid-gas mixtures and have an even simpler form.

Nevertheless, it is worth mentioning that a variety of other algebraic EoS have been developed, either for other purposes, e.g. solid-state EoS like the Mie-Grüneisen EoS, or taking more complex forms than the cubic EoS (2.2.17), e.g. the Benedict-Webb-Rubin EoS. Although not exhaustive, [Poling et al., 2001] provides a good overview of the different EoS that can be applied to describe liquids and gases.

2.3 Thermodynamic equilibrium for a single-component fluid

The description of the thermodynamics of two-phase mixtures is a cornerstone of diffuse interface models addressing phase change phenomena [Saurel et al., 2008,Le Martelot et al., 2014]. This section recalls the notion of thermodynamic equilibrium and details its practical computation.

2.3.1 Thermodynamic stability and equilibrium

2.3.1.1 Gibbs-Duhem stability criterion

According to the second principle, the spontaneous evolution of a system always tends to maximize its entropy. The thermodynamic equilibrium then naturally corresponds to the maximum entropy state of the system. Let Ω be a closed thermodynamic system (cf. Figure 2.1 page 7). Ω is surrounded by Ω^c, so that the global system $\Omega \cup \Omega^c$ is isolated. Assume that Ω^c is much larger than Ω so that it is at constant pressure and temperature P_0, T_0. If Ω spontaneously exchanges small amounts of work ΔW and heat ΔQ with Ω^c, its sensible energy will change, by virtue of the First Law (see section 2.1.1 page 7), as

$$\Delta E_s = \Delta Q + \Delta W \tag{2.3.1}$$

The work is associated with a variation of the molar volume ΔV that verifies $\Delta W = -P_0 \Delta V$. The heat is associated with a variation of entropy $\Delta Q = T_0 \Delta S_{\text{rev}}$ and the total entropy variation is given by $\Delta S = \Delta S_{\text{rev}} + \Delta S_{\text{irr}}$, the sum of the reversible and irreversible entropy changes. Finally, Equation (2.3.1) becomes:

$$\Delta E_s - T_0 \Delta S + P_0 \Delta V = -T_0 \Delta S_{\text{irr}}, \tag{2.3.2}$$

From the Second Law (see section 2.1.2), this yields an inequality ruling the spontaneous evolution of the system Ω:

$$\Delta E_s - T_0 \Delta S + P_0 \Delta V \leq 0. \tag{2.3.3}$$

Now, the condition for the system to be thermodynamically stable is that it *cannot* spontaneously evolve. Then, the system is stable under the *Gibbs-Duhem stability condition*, when

$$\Delta E_s - T_0 \Delta S + P_0 \Delta V \geq 0. \tag{2.3.4}$$

This condition can then be applied to various systems. For the simplest case of a closed and isolated system (i.e. with constant volume and energy), (2.3.4) becomes

$$\Delta S \leq 0, \tag{2.3.5}$$

so that the system is stable when its entropy is maximum. If the system is isobaric and isothermal, (2.3.4) boils down to

$$\Delta G \geq 0, \tag{2.3.6}$$

so that the system is stable when its Gibbs energy is minimum.

Similarly, for a system at constant volume and temperature, the stability corresponds to a minimum Helmoltz energy F_s. For a system at constant entropy and pressure, the stability consists in a minimum enthalpy H_s state, and for a system at constant volume and entropy, it corresponds to a minimum sensible energy E_s state.

2.3.1.2 Thermodynamic stability for cubic EoS at given (T, P)

The cubic nature of VDW, PR and SRK EoS implies the possible existence of up to three candidate values for the density, for a given couple (T, P), as described in Appendix A.2 and as depicted in Figure 2.7 page 19. Among the solutions, the globally stable one is the one of minimal Gibbs energy g, as illustrated in Figure 2.9.

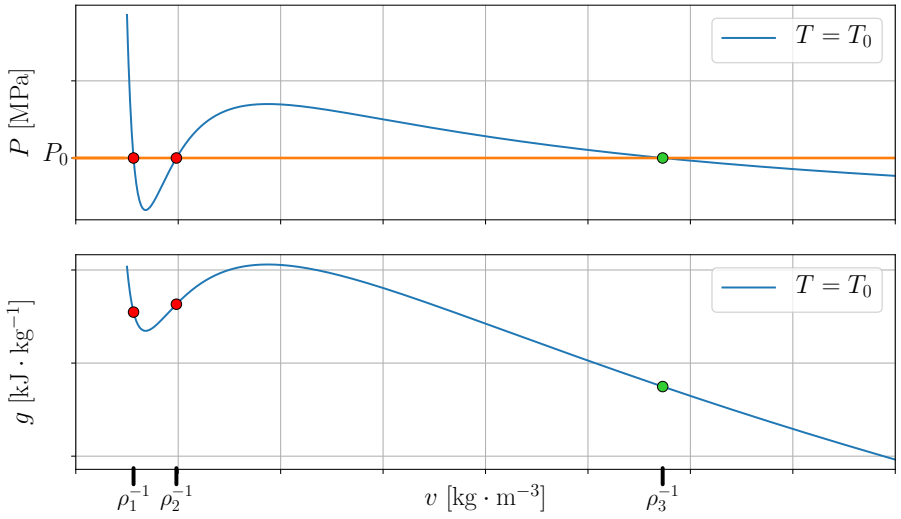

Figure 2.9: Determination of the stable root of a cubic EoS when multiple positive density roots are found. Here, ρ_3 is the solution of minimum Gibbs energy and is then the stable solution, corresponding to a gas state.

2.3.1.3 Local thermodynamic stability condition

The stability criterion of a phase can be expressed in terms of the Hessian matrix of the sensible energy. Indeed, from the stability condition (2.3.4), a second-order Taylor-expansion of the internal energy around its equilibrium value yields

$$\begin{aligned}\Delta E_s = &\left[\left.\frac{\partial E_s}{\partial S}\right|_V - T_0\right]\Delta S + \left[\left.\frac{\partial E_s}{\partial V}\right|_S + P_0\right]\Delta V \\ &+ \frac{1}{2}\left.\frac{\partial^2 E_s}{\partial S^2}\right|_V \Delta S^2 + \frac{\partial^2 E_s}{\partial S \partial V}\Delta S \Delta V + \frac{1}{2}\left.\frac{\partial^2 E_s}{\partial V^2}\right|_S \Delta V^2 \geq 0.\end{aligned} \tag{2.3.7}$$

Using the definitions of the partial derivatives of E_s with respect to S and V, which are respectively T_0 and $-P_0$, one has immediately

$$\frac{1}{2}\left.\frac{\partial^2 E_s}{\partial S^2}\right|_V \Delta S^2 + \frac{\partial^2 E_s}{\partial S \partial V}\Delta S \Delta V + \frac{1}{2}\left.\frac{\partial^2 E_s}{\partial V^2}\right|_S \Delta V^2 \geq 0. \tag{2.3.8}$$

Hence, the Hessian matrix of the sensible energy must be positive definite, which corresponds to

$$\begin{cases} \left.\dfrac{\partial^2 E_s}{\partial S^2}\right|_V \geq 0, & \text{(2.3.9a)} \\ \left.\dfrac{\partial^2 E_s}{\partial V^2}\right|_S \left.\dfrac{\partial^2 E_s}{\partial S^2}\right|_V - \left[\dfrac{\partial^2 E_s}{\partial S \partial V}\right]^2 \geq 0, & \text{(2.3.9b)} \end{cases}$$

which, using Maxwell's relations (2.1.23), boils down to

$$\begin{cases} \dfrac{T}{C_v} \geq 0, & \text{(2.3.10a)} \\ \dfrac{1}{\rho\beta} \geq 0. & \text{(2.3.10b)} \end{cases}$$

Finally, the single-component phase local stability condition is

$$\begin{cases} C_v \geq 0, & \text{(2.3.11a)} \\ \beta \geq 0. & \text{(2.3.11b)} \end{cases}$$

The first condition (2.3.11a) is actually always verified. Yet, the second condition, (2.3.11b) appears to be violated in some cases by the cubic EoS, as it can be seen in Figure 2.9. Indeed, by its definition (2.2.51), the positivity of beta is equivalent to a negative slope in the Clapeyron diagram (P, v). This criterion is then verified everywhere except between the extrema of the subcritical isothermal lines. Hence, when the cubic EoS has three roots, the intermediate value always corresponds to an unstable state. The minimum Gibbs energy is the stable state, and the other one is in a *metastable* state: it is locally stable from condition (2.3.11), but globally unstable as there exists a more stable state.

2.3.1.4 Two-phase equilibrium

We consider now an isolated system containing two phases. The liquid phase properties are indexed by ℓ and the vapour phase properties by v. The mass, volume, energy and entropy of the system can be decomposed as

$$\begin{aligned} m &= m_\ell + m_v, & \text{(2.3.12a)} \\ \mathcal{V} &= \mathcal{V}_\ell + \mathcal{V}_v, & \text{(2.3.12b)} \\ \mathcal{E}_s &= \mathcal{E}_{s,\ell} + \mathcal{E}_{s,v}, & \text{(2.3.12c)} \\ \mathcal{S} &= \mathcal{S}_\ell + \mathcal{S}_v. & \text{(2.3.12d)} \end{aligned}$$

and, the system being isolated,

$$\begin{aligned} \mathrm{d}m = \mathrm{d}m_\ell + \mathrm{d}m_v &= 0, & \text{(2.3.13a)} \\ \mathrm{d}\mathcal{V} = \mathrm{d}\mathcal{V}_\ell + \mathrm{d}\mathcal{V}_v &= 0, & \text{(2.3.13b)} \\ \mathrm{d}\mathcal{E}_s = \mathrm{d}\mathcal{E}_{s,\ell} + \mathrm{d}\mathcal{E}_{s,v} &= 0. & \text{(2.3.13c)} \end{aligned}$$

The gibbs relation (2.1.7) applied to each phase writes

$$\begin{cases} \mathrm{d}\mathcal{E}_{s,\ell} = T_\ell \,\mathrm{d}\mathcal{S}_\ell - P_\ell \,\mathrm{d}\mathcal{V}_\ell + g_\ell \,\mathrm{d}m_\ell, & \text{(2.3.14a)} \\ \mathrm{d}\mathcal{E}_{s,v} = T_v \,\mathrm{d}\mathcal{S}_v - P_v \,\mathrm{d}\mathcal{V}_v + g_\ell \,\mathrm{d}m_v. & \text{(2.3.14b)} \end{cases}$$

The equilibrium condition implies that the total entropy differential is zero. Combined with (2.3.13) and (2.3.14), it yields:

$$(T_\ell - T_v)\,\mathrm{d}\mathcal{S}_\ell - (P_\ell - P_v)\,\mathrm{d}\mathcal{V}_\ell + (g_\ell - g_v)\,\mathrm{d}m_\ell = 0. \tag{2.3.15}$$

This relation must be verified for any transformation, hence the *liquid-vapour equilibrium condition*:

$$\begin{cases} P_\ell = P_v, & \text{(2.3.16a)} \\ T_\ell = T_v, & \text{(2.3.16b)} \\ g_\ell = g_v. & \text{(2.3.16c)} \end{cases}$$

For a two-phase system at thermodynamic equilibrium, this defines the equilibrium pressure $P = P_\ell = P_v$ and the equilibrium temperature $T = T_\ell = T_v$. The liquid fractions can be defined as:

$$x_\ell = \frac{n_\ell}{n} \quad ; \quad y_\ell = \frac{m_\ell}{m} \quad ; \quad z_\ell = \frac{\mathcal{V}_\ell}{\mathcal{V}}, \tag{2.3.17}$$

which are respectively the *liquid mole fraction*, the *liquid mass fraction* and the *liquid volume fraction*. Obviously, the vapour fractions verify $x_v = (1 - x_\ell)$, $y_v = (1 - y_\ell)$ and $z_v = (1 - z_\ell)$.

The two-phase mixture density is then

$$\rho = \frac{m}{\mathcal{V}} = z_\ell \rho_\ell + (1 - z_\ell)\rho_v. \tag{2.3.18}$$

Similarly, the mass-specific volume of the mixture is

$$v = \frac{\mathcal{V}}{m} = y_\ell v_\ell + (1 - y_\ell)v_v. \tag{2.3.19}$$

More generally, any mass-specific quantity (thermodynamic potentials, entropy) is computed as a barycenter between their liquid and vapour counterpart with respective weights y_ℓ and $(1 - y_\ell)$.

2.3.1.5 Spinodal and binodal regions

From the previous paragraphs, it appears that in the (P, v) Clapeyron diagram, the region of instability, called the *spinodal region* and the region of metastability, called the *binodal region* can be delimited. *Metastability* characterizes thermodynamic states that are locally stable in the sense of (2.3.11), but globally unstable, as they do not satisfy the Gibbs-Duhem stability criterion (2.3.4).

This representation is depicted in Figure 2.10. It appears that the spinodal and binodal envelopes meet at the critical point. The area over the critical point contains the supercritical states. The area on the left of the binodal envelope contains the stable liquid phase, whereas the grey hatched area on the left side of the spinodal envelope contains the metastable liquid. The area on the right of the binodal envelope contains the stable vapour states, and the grey hatched area on the right side of the spinodal envelope contains the metastable vapour.

For a given subcritical pressure P, the two intersections with the binodal dome belong to the same isothermal line: it corresponds to the saturation temperature of pressure P, written $T^{\mathrm{sat}}(P)$. The two points correspond to the saturated liquid and vapour densities $\rho_\ell(P)$ and $\rho_v(P)$. Note that, by duality, the system can be equivalently defined with respect to the temperature, by defining its saturation pressure $T^{\mathrm{sat}}(P)$ and saturated liquid and vapour densities $\rho_\ell(T)$ and $\rho_v(T)$.

2.3.1.6 Clausius-Clapeyron relation and saturation derivatives

As demonstrated in paragraph 2.3.1.4, the two-phase equilibria obey System (2.3.16). In particular, their Gibbs energies remain equal. Then, for an infinitesimal evolution of the system state, the two-phase equilibrium will evolve following

$$\mathrm{d}g_\ell = \mathrm{d}g_v. \tag{2.3.20}$$

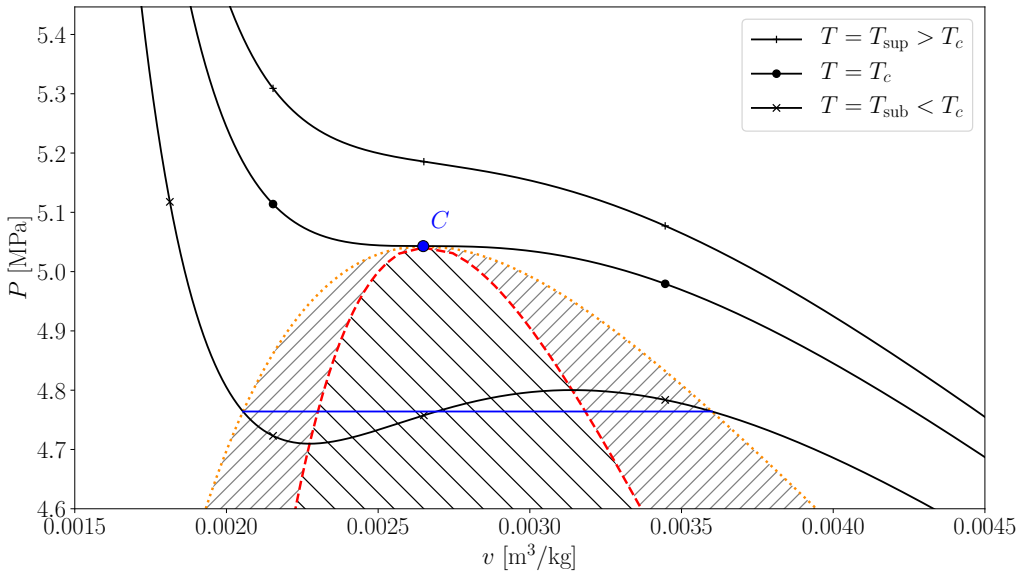

Figure 2.10: Clapeyron diagram for O_2. Black lines denote the isotherms predicted by the cubic (here SRK) EoS. The blue line is the saturated pressure corresponding to the subcritical isotherm T_{sub}. The orange dotted line is the binodal envelope. The red dashed line is the spinodal envelope. The spinodal region of thermodynamic instability is hatched with black lines [\\], while the binodal region of metastable is hatched with gray lines [//]. The critical point is denoted by C.

Developping the expression of the Gibbs energy (2.1.25d) for each phase yields

$$-s_\ell \, \mathrm{d}T + \frac{1}{\rho_\ell} \, \mathrm{d}P = -s_v \, \mathrm{d}T + \frac{1}{\rho_v} \, \mathrm{d}P, \tag{2.3.21}$$

which gives an analytic expression that rules the variations of the temperature and pressure for a two-phase system at equilibrium:

$$\left.\frac{\mathrm{d}T}{\mathrm{d}P}\right|_{\text{sat}} = \frac{\rho_\ell - \rho_v}{\rho_v \rho_\ell \, (s_v - s_\ell)}. \tag{2.3.22}$$

Using the equality of the Gibbs energies and of the temperatures, the entropy can be substituted to obtain the Clausius-Clapeyron relation:

$$\boxed{\left.\frac{\mathrm{d}T}{\mathrm{d}P}\right|_{\text{sat}} = \frac{T \, (\rho_\ell - \rho_v)}{\rho_v \rho_\ell \, (h_v - h_\ell)}.} \tag{2.3.23}$$

This very important relation allows to compute the variations of any phase quantity for two-phase systems in equilibrium. The *saturation derivatives* can then be defined: for a thermodynamic quantity ξ_ϕ of phase $\phi \in \{\ell, v\}$, one defines

$$\left.\frac{\mathrm{d}\xi_\phi}{\mathrm{d}T}\right|_{\text{sat}} = \frac{\mathrm{d}\xi_\phi(T, P^{\text{sat}}(T))}{\mathrm{d}T} = \left.\frac{\partial \xi_\phi}{\partial T}\right|_P + \left.\frac{\mathrm{d}P}{\mathrm{d}T}\right|_{\text{sat}} \left.\frac{\partial \xi_\phi}{\partial P}\right|_T \tag{2.3.24}$$

and

$$\left.\frac{\mathrm{d}\xi_\phi}{\mathrm{d}P}\right|_{\text{sat}} = \frac{\mathrm{d}\xi_\phi(T^{\text{sat}}(P), P)}{\mathrm{d}P} = \left.\frac{\mathrm{d}T}{\mathrm{d}P}\right|_{\text{sat}} \left.\frac{\partial \xi_\phi}{\partial P}\right|_T + \left.\frac{\partial \xi_\phi}{\partial T}\right|_P \tag{2.3.25}$$

For example for the density of the phase $\phi \in \{\ell, v\}$, it reads

$$\left.\frac{\mathrm{d}\rho_\phi}{\mathrm{d}T}\right|_{\text{sat}} = \left.\frac{\partial\rho_\phi}{\partial T}\right|_P + \left.\frac{\mathrm{d}P}{\mathrm{d}T}\right|_{\text{sat}} \left.\frac{\partial\rho_\phi}{\partial P}\right|_T = -\rho_\phi\alpha_\phi + \rho_\phi\beta_\phi \left.\frac{\mathrm{d}P}{\mathrm{d}T}\right|_{\text{sat}}. \tag{2.3.26}$$

Similarly, the variations of the sensible energy of the phase $\phi \in \{\ell, v\}$ at saturation is given by:

$$\left.\frac{\mathrm{d}e_\phi}{\mathrm{d}T}\right|_{\text{sat}} = \left.\frac{\partial e_\phi}{\partial T}\right|_P + \left.\frac{\mathrm{d}P}{\mathrm{d}T}\right|_{\text{sat}} \left.\frac{\partial e_\phi}{\partial P}\right|_T = \frac{\beta_\phi P - \alpha_\phi T}{\rho_\phi} + \left(c_{p,\phi} - \frac{\alpha_\phi P}{\rho_\phi}\right) \left.\frac{\mathrm{d}T}{\mathrm{d}P}\right|_{\text{sat}}. \tag{2.3.27}$$

Another important differential is that of the liquid volume fraction at saturation, given by:

$$\mathrm{d}z_\ell = -\frac{1}{\rho_\ell - \rho_v}\left[z_\ell \left.\frac{\mathrm{d}\rho_\ell}{\mathrm{d}T}\right|_{\text{sat}} + (1 - z_\ell) \left.\frac{\mathrm{d}\rho_v}{\mathrm{d}T}\right|_{\text{sat}}\right]\mathrm{d}T + \frac{1}{\rho_\ell - \rho_v}\mathrm{d}\rho. \tag{2.3.28}$$

2.3.2 Practical computation of the equilibrium

2.3.2.1 Computation for cubic EoS using the *corresponding states principle* (CSP)

To describe the saturation for cubic EoS, it is actually interesting to reduce the problem thanks to a change of variables. Indeed, similarly to the usual cubic EoS computations that can be unified for all chemical components through the *corresponding states principle* (CSP), it is possible to reduce the search for the saturated states of any pure component to a unique universal computation.

There is yet a subtlety compared to the usual reduced variables presented with the van der Waals EoS. Indeed, for SRK and PR EoS, since the attractive coefficient depends on the temperature, and the acentric factor was introduced (see Section 2.2.1.4), the usual system of reduced variables $T_r = \frac{T}{T_c}, P_r = \frac{P}{P_c}, V_r = \frac{V}{V_c}$ does not allow to formulate a unique saturated state definition for all components. In order to overcome this, the following reduced-saturation (Rsat) variables are introduced in the present work:

$$\begin{cases} \nu \triangleq \dfrac{1}{\bar{b}\rho}, & \text{(2.3.29a)} \\ \pi \triangleq \dfrac{P\bar{b}}{\bar{r}T}, & \text{(2.3.29b)} \\ \theta \triangleq \dfrac{\bar{a}(T)}{\bar{b}\bar{r}T}. & \text{(2.3.29c)} \end{cases}$$

ν will be called the Rsat-volume, π the Rsat-pressure, and θ the Rsat-temperature (although it has the dimension of the inverse of a temperature).

The cubic EoS may then be rewritten under the form:

$$\pi(\nu, \theta) = \frac{1}{\nu - 1} - \frac{\theta}{\nu^2 + \varepsilon_1\nu - \varepsilon_2}, \tag{2.3.30}$$

and the fugacity coefficient expression also reduces to:

$$\varphi(\nu, \theta) = \frac{1}{\pi(\nu - 1)}\left[\frac{2\nu + \varepsilon_1 - \varepsilon_{12}}{2\nu + \varepsilon_1 + \varepsilon_{12}}\right]^{\left(\frac{\theta}{\varepsilon_{12}}\right)} \exp\left(\pi\nu - 1\right). \tag{2.3.31}$$

This shows that the search for the saturation pressure takes the same form for any mixture. Indeed, it appears in equations (2.3.30) and (2.3.31) that only the EoS-specific parameters are left: the species-specific parameters do no longer appear. Global properties of the reduced cubic EoS are further analyzed in Appendix A.3.

For a given mixture at a given temperature, θ is known. Determination of the Rsat-pressure π at saturation requires to find π^{sat} such that:

$$\varphi\big(\pi^{\mathrm{sat}}, \nu^{\min}(\pi^{\mathrm{sat}}, \theta)\big) = \varphi\big(\pi^{\mathrm{sat}}, \nu^{\max}(\pi^{\mathrm{sat}}, \theta)\big), \tag{2.3.32}$$

where $\nu^{\min}(\pi, \theta)$ and $\nu^{\max}(\pi, \theta)$ are the minimum and maximum positive roots of the reduced cubic equation

$$\nu^3 + \left[\varepsilon_1 - 1 - \frac{1}{\pi}\right]\nu^2 + \left[\frac{\theta - \varepsilon_1}{\pi} - (\varepsilon_1 + \varepsilon_2)\right]\nu + \left[\varepsilon_2\left(\frac{1}{\pi} + 1\right) - \frac{\theta}{\pi}\right] = 0. \tag{2.3.33}$$

Note that for $\pi = \pi^{\mathrm{sat}}(\theta)$, one has

$$\begin{cases} \nu^{\min}(\pi^{\mathrm{sat}}, \theta) = \nu_\ell(\theta) = \dfrac{1}{\bar{b}\rho_\ell}, & \text{(2.3.34a)} \\ \nu^{\max}(\pi^{\mathrm{sat}}, \theta) = \nu_v(\theta) = \dfrac{1}{\bar{b}\rho_v}. & \text{(2.3.34b)} \end{cases}$$

The following notation is used:

$$\begin{cases} \varphi_\ell(\pi) = \varphi\big(\pi, \nu^{\min}(\pi, \theta)\big), & \text{(2.3.35a)} \\ \varphi_v(\pi) = \varphi\big(\pi, \nu^{\max}(\pi, \theta)\big). & \text{(2.3.35b)} \end{cases}$$

To solve this problem, a Newton-Raphson procedure may be used. The function to be canceled is given by

$$f_\theta : \pi \mapsto \varphi_\ell(\pi, \theta) - \varphi_v(\pi, \theta), \tag{2.3.36}$$

the derivative of which is

$$f'_\theta(\pi) = \left(\nu^{\min}(\pi, \theta) - \frac{1}{\pi}\right)\varphi_\ell(\pi, \theta) - \left(\nu^{\max}(\pi, \theta) - \frac{1}{\pi}\right)\varphi_v(\pi, \theta). \tag{2.3.37}$$

If $\pi^{(k)}$ is the k^{th} iterate, its update reads

$$\pi^{(k+1)} = \pi^{(k)} - \frac{f_\theta(\pi^{(k)})}{f'_\theta(\pi^{(k)})} = 2\pi^{(k)} - \frac{\varphi_\ell(\pi^{(k)}, \theta) - \varphi_v(\pi^{(k)}, \theta)}{\nu^{\min}(\pi^{(k)}, \theta)\varphi_\ell(\pi^{(k)}, \theta) - \nu^{\max}(\pi^{(k)}, \theta)\varphi_v(\pi^{(k)}, \theta)}. \tag{2.3.38}$$

The solver iterates until the relative difference of the fugacity coefficients is under a tolerance value

$$\frac{\varphi_\ell - \varphi_v}{\max(\varphi_\ell, \varphi_v)} < \epsilon_{\mathrm{tol}}. \tag{2.3.39}$$

In practice, this saturation computation is processed outline once and for all, for any component. It is then stored in a table that contains $\theta, \nu_\ell(\theta), \nu_v(\theta)$, and also $\frac{\mathrm{d}\nu_\ell}{\mathrm{d}\theta}$, $\frac{\mathrm{d}\nu_v}{\mathrm{d}\theta}$, to allow cubic polynomial interpolation. There is no need to store $\pi(\theta)$ since the saturation pressure can be directly computed from the EoS knowing the temperature and phases densities.

2.3.2.2 Computing the equilibrium using the tabulated CSP-reduced saturation

The table being computed, the practical equilibrium calculation is now described. The different cases depend on the nature of the input data for which the thermodynamic equilibrium must be computed.

Case 1: When, for a given chemical species, **the temperature and the density** (ρ, T) are known, reading the table is straightforward.

(i) First of all, when the temperature is higher than the critical temperature of the fluid, the state is always stable and it can be computed directly from the cubic EoS. This corresponds to the case $\theta(T) < \theta^c$, with θ^c given in Appendices A.3.2, A.3.3 and A.3.4 for the different cubic EoS.

(ii) Before using the table, it is necessary to check if the one-phase solution is the stable solution. This is done by computing the one phase pressure $P^{1\phi}$ directly from the cubic EoS (2.2.17). Then, the roots of the EoS corresponding to $(T, P^{1\phi})$ are computed. If only one root is positive, it is necessarily ρ and the one-phase state is then stable. If multiple roots are found, their fugacity coefficients are compared. If the input density ρ is the root that minimizes the fugacity coefficient, then the one-phase state is stable. Otherwise, the equilibrium corresponds to a two-phase state and the table must be read.

(iii) If a two-phase state was found in the previous stability test, the equilibrium state must be evaluated. First, the Rsat-temperature should be computed from Equation (2.3.29c). The corresponding values $\nu_\ell(\theta)$ and $\nu_v(\theta)$ are obtained using a cubic polynomial interpolation between the table points. Then, the saturated values ρ_ℓ and ρ_v are computed by inverting equation (2.3.29a). The system pressure is then necessarily the saturation pressure, which can be computed using the EoS, evaluated as $P^{\text{sat}} = P(\rho_\ell, T) = P(\rho_v, T)$. The sensitivity of the pressure with respect to density being much lower in the vapour phase than in the liquid phase – because of the latter lower compressibility – it is better to evaluate the pressure using the vapour density ρ_v.

(iv) Else, if the density is higher than ρ_ℓ, the state (ρ, T) is a stable liquid state and the pressure is directly computed from the EoS, as $P(\rho, T)$. Similar computation is done if $\rho < \rho_v(T)$, when the state (ρ, T) corresponds to a stable vapour state.

Case 2: For a given chemical species, **given the pressure and the density** (ρ, P), it is necessary to find the temperature value of the saturation. Indeed, it would not be possible to directly tabulate and read the Rsat-pressure, since its value depends on the temperature, which is not known at the moment. The proposed strategy is described below.

(i) First, the single-phase temperature $T^{1\phi}$ is computed directly from the EoS. The corresponding Rsat-temperature $\theta(T^{1\phi})$ is then compared to the critical Rsat-temperature of the EoS. If $\theta(T^{1\phi}) \leq \theta^c$, then the solution is necessarily stable since the fluid is in a supercritical state. In the subcritical case $\theta(T^{1\phi}) > \theta^c$, the input density ρ is compared to the saturated liquid and vapour densities: if $\rho \notin \left[\rho_v(T^{1\phi}), \rho_\ell(T^{1\phi})\right]$, then the single-phase solution is the stable solution. Otherwise, a two-phase state must be computed.

(ii) If the stable solution corresponds to a two-phase equilibrium, the saturation temperature must be obtained by a Newton-Raphson method. From a first-guess value of temperature T^0, the update of the temperature is defined as

$$T^{k+1} = T^k - \frac{P^{\text{sat}}(T^k) - P}{\frac{\mathrm{d}P^{\text{sat}}}{\mathrm{d}T}}. \tag{2.3.40}$$

The derivative of the saturation pressure with respect to the temperature $\frac{\mathrm{d}P^{\text{sat}}}{\mathrm{d}T}$ is given by the Clausius-Clapeyron relation (2.3.23), and the quantity $P^{\text{sat}}(T^k)$ is evaluated by reading the table. The iterations run until the convergence condition is met, defined by $\frac{P^{\text{sat}}(T^k)-P}{P} < \epsilon_{\text{tol}}$.

Case 3: The last case is the search for the equilibrium state **given the density and the sensible energy** (ρ, e_s). This case is important because it corresponds to the situation that occurs in two-phase simulations, as the solver transports the conservative quantities.

(i) First, a Newton-Raphson method is performed directly on the EoS to find the temperature $T^{1\phi}$, assuming a single-phase state. Then, the stability of the couple $(\rho, T^{1\phi})$ is evaluated as in *Case 1*. If the single-phase state is stable, the solution temperature $T^{1\phi}$ is kept. If the state is unstable, it is necessary to undergo another iterative method.

(ii) A Newton-Raphson method is used to retrieve the two-phase equilibrium, the update of which

being

$$T^{k+1} = T^k - \frac{e_s(\rho, T^k) - e_s}{\left.\frac{\partial e_s}{\partial T}\right|_\rho}, \tag{2.3.41}$$

with the mixture sensible energy given by $e_s(T^k) = \frac{1}{\rho}\left[z_\ell \rho_\ell e_\ell(T^k) + (1-z_\ell)\rho_v e_v(T^k)\right]$ and the liquid mass fraction $z_\ell = \frac{\rho - \rho_v(T^k)}{\rho_\ell(T^k) - \rho_v(T^k)}$. The derivative is evaluated as

$$\left.\frac{\partial e_s}{\partial T}\right|_\rho = \frac{1}{\rho}\left[(\rho_\ell e_\ell - \rho_v e_v)\left.\frac{\partial z_\ell}{\partial T}\right|_\rho + z_\ell \left.\frac{\mathrm{d}\rho_\ell e_\ell}{\mathrm{d}T}\right|_{\mathrm{sat}} + (1-z_\ell)\left.\frac{\mathrm{d}\rho_v e_v}{\mathrm{d}T}\right|_{\mathrm{sat}}\right] \tag{2.3.42}$$

$$\left.\frac{\partial e_s}{\partial T}\right|_\rho = \frac{1}{\rho}\left[\frac{e_v - e_\ell}{\rho_\ell - \rho_v}\left(z_\ell \rho_v \left.\frac{\mathrm{d}\rho_\ell}{\mathrm{d}T}\right|_{\mathrm{sat}} + (1-z_\ell)\rho_\ell \left.\frac{\mathrm{d}\rho_v}{\mathrm{d}T}\right|_{\mathrm{sat}}\right)\right. \tag{2.3.43}$$

$$\left. + z_\ell \rho_\ell \left.\frac{\mathrm{d}e_\ell}{\mathrm{d}T}\right|_{\mathrm{sat}} + (1-z_\ell)\rho_v \left.\frac{\mathrm{d}e_v}{\mathrm{d}T}\right|_{\mathrm{sat}}\right] \tag{2.3.44}$$

The saturation derivatives are given in paragraph 2.3.1.6.

(iii) In practice, it happens that the convergence is somehow hard to reach, especially when the input state (ρ, e_s) corresponds to a near-critical point or a near-pure state.
To overcome the possible convergence issues, when two successive sensible energy iterates $e_s^{(k-1)} = e_s(\rho, T^{(k-1)})$ and $e_s^{(k)} = e_s(\rho, T^{(k)})$ are around the target value e_s, that is to say $e_s \in \left[e_s^{(k-1)}, e_s^{(k)}\right]$, the zero-finding numerical method is switched to a Brent-like method. In more details, the following bounding values are introduced:

$$\begin{cases} e_s^{\inf} = \min\left(e_s^{(k-1)}, e_s^{(k)}\right), & e_s^{\sup} = \max\left(e_s^{(k-1)}, e_s^{(k)}\right), \quad (2.3.45a) \\ T^{\inf} = \min\left(T^{(k-1)}, T^{(k)}\right), & T^{\sup} = \max\left(T^{(k-1)}, T^{(k)}\right). \quad (2.3.45b) \end{cases}$$

The next iteration is then obtained by computing a Newton-Raphson step at the midpoint $T^{\mathrm{mid}} = \frac{T^{\inf} + T^{\sup}}{2}$, so that

$$T^{\mathrm{NR}} = T^{\mathrm{mid}} - \frac{e_s(\rho, T^{\mathrm{mid}}) - e_s}{\left.\frac{\partial e_s}{\partial T}\right|_\rho}. \tag{2.3.46}$$

The update is then taken as:

$$T^{(k+1)} = \begin{cases} T^{\mathrm{NR}} & \text{if } T^{\mathrm{NR}} \in \left[T^{\inf}, T^{\sup}\right], \\ T^{\mathrm{mid}} & \text{otherwise.} \end{cases} \tag{2.3.47}$$

Finally, the research interval is reduced as follows: if $e_s^{(k+1)} < e_s$, then $T^{\inf} = T^{(k+1)}$ and $e_s^{\inf} = e_s^{(k+1)}$; otherwise $T^{\sup} = T^{(k+1)}$ and $e_s^{\sup} = e_s^{(k+1)}$.

2.3.3 Approximate multicomponent two-phase equilibrium for Cubic EoS

2.3.3.1 Motivation and nature of the approximation

Because the target applications of the present work consist in simulating reactive flows, it is necessary to deal with multicomponent mixtures. Yet, the exact computation of a multiphase equilibrium in

the case of a multicomponent mixtures – which is detailed in section 2.4 – can become a tedious task and represent a heavy computational cost. Indeed, the computation of the equilibrium requires to search for the global minimum of a function of N_s variables to evaluate the stability of the single-phase mixture, and then requires an additional iterative method in N_s dimensions to find the stable multiphase state [Michelsen and Mollerup, 2004]. In this respect, the exact multiphase equilibrium computation for multicomponent flows, especially when going towards detailed chemical mechanisms for combustion, may become computationally out of range.

Furthermore, this work uses diffuse interface models (see section 3.3.2 for more details), in which the interface region where the two-phase states may be encountered, consists in an artificial mixture. The main requirement for this artificial mixture is to include a thermodynamic closure that guarantees the global hyperbolicity of the transport equations, as shown in Chapter 5.

This work then proposes an approximate equilibrium formulation that guarantees the hyperbolicity of the system while keeping an identical algorithm complexity for any number of components.

The approximated equilibrium consists in imposing that both phases have equal composition. In other words, the i^{th} species mass fraction within the liquid phase $Y_i^\ell = \frac{m_i^\ell}{m_\ell}$ and the species mass fraction within the vapour phase $Y_i^v = \frac{m_i^v}{m_v}$ are assumed to be equal $Y_i^\ell = Y_i^v$. Then, they are equal to the overall species mass fraction, and the approximated equilibrium can be summarized by the following assumption:

$$Y_i = Y_i^\ell = Y_i^v. \tag{2.3.48}$$

2.3.3.2 Approximate equilibrium condition

Starting from the former simplifying hypothesis, we now derive the equilibrium condition from considerations similar to section 2.3.1.4. We consider an isolated system containing two phases and N_s chemical species respecting hypothesis (2.3.48). The liquid phase properties are indexed by ℓ and the vapour phase properties by v. The mass, volume, energy and entropy of the system can be decomposed as

$$m_i = m_i^\ell + m_i^v \qquad \text{for all } i \in \{1..N_s\}, \tag{2.3.49a}$$
$$\mathcal{V} = \mathcal{V}_\ell + \mathcal{V}_v, \tag{2.3.49b}$$
$$\mathcal{E}_s = \mathcal{E}_{s,\ell} + \mathcal{E}_{s,v}, \tag{2.3.49c}$$
$$\mathcal{S} = \mathcal{S}_\ell + \mathcal{S}_v, \tag{2.3.49d}$$

where m_i^ℓ and m_i^v denote respectively the mass of the i^{th} species in the liquid and in the vapour phases. As in section 2.3.1.4, the system being isolated, the following differentials are zero:

$$\mathrm{d}m = \mathrm{d}m_\ell + \mathrm{d}m_v \;= 0 \tag{2.3.50a}$$
$$\mathrm{d}\mathcal{V} = \mathrm{d}\mathcal{V}_\ell + \mathrm{d}\mathcal{V}_v \;= 0 \tag{2.3.50b}$$
$$\mathrm{d}\mathcal{E}_s = \mathrm{d}\mathcal{E}_{s,\ell} + \mathrm{d}\mathcal{E}_{s,v} = 0 \tag{2.3.50c}$$

Writing the Gibbs relation (2.1.7) applied to each phase, one has

$$\begin{cases} \mathrm{d}\mathcal{E}_{s,\ell} = T_\ell\,\mathrm{d}\mathcal{S}_\ell - P_\ell\,\mathrm{d}\mathcal{V}_\ell + \displaystyle\sum_{i=1}^{N_s} g_{\ell,i}\,\mathrm{d}m_i^\ell, & \text{(2.3.51a)} \\ \mathrm{d}\mathcal{E}_{s,v} = T_v\,\mathrm{d}\mathcal{S}_v - P_v\,\mathrm{d}\mathcal{V}_v + \displaystyle\sum_{i=1}^{N_s} g_{v,i}\,\mathrm{d}m_i^v. & \text{(2.3.51b)} \end{cases}$$

Using hypothesis (2.3.48), the components mass within the phases verify

$$\begin{cases} m_i^\ell = Y_i^\ell m_\ell = Y_i m_\ell & \text{(2.3.52a)} \\ m_i^v = Y_i^v m_v = Y_i m_v. & \text{(2.3.52b)} \end{cases}$$

The global composition $\underline{\boldsymbol{Y}}$ of a closed system being constant, one has

$$\begin{cases} \mathrm{d}m_i^\ell = \mathrm{d}(Y_i m_\ell) = Y_i \,\mathrm{d}m_\ell & \text{(2.3.53a)} \\ \mathrm{d}m_i^v = \mathrm{d}(Y_i m_v) = Y_i \,\mathrm{d}m_v. & \text{(2.3.53b)} \end{cases}$$

Then, using the identities

$$\sum_{i=1}^{N_s} Y_i g_{\ell,i} = g_\ell \qquad \text{and} \qquad \sum_{i=1}^{N_s} Y_i g_{v,i} = g_v, \tag{2.3.54}$$

system (2.3.51) becomes

$$\begin{cases} \mathrm{d}\mathcal{E}_{s,\ell} = T_\ell \,\mathrm{d}\mathcal{S}_\ell - P_\ell \,\mathrm{d}\mathcal{V}_\ell + g_\ell \,\mathrm{d}m_\ell, & \text{(2.3.55a)} \\ \mathrm{d}\mathcal{E}_{s,v} = T_v \,\mathrm{d}\mathcal{S}_v - P_v \,\mathrm{d}\mathcal{V}_v + g_v \,\mathrm{d}m_v. & \text{(2.3.55b)} \end{cases}$$

The equilibrium condition corresponds to a maximum entropy state. Then, the total entropy differential is zero, which, combined with equations (2.3.50) and (2.3.51), corresponds to

$$(T_\ell - T_v)\,\mathrm{d}\mathcal{S}_\ell - (P_\ell - P_v)\,\mathrm{d}\mathcal{V}_\ell + (g_\ell - g_v)\,\mathrm{d}m_\ell = 0. \tag{2.3.56}$$

This relation must be verified for any transformation, hence the *simplified liquid-vapour equilibrium condition*:

$$\begin{cases} P_\ell = P_v, & \text{(2.3.57a)} \\ T_\ell = T_v, & \text{(2.3.57b)} \\ g_\ell = g_v. & \text{(2.3.57c)} \end{cases}$$

This criterion has eventually the same expression as criterion (2.3.16), except that it is now applied in the context of multicomponent mixtures.

2.3.3.3 Extended Clausius-Clapeyron relation

Applying the simplified equilibrium hypotheses allows to formulate a relation that links the derivatives of the quantities $P, T, \underline{\boldsymbol{Y}}$ together for two-phase states. As in paragraph 2.3.1.6, one can use the equilibrium condition (2.3.57) to obtain

$$\mathrm{d}g_\ell = \mathrm{d}g_v. \tag{2.3.58}$$

Developping the expression of the Gibbs energy (2.1.25d) for each phase yields

$$-s_\ell \,\mathrm{d}T + \frac{1}{\rho_\ell}\,\mathrm{d}P + \sum_{i=1}^{N_s} g_{\ell,i}\,\mathrm{d}Y_i = -s_v \,\mathrm{d}T + \frac{1}{\rho_v}\,\mathrm{d}P + \sum_{i=1}^{N_s} g_{v,i}\,\mathrm{d}Y_i, \tag{2.3.59}$$

which provides an *extended Clausius-Clapeyron relation* for multicomponent mixture assuming simplified equilibrium, formulated as

$$\mathrm{d}T = \frac{\rho_\ell - \rho_v}{\rho_\ell \rho_v \,(s_v - s_\ell)}\,\mathrm{d}P + \sum_{i=1}^{N_s} \frac{g_{v,i} - g_{\ell,i}}{s_v - s_\ell}\,\mathrm{d}Y_i. \tag{2.3.60}$$

The existence of such relation is another advantage of the simplified equilibrium, since *there exists no equivalent analytic relation for the exact multicomponent equilibrium.*

2.3.3.4 Practical computation of the equilibrium

The practical computation of the equilibrium is identical to the single-species one. Indeed, the reduced variables ν, θ, π defined in equation (2.3.29) allow, even for a multicomponent mixture, to derive a unique formulation of the equilibrium, regardless of the mixture composition.

Under the simplified equilibrium hypothesis (2.3.48), the stability condition of a phase is similar to the single-component case. Thus, the methods presented in paragraph 2.3.2.2 for the different input data can be directly transposed to the multi-component case, in order to compute the simplified equilibrium.

2.4 Exact two-phase multicomponent equilibrium

In this section, the exact multicomponent two-phase equilibrium computation is described. For a comprehensive description and review of the methods used to find the multiphase multicomponent equilibrium, the reader is referred to [Michelsen and Mollerup, 2004]. Part of the work presented in this section, namely the *tangent plane distance* stability analysis and the equilibrium computation for a given state $(T, P, \underline{\boldsymbol{X}})$ was implemented in collaboration with Thomas Laroche, Ph.D student at CERFACS (Toulouse), whose contribution is warmly acknowledged.

2.4.1 Equilibrium formulation

2.4.1.1 Equilibrium condition

As for the previous equilibrium characterizations, a closed and isolated two-phase system Ω is considered. The global system quantities can again be decomposed into

$$m_i = m_i^\ell + m_i^v \qquad \text{for all } i \in \{1..N_s\}\,, \tag{2.4.1a}$$
$$\mathcal{V} = \mathcal{V}_\ell + \mathcal{V}_v, \tag{2.4.1b}$$
$$\mathcal{E}_s = \mathcal{E}_{s,\ell} + \mathcal{E}_{s,v}, \tag{2.4.1c}$$
$$\mathcal{S} = \mathcal{S}_\ell + \mathcal{S}_v. \tag{2.4.1d}$$

As in section 2.3.3.2, the system Ω being isolated, the following differentials are zero:

$$\mathrm{d}m_i = \mathrm{d}m_i^\ell + \mathrm{d}m_i^v = 0 \qquad \text{for all } i \in \{1..N_s\}\,, \tag{2.4.2a}$$
$$\mathrm{d}\mathcal{V} = \mathrm{d}\mathcal{V}_\ell + \mathrm{d}\mathcal{V}_v = 0, \tag{2.4.2b}$$
$$\mathrm{d}\mathcal{E}_s = \mathrm{d}\mathcal{E}_{s,\ell} + \mathrm{d}\mathcal{E}_{s,v} = 0. \tag{2.4.2c}$$

Writing the gibbs relation (2.1.7) applied to each phase, one has

$$\begin{cases} \mathrm{d}\mathcal{E}_{s,\ell} = T_\ell\,\mathrm{d}\mathcal{S}_\ell - P_\ell\,\mathrm{d}\mathcal{V}_\ell + \displaystyle\sum_{i=1}^{N_s} g_{\ell,i}\,\mathrm{d}m_i^\ell, & \text{(2.4.3a)} \\ \mathrm{d}\mathcal{E}_{s,v} = T_v\,\mathrm{d}\mathcal{S}_v - P_v\,\mathrm{d}\mathcal{V}_v + \displaystyle\sum_{i=1}^{N_s} g_{v,i}\,\mathrm{d}m_i^v. & \text{(2.4.3b)} \end{cases}$$

Since the thermodynamic equilibrium of the isolated system Ω is reached at maximum entropy, $\mathrm{d}\mathcal{S} = 0$, and combining $\big[(2.4.3a) + (2.4.3b)\big]$ with (2.4.2) yields

$$(T_\ell - T_v)\,\mathrm{d}\mathcal{S}_\ell - (P_\ell - P_v)\,\mathrm{d}\mathcal{V}_\ell + \sum_{i=1}^{N_s} \big(g_{\ell,i} - g_{v,i}\big)\,\mathrm{d}m_i^\ell = 0. \tag{2.4.4}$$

This relation must be verified for any transformation $(\mathrm{d}\mathcal{S}_\ell, \mathrm{d}\mathcal{V}_\ell, \mathrm{d}m_i^\ell)$, hence the *liquid-vapour equilibrium necessary condition*:

$$\begin{cases} P_\ell = P_v, & \text{(2.4.5a)} \\ T_\ell = T_v, & \text{(2.4.5b)} \\ g_i^\ell = g_i^v \qquad \text{for all } i \in \{1..N_s\}\,. & \text{(2.4.5c)} \end{cases}$$

Note that this is only a necessary condition: different compositions may verify this relation. Indeed, the condition $\mathrm{d}\mathcal{S} = 0$ is only a necessary condition for the composition to maximize the entropy. The only globally stable equilibrium state is characterized by the one being the global minimum of the Gibbs energy.

2.4.1.2 Alternative formulation of the equilibrium

The two-phase multicomponent equilibrium condition can be reformulated in a convenient way for computing the equilibrium compositions, by introducing the K-factors. At a given temperature and pressure, the stability of a two-phase mixture (2.4.5) can be expressed in terms of the fugacities, and summarized into

$$\begin{cases} \hat{f}_i^\ell(T, P, \underline{\boldsymbol{X}}^\ell) = \hat{f}_i^v(T, P, \underline{\boldsymbol{X}}^v) \qquad \text{for all } i \in \{1...N_s\}\,, & \text{(2.4.6a)} \\ x_\ell \underline{\boldsymbol{X}}^\ell + (1 - x_\ell)\underline{\boldsymbol{X}}^v = \underline{\boldsymbol{X}}, & \text{(2.4.6b)} \\ \displaystyle\sum_{i=1}^{N_s} \left(X_i^\ell - X_i^v\right) = 0, & \text{(2.4.6c)} \end{cases}$$

where the last equation expresses the fact that mole fractions of liquid and vapour phases sum to unity. The K-factors are now defined as

$$K_i = \frac{X_i^v}{X_i^\ell}, \tag{2.4.7}$$

so that equation (2.4.6b) can be rewritten as

$$\begin{cases} X_i^\ell = \dfrac{X_i}{x_\ell + (1 - x_\ell)K_i}, & \text{(2.4.8a)} \\ X_i^v = \dfrac{K_i X_i}{x_\ell + (1 - x_\ell)K_i}. & \text{(2.4.8b)} \end{cases}$$

Using the fugacity coefficients φ, since $\hat{f}_i^\ell = X_i^\ell \varphi_i^\ell P$ and $\hat{f}_i^v = X_i^v \varphi_i^v P$, the equilibrium condition (2.4.6a) can be combined to the definition of the K-factors (2.4.7) to yield

$$K_i = \frac{\varphi_i^\ell}{\varphi_i^v}. \tag{2.4.9}$$

and (2.4.6c) becomes

$$\sum_{i=1}^{N_s} \frac{X_i\,(K_i - 1)}{x_\ell + (1 - x_\ell)\,K_i} = 0. \tag{2.4.10}$$

These last two equations characterize the equilibrium for a given $(T, P, \underline{\boldsymbol{X}})$. Equation (2.4.10) is called the *Rachford-Rice* equation, and will be useful in finding the equilibrium, which is the purpose of the next section.

2.4.2 Stability analysis

2.4.2.1 Gibbs' *tangent plane condition* of stability

According to paragraph 2.4.1.1, a mathematical formulation for the stability test must be formulated. In order to evaluate the stability of a one-phase mixture for a given temperature, pressure and molar composition $(T, P, \underline{\boldsymbol{X}})$, one can consider the Gibbs energy variation that would yield the formation of an infinitesimal amount $\delta n_{\phi'}$ moles of a new phase ϕ' of composition $\underline{\boldsymbol{\xi}}$, where ξ_i is the mole fraction of the i^{th} component within phase ϕ'. This transformation is depicted in Figure 2.11. As it is convenient here to work with molar quantities instead of mass-specific quantities, the *chemical potential* $\left(\mu_i^\phi\right)_{i\in[\![1,N_s]\!];\phi=\ell,v}$ of each species is preferred to its mass-specific counterpart that is the specific Gibbs energy $\left(g_i^\phi\right)_{i\in[\![1,N_s]\!];\phi=\ell,v}$. The definition of the chemical potential is given in equation (2.1.21a).

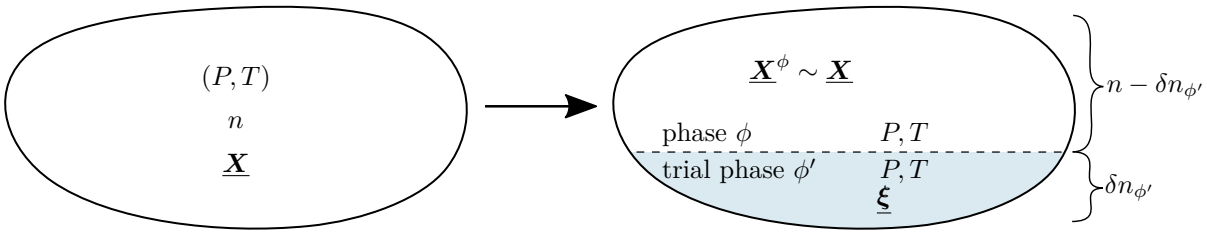

Figure 2.11: Transformation corresponding to the formation of $\delta n_{\phi'}$ of a *trial phase* ϕ'.

The change in the Gibbs energy of the system due to this isothermal and isobaric transformation is:

$$\delta G = \delta n_{\phi'} \sum_{i=1}^{N_s} \xi_i \left[\mu_i(T,P,\underline{\boldsymbol{\xi}}) - \mu_i(T,P,\underline{\boldsymbol{X}})\right]. \tag{2.4.11}$$

The single-phase solution is known to be thermodynamically stable if it is the composition that minimizes the system Gibbs energy. Then, for the one-phase state to be stable, the variation of Gibbs energy due to the formation of phase ϕ' should be necessarily positive.

This allows to formulate the Gibbs' *tangent plane condition* of stability for a single-phase solution [Michelsen and Mollerup, 2004]: the single-phase composition stability is characterized by

$$\forall\ \underline{\boldsymbol{\xi}}, \qquad \sum_{i=1}^{N_s} \xi_i \left[\mu_i(T,P,\underline{\boldsymbol{\xi}}) - \mu_i(T,P,\underline{\boldsymbol{X}})\right] \geq 0. \tag{2.4.12}$$

2.4.2.2 The tangent plane distance

From the previous section, it appears relevant to define the *tangent plane distance* function TPD as a function of the trial phase composition $\underline{\boldsymbol{\xi}}$ for a given initial state $(T, P, \underline{\boldsymbol{X}})$, as:

$$\mathrm{TPD}(\underline{\boldsymbol{\xi}}) = \sum_{i=1}^{N_s} \xi_i(\mu_i(T,P,\underline{\boldsymbol{\xi}}) - \mu_i(T,P,\underline{\boldsymbol{X}})). \tag{2.4.13}$$

The TPD function corresponds to the relative position of the Gibbs energy function with respect to its tangent plane at $(T, P, \underline{\boldsymbol{X}})$, as depicted in Figure 2.12a.

Note that a dimensionless version of the TPD function, $\mathrm{tpd} = \frac{\mathrm{TPD}}{\mathcal{R}T}$, can be defined in terms of the fugacity coefficient:

$$\mathrm{tpd}(\underline{\boldsymbol{\xi}}) = \frac{\mathrm{TPD}(\underline{\boldsymbol{\xi}})}{\mathcal{R}T} = \sum_{i=1}^{N_s} \xi_i \left[\ln(\xi_i) + \ln\left(\varphi_i(T,P,\underline{\boldsymbol{\xi}})\right) - d_i\right], \tag{2.4.14}$$

with $d_i = \ln(X_i) + \ln\left(\varphi_i(T,P,\underline{\boldsymbol{X}})\right)$.

The TPD function allows for a convenient graphical interpretation of the stability test for a binary mixture. To this purpose, if one defines the *Gibbs energy of mixing* $G^{\text{mix}}(\xi_1)$ of a solution in the state (T,P) and composition $(\xi_1, 1-\xi_1)$ as

$$G^{\text{mix}}(\xi_1) = \xi_1\left[\mu_1(T,P,\xi_1) - \mu_1^0(T,P)\right] + (1-\xi_1)\left[\mu_2(T,P,\xi_1) - \mu_2^0(T,P)\right], \tag{2.4.15}$$

where $\mu_i^0(T,P) = \mu_i(T,P,\xi_i=1) = G(T,P,\xi_i=1)$ denotes the value of the chemical potential of the pure component i in the state (T,P). Note that the minimization of Gibbs energy G is equivalent to the minimization of the Gibbs energy of mixing G^{mix}, since the latter is equal to the former shifted by the quantity $\mu_2^0 + \xi_1(\mu_1 - \mu_2)$. This linear modification obviously does not modify the tpd values and, subsequently, preserves the stability analysis conclusions. The introduction of the Gibbs energy of mixing is just more convenient for graphical representation purposes.

A graphical representation of the tpd test is provided in Figure 2.12. The tangent plane being a hyperplane of a N_s-dimension space, it corresponds to a straight line in the binary mixture case. This illustrative tpd test shows an unstable case as negative values of the tpd-function are found in Figure 2.12a.

It appears in Figure 2.12b that the two-phase equilibrium states correspond to the convex hull of the Gibbs energy of mixing.

2.4.3 Computing the equilibrium at given $(T, P, \boldsymbol{X})$

2.4.3.1 Stability test

2.4.3.1.1 Description of the method

Before attempting to compute a two-phase equilibrium state, it is necessary to verify the stability of the single-phase state $(T,P,\underline{\boldsymbol{X}})$. The tpd stability analysis can be reduced to the evaluation of the tpd function sign at its minima. The strategy then consists in the following steps:

i) Find the location of each local minimum of the tpd function

ii) Evaluate the sign of the tpd function at each local minimum

The search for the minimum of $\text{tpd}(\underline{\boldsymbol{\xi}})$ for $\underline{\boldsymbol{\xi}} \in [0,1]$ must obey the following constraint:

$$\sum_{i=1}^{N_s} \xi_i - 1 = 0. \tag{2.4.16}$$

This constraint can be addressed by introducing the Lagrangian function $\mathcal{L}$:

$$\mathcal{L}(\underline{\boldsymbol{\xi}},\lambda) = \text{tpd}(\underline{\boldsymbol{\xi}}) - \lambda\left(\sum_{i=1}^{N_s}\xi_i - 1\right) = \sum_{i=1}^{N_s}\xi_i(\ln\xi_i + \ln\varphi_i - d_i) - \lambda\left(\sum_{i=1}^{N_s}\xi_i - 1\right). \tag{2.4.17}$$

The stationary points of function $\mathcal{L}$, i.e. its minima, maxima and saddle points, represent the stationary points of the tpd and hence contain the tpd local minima. The partial derivatives of $\mathcal{L}$ at stationary points are such that :

$$\begin{cases} \dfrac{\partial\mathcal{L}}{\partial\xi_i} = \ln\xi_i + \ln\varphi_i - d_i + 1 - \lambda, \quad i = 1,2,...,N_s, & \text{(2.4.18a)} \\ \dfrac{\partial\mathcal{L}}{\partial\lambda} = -\displaystyle\sum_{i=1}^{N_s}\xi_i + 1 = 0. & \text{(2.4.18b)} \end{cases}$$

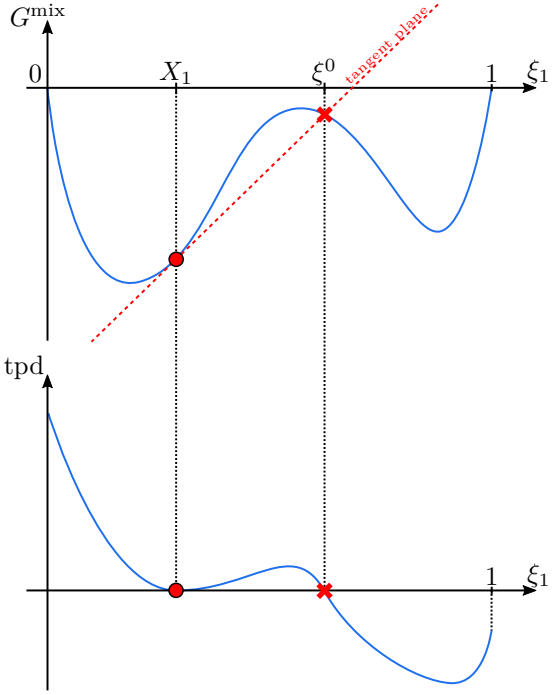

(a) Graphical representation of the tpd function which tests the stability of the composition $\underline{\boldsymbol{X}} = (X_1, 1 - X_1)$. This state is unstable, as there exist compositions (actually any composition with $\xi_1 > \xi^0$) for which the tpd function takes negative values. An example of a two-phase state minimizing the Gibbs energy, corresponding to this example, is displayed in the top Figure 2.12b.

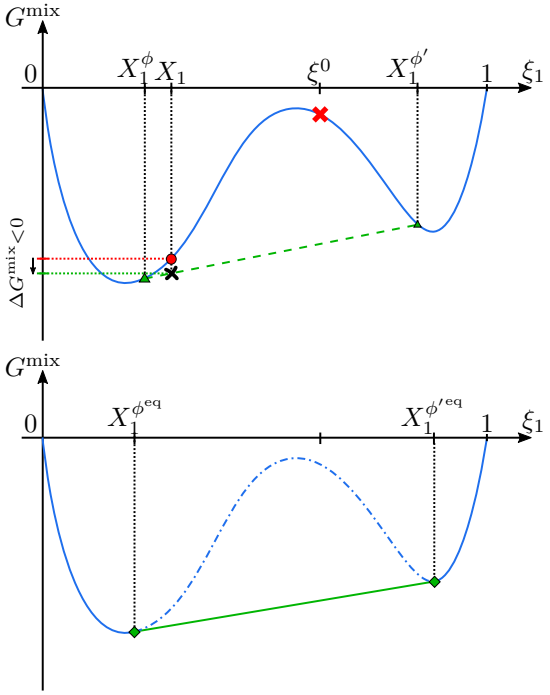

(b) **Top diagram:** an example of two-phase mixture of respective compositions $\underline{\boldsymbol{X}}^{\phi}$ and $\underline{\boldsymbol{X}}^{\phi'}$. The thick black cross at abscissa X_1 represents the two-phase mixture Gibbs energy of mixing. **Bottom diagram:** the equilibrium Gibbs energy of mixing is represented in solid lines. The green region corresponds to a two-phase mixture. The dot-dashed line shows the unstable one-phase region. The equilibrium compositions of the two-phase mixtures are $\underline{\boldsymbol{X}}^{\phi^{\text{eq}}}$ and $\underline{\boldsymbol{X}}^{\phi'^{\text{eq}}}$.

Figure 2.12: Graphical representation of the stability analysis and two-phase equilibrium for a binary mixture.

Finally, at the stationary points of $\mathcal{L}$ denoted $(\underline{\boldsymbol{\xi}}^{\text{S}}, \lambda^{\text{S}})$, the tpd-function verifies

$$\text{tpd}(\underline{\boldsymbol{\xi}}^{\text{S}}) = \sum_{i=1}^{N_s} \xi_i^{\text{S}} (\ln \xi_i^{\text{S}} + \ln \varphi_i - d_i) = \sum_{i=1}^{N_s} \xi_i^{\text{S}} (\lambda^{\text{S}} - 1) = \lambda^{\text{S}} - 1. \tag{2.4.19}$$

The stability condition is then that for all stationary points of $\mathcal{L}$, $\lambda^{\text{S}} \geq 1$.

In practice, an unconstrained formulation is actually preferred. Instead of working with the mole fractions $\underline{\boldsymbol{\xi}}$ of the incipient phase, its extensive composition $\underline{\boldsymbol{n}}' = \{n_i'\}_{i=1\ldots N_s}$ (in terms of amount of substance) can be used directly, so that $n' \underline{\boldsymbol{\xi}} = \underline{\boldsymbol{n}}'$, with $n' = \sum_{i=1}^{N_s} n_i'$. The function tm is defined as

$$\text{tm}(\underline{\boldsymbol{n}}') = (1 - n' + n' \ln (n')) + n' \text{tpd}\left(\frac{\underline{\boldsymbol{n}}'}{n'}\right), \tag{2.4.20a}$$

$$\text{tm}(\underline{\boldsymbol{n}}') = 1 + \sum_{i=1}^{N_s} n_i' \left(\ln (n_i') + \ln (\varphi_i(\underline{\boldsymbol{n}}')) - d_i - 1\right). \tag{2.4.20b}$$

The stationary points $\underline{\boldsymbol{n}}'^{\mathrm{S}}$ of tm satisfy :

$$\frac{\partial \mathrm{tm}}{\partial n_i'} = \ln\left(n_i'^{\mathrm{S}}\right) + \ln\left(\varphi_i\left(\underline{\boldsymbol{n}}'^{\mathrm{S}}\right)\right) - d_i = 0, \quad i = 1, 2, ..., N_s. \tag{2.4.21}$$

At the stationary points we obtain :

$$\mathrm{tm}\left(\underline{\boldsymbol{n}}'^{\mathrm{S}}\right) = 1 - n'^{\mathrm{S}}. \tag{2.4.22}$$

So that finally, the condition for stability is that at each stationary points of tm, the total amount of substance is such that $n' \leq 1$. In the scope of this work, the research of the stationary points of tm is made by a *successive substitution method*. From a first-guess trial composition $\underline{\boldsymbol{n}}'^{(0)}$, the update for the composition at iteration $(k+1)$ is obtained from

$$\ln\left(n_i'^{(k+1)}\right) = d_i - \ln\left(\varphi_i\left(\underline{\boldsymbol{n}}'^{(k)}\right)\right), \tag{2.4.23}$$

for $i \in \{1...N_s\}$. The values of the first guess are computed, as recommended in [Michelsen and Mollerup, 2004] and used in [Matheis and Hickel, 2018] using Wilson's approximation of the K-factors, which reads

$$\ln\left(K_i\right) = \ln\left(\frac{P_{c,i}}{P}\right) + 5.373\left(1+\omega_i\right)\left(1 - \frac{T_{c,i}}{T}\right). \tag{2.4.24}$$

This approximation is based on a vapour pressure correlation of the form $\ln(P) = A - \frac{B}{T}$ (more details can be found in [Michelsen and Mollerup, 2004], Chapter 10). Two initial guesses are then used:

$$n_i' = X_i K_i, \qquad \text{and} \qquad n_i' = \frac{X_i}{K_i}. \tag{2.4.25}$$

2.4.3.1.2 Example of stability test

In order to illustrate the results from TPD stability tests, the stability region of a H_2-N_2 mixture is now compared with results from [Matuszewski, 2011]. The results are presented in figure 2.13, and are correspond properly to the expected results.

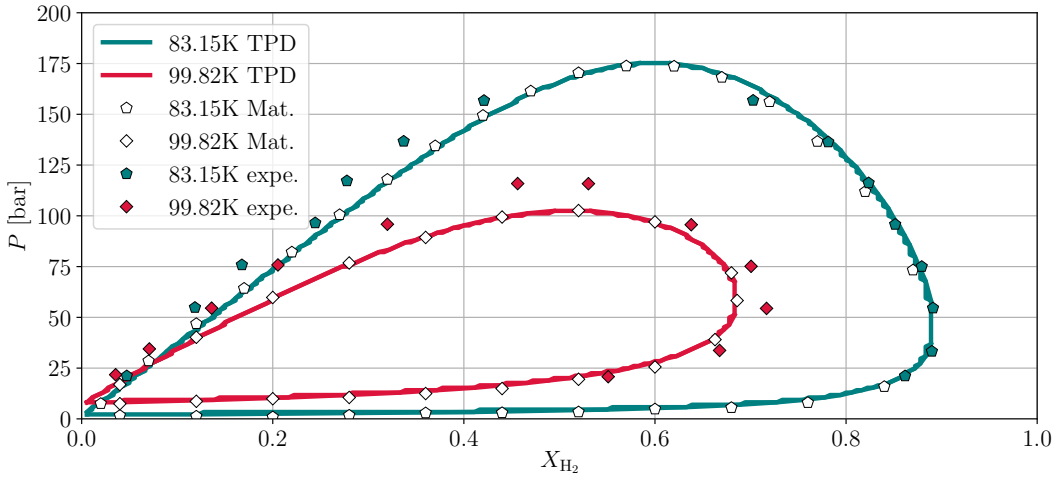

Figure 2.13: Stability region of a H2-N2 mixture obtained from the TPD analysis. The results from the TPD analysis are displayed in solid lines. Comparison data consist in experimental points (filled symbols) and computation results (white symbols) both taken from [Matuszewski, 2011].

2.4.3.1.3 Remark on the stability of multicomponent mixtures

The thermodynamic instabilities of single-component mixtures are of mechanical nature, in the sense that they correspond to a negative isothermal compressibility coefficient β. For multicomponent mixtures, the instabilities may also be of chemical nature, in the sense that they can be driven by variations of the chemical composition of the phases.

This higher complexity in the instabilities of multicomponent mixtures results in more complex phase behaviours than for the single-component instabilities. In this respect, [Van Konynenburg and Scott, 1980] showed that the cubic equations of state are able to predict the various phase stability patterns in the case of binary mixtures, and classified them into different types. This classification is summarized in figure 2.14, which shows a projection on the (T, P) plane of the stability regions for binary mixtures. The white-filled areas correspond to regions where the mixture is stable for any composition. Blue-filled areas correspond to thermodynamic points (T, P) for which there exist mixture compositions that lead to liquid-vapour phase separation. Red-filled areas correspond to thermodynamic points for which there exist mixture compositions that lead to liquid-liquid phase separation (non-miscible liquids). The blue lines correspond to the saturation curves for the pure components (denoted 1 and 2). The red lines denote thermodynamic points along which there exist compositions that lead to the coexistence of three phases (two liquid phases and one vapour phase).

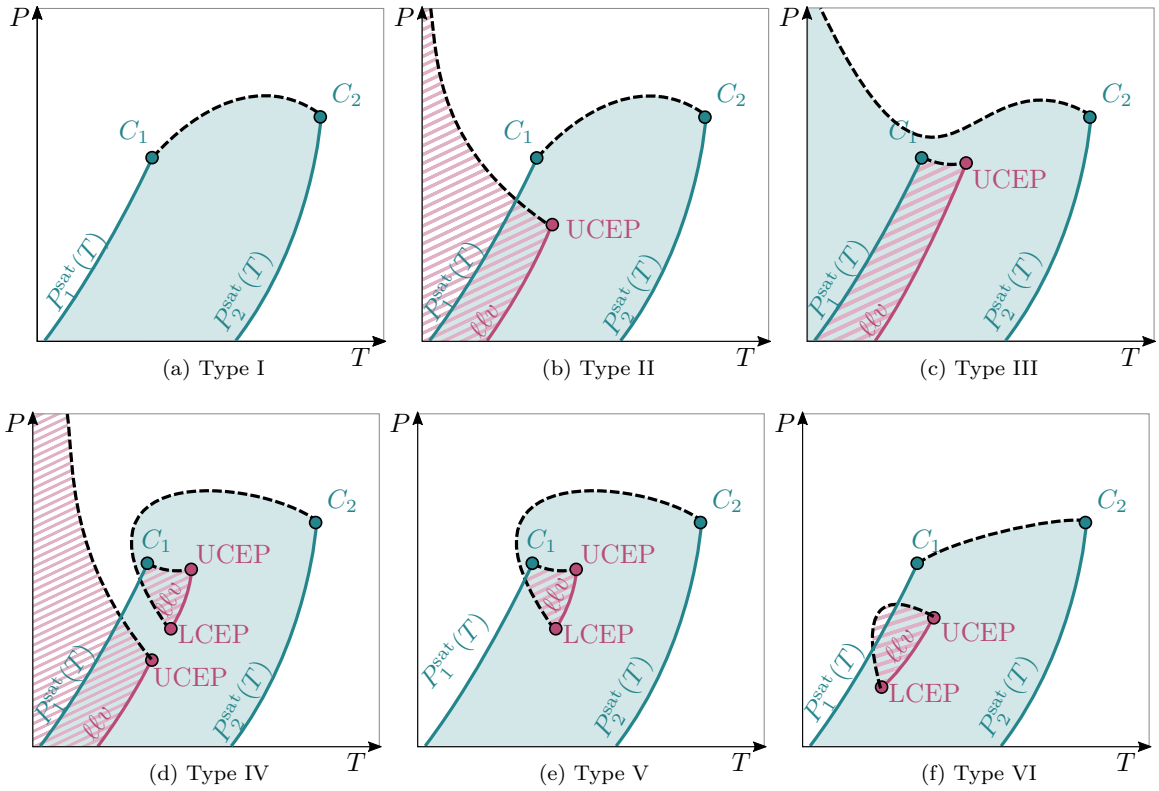

Figure 2.14: Classification of the patterns of thermodynamic instability regions of binary mixtures. Projection on the (T, P) plane of the (X_1, T, P) three-dimensional phase stability diagram. $\ell\ell v$ denote denotes the line along which two liquid phases and a vapour phase can coexist for certain compositions. UCEP stands for *upper critical end point* and LCEP for *lower critical end point*, the points where two of the three coexisting phase become identical. For more details, the reader is referred to [Prausnitz et al., 1998].

More details about the different instability patterns can be found in chapter 12 of [Prausnitz et al., 1998].

It is worth noting that the implemented multicomponent solver for the present work is restricted to equilibriums between two phases, so that three-phase coexistence points are not considered at the moment. The reader is referred to [Michelsen and Mollerup, 2004] for more details on N-phase stability analysis and equilibrium computations.

2.4.3.2 Finding the equilibrium two-phase composition for unstable states

Once an unstable state has been spotted, it is necessary to find the compositions of the two equilibrium phases. This can be achieved by means of a *successive substitution method* using the K-factors defined in equation (2.4.7). Starting from an initial guess for the K-factors, $K_i^{(0)}$, the following iterative procedure is used to find the equilibrium.

From values of the K-factors $K_i^{(k)}$ obtained at iteration (k), the estimates of the phases composition $\underline{\boldsymbol{X}}^{\ell(k)}$ and $\underline{\boldsymbol{X}}^{v(k)}$ can be computed by solving the Rachford-Rice equation (2.4.10). This is done by finding the zero of function $\mathrm{RR}(x_\ell)$, defined by:

$$\mathrm{RR}(x_\ell) = \sum_{i=1}^{N_s} \frac{X_i \left(K_i^{(k)} - 1\right)}{x_\ell + (1 - x_\ell)\, K_i^{(k)}}. \tag{2.4.26}$$

The derivative of this function reads

$$\mathrm{RR}'(x_\ell) = \sum_{i=1}^{N_s} \frac{X_i \left(K_i^{(k)} - 1\right)^2}{\left[x_\ell + (1 - x_\ell)\, K_i^{(k)}\right]^2} > 0. \tag{2.4.27}$$

This monotonically increasing function then has one zero for $x_\ell \in [0,1]$ provided $\mathrm{RR}(0) < 0$ and $\mathrm{RR}(1) > 0$.

The solution x_ℓ of the Rachford-Rice equation is then used to compute the phases compositions as

$$\begin{cases} X_i^{\ell(k)} = \dfrac{X_i}{x_\ell + (1 - x_\ell) K_i^{(k)}}, & \text{(2.4.28a)} \\ X_i^{v(k)} = \dfrac{X_i K_i^{(k)}}{x_\ell + (1 - x_\ell) K_i^{(k)}}. & \text{(2.4.28b)} \end{cases}$$

Note that the interval in which the solution should be searched for can be reduced using the consistency of phases' mole fractions $X_i^\ell \leq 1$ and $X_i^v \leq 1$. Indeed, for any component i with a K-factor smaller than unity, the consistency of the liquid mole fraction gives

$$x_\ell \geq \frac{X_i - K_i^{(k)}}{1 - K_i^{(k)}}, \tag{2.4.29a}$$

and the one of the vapour mole fraction

$$x_\ell \leq \frac{K_i^{(k)}\,(1 - X_i)}{K_i^{(k)} - 1}. \tag{2.4.29b}$$

The initial bounds for the zero-finding are then

$$\begin{cases} x_\ell^{\min} = \max\left(\max\limits_{i=1..N_s}\left\{\dfrac{X_i - K_i^{(k)}}{1 - K_i^{(k)}}\right\}, 0\right), & \text{(2.4.30a)} \\ x_\ell^{\max} = \min\left(\min\limits_{i=1..N_s}\left\{\dfrac{K_i^{(k)}\,(1 - X_i)}{K_i^{(k)} - 1}\right\}, 1\right). & \text{(2.4.30b)} \end{cases}$$

If $\mathrm{RR}(x_\ell^{\min}) > 0$ or $\mathrm{RR}(x_\ell^{\max}) < 0$, the problem has no solution within $[0, 1]$ and the computation fails for the current value of the K-factors. A better initial guess for the K-factors is then required. Note that for the practical cases computed in the scope of this work, there have always been at least one initial guess $\underline{\boldsymbol{K}}^{(0)}$, defined from Wilson's K-factors (2.4.24) that achieved convergence.

If one has the conform inequalities $\mathrm{RR}(x_\ell^{\min}) < 0$ or $\mathrm{RR}(x_\ell^{\max}) > 0$, these quantities are used as initial bounds for the iterative zero-finding method. It is then successively updated by computing a Newton step from the midpoint value $x_\ell^{\mathrm{new}} = x_\ell - \frac{\mathrm{RR}(x_\ell)}{\mathrm{RR}'(x_\ell)}$, with $x_\ell = \frac{x_\ell^{\min} + x_\ell^{\max}}{2}$. If $\mathrm{RR}(x_\ell^{\mathrm{new}}) < 0$, then $x_\ell^{\min}$ is updated to $x_\ell^{\min} = x_\ell^{\mathrm{new}}$. Otherwise, $x_\ell^{\max}$ is updated to $x_\ell^{\max} = x_\ell^{\mathrm{new}}$, until a convergence criterion is met. The global *successive substitution method* is convergent provided the initial guesses are good enough. For more details about convergence, the reader is referred to Chapter 10 of [Michelsen and Mollerup, 2004].

2.4.4 Computing the equilibrium at given $(\rho, e_s, \boldsymbol{X})$

This section describes the practical implementation of the equilibrium within the hyperbolic solver, that allows to retrieve the thermodynamic equilibrium state from the transported conservative variables. In order to retrieve the thermodynamic equilibrium state from given $(\rho, e_s, \underline{\boldsymbol{X}})$, an *outer-loop* based on a Newton-Raphson algorithm is used.

2.4.4.1 Preliminary checks

2.4.4.1.1 The case of single-component and quasi-single-component mixtures

Before effectively applying the iterative solver to search for a possible two-phase equilibrium, the maximum value of the species mole fractions $X_{\max} = \max_{i \in [1, N_s]} \{X_i\}$ is computed. The mixture composition is considered to be very close to a single-component mixture if

$$X_{\max} > 1 - \epsilon_{1\mathrm{c}}, \tag{2.4.31}$$

with $\epsilon_{1\mathrm{c}}$ a threshold value typically set to $\epsilon_{1\mathrm{c}} = 10^{-4}$ in the present work. In this case, the exact multicomponent equilibrium is not computed. Instead, the approximate thermodynamic equilibrium of section 2.3.3 is considered. This allows to save time and also to avoid convergence issue, since in practice the exact multicomponent equilibrium computation is observed to have difficulties to converge when the mixture is very close to a single-component one. The stability test for approximate equilibrium is then applied and, if the mixture is found to be unstable, the approximate two-phase equilibrium is computed.

Note that this differs from the strategy of [Matheis and Hickel, 2018], who simply assume the phase to be stable when condition (2.4.31) is verified. This may yield the wrong fluid state for example if the flow is such that a single-component region undergoes cavitation. Conversely, the method presently described allows to find any unstable state, whether the fluid is a single-component or multicomponent mixture.

2.4.4.1.2 Evaluating the stability of the single-phase solution

If condition (2.4.31) is not met, the single-phase state $T^{\text{1-phase}}, P^{\text{1-phase}}$ corresponding to the given dataset $(\rho, e_s, \underline{\boldsymbol{X}})$ is computed. Then, the stability test of section 2.4.3.1.1 is applied to the obtained state $(T^{\text{1-phase}}, P^{\text{1-phase}}, \underline{\boldsymbol{X}})$. If the mixture is stable, the single-phase solution is kept. Otherwise, the two-phase state at equilibrium must be computed, by means of an iterative procedure. This is described in the following.

2.4.4.2 Iterative loop

2.4.4.2.1 First guess

An initial guess $\left(T^{(0)}, P^{(0)}, \underline{\boldsymbol{X}}^{(0)}\right)$ of the fluid state is used, typically taken from the previous iteration n:

$$\left(T^{(0)}, P^{(0)}, \underline{\boldsymbol{X}}^{(0)}\right) = \left(T^{n}, P^{n}, \underline{\boldsymbol{X}}^{n}\right). \tag{2.4.32}$$

2.4.4.2.2 Iterations

A two-dimensional Newton-Raphson iterative strategy is then applied. The objective function considered is

$$f^{\text{obj}}\left(\begin{bmatrix} T^{(k)} \\ P^{(k)} \end{bmatrix}\right) = \begin{bmatrix} \rho\left(T^{(k)}, P^{(k)}, \underline{\boldsymbol{X}}^{n+1}\right) - \rho^{n+1} \\ e_s\left(T^{(k)}, P^{(k)}, \underline{\boldsymbol{X}}^{n+1}\right) - e_s^{n+1} \end{bmatrix}, \tag{2.4.33}$$

where $\rho\left(T^{(k)}, P^{(k)}, \underline{\boldsymbol{X}}^{n+1}\right)$ and $e_s\left(T^{(k)}, P^{(k)}, \underline{\boldsymbol{X}}^{n+1}\right)$ are the two-phase mixture density and sensible energy, obtained from the equilibrium computation of section 2.4.3.2, applied to the current iteration state $\left(T^{(k)}, P^{(k)}, \underline{\boldsymbol{X}}^{n+1}\right)$.

The Jacobian matrix $\mathcal{J}^{\text{obj}}$ of the objective function f^{obj} is computed numerically, as no analytic formulation for this function is available. It reads

$$\mathcal{J}^{\text{obj}} \approx \begin{bmatrix} \frac{\rho\left(T^{(k)}+\Delta T, P^{(k)}, \underline{\boldsymbol{X}}^{n+1}\right) - \rho\left(T^{(k)}-\Delta T, P^{(k)}, \underline{\boldsymbol{X}}^{n+1}\right)}{2\Delta T} & \frac{\rho\left(T^{(k)}, P^{(k)}+\Delta P, \underline{\boldsymbol{X}}^{n+1}\right) - \rho\left(T^{(k)}, P^{(k)}-\Delta P, \underline{\boldsymbol{X}}^{n+1}\right)}{2\Delta P} \\ \frac{e_s\left(T^{(k)}+\Delta T, P^{(k)}, \underline{\boldsymbol{X}}^{n+1}\right) - e_s\left(T^{(k)}-\Delta T, P^{(k)}, \underline{\boldsymbol{X}}^{n+1}\right)}{2\Delta T} & \frac{e_s\left(T^{(k)}, P^{(k)}+\Delta P, \underline{\boldsymbol{X}}^{n+1}\right) - e_s\left(T^{(k)}, P^{(k)}-\Delta P, \underline{\boldsymbol{X}}^{n+1}\right)}{2\Delta P} \end{bmatrix}. \tag{2.4.34}$$

2.4.4.2.3 Final state

The solver iterates until the following criterion is fulfilled:

$$\begin{cases} \dfrac{\rho\left(T^{(k)}, P^{(k)}, \underline{\boldsymbol{X}}^{n+1}\right) - \rho^{n+1}}{\rho^{n+1}} < \epsilon, & \text{(2.4.35a)} \\ \dfrac{e_s\left(T^{(k)}, P^{(k)}, \underline{\boldsymbol{X}}^{n+1}\right) - e_s^{n+1}}{e_s^{n+1}} < \epsilon, & \text{(2.4.35b)} \end{cases}$$

with ϵ a convergence threshold.

2.4.5 Illustration of the different equilibrium computations

2.4.5.1 H_2-O_2 mixture

We now consider a H_2-O_2 interface, for which we compute both the exact and approximate equilibriums. The pressure is set to $P = 10$ bar, as this will be the operating pressure for simulations of Chapter 6. The input profile for the density and species is given as:

$$\begin{cases} \rho Y_{H_2}(x) = \rho^0_{H_2}\left[1 - f_\rho(x)\right], & \text{(2.4.36a)} \\ \rho Y_{O_2}(x) = \rho^0_{O_2} f_\rho(x), & \text{(2.4.36b)} \end{cases}$$

with the values $\rho^0_{H_2} = 0.8$ kg/m^3 and $\rho^0_{O_2} = 1200$ kg/m^3. The profile f_ρ is given by:

$$f_\rho(x) = \frac{1}{2}\left[1 + \mathrm{erf}\left(10\left(x - 1/2\right)\right)\right], \tag{2.4.37}$$

where erf is the *error function*, defined as

$$\mathrm{erf}(x) = \frac{1}{\sqrt{\pi}} \int_{-x}^{x} e^{-\tau^2}\, \mathrm{d}\tau. \tag{2.4.38}$$

The results of the equilibrium computations are presented in figure 2.15.

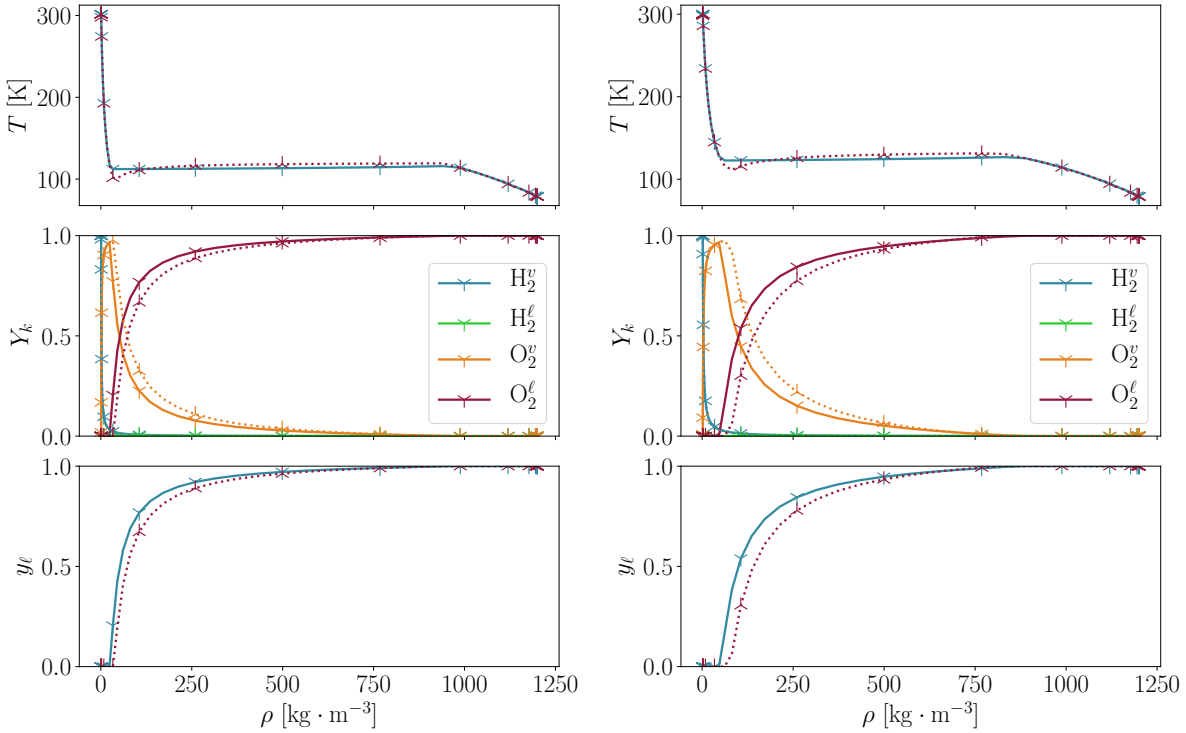

(a) 10 bar (b) 20 bar

Figure 2.15: Comparison of the thermodynamic quantities within an interface at $P = 10$ bar and $P = 20$ bar for the exact and approximate equilibriums, considering an H_2-O_2 mixture. Solid lines denote the profiles for the exact equilibrium computation. Dotted lines represent the approximate equilibrium computations.

The obtained profiles are very similar. The approximate equilibrium tends to slightly shift the profiles towards the cold/pure-O_2 region. The temperature values obtained within the interface are close, and the widths of the two-phase diffuse interface region, where $y_\ell \in]0, 1[$ are almost equal.

This validates the use of the approximate equilibrium formulation for the liquid rocket engine injection simulations that will be proposed in Chapter 6.

Note that when going to higher pressures, typically above the critical pressure of the pure components (see figure 2.16b), the approximate computation appears not to retrieve a two-phase region, the liquid volume fraction switching directly from zero to one without intermediary values. This can be explained by the fact that the approximate equilibrium formulation, being similar to a single-component computation, addresses mechanical instabilities but not chemical instabilities. As the mechanical instabilities vanish when the pressure is too high compared to the critical pressure of the pure components, the

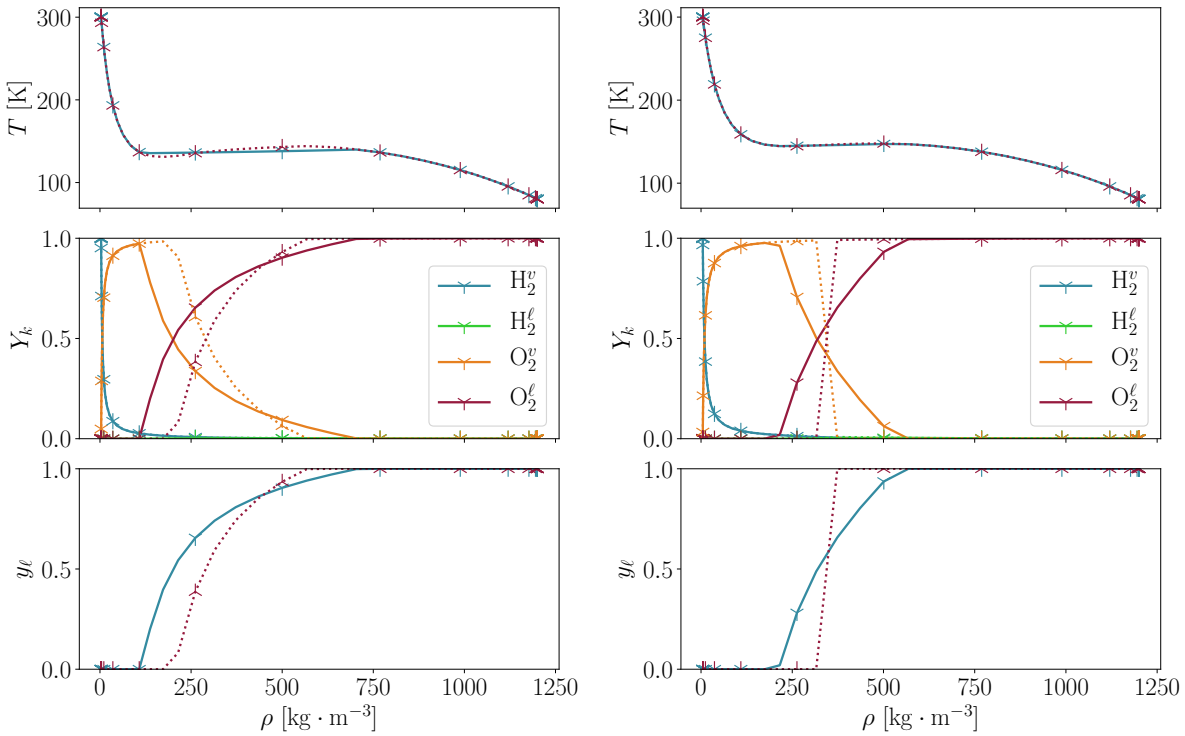

(a) 40 bar (b) 60 bar

Figure 2.16: Comparison of the thermodynamic quantities within an interface at $P = 40$ bar and $P = 60$ bar for the exact and approximate equilibriums, considering an H_2-O_2 mixture. Solid lines denote the profiles for the exact equilibrium computation. Dotted lines represent the approximate equilibrium computations. The approximate computation at 60 bar displays no thermodynamic instability, switching from pure "vapour-like" fluid with $y_\ell = 0$ to pure "liquid-like" fluid with $y_\ell = 1$.

approximate equilibrium formulation does not allow to retrieve the unstable zone. Therefore, computations in pressure ranges above the pure components critical pressures require the exact multicomponent equilibrium computation.

Note that at higher pressures (see figure 2.17), there is no more instability, even for the exact formulation, so that both computations predict the same thermodynamic state.

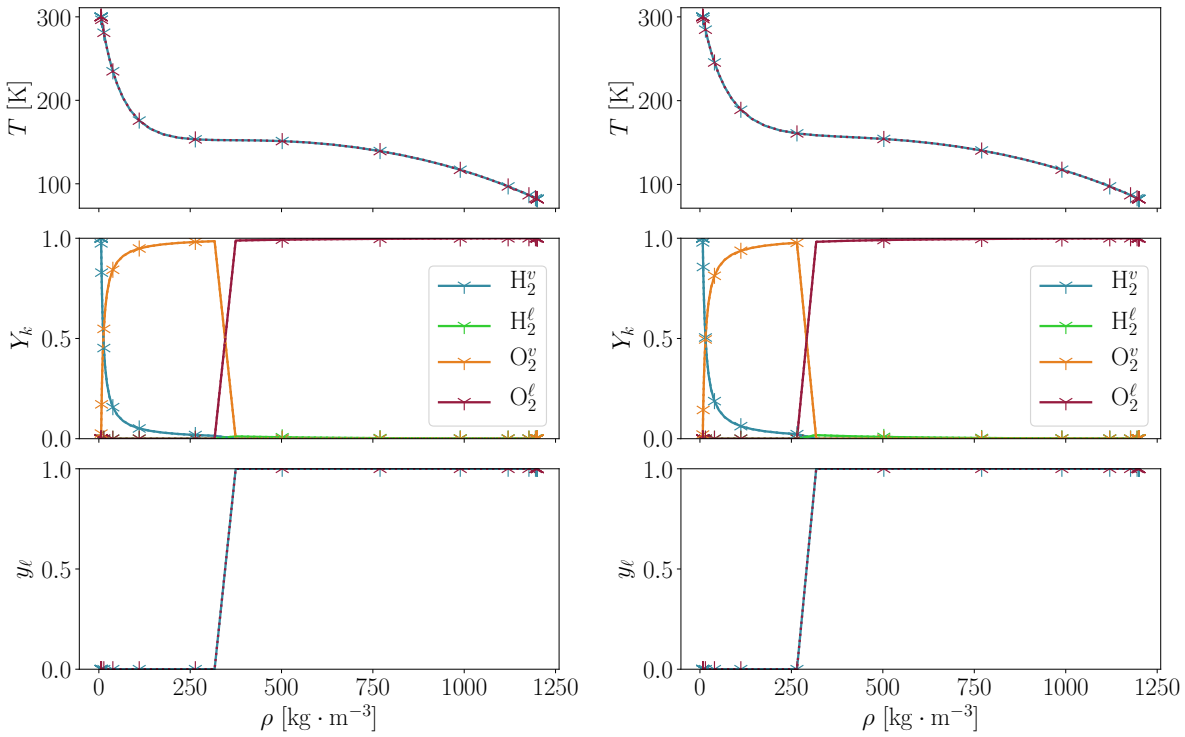

(a) 80 bar

(b) 100 bar

Figure 2.17: Comparison of the thermodynamic quantities within an interface at $P = 80$ bar and $P = 100$ bar for the exact and approximate equilibriums, considering an H_2-O_2 mixture. Solid lines denote the profiles for the exact equilibrium computation. Dotted lines represent the approximate equilibrium computations.

2.4.5.2 CH_4-O_2 mixture

An additional illustration of comparisons between the approximate and exact equilibriums for a CH_4-O_2 mixture is displayed through figures 2.18 to 2.20. Similar density and species profiles are considered, with value $\rho^0_{CH_4} = 10$ kg/m^3 all other input values being identical to the previous H_2-O_2 case.

Again, very similar results are observed with the two formulations at low pressures (see figures 2.18 and 2.19a). Above the pure components critical pressure, as observed in the previous paragraph, the approximate equilibrium computation does not retrieve the two-phase region (see figure 2.19b). The results become identical again at higher pressures, where there is no more instability, for the simplified as well as for the exact formulation (see figure 2.20).

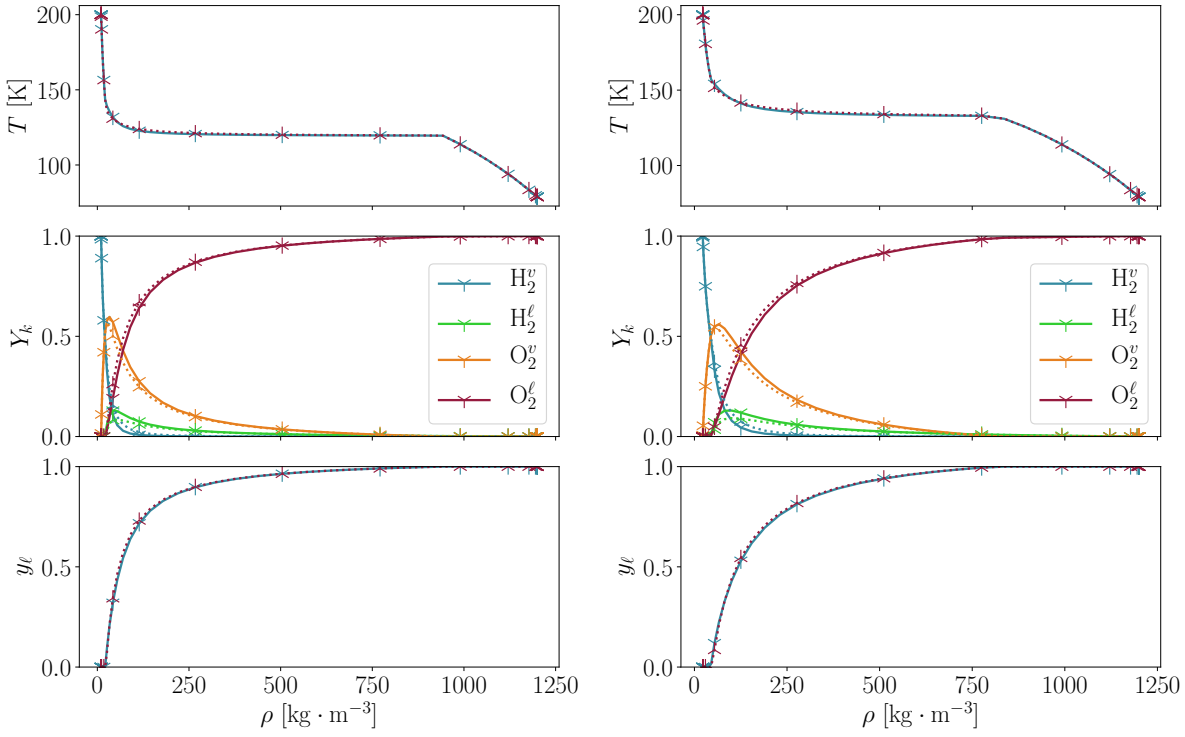

(a) 10 bar

(b) 20 bar

Figure 2.18: Comparison of the thermodynamic quantities within an interface at $P = 10$ bar and $P = 20$ bar for the exact and approximate equilibriums, considering an CH_4-O_2 mixture. Solid lines denote the profiles for the exact equilibrium computation. Dotted lines represent the approximate equilibrium computations.

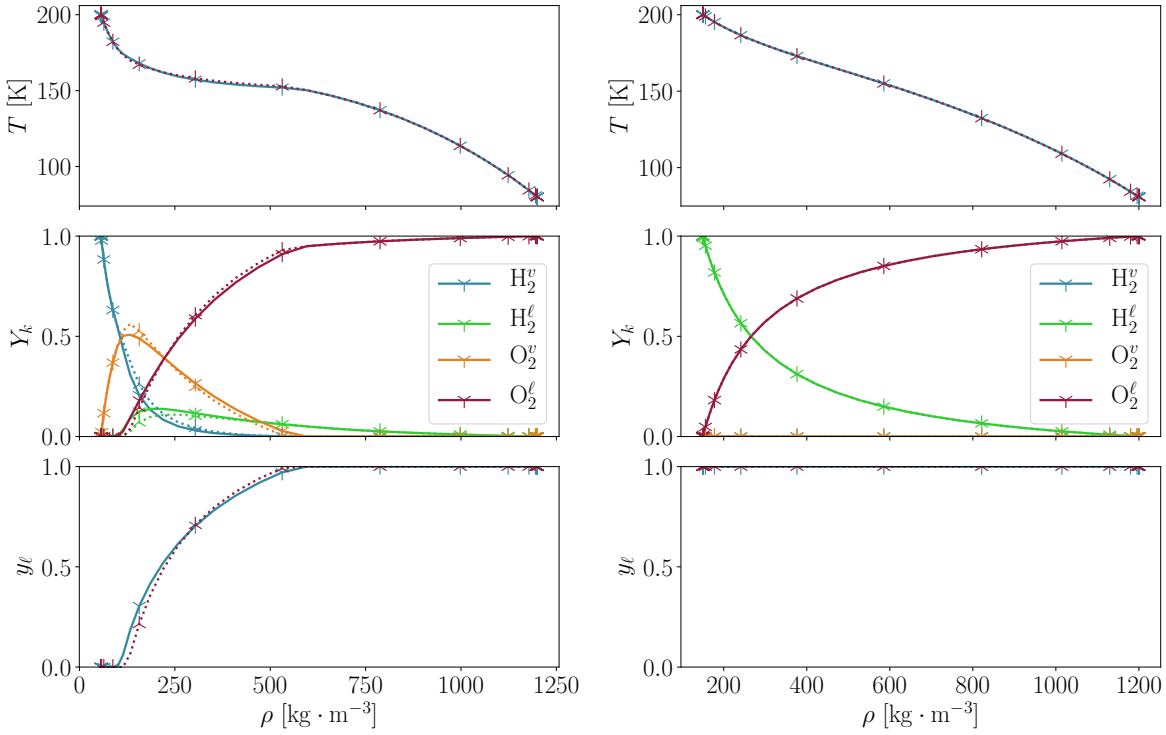

(a) 40 bar (b) 60 bar

Figure 2.19: Comparison of the thermodynamic quantities within an interface at $P = 40$ bar and $P = 60$ bar for the exact and approximate equilibriums, considering an CH_4-O_2 mixture. Solid lines denote the profiles for the exact equilibrium computation. Dotted lines represent the approximate equilibrium computations.

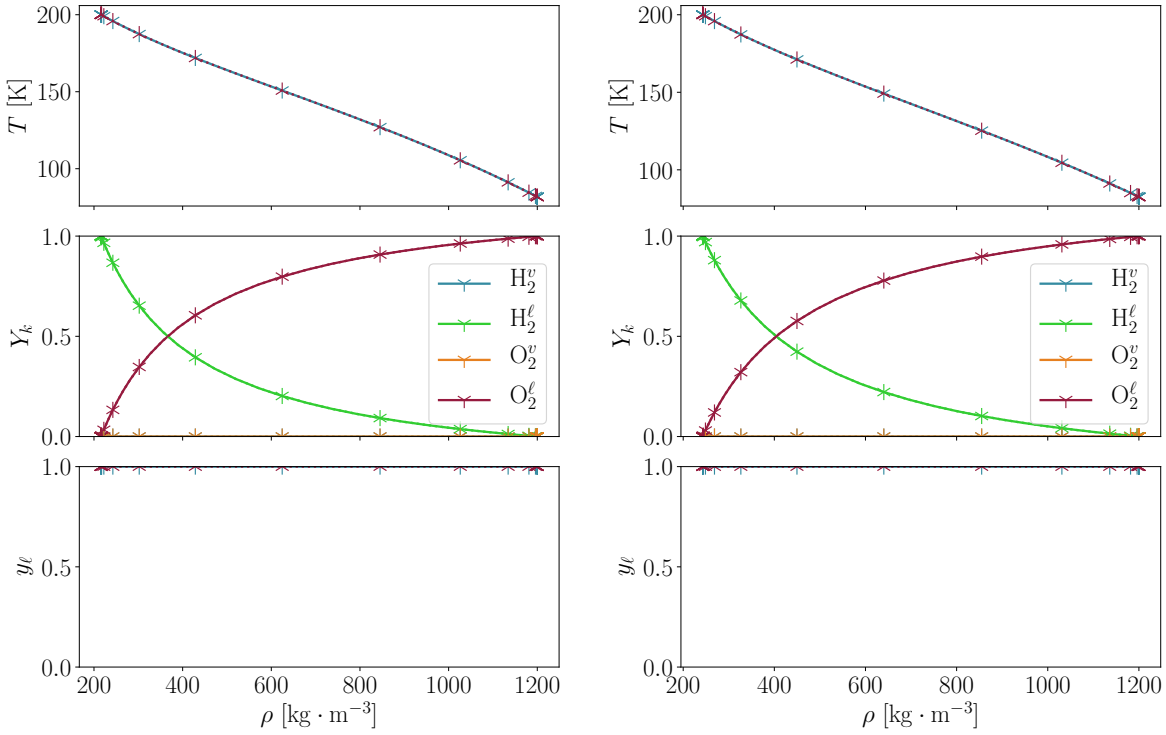

(a) 80 bar

(b) 100 bar

Figure 2.20: Comparison of the thermodynamic quantities within an interface at $P = 80$ bar and $P = 100$ bar for the exact and approximate equilibriums, considering an CH_4-O_2 mixture. Solid lines denote the profiles for the exact equilibrium computation. Dotted lines represent the approximate equilibrium computations.

2.5 Conclusion

This chapter recalled the basic principles of thermodynamics, and the theoretical background that allows to address non-ideal thermodynamics. In particular, the family of cubic EoS was carefully studied, as they provide a relevant framework for the target applications.

Then, thermodynamic stability has been introduced, in the cases of single-component and multicomponent mixtures. The two-phase equilibrium condition for unstable states has been described, and its practical computation has been presented. In particular, the *tangent plane distance* stability test and the algorithm for the computation of the two-phase equilibrium have been described, requiring rather complex calculations.

In order to reduce the complexity of equilibrium calculations, an approximate formulation of the thermodynamic equilibrium has been proposed, and its relevance in the case of a H_2-O_2 mixture in the operating conditions of a case of interest – to be described in chapter 6 – has been evidenced. For this simplified equilibrium formulation, a efficient computational method was proposed, based on *reduced saturation* properties.

After this description of the thermodynamics, the subsequent chapter focuses on the state-of-the-art of interface modeling techniques.

Chapter 3

Interface modeling

This chapter proposes a brief overview of the most commonly used methods for the modeling of separate two-phase flows. In particular, the representation of the interface and the description of pure phases are recalled for the different modeling strategies, and their range of interest is recalled.

3.1 Introduction

Liquid injection is encountered in a majority of internal combustion engines. The efficiency and quality of the combustion process is tightly related with the effectiveness of the injection, atomization and evaporation of the liquid reactant. If the modeling and simulation of such flows are of primary importance for industrial applications, they also represent a theoretical challenge that is actively faced by many research groups.

The typical topology encountered when atomizing a liquid jet with coaxial injection is displayed in Figure 3.1. The first part of the jet consists of a *potential core* which further destabilizes. The joint

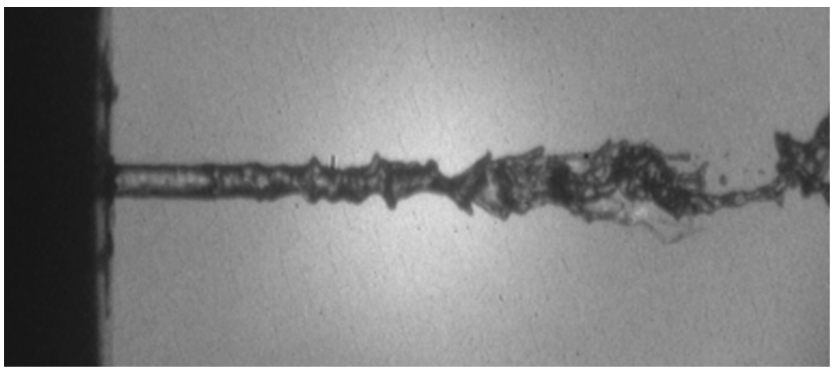

Figure 3.1: Experimental case of a liquid water jet breakup by high-speed coaxial annular air flow (picture taken from [Charalampous et al., 2009]).

contributions of the shear stresses due to the velocity difference and of the surface tension lead to a primary breakup of the jet. The resulting liquid ligaments and large droplets are then subject to a secondary breakup process, that yields the smaller droplets. These dynamics eventually increase the total surface of the liquid-vapour interface, enhancing the evaporation process that is of major importance in the context of combustion systems.

Three main regimes are typically encountered along the atomization of a liquid jet, as depicted in Figure 3.2. The present work focuses on the modeling of the separate two-phase flow regime. In

this context, the flow to be solved consists in regions of single-phase flows (the bulk phases), that are separated by an interface. The typical order of magnitude of the liquid-vapour interface thickness, is

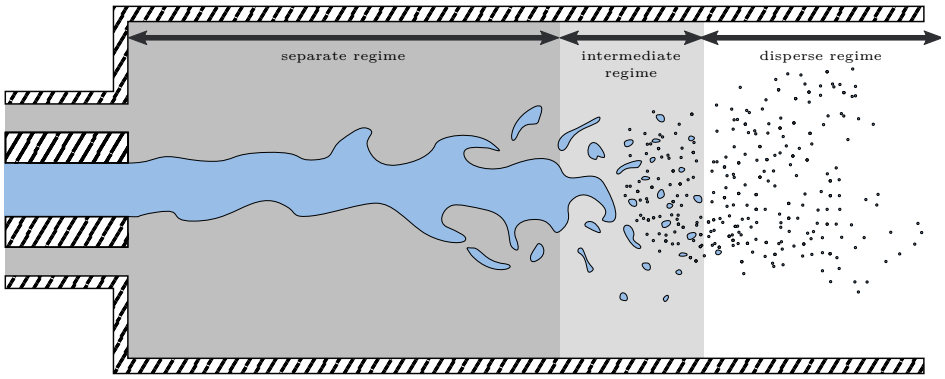

Figure 3.2: Schematic representation of the different two-phase flow regimes encountered in a liquid jet atomization.

about 10^{-10} m to 10^{-6} m. In this respect, the modeling of two-phase flows within industrial burners of a typical size of 10^{-1} m involves huge scale disparities, which are largely non-affordable for direct computation.

In order to overcome this issue, different strategies have been considered and are briefly summarized in what follows. First section 3.2 presents the family of *sharp-interface methods*. Such methods represent the interface as a discontinuity between the liquid and the gas phases. Then, section 3.3 is dedicated to the description of the family of *diffuse-interface methods*, which treat the liquid-vapour interface as a diffuse medium with a proper thickness. This will allow in particular to support the choice of the present work to use a diffuse-interface method, namely a *multifluid method*.

3.2 Sharp-interface methods

The family of sharp-interface methods (SIM) represent the interface as a sharp discontinuity between the phases. From this idea, a variety of strategies can be used to transport the interface, reconstruct its topology, and address the coupling between the evolution of the phases and the interface. In the present section, overviews of the three main SIM strategies are presented sequentially, each of them having multiple variants.

First, the *level-set method* is presented in section 3.2.1. It is based on the representation of the interface as an iso-value of the *level-set function*, e.g. the zero-value line of the signed distance to the interface. This level-set function is then transported and frequently re-initialized to remain representative of the signed distance value. Although this strategy is very straightforward to implement, it suffers relatively strong mass-conservation issues. Advanced formulations, using other level-set function formulations and re-initialization strategies, allow to reduce the mass-conservation errors, to the cost of an increased complexity. Such methods usually need to be combined with high-order numerical methods.

Then, section 3.2.2 describes the *volume-of-fluid method*. This method is dedicated to the simulation of incompressible flows. It consists in transporting the phases volume fraction to reconstruct the interface topology. The interface reconstruction is performed by means of optimization methods. Once obtained, the interface geometry is used to transport the volume fraction using a semi-Lagrangian transport. Such transport is typically performed by dimensional splitting strategies for structured meshes. In the unstructured case, geometric methods are required, leading to an increasing complexity with the number of dimensions. The advantage of the volume-of-fluid method is that, the volume fraction being directly transported, it ensures discrete mass conservation.

Finally, the *front-tracking method* is studied in section 3.2.3. This method can be used for both incom-

pressible and compressible two-phase flows. In a nutshell, it consists in tracking the interface positions by means of Lagrangian markers carried with the flow. The markers transport is straightforward and allow for an efficient tracking of the interface. Conversely, such method is subject to mass-conservation issues. Also, the markers regularly need to be redistributed homogeneously along the interface when the deformation is strong or when interfaces merge, which can deteriorate the simplicity and effectiveness of the method.

3.2.1 Level-set methods

The level-set (LS) method consists in representing the interface as an isocontour of a smooth quantity Φ (the LS function). This idea was first proposed by [Osher and Sethian, 1988] to address front propagation in combustion and crystal growth problems. Then, [Mulder et al., 1992] and [Sussman et al., 1994] extended this idea to treat Rayleigh-Taylor instabilities in the context of two-phase flows. More recently, the idea was further improved by [Olsson and Kreiss, 2005, Desjardins et al., 2008] to provide formulations that conserves the level-set function and enhance mass conservation.

3.2.1.1 Signed-distance level-set method

Early works, e.g. [Sussman et al., 1994], used to define the LS function Φ as the signed normal distance d to the interface Γ_I, so that

$$\left|\Phi(\vec{x},t)\right| = \left|d(\vec{x},\Gamma_I(t))\right| = \min_{\vec{x}_I\in\Gamma_I(t)} \left|\vec{x}-\vec{x}_I\right|, \tag{3.2.1}$$

with for instance $\Phi(\vec{x},t) < 0$ on the liquid side and $\Phi(\vec{x},t) > 0$ on the vapour side. This distance function obviously fulfills the following conditions:

$$\begin{cases} \left|\vec{\boldsymbol{\nabla}} d\right| = 1 & \text{for } \vec{x}\in\Omega, \\ d = 0 & \text{for } \vec{x}\in\Gamma_I(t), \end{cases} \tag{3.2.2}$$

where Ω is the computational domain.

The interface corresponds to the iso-level $\Phi = 0$. The interface position is then tracked by solving the following evolution equation for the level-set function:

$$\frac{\partial\Phi}{\partial t} + \nabla\cdot(\Phi\vec{u}) = 0. \tag{3.2.3}$$

Naturally, equation (3.2.3) does not generally guarantee that Φ remains a distance function. Therefore, a *reinitialization step* is performed after each transport iteration to overcome this issue. The reinitialization step is formulated by [Sussman et al., 1994] as the steady-state resolution of the following equation:

$$\frac{\partial\Phi}{\partial\tau} = \text{sign}\,(\Phi)\left(1-\left|\vec{\boldsymbol{\nabla}}\Phi\right|\right), \tag{3.2.4}$$

with the sign function defined as

$$\text{sign}\,(\Phi) = \begin{cases} -1 & \text{if } \Phi < 0, \\ 0 & \text{if } \Phi = 0, \\ 1 & \text{if } \Phi > 0. \end{cases} \tag{3.2.5}$$

It is clear that the exact resolution of equation (3.2.4) preserves the 0-LS function isovalue and does not modify the interface location. Nonetheless, the numerical errors made with the resolution of (3.2.4) induce modifications in the 0-LS function isovalue. In such method, both the LS transport (3.2.3) and its reinitialization generate mass conservation errors which are unacceptably high, hence a need for improved LS methods.

3.2.1.2 Conservative level-set method

As pointed out by [Olsson and Kreiss, 2005], if the LS function were instead a Heaviside function, and if the numerical resolution of the transport equation (3.2.3) were conservative, the interface location would be exactly transported and there would be no mass conservation error. As it is not possible to transport a Heaviside function accurately using classic hyperbolic numerical methods, the following smoothed Heaviside function H_s is used instead:

$$H_s(\Psi) = \begin{cases} 0, & \Psi < -\varepsilon, \\ \frac{1}{2} + \frac{\Psi}{2\varepsilon} + \frac{1}{2\pi}\sin\left(\frac{\pi\Psi}{\varepsilon}\right) & -\varepsilon \leq \Psi \leq \varepsilon, \\ 1, & \Psi > \varepsilon, \end{cases} \tag{3.2.6}$$

with ε a smearing parameter. The LS function is defined as

$$\Phi(\vec{x}, t) = H_s(d(\vec{x}, \Gamma_I(t))), \tag{3.2.7}$$

in which case the interface corresponds to $\Phi = 0.5$. Similarly, the LS function can be defined using a hyperbolic tangent function, as in [Desjardins et al., 2008]:

$$\Phi(\vec{x}, t) = \frac{1}{2}\left[1 + \tanh\left(\frac{d(\vec{x}, \Gamma_I(t))}{2\varepsilon}\right)\right], \tag{3.2.8}$$

Again, the interface corresponds to the isolevel $\Phi = 0.5$.

The smearing parameter ε is then defined relatively to the mesh size, for the variations of the initial level-set profile $\Phi_0(\vec{x})$ to be resolved. This definition allows to directly use function Φ to represent the density and viscosity variations across the interface, without having to use the distance $d(\vec{x}, \Gamma_{I_0})$.

In [Olsson and Kreiss, 2005], the re-initialization step consists in the following evolution equation:

$$\frac{\partial \Phi}{\partial \tau} + \nabla \cdot \left(\Phi\left(1 - \Phi\right)\vec{n}\right) = \varepsilon \Delta \Phi. \tag{3.2.9}$$

This equation is solved in the pseudo-time τ until the stationary solution is reached. The divergence term on the left-hand side acts as a compressive term to prevent the numerical diffusion of the profile. The right-hand side term is a diffusive term. The two adverse contributions of the compressive and diffusive terms maintain the interface thickness to a typical value close to 2ε.

Since both the transport (3.2.3) and reinitialization (3.2.9) are conservative, this method is called the *conservative level-set* method. Nevertheless, this denomination refers to the exact conservation of the LS function and is not to be mistaken with the mass conservation, which is not exactly guaranteed.

The reinitialization (3.2.9) involves an isotropic diffusion, causing modifications of the LS function in the direction tangent to the interface that are not counterbalanced by the compressive term which only acts on the normal direction, generating mass conservation error. In order to overcome this problem, [Olsson et al., 2007] proposed the following anisotropic-diffusion version of the re-initialization equation:

$$\frac{\partial \Phi}{\partial \tau} + \nabla \cdot \left(\Phi\left(1 - \Phi\right)\vec{n}\right) = \nabla \cdot \left(\varepsilon\left(\nabla\Phi \cdot \vec{n}\right)\vec{n}\right). \tag{3.2.10}$$

From a given LS function field, different strategies can be adopted to approximate the interface normals on the grid. Early methods use the normalized gradient of the LS function as the interface normal,

$$\vec{n} = \frac{\vec{\boldsymbol{\nabla}}\Phi}{\left|\vec{\boldsymbol{\nabla}}\Phi\right|}. \tag{3.2.11}$$

In [Desjardins et al., 2008], it is observed that the direct computation of the normals from the transported LS function leads to improper approximations of the normals, as soon as spurious oscillations are present on Φ. In this case, an additional reinitialization step is processed as a pre-treatment to rebuild the distance function d from the LS function Φ using a *fast marching method*. The interface normals are then computed as

$$\vec{n} = \frac{\vec{\nabla} d}{\left|\vec{\nabla} d\right|}. \tag{3.2.12}$$

The obtained normal vector is kept constant throughout the iterations of the reinitialization step described by equation (3.2.10).

3.2.1.3 Numerical methods

The fundamental advantage of the LS method is that the quantity transported to represent the sharp interface is smooth, allowing for a well-behaved numerical transport. In the conservative LS method of [Olsson et al., 2007], as the normals are computed using the conservative LS function (3.2.11), it is important to prevent numerical oscillations on Φ. In this context, high-order accuracy can be achieved either by means of non-linear *total variation diminishing* (TVD) methods, such as the MUSCL scheme of [van Leer, 1979], combined with a flux limiter [Sweby, 1984] or using higher-order *weighted essentially non-oscillatory* (WENO) schemes from [Liu et al., 1994].

In their *accurate conservative level-set* formulation, [Desjardins et al., 2008] take advantage of their robust interface normal approximation from equation (3.2.12). As this method is radically less sensitive to numerical oscillations, a non-oscillatory numerical scheme is not absolutely necessary, hence their choice for cheaper higher-order methods such as the *high-order upstream centered schemes* (HOUC) exploited in [Nourgaliev and Theofanous, 2007].

A computational example from [Desjardins et al., 2008] is provided in Figure 3.3.

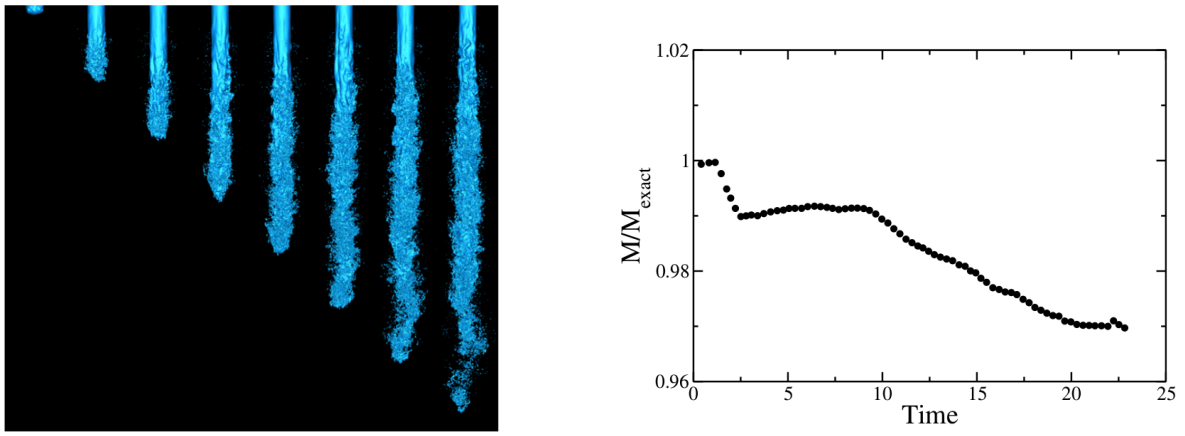

(a) Snapshots of the interface.

(b) Mass conservation error with respect to time.

Figure 3.3: Level-set simulation of the turbulent atomization of a liquid Diesel jet, taken from [Desjardins et al., 2008].

3.2.1.4 Compressible flows

The LS method can also be formulated in the context of compressible flows [Fedkiw et al., 1999, Abgrall and Karni, 2001, Kinzel et al., 2018]. Because of the strong variations of the thermodynamic properties between the liquid and gas phases, the direct computation of the fluid transport using classic numerical

methods yields high numerical errors and leads to strong pressure errors. This issue can be addressed by means of the *ghost-fluid method* of [Fedkiw et al., 1999]. In this method, the flux computations at the interface for each phase is done by considering the other phase's volume as filled with a "ghost" version of the former phase. This way, the flux computations do not suffer from the strong variations of the fluid properties, and spurious pressure oscillations are prevented. The ghost-fluid state is computed by using the real fluids pressure and velocity values, and by extrapolating the entropy, as depicted in Figure 3.4. In [Fedkiw et al., 1999], a constant entropy extrapolation is used. Once the fluxes have

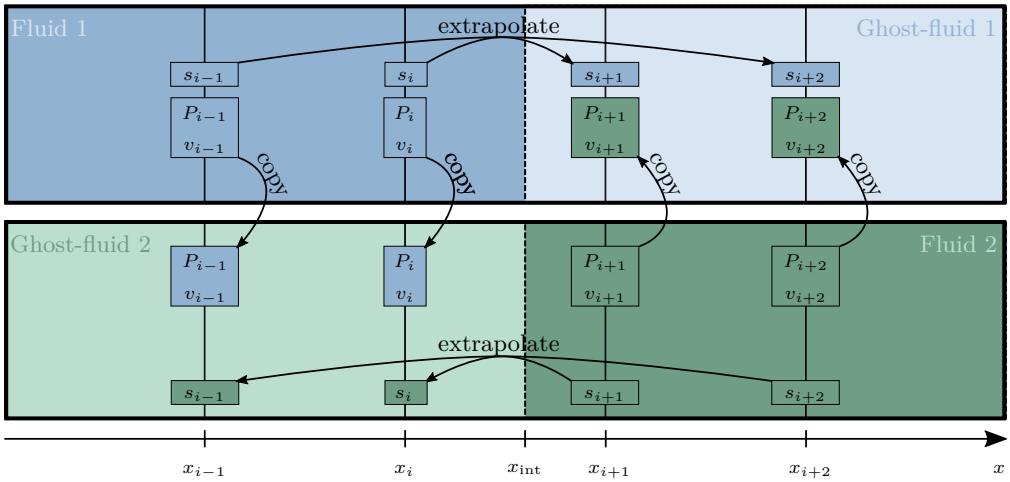

Figure 3.4: Illustration of the ghost-fluid method. *Fluid 1* and *Fluid 2* refer to the transported phases (e.g. liquid and vapour). The dashed line represents the interface between phases.

been computed for each phase, the solutions are combined to rebuild the actual real fluid using the LS function. This treatment is not conservative (in all three variables mass, momentum and energy), similarly to the incompressible LS formulation. In order to allow for an increased grid resolution in zones where the LS function evolution leads to mass-conservation errors, the LS method can be used in combination with *adaptive mesh refinement* (AMR) techniques. This strategy is applied in [Fedkiw et al., 1999] in a compressible context and a snapshot of the computation is displayed in Figure 3.5. It is

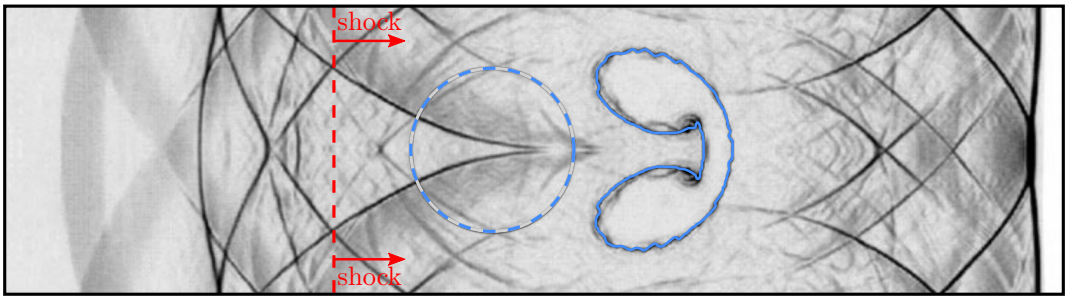

Figure 3.5: Schlieren image of a bubble-shock interaction using the level-set ghost-fluid method. The dashed lines represent the initial conditions, the red one displaying the initial shock front position and the blue one the initial interface location. The blue solid line displays the interface state at the time of the snapshot. Image taken from [Fedkiw et al., 1999].

worth mentioning that the appearance/disappearance of phases (e.g. in the case of boiling or cavitating flows) is not addressed by the LS method, since the LS function is only advected and reinitialized.

3.2.1.5 Conclusions

The level-set method provides a convenient framework that is relatively simple to formulate and implement, and allows to simulate atomization, coalescence of jets with complex geometries, provided a fine enough grid. The compressible formulation of the LS method also provides an interesting framework towards the simulation.

The major drawback of such method is the absence of discrete mass conservation due to the non-conservation of the volume bounded by the isosurface representing the interface. In the compressible context, all the transported variables are subject to conservation errors, which may harm the computational accuracy after a certain physical time.

3.2.2 Volume-of-fluid methods

The volume-of-fluid methods (VoF) find their origins in the works of [DeBar, 1974, Noh and Woodward, 1976, Hirt and Nichols, 1981]. This methods consists in reconstructing the interface geometry, using the knowledge of the liquid volume fraction z_ℓ (also called VoF function in this context) within each cell volume $\mathcal{V}_{ij}$, defined as

$$z_{\ell,ij}(t) = \frac{\mathcal{V}_{\ell,ij}}{\mathcal{V}_{ij}} = \frac{1}{\mathcal{V}_{ij}} \int_{\mathcal{V}_{ij}} \chi_\ell(\vec{x}, t)\, \mathrm{d}\vec{x}, \tag{3.2.13}$$

where $\mathcal{V}$ is the volume of the considered cell and χ_ℓ the characteristic function of the presence of the liquid, that is

$$\chi_\ell(\vec{x}, t) = \begin{cases} 1 & \text{if the liquid phase is present at position } \vec{x} \text{ and time } t, \\ 0 & \text{otherwise.} \end{cases} \tag{3.2.14}$$

3.2.2.1 Interface representation

The VoF method relies on an interface reconstruction, in order to obtain the sharp interface topology from the knowledge of the VoF function. A simple and widely used strategy is to approximate the sharp interface by a linear function within each cell (a line in 2D or a plane in 3D). This interface representation is referred to as the *Piecewise Linear Interface Calculation* (PLIC) method, introduced in [Youngs, 1982]. An even more elementary method, called *Simple Line Interface Reconstruction* (SLIC) [Noh and Woodward, 1976], consists in considering that the interface is parallel to a cell face, allowing for a more straightforward implementation at the cost of the accuarcy of the reconstruction. These techniques are depicted in Figure 3.6.

In order to perform PLIC reconstruction, the normal vector to the interface must be computed.

3.2.2.2 Interface normal reconstruction

The basic idea driving the interface normal reconstruction strategies is to use the neighbouring cells VoF function values in order to find the best approximation of the local interface position and direction.

The Parker's and Youngs' method [Parker and Youngs, 1992] proposes a direct computation of the interface normal by considering that the interface normal is colinear to ∇z_ℓ. This gradient is approximated from central differences of the VoF function. The details of this method can be found in [Pilliod Jr and Puckett, 2004], in which it is also shown that the Parker and Youngs' method is unable to reconstruct all linear interfaces exactly – a necessary condition for the method to be second-order accurate.

Conversely, the *Least-square VoF interface reconstruction algorithm* (LVIRA), achieves second-order accurate reconstruction of curved interfaces through an iterative procedure. It consists in finding the interface normal $\vec{n}_{ij}$ which, for a linear interface extrapolation over the direct neighbours, minimizes the

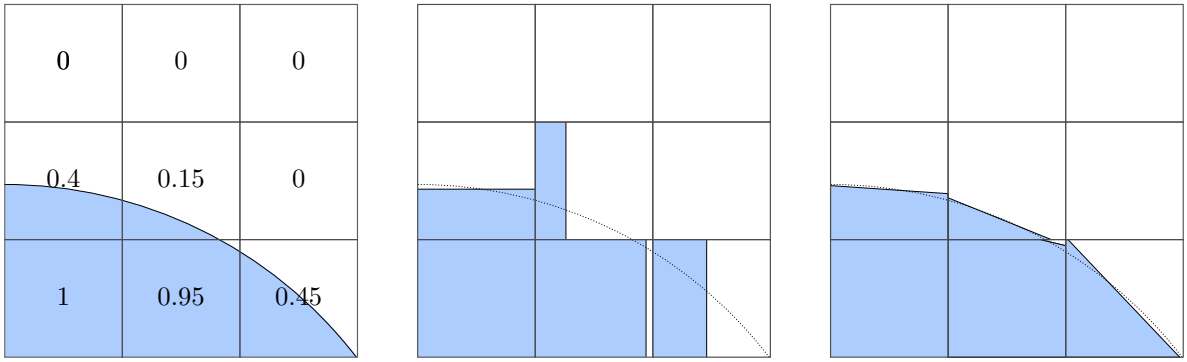

(a) Actual interface topology (b) SLIC-reconstructed interface (c) PLIC-reconstructed interface

Figure 3.6: VoF reconstruction of an interface within a mesh. The numbers indicate the value of the VoF function z_ℓ.

discrete L^2 error E_{ij}^2 between the VoF function values in direct neighbours $z_{\ell_{i'j'}}$ and its extrapolated values $z^{\text{ext}}_{\ell_{i'j'}}(\vec{n_{ij}})$.

$$E_{ij}^2 = \left[\sum_{k,l=-1}^{1} \left(z^{\text{ext}}_{\ell_{i+k,j+l}}(\vec{n}) - z_{\ell_{i+k,j+l}} \right)^2 \right]^{\frac{1}{2}} \tag{3.2.15}$$

For structured grids, the *efficient LVIRA* method (ELVIRA) consists in reducing this minimization problem to only six candidate normal reconstructions. These candidates are obtained from finite differences of the VoF function values within the neighbour cells and is shown to maintain second-order accuracy by [Pilliod Jr and Puckett, 2004].

For unstructured grids, the *geometric least-squares* method (GLS) of [Mosso et al., 1996] is able to reconstruct all linear interfaces exactly. It consists in iteratively approaching the normal to the interface. For a cell containing an interface, the middle of the interface within each neighbour is taken. For each pair of neighbours, the interface middles are connected by a straight line (in 2D). The normal to this straight line is used to define an approximate interface normal. The normal update is obtained from a least-square regression from all such approximate normals obtained for each pair of neighbours. This process is repeated until convergence. It achieves second-order accuracy in unstructured meshes, at the cost of expensive iterations, since each iteration requires the reconstruction of the whole interface.

Although these classic methods are still commonly used (see for instance [Owkes and Desjardins, 2014]), it is worth mentioning that the development of interface normal reconstruction techniques is still an active research topic among VoF-related works (e.g. the *embedded height-function* method of [Ivey and Moin, 2015]), in order to provide efficient and accurate methods for 3D unstructured hybrid meshes.

Another interesting strategy to obtain the interface normal is to transport the material centroid in addition to the VoF function, which relates to the first-order moment of the characteristic function χ_ℓ [Dyadechko and Shashkov, 2005]. This method is called the Moment-of-Fluid method and allows for a straightforward reconstruction of the normal at the cost of an additional transport equation.

The *coupled level-set and volume-of-fluid* (CLSVOF) strategy of [Sussman and Puckett, 2000] transports a level-set function in addition to the VoF function. The level-set function is then used to compute the interface normal. The interface is then obtained as having this normal and is positioned in the cell to match the value of the VoF function.

3.2.2.3 Interface transport

This method applies to incompressible flows, and is described by the set of equations

$$\begin{cases} \dfrac{\partial \rho}{\partial t} + \vec{u} \cdot \nabla \rho = 0, & \text{(3.2.16a)} \\ \nabla \cdot \vec{u} = 0, & \text{(3.2.16b)} \\ \dfrac{\partial \vec{u}}{\partial t} + (\nabla \vec{u}) \cdot \vec{u} + \dfrac{1}{\rho} \nabla P = 0, & \text{(3.2.16c)} \\ \dfrac{\partial z_\ell}{\partial t} + \vec{u} \cdot \nabla z_\ell = 0. & \text{(3.2.16d)} \end{cases}$$

Unlike the mass and momentum transports, the VoF function evolution is evaluated using the knowledge of the interface topology thanks to a *semi-Lagrangian* transport.

If the one-dimensional semi-Lagrangian transport allows for a straigthforward computation of the VoF function flux, the multidimensional case raises non-trivial issues, that are still currently studied. Historically, as the first VoF methods were applied to structured meshes, dimensional splitting methods have been considered [Hirt and Nichols, 1981]. Such methods require to perform an interface reconstruction after the transport along each dimension. A particular care must be taken to ensure conservation when using dimensional splitting. Indeed, although the multi-dimensional velocity fluid is solenoidal, there is no reason for the velocity fluid along each separate direction to be divergence-free. In this respect, [Weymouth and Yue, 2010] describes a dimensional-splitting strategy that preserves mass conservation.

In order to get rid of the splitting error, unsplit transport methods, relying on geometric considerations have been introduced by [Pilliod Jr and Puckett, 2004] for two-dimensional cases. Unsplit methods are still an active research field – see for example [Hernández et al., 2008, Owkes and Desjardins, 2014, Ivey and Moin, 2017] – for the development of three-dimensional computationally efficient methods. One of the main challenges in such methods is to avoid the VoF function fluxes to be overlapping, which would jeopardize the conservation of the VoF function. For example, in [Owkes and Desjardins, 2014], the velocities are evaluated at the cell's vertices. This is illustrated in Figure 3.7.

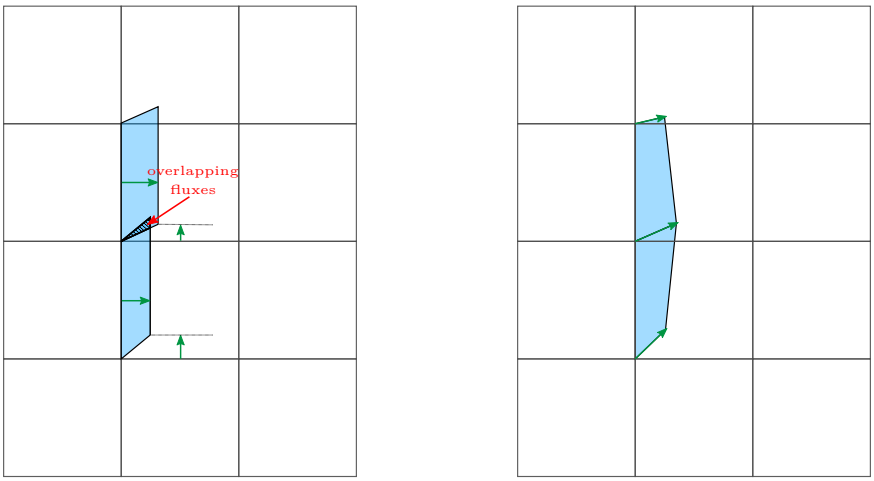

(a) Overlapping fluxes when using face velocities (green arrows)

(b) Non-overlapping fluxes using vertex velocities (green arrows)

Figure 3.7: Unsplit strategy for VoF function fluxes evaluation

In this latter reference, the three-dimensional extension is achieved by decomposing the flux volume

into a collection of simplices (tetrahedron) in each of which the amount of liquid is evaluated. This approach also requires to correct the flux volume in order to guarantee discrete conservation.

3.2.2.4 Example of volume-of-fluid application

An example of application is depicted in Figure 3.8. It shows the ability of the volume-of-fluid method to predict the primary and secondary breakups of the jet. Ligaments are formed, and break up into small droplets.

Figure 3.8: Atomization of a water jet in quiescent air. Taken from [Le Chenadec and Pitsch, 2013].

3.2.2.5 Conclusion

The VoF method is a currently actively studied method that allows for a conservative transport in the context of incompressible flows. Although the underlying idea is simple, its application requires to take specific care. In particular, increased complexity is encountered when dealing with unstructured multidimensional implementations.

3.2.3 Front-tracking methods

The *front-tracking* method [Glimm et al., 1981] consists in using Lagrangian markers to track the position of the interface. The interface is then assimilated to a line (in 2D) or a surface (in 3D) connecting the markers together, obtained either by linear or higher-order interpolation.

This method has the ability to solve incompressible or compressible flows. Unlike the VOF method for incompressible flows, the conservation of mass and energy for the phases is not guaranteed, as the transport of the front markers and the reconstruction of the interface do not guarantee such conservation. In addition, the method requires intensive transfers of information between the Lagrangian markers and the flow field.

The different operations applied to the markers in the front-tracking method are now briefly described. These operations – and in particular the involved data management – are responsible for the high complexity of implementation for this method, which is one of its main drawbacks.

3.2.3.1 Transporting the markers

The propagation of the markers is performed by integrating the local flow velocity over time. For example, Runge-Kutta methods can be used. For a marker m, and the classical RK4 method, this writes

$$\vec{x}_m^{n+1} = \vec{x}_m^n + \frac{1}{6}\left(\vec{u}_1 + 2\vec{u}_2 + 2\vec{u}_3 + \vec{u}_4\right)\Delta t, \tag{3.2.17}$$

with

$$\begin{cases} \vec{u}_1 = \vec{u}\left(\vec{x}_m^n, t\right), & \text{(3.2.18a)} \\ \vec{u}_2 = \vec{u}\left(\vec{x}_m^n + \frac{\Delta t}{2}\vec{u}_1, t + \frac{\Delta t}{2}\right), & \text{(3.2.18b)} \\ \vec{u}_3 = \vec{u}\left(\vec{x}_m^n + \frac{\Delta t}{2}\vec{u}_2, t + \frac{\Delta t}{2}\right), & \text{(3.2.18c)} \\ \vec{u}_4 = \vec{u}\left(\vec{x}_m^n + \Delta t\vec{u}_3, t + \Delta t\right), & \text{(3.2.18d)} \end{cases}$$

where $\vec{u}\left(\vec{x}, t\right)$ is an approximated local flow velocity at point $\vec{x}$ and time t.

It is readily seen that this method has no reason to strictly guarantee mass conservation for the phases. In addition, each marker being advected separately, any error made on the marker transport causes the mass bounded by the finally reconstructed interface to vary from its initial value. Two issues can be responsible for transport errors. First, the discrete integration scheme, for instance (3.2.17), introduces numerical errors. High-order methods naturally lead to reduced numerical errors and improve mass conservation. Second, the interpolation method used to approximate the local flow velocity $\underline{\boldsymbol{v}}\left(\underline{\boldsymbol{x}}, t\right)$ from the values of the velocity at the grid points can lead to errors. Indeed, a non-solenoidal approximate velocity field can be obtained even though a divergence-free velocity field has been guaranteed by the Eulerian transport scheme at grid points. For this reason, one can take advantage of the improved interpolation methods developed by the Immersed Boundary Method community ([Peskin and Printz, 1993, Muldoon and Acharya, 2008]) to provide divergence-free velocity at the marker positions.

3.2.3.2 Reseeding the interface markers

Once the markers have been transported, the deformations of the interface may lead to an unbalanced marker distribution along the interface. In order to maintain a satisfying representation of the interface, it can be necessary to *reseed* the markers, by removing and/or adding some of them [Popinet and Zaleski, 1999].

This requires to have a versatile data structure to aggregate the interface data, that must typically contain the marker indices, their position and their neighbouring markers they are connected to. Reseeding causes this data structure to be modified at various point and the links between neighbouring markers must be properly updated. In addition, when two interfaces collide, a merging must be performed, and the interface data must be updated in this respect. Similarly, when the flow dynamics pinch off a phase inclusion, the corresponding interface must split in two different interfaces to render the break-up. For example, the results of [Shin and Juric, 2002] for the simulation of such interface topology changes are depicted in Figure 3.9.

3.2.3.3 Retro-coupling with the flow

Once the interface markers have been transported, the interface is reconstructed using interpolation methods such as cubic spline interpolation. The new interface position and topology is then used to evaluate the Eulerian flow properties to solve for the Navier-Stokes equations.

In the incompressible case, the interface location allows to directly update the density values, since it is assumed constant within each phase. The velocities and pressure are updated subsequently.

In the compressible case, it is possible to use the interface position information to update the flow fields using a ghost-fluid method (see Paragraph 3.2.1.4) to transport the phases, as done in [Terashima and Tryggvason, 2009]. The two-phase Navier-Stokes equations are then solved for both fluids and their respective ghost-fluids and combined back into the flow field solution. Note that, again, the inexact evaluation of the interface position results in conservation errors. A bubble-shock interaction example solved using this strategy is depicted in Figure 3.10.

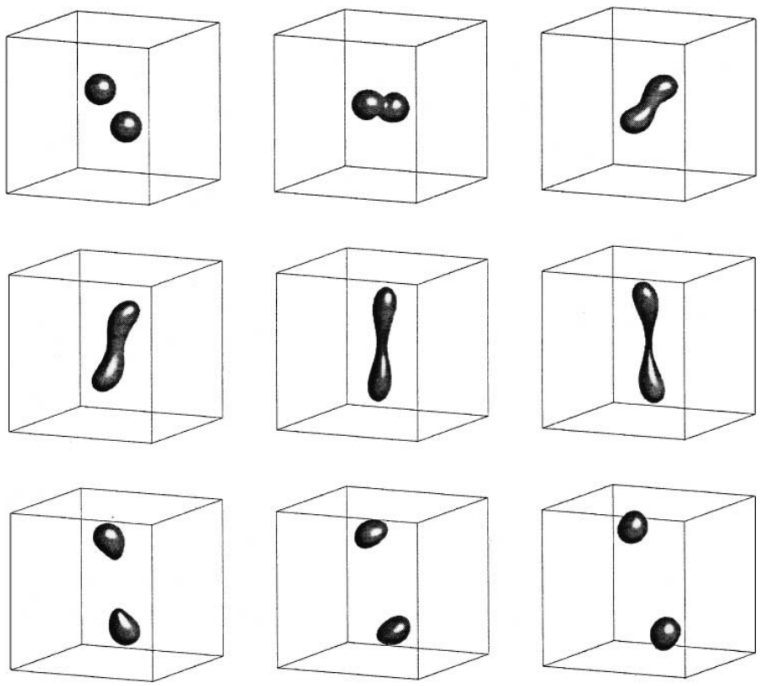

Figure 3.9: Results of a grazing droplet collision front-tracking simulation. The droplets first coalesce and then break-up into two droplets. Taken from [Shin and Juric, 2002]

3.2.3.4 Conclusion on the front-tracking methods

The front-tracking method have been used in various situations and can provide satisfying results to both compressible and incompressible flow simulations. If the interface transport is easy to formulate, one must be careful with the treatment of high interface deformations and topology changes, in order to always maintain a satisfying distribution of the markers along the interface. As for the level-set method, the front-tracking strategy does not guarantee discrete mass conservation. Finally, one of the main drawbacks of the front-tracking methods is the very high complexity of the implementation, requiring a specific data structure for the interfaces and complex operations for the markers reseeding, interface reconstruction and dynamic coupling with the flow model.

3.2.4 Conclusion

Among the sharp interface methods, only the volume-of-fluid method has the property to guarantee discrete mass conservation to the cost of intensive geometric computations when used with unstructured meshes. Also, this method is only functional in the incompressible context.

On the other hand, the level-set and front-tracking methods track the interface by means of, respectively, Eulerian or Lagrangian transports. Such methods can be adapted to compressible cases by means of the ghost-fluid method, which unfortunately suffer conservation issues. Also, these methods do not address interface formation or disappearance as they require an initially existing interface that will further evolve with transport and reinitialization/reseeding processes.

In order to elude such drawbacks, the diffuse interface methods are now considered.

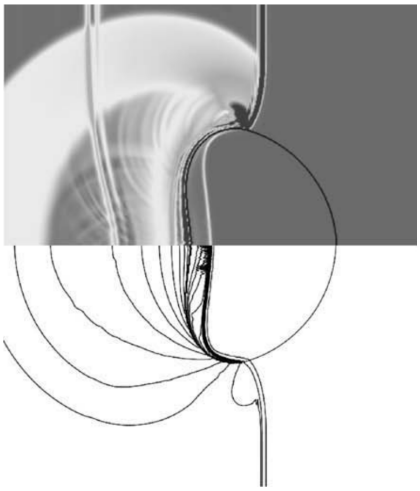

(a) Snapshot at time $t = 3.1$ μs. The upper image shows the density gradients, while the lower image displays pressure contours.

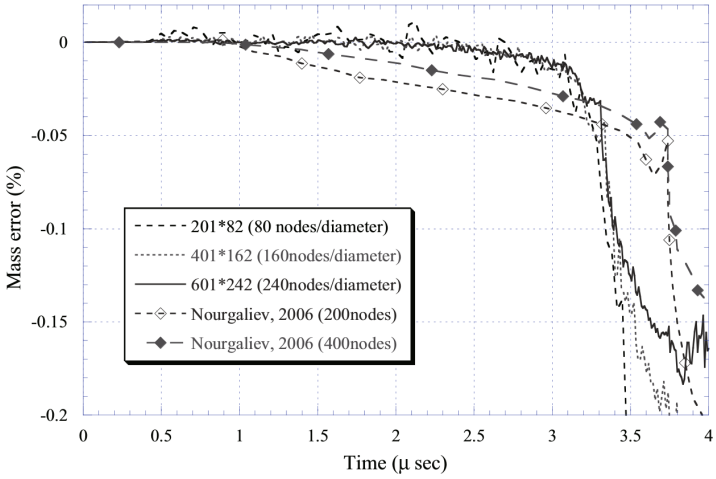

(b) Mass conservation for different mesh refinements. When the interface gets deformed, increasing mass-conservation errors appear.

Figure 3.10: Compressible front-tracking simulation of an air bubble in water hit by a shock. The pictures are taken from [Terashima and Tryggvason, 2009].

3.3 Diffuse-interface methods

Among the Diffuse Interface Methods, two major subfamilies can be defined. The first one, called *phase field methods*, relies on an enhanced physical description of the interface thermodynamics. This interface model thereby intrinsically contains the physical phenomena that characterize the interface – in particular the surface tension. In this context, the interface thickness must be resolved on the computational grid, or methods must be found to artificially thicken the interface. This class of methods has a strong theoretical interest as its construction is anchored in the physics occurring at the interface, but still raises numerical questions.

The other class of methods is called *multifluid methods*. They consist in representing the interface at a macroscopic level by numerically smearing the interface thickness. The artificially diffused interface zone then requires particular care to be treated, in order to avoid this zone to spread nonphysically across the domain. In this framework, the physical properties of the interface, such as the surface tension, can be incorporated afterwards to the model, which benefits from its high modularity.

This section presents an overview of the concepts and achievements of both methods, with a particular emphasis put on multifluid models, since the present work can be related to such methods.

3.3.1 Phase field methods

The phase field (PF) methods consist in introducing an *order parameter* Φ, a smoothly varying color function to characterize each phase. Unlike the level-set function used in the eponymous method presented in section 3.2.1, this color function is representative of a thermodynamic quantity and varies gradually from one phase to the other. The example of a liquid-gas mixture, assuming $\Phi = \Phi_\ell$ in the liquid and $\Phi = \Phi_g$ in the gas phase, modeled by a PF method is displayed in Figure 3.11.

In the framework of PF models, the capillary effects are intrinsically contained in the interface description. Thereby, unlike the interface representation for sharp interface methods (cf. Section 3.2), the interface description for PF methods and the capillary effects cannot be treated separately.

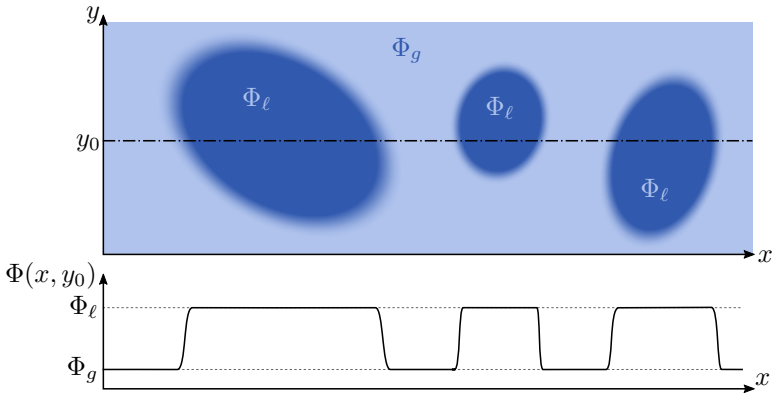

Figure 3.11: Gradually varying thermodynamic quantity Φ used as a phase field to represent the fluid topology and thermodynamics.

3.3.1.1 Single-component mixtures

For a single-component inviscid mixture, the fluid density can be used as the order parameter $\Phi = \rho$. The continuous representation of interfaces in single-component fluids was developed by [Rayleigh, 1892] and [van der Waals, 1893], who inferred gradient theories based on the van der Waals EoS. In this theory, the interface is identified by the gradient of the density. The capillary effects are interpreted as an additional capillary energy, corresponding to a potential energy of capillarity. In this respect, the volume-specific Helmoltz energy $\hat{f}_s^c$ of a capillary fluid is derived:

$$\hat{f}_s^c(T, \rho, \vec{\boldsymbol{\nabla}}\rho) = \hat{f}_s(T, \rho) + \frac{\lambda}{2}\left(\vec{\boldsymbol{\nabla}}\rho\right)^2, \tag{3.3.1}$$

with $\hat{f}_s$ the Helmoltz energy defined in (2.1.22a) with λ the *capillary coefficient*, in $\mathrm{m}^7 \cdot \mathrm{s}^{-2}$. One can then show that the enthalpy and Gibbs energy are not modified by the capillary energy. Conversely, the mass-specific sensible energy and Helmoltz energy of a capillary fluid read:

$$e_s^c(T, \rho, \vec{\boldsymbol{\nabla}}\rho) = e_s(T, \rho) + \frac{\lambda}{2\rho}\left(\vec{\boldsymbol{\nabla}}\rho\right)^2, \tag{3.3.2a}$$

$$f_s^c(T, \rho, \vec{\boldsymbol{\nabla}}\rho) = f_s(T, \rho) + \frac{\lambda}{2\rho}\left(\vec{\boldsymbol{\nabla}}\rho\right)^2, \tag{3.3.2b}$$

and the corresponding pressure is

$$P^c(T, \rho, \vec{\boldsymbol{\nabla}}\rho) = P(T, \rho) - \frac{\lambda}{2}\left(\vec{\boldsymbol{\nabla}}\rho\right)^2. \tag{3.3.3}$$

It is worth noting that, since the capillary effects do not modify the Gibbs energy, the bulk phases state of a liquid-vapour interface at equilibrium corresponds to the saturation values predicted by the EoS.

In [van der Waals, 1893], it is shown that a direct expression of the surface tension coefficient σ can be formulated. Considering a liquid-vapour interface at temperature T, throughout which the density gradually evolves from the liquid density $\rho_\ell^{\mathrm{sat}}(T)$ at position $\vec{x}_\ell$ to the vapour density $\rho_v^{\mathrm{sat}}(T)$ at position $\vec{x}_v$, the surface tension coefficient reads

$$\sigma = \int_{\vec{x}_\ell}^{\vec{x}_v} \lambda \left(\vec{\boldsymbol{\nabla}}\rho\right)^2 \vec{n} \cdot \mathrm{d}\vec{x}, \tag{3.3.4}$$

where $\vec{n}$ is the interface normal.

This enhanced thermodynamic description involves a modification of the stress tensor of the capillary fluid, as shown by [Korteweg, 1901, Rocard, 1967]. Thereby, enhanced conservation equations can be obtained by application of the *virtual power principle* [Seppecher, 1987]:

$$\begin{cases} \dfrac{\partial \rho}{\partial t} + \vec{\boldsymbol{\nabla}} \cdot (\rho \vec{u}) = 0, & \text{(3.3.5a)} \\ \dfrac{\partial \rho \vec{u}}{\partial t} + \vec{\boldsymbol{\nabla}} \cdot \left[\rho \vec{u} \otimes \vec{u} + P^{\mathrm{m}} \boldsymbol{\mathcal{I}} + \lambda \vec{\boldsymbol{\nabla}} \rho \otimes \vec{\boldsymbol{\nabla}} \rho \right] = 0, & \text{(3.3.5b)} \\ \dfrac{\partial \rho e_{\mathrm{t}}^c}{\partial t} + \vec{\boldsymbol{\nabla}} \cdot \left[\left(\rho e_{\mathrm{t}}^c + P^{\mathrm{m}} \right) \vec{u} + \lambda \left(\vec{\boldsymbol{\nabla}} \rho \otimes \vec{\boldsymbol{\nabla}} \rho \right) \cdot \vec{u} + \lambda \rho \vec{\boldsymbol{\nabla}} \rho \left(\vec{\boldsymbol{\nabla}} \cdot \vec{u} \right) \right] = 0. & \text{(3.3.5c)} \end{cases}$$

The tensor $\lambda \left(\vec{\boldsymbol{\nabla}} \rho \otimes \vec{\boldsymbol{\nabla}} \rho \right)$ is usually referred to as *Korteweg's tensor*. The total energy e_{t}^c of the capillary fluid is the sum of its internal and kinetic energies:

$$e_{\mathrm{t}}^c = e_s^c(T, \rho, \vec{\boldsymbol{\nabla}} \rho) + e_c. \tag{3.3.6}$$

A *mechanical pressure* term P^{m} appears in (3.3.5), which is defined as the isotropic part of the stress tensor:

$$P^{\mathrm{m}} = P^c + \frac{\lambda}{2} \left(\vec{\boldsymbol{\nabla}} \rho \right)^2 - \rho \vec{\boldsymbol{\nabla}} \cdot \left(\lambda \vec{\boldsymbol{\nabla}} \rho \right). \tag{3.3.7}$$

For an isothermal subcritical interface, the stationary solution of system (3.3.5) implies that the interface has a proper thickness h_{int}, which depends on the temperature and the value of the capillary coefficient [Jamet, 1998].

This theory is very promising as it provides a continuous formulation of two-phase flows conservation equations, which natively includes the interface physics. Nonetheless, typical values for the interface width being of the order of 10^{-9} m to 10^{-7} m for subcritical temperatures far from the critical point. Then, it is practically non-affordable to use a mesh to resolve the interface width for direct numerical simulations of turbulent flows in which the Kolmogorov scales typically range from 10^{-6} m to 10^{-4} m, so that the smallest flow scales are typically 3 orders of magnitude larger than the interface scale.

This motivated the works of [Jamet, 1998], who proposed a strategy to thicken the interface without modifying its global dynamic properties (typically surface tension). Yet, this method was only applicable in the vicinity of the critical point. Later on, the same author [Jamet et al., 2001] proposed a more general strategy which consists in modifying the thermodynamics within the interface, resulting in a greatly increased complexity and computational cost. The recent work of [Nayigizente et al., 2018] introduced a more efficient thickening method. An example of the destabilization and atomization of a liquid jet in a periodic domain using this latter method is depicted in Figure 3.12.

However, despite these promising works on the second gradient theory, there remain obstacles to overcome. The main one concerns the mathematical characterization of system (3.3.5) to properly derive adapted numerical methods and boundary conditions. Indeed, this system does not fall under the PDE classifications classically used in fluid mechanics as it involves third-order spatial derivatives of transported quantities. In particular, the question of the speed of sound within the interface is unclear.

3.3.1.2 Multicomponent mixtures

The extension to multicomponent mixtures, which is of major importance towards combustion modeling applications, has been studied by [Fouillet, 2003], [Gaillard, 2015] for binary mixtures. Despite the additional complexity arising from the multicomponent character of the mixture, these studies keep only a single order parameter, the density, as for the single-component case.

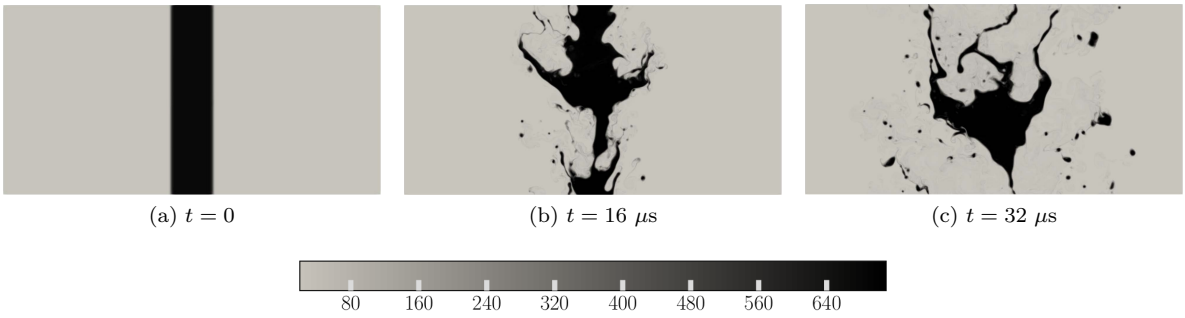

(a) $t = 0$ (b) $t = 16$ μs (c) $t = 32$ μs

(d) Density colorbar

Figure 3.12: Atomization of a liquid N_2 jet in a gaseous N_2 environment. Taken from [Nayigizente et al., 2018]

Conversely, the Cahn-Hilliard equation proposed in [Cahn and Hilliard, 1958], in the context of phase separation problems in binary alloys, uses the concentration x_1 of the component 1 as the order parameter. This equation reads [Jacqmin, 1999]:

$$\frac{\partial x_1}{\partial t} + \vec{u} \cdot \vec{\boldsymbol{\nabla}} x_1 = \kappa \nabla^2 \mu_1^c, \tag{3.3.8}$$

with $\vec{u}$ the flow velocity, κ a diffusion coefficient and μ_1^c the chemical potential of component 1, which reads

$$\mu_1^c = \mu_1 - \lambda \nabla^2 x_1 = \frac{\mathrm{d}F_s(x_1)}{\mathrm{d}x_1} - \lambda \nabla^2 x_1, \tag{3.3.9}$$

with the capillary term $-\lambda \nabla^2 x_1$. The quantity $F_s(x_1)$ denotes the molar Helmoltz energy of the homogeneous system with composition x_1, and is assumed to have the usual form given in Figure 3.13. In this respect, the equilibrium of a mixture made of two phases ϕ and ϕ' corresponds to the respective concentrations $(x_1^{\phi})^{\mathrm{eq}}$ and $(x_1^{\phi'})^{\mathrm{eq}}$.

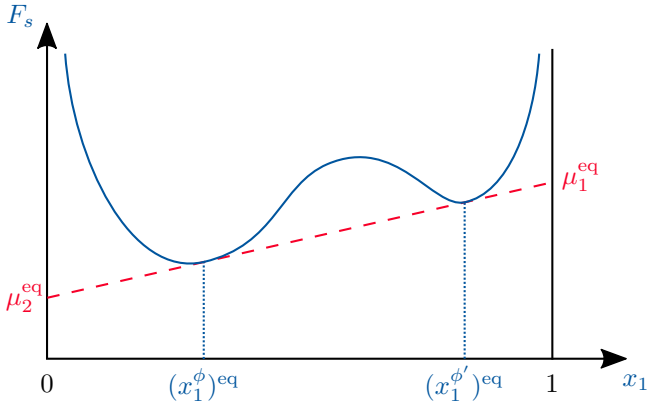

Figure 3.13: Helmoltz energy of the binary mixture.

The Helmoltz energy for the Cahn-Hilliard model reads, including the capillary effects:

$$F_s^c = F_s + \frac{\lambda}{2} \left(\vec{\boldsymbol{\nabla}} x_1 \right)^2. \tag{3.3.10}$$

This form is similar to equation (3.3.2b) with the order parameter being x_1. An example of application for this model is the spinodal decomposition in a binary alloy shown in Figure 3.14.

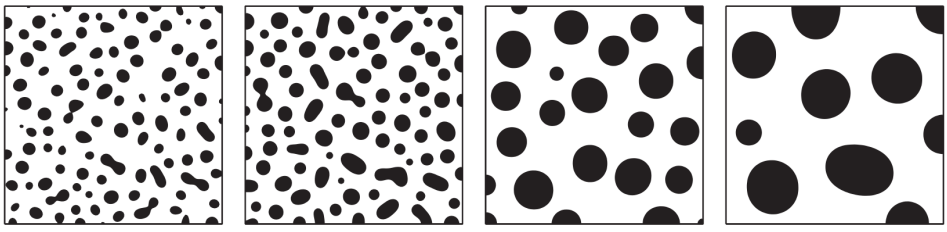

Figure 3.14: Simulation of a spinodal decomposition using the Cahn-Hilliard equation by [Kim et al., 2016]

Despite the numerous applications of the Cahn-Hilliard equation, no compressible formulation based on this model have been found. This limits the relevance of this method in the context of the present work.

3.3.2 Multifluid methods

The multifluid methods have been introduced to address the need for two-phase models able to treat compressible flows. It is thus natural that such models emerged in the context of deflagration-to-detonation transition studies in the two-phase conditions of reactive granular materials flows. In their pioneering work [Baer and Nunziato, 1986], Baer and Nunziato (BN) propose a two-phase flow model that can be derived by averaging the phases' transport equations around the interface, as reviewed in [Drew, 1983]. By doing so, the interface – similar to a discontinuity at the flow typical lengthscale – is smeared out and hence described by a diffuse region.

This makes possible the formulation of a continuous Eulerian description of the flow, so that the numerical methods for the transport of single-phase flows can be adapted to treat the obtained hyperbolic system. This seminal formulation has then been branched into a variety of reduced models with simplified formulations for certain applications. A global overview of the methods, their properties and applications is proposed in the following.

3.3.2.1 Transport models

3.3.2.1.1 The general non-equilibrium model

The BN model has been reformulated in various ways since its initial expression in [Baer and Nunziato, 1986]. A classic formulation [Saurel and Abgrall, 1999] of the 7-equation transport model of Baer and Nunziato applied to a separate liquid-gas flow in one-dimension, for a single-component fluid and

without phase change, is:

$$\frac{\partial z_\ell \rho_\ell}{\partial t} + \frac{\partial z_\ell \rho_\ell u_\ell}{\partial x} = 0 \tag{3.3.11a}$$

$$\frac{\partial z_v \rho_v}{\partial t} + \frac{\partial z_v \rho_v u_v}{\partial x} = 0 \tag{3.3.11b}$$

$$\frac{\partial z_\ell \rho_\ell u_\ell}{\partial t} + \frac{\partial z_\ell \rho_\ell u_\ell^2 + z_\ell P_\ell}{\partial x} = +P_I \frac{\partial z_\ell}{\partial x} + \kappa_u (u_v - u_\ell) \tag{3.3.11c}$$

$$\frac{\partial z_v \rho_v u_v}{\partial t} + \frac{\partial z_v \rho_v u_v^2 + z_v P_v}{\partial x} = -P_I \frac{\partial z_\ell}{\partial x} - \kappa_u (u_v - u_\ell) \tag{3.3.11d}$$

$$\frac{\partial z_\ell \rho_\ell e_{\mathrm{t},\ell}}{\partial t} + \frac{\partial (z_\ell \rho_\ell e_{\mathrm{t},\ell} + z_\ell P_\ell) u_\ell}{\partial x} = +P_I u_I \frac{\partial z_\ell}{\partial x} + \kappa_P P_I \left(P_\ell - P_v\right) + \kappa_u u_I (u_v - u_\ell) \tag{3.3.11e}$$

$$\frac{\partial z_v \rho_v e_{\mathrm{t},v}}{\partial t} + \frac{\partial (z_v \rho_v e_{\mathrm{t},v} + z_v P_v) u_v}{\partial x} = -P_I u_I \frac{\partial z_\ell}{\partial x} - \kappa_P P_I \left(P_\ell - P_v\right) - \kappa_u u_I (u_v - u_\ell) \tag{3.3.11f}$$

$$\frac{\partial z_\ell}{\partial t} + u_I \frac{\partial z_\ell}{\partial x} = +\kappa_P (P_\ell - P_v), \tag{3.3.11g}$$

This model is usually referred to as the nonequilibrium model since the two phases are let free to take different velocities, pressures, temperatures and chemical potentials. The left-hand side of equations (3.3.11a) to (3.3.11f) represent the conservative transport of mass, momentum and energy for each phase, while their right-hand side contains the conservative exchange terms, the sum of which being zero. The last equation, (3.3.11g), is called the compaction equation. It renders the variations of the phases' volume, including in particular advective and compressibility-related effects.

This system of equations involves non-conservative terms that require a careful treatment for a proper numerical resolution. This will be further mentioned in paragraph 3.3.2.3.

In addition to the phases' quantities, this model contains two additional variables, the interface velocity u_I and the interface pressure P_I. Since the terms in which they appear involve the gradient of a transported quantity, $\frac{\partial z_\ell}{\partial x}$, their value has an impact on the hyperbolic nature of the flow. For instance, as mentioned by [Saurel and Abgrall, 1999], considering the liquid to be incompressible and assuming $P_I = P_v$ results in a non-hyperbolic system. In this respect, [Abgrall and Saurel, 2003] eludes the need for these closures by formulating the source terms of (3.3.11) in terms of averaged values of the local flow properties. In [Saurel and Abgrall, 1999], it is observed that across an liquid-gas interface, the typical relaxation time of the velocity and pressure is short compared to the flow timescales. In this respect, *stiff mechanical relaxation* is considered and constrains the phases to evolve with the same pressure and velocity, imposed by an operator-splitting strategy, so that when the fluxes must be computed, one necessarily has $P_\ell = P_I = P_v$ and $u_\ell = u_I = u_v$. The authors show that such treatment allows to recover the hyperbolicity of the system.

3.3.2.1.2 Velocity-pressure equilibrium model

Following the idea of [Saurel and Abgrall, 1999], Kapila's model [Kapila et al., 2001] proposes a reduced 5-equation model with a single pressure and velocity for both phases. A thorough mathematical analysis of this latter model has been subsequently provided by [Murrone and Guillard, 2005]. Kapila's model corresponds to an asymptotic limit of the BN model (3.3.11) with pressure and velocity relaxation. It

reads

$$\frac{\partial z_v \rho_v}{\partial t} + \frac{\partial z_v \rho_v u}{\partial x} = 0 \tag{3.3.12a}$$

$$\frac{\partial z_\ell \rho_\ell}{\partial t} + \frac{\partial z_\ell \rho_\ell u}{\partial x} = 0 \tag{3.3.12b}$$

$$\frac{\partial \rho u}{\partial t} + \frac{\partial \rho u^2 + P}{\partial x} = 0 \tag{3.3.12c}$$

$$\frac{\partial \rho e_\mathrm{t}}{\partial t} + \frac{\partial \left(\rho e_\mathrm{t} + P\right) u}{\partial x} = 0 \tag{3.3.12d}$$

$$\frac{\partial z_\ell}{\partial t} + u \frac{\partial z_\ell}{\partial x} = z_\ell (1 - z_\ell) \frac{\rho_v c_v^2 - \rho_\ell c_\ell^2}{\sum_{\phi=\ell,v} (1 - z_\phi) \rho_\phi c_\phi^2} \frac{\partial u}{\partial x}. \tag{3.3.12e}$$

This system is hyperbolic provided the EoS used to close the phase-wise thermodynamics are convex. Although pressures and velocities are kept equal between the liquid and gas phases, there remain degrees of freedom in the disequilibrium between phases. In particular, the phases can take different temperatures. It will be observed in Section 7.2 that this degree of freedom allows to avoid pressure noise when transporting contact discontinuities.

A similar model was proposed by [Allaire et al., 2002]. This model is not strictly derived from the BN model as it does not correspond to its asymptotic limit. It yet consists in a 5-equation model derived from a phenomenological approach for which the compaction equation (3.3.12e) reduces to

$$\frac{\partial z_\ell}{\partial t} + u \frac{\partial z_\ell}{\partial x} = 0. \tag{3.3.13}$$

This allows to get rid of the non-conservative term on the right-hand side of (3.3.12e) which is hard to handle numerically. The consequences of this modification are that the characteristic waves of the system are strongly modified, as shown by [Murrone and Guillard, 2005]. Indeed, the speed of sound for Kapila's model (3.3.12) is given by Wood's speed of sound c_w

$$\rho c_\mathrm{w}^2 = \frac{1}{\frac{z_\ell}{\rho_\ell c_\ell^2} + \frac{z_v}{\rho_v c_v^2}}, \tag{3.3.14}$$

whilst the speed of sound for Allaire's model is

$$\rho c_\mathrm{a}^2 = \frac{z_\ell \xi_\ell \rho_\ell c_\ell^2 + z_v \xi_v \rho_v c_v^2}{z_\ell \xi_\ell + z_v \xi_v}, \tag{3.3.15}$$

with coefficients ξ_ϕ defined for $\phi \in \{\ell, v\}$ as

$$\xi_\phi = \left.\frac{\partial \rho_\phi e_\phi}{\partial P}\right|_{\rho_\phi}. \tag{3.3.16}$$

Another strategy introduced by [Saurel et al., 2009] consists in taking one step back to a 6-equation model which assumes only velocity equilibrium, and treat the pressure equilibrium assumption by stiff relaxation. This way, the form of the compaction equation of the 6-equation model is equivalent to the one of the 7-equation (3.3.11g), which is easier to compute than the 5-equation compaction equation (3.3.12e). Note that the corresponding speed of sound is also different from Wood's, and reads

$$\rho c_\mathrm{6eq}^2 = z_\ell \rho_\ell c_\ell^2 + z_v \rho_v c_v^2. \tag{3.3.17}$$

3.3.2.1.3 Further reduced models: the 4-equation and 3-equation models

When the assuming temperature equilibrium in addition to the velocity-pressure equilibrium, the 4-equation model is obtained, which reads

$$\frac{\partial z_v \rho_v}{\partial t} + \frac{\partial z_v \rho_v u}{\partial x} = 0, \tag{3.3.18a}$$
$$\frac{\partial z_\ell \rho_\ell}{\partial t} + \frac{\partial z_\ell \rho_\ell u}{\partial x} = 0, \tag{3.3.18b}$$
$$\frac{\partial \rho u}{\partial t} + \frac{\partial \rho u^2 + P}{\partial x} = 0, \tag{3.3.18c}$$
$$\frac{\partial \rho e_{\mathrm{t}}}{\partial t} + \frac{\partial \left(\rho e_{\mathrm{t}} + P\right) u}{\partial x} = 0, \tag{3.3.18d}$$

Considering in addition the equilibrium of chemical potentials between phases yields the 3-equation model, also called the *homogeneous equilibrium model*, which has a form similar to the Euler equations:

$$\frac{\partial \rho}{\partial t} + \frac{\partial \rho u}{\partial x} = 0, \tag{3.3.19a}$$
$$\frac{\partial \rho u}{\partial t} + \frac{\partial \rho u^2 + P}{\partial x} = 0, \tag{3.3.19b}$$
$$\frac{\partial \rho e_{\mathrm{t}}}{\partial t} + \frac{\partial \left(\rho e_{\mathrm{t}} + P\right) u}{\partial x} = 0. \tag{3.3.19c}$$

These models will be described in more details in paragraphs 3.3.2.2.1 and 3.3.2.2.2.

3.3.2.1.4 Hierarchy of the models and subcharacteristic condition

Multifluid models inherited from the nonequilibrium model (3.3.11) can be studied through the prism of the *subcharacteristic condition* introduced by [Liu, 1987]. In order to formulate this condition [Lund, 2012], consider a PDE with hyperbolic transport and relaxation source terms (e.g. the BN model (3.3.11)), which reads:

$$\frac{\partial \mathbf{U}}{\partial t} + \mathcal{H}\left(\mathbf{U}\right) \frac{\partial \mathbf{U}}{\partial x} = \frac{1}{\tau_R} \boldsymbol{R}\left(\mathbf{U}\right), \tag{3.3.20}$$

with the hyperbolic operator $\mathcal{H}$, the relaxation operator $\boldsymbol{R}$, the relaxation characteristic time τ_R and the N transported variables $\mathbf{U}$. From system (3.3.20), define the corresponding equilibrium system, as

$$\begin{cases} \dfrac{\partial \tilde{\mathbf{U}}}{\partial t} + \mathcal{G}\left(\tilde{\mathbf{U}}\right) \dfrac{\partial \tilde{\mathbf{U}}}{\partial x} = 0 & \text{(3.3.21a)} \\ \mathbf{U} = \mathrm{eq}(\tilde{\mathbf{U}}), & \text{(3.3.21b)} \end{cases}$$

where $\tilde{\mathbf{U}}$ is the reduced set of $n \leq N$ variables of the equilibrium system. $\mathbf{U} = \mathrm{eq}(\tilde{\mathbf{U}})$ is the equilibrium state that cancels the relaxation terms $\boldsymbol{R}\left(\mathrm{eq}(\tilde{\mathbf{U}})\right) = 0$, and $\mathcal{G}$ is the transport operator of the reduced equilibrium system. For instance, if (3.3.20) represents the BN model, then (3.3.21a) can be Kapila's model (3.3.12)

Let the eigenvalues of $\mathcal{H}$, evaluated at an equilibrium state $\mathbf{U} = \mathrm{eq}(\tilde{\mathbf{U}})$, be given by

$$\Lambda_1 \leq \cdots \leq \Lambda_i \leq \cdots \leq \Lambda_N, \tag{3.3.22}$$

and the eigenvalues of $\mathcal{G}$ evaluated at the corresponding reduced state $\tilde{\mathbf{U}}$ be given by

$$\lambda_1 \leq \cdots \leq \lambda_i \leq \cdots \leq \lambda_n. \tag{3.3.23}$$

The equilibrium system (3.3.21) is said to fulfill the *subcharacteristic condition* with respect to the relaxation system (3.3.20) if the eigenvalues verify

$$\forall i \in \{1...n\}, \quad \Lambda_i \leq \lambda_i \leq \Lambda_{i+N-n}. \tag{3.3.24}$$

Under such considerations, it has been shown by [Lund, 2012] that the different models derived from the single-velocity 6-equation version of the BN model by assuming equilibrium of pressure, temperature and/or chemical potential do fulfill the subcharacteristic condition. In other words, the speed of sound decreases as the number of equations of the model decreases, as displayed in Figure 3.15.

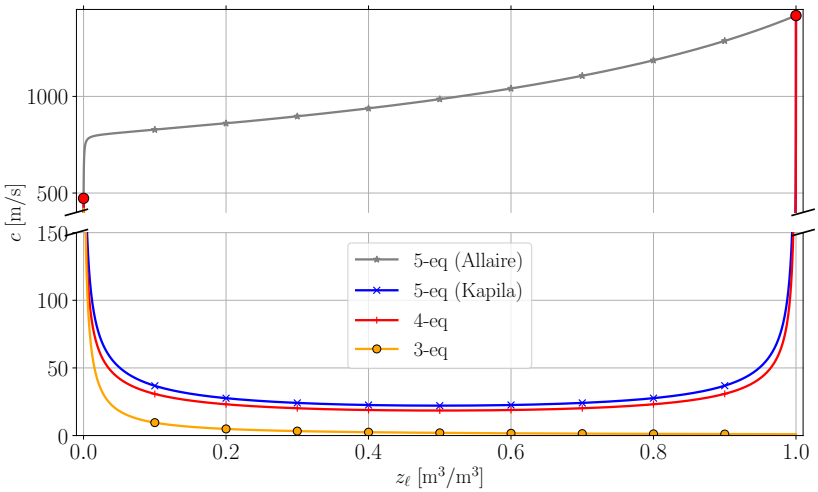

Figure 3.15: Speed of sound for the 5-equation model of Allaire, the 5-equation model of Kapila, the velocity-pressure-temperature equilibrium 4-equation model and the velocity-pressure-temperature-Gibbs free energy equilibrium 3-equation model.

3.3.2.2 Addressing additional physical phenomena

The fundamental multifluid models and their relations with sub-models have been recalled. It is now important to mention the ability of this class of models to incorporate additional physical phenomena required by the possibly targeted applications.

3.3.2.2.1 Heat transfer

In order to incorporate heat transfer into the model, [Le Martelot et al., 2014] formulated Kapila's system (3.3.12) with the energy equation simply modified as

$$\frac{\partial \rho e_{\mathrm{t}}}{\partial t} + \frac{\partial \left(\rho e_{\mathrm{t}} + P\right) u - \lambda_{\mathrm{mix}} \frac{\partial T}{\partial x}}{\partial x} = 0, \tag{3.3.25}$$

$\lambda_{\mathrm{mix}} = z_\ell \lambda_\ell + z_v \lambda_v$ being the mixture's thermal conductivity coefficient.
Additionally, heat exchange between phases can be addressed following [Saurel et al., 2008]. It is modeled in a relaxation form, as $Q_v^\ell = \kappa_T (T_v - T_\ell)$ with κ_T a relaxation coefficient. This energy transfer does not appear in the energy equation since it consists in a simple exchange between the phases. Nevertheless, it modifies the compaction equation through its effect on the phases' volume. This reads

$$\frac{\partial z_\ell}{\partial t} + u \frac{\partial z_\ell}{\partial x} = z_\ell (1 - z_\ell) \frac{\rho_v c_v^2 - \rho_\ell c_\ell^2}{\sum_{\phi=\ell,v} (1 - z_\phi) \rho_\phi c_\phi^2} \frac{\partial u}{\partial x} + \frac{\frac{1}{\xi_\ell z_\ell} + \frac{1}{\xi_v z_v}}{z_v \rho_\ell c_\ell^2 + z_\ell \rho_v c_v^2} \kappa_T \left(T_v - T_\ell\right), \tag{3.3.26}$$

with the coefficients ξ_ϕ defined by (3.3.16).

In the limit of stiff thermal relaxation, the (velocity-)pressure-temperature equilibrium system is obtained. It naturally reduces to the 4-equation model (3.3.18), which consists in a fully conservative transport system. It is made of conservation equations for the whole mixture's momentum and energy, and conservation of each phases' mass.

3.3.2.2.2 Phase change

In addition, phase change can be taken into account. This is usually achieved by considering a stiff relaxation towards thermodynamic equilibrium [Saurel et al., 2008, Le Martelot et al., 2014, Chiapolino et al., 2016, Chiapolino et al., 2017]. In this respect, the 4-equation model (3.3.18) is supplemented with a relaxation term on the Gibbs free energy $\kappa_g \left(g_\ell - g_v\right)$ to describe mass transfer between phases, where κ_g is the relaxation rate. The model reads

$$\frac{\partial z_v \rho_v}{\partial t} + \frac{\partial z_v \rho_v u}{\partial x} = \rho \kappa_g \left(g_\ell - g_v\right) \tag{3.3.27a}$$

$$\frac{\partial z_\ell \rho_\ell}{\partial t} + \frac{\partial z_\ell \rho_\ell u}{\partial x} = -\rho \kappa_g \left(g_\ell - g_v\right) \tag{3.3.27b}$$

$$\frac{\partial \rho u}{\partial t} + \frac{\partial \rho u^2 + P}{\partial x} = 0 \tag{3.3.27c}$$

$$\frac{\partial \rho e_\mathrm{t}}{\partial t} + \frac{\partial \left(\rho e_\mathrm{t} + P\right) u}{\partial x} = 0. \tag{3.3.27d}$$

After the hyperbolic transport corresponding to system (3.3.18), the operator splitting procedure is applied to compute the stiff relaxation to thermodynamic equilibrium, which is computed by solving

$$g_\ell(\rho_\ell^{\mathrm{eq}}, e_\ell^{\mathrm{eq}}) = g_v(\rho_v^{\mathrm{eq}}, e_v^{\mathrm{eq}}), \tag{3.3.28}$$

with equilibrium values corresponding to the transported density and energy:

$$z_\ell^{\mathrm{eq}} \rho_\ell^{\mathrm{eq}} + z_v^{\mathrm{eq}} \rho_v^{\mathrm{eq}} = \rho \tag{3.3.29a}$$

$$z_\ell^{\mathrm{eq}} \rho_\ell^{\mathrm{eq}} e_\ell^{\mathrm{eq}} + z_v^{\mathrm{eq}} \rho_v^{\mathrm{eq}} e_v^{\mathrm{eq}} = \rho e_s. \tag{3.3.29b}$$

[Saurel et al., 2008, Le Martelot et al., 2014] solve this for Stiffened Gas EoS closures using a Newton-Raphson solver, while [Chiapolino et al., 2016, Chiapolino et al., 2017] propose an approximate single-step resolution. Note that [Le Martelot et al., 2014] achieves the computation of a boiling flow as depicted in Figure 3.16 by adding surface tension (see next paragraph) and gravity effects to the flow.

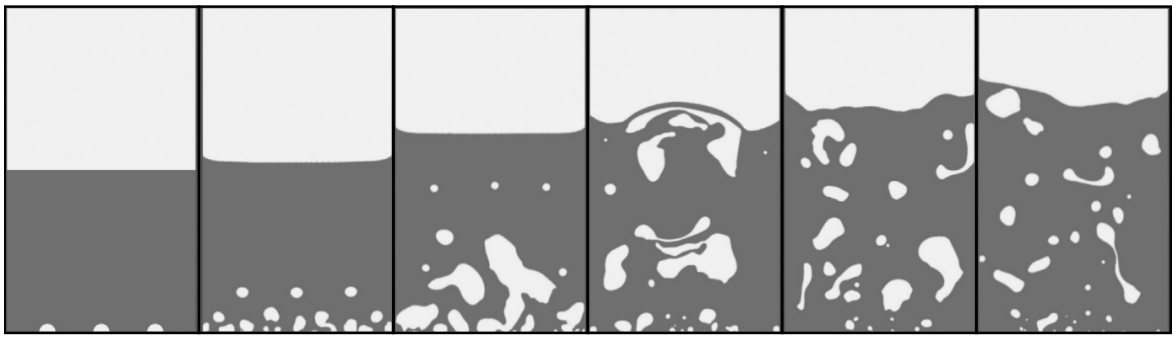

Figure 3.16: Boiling flow simulation by [Le Martelot et al., 2014], addressing phase change, surface tension and gravity.

Note that some particular canonical cases allow for a more accurate resolution of the equilibrium, as empirical relations are available to model finite-time relaxation processes in the BN model (3.3.11). For instance, in [Furfaro and Saurel, 2016], the BN model is used with phase change and temperature relaxation terms to achieve a direct simulation of phase change for a droplet. Finite temperature and phase change relaxation rates are evaluated by means of Sherwood and Nusselt numbers correlations, following [Abramzon and Sirignano, 1989].

Also, very recent work of [Matheis and Hickel, 2018], inspired by the two-phase equilibrium computations of [Qiu et al., 2014], can be related to the family of multifluid methods, although the authors do not claim such affiliation. The conservative evolution model would correspond to the equilibrium version of system (3.3.27), which yields the 3-equation *homogeneous equilibrium* model (3.3.19). This system is expressed by [Matheis and Hickel, 2018] in a multicomponent real gas context. Interesting results were obtained for the large-eddy simulation of the ECN Spray A [Pickett et al., 2010].

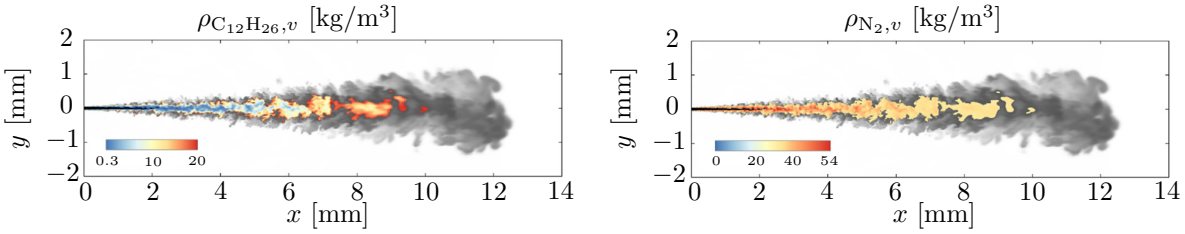

Figure 3.17: Large-eddy simulation of the *Spray A* test configuration of the *Engine Combustion Network* (ECN) [Pickett et al., 2010]. These snapshots taken from [Matheis and Hickel, 2018] display the n-dodecane and nitrogen partial densities within the vapour phase (coloured fields), while the temperature field is displayed in a gray scale where $z_\ell \notin [0.01, 0.99]$.

3.3.2.2.3 Surface Tension

Surface tension effects can be incorporated into the model. In the context of Sharp Interface Methods, it is represented as a surface force located at the interface. At a liquid-vapour interface, [Landau and Lifshitz, 1987] provide an expression of the force balance, as:

$$(P_\ell - P_v + \sigma\kappa)\vec{n} = (\boldsymbol{\tau}_\ell - \boldsymbol{\tau}_v)\vec{n} + \vec{\nabla}_s\sigma, \tag{3.3.30}$$

with P_ϕ the pressures in the bulk phase $\phi \in \{\ell, v\}$, σ the surface tension coefficient, κ the interface curvature, $\vec{n}$ the vector normal to the interface pointing from liquid to vapour and $\boldsymbol{\tau}_\phi$ the viscous stress tensor in phase ϕ.

As presented by [Brackbill et al., 1992], when neglecting the variations of the surface tension coefficient and the viscous stress contributions along the interface, the surface force $\vec{f_s}$ is normal to the interface and writes

$$\vec{f_s} = \sigma\kappa\vec{n}. \tag{3.3.31}$$

In the current context of Diffuse Interface Methods, the interface is represented with a finite thickness δ_s. In this respect, the surface tension expression has to be formulated as a volume force $\vec{f_v}$, the integral of which across the interface should yield the surface force as the interface thickness tends to zero. In other words,

$$\lim_{\delta_s \to 0} \int_{\mathcal{V}} \vec{f_v}\, \mathrm{d}\vec{x} = \int_{\mathcal{A}} \vec{f_s}\, \mathrm{d}\vec{x}_s, \tag{3.3.32}$$

with $\mathcal{A}$ an interfacial surface and $\mathcal{V}$ the corresponding volume of thickness δ_s. [Brackbill et al., 1992] then shows that such volume force can be expressed by means of the variations of a color function

across the interface. A natural choice for such color function is for instance the liquid volume fraction z_ℓ. This *Continuum Surface Force* (CSF) reads

$$\vec{f_v} = \sigma\kappa(\vec{x})\vec{\nabla}z_\ell, \tag{3.3.33}$$

where the local interface curvature is approximated by

$$\kappa(\vec{x}) = \vec{\nabla}\cdot\left(\frac{\vec{\nabla}z_\ell}{\left\|\vec{\nabla}z_\ell\right\|}\right), \tag{3.3.34}$$

as the term within the divergence operator represents the vector normal to the interface.

Further developments have been led in order to improve the behaviour of the model. First, [Gueyffier et al., 1999] proposed a conservative form of the surface force in the momentum equation. This reads, in two or three dimensions,

$$\frac{\partial\rho\vec{u}}{\partial t} + \vec{\nabla}\cdot(\rho\vec{u}\otimes\vec{u} + P\mathfrak{J} - \sigma\boldsymbol{\tau}_\sigma) = 0, \tag{3.3.35}$$

with the surface tension tensor $\boldsymbol{\tau}_\sigma$ defined as

$$\boldsymbol{\tau}_\sigma = \left|\vec{\nabla}z_\ell\right|\mathfrak{J} - \frac{\vec{\nabla}z_\ell\otimes\vec{\nabla}z_\ell}{\left|\vec{\nabla}z_\ell\right|} \tag{3.3.36}$$

Later-on, a conservative form was proposed by [Perigaud and Saurel, 2005] for the total energy equation, in the context of a 5-equation multifluid model. This requires to inject a surface tension potential energy e_σ into the transported total energy $e_\mathrm{t} = e_s + e_c + e_\sigma$, of the form

$$e_\sigma = \frac{\sigma}{\rho}\left|\vec{\nabla}z_\ell\right|, \tag{3.3.37}$$

so that the energy conservation becomes

$$\frac{\partial\rho e_\mathrm{t}}{\partial t} + \vec{\nabla}\cdot\left(\left(\rho e_\mathrm{t} + P\right)\vec{u} - \sigma\boldsymbol{\tau}_\sigma\cdot\vec{u}\right) = 0. \tag{3.3.38}$$

Although this formulation is better than a mere source-term implementation of the surface tension, the computation of the curvature from equation (3.3.34) is very sensitive to the local liquid mass fraction topology, and may be ill-behaved when high-frequency numerical oscillations are present. In this respect, the surface tension computations require a well resolved interface thickness – or, in other words, a relatively diffused interface profile – for the curvature to be satisfyingly computed.

3.3.2.3 Numerical Methods

3.3.2.3.1 Hyperbolic transport

In its initial formulation [Baer and Nunziato, 1986], the non-equilibrium model was solved using an 'old fashioned' *method of lines* together with an implicit ODE solver. The more recent methods are mostly based on a finite-volume method for space discretization, as reviewed in [Saurel and Pantano, 2018], as it provides a relevant framework for the study of wave propagation and shock–waves interactions. The different multifluid systems can be summarized under the form (see e.g. [Murrone and Guillard, 2005]):

$$\frac{\partial\mathbf{U}}{\partial t} + \vec{\nabla}\cdot\boldsymbol{F}(\mathbf{U}) + \mathfrak{M}(\mathbf{U})\cdot\vec{\nabla}\mathbf{U} = \boldsymbol{S}(\mathbf{U}), \tag{3.3.39}$$

where $\mathbf{U}$ are the transported variables, $\boldsymbol{F}(\mathbf{U})$ the conservative flux, $\mathfrak{M}(\mathbf{U})$ the non-conservative transport operator, and $\boldsymbol{S}$ the source terms operator (including the relaxation terms). The finite-volume method framework consists in computing the evolution of the mean value $\mathbf{U}_j^n$, defined as

$$\mathbf{U}_j^n = \frac{1}{\mathcal{V}_{\mathcal{C}_j}} \int_{\mathcal{C}_j} \mathbf{U}(\vec{x}, t^n)\, \mathrm{d}\vec{x} \tag{3.3.40}$$

where the index j denotes the j^{th} cell of the computational grid. Equation (3.3.39) is then integrated. This yields,

$$\begin{aligned} \mathbf{U}_j^{n+1} = \mathbf{U}_j^n - \frac{1}{\mathcal{V}_{\mathcal{C}_j}} \int_{t^n}^{t^{n+1}} \int_{\partial\mathcal{C}_j} \mathcal{F}(\mathbf{U})\vec{n}\, \mathrm{d}S\, \mathrm{d}t - \frac{1}{\mathcal{V}_{\mathcal{C}_j}} \int_{t^n}^{t^{n+1}} \int_{\mathcal{C}_j} \mathfrak{M}(\mathbf{U}) \cdot \vec{\nabla}\mathbf{U}\, \mathrm{d}\mathbf{U}\, \mathrm{d}t \\ + \frac{1}{\mathcal{V}_{\mathcal{C}_j}} \int_{t^n}^{t^{n+1}} \int_{\mathcal{C}_j} \boldsymbol{S}(\mathbf{U})\, \mathrm{d}\vec{x}\, \mathrm{d}t \end{aligned} \tag{3.3.41}$$

The numerical resolution of this system is then generally performed using an operator-splitting strategy. First order resolution typically consists in:

(i) computing the hyperbolic transport (including the non-conservative terms) by means of a Godunov-type method. This requires to solve for a Riemann problem at cells' boundaries, either exactly or approximately, in order to evaluate the numerical fluxes involved in the update formulation.

(ii) computing the source terms from the obtained state.

Note that the need for solving Riemann problems for the typically used Godunov-like methods is one of the motivations to carry out the systematic characteristic analysis of the multifluid systems, as done in [Saurel and Abgrall, 1999, Allaire et al., 2002, Murrone and Guillard, 2005, Le Martelot et al., 2014]. The Riemann problem is usually solved approximately using the classic HLL [Harten et al., 1983] and HLLC [Toro et al., 1994] solvers, or the Roe method [Roe, 1986].

Higher-order resolution is often achieved using a MUSCL scheme [van Leer, 1979] with limiters. In presence of source terms, an advanced operator-splitting procedure [Strang, 1968] can be used, as done in [Saurel and Abgrall, 1999].

3.3.2.3.2 Limiting the interface smearing

Although the liquid-gas interface is by definition of the method a *diffuse* zone, this artificial mixing zone should remain constrained to a relatively thin zone during computation. In order to avoid the numerical smearing of the interface, different strategies have been developed for 5-equation pressure-velocity equilibrium models (3.3.12).

A first strategy consists in using a strongly anti-diffusive TVD transport for the transport of the phases' volume fraction. Instead of transporting the volume fraction z_ℓ using a MUSCL scheme with second-order TVD limiter, [Chiapolino et al., 2017] uses the *Overbee* limiter which is the most anti-diffusive TVD limiter according to Sweby's theory [Sweby, 1984]. The classic Minmod and Superbee limiters are displayed together with the Overbee limiter in Figure 3.18. Minmod represents the most diffusive second-order TVD method, while Superbee is the most anti-diffusive second-order TVD method. Overbee goes beyond the second-order limit and consists in the most anti-diffusive TVD method. This strategy is thus extremely straightforward to formulate since it only consists in changing the limiter used in the MUSCL scheme. The results obtained from such method are shown in Figure 3.19. The numerical smearing appears to be satisfyingly reduced compared to the case using the Superbee limiter.

One drawback of such method is the absence of explicit control of the diffuse interface thickness. This can be obtained by another strategy, which consists in artificially compressing the interface by

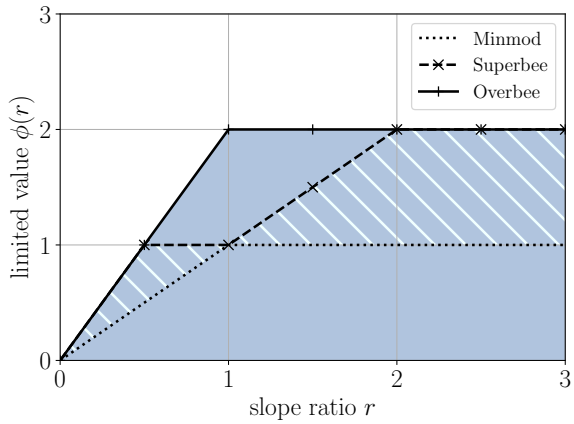

Figure 3.18: Sweby's diagram [Sweby, 1984] for Minmod, Superbee and Overbee limiters. Coloured region represents the TVD region. Hatched region is the second-order TVD region.

introduction of a source term into the volume fraction transport equation [Shukla et al., 2010]. This strategy is close to the *re-initialization* step used by [Desjardins et al., 2008] for the Level-Set method, and the compressive source term is similar to the one appearing for the Level-Set method, in equation (3.2.9). The obtained transport-compressive evolution equation for the liquid volume fraction is then

$$\frac{\partial z_\ell}{\partial t} + \vec{u}\cdot\vec{\nabla} z_\ell = \mathcal{U}_0 \vec{\nabla}\cdot\left[\epsilon_h \left|\vec{\nabla} z_\ell\right| - z_\ell\left(1-z_\ell\right)\vec{n}\right], \tag{3.3.42}$$

where the interface normal is $\vec{n} = \frac{\vec{\nabla} z_\ell}{\left|\vec{\nabla} z_\ell\right|}$, and $\mathcal{U}_0$ is a *characteristic compression velocity* of the interface, which is typically set to a much larger value than the flow velocity. In this respect, the solution is always driven towards the compressed interface solution

$$z_\ell = \frac{1}{2}\left(1 + \tanh\left(\frac{n}{2\epsilon_h}\right)\right). \tag{3.3.43}$$

Note that the mixture's density must take into account this interface compression. Its transport equation is thereby supplemented with an corresponding compressive term, which finally reads

$$\frac{\partial \rho}{\partial t} + \vec{\nabla}\cdot\rho\vec{u} = H(z_\ell)\mathcal{U}_0\vec{n}\cdot\left[\vec{\nabla}\left(\epsilon_h \vec{n}\cdot\vec{\nabla}\rho\right) - \left(1-2z_\ell\right)\vec{\nabla}\rho\right], \tag{3.3.44}$$

where $H(z_\ell)$ is an indicative function of the interface region, that aims at preserving a classic ρ transport away from the interface. Its value is taken by [Shukla et al., 2010] as

$$H(z_\ell) = \tanh\left[\left(\frac{z_\ell(1-z_\ell)}{10^{-2}}\right)^2\right]. \tag{3.3.45}$$

The improvement of the results obtained with this methods are displayed in Figure 3.20. Note that this method is unfortunately not conservative, as the total energy field of the sharpened solution is recomputed from the pressure field and the sharpened density field.

3.3.2.4 Conclusion on the multifluid methods

The family of multifluid methods have been presented. It appears that this class of models, dedicated to compressible flows, can address a wide variety of physical processes. In particular, it can be efficiently

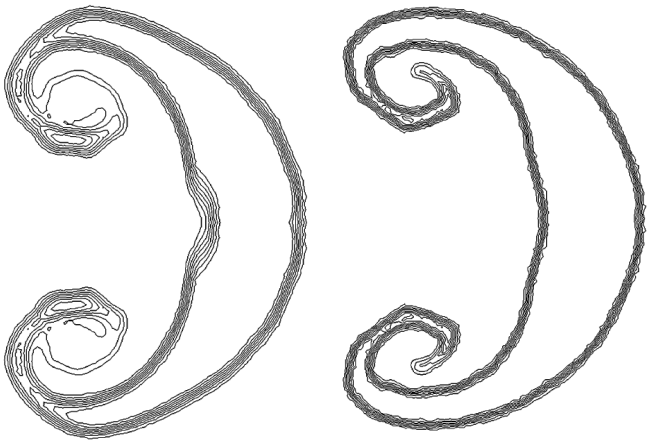

(a) Superbee limiter (b) Overbee limiter

Figure 3.19: Comparison of air-krypton bubble-shock interaction simulations with either Superbee or Overbee slope limiters. Isolines of the liquid volume fraction are displayed. Image taken from [Chiapolino et al., 2017].

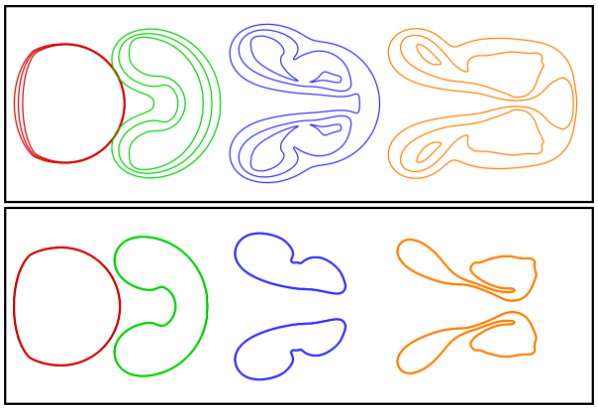

Figure 3.20: Liquid-volume fraction isolines for a Mach 1.22 air-helium shock-bubble interaction. Reduction of the numerical smearing is observed between the top (no specific treatment) and bottom (compressive term added) fields. Taken from [Shukla et al., 2010].

used for simulations involving phase change. Another advantage for such method is that it ensures discrete conservation of the transported quantities. Conversely, its use generally requires to prevent the interface smearing in order to avoid the artificial mixture of the diffuse interface to spread across the computational domain. Also, several cells are needed in the direction normal to the interface to represent it while only a single cell suffices for a volume-of-fluid or front-tracking model.

3.4 Conclusion

In this section, an overview of available two-phase models has been presented. The main properties of the method according to the target application – which consists in LES computations of compressible high-pressure flows in subcritical and supercritical conditions – are summarized in table 3.1. While the volume of fluid method is not relevant for compressible applications, the level-set and front-tracking methods violate mass, momentum and energy conservation. In addition, phase-field methods are a promising family of models but still suffer some limitations as the interface needs to be artificially

thickened. Also, the discretization of the governing equations for non-isothermal flows given by the second-gradient theory is not straightforward as their mathematical structure does not correspond to classically encountered PDEs in fluid mechanics. Finally, the multifluid methods have been presented. They offer a versatile framework to deal with two-phase flows, as different levels of disequilibrium between phases can be addressed, and physical effects (e.g. surface tension, phase change) can be integrated. They are also able to treat formation and disappearance of interfaces. For these reasons, they are suitable considering the target application, although they have some limitations. In particular, they require several grid cells to capture the interface and are subject to progressive interface smearing. The next chapter is dedicated to the description of the formulation of a multifluid method in the present

Method	Discrete conservation	Compressible formulation	Main advantage	Main drawback
Level-set	✗	✓(ghost-fluid)	Simple in multiple dimensions	Conservation error
Volume-of-Fluid	✓	✗	Mass-conserving	Not compressible
Front-tracking	✗	✓(ghost-fluid)	Straightforward interface transport	Conservation error
Phase-field	✓	✓	Intrinsic interface physics	Required resolution scale
Multifluid	✓	✓	Versatility & fulfills conservation	Interface smearing

Table 3.1: Summary of the main properties of the different interface methods.

context, providing the required developments for its use within the target LES solver.

Chapter 4

Numerical methods for hyperbolic conservation laws

The present chapter presents the various numerical methods that have been implemented and used in this Ph.D work. In particular, finite volume, finite element, discontinuous Galerkin and residual distribution schemes are presented. Furthermore, a brief study of monotonicity issues is conducted.

4.1 Introduction

Numerical analysis is a major field of applied mathematics, which addresses a great number of applications, especially in physics. In particular, flow modeling is a very demanding topic for numerical methods, which obviously benefits from the boom in computational resources and capacities. The development of numerical methods involves by nature different scientific fields and must typically take into account multiple constraints such as mathematical constraints (e.g. stability, accuracy), physical constraints (e.g. preservation of positivity of the density and pressure fields, conservation principles, entropy) and computational constraints (e.g. parallel computing efficiency, low memory requirements).

First, section 4.2 introduces useful concepts and results for the study of hyperbolic conservation laws. Then, section 4.3 defines global concepts of numerical analysis and discretization of the solution. Section 4.4 is dedicated to the description of cell-centered methods, namely finite volume and discontinuous Galerkin methods. Finally, section 4.5 presents vertex-centered methods, and more specifically finite element methods among which the Taylor-Galerkin of the AVBP solver.

4.2 Hyperbolic conservation laws

The present work focuses in particular on the numerical resolution of *hyperbolic* partial differential equations (PDE), and more particularly on hyperbolic *conservation laws*. This section briefly introduces these concepts and the corresponding notations.

4.2.1 Definitions

4.2.1.1 Conservation laws

Let $d \in \mathbb{N}^*$ be the number of spatial dimensions and $\Omega \subset \mathbb{R}^d$ be the domain of study. $\partial\Omega$ denotes the frontiers of the domain.

Let $N_\mathrm{t} \in \mathbb{N}^*$ be the number of conserved variables and $\mathbf{U} \in \boldsymbol{\mathcal{U}}$ the vector of these variables, expressed

as a function of the position and time:

$$\mathbf{U} : \mathbb{R}^d \times \mathbb{R}^+ \longrightarrow \boldsymbol{\mathcal{S}}, \tag{4.2.1}$$

$$(\vec{x}, t) \quad \longmapsto \mathbf{U}(\vec{x}, t), \tag{4.2.2}$$

where $\boldsymbol{\mathcal{S}} \subset \mathbb{R}^{N_\mathrm{t}}$ denotes the admissible states for the conserved variables (e.g. verifying positivity of the density, validity of the species mass fractions $Y_k \in [0,1]$), and $\boldsymbol{\mathcal{U}}$ is the space of functions from $\mathbb{R}^d \times \mathbb{R}^+$ into $\boldsymbol{\mathcal{S}}$.

Then, $\mathbf{U}$ is ruled by a *Conservation Law* if there exists a *Flux Function*

$$\vec{\mathcal{F}} : \left\{ \begin{array}{ccc} \boldsymbol{\mathcal{S}} & \longrightarrow & \left(\mathbb{R}^{N_\mathrm{t}}\right)^d, \\ \mathbf{U} & \longmapsto & \vec{\mathcal{F}}(\mathbf{U}), \end{array} \right. \tag{4.2.3}$$

such that $\mathbf{U}$ verifies the PDE:

$$\frac{\partial \mathbf{U}}{\partial t} + \vec{\boldsymbol{\nabla}} \cdot \vec{\mathcal{F}}(\mathbf{U}) = 0. \tag{4.2.4}$$

Note that in this entire chapter, the vector "arrow" symbol $\vec{\cdot}$ indicates quantities having components along the d spatial dimensions, whereas bold font indicates vectors of multiple variables. Obviously, these notations can be continued so that the dot product notation $\cdot$ relates to the dot product over spatial dimensions, and the double contraction product : also refers to spatial dimensions.

Problems involving conservation laws must be provided with initial and/or boundary conditions, leading to the typical *boundary value problem*:

$$\begin{cases} \dfrac{\partial \mathbf{U}}{\partial t} + \vec{\boldsymbol{\nabla}} \cdot \vec{\mathcal{F}}(\mathbf{U}) = 0, & \text{for } (\vec{x}, t) \in \Omega \times \mathbb{R}^*_+, & \text{(4.2.5a)} \\ \text{Boundary Conditions (Dirichlet, Neumann, mixed...)}, & \text{for } (\vec{x}, t) \in \partial\Omega \times \mathbb{R}^*_+, & \text{(4.2.5b)} \\ \text{Initial conditions}, & \text{for } \vec{x} \in \Omega, t = 0. & \text{(4.2.5c)} \end{cases}$$

4.2.1.2 Hyperbolicity

The directional Jacobian matrix of the flux function $\vec{\boldsymbol{\jmath}}_{\vec{n}}(\mathbf{U})$ is defined as

$$\vec{\boldsymbol{\jmath}}_{\vec{n}}(\mathbf{U}) = \frac{\partial \vec{\mathcal{F}}}{\partial \mathbf{U}} \cdot \vec{n}, \tag{4.2.6}$$

with $\vec{n}$ the direction unit-vector of $\mathbb{R}^d$.

A conservation law is said to be *hyperbolic*, if the directional Jacobian matrix of the flux function is diagonalizable with real eigenvalues [LeVeque, 1992]. In this case, we denote $\nu_{\vec{n}}$ the *spectral radius* of $\vec{\boldsymbol{\jmath}}_{\vec{n}}$:

$$\nu_{\vec{n}}(\mathbf{U}) = \max\left\{ |\lambda_{\vec{n}}|, \ \exists \boldsymbol{V} \in \mathbb{R}^{N_\mathrm{t}} \text{ such that } \vec{\boldsymbol{\jmath}}_{\vec{n}}(\mathbf{U}) \cdot \boldsymbol{V} = \lambda_{\vec{n}} \boldsymbol{V} \right\}. \tag{4.2.7}$$

4.2.1.3 Linear advection

For instance, the most simple hyperbolic equation consists in the linear advection of a scalar quantity u at a constant velocity c_0.

$$d = 1, \quad N_\mathrm{t} = 1 \quad \text{and} \quad f(u) = c_0 u, \tag{4.2.8}$$

so that equation (4.2.4) writes:

$$\frac{\partial u}{\partial t} + c_0 \frac{\partial u}{\partial x} = 0. \tag{4.2.9}$$

This simple equation is very convenient as it admits an analytical solution. Indeed, for an initial solution profile $u(x, t = 0) = u_0(x)$, the unique solution of (4.2.9) is given by:

$$\forall t \geq 0, \quad u(x, t) = u_0(x - c_0 t). \tag{4.2.10}$$

The linear advection equation – for its theoretical interest and simplicity – and Euler equations – for its theoretical interest in flow modeling – are the two hyperbolic conservation laws that will be studied in the present chapter. The next section is dedicated to the mathematical description of the Euler equations.

4.2.2 Euler equations

Hyperbolic PDEs are widely studied as they are tightly related with the modeling of transport phenomena in physics. In particular, the Euler equations are an hyperbolic conservation law, provided the convexity of the EoS as studied in Chapter **5**. In the three-dimensional Cartesian case for a multi-component fluid, the conservative variables and the corresponding flux function read:

$$\mathbf{U} = \begin{bmatrix} \rho Y_1 \\ \vdots \\ \rho Y_{N_s} \\ \rho u \\ \rho v \\ \rho w \\ \rho e_{\mathrm{t}} \end{bmatrix} \quad \text{and} \quad \vec{\mathcal{F}}(\mathbf{U}) = \begin{bmatrix} \rho u Y_1 & \rho v Y_1 & \rho w Y_1 \\ \vdots & \vdots & \vdots \\ \rho u Y_{N_s} & \rho v Y_{N_s} & \rho w Y_{N_s} \\ \rho u^2 + P & \rho v u & \rho w u \\ \rho u v & \rho v^2 + P & \rho w v \\ \rho u w & \rho v w & \rho w^2 + P \\ (\rho e_{\mathrm{t}} + P) u & (\rho e_{\mathrm{t}} + P) v & (\rho e_{\mathrm{t}} + P) w \end{bmatrix}. \tag{4.2.11}$$

with ρ the fluid density, u the velocity, e_{t} the total energy $e_{\mathrm{t}} = e_s + e_c$, where the kinetic energy is given by $e_c = \frac{1}{2}\underline{\boldsymbol{u}}^2$.

Note that it can be convenient to introduce the fluxes along each space dimension x, y, z, $\mathcal{F}_x(\mathbf{U})$, $\mathcal{F}_y(\mathbf{U})$ and $\mathcal{F}_z(\mathbf{U})$, which correspond to the columns of the flux tensor given in (4.2.11), so that (4.2.4) can be rewritten as

$$\frac{\partial \mathbf{U}}{\partial t} + \frac{\partial \mathcal{F}_x(\mathbf{U})}{\partial x} + \frac{\partial \mathcal{F}_y(\mathbf{U})}{\partial y} + \frac{\partial \mathcal{F}_z(\mathbf{U})}{\partial z} = 0, \tag{4.2.12}$$

which is a more adapted form for the subsequent developments.

4.2.2.1 Pseudo-linearized form in conservative variables

The numerical resolution of hyperbolic systems requires to analyse their characteristic structure. This can be done by expressing the conservative system of equations (4.2.12) in a pseudo-linear form, which writes

$$\frac{\partial \mathbf{U}}{\partial t} + \mathcal{A}_x(\mathbf{U}) \cdot \frac{\partial \mathbf{U}}{\partial x} + \mathcal{A}_y(\mathbf{U}) \cdot \frac{\partial \mathbf{U}}{\partial y} + \mathcal{A}_z(\mathbf{U}) \cdot \frac{\partial \mathbf{U}}{\partial z} = 0, \tag{4.2.13}$$

where the matrices $\mathcal{A}_x(\mathbf{U})$, $\mathcal{A}_y(\mathbf{U})$ and $\mathcal{A}_z(\mathbf{U})$ represent Jacobian matrices of the flux vectors along each dimension. Only the expression of $\mathcal{A}_x(\mathbf{U})$ is now presented, as the other Jacobian matrices can

be derived from it by a permutation of the dimensions and the corresponding velocities. Its entries read

$$\left(\mathcal{A}_x(\mathbf{U})\right)_{ij} = \left.\frac{\partial \mathcal{F}_x\left(\mathbf{U}\right)_i}{\partial \mathrm{U}_j}\right|_{\mathrm{U}_{k\neq j}} \tag{4.2.14}$$

and its expression can be determined by developing the differential of the conservative volume-specific total energy $\mathrm{d}(\rho e_\mathrm{t})$, as

$$\mathrm{d}(\rho e_\mathrm{t}) = \mathrm{d}(\rho e_s) + \mathrm{d}\left(\frac{\rho\left(u^2+v^2+w^2\right)}{2}\right) = \mathrm{d}(\rho e_s) + u\,\mathrm{d}(\rho u) + v\,\mathrm{d}(\rho v) + w\,\mathrm{d}(\rho w) - e_c\,\mathrm{d}\rho, \tag{4.2.15}$$

which, expressing the differentials of ρe_s and ρ using $(P, \rho Y_1, .., \rho Y_{N_s})$ as independent variables, yields

$$\mathrm{d}(\rho e_\mathrm{t}) = \sum_{i=1}^{N_s}\left[\left.\frac{\partial\left(\rho e_s\right)}{\partial \rho Y_i}\right|_{P,\rho Y_{j\neq i}} - e_c\right]\mathrm{d}(\rho Y_i) + \left.\frac{\partial\left(\rho e_s\right)}{\partial P}\right|_{\rho Y_j}\mathrm{d}P + u\,\mathrm{d}(\rho u) + v\,\mathrm{d}(\rho v) + w\,\mathrm{d}(\rho w)\,. \tag{4.2.16}$$

Introducing the coefficients ζ and $(\xi_i)_{i=1\ldots N_s}$ defined by

$$\begin{cases} \zeta = \left.\dfrac{\partial P}{\partial \rho e_s}\right|_{\rho, Y_j}, & \text{(4.2.17a)} \\ \xi_i = \left.\dfrac{\partial \rho e_s}{\partial \rho Y_i}\right|_{P,\rho Y_{j\neq i}}, & \text{(4.2.17b)} \end{cases}$$

it comes that

$$\mathrm{d}(\rho e_\mathrm{t}) = \sum_{i=1}^{N_s}\left(\xi_i - e_c\right)\mathrm{d}(\rho Y_i) + \frac{1}{\zeta}\,\mathrm{d}P + u\,\mathrm{d}(\rho u) + v\,\mathrm{d}(\rho v) + w\,\mathrm{d}(\rho w)\,. \tag{4.2.18}$$

and the Jacobian matrix finally reads

$$\mathcal{A}_x(\mathbf{U}) = \begin{bmatrix} \left(1-Y_1\right)u & \cdots & -Y_{N_s}u & Y_1 & 0 & 0 & 0 \\ \vdots & \ddots & \vdots & \vdots & \vdots & \vdots & \vdots \\ -Y_1 u & \cdots & \left(1-Y_{N_s}\right)u & Y_{N_s} & 0 & 0 & 0 \\ -u^2+\zeta\left(e_c-\xi_1\right) & \cdots & -u^2+\zeta\left(e_c-\xi_{N_s}\right) & \left(2-\zeta\right)u & -\zeta v & -\zeta w & \zeta \\ -uv & \cdots & -uv & v & u & 0 & 0 \\ -uw & \cdots & -uw & w & 0 & u & 0 \\ \left[\left(e_c-\xi_1\right)\zeta - h_\mathrm{t}\right]u & \cdots & \left[\left(e_c-\xi_{N_s}\right)\zeta - h_\mathrm{t}\right]u & h_\mathrm{t}-u^2\zeta & -\zeta v & -\zeta w & \left(1+\zeta\right)u \end{bmatrix}. \tag{4.2.19}$$

It is worth mentioning that the form of the Jacobian matrix expressed in (4.2.19) stands for any thermodynamic closure. The expression of coefficients ζ and ξ_i, which somehow encapsulate the thermodynamic closure of the system, can then be obtained by expressing the differential of the sensible energy with respect to pressure and the quantities ρY_i. By (4.2.16) and (4.2.18), it writes

$$\mathrm{d}(\rho e_s) = \frac{1}{\zeta}\,\mathrm{d}P + \sum_{i=1}^{N_s}\xi_i\,\mathrm{d}(\rho Y_i) \tag{4.2.20}$$

In the case of a cubic EoS, this yields

$$\mathrm{d}(\rho e_s) = \frac{\rho\beta c_v}{\alpha}\,\mathrm{d}P + \sum_{i=1}^{N_s}\left[\frac{\rho c_p}{\alpha}v_i - h_{s,i}\right]\mathrm{d}(\rho Y_i) \tag{4.2.21}$$

so that

$$\begin{cases} \zeta = \dfrac{\alpha}{\rho\beta c_v}, & \text{(4.2.22a)} \\ \xi_i = \dfrac{\rho c_p}{\alpha} v_i - h_{s,i}. & \text{(4.2.22b)} \end{cases}$$

4.2.2.2 Pseudo-linearized form in primitive variables

In order to further analyze the characteristic structure of equation (4.2.12), it is convenient to rewrite equation (4.2.13) in terms of the primitive variables $\boldsymbol{V}$, defined by

$$\boldsymbol{V} = \begin{bmatrix} \rho Y_1 \\ \vdots \\ \rho Y_{N_s} \\ u \\ v \\ w \\ P \end{bmatrix}. \tag{4.2.23}$$

This writes

$$\frac{\partial \boldsymbol{V}}{\partial t} + \mathcal{B}_x(\boldsymbol{V}) \cdot \frac{\partial \boldsymbol{V}}{\partial x} + \mathcal{B}_y(\boldsymbol{V}) \cdot \frac{\partial \boldsymbol{V}}{\partial y} + \mathcal{B}_z(\boldsymbol{V}) \cdot \frac{\partial \boldsymbol{V}}{\partial z} = 0, \tag{4.2.24}$$

and the matrices $\mathcal{B}_x$, $\mathcal{B}_y$ and $\mathcal{B}_z$ are obtained by means of a *change of basis*. The transformation matrix $\mathcal{T}_{\boldsymbol{V}\mathbf{U}}$ associated with the change of basis is obtained from

$$\mathcal{T}_{\boldsymbol{V}\mathbf{U}} = \left[\left. \frac{\partial \mathbf{U}_i}{\partial \boldsymbol{V}_j} \right|_{\boldsymbol{V}_{k \neq j}} \right], \tag{4.2.25}$$

which yields

$$\mathcal{T}_{\boldsymbol{V}\mathbf{U}} = \begin{bmatrix} 1 & \cdots & 0 & 0 & 0 & 0 & 0 \\ \vdots & \ddots & \vdots & \vdots & \vdots & \vdots & \vdots \\ 0 & \cdots & 1 & 0 & 0 & 0 & 0 \\ u & \cdots & u & \rho & 0 & 0 & 0 \\ v & \cdots & v & 0 & \rho & 0 & 0 \\ w & \cdots & w & 0 & 0 & \rho & 0 \\ (e_c + \xi_1) & \cdots & (e_c + \xi_{N_s}) & \rho u & \rho v & \rho w & \frac{1}{\zeta} \end{bmatrix}, \tag{4.2.26a}$$

and

$$\mathcal{T}_{\mathbf{U}\boldsymbol{V}} = \mathcal{T}_{\boldsymbol{V}\mathbf{U}}^{-1} = \begin{bmatrix} 1 & \cdots & 0 & 0 & 0 & 0 & 0 \\ \vdots & \ddots & \vdots & \vdots & \vdots & \vdots & \vdots \\ 0 & \cdots & 1 & 0 & 0 & 0 & 0 \\ -u/\rho & \cdots & -u/\rho & 1/\rho & 0 & 0 & 0 \\ -v/\rho & \cdots & -v/\rho & 0 & 1/\rho & 0 & 0 \\ -w/\rho & \cdots & -w/\rho & 0 & 0 & 1/\rho & 0 \\ \zeta\,(e_c - \xi_1) & \cdots & \zeta\,(e_c - \xi_{N_s}) & -\zeta u & -\zeta v & -\zeta w & \zeta \end{bmatrix}. \tag{4.2.26b}$$

The Jacobian matrices in primitive variables can then be computed as

$$\mathcal{B}_x(\boldsymbol{V}) = \mathcal{T}_{\boldsymbol{V}\mathbf{U}}^{-1} \mathcal{A}_x(\mathbf{U})\, \mathcal{T}_{\boldsymbol{V}\mathbf{U}}, \tag{4.2.27}$$

and one gets

$$\mathcal{B}_x(\boldsymbol{V}) = \begin{bmatrix} u & \cdots & 0 & \rho Y_1 & 0 & 0 & 0 \\ \vdots & \ddots & \vdots & \vdots & \vdots & \vdots & \vdots \\ 0 & \cdots & u & \rho Y_{N_s} & 0 & 0 & 0 \\ 0 & \cdots & 0 & u & 0 & 0 & 1/\rho \\ 0 & \cdots & 0 & 0 & u & 0 & 0 \\ 0 & \cdots & 0 & 0 & 0 & u & 0 \\ 0 & \cdots & 0 & \rho\zeta\left(h_s - \overline{\xi}\right) & 0 & 0 & u \end{bmatrix}, \tag{4.2.28}$$

with $\overline{\xi} = \sum_{i=1}^{N_s} Y_i \xi_i$. Once again, this form is generic and stands for any thermodynamic closure.

4.2.2.3 Characteristic form and the speed of sound

Finally, the characteristic form is obtained by diagonalizing the matrix $\mathcal{B}_x$, which boils down to

$$\Lambda_x(\mathbf{W}) = \mathcal{T}_{\boldsymbol{V}\mathbf{W}}\ \mathcal{B}_x(\boldsymbol{V})\ \mathcal{T}_{\mathbf{W}\boldsymbol{V}}. \tag{4.2.29}$$

This implies that there exist a set of variables $\mathbf{W}$ such that the Jacobian matrix of the system is diagonalizable in these variables. Such variables are called the *characteristic variables*.
In characteristic variables, the diagonal Jacobian matrix reads:

$$\Lambda_x(\mathbf{W}) = \mathrm{diag}\left(u, \cdots, u, u - \sqrt{\zeta\left(h_s - \overline{\xi}\right)}, u + \sqrt{\zeta\left(h_s - \overline{\xi}\right)}\right). \tag{4.2.30}$$

Here appears the speed of sound c_H of the hyperbolic system (4.2.12):

$$c_H = \sqrt{\zeta\left(h_s - \overline{\xi}\right)}. \tag{4.2.31}$$

This expression can be recast into the following form:

$$c_H^2 = c^2 + \left.\frac{\partial P}{\partial e_s}\right|_{\rho,\underline{\boldsymbol{Y}}} \left(\frac{P}{\rho^2} - \left.\frac{\partial e_s}{\partial \rho}\right|_{s,\underline{\boldsymbol{Y}}}\right). \tag{4.2.32}$$

with $c^2 = \left.\frac{\partial P}{\partial \rho}\right|_{s,\underline{\boldsymbol{Y}}}$ the square of the isentropic speed of sound.

Proof:

First, it can be shown that $\overline{\xi} = \left.\frac{\partial(\rho e_s)}{\partial \rho}\right|_{P,\underline{\boldsymbol{Y}}}$, using equation (4.2.20), as

$$\begin{aligned} \mathrm{d}(\rho e_s) &= \frac{1}{\zeta}\,\mathrm{d}P + \sum_{i=1}^{N_s} \left.\frac{\partial(\rho e_s)}{\partial \rho Y_i}\right|_{P,\rho Y_{j\neq i}} \mathrm{d}(\rho Y_i), \\ &= \frac{1}{\zeta}\,\mathrm{d}P + \underbrace{\sum_{i=1}^{N_s} Y_i \left.\frac{\partial(\rho e_s)}{\partial \rho Y_i}\right|_{P,\rho Y_{j\neq i}}}_{=\overline{\xi}} \mathrm{d}\rho + \rho \sum_{i=1}^{N_s} \left.\frac{\partial(\rho e_s)}{\partial \rho Y_i}\right|_{P,\rho Y_{j\neq i}} \mathrm{d}Y_i. \end{aligned}$$

Since $\underline{\boldsymbol{Y}}$ verifies $Y_{N_s} = 1 - \sum_{j=1}^{N_s-1} Y_j$, this relation becomes

$$\mathrm{d}(\rho e_s) = \frac{1}{\zeta}\,\mathrm{d}P + \overline{\xi}\,\mathrm{d}\rho + \rho \sum_{i=1}^{N_s-1} \left[\left.\frac{\partial(\rho e_s)}{\partial \rho Y_i}\right|_{P,\rho Y_{j\neq i}} - \left.\frac{\partial(\rho e_s)}{\partial \rho Y_{N_s}}\right|_{P,\rho Y_{j\neq N_s}} \right] \mathrm{d}Y_i,$$

in which the differentiating variables $P, \rho, (Y_i)_{i=1..N_s-1}$ are independent. This directly yields

$$\overline{\xi} = \left.\frac{\partial(\rho e_s)}{\partial \rho}\right|_{P,\underline{\boldsymbol{Y}}} \tag{4.2.33}$$

Then, using the definitions of ζ, one has:

$$\begin{aligned} c_H^2 &= \left.\frac{\partial P}{\partial(\rho e_s)}\right|_{\rho\underline{\boldsymbol{Y}}} \left(e_s + \frac{P}{\rho} - \left.\frac{\partial(\rho e_s)}{\partial \rho}\right|_{P,\underline{\boldsymbol{Y}}} \right) \\ &= \frac{1}{\rho} \left.\frac{\partial P}{\partial e_s}\right|_{\rho\underline{\boldsymbol{Y}}} \left(e_s + \frac{P}{\rho} - \rho \left.\frac{\partial e_s}{\partial \rho}\right|_{P,\underline{\boldsymbol{Y}}} - e_s \right) \\ &= \frac{P}{\rho^2} \left.\frac{\partial P}{\partial e_s}\right|_{\rho\underline{\boldsymbol{Y}}} - \left.\frac{\partial P}{\partial e_s}\right|_{\underline{\boldsymbol{Y}}} \left.\frac{\partial e_s}{\partial \rho}\right|_{P,\underline{\boldsymbol{Y}}} \end{aligned}$$

Using a classic result of differential calculus, one has $\left.\frac{\partial P}{\partial e_s}\right|_{\rho\underline{\boldsymbol{Y}}} \left.\frac{\partial e_s}{\partial \rho}\right|_{P,\underline{\boldsymbol{Y}}} = -\left.\frac{\partial P}{\partial \rho}\right|_{e_s,\underline{\boldsymbol{Y}}}$ and

$$c_H^2 = \frac{P}{\rho^2} \left.\frac{\partial P}{\partial e_s}\right|_{\rho\underline{\boldsymbol{Y}}} + \left.\frac{\partial P}{\partial \rho}\right|_{e_s,\underline{\boldsymbol{Y}}}$$

Another classic rule of differential calculus states that

$$\left.\frac{\partial P}{\partial \rho}\right|_{e_s,\underline{\boldsymbol{Y}}} = \left.\frac{\partial P}{\partial \rho}\right|_{s,\underline{\boldsymbol{Y}}} + \left.\frac{\partial P}{\partial s}\right|_{\rho,\underline{\boldsymbol{Y}}} \left.\frac{\partial s}{\partial \rho}\right|_{e_s,\underline{\boldsymbol{Y}}}$$

so that

$$\begin{aligned} c_H^2 &= \frac{P}{\rho^2} \left.\frac{\partial P}{\partial e_s}\right|_{\rho,\underline{\boldsymbol{Y}}} + \left.\frac{\partial P}{\partial \rho}\right|_{s,\underline{\boldsymbol{Y}}} + \left.\frac{\partial P}{\partial s}\right|_{\rho,\underline{\boldsymbol{Y}}} \left.\frac{\partial s}{\partial \rho}\right|_{e_s,\underline{\boldsymbol{Y}}} \\ &= \left.\frac{\partial P}{\partial \rho}\right|_{s,\underline{\boldsymbol{Y}}} + \left.\frac{\partial P}{\partial e_s}\right|_{\rho,\underline{\boldsymbol{Y}}} \left(\frac{P}{\rho^2} + \left.\frac{\partial e_s}{\partial P}\right|_{\rho,\underline{\boldsymbol{Y}}} \left.\frac{\partial P}{\partial s}\right|_{\rho,\underline{\boldsymbol{Y}}} \left.\frac{\partial s}{\partial \rho}\right|_{e_s,\underline{\boldsymbol{Y}}} \right) \\ &= \left.\frac{\partial P}{\partial \rho}\right|_{s,\underline{\boldsymbol{Y}}} + \left.\frac{\partial P}{\partial e_s}\right|_{\rho,\underline{\boldsymbol{Y}}} \left(\frac{P}{\rho^2} + \left.\frac{\partial e_s}{\partial s}\right|_{\rho,\underline{\boldsymbol{Y}}} \left.\frac{\partial s}{\partial \rho}\right|_{e_s,\underline{\boldsymbol{Y}}} \right) \\ &= \left.\frac{\partial P}{\partial \rho}\right|_{s,\underline{\boldsymbol{Y}}} + \left.\frac{\partial P}{\partial e_s}\right|_{\rho,\underline{\boldsymbol{Y}}} \left(\frac{P}{\rho^2} - \left.\frac{\partial e_s}{\partial \rho}\right|_{s,\underline{\boldsymbol{Y}}} \right) \end{aligned}$$

Finally, this hyperbolic system speed of sound reads

$$c_H^2 = c^2 + \left.\frac{\partial P}{\partial e_s}\right|_{\rho,\underline{\boldsymbol{Y}}} \left(\frac{P}{\rho^2} - \left.\frac{\partial e_s}{\partial \rho}\right|_{s,\underline{\boldsymbol{Y}}} \right). \tag{4.2.34}$$

Note that once again, this form has been obtained without any assumption on the thermodynamic

closure. However, for a single-phase mixture, the term between parentheses is zero, by virtue of the mass-specific Gibbs relation (2.1.25a), and the classic result is found: the sound speed of the hyperbolic system is equal to the thermodynamic isentropic sound speed, so that the diagonal matrix of eigenvalues reads

$$\Lambda_x(\mathbf{W}) = \operatorname{diag}\left(u, \cdots, u, u-c, u+c\right), \tag{4.2.35}$$

the matrix of left and right eigenvectors being respectively given by

$$\mathcal{T}_{\boldsymbol{V}\mathbf{W}} = \begin{bmatrix} 1 & \cdots & 0 & -Y_1/c^2 & 0 & 0 & 0 \\ \vdots & \ddots & \vdots & \vdots & \vdots & \vdots & \vdots \\ 0 & \cdots & 1 & -Y_{N_s}/c^2 & 0 & 0 & 0 \\ 0 & \cdots & 0 & 0 & 1 & 0 & 0 \\ 0 & \cdots & 0 & 0 & 0 & 1 & 0 \\ 0 & \cdots & 0 & 1/\rho c & 0 & 0 & -1 \\ 0 & \cdots & 0 & 1/\rho c & 0 & 0 & 1 \end{bmatrix}, \tag{4.2.36}$$

$$\mathcal{T}_{\mathbf{W}\boldsymbol{V}} = \mathcal{T}_{\boldsymbol{V}\mathbf{W}}^{-1} = \begin{bmatrix} 1 & \cdots & 0 & 0 & 0 & \rho Y_1/2c & \rho Y_1/2c \\ \vdots & \ddots & \vdots & \vdots & \vdots & \vdots & \vdots \\ 0 & \cdots & 1 & 0 & 0 & \rho Y_{N_s}/2c & \rho Y_{N_s}/2c \\ 0 & \cdots & 0 & 0 & 0 & \rho c/2 & \rho c/2 \\ 0 & \cdots & 0 & 1 & 0 & 0 & 0 \\ 0 & \cdots & 0 & 0 & 1 & 0 & 0 \\ 0 & \cdots & 0 & 0 & 0 & -1/2 & 1/2 \end{bmatrix}. \tag{4.2.37}$$

4.2.3 The Riemann problem

The Riemann problem is a fundamental mathematical problem that is of major importance for the understanding and the resolution of hyperbolic problems. It consists in an *boundary value problem* (BVP) involving two constant initial states. For example in 1D, for $(x,t) \in \mathbb{R} \times \mathbb{R}^+$ by

$$\begin{cases} \dfrac{\partial \mathbf{U}}{\partial t} + \dfrac{\partial \mathcal{F}(\mathbf{U})}{\partial x} = 0, & \text{(4.2.38a)} \\ \mathbf{U}(x,0) = \mathbf{U}_0(x) = \begin{cases} \mathbf{U}_L \text{ if } x < 0, \\ \mathbf{U}_R \text{ if } x \geq 0, \end{cases} & \text{(4.2.38b)} \end{cases}$$

where $\mathbf{U}_L$ and $\mathbf{U}_R$ denote the constant *left* and *right* states respectively. For each component $k \in [\![1, N_t]\!]$ of the conserved variables, the initial state is illustrated by Figure 4.1.

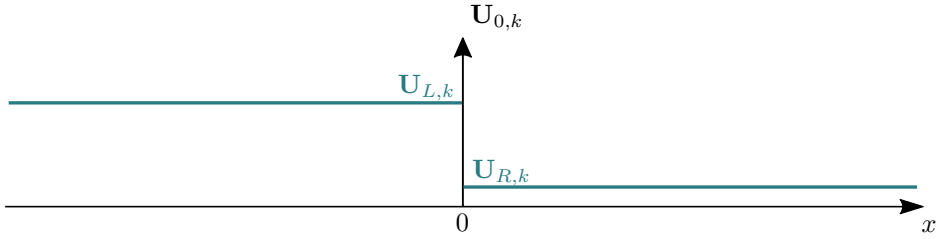

Figure 4.1: Typical form of the initial solution of the Riemann problem for any conserved variable $(\mathbf{U}_k)_{k\in[\![1,N_t]\!]}$.

4.2.3.1 The Riemann problem for a linear conservation equation

When considering a linear conservation equation, the Riemann problem is formulated as

$$\begin{cases} \dfrac{\partial \mathbf{U}}{\partial t} + \mathcal{C}\dfrac{\partial \mathbf{U}}{\partial x} = 0, & \text{(4.2.39a)} \\ \mathbf{U}(x,0) = \mathbf{U}_0(x) = \begin{cases} \mathbf{U}_L \text{ if } x < 0 \\ \mathbf{U}_R \text{ if } x \geq 0 \end{cases} & \text{(4.2.39b)} \end{cases}$$

where $\mathcal{C}$ is a constant diagonalizable matrix. Denoting by $\mathbf{\Lambda}$ its eigenvalues matrix sorted in ascending order, one has

$$\mathcal{C} = \mathcal{R}\,\mathbf{\Lambda}\,\mathcal{L}. \tag{4.2.40}$$

The characteristic variables defined by $\mathbf{W} = \mathcal{L}\mathbf{U}$ are then solution of the equivalent BVP

$$\begin{cases} \dfrac{\partial \mathbf{W}}{\partial t} + \mathbf{\Lambda}\dfrac{\partial \mathbf{W}}{\partial x} = 0, & \text{(4.2.41a)} \\ \mathbf{W}(x,0) = \mathbf{W}_0(x) = \begin{cases} \mathbf{W}_L = \mathcal{L}\mathbf{U}_L \text{ if } x < 0, \\ \mathbf{W}_R = \mathcal{L}\mathbf{U}_R \text{ if } x \geq 0, \end{cases} & \text{(4.2.41b)} \end{cases}$$

which is a set of N_t independent equations equivalent to the linear advection equation (4.2.9). At a given time t and for each eigenvalue $k \in [\![1, N_\mathrm{t}]\!]$, the corresponding characteristic variable W_k is piecewise constant, and the position $x_k(t)$ where its value switches from $\mathrm{W}_{k,L}$ to $\mathrm{W}_{k,R}$ is given by $x_k(t) = \lambda_k t$. This is illustrated by Figure 4.2 in the case $N_\mathrm{t} = 3$. The solution of the Riemann problem (4.2.39) is then obtained by a change of variable from the characteristic variables to the conservative variables:

$$\mathbf{U}(x,t) = \mathcal{R} \cdot \mathbf{W}(x,t), \tag{4.2.42}$$

where

$$\mathrm{W}_k(x,t) = \begin{cases} \mathrm{W}_{k,L} \text{ if } x < \lambda_k t, \\ \mathrm{W}_{k,R} \text{ if } x \geq \lambda_k t. \end{cases} \tag{4.2.43}$$

4.2.3.2 The Riemann problem for the Euler equations

4.2.3.2.1 Description of the Riemann problem

The Riemann problem for the Euler equations is now studied, and the main results are briefly recalled. For the sake of clarity, all the notions introduced here consider a one-dimensional configuration and a single-component fluid, so that the Euler equations reduce to a three-equation system. The reader is referred to [Toro, 2013] and [LeVeque, 1992] for more details. The nonlinear nature of the Euler equations does not allow for an analytical formulation of the solution. Also, unlike the case of linear hyperbolic conservation equations, the Euler equations involve more complex waves. Three types of waves are possible:

- *Shock Waves* (SW), which consist in a discontinuous wave associated with a genuinely non-linear field corresponding to the eigenvalues $u - c$ or $u + c$. Along a shock wave, the characteristics from both sides converge to the shock. Note that although a shock wave is *associated* with the eigenvalue $u - c$ or $u + c$, its actual propagation speed is generally not equal to this characteristic speed.
- *Rarefaction Waves* (RW), which consist in a continuous wave associated with a genuinely non-linear field corresponding to the eigenvalues $u - c$ or $u + c$. The characteristics on both sides of a rarefaction waves are divergent and are connected by a *rarefaction fan*.

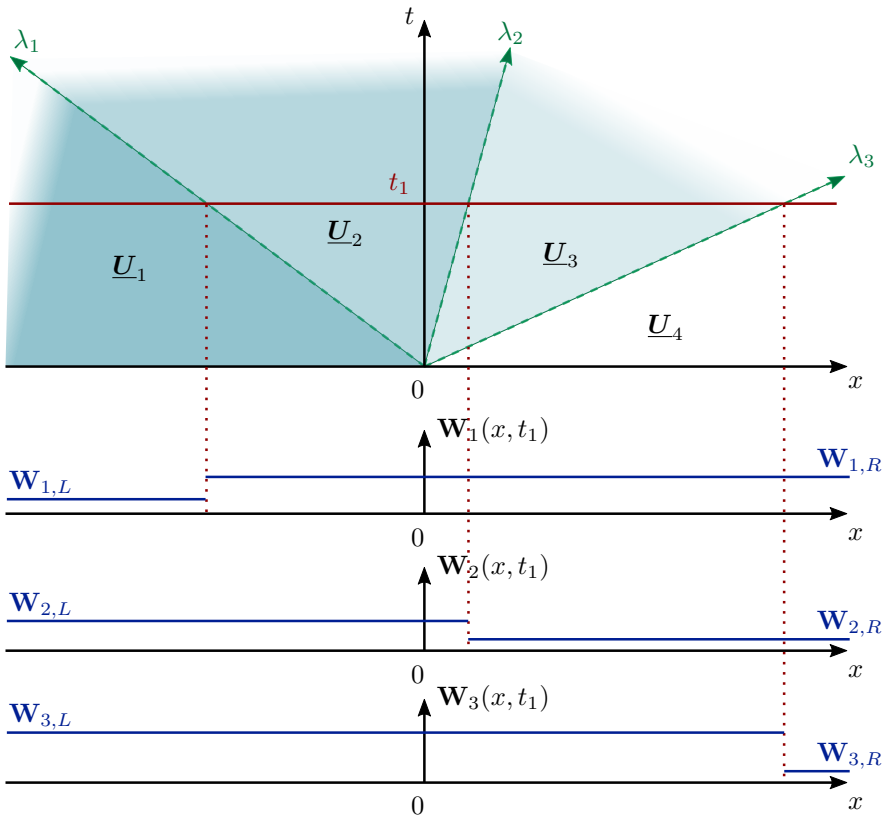

Figure 4.2: Riemann problem for a hyperbolic conservation law, with $N_\mathrm{t} = 3$. Top diagram depicts the propagation of the characteristics at different speeds $\lambda_{\{1,2,3\}}$ in the (x,t) diagram. Bottom diagram shows the values of the characteristic quantities at time $t_1 > 0$

– *Contact Discontinuities* (CD), wave associated with the linearly degenerate field corresponding to the eigenvalue u. Through a contact discontinuity, the pressure and velocity fields are constant but the density field – or, equivalently, the entropy field – can be discontinuous.

Due to the conservation constraints, the propagation speed S_SW of a shock wave is connected to the pre-shock and post-shock states, $\mathbf{U}_\mathrm{pre}$ and $\mathbf{U}_\mathrm{post}$ by the *Rankine-Hugoniot* relation:

$$\mathcal{F}\left(\mathbf{U}_\mathrm{post}\right) - \mathcal{F}\left(\mathbf{U}_\mathrm{pre}\right) = S_\mathrm{SW}\left(\mathbf{U}_\mathrm{post} - \mathbf{U}_\mathrm{pre}\right) \tag{4.2.44}$$

The typical pattern of the Riemann problem for the Euler equations is depicted in Figure 4.3. While the leftmost and rightmost waves (numbered respectively 1 and 3), corresponding to the genuinely non-linear fields, may be either a shock wave or a rarefaction wave, the center wave (number 2), corresponding to the linearly degenerate field, is *always* a contact discontinuity. The *star region* denotes the area between the two non-linear waves. The left-star and right-star states $\mathbf{U}_L^*$ and $\mathbf{U}_R^*$ denote the (constant) states on both sides of the contact discontinuity: these are the unknowns of the Riemann problem.

The different wave configurations that can be encountered are summarized in Figure 4.4. Note that the patterns 4.4a or 4.4c correspond to the physical test configuration of a shock tube, where the initial velocities are zero.

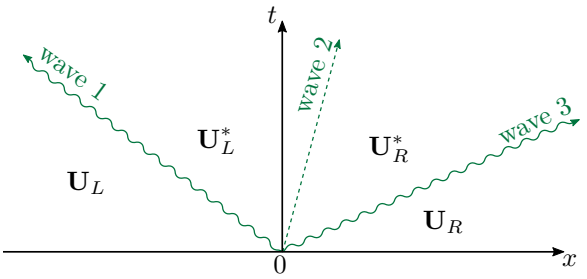

Figure 4.3: The Riemann problem characteristic pattern for the Euler equations. Curly lines are used to represent the waves of unknown nature. The dashed line represents the contact discontinuity.

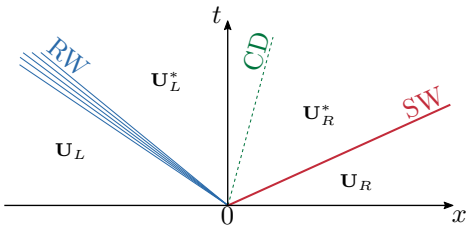

(a) RW-CD-SW pattern. Obtained for instance when $P_L > P_R$ and $u_L = u_R$

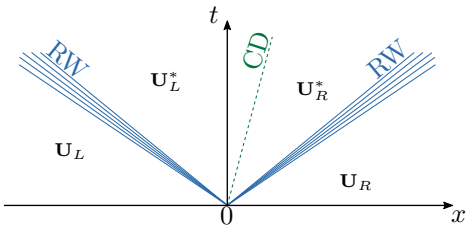

(b) RW-CD-RW pattern. Obtained for instance when $P_L = P_R$ and $u_L < u_R$

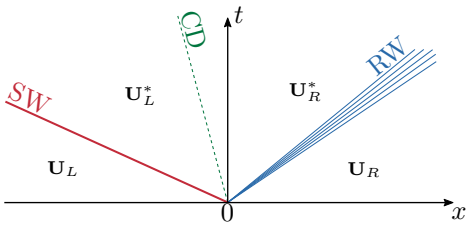

(c) SW-CD-RW pattern. Obtained for instance when $P_L < P_R$ and $u_L = u_R$

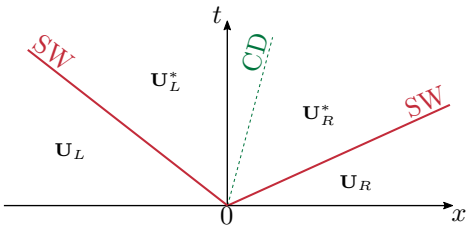

(d) SW-CD-SW pattern. Obtained for instance when $P_L = P_R$ and $u_L > u_R$

Figure 4.4: The different wave patterns that are possible for the Riemann problem with Euler equations. Note that depending on the flow velocity, the three waves can be on the same side of the t axis: only the order of the different waves is important in this illustration and the case of a *subsonic* Riemann problem is arbitrarily chosen to display the wave patterns.

4.2.3.2.2 Interest for the numerical methods

For finite-volume methods or discontinuous-Galerkin methods (see section 4.4) to quote but a few, the solution is discontinuous across cells boundaries. In this respect, it is necessary to evaluate the flux of conservative variables that flows across the cells boundaries during a time step. As depicted in Figure 4.5, this situation can be interpreted locally as a Riemann problem. Indeed, although the Riemann problem assumes constant states for $x \in]-\infty, 0[$ and $x \in [0, +\infty[$, an analogue situation is found when "zooming" enough on each cell boundary. As long as no characteristic wave resulting from interactions with the neighbour intercells reach the considered intercell, the flux corresponds to the physical flux at the considered intercell location $x_{e+1/2}$ obtained by the resolution of the Riemann problem. This is precisely the idea of Godunov, who proposed to evaluate the *intercell flux*, or *numerical flux* by solving for a Riemann problem between states $\mathbf{U}_e$ and $\mathbf{U}_{e+1}$ and estimating the flux flowing through the cell boundary (corresponding to $x = 0$ in the Riemann problem frame) during the time step. The condition of non-interaction with the characteristic waves resulting from neighbour intercell

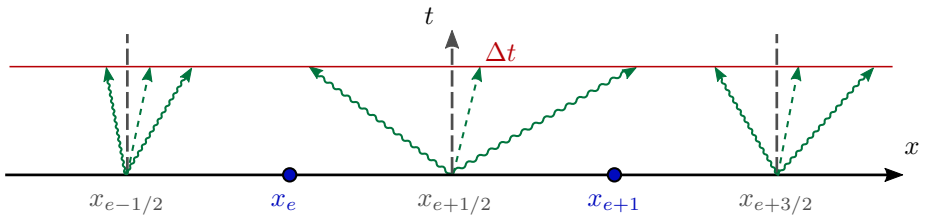

Figure 4.5: Riemann problem representation of the intercell fluxes

Riemann problems is analogue to a CFL condition (see paragraph 4.3.3.3), which writes

$$\frac{\nu \Delta t}{\Delta x} \leq 1, \tag{4.2.45}$$

with ν the speed of the fastest traveling wave within the whole mesh.

In his seminal paper [Godunov, 1959], Godunov provides an efficient iterative method that resolves exactly the Riemann problem. The value of the intercell flux $\mathbf{F}_{\text{God}}$ is then computed as

$$\mathbf{F}_{\text{God}} = \mathcal{F}\left(\mathbf{U}(0)\right) \tag{4.2.46}$$

Despite its efficiency, the complexity and computational cost of this resolution can be reduced by considering approximate resolutions of the Riemann problem. Some examples of this strategy are now presented.

4.2.3.3 Approximate resolution and numerical fluxes

4.2.3.3.1 The Harten-Lax-van Leer (HLL) approximation

The HLL approximate Riemann solver of [Harten et al., 1983] consists in approximating the Riemann problem by a two-wave problem. The contact discontinuity is omitted and a single "star" state is considered at the center region, as shown in Figure 4.6. This simplified representation of the Riemann

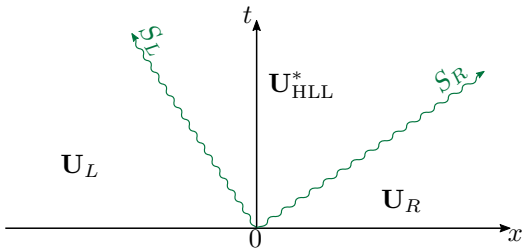

Figure 4.6: Approximation of the Riemann problem solution by the HLL flux.

problem is actually based on the following observation: considering S_L and S_R the fastest signal propagation speeds to the left and right directions, the integral of the conservation law (4.2.4) over the control volume $[S_L t_0, S_R t_0] \times [0, t_0]$ for any time $t_0 > 0$ reads

$$\int_{S_L t_0}^{S_R t_0} \mathbf{U}\left(x, t_0\right) \mathrm{d}x - \int_{S_L t_0}^{S_R t_0} \mathbf{U}\left(x, 0\right) \mathrm{d}x + \int_0^{t_0} \mathcal{F}\left(\mathbf{U}\left(S_R t_0, \tau\right)\right) \mathrm{d}\tau - \int_0^{t_0} \mathcal{F}\left(\mathbf{U}\left(S_L t_0, \tau\right)\right) \mathrm{d}\tau = 0. \tag{4.2.47}$$

This directly reduces to

$$\int_{S_L t_0}^{S_R t_0} \mathbf{U}\left(x, t_0\right) = t_0 \left(S_R \mathbf{U}_R - S_L \mathbf{U}_L + \mathbf{F}_L - \mathbf{F}_R\right), \tag{4.2.48}$$

which, divided by the width of the wave signal of the Riemann problem $t_0 (S_R - S_L)$ yields

$$\frac{1}{t_0 (S_R - S_L)} \int_{S_L t_0}^{S_R t_0} \mathbf{U}(x, t_0) = \frac{S_R \mathbf{U}_R - S_L \mathbf{U}_L + \mathbf{F}_L - \mathbf{F}_R}{S_R - S_L}. \tag{4.2.49}$$

This quantity happens to be independent of the time t_0, and defines the approximate intermediate state $\mathbf{U}^*_{\text{HLL}}$:

$$\mathbf{U}^*_{\text{HLL}} = \frac{S_R \mathbf{U}_R - S_L \mathbf{U}_L + \mathbf{F}_L - \mathbf{F}_R}{S_R - S_L}. \tag{4.2.50}$$

The intercell flux $\mathbf{F}_{\text{HLL}}$ is then defined as

$$\mathbf{F}_{\text{HLL}} = \begin{cases} \mathbf{F}_L & \text{if } 0 \leq S_L, \\ \mathbf{F}^*_{\text{HLL}} & \text{if } S_L < 0 < S_R, \\ \mathbf{F}_R & \text{if } S_R \leq 0, \end{cases} \tag{4.2.51}$$

where, unlike for the Godunov flux, the intermediate flux in the subsonic case $\mathbf{F}^*_{\text{HLL}}$ is not equal to $\mathcal{F}\left(\mathbf{U}^*_{\text{HLL}}\right)$, but to

$$\mathbf{F}^*_{\text{HLL}} = \frac{S_R \mathbf{F}_L - S_L \mathbf{F}_R + S_R S_L (U_R - U_L)}{S_R - S_L}, \tag{4.2.52}$$

which is obtained by applying the Rankine-Hugoniot jump relations across the left or, equivalently, the right wave.

The estimation of the wave speeds is then the following:

$$\begin{cases} S_L = \max\{u_R - c_R, u_L - c_L\}, & \text{(4.2.53a)} \\ S_R = \max\{u_R + c_R, u_L + c_L\}. & \text{(4.2.53b)} \end{cases}$$

4.2.3.3.2 Approximate Riemann problem corresponding to the Rusanov numerical flux

The previous approximate Riemann problem can be even further simplified, by considering a unique fastest signal speed S for both sides, so that $S_L = -S$ and $S_R = +S$. This provides the Rusanov intercell flux, see Figure 4.7. As the propagation speed magnitude S should be an upper bound of

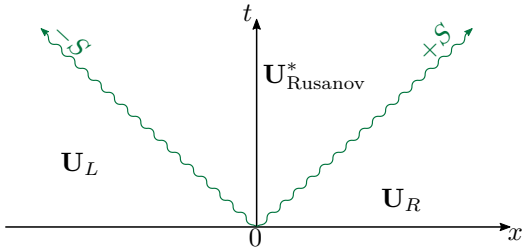

Figure 4.7: Approximation of the Riemann problem solution by the Rusanov flux.

the actual propagation speed of information of the exact Riemann problem, the value used by [Davis, 1988] is the following:

$$S = \max\left\{|u_L - c_L|, |u_L + c_L|, |u_R - c_R|, |u_R + c_R|\right\}. \tag{4.2.54}$$

One can also use [Toro, 2013]

$$S = \max\left\{|u_L| + c_L, |u_R| + c_R\right\}. \tag{4.2.55}$$

Then, the intermediate state for the approximate Riemann problem is

$$\mathbf{U}^*_{\text{Rus}} = \frac{1}{2}\left(\mathbf{U}_R + \mathbf{U}_L\right) + \frac{1}{2S}\left(\mathbf{F}_L - \mathbf{F}_R\right), \tag{4.2.56}$$

and from equation (4.2.52), the Rusanov flux is

$$\mathbf{F}^*_{\text{Rus}} = \frac{1}{2}\left(\mathbf{F}_L + \mathbf{F}_R\right) - \frac{1}{2}S\left(U_R - U_L\right). \tag{4.2.57}$$

As they do not account for the presence of a contact discontinuity, approximating an intercell flux by the HLL flux (4.2.52) or Rusanov flux (4.2.57) will strongly smear the information carried by the linearly degenerate field at velocity u, especially when $|u| \ll c$. Next section describes another classic approximate Riemann solver that restores the three-wave pattern, conform with the exact Riemann problem.

4.2.3.3.3 The Harten-Lax-van Leer + contact (HLLC) approximation

In order to provide a better representation of the approximate solution, [Toro et al., 1994] proposed a three-wave formulation, improving the HLL approximation by restoring the contact-discontinuity propagation. This strategy, called HLLC, is illustrated by Figure 4.8. The approximate solution of the

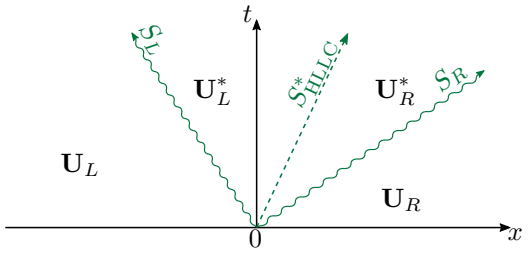

Figure 4.8: Approximation of the Riemann problem solution by the HLLC flux.

Riemann problem is given by

$$\mathbf{U}\left(x,t\right) = \begin{cases} \mathbf{U}_L & \text{if } x/t \leq S_L \\ \mathbf{U}^*_{\text{HLLC},L} & \text{if } S_L < x/t \leq S^*_{\text{HLLC}} \\ \mathbf{U}^*_{\text{HLLC},R} & \text{if } S^*_{\text{HLLC}} < x/t < S_R \\ \mathbf{U}_R & \text{if } S_R \leq x/t \end{cases} \tag{4.2.58}$$

The center wave being a contact discontinuity, the states on both sides $\mathbf{U}^*_{\text{HLLC},L}$ and $\mathbf{U}^*_{\text{HLLC},R}$ shall have the same pressure and velocity

$$\begin{cases} u^*_{\text{HLLC}} = u^*_{\text{HLLC},L} = u^*_{\text{HLLC},R}, & \text{(4.2.59a)} \\ P^*_{\text{HLLC}} = P^*_{\text{HLLC},L} = P^*_{\text{HLLC},R}, & \text{(4.2.59b)} \end{cases}$$

and the propagation speed of the contact discontinuity is the intermediate flow velocity $S^*_{\text{HLLC}} = u^*_{\text{HLLC}}$.
The Rankine-Hugoniot relation (4.2.44) applied across the left and right waves yields

$$\begin{cases} S_L\mathbf{U}^*_{\text{HLLC},L} - \mathcal{F}(\mathbf{U}^*_{\text{HLLC},L}) = S_L\mathbf{U}_L - \mathcal{F}(\mathbf{U}_L), & \text{(4.2.60a)} \\ S_R\mathbf{U}^*_{\text{HLLC},R} - \mathcal{F}(\mathbf{U}^*_{\text{HLLC},R}) = S_R\mathbf{U}_R - \mathcal{F}(\mathbf{U}_R), & \text{(4.2.60b)} \end{cases}$$

which can be expressed in terms of pressure relations

$$\begin{cases} P^*_{\mathrm{HLLC},L} = P_L + \rho_L \left(S_L - u_L\right)\left(S^*_{\mathrm{HLLC}} - u_L\right), & (4.2.61a) \\ P^*_{\mathrm{HLLC},R} = P_R + \rho_R \left(S_R - u_R\right)\left(S^*_{\mathrm{HLLC}} - u_R\right). & (4.2.61b) \end{cases}$$

Using the pressure equality (4.2.59), the contact discontinuity propagation speed is finally

$$S^*_{\mathrm{HLLC}} = \frac{P_R - P_L + \rho_L u_L \left(S_L - u_L\right) - \rho_R u_R \left(S_R - u_R\right)}{\rho_L \left(S_L - u_L\right) - \rho_R \left(S_R - u_R\right)}. \tag{4.2.62}$$

The intermediate states are obtained using equation (4.2.60) and read

$$\begin{cases} \mathbf{U}^*_L = \dfrac{S_L - u_L}{S_L - S^*_{\mathrm{HLLC}}} \begin{bmatrix} \rho_L \\ \rho_L S^*_{\mathrm{HLLC}} \\ \rho_L e_{\mathrm{t},L} + \left(S^*_{\mathrm{HLLC}} - u_L\right)\left(\rho_L S^*_{\mathrm{HLLC}} + \frac{P_L}{S_L - u_L}\right) \end{bmatrix}, & (4.2.63a) \\ \mathbf{U}^*_R = \dfrac{S_R - u_R}{S_R - S^*_{\mathrm{HLLC}}} \begin{bmatrix} \rho_R \\ \rho_R S^*_{\mathrm{HLLC}} \\ \rho_R e_{\mathrm{t},R} + \left(S^*_{\mathrm{HLLC}} - u_R\right)\left(\rho_R S^*_{\mathrm{HLLC}} + \frac{P_R}{S_R - u_R}\right) \end{bmatrix}. & (4.2.63b) \end{cases}$$

The intercell flux is finally obtained, as for the Godunov flux, by taking its value at abscissa $x = 0$, so that

$$\mathbf{F}_{\mathrm{HLLC}} = \begin{cases} \mathbf{F}_L & \text{if } 0 \leq S_L, \\ \mathbf{F}^*_{\mathrm{HLLC},L} & \text{if } S_L < 0 \leq S^*_{\mathrm{HLLC}}, \\ \mathbf{F}^*_{\mathrm{HLLC},R} & \text{if } S^*_{\mathrm{HLLC}} < 0 < S_R, \\ \mathbf{F}_R & \text{if } S_R \leq 0, \end{cases} \tag{4.2.64}$$

and by conservation requirements, the HLLC fluxes for the intermediate states read, from the Rankine-Hugoniot relation,

$$\begin{cases} \mathbf{F}^*_{\mathrm{HLLC},L} = \mathcal{F}\left(\mathbf{U}_L\right) + S_L \left(\mathbf{U}^*_{\mathrm{HLLC},L} - \mathbf{U}_L\right), & (4.2.65a) \\ \mathbf{F}^*_{\mathrm{HLLC},R} = \mathcal{F}\left(\mathbf{U}_R\right) + S_R \left(\mathbf{U}^*_{\mathrm{HLLC},R} - \mathbf{U}_R\right). & (4.2.65b) \end{cases}$$

4.2.3.3.4 The Roe flux

The last intercell flux to be presented in this section is the *Roe flux* [Roe, 1986]. Such method is for instance applied, in a multifluid context, in the work of [Allaire et al., 2002]. It relies on a philosophy different from the previously described approximate Riemann solvers. In a nutshell, it consists in reformulating the exact Riemann problem by writing the conservation equation in its quasi-linear form:

$$\frac{\partial \mathbf{U}}{\partial t} + \mathcal{A}_x\left(\mathbf{U}\right)\frac{\partial \mathbf{U}}{\partial x} = 0, \tag{4.2.66}$$

and approximating the jacobian matrix of the flux function $\mathcal{A}_x$ as being constant:

$$\mathcal{A}_x\left(\mathbf{U}\right) \approx \tilde{\mathcal{A}}_x, \tag{4.2.67}$$

where the constant value is estimated from the left and right initial states $\tilde{\mathcal{A}}_x = \tilde{\mathcal{A}}_x\left(\mathbf{U}_L, \mathbf{U}_R\right)$, and verifies the consistency condition $\tilde{\mathcal{A}}_x\left(\mathbf{U}, \mathbf{U}\right) = \mathcal{A}_x\left(\mathbf{U}\right)$. The obtained Riemann problem is then solved *exactly*, as it consists in a linear Riemann problem, similar to (4.2.39).

The comprehensive derivation of the Roe method can be found in [Toro, 2013], and the resulting numerical flux can be written under the following form:

$$\mathbf{F}_{\text{Roe}} = \frac{1}{2}\left[\mathcal{F}(\mathbf{U}_L) + \mathcal{F}(\mathbf{U}_R)\right] - \frac{1}{2}\boldsymbol{R}(\mathbf{U}_L, \mathbf{U}_R), \tag{4.2.68}$$

where $\boldsymbol{R}$ is given as a function of left and right states of the Riemann problem:

$$\boldsymbol{R}(\mathbf{U}_L, \mathbf{U}_R) = |\bar{u} - c^*|\,\xi_\ominus \begin{bmatrix} 1 \\ \bar{u} - c^* \\ \bar{h}_{\text{tot}} - \bar{u}c^* \end{bmatrix} + |\bar{u}| \begin{bmatrix} \xi_\rho \\ \xi_\rho \bar{u} \\ B \end{bmatrix} + |\bar{u} + c^*|\,\xi_\oplus \begin{bmatrix} 1 \\ \bar{u} + c^* \\ \bar{h}_{\text{tot}} + \bar{u}c^* \end{bmatrix} \tag{4.2.69}$$

In the above expression, the coefficients $(\xi_j)_{j=1..5}$ and B are defined by

$$\xi_\ominus = \frac{1}{2c^{*2}}\left(\Delta P - \underline{\rho} c^* \Delta u\right) \tag{4.2.70a}$$

$$\xi_\rho = \Delta(\rho) - \frac{\Delta P}{c^{*2}} \tag{4.2.70b}$$

$$\xi_\oplus = \frac{1}{2c^{*2}}\left(\Delta P + \underline{\rho} c^* \Delta u\right) \tag{4.2.70c}$$

$$B = \frac{\overline{u}^2}{2}\Delta\rho + \Delta(\rho e_s) - \frac{\overline{h_{\text{t}}}}{c^{*2}}\Delta P \tag{4.2.70d}$$

with the jump $\Delta\varphi$ for any quantity φ defined by $\Delta\varphi = \varphi_R - \varphi_L$, the Roe mean values

$$\overline{\varphi} = \frac{\sqrt{\rho_L}\varphi_L + \sqrt{\rho_R}\varphi_R}{\sqrt{\rho_L} + \sqrt{\rho_R}}, \tag{4.2.71a}$$

$$\underline{\varphi} = \frac{\sqrt{\rho_L}\varphi_R + \sqrt{\rho_R}\varphi_L}{\sqrt{\rho_L} + \sqrt{\rho_R}}. \tag{4.2.71b}$$

Different choices are possible for the speed of sound. Since the Roe flux is used in the present work to reproduce some results of [Allaire et al., 2002], the same approximation is used, which reads

$$c^* = \sqrt{\frac{\overline{(\zeta c^2)}}{\overline{\zeta}}}, \qquad \text{with } \zeta = \left.\frac{\partial(\rho e_s)}{\partial P}\right|_\rho \tag{4.2.72}$$

At this point, the main properties of hyperbolic conservation laws have been introduced, and the approximate Riemann solvers that are extensively applied to solve multifluid diffuse interface models have been presented. The next section introduces the important concepts and notations that will be used for the different numerical methods.

4.3 Numerical methods: preliminary definitions

4.3.1 Discretization

Finding an analytical solution to the initial value problem (4.2.5) is generally not possible, especially for multidimensional cases. A common strategy is then to solve the problem approximately. This can be done by introducing an approximate solution space $\boldsymbol{\mathcal{V}}_\Delta$, in order to represent the solution by means of a finite set of values to be determined computationally. This set of values is called the *degrees of freedom* (DoF) of the solution.

The DoF can represent the values taken by the solution field at given spatial positions and given times, which corresponds to a *nodal* discretization. Instead, the DoF can consist in the scalar coordinates of the numerical solution in a chosen functional basis of a finite-dimensional space, typically a polynomial basis (e.g. Legendre polynomials up to a certain order), or a trigonometric basis. This formulation is called a *modal* discretization. The approximate finite-dimensional space $\boldsymbol{\mathcal{V}}_\Delta$ must then be provided with an approximate form of the differential operators constituting the hyperbolic conservation law (possibly written under its weak form, as presented in paragraph 4.4.2.1.1).

This whole procedure is called a *numerical method*. Note that for finite-element methods, the approximate space for the test functions may be either $\boldsymbol{\mathcal{V}}_\Delta$ (which corresponds to the Galerkin method, see section 4.5.1) or a different finite-dimensional space (as for the Petrov-Galerkin methods, see e.g. [Donea and Huerta, 2003]).

Although there exist spectral methods that use a global modal discretization of the domain, most methods are based on a spatial division of the fluid domain Ω. Such division, called the *mesh* or the *grid*, is described by a vocabulary and various features that are now briefly introduced.

4.3.1.1 Computational meshes

A computational mesh is defined as a *tessellation* $\mathcal{T}_h$ of the fluid domain Ω. In other words, it is a set of *elements* $\mathcal{E}$ such that

$$\begin{cases} \Omega = \bigcup\limits_{\mathcal{E}\in\mathcal{T}_h} \mathcal{E}, & \text{(4.3.1a)} \\ \forall \left(\mathcal{E}, \mathcal{E}'\right) \in \mathcal{T}_h^2, \quad \mathcal{E} \neq \mathcal{E}' \implies \dim\left(\mathcal{E} \cap \mathcal{E}'\right) < \dim\left(\Omega\right) . & \text{(4.3.1b)} \end{cases}$$

Although there is no theoretical limitation in the geometric nature of the mesh elements $\mathcal{E}$, all elements considered in this work are delimited by straight lines: polygons in 2D, polyhedrons in 3D. The volume enclosed in the e^{th} element $\mathcal{E}_e$ is denoted $\mathcal{V}_e$.

Two families of meshes are defined depending on the nature of the arrangement of the elements:

- *structured meshes* consist of elements defined by a division of the domain Ω from a collection of regular lines or planes. In a structured mesh, all the vertices are surrounded by a constant number of neighbouring elements (except at the boundaries). The numbering and identification of the elements (or vertices) and their neighbours is straightforward, as depicted in Figure 4.9a;
- *unstructured meshes* consist of a collection of elements in which the different vertices can have various numbers of direct neighbours. Unstructured meshes require to store the position and neighbours of the elements in a *connectivity table*. The use of such meshes generally restricts the choice of numerical schemes to the ones of *compact stencil* (see paragraph 4.3.3.1), as it is cumbersome and computationally expensive to find indirect neighbours of a cell or a node.

Structured meshes are very convenient for academic studies and the development of numerical methods, as they are straightforward to implement and use. Although slightly more complex geometries than a mere rectangle can be discretized using a structured mesh, e.g. by defining multiple structured patches, their use is very limited regarding industrial configurations that involve complex geometries. Unstructured meshes are best suited in this case, and they also offer more flexible local mesh refinement capabilities.

Some useful notations are now introduced regardless of the considered type of mesh. For a vertex i, its neighbouring elements (or, by abuse of language, its direct neighbour vertices) are denoted $\mathcal{D}_i$. Every node i is associated with a *dual cell* $\mathcal{C}_i$ (by opposition to the *primal cells* $\mathcal{E}$). Different methods can be used to construct the dual cells. A common and simple one is to join the middles of the edges connected to i with the centroids of the elements of $\mathcal{D}_i$, as displayed in Figure 4.10. Note that the set of dual cells forms the *dual mesh* which also verifies the definition (4.3.1).

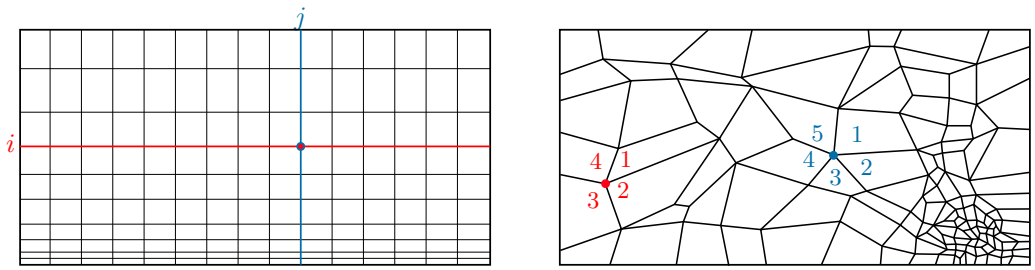

(a) Structured mesh defined by two collections of vertical and horizontal lines. A vertex and its neighbours can be easily identified by numbering the lines of each collection. All vertices (except at boundaries) have four direct neighbour elements.

(b) Unstructured mesh. The red and blue vertices have different number of direct neighbour elements.

Figure 4.9: Structured and unstructured quadrangular meshes.

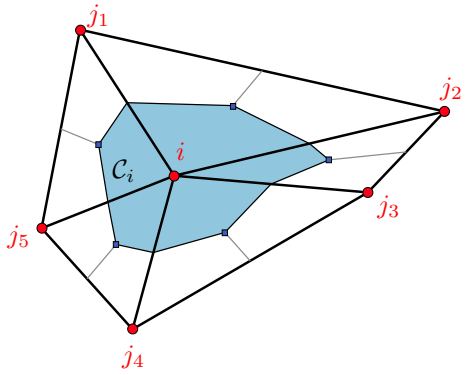

Figure 4.10: The dual cell associated with node i. The neighbour nodes $j_1, ..., j_5 \in \mathcal{D}_i$ are represented. They are connected by thick lines representing the primal mesh. Thin lines correspond to the dual mesh.

4.3.2 Representation of the solution

Once the geometry of the mesh has been defined, various options still remain to define the finite-dimensional approximate space $\boldsymbol{\mathcal{V}}_\Delta$, as different sets of degrees of freedom (DoF) may be picked. The different options are typically split into three families:

- *cell-centered methods* describe the solution properties cell by cell. The most common cell-centered methods are *finite-volume* (FV) methods, for which the DoF correspond to the mean (integral) value of the conserved variables within each cell, as illustrated by Figure 4.11a. Higher-order representations of the solution within each cell are possible, e.g. in the framework of *discontinuous Galerkin* (DG) methods, which rely on a cell-wise polynomial representation of the solution using additional DoF within the cell. These methods are further described in section 4.4;
- *vertex-centered methods*, illustrated in Figure 4.11b, are the methods that represents the solution by its values at the mesh nodes. This is typically the case of finite-difference methods, as well as *Galerkin methods*, also called *finite-element* (FE) methods. These methods are further described in section 4.5;

In this manuscript, only piecewise-polynomial representations of the solution are considered.

Although this way of sorting the numerical methods is convenient for their description, the difference between them appears somehow blurry. For instance, it has been shown by [Mavriplis and Jameson, 1990] that, considering a regular triangular mesh in 2D, the $\mathbb{P}_1$-Galerkin method is equivalent to a finite-volume method applied on the dual mesh.

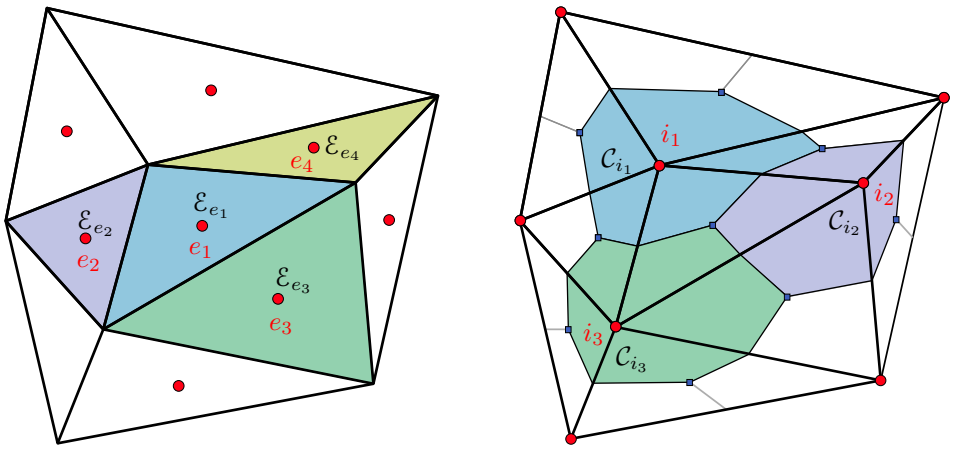

(a) Cell-centered method (b) Vertex-centered formulation

Figure 4.11: Illustration of the control volumes (filled areas) and data points (red dots) corresponding to different formulations.

4.3.3 Properties of the numerical methods

4.3.3.1 Stencil

For a given DoF i, the set of nodes that are used to compute the update u_i^{n+1} is called the *stencil* of the numerical method. According to formula (4.3.11), it corresponds for a given i to the ensemble of DoF j such that $c_{ij} \neq 0$. A stencil is said to be *compact* when the update of the solution at a given DoF i only depends on its direct neighbours $\mathcal{D}_i$.

The compactness of the stencil is an important feature in the context of unstructured meshes and parallel computing, as it can be cumbersome and expensive to gather the values of the solution at indirect neighbour DoF for non-compact stencils.

4.3.3.2 Numerical errors

4.3.3.2.1 Global error and consistency

For any kind of discretization and numerical scheme, the solution is expected to be closer and closer to the solution as the number of DoF increases. This property is called the *consistency* of the numerical method. The *global error* is measured as

$$\epsilon_g = \|\mathbf{U}_\Delta - \mathbf{U}\|, \tag{4.3.2}$$

with $\mathbf{U}$ the exact solution and $\mathbf{U}_\Delta$ its discrete approximation obtained from the numerical method.

As the DoF are associated with a spatial discretization, the number of DoF can be associated with the characteristic length of the mesh cells Δx – provided the uniformity of the mesh refinement. The spatial and temporal *orders* of a numerical method are the exponents r_x and r_t such that

$$\begin{cases} \epsilon_g = \mathcal{O}(\Delta x^{r_x}) & \text{where } \Delta x \to 0, \quad (4.3.3a) \\ \epsilon_g = \mathcal{O}(\Delta t^{r_t}) & \text{where } \Delta t \to 0. \quad (4.3.3b) \end{cases}$$

4.3.3.2.2 Projection and truncation errors

To analyze the numerical error, it is relevant to introduce the projection of the exact solution over the approximate space $\mathcal{P}_\Delta(\mathbf{U})$. Applying the triangle inequality, the global error ϵ_g can then be decomposed into

$$\epsilon_\mathrm{g} \leq \epsilon_\mathcal{P} + \epsilon_\mathrm{t}, \tag{4.3.4}$$

with

$$\begin{cases} \epsilon_\mathcal{P} = \left\| \mathbf{U} - \mathcal{P}_\Delta(\mathbf{U}) \right\|, & \text{(4.3.5a)} \\ \epsilon_\mathrm{t} = \left\| \mathcal{P}_\Delta(\mathbf{U}) - \mathbf{U}_\Delta \right\|. & \text{(4.3.5b)} \end{cases}$$

The error $\epsilon_\mathcal{P}$ is called the *projection error*. It is typically dominated by Δx^{p+1}, where p is the polynomial order of reconstruction of $\boldsymbol{\mathcal{V}}_\Delta$. It measures the ability of the discrete solution space to approximate accurately the exact solution.

The error ϵ_t is called the *truncation error*. This error measures the ability of the numerical method to compute accurately the evolution of the discrete solution.

Asymptotically, a numerical method *of order* r_x is then a numerical method for which both the projection and truncation errors decrease with rate r_x, i.e.

$$\epsilon_\mathcal{P} \leq \mathcal{O}\left(\Delta x^{r_x}\right) \quad \text{and} \quad \epsilon_\mathrm{t} \leq \mathcal{O}\left(\Delta x^{r_x}\right) \quad \text{when } \Delta x \to 0 \tag{4.3.6}$$

4.3.3.3 Stability

A numerical method is said to be *stable* when the discrete solution remains *controllable*, in the sense that it does not blow up to infinity. This condition reads

$$\exists C > 0 \ : \forall n \in \mathbb{N}^*, \quad \|\mathbf{U}^n\| \leq C \left\| \mathbf{U}^0 \right\| \tag{4.3.7}$$

with $\|\cdot\|$ a chosen norm over the finite-dimensional space $\boldsymbol{\mathcal{V}}_\Delta$, for instance a component-wise $\mathcal{L}^K$-norm, $K \in \mathbb{N}^*$:

$$\|\mathbf{U}^n\|_K = \left(\sum_{i=1}^{n_\mathrm{DoF}} |\mathbf{U}_i^n|^K \right)^{1/K}, \tag{4.3.8}$$

or the $\mathcal{L}^\infty$ norm:

$$\|\mathbf{U}^n\|_K = \max_{i \in [\![1, n_\mathrm{DoF}]\!]} |\mathbf{U}_i^n|. \tag{4.3.9}$$

The stability of the numerical methods may depend on the time step Δt. For explicit hyperbolic numerical methods, a linear stability condition can generally be formulated as a condition on the *Courant-Friedrich-Lewy* (CFL) number η_C, defined as

$$\eta_C = \frac{\nu \Delta t}{\Delta x}, \tag{4.3.10}$$

with Δx the mesh spatial step and ν the spectral radius of Jacobian matrix of the physical flux $\mathcal{F}$.

4.3.3.4 Realizability of the solution

In addition to the order of accuracy, the stability and the convergence properties of the numerical method, which are genuinely mathematical notions, a numerical method for a flow problem should respect physical constraints. In particular, the pressure and density should remain positive quantities and the mass fractions – of the species and the possibly transported phases – should remain within $[0, 1]$. Such constraints are referred to as the *realizability constraints*.

Consider now an explicit conservative numerical method of a scalar conservation law, assuming the following form for the update:

$$\forall i \in [\![1, n_{\mathrm{DoF}}]\!], \quad u_i^{n+1} = u_i^n + \Delta t \sum_{j \neq i} c_{ij}\left(u^n\right)\left(u_j^n - u_i^n\right). \tag{4.3.11}$$

The following introduces some relevant properties of numerical schemes. For the sake of simplicity, they are introduced in assuming a one-dimensional context.

4.3.3.4.1 Monotone schemes

Following the nomenclature of [Hirsch, 1997], section 21.2, a numerical method of the form

$$u_i^{n+1} = \mathcal{N}_i\left(u^n\right) \tag{4.3.12}$$

is said to be *monotone* if

$$\forall i \in [1, n_{\mathrm{DoF}}], \quad \left.\frac{\partial \mathcal{N}_i}{\partial u_j^n}\right|_{\left(u_k^n\right)_{k \neq j}} \geq 0, \tag{4.3.13}$$

which can be rewritten, using (4.3.11), as

$$\forall\,(i, j) \in [1, n_{\mathrm{DoF}}]^2, \quad c_{ij} \geq 0. \tag{4.3.14}$$

4.3.3.4.2 Total variation diminishing (TVD) schemes

A numerical method is said to be *total variation diminishing* (TVD) if the *total variation* TV of the approximate solution decreases along iterations. The total variation $TV(u)$ of a scalar field u is defined by

$$TV(u) = \int_\Omega \left|\frac{\partial u}{\partial x}\right| \mathrm{d}x. \tag{4.3.15}$$

For example, for a piecewise-linear solution, the discrete total variation of the approximate solution u^n reads

$$TV(u^n) = \sum_{i=1}^{n_{\mathrm{DoF}}-1} \left|u_{i+1}^n - u_i^n\right|. \tag{4.3.16}$$

The TVD property of the numerical method then reads:

$$TV(u^{n+1}) \leq TV(u^n) \leq TV(u^0). \tag{4.3.17}$$

4.3.3.4.3 Monotonicity preserving schemes

A numerical method is said to be *monotonicity preserving* if for any monotonic discrete solution u^n, the update is u^{n+1} is a monotonic discrete solution. Monotonicity preservation is equivalently characterized by the two conditions: *no new local extrema in x can be created as time evolves; the value of a local minimum is non-decreasing and the value of a local maximum is non-increasing.*

4.3.3.4.4 Hierarchy of the monotonicity properties

It is interesting to point out that the monotonicity properties can be ordered as follows (cf. [Hirsch, 1997], chapter 21):

$$\Big\{\text{Monotonicity preserving schemes}\Big\} \subset \Big\{\text{TVD schemes}\Big\} \subset \Big\{\text{Monotone schemes}\Big\}. \tag{4.3.18}$$

4.3.3.4.5 Godunov's theorem

A numerical scheme is said to be *linear* if the coefficients $\left(c_{ij}\right)_{(i,j)\in[\![1,n_{\text{DoF}}]\!]^2}$ are independent of the solution. For instance, the first-order Godunov-like schemes of section 4.4.1.2, the Galerkin-Runge-Kutta and Taylor-Galerkin schemes of sections 4.5.1.2.2 and 4.5.1.3, and the Runge-Kutta Discontinuous Galerkin schemes presented in 4.4.2 are linear.

Linear schemes are convenient regarding the relative simplicity of their formulation. Nonetheless, an important drawback is formulated by Godunov's theorem, which states that *a monotonicity preserving linear scheme is at most first-order*. In other words, the use of linear scheme implies a choice between having a high-order scheme or a monotonicity-preserving scheme.

4.4 Cell-centered methods

4.4.1 Finite-volume methods

4.4.1.1 Finite-volume discretization

Finite-volume methods consist in approximating the solution by its mean value over an element. The discrete solution is then piecewise constant and the value taken in a cell $\mathcal{E}_e$ is:

$$\mathbf{U}_e(t) = \frac{1}{\mathcal{V}_e}\int_{\mathcal{E}_e} \mathbf{U}\left(x,t\right) \mathrm{d}\mathcal{V}. \tag{4.4.1}$$

Integration of the conservation law (4.2.4) over a cell $\mathcal{E}_e$ reads:

$$\frac{\partial \mathbf{U}_e}{\partial t} + \frac{1}{\mathcal{V}_e}\int_{\mathcal{E}_e} \vec{\nabla}\cdot\mathcal{F}\left(\mathbf{U}(x,t)\right) \mathrm{d}\mathcal{V} = 0. \tag{4.4.2}$$

Applying the Green-Gauss theorem yields

$$\frac{\partial \mathbf{U}_e}{\partial t} + \frac{1}{\mathcal{V}_e}\int_{\partial\mathcal{E}_e} \mathcal{F}\left(\mathbf{U}(x,t)\right)\cdot\vec{n}\,\mathrm{d}\mathcal{S} = 0. \tag{4.4.3}$$

The ordinary differential equation (4.4.3) is then discretized by a Forward-Euler method[1]

$$\mathbf{U}_e^{n+1} = \mathbf{U}_e^{n} - \frac{\Delta t}{\mathcal{V}_e}\int_{\partial\mathcal{E}_e} \mathcal{F}\left(\mathbf{U}(x,t)\right)\cdot\vec{n}\,\mathrm{d}\mathcal{S}. \tag{4.4.4}$$

Under the piecewise-constant representation of the solution, the evaluation of the flux at the cell faces is not trivial, since the solution is discontinous at such point. In this respect, the normal flux across the interface between two cells $\mathcal{E}_e$ and $\mathcal{E}_f$ is approximated by a *numerical flux* $\mathbf{F}\left(\mathbf{U}_e,\mathbf{U}_f,\vec{n}\right)$. This numerical flux is said to be *consistent* with the physical flux, if

$$\forall\mathbf{U},\ \forall\vec{n},\quad \mathbf{F}(\mathbf{U},\mathbf{U},\vec{n}) = \mathcal{F}\left(\mathbf{U}\right)\cdot\vec{n}. \tag{4.4.5}$$

This implies that the spatial discretization is consistent in the sense of 4.3.3.2.1. Different choices of numerical fluxes are then possible, as described in the next paragraphs.

[1] Note that instead of this latter first-order time marching scheme, higher-order Runge-Kutta methods (given in Appendix C) can be used in conjunction with high-order spatial reconstruction to achieve higher-order accuracy.

4.4.1.2 Godunov-like methods

4.4.1.2.1 The Godunov method

The Godunov method corresponds to the finite-volume discrete scheme (4.4.4), written

$$\mathbf{U}_e^{n+1} = \mathbf{U}_e^n - \frac{\Delta t}{\mathcal{V}_e} \sum_{\mathcal{E}_f \in \mathcal{N}_e} \mathbf{F}\left(\mathbf{U}_e, \mathbf{U}_f, \vec{n}\right) \mathcal{S}_{ef}, \tag{4.4.6}$$

where S_{ef} is the area of the face separating cells $\mathcal{E}_e$ and $\mathcal{E}_f$, and $\vec{n}$ the normal vector, pointing from $\mathcal{E}_e$ to $\mathcal{E}_f$. The solution being discontinuous at the cell faces, the idea of Godunov [Godunov, 1959] is to interpret this configuration as a Riemann problem across the cell faces, as mentioned in paragraph 4.2.3.2. The numerical flux $\mathbf{F}\left(\mathbf{U}_e, \mathbf{U}_f, \vec{n}\right)$ is then the physical flux $\mathcal{F}$ at the face position, as given by equation (4.2.46). It is obviously consistent.

This numerical method is stable under the CFL condition $\eta_C \leq 1$.

4.4.1.2.2 Approximate numerical fluxes

In order to lighten the computation effort needed to evaluate the numerous numerical fluxes, approximate Riemann solvers can be used. In particular, description of the *Harten-Lax-van Leer* (HLL) flux is provided in paragraph 4.2.3.3.1, and description of the *HLL + contact* (HLLC) flux is provided in paragraph 4.2.3.3.3. An even simpler – yet the most diffusive – numerical flux is the Rusanov flux which is mentioned in paragraph 4.2.3.3.2.

The interested reader shall find a rather comprehensive description of the various intercell fluxes in [Toro, 2013].

4.4.1.3 Higher-order methods

The Godunov-like methods described above are very robust shock-capturing methods. Nonetheless, they are only first-order in space [Toro, 2013]. It is yet possible to formulate higher-order methods in the finite-volume context. This is typically done by improving the local representation of the data.

4.4.1.3.1 Monotonic upwind schemes for conservation laws (MUSCL)

The *monotonic upwind scheme for conservation laws* (MUSCL), proposed by Bram van Leer in [van Leer, 1979], uses the values in neighbour cells to reconstruct a piecewise linear approximate solution. For the sake of clarity, it is presented here in a one-dimensional context. The domain $\Omega = [0, L]$ is discretized into cells $\mathcal{E}_e = \left[x_{e-1/2}, x_{e+1/2}\right]$ of length $\Delta x = L/n_{\mathcal{E}}$, with $e \in [\![1, n_{\mathcal{E}}]\!]$. The abscissas of the bounds of the elements are $x_{e+1/2} = e\Delta x$ and their center is located at $x_e = \left(e + 1/2\right)\Delta x$.

In the one-dimensional scalar case, the reconstructed solution reads

$$u_e(x) = u_e^n + \frac{x - x_e}{\Delta x}\sigma_e^n \text{ for } x \in \left[x_{e-1/2}, x_{e+1/2}\right] \tag{4.4.7}$$

where σ_e^n is an evaluation of the local variations of the solution, typically

$$\sigma_e^n = u_{e+1}^n - u_e^n \tag{4.4.8}$$

The reconstruction is depicted in Figure 4.12.

As the reconstruction yields non-constant states within the cells, the Godunov strategy can be adapted to the *generalized Riemann problem* as evoked by [Toro, 2013]. Yet, simpler formulations allow to elude the resolution of the generalized Riemann problem. This is the case of the MUSCL-Hancock scheme, which consists in the following steps

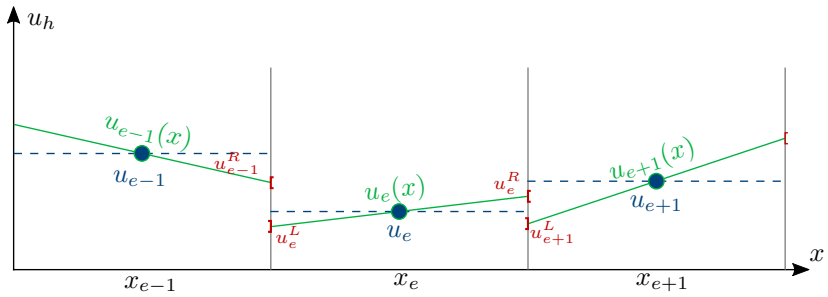

Figure 4.12: Piecewise-linear MUSCL reconstruction for a scalar solution.

(i) reconstruct the piecewise-linear solution by

$$u_e^L = u_e^n - \frac{\sigma_e^n}{2} \quad , \quad u_e^R = u_e^n + \frac{\sigma_e^n}{2}, \tag{4.4.9}$$

(ii) estimate intermediate state at time $\Delta t/2$

$$\begin{cases} \tilde{u}_e^L = u_e^L + \dfrac{\Delta t}{2\Delta x}\left[\mathcal{F}\left(u_e^L\right) - \mathcal{F}\left(u_e^R\right)\right], & \text{(4.4.10a)} \\ \tilde{u}_e^R = u_e^R + \dfrac{\Delta t}{2\Delta x}\left[\mathcal{F}\left(u_e^L\right) - \mathcal{F}\left(u_e^R\right)\right], & \text{(4.4.10b)} \end{cases}$$

(iii) solve for the Riemann problem (4.2.38) – either exactly or approximately – at face $x_{e+1/2}$ with left and right values $\tilde{u}_e^R, \tilde{u}_{e+1}^L$ to get the intercell flux $F_{e+1/2}$,

(iv) update the solution with

$$u_e^{n+1} = u_e^n - \frac{\Delta t}{\Delta x}\left[F_{e+1/2} - F_{e-1/2}\right]. \tag{4.4.11}$$

4.4.1.3.2 Slope limitation

Reconstructing the slope with formula (4.4.8) yields a solution for which the *total variation* is generally higher than the total variation of the piecewise-constant solution. This may imply overshoots and undershoots of the solution, in particular near local extrema. The global consequence of this issue is that the scheme produces spurious oscillations that pollute the solution and may violate some realizability constraints.

This unwanted behaviour is prevented by guaranteeing a reconstructed solution with total variation smaller than the piecewise-constant solution. Instead of using directly formula (4.4.8) to evaluate the local slope σ_e^n, the following *limitation* is performed:

$$\sigma_e^n = \phi(r_e^n)\left(u_{e+1}^n - u_e^n\right), \tag{4.4.12}$$

where $\phi : \mathbb{R} \to \mathbb{R}^+$ is the slope limiter and r_e^n denotes the slope ratio

$$r_e^n = \frac{u_e^n - u_{e-1}^n}{u_{e+1}^n - u_e^n}. \tag{4.4.13}$$

Different choices of slope limiters are possible. To quote but a few:

$$\textit{minmod:} \qquad \phi : r \mapsto \max\left\{0, \min\left\{1, r\right\}\right\}, \tag{4.4.14a}$$

$$\textit{superbee:} \qquad \phi : r \mapsto \max\left\{0, \min\left\{1, 2r\right\}, \min\left\{2, r\right\}\right\}, \tag{4.4.14b}$$

$$\textit{overbee:} \qquad \phi : r \mapsto \max\left\{0, \min\left\{2, 2r\right\}\right\}, \tag{4.4.14c}$$

$$\textit{van Leer:} \qquad \phi : r \mapsto \frac{r + |r|}{1 + |r|}. \tag{4.4.14d}$$

It is worth to mention that any negative value of the ratio r yields a zero value of the slope, which means that any local extremum (corresponding to $r_e^n < 0$) will lead to a locally constant reconstruction, preventing further increase of the local extremum, but capping at first-order the accuracy of the scheme at extrema. The various choices of the slope limiters can be represented in a *Sweby diagram* from [Sweby, 1984], see Figure 4.13. In particular, the higher the values of a slope limiter, the more anti-diffusive the obtained scheme will be. Conversely, lower the values of the limiter mean higher numerical diffusion. In this respect, the minmod and superbee limiters yield respectively the most and less diffusive methods among second-order TVD schemes. As mentioned in paragraph 3.3.2.3.2, [Chiapolino et al., 2017] give up the second-order reconstruction for the liquid volume fraction in the 5-equation model (3.3.12) and prefers the overbee limiter, which is the most antidiffusive TVD limiter.

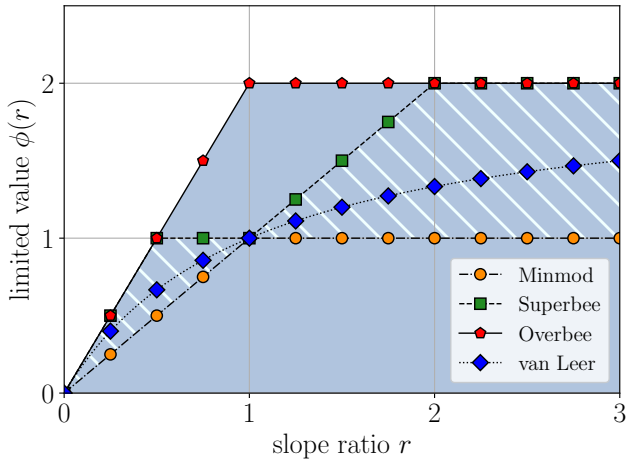

Figure 4.13: Sweby diagram [Sweby, 1984]. Any limiter lying within the filled region is TVD. In addition, any limiter lying within the hatched region provides a second-order reconstruction.

4.4.1.3.3 A word on higher-order FV methods

There exists a zoology of higher-order FV methods. In the framework of MUSCL, higher degree polynomial reconstructions may be considered. Quadratic functions are used in the *piecewise-parabolic method* proposed by [Colella and Woodward, 1984]. The ENO and WENO methods of [Harten et al., 1987] provide a framework for arbitrary-order polynomial reconstruction, adapting the reconstruction stencil to prevent numerical oscillations.

On the other hand, a more recent method called *multidimensional optimal order detection* (MOOD) method [Clain et al., 2011] achieves monotonicity by *a posteriori* limiting the order of reconstruction within each cell. Starting from a polynomial reconstruction of degree p of the solution, the update is evaluated. If an increase of the total variation is detected on the obtained update, the degree of the reconstruction is decremented. The update is re-evaluated, until a solution is found which does not increase the total variation.

4.4.2 Runge-Kutta discontinuous Galerkin (RKDG) methods

The family of Runge-Kutta discontinuous Galerkin methods is now presented [Cockburn and Shu, 1998]. It consists in representing the solution by a polynomial function within each cell, without requiring the solution to be continuous across the cells boundaries.

RKDG methods provide a convenient framework to achieve high-order transport, which will be useful for the developments led in Chapter 8. First, the derivation of the RKDG method is presented in section 4.4.2.1. This is done in a one-dimensional context, although the formalism allows for multi-dimensional methods if considering multidimensional polynomial functions [Cockburn and Shu, 1998]. Then, in section 4.4.2.2, test cases and a convergence study are led to validate the implementation of this numerical method, which be used later in this manuscript.

4.4.2.1 Derivation of the method

4.4.2.1.1 Weak formulation

In order to derive discontinuous-Galerkin methods, the first step is to express the PDE (4.2.4) in a weak form, considering the functional space

$$\boldsymbol{\mathcal{V}} = \left\{ \phi : \Omega \to \mathbb{R}^{N_{\mathrm{t}}} \mid \phi \in \mathcal{C}^1(\Omega) \text{ is of compact support} \right\}. \tag{4.4.15}$$

A function $\phi : \Omega \subset \mathbb{R}^d \longrightarrow \mathbb{R}^{N_{\mathrm{t}}}$ is said to be of compact support when there exists a compact – i.e. closed and bounded – subset $\Omega_{\mathrm{supp}} \subset \Omega$ such that:

$$\forall x \in \Omega \setminus \Omega_{\mathrm{supp}}, \phi(x) = 0. \tag{4.4.16}$$

For the sake of clarity, boundary conditions are ignored for the moment. One may for example claim that the space domain Ω is periodic. The problem is reformulated as:

$$\begin{aligned} &\textit{Find } \mathbf{U} \textit{ such that for any } \text{test } \textit{function } \boldsymbol{w} \in \boldsymbol{\mathcal{V}}, \forall t \in \mathbb{R}_+^*, \\ &\int_\Omega \left(\boldsymbol{w} \frac{\partial \mathbf{U}}{\partial t} + \boldsymbol{w} \frac{\partial \left(\mathcal{F}\left(\mathbf{U}\right) \right)}{\partial x} \right) \mathrm{d}x = 0. \end{aligned} \tag{4.4.17}$$

Applying an integration by parts, one obtains the *weak formulation* of the problem:

$$\begin{aligned} &\textit{Find } \mathbf{U} \textit{ such that for any } \text{test } \textit{function } \boldsymbol{w} \in \boldsymbol{\mathcal{V}}, \forall t \in \mathbb{R}_+^*, \\ &\int_\Omega \left(\boldsymbol{w} \frac{\partial \mathbf{U}}{\partial t} - \frac{\partial \boldsymbol{w}}{\partial x} \mathcal{F}\left(\mathbf{U}\right) \right) \mathrm{d}x = 0. \end{aligned} \tag{4.4.18}$$

Let $(\psi_i^e)_{i=1..p}$ denote a basis of $\mathbb{P}^p(\mathcal{E}_e)$, the vector space (of dimension $p+1$) of degree p polynomials over element $\mathcal{E}_e$. Such basis allows to define the finite dimensional vector space

$$\boldsymbol{\mathcal{V}}_e = \left\{ \phi_e : \mathcal{E}_e \to \mathbb{R}, \phi_e = \chi_e \sum_{i=0}^{p} \psi_i^e v_i^e \quad ; \quad (v_i^e)_{i \in [\![0,p]\!]} \in \mathbb{R}^{p+1} \right\}, \tag{4.4.19}$$

with χ_e the *characteristic function* of element $\mathcal{E}_e$, defined by

$$\chi_e(x) = \begin{cases} 1 & \text{if } x \in \mathcal{E}_e, \\ 0 & \text{otherwise.} \end{cases} \tag{4.4.20}$$

An approximate solution of (4.4.18) can be obtained by projection of the solution onto the finite dimension space

$$\boldsymbol{\mathcal{V}}_\Delta = \left\{ \phi : \Omega \to \mathbb{R}, \phi = \sum_{e=1}^{n^e} \chi_e \sum_{i=0}^{p} \psi_i^e v_i^e \quad ; \quad (v_i^e)_{i\in[\![1,p]\!],e\in[\![1,n^e]\!]} \in \mathbb{R}^{(p+1)\times n^e} \right\}, \tag{4.4.21}$$

using the polynomial basis $(\psi_i^e)_{i\in[\![0,p]\!]}$ as test functions.
The weak form (4.4.18) then yields the following semi-discrete problem:

$$\begin{aligned} &\textit{Find } \mathbf{U}_\Delta(x,t) = \sum_{e=1}^{n^e} \chi_e(x) \sum_{i=0}^{p} \psi_i^e(x) \mathbf{U}_i^e(t) \textit{ such that} \\ &\forall e \in \{1..n^e\}, \forall i \in \{0..p\}, \quad \sum_{j=0}^{p} \left(\int_{\mathcal{E}_e} \psi_i^e \psi_j^e \,\mathrm{d}x \right) \frac{\mathrm{d}\mathbf{U}_j^e}{\mathrm{d}t} + \int_{\mathcal{E}_e} \psi_i^e \frac{\partial \mathcal{F}(\mathbf{U}_\Delta)}{\partial x} \,\mathrm{d}x = 0. \end{aligned} \tag{4.4.22}$$

Integrating by parts the flux divergence integral yields:

$$\underbrace{\sum_{j=0}^{p} \left(\int_{\mathcal{E}_e} \psi_i^k \psi_j^e \,\mathrm{d}x \right) \frac{\mathrm{d}\mathbf{U}_j^e}{\mathrm{d}t}}_{\text{(M)}} + \underbrace{\left[\psi_i^e(x) \mathcal{F}(\mathbf{U}_\Delta)(x) \right]_{x_{e-1/2}}^{x_{e+1/2}}}_{\text{(B)}} - \underbrace{\int_{\mathcal{E}_e} \mathcal{F}(\mathbf{U}_\Delta) \frac{\partial \psi_i^e}{\partial x} \,\mathrm{d}x}_{\text{(V)}} = 0, \tag{4.4.23}$$

where the first term (M) involves the mass matrix $\mathcal{M}_e$ over element $\mathcal{E}_e$, the entries of which read

$$\mathcal{M}_{ij} = \int_{\mathcal{E}_e} \psi_i^e \psi_j^e \,\mathrm{d}x. \tag{4.4.24}$$

The second term (B) represents the *border terms*, while the *volume terms* correspond to the last term (V).

4.4.2.1.2 Volume integral

The flux function in the volume integral is approximated by its projection over $\boldsymbol{\mathcal{V}}_\Delta$:

$$\mathcal{F}\left(\mathbf{U}_\Delta(x,t)\right) = \sum_{e=1}^{n^e} \chi_e \sum_{i=0}^{p} \psi_i^e(x) \mathbf{F}_i^e(t), \tag{4.4.25}$$

and the volume integral can then be evaluated thanks to quadrature rules using change of variable $\tilde{x} = \frac{2(x-x_e)}{\Delta x} - 1$:

$$\int_{\mathcal{E}_e} \sum_{j=0}^{p} \frac{\partial \psi_i^e}{\partial x} \psi_j^e \mathbf{F}_j^e(t) \,\mathrm{d}x = \frac{\Delta x}{2} \sum_{j=0}^{p} \mathbf{F}_j^e(t) \int_{-1}^{1} \frac{\partial \psi_i^e}{\partial x}\big(x(\tilde{x})\big) \psi_j^e\big(x(\tilde{x})\big) \,\mathrm{d}\tilde{x} \tag{4.4.26a}$$

$$= \frac{\Delta x}{2} \sum_{j=0}^{p} \mathbf{F}_j^e(t) \sum_{q=0}^{n^Q} \frac{\partial \psi_i^e}{\partial x}\big(x(\tilde{x}_q)\big) \psi_j^e\big(x(\tilde{x}_q)\big) \omega_q, \tag{4.4.26b}$$

where $\tilde{x}_q$ and ω_q are respectively the n^Q quadrature points in the reference element $[-1,1]$ and the associated weights. Details on the quadrature methods are given in appendix C.2. Gauss-Legendre quadrature are used here, as they provide a high *degree of exactness* (equal to $2n^Q - 1$).
The polynomial approximation of the flux function (4.4.25) is made so that the right hand side of (4.4.26b) can be precomputed. Of course, such approximation is not mandatory, and one can instead compute at each time step the volume terms of (4.4.23) with a numerical quadrature.

4.4.2.1.3 Border terms

Border terms in (4.4.23) require to evaluate the flux at the faces[2] of the elements. The jump in cell values can be treated as a Riemann problem that may be solved exactly or approximately. The resulting *numerical flux* is then used at element faces. In the present work, either the HLLC flux or the Rusanov flux are used (cf. section 4.2.3.3).

Note that the one-dimensional context greatly simplifies the border terms evaluation. Indeed, in the multi-dimensional case, the border terms evaluation require to compute the integral of the numerical flux over the boundary, along which the solution varies, e.g. by means of a quadrature rule.

4.4.2.1.4 Choice of the polynomial basis

The choice of the polynomial basis can follow two strategies. The first possibility, called **nodal DG** methods, use a Lagrange polynomial basis. In this case, the coefficients $\mathbf{U}_i^e$ correspond to actual values of the solution at some chosen nodes for each element $e \in [\![1, n_\mathcal{E}]\!]$, $\left(x_i^e\right)_{i\in[\![0,p]\!]}$. In this context, the basis functions $\left(\psi_i^e\right)_{i\in[\![0,p]\!],e\in[\![1,n_\mathcal{E}]\!]}$ representation of degree p is given by

$$\psi_i^e = \prod_{\substack{j\in[\![0,p]\!]\\ j\neq i}} \frac{x - x_j^e}{x_i^e - x_j^e}. \tag{4.4.27}$$

As the Lagrange polynomials are not orthogonal in general, the mass matrix will not be diagonal. Yet, since the choice of the Lagrange polynomials nodes is free, two possibilities will enhance the computational efficiency:

- defining Lagrange nodes at Gauss-Legendre quadrature points for an efficient computation of the volume integral term,
- defining Lagrange nodes at Gauss-Lobatto quadrature points for an efficient computation of edge values, as edge points belong to the set of Gauss-Lobatto quadrature points.

Conversely, if the polynomial basis does not correspond to the Lagrange polynomial at the DoF, it is called a **modal DG** method. In this context, one can choose – although this is not mandatory – an orthogonal basis, which leads to a convenient diagonal *mass* matrix, that can be costlessly inverted. For instance, one can choose the orthogonal family of Legendre polynomials:

$$\psi_i^e = \frac{1}{2^i} \sum_{j=0}^{i} \binom{n}{k}^2 (x-1)^{n-k} (x+1)^k. \tag{4.4.28}$$

Despite its computational advantage for the *mass* matrix inversion, it requires a computational effort to evaluate the physical fluxes at Gauss quadrature points for the volume integral and for the boundary terms calculation.

4.4.2.1.5 Summary

In this work, the following choices are made:

- The polynomial basis used to represent the approximate solution is the Lagrange Polynomials set defined at Gauss-Legendre quadrature points,
- The Numerical Flux used is the Rusanov Flux.

[2] Note that the faces reduce to points in one dimension and to lines in two dimensions.

4.4.2.2 Convergence order and validation

The error of a RKDG method in space evolves with a rate of convergence of $\mathcal{O}(\Delta x^{p+1})$, for a $\mathbb{P}^p$ DG space discretization. The rate of convergence time is given by the order of the RK method. In practice, a RK-$(p+1)$ method is used to achieve space-time convergence of order $(p+1)$ [Cockburn et al., 2000].

In order to validate the implementation of the RKDG method, mesh refinement numerical experiments are led to verify that the theoretical convergence order is achieved by the solver.

4.4.2.2.1 Linear advection

The initial profile u_0 used to test the RKDG with linear advection is $u_0(x) = 1+f(x)$ with the following profile function:

$$f(x) = \begin{cases} \left[\cos\left(2\pi\left(x-0.5\right)\right)\right]^8 & \text{if } x \in [0.25, 0.75]\,, \\ 0 & \text{otherwise.} \end{cases} \tag{4.4.29}$$

Such profile has a $\mathcal{C}^8$ regularity, allowing to perform high-order convergence analyses. Test cases are made on a unitary-length periodic domain. The constant advection speed is $c_0 = 1$ m/s.

The results of the linear advection using RKDG schemes from order 1 to 3 are depicted in Figure 4.14. For all three simulations, the spatial discretization consists in 20 elements. The CFL number for all simulations is cfl $= 0.2$. The first-order RKDG method is equivalent to a finite volume method with the Rusanov flux, which is also equivalent for the one-dimensional linear advection case to a finite-difference upwind scheme in space with a forward-Euler time-marching. It is then natural to obtain a bounded solution that is highly diffused in Figure 4.14a. The second-order scheme, using $\mathbb{P}^1$ elements, is much less diffusive but introduces a dispersion error. It is not monotonicity-preserving but guarantees a higher-fidelity transport, as illustrated in Figure 4.14b. Finally, the third-order scheme is even more accurate. Like the second-order scheme, it is not monotonicity-preserving, although neither overshoot nor undershoot are clearly visible in Figure 4.14c.

The convergence rate of the different methods is evaluated numerically. The results are depicted in Figure 4.15. The expected orders are retrieved, validating the implementation of the method.

The similar validation strategy is then applied in the case of Euler equations.

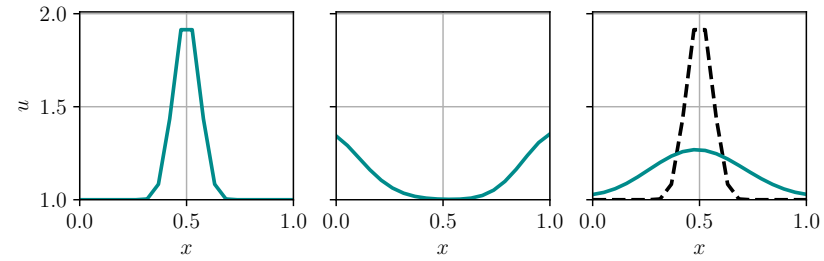

(a) 1st-order RKDG

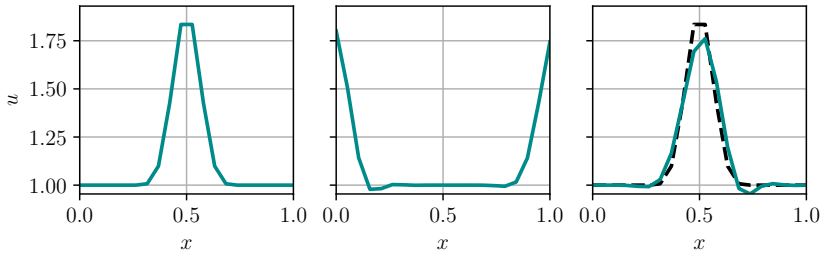

(b) 2nd-order RKDG

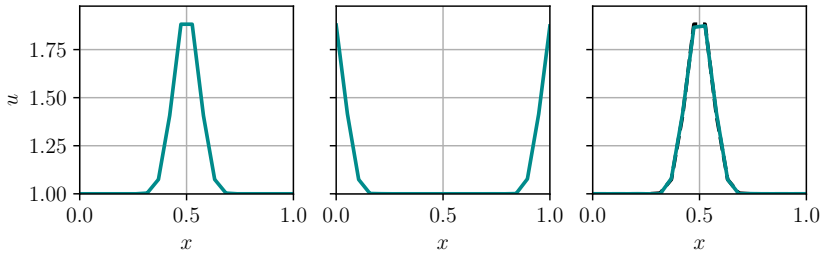

(c) 3rd-order RKDG

Figure 4.14: Linear advection snapshots taken at $t = 0$, $t = 1/2$ and $t = 1$.

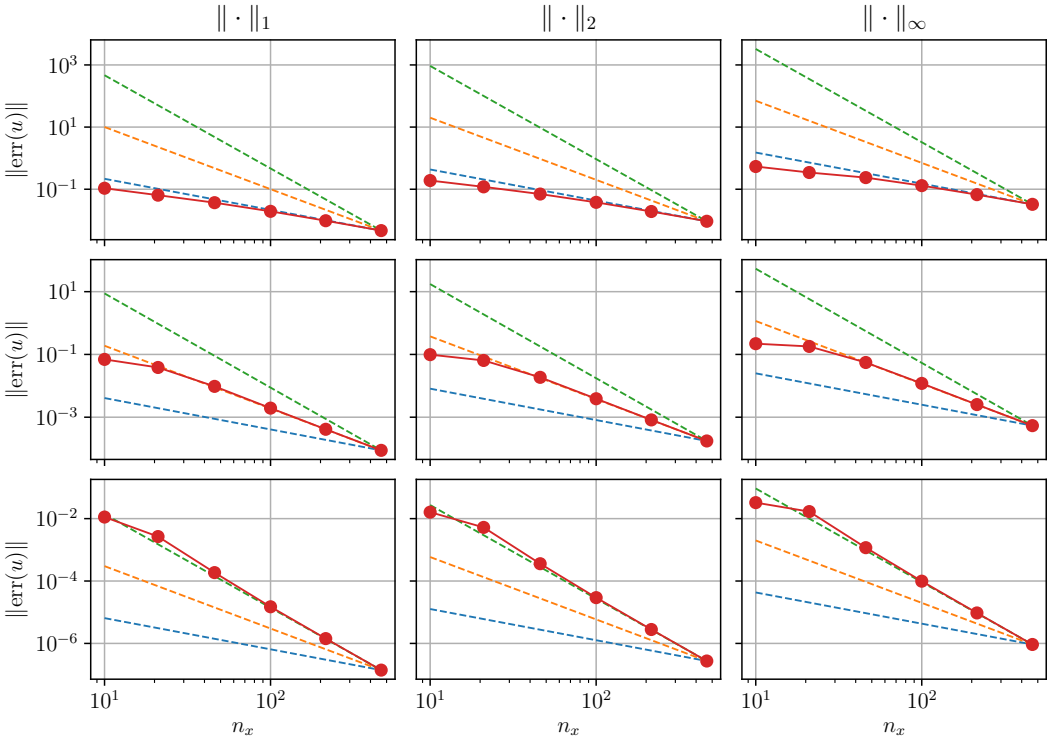

Figure 4.15: Convergence order for the linear advection equation. From top to bottom, the convergence results for RKDG1, RKDG2 and RKDG3 are displayed. The columns correspond, from left to right, to the L_1-norm, the L_2-norm, and the L_∞-norm. Dashed lines correspond to the expected slopes of order 1 in blue, 2 in orange and 3 in green.

4.4.2.2.2 Euler equations

The test configuration which is now considered is the transport of a regular density perturbation in a domain with constant pressure and velocity.

The NASG EoS presented in section 2.2.3.2 is used as the thermodynamic closure for the validation test. The coefficients chosen are those of liquid O_2, taken from the data provided by [Le Métayer and Saurel, 2016] and displayed in table 4.1.

	P_∞ [Pa]	b [$m^3 \cdot kg^{-1}$]	c_v [$J \cdot K^{-1} \cdot kg^{-1}$]	γ	e_0 [$J \cdot kg^{-1}$]
liquid	2036×10^5	4.57×10^{-4}	791	2.2	-290222
vapour	0	0	299	1.85	29274

Table 4.1: NASG coefficients for O_2.

The length of the periodic domain is $L = 1$ m. The initial density profile is given by

$$\rho_0(x) = \rho_b + \rho_\Delta f(x), \tag{4.4.30}$$

with $f(x)$ the regular profile given in (4.4.29). The numerical values are chosen to be in the liquid phase according to [Le Métayer and Saurel, 2016], that is $\rho_b = 1100$ [$kg \cdot m^{-3}$] and $\rho_\Delta = 100$ [$kg \cdot m^{-3}$]. The initial pressure value is $P_0(x) = 10$ bar and the initial velocity is $u_0(x) = 20$ m/s.

The number of elements in the mesh is $n_x = 20$. Simulations are run using RKDG1, RKDG2 and RKDG3 schemes, with a Rusanov numerical flux. The results are displayed in Figure 4.16. Since the velocity and pressure fields are preserved up to machine error, they are not displayed. As for the linear advection case, the first-order scheme is diffusive. Actually, the amount of numerical diffusion is much higher than for the linear advection case and a flat profile is already obtained after advection over half the domain length. This is due to the use of a Rusanov flux, which achieves upwinding by adding enough diffusion to compensate the highest propagation speed of information, which is $u + c$ in this case. As the speed of sound is such that $c \gg u$ here, the numerical diffusion flattens the solution.

The numerical diffusion for the first-order scheme can be reduced by computing more accurately the solution of the Riemann problem at the interface between cells, using for example a HLLC solver [Toro et al., 1994]. Yet, as the object of this study focuses mainly on higher-order transport, the Rusanov flux is sufficient to carry out the study as high-order space discretization is achieved by the high-order polynomial representation of the solution.

Once again, the second-order scheme displays a better fidelity but has a relatively high dispersion error. The third-order is naturally even more accurate, almost exactly fitting the analytical solution. This is an noteworthy behaviour of the high-order methods: despite the high difference between the transport velocity and the highest characteristic velocity, the high-order representation of the states at elements boundaries prevent the smearing of the solution despite the use of a very diffusive numerical flux.

The errors after 50 ms evaluated with the L_1-norm, L_2-norm and L_∞-norm are computed for all three conservative variables (ρ, ρu and ρe_t). The results for the second-order and third-order RKDG schemes are displayed in Figure 4.17. The observed convergence rate is in agreement with the respectively expected second- and third-order. This validates the implementation of the RKDG method with the Euler equations.

4.4.2.3 A word on high-order positivity preserving DG methods

As the positivity preservation is an important issue in the numerical resolution of flow models, positivity preserving schemes have been developed within the DG framework. The pioneering work of [Zhang and Shu, 2010a] in this direction provided a DG scheme that preserves the positivity of the mean value

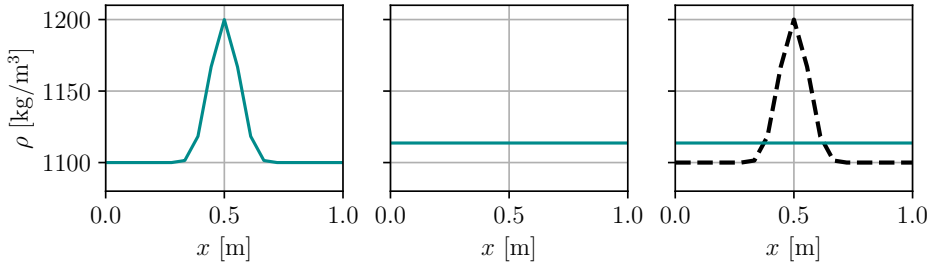

(a) RKDG1 transport: $\mathbb{P}^0$ elements are used for space discretization (piecewise constant), with a RK1 (forward-Euler) time-marching update.

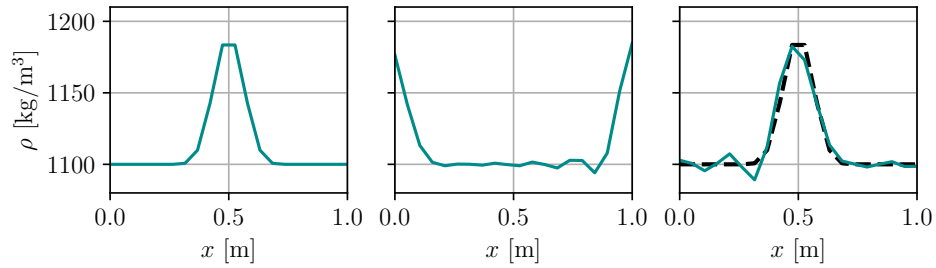

(b) RKDG2 transport: $\mathbb{P}^1$ elements are used for space discretization (piecewise linear), with a RK2 time-marching update.

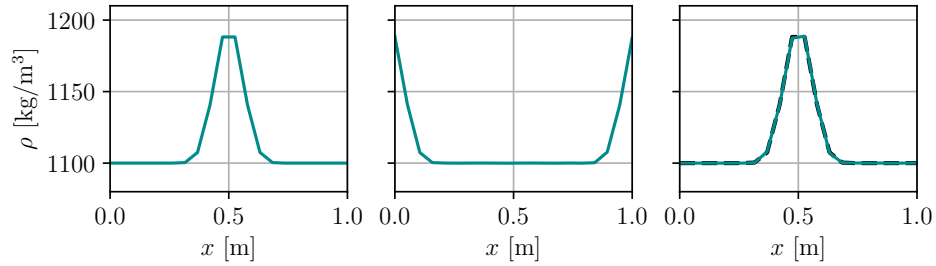

(c) RKDG3 transport: $\mathbb{P}^2$ elements are used for space discretization (piecewise quadratic), with a RK3 time-marching update.

Figure 4.16: Transport of a density perturbation with RKDG3 ($\mathbb{P}^2$ elements). Snapshots are taken at $t = 0$, $t = 25$ ms and $t = 50$ ms. The black dashed line represents the analytical solution, identical to the initial solution.

within each element, for a scalar conservation law. This requires the evaluation of the solution at a finite number of points to perform a limitation that guarantees positivity. Later on, the same team extended this idea to Euler equations over quadrangular elements [Zhang and Shu, 2010b] and over triangular elements [Zhang et al., 2013]. These methods allow for preserve the order of accuracy of the numerical method, but impose a more restrictive CFL constraint than classic DG methods.

4.4.2.4 Remark on the implementation of RKDG methods

In addition to the implementation of the RKDG methods used for the results presented in this manuscript, an implementation of these methods has been carried out during this Ph.D thesis, in the context of project *HODINS* at the CEMRACS mathematics summer program, in 2016. This project was dedicated to the implementation of a numerical solver in a task-programming framework, within the runtime StarPU [Augonnet et al., 2011], which allows for high-performance computing on heterogeneous architectures. The results of this project have been published in [Essadki et al., 2018], although for the sake of clarity, only a finite-volume method is described in the paper.

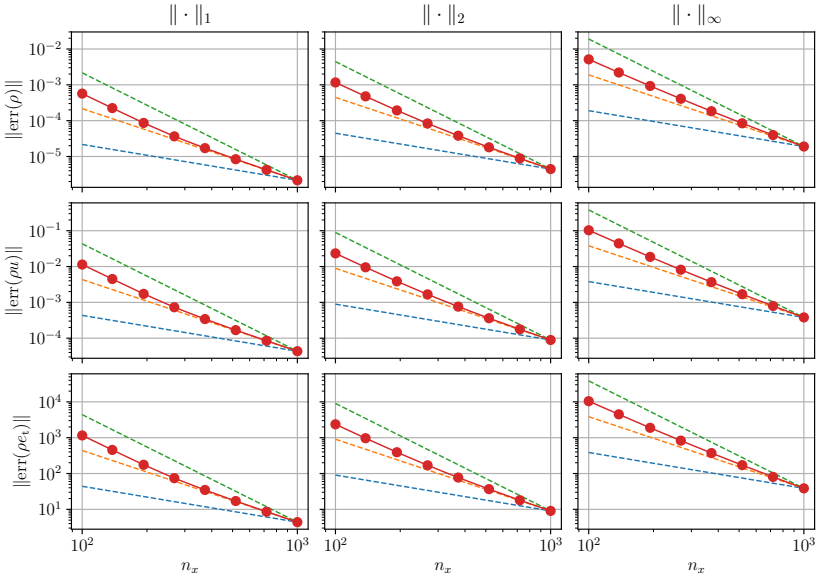

(a) Second-order RKDG

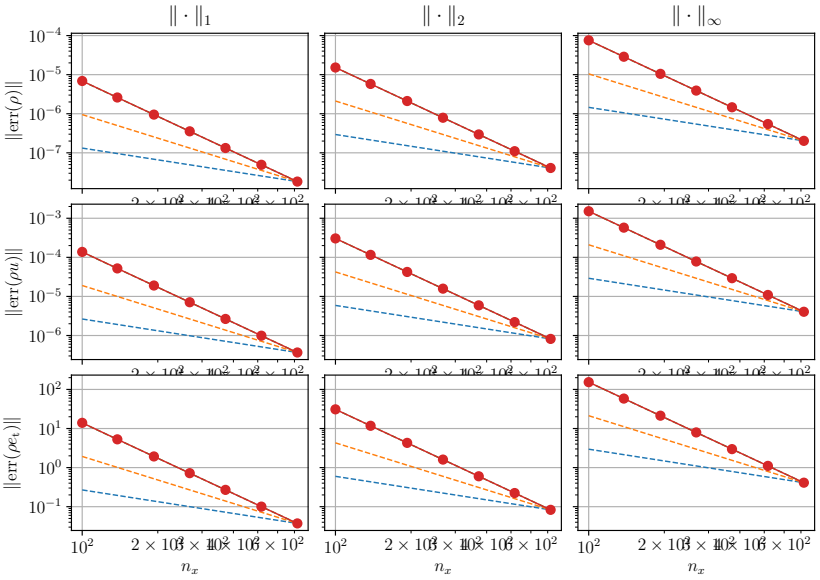

(b) Third-order RKDG

Figure 4.17: Convergence analysis for the Euler equations with NASG thermodynamic closure.

4.5 Vertex-centered numerical methods

Vertex-centered numerical methods use the solution values at the grid nodes as degrees of freedom. This formalism is closely related with classical finite-differences methods, and the Galerkin finite-element method. Vertex-centered methods are relatively close to cell-centered methods, as it was for instance shown by [Mavriplis and Jameson, 1990]: when applied on a regular triangular mesh, the $\mathbb{P}_1$ Galerkin method is equivalent to a vertex-centered finite-volume scheme applied on the dual mesh.

Although the FV methods have been the most popular techniques for flow modeling with a very active community, some authors such as [Donea, 1984], [Löhner et al., 1984], and more recently [Colin and Rudgyard, 2000] pushed forward the application of FE methods to flow modeling. These works provided efficient high-order schemes with low-dissipation, which makes them suitable for applications to LES.

Section 4.5.1 presents the classic Galerkin finite element method, introducing the family of two-step Taylor-Galerkin schemes called TTG, that are implemented in the compressible and unstructured HPC solver AVBP, used in Chapters **5** and **6**. Then, section 4.5.2 presents some developments that aim to construct a high-order finite-element monotonicity-preserving scheme.

4.5.1 Galerkin method

4.5.1.1 Weak formulation

The *finite element method* of Galerkin (FEM), similarly to its discontinuous counterpart described in section 4.4.2, relies on a weak formulation of the conservation law. First, the problem is rewritten as:

$$\forall \boldsymbol{w} \in \boldsymbol{\mathcal{V}},\ \forall t \in \mathbb{R}_+^*,\ \int_\Omega \left(\boldsymbol{w} \cdot \frac{\partial \mathbf{U}}{\partial t} + \boldsymbol{w} \cdot \left[\vec{\nabla} \cdot \vec{\mathcal{F}}\left(\mathbf{U}\right) \right] \right) \mathrm{d}\mathcal{V} = 0, \tag{4.5.1}$$

where $\boldsymbol{w}$ is called a *test function*, belonging to a chosen set $\boldsymbol{\mathcal{V}}$. Then, the weak solution $\mathbf{U}$ of the problem is characterized by:

$$\forall \boldsymbol{w} \in \boldsymbol{\mathcal{V}},\ \forall t \in \mathbb{R}_+^*,\ \int_\Omega \left(\boldsymbol{w} \cdot \frac{\partial \mathbf{U}}{\partial t} - \vec{\nabla}\boldsymbol{w} \cdot \vec{\mathcal{F}}\left(\mathbf{U}\right) \right) \mathrm{d}\mathcal{V} = 0, \tag{4.5.2}$$

obtained using an integration by parts.

4.5.1.2 Galerkin semi-discretization

4.5.1.2.1 The Galerkin approximation

The FEM consists in approaching the solution $\mathbf{U} \in \boldsymbol{\mathcal{U}}$ by the approximate one $\mathbf{U}_\Delta \in \boldsymbol{\mathcal{V}}_\Delta$, where $\boldsymbol{\mathcal{V}}_\Delta = \mathbb{P}^k(\mathcal{T}_h)$ is the finite-dimension functional space of piecewise-polynomial functions over the mesh. The approximate solution can be expressed as

$$\mathbf{U}_\Delta\left(\vec{x}, t\right) = \sum_{j=1}^{n_{\mathrm{DoF}}} \mathbf{U}_j(t) \hat{\phi}_j\left(\vec{x}\right), \tag{4.5.3}$$

where $\hat{\phi}_i$ is the basis function associated with the i^{th} DoF. The present work focuses on the $\mathbb{P}^1$ case, representing the solution by piecewise linear functions. The corresponding basis functions $\left(\hat{\phi}_j\right)_{j \in [\![1, n_{\mathrm{DoF}}]\!]}$ are then the *hat* functions associated with the mesh vertices, as illustrated by figure 4.18. Function $\hat{\phi}_j$ consists in the unique piecewise-linear function that verifies

$$\hat{\phi}_j(\vec{x}_i) = \delta_{ij} = \begin{cases} 1 \text{ if } i = j, \\ 0 \text{ otherwise,} \end{cases} \tag{4.5.4}$$

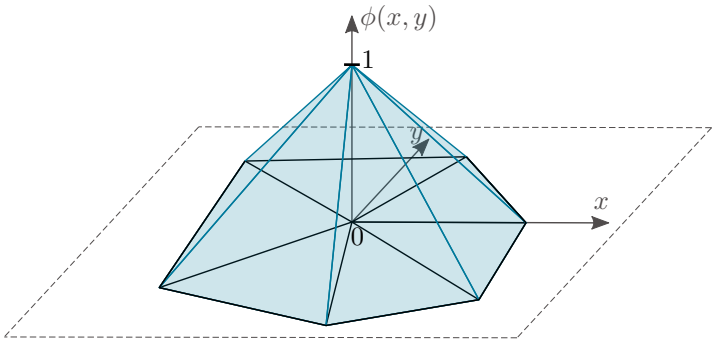

Figure 4.18: Illustration of a basis function for the $\mathbb{P}^1$ Galerkin method, for a 2D triangular mesh.

with δ_{ij} the Kronecker operator.

Unlike the DG representation of the solution $\mathbf{U}_\Delta$ that appears in (4.4.22), the Galerkin formulation consists in a continuous approximation of the solution (4.5.3). In this respect, the $\mathbb{P}^1$-DG is not equivalent to the $\mathbb{P}^1$-Galerkin representation.

In the present work, the flux function (in the three-dimensional case) is approximated under the *group representation* [Donea and Huerta, 2003], as done in [Colin and Rudgyard, 2000], which consists in writing

$$\vec{\mathcal{F}}\left(\mathbf{U}\left(\vec{x},t\right)\right) \approx \sum_{j=1}^{n_{\mathrm{DoF}}} \vec{\mathcal{F}}\left(\mathbf{U}_j(t)\right)\hat{\phi}_j\left(\vec{x}\right). \tag{4.5.5}$$

and the following notation is used (in the three-dimensional case):

$$\vec{\mathcal{F}}\left(\mathbf{U}_j(t)\right) = \begin{bmatrix} \mathbf{F}_j^x(t) \\ \mathbf{F}_j^y(t) \\ \mathbf{F}_j^z(t) \end{bmatrix} = \vec{\mathbf{F}}_j(t) \tag{4.5.6}$$

Note that although relation (4.5.5) is exact only when the considered numerical flux is linear, it allows for substantial computational gain, as underlined by [Fletcher, 1996]. This latter reference states that the accuracy of the solution is not deteriorated by such approximation provided the two conditions:

(i) the equations are solved in their conservative form,

(ii) the same polynomial interpolation is used for all the terms appearing in the differential terms of the conservation law.

In particular, the order of the solution is the same whether approximation (4.5.5) is used or not.

Following the Galerkin method, the space of the test functions is also reduced to $\boldsymbol{\mathcal{V}}_\Delta$.

$$\forall \boldsymbol{w} \in \boldsymbol{\mathcal{V}}_\Delta,\ \forall t \in \mathbb{R}_+^*,\ \sum_{j=1}^{n_{\mathrm{DoF}}} \int_\Omega \left(\boldsymbol{w} \cdot \frac{\mathrm{d}\mathbf{U}_j}{\mathrm{d}t}\hat{\phi}_j - \vec{\nabla}\boldsymbol{w} \cdot \left(\vec{\mathbf{F}}_j(t)\,\hat{\phi}_j\right)\right) \mathrm{d}\mathcal{V} = 0. \tag{4.5.7}$$

Since $\boldsymbol{\mathcal{V}}_\Delta$ is spanned by the $\left(\hat{\phi}_j\right)_{j=1,n_{\mathrm{DoF}}}$, verifying equation (4.5.7) for any $\boldsymbol{w} \in \boldsymbol{\mathcal{V}}_\Delta$ is equivalent to:

$$\forall i \in [\![1, n_{\mathrm{DoF}}]\!],\ \forall t \in \mathbb{R}_+^*,\ \sum_{j=1}^{n_{\mathrm{DoF}}} \int_\Omega \left(\frac{\mathrm{d}\mathbf{U}_j}{\mathrm{d}t}\hat{\phi}_i\hat{\phi}_j - \vec{\mathbf{F}}_j(t) \cdot \left(\hat{\phi}_j\vec{\nabla}\hat{\phi}_i\right)\right) \mathrm{d}\mathcal{V} = 0, \tag{4.5.8}$$

which is equivalent to

$$\forall i \in [\![1, n_{\mathrm{DoF}}]\!],\ \forall t \in \mathbb{R}_+^*,\quad \sum_{e=1}^{n_\mathcal{E}} \sum_{j=1}^{n_{\mathrm{DoF}}} \frac{\mathrm{d}\mathbf{U}_j}{\mathrm{d}t} \left[\int_{\mathcal{E}_e} \hat{\phi}_i\hat{\phi}_j\,\mathrm{d}\mathcal{V}\right] + \sum_{e=1}^{n_\mathcal{E}} \sum_{j=1}^{n_{\mathrm{DoF}}} \left[\int_{\mathcal{E}_e} \hat{\phi}_i\vec{\nabla}\hat{\phi}_j\,\mathrm{d}\mathcal{V}\right] \cdot \vec{\mathbf{F}}_j(t) = 0. \tag{4.5.9}$$

In (4.5.9) appears the Galerkin *mass matrix* $\boldsymbol{\mathcal{M}}$ and *advection operator* $\boldsymbol{\mathcal{T}}$, defined by

$$\boldsymbol{\mathcal{M}}_{ij} = \sum_{e=1}^{n_\mathcal{E}} \boldsymbol{\mathcal{M}}_{ij}^e, \qquad \text{with} \qquad \boldsymbol{\mathcal{M}}_{ij}^e = \int_{\mathcal{E}_e} \hat{\phi}_i \hat{\phi}_j \, \mathrm{d}\mathcal{V}, \tag{4.5.10}$$

$$\boldsymbol{\mathcal{T}}_{ij} = \sum_{e=1}^{n_\mathcal{E}} \boldsymbol{\mathcal{T}}_{ij}^e, \qquad \text{with} \qquad \boldsymbol{\mathcal{T}}_{ij}^e = \int_{\mathcal{E}_e} \hat{\phi}_i \vec{\nabla} \hat{\phi}_j \, \mathrm{d}\mathcal{V}. \tag{4.5.11}$$

The semi-discrete equation eventually writes in the vectorial form:

$$\boldsymbol{\mathcal{M}} \frac{\mathrm{d}\left\lfloor \mathbf{U} \right\rceil}{\mathrm{d}t} + \boldsymbol{\mathcal{T}} \cdot \left\lfloor \vec{\mathbf{F}} \right\rceil = 0, \tag{4.5.12}$$

where the notation $\left\lfloor \mathbf{U} \right\rceil$ denotes vector of $\mathbb{R}^{n_{\mathrm{DoF}} \times N_\mathrm{t}}$ containing the solution values at the n_{DoF} nodes. It is worth emphasizing that both $\boldsymbol{\mathcal{M}}$ and $\boldsymbol{\mathcal{T}}$ are constant for a given computational grid and Galerkin polynomial order, and do not depend on the solution and flux values. In addition, these matrices are sparse, since for any $j \notin \mathcal{D}_i$, $\boldsymbol{\mathcal{M}}_{ij} = \boldsymbol{\mathcal{T}}_{ij} = 0$.

4.5.1.2.2 The Galerkin-Runge-Kutta (GRK) scheme

The semi-discrete form (4.5.12) consists in a large system of ordinary differential equation, which can be solved by means of a Runge-Kutta (RK) method. When $\mathbb{P}^1$ elements are used for the Galerkin discretization, a third-order scheme in space and time can be obtained [Donea and Huerta, 2003] using the RK3 method for the time-marching scheme.

The corresponding scheme then writes

$$\begin{cases} \left\lfloor \mathbf{U} \right\rceil^{n+\frac{1}{3}} = \left\lfloor \mathbf{U} \right\rceil^{n} + \dfrac{\Delta t}{3} \left\lfloor \boldsymbol{H} \right\rceil^{n}, & \text{(4.5.13a)} \\ \left\lfloor \mathbf{U} \right\rceil^{n+\frac{1}{2}} = \left\lfloor \mathbf{U} \right\rceil^{n} + \dfrac{\Delta t}{2} \left\lfloor \boldsymbol{H} \right\rceil^{n+\frac{1}{3}}, & \text{(4.5.13b)} \\ \left\lfloor \mathbf{U} \right\rceil^{n+1} = \left\lfloor \mathbf{U} \right\rceil^{n} + \Delta t \left\lfloor \boldsymbol{H} \right\rceil^{n+\frac{1}{2}}, & \text{(4.5.13c)} \end{cases}$$

with

$$\left\lfloor \boldsymbol{H} \right\rceil^{k} = -\boldsymbol{\mathcal{M}}^{-1} \boldsymbol{\mathcal{T}} \cdot \left\lfloor \vec{\mathbf{F}} \right\rceil^{k}. \tag{4.5.14}$$

This scheme is stable under the CFL constraint $\eta_C \leq 1$.

4.5.1.3 Taylor-Galerkin (TG) schemes

The family of Taylor-Galerkin schemes is based on a strategy similar to the Lax-Wendroff scheme. Instead of the GRK scheme presented in paragraph 4.5.1.2.2, which consists in performing first a spatial semi-discretization and then using a time-marching method for the temporal discretization, TG schemes are built first on a temporal semi-discretization using a Taylor expansion, and then a spatial discretization of the resulting semi-discrete differential equation.

4.5.1.3.1 The Lax-Wendroff-Galerkin scheme

The derivation of the second-order TG scheme [Donea and Huerta, 2003], called Lax-Wendroff-Galerkin (or TG2) scheme is now presented. It can be summarized into the three steps given below.

The first step consists in writing the Taylor expansion in time of the vector of conservative variables $\mathbf{U}$ up to order 2:

$$\mathbf{U}(\vec{x}, t^{n+1}) = \mathbf{U}(\vec{x}, t^n) + \Delta t \left(\frac{\partial \mathbf{U}}{\partial t}\right)_{(\vec{x},t^n)} + \frac{\Delta t^2}{2}\left(\frac{\partial^2 \mathbf{U}}{\partial t^2}\right)_{(\vec{x},t^n)} + \mathcal{O}\left(\Delta t^3\right) \tag{4.5.15}$$

The second step is to apply the *Cauchy-Kowalevski* procedure, which consists in turning the temporal derivatives of (4.5.15) into spatial derivatives by means of the conservation law (4.2.4). The first-order derivative is then given by

$$\left(\frac{\partial \mathbf{U}}{\partial t}\right)_{(\vec{x},t^n)} = -\vec{\nabla}\cdot\vec{\mathcal{F}}\left(\mathbf{U}\right) \tag{4.5.16}$$

and the second-order derivative is

$$\left(\frac{\partial^2 \mathbf{U}}{\partial t^2}\right)_{(\vec{x},t^n)} = -\vec{\nabla}\cdot\left(\frac{\partial \vec{\mathcal{F}}\left(\mathbf{U}\right)}{\partial t}\right)_{(\vec{x},t^n)} = -\vec{\nabla}\cdot\left(\vec{\mathcal{J}}\left(\mathbf{U}\right)\left(\frac{\partial \mathbf{U}}{\partial t}\right)_{(\vec{x},t^n)}\right) = \vec{\nabla}\cdot\left[\vec{\mathcal{J}}\left(\mathbf{U}\right)\vec{\nabla}\cdot\vec{\mathcal{F}}\left(\mathbf{U}\right)\right]. \tag{4.5.17}$$

The approximate vector of conservative variables $\mathbf{U}_\Delta^{n+1}(\vec{x})$ at time t^{n+1} then reads

$$\mathbf{U}_\Delta^{n+1}(\vec{x}) = \mathbf{U}_\Delta^{n}(\vec{x}) - \Delta t\vec{\nabla}\cdot\vec{\mathcal{F}}\left(\mathbf{U}_\Delta^n\right) + \frac{\Delta t^2}{2}\vec{\nabla}\cdot\left[\vec{\mathcal{J}}\left(\mathbf{U}_\Delta^n\right)\vec{\nabla}\cdot\vec{\mathcal{F}}\left(\mathbf{U}_\Delta^n\right)\right]. \tag{4.5.18}$$

The resulting differential equation (4.5.18) only involves functions and derivatives along spatial variables. The third and final step consists in the discretization of (4.5.18), following a similar Galerkin procedure as the one described in section 4.5.1.2. The conservative variables and the associated flux are approximated following (4.5.3) and (4.5.5). In addition, the Jacobian matrix $\vec{\mathcal{J}}\left(\mathbf{U}_\Delta^n\left(\vec{x}\right)\right)$ is approximated by its mean value over the containing element $\mathcal{E}_e \ni x$:

$$\vec{\mathcal{J}}\left(\mathbf{U}_\Delta^n\left(\vec{x}\right)\right) \approx \vec{\mathcal{J}}_e^n = \frac{1}{n_{\mathrm{v}}^e}\sum_{j\in\mathcal{E}_e}\vec{\mathcal{J}}(\mathbf{U}_j^n), \tag{4.5.19}$$

with n_{v}^e the number of vertices in element $\mathcal{E}_e$. The weak form of equation (4.5.18) under these approximations reads:

$$\begin{aligned}&\forall i \in [\![1, n_{\mathrm{DoF}}]\!],\\ &\sum_{e=1}^{n_\mathcal{E}}\sum_{j=1}^{n_{\mathrm{DoF}}}\int_{\mathcal{E}_e}\left(\left(\mathbf{U}_j^{n+1}-\mathbf{U}_j^n\right)\hat{\phi}_i\hat{\phi}_j + \Delta t\vec{\mathbf{F}}_j^n\cdot\left(\hat{\phi}_i\vec{\nabla}\hat{\phi}_j\right) - \frac{\Delta t^2}{2}\vec{\nabla}\cdot\left[\vec{\mathcal{J}}_e^n\left(\vec{\mathbf{F}}_j^n\cdot\vec{\nabla}\hat{\phi}_j\right)\right]\hat{\phi}_i\right)\mathrm{d}\mathcal{V} = 0.\end{aligned} \tag{4.5.20}$$

Which can be written, using the notations of [Colin and Rudgyard, 2000], as

$$\boldsymbol{\mathcal{M}}\left[\mathbf{U}^{n+1}\right] = \boldsymbol{\mathcal{M}}\left[\mathbf{U}^n\right] - \Delta t\left[\mathbf{L}\left(\mathbf{U}^n\right)\right] - \frac{\Delta t^2}{2}\left[\mathbf{LL}\left(\mathbf{U}^n\right)\right], \tag{4.5.21}$$

where the mass matrix $\boldsymbol{\mathcal{M}}$ is defined by equation (4.5.10). The first-order term $\mathbf{L}\left(\mathbf{U}^n\right)$ and second-order term $\mathbf{LL}\left(\mathbf{U}^n\right)$ are given by

$$\mathbf{L}\left(\mathbf{U}_i^n\right) = \sum_{e=1}^{n_\mathcal{E}}\sum_{j=1}^{n_{\mathrm{DoF}}}\vec{\mathbf{F}}_j^n\cdot\int_{\mathcal{E}_e}\hat{\phi}_i\vec{\nabla}\hat{\phi}_j\,\mathrm{d}\mathcal{V} = \left(\boldsymbol{\mathcal{T}}\cdot\left[\vec{\mathbf{F}}^n\right]\right)_i, \tag{4.5.22a}$$

$$\mathbf{LL}\left(\mathbf{U}_i^n\right) = \sum_{e=1}^{n_\mathcal{E}}\sum_{j=1}^{n_{\mathrm{DoF}}}\int_{\mathcal{E}_e}\vec{\nabla}\cdot\left[\vec{\mathcal{J}}_e^n\vec{\nabla}\cdot\left(\vec{\mathbf{F}}_j^n\hat{\phi}_j\right)\right]\hat{\phi}_i\,\mathrm{d}\mathcal{V}, \tag{4.5.22b}$$

The second-order term $\mathbf{LL}(\mathbf{U}^n)$ is computed by integration by parts, which reads

$$\begin{aligned}\mathbf{LL}(\mathbf{U}_i^n) = &-\sum_{e=1}^{n_\mathcal{E}}\sum_{j=1}^{n_{\mathrm{DoF}}} \vec{\mathcal{J}}_e^n \int_{\mathcal{E}_e} \left[\vec{\mathbf{F}}_j^n \cdot \vec{\nabla}\hat{\phi}_j\right] \vec{\nabla}\hat{\phi}_i \,\mathrm{d}\mathcal{V},\\ &+\sum_{e=1}^{n_\mathcal{E}}\sum_{j=1}^{n_{\mathrm{DoF}}} \int_{\partial\mathcal{E}_e\cap\partial\Omega} \vec{\mathcal{J}}_e^n \left(\vec{\mathbf{F}}_j^n \cdot \vec{\nabla}\hat{\phi}_j\right) \hat{\phi}_i \cdot \vec{n} \,\mathrm{d}\mathcal{S}.\end{aligned} \tag{4.5.23}$$

The second term of (4.5.23), containing the boundary terms, will be described in paragraph (4.5.1.3.2). Equation (4.5.21) defines the *Lax-Wendroff-Galerkin* scheme, also called the LW-FE or the TG2 (for TG 2$^{\mathrm{nd}}$-order) scheme [Donea and Huerta, 2003].

4.5.1.3.2 Boundary terms

The values of the boundary terms arising from the integration by parts (4.5.23) must be provided. Such terms should not require the formulation of additional "physical" boundary conditions, since the system of Euler equations is already completely determined by the considered Cauchy problem. Nonetheless, a value must be attributed to these terms. In this respect, two different assumptions have been considered by [Lamarque, 2007] and are available in AVBP:

(i) *uncancelled second-order term* (USOT), which consists in neglecting the boundary terms, so that at all grid nodes (and, in particular, even at the boundary nodes), one has

$$\mathbf{LL}(\mathbf{U}_i^n) = -\sum_{e=1}^{n_\mathcal{E}}\sum_{j=1}^{n_{\mathrm{DoF}}} \vec{\mathcal{J}}_e^n \int_{\mathcal{E}_e} \left[\vec{\mathbf{F}}_j^n \cdot \vec{\nabla}\hat{\phi}_j\right] \vec{\nabla}\hat{\phi}_i \,\mathrm{d}\mathcal{V} \tag{4.5.24}$$

(ii) *cancelled second-order term* (CSOT), which assume a zero-valued second-order term at boundary nodes, so that

$$\forall \vec{x}_i \in \partial\Omega, \mathbf{LL}(\mathbf{U}_i^n) = 0. \tag{4.5.25}$$

4.5.1.3.3 Matrix formulation

It is possible to express the update (4.5.21) in the following form:

$$\begin{aligned}\sum_{e=1}^{n_\mathcal{E}}\sum_{j=1}^{n_{\mathrm{DoF}}} \int_{\mathcal{E}_e} \vec{\nabla}\cdot\left[\vec{\mathcal{J}}_e^n \vec{\nabla}\cdot\left(\vec{\mathbf{F}}_j^n \hat{\phi}_j\right)\right] \hat{\phi}_i \,\mathrm{d}\mathcal{V} = &-\sum_{e=1}^{n_\mathcal{E}}\sum_{j=1}^{n_{\mathrm{DoF}}} \left(\int_{\mathcal{E}_e} \left[\vec{\nabla}\hat{\phi}_i \otimes \vec{\nabla}\hat{\phi}_j\right] \mathrm{d}\mathcal{V}\right) : \left(\vec{\mathcal{J}}_e^n \,{}^{\mathrm{t}}\vec{\mathbf{F}}_j^n\right)\\ &+\sum_{e=1}^{n_\mathcal{E}}\sum_{j=1}^{n_{\mathrm{DoF}}} \int_{\partial\mathcal{E}_e\cap\partial\Omega} \vec{\mathcal{J}}_e^n \left(\vec{\mathbf{F}}_j^n \cdot \vec{\nabla}\hat{\phi}_j\right) \hat{\phi}_i \cdot \vec{n} \,\mathrm{d}\mathcal{S}\end{aligned} \tag{4.5.26}$$

, with the double contraction product defined over the spatial dimensions:

$$\vec{\vec{A}} : \vec{\vec{B}} = \mathrm{Tr}\left(\vec{\vec{A}} \cdot \vec{\vec{B}}\right) = \sum_{k=1}^{d}\sum_{l=1}^{d} A_{kl} B_{lk} \tag{4.5.27}$$

which can be summarized as

$$\boldsymbol{\mathcal{M}}\left[\mathbf{U}^{n+1}\right] = \boldsymbol{\mathcal{M}}\left[\mathbf{U}^n\right] - \Delta t \boldsymbol{\mathcal{T}} \cdot \left[\mathbf{F}^n\right] - \frac{\Delta t}{2}\boldsymbol{\mathcal{D}} : \left[\vec{\boldsymbol{\mathcal{J}}}^n \cdot \mathbf{F}^n\right] + \left[\mathrm{BT}^n\right] \tag{4.5.28}$$

with the *diffusion operator* defined as

$$\boldsymbol{\mathcal{D}}_{ij} = \sum_{e=1}^{n_\mathcal{E}} \boldsymbol{\mathcal{D}}_{ij}^e, \qquad \text{with} \qquad \boldsymbol{\mathcal{D}}_{ij}^e = \int_{\mathcal{E}_e} \vec{\nabla}\hat{\phi}_i \otimes \vec{\nabla}\hat{\phi}_j \,\mathrm{d}\mathcal{V}. \tag{4.5.29}$$

In this formulation, the different operators $\mathfrak{M}$, $\mathcal{T}$ and $\mathfrak{D}$ are constant once the mesh and basis functions are fixed.

4.5.1.3.4 Two-step Taylor-Galerkin (TTG) schemes

Higher-order convergence can be obtained with so-called TTG schemes. This strategy was initiated by [Selmin, 1987], and further explored and formalized by [Colin and Rudgyard, 2000]. In this latter reference, a general form of the TTG schemes is provided. It is based on an alternative form of the truncated Taylor expansion (4.5.15), which introduces an intermediate step $\tilde{U}$, so that the state at time t^{n+1} is given by

$$\begin{cases} \tilde{\mathbf{U}}^n(\vec{x}) &= \mathbf{U}^n(\vec{x}) - \alpha_{\mathrm{TTG}}\Delta t\dfrac{\partial \mathbf{U}^n}{\partial t} + \beta_{\mathrm{TTG}}\Delta t^2\dfrac{\partial^2 \mathbf{U}^n}{\partial t^2}, & \text{(4.5.30a)} \\ \mathbf{U}^{n+1}(\vec{x}) &= \mathbf{U}^n(\vec{x}) - \Delta t\left(\theta_{\mathrm{TTG}}\dfrac{\partial \mathbf{U}^n}{\partial t} + \tilde{\theta}_{\mathrm{TTG}}\dfrac{\partial \tilde{\mathbf{U}}^n}{\partial t}\right) + \Delta t^2\left(\varepsilon_{\mathrm{TTG}}\dfrac{\partial^2 \mathbf{U}^n}{\partial t^2} + \tilde{\varepsilon}_{\mathrm{TTG}}\dfrac{\partial^2 \tilde{\mathbf{U}}^n}{\partial t^2}\right), & \text{(4.5.30b)} \end{cases}$$

where the coefficients α_{TTG}, β_{TTG}, θ_{TTG}, $\tilde{\theta}_{\mathrm{TTG}}$, $\varepsilon_{\mathrm{TTG}}$ and $\tilde{\varepsilon}_{\mathrm{TTG}}$ are constant parameters of the TTG method. Following the same Galerkin discretization technique as described in paragraph 4.5.1.3.1, one obtains the following expression for the TTG scheme:

$$\begin{cases} \mathfrak{M}\left[\tilde{\mathbf{U}}^n\right] &= \mathfrak{M}\left[\mathbf{U}^n\right] - \alpha_{\mathrm{TTG}}\Delta t\left[\mathbf{L}\left(\mathbf{U}^n\right)\right] + \beta_{\mathrm{TTG}}\Delta t^2\left[\mathbf{LL}\left(\mathbf{U}^n\right)\right], & \text{(4.5.31a)} \\ \mathfrak{M}\left[\mathbf{U}^{n+1}\right] &= \mathfrak{M}\left[\mathbf{U}^n\right] - \Delta t\left(\theta_{\mathrm{TTG}}\left[\mathbf{L}\left(\mathbf{U}^n\right)\right] + \tilde{\theta}_{\mathrm{TTG}}\left[\mathbf{L}\left(\tilde{\mathbf{U}}^n\right)\right]\right) & \text{(4.5.31b)} \\ & \quad + \Delta t^2\left(\varepsilon_{\mathrm{TTG}}\left[\mathbf{LL}\left(\mathbf{U}^n\right)\right] + \tilde{\varepsilon}_{\mathrm{TTG}}\left[\mathbf{LL}\left(\tilde{\mathbf{U}}^n\right)\right]\right). \end{cases}$$

The choice of the coefficients yields the different TTG schemes, resulting in various behaviours in terms of diffusion and dispersion [Colin and Rudgyard, 2000]. The different parameter combinations are recalled in Table 4.2.

Scheme	α_{TTG}	β_{TTG}	θ_{TTG}	$\tilde{\theta}_{\mathrm{TTG}}$	$\varepsilon_{\mathrm{TTG}}$	$\tilde{\varepsilon}_{\mathrm{TTG}}$
LW-FE	-	-	1	-	$1/2$	-
TTG3	$1/3$	$1/9$	1	0	0	$1/2$
TTG4A	$1/3$	$1/12$	1	0	0	$1/2$
TTG4B	0.1409714	0.1160538	0	1	0	0.3590284
TTGC	$1/2 - \gamma_{\mathrm{TTG}}$	$1/6$	0	1	γ_{TTG}	0

Table 4.2: Sets of coefficients defining the different TTG schemes and the LW-FE scheme. This latter scheme being a one-step scheme, only the relevant coefficients are provided.

In particular, it is shown by [Colin and Rudgyard, 2000] that if the coefficients are such that

$$\begin{cases} \theta_{\mathrm{TTG}} + \tilde{\theta}_{\mathrm{TTG}} = 1, & \text{(4.5.32a)} \\ \varepsilon_{\mathrm{TTG}} + \tilde{\varepsilon}_{\mathrm{TTG}} + \alpha_{\mathrm{TTG}}(1 - \theta_{\mathrm{TTG}}) = \dfrac{1}{2}, & \text{(4.5.32b)} \\ \dfrac{1}{2}\alpha_{\mathrm{TTG}}\left(1 - 2\varepsilon_{\mathrm{TTG}}\right) + (1 - \theta_{\mathrm{TTG}})\left(\beta_{\mathrm{TTG}} - \alpha_{\mathrm{TTG}}^2\right) = \dfrac{1}{6}, & \text{(4.5.32c)} \end{cases}$$

the scheme is third-order accurate, which is the case for all TTG schemes of Table 4.2. Note that the TTGC formulation actually corresponds to a family of schemes defined by the parameter γ_{TTG}. This paramter has an impact on the dissipation of the scheme – especially at high frequencies – and on the CFL stability criterion [Colin and Rudgyard, 2000]. Following [Colin and Rudgyard, 2000], $\gamma_{\mathrm{TTG}} = 0.01$ achieves low dissipation and has a high stability limit, slightly above $\eta_C = 1$.

4.5.1.4 Conclusion

This section allowed to introduce the class of TTG schemes, which will be used in the computations of Chapters **5** and **6**, in the AVBP solver. Their derivation and properties have been briefly described.

The next section presents an original work led in order to investigate the possibility to formulate a high-order monotonicity-preserving TTG method.

4.5.2 Finite element methods with flux-corrected transport (FEM-FCT)

The present section is dedicated to the description of the FEM-FCT framework and presents the development of a numerical method within this framework. For the sake of simplicity, the following study is conducted on the advection equation, over a one-dimensional periodic domain and a regular mesh.

4.5.2.1 Motivation and principle of the method

The FEM-FCT strategy aims at preventing the oscillatory behaviour of the classical centered FE methods such as those described in the previous section 4.5.1 when under-resolved gradients are present in the solution. This oscillatory behaviour is highlighted in figure 4.19 in the limit case of the transport of a step profile. In this test case, spurious oscillations of the solution are generated near the discontinuities, resulting in overshoots ($u > 1$) and undershoots ($u < 0$) of the approximate solution.

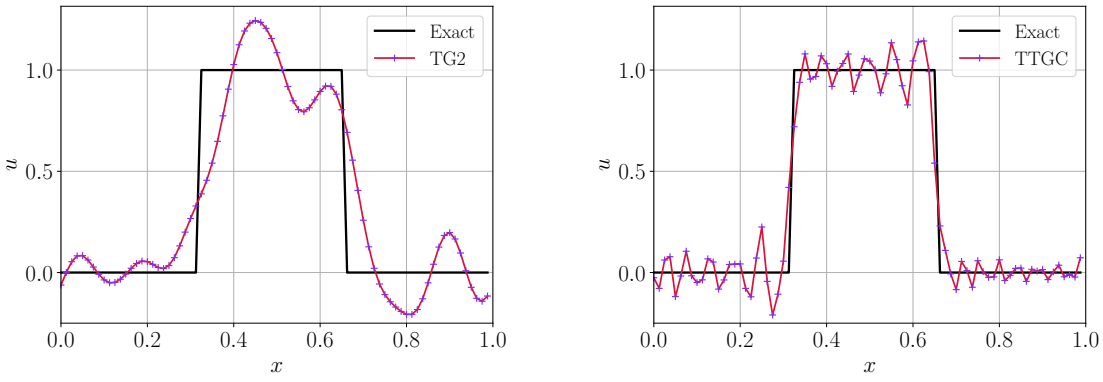

(a) TG2 (2^{nd}-order) (b) TTGC (3^{rd}-order)

Figure 4.19: Transport of a step function in a periodic domain using centered FE methods.

Because of Godunov's Theorem recalled in paragraph 4.3.3.4.5, among linear methods, only first-order methods ensure monotonicity preservation and avoid such spurious oscillations. The idea of *flux-corrected transport* (FCT), proposed in [Boris and Book, 1973], was then to have the best of both worlds by using a monotonicity-preserving low-order method to *restrain* the high-order FE method where it oscillates, providing a high-order non-oscillatory method. This idea has been further developed by the work of [Zalesak, 1979], extending the FEM-FCT formulation to multi-dimensional problems on a

regular mesh. Subsequently, [Löhner et al., 1988] provided an extension to unstructured meshes. More recently, the works of [Kuzmin and Turek, 2002] rigorously reformulated the FEM-FCT framework and proposed an extension to implicit schemes guaranteeing positivity preservation even for high CFL numbers. In the context of this Ph.D work, a preliminary study of FEM-FCT schemes is led in order to investigate the possibility of implementing a high-order monotonicity preserving method into the AVBP solver, based on the preexisting TTGC/TTG4A third-order FE methods.

4.5.2.2 Original formulation

The typical formulation of FEM-FCT methods [Zalesak, 1979] is summarized in the following steps:

1. Compute a high-order update $\lfloor u^H \rfloor$ using a FE discretization of the conservation law;
2. Compute a low-order update $\lfloor u^L \rfloor$ using a non-oscillatory first-order upwinded version of the high-order method, typically by *lumping* the mass matrix and adding enough numerical diffusion [Kuzmin, 2009];
3. Compute the anti-diffusive contributions ψ_{ij} between each pair of DoF (i, j) that restore the original high-order update;
4. Limit these anti-diffusive contributions in order to prevent the formation of new local extrema and to avoid the increase of the existing local extrema;
5. Compute the final update $\lfloor u^{n+1} \rfloor$ by adding the limited anti-diffusive contributions to the low-order solution $\lfloor u^L \rfloor$.

These five steps are now detailed in the following paragraphs.

Step 1 – formulation of the high-order FE method

The one-step "Lax-Wendroff" TG2 scheme (4.5.21) is used here, on which the formulation of [Kuzmin, 2009] is applied. In the case of a one-dimensional advection equation on a regular periodic mesh of step Δx, it reads:

$$\mathcal{M}\lfloor u^H \rfloor = \mathcal{M}\lfloor u^n \rfloor + (a\Delta t)\,\mathcal{T}\lfloor u^n \rfloor + \frac{1}{2}a^2\Delta t^2 \mathcal{D}\lfloor u^n \rfloor. \tag{4.5.33}$$

In the one-dimensional case, the operators $\mathcal{M}$, $\mathcal{T}$ and $\mathcal{D}$ – respectively the mass, advection and diffusion matrices – are all tridiagonal $(n_{\text{DoF}} \times n_{\text{DoF}})$ matrices (except the corner entries that are non-zero due to the periodicity of the domain) which have the following expressions:

$$\mathcal{M} = \Delta x \mathcal{M}_0; \qquad \mathcal{T} = \mathcal{T}_0; \qquad \mathcal{D} = \frac{1}{\Delta x}\mathcal{D}_0 \tag{4.5.34a}$$

with

$$\mathcal{M}_0 = \frac{1}{6}\begin{bmatrix} 4 & 1 & 0 & 1 \\ 1 & \ddots & \ddots & 0 \\ 0 & \ddots & \ddots & 1 \\ 1 & 0 & 1 & 4 \end{bmatrix}; \quad \mathcal{T}_0 = \frac{1}{2}\begin{bmatrix} 0 & -1 & 0 & 1 \\ 1 & \ddots & \ddots & 0 \\ 0 & \ddots & \ddots & -1 \\ -1 & 0 & 1 & 0 \end{bmatrix}; \quad \mathcal{D}_0 = \begin{bmatrix} -2 & 1 & 0 & 1 \\ 1 & \ddots & \ddots & 0 \\ 0 & \ddots & \ddots & 1 \\ 1 & 0 & 1 & -2 \end{bmatrix}. \tag{4.5.34b}$$

Introducing the CFL number $\eta_C = a\frac{\Delta t}{\Delta x}$ and the *stiffness* matrix $\mathcal{K}_0$

$$\mathcal{K}_0 = \mathcal{T}_0 + \frac{1}{2}\eta_C \mathcal{D}_0, \tag{4.5.35}$$

equation (4.5.33) becomes

$$\mathcal{M}_0\lfloor u^H \rfloor = \mathcal{M}_0\lfloor u^n \rfloor + \eta_C \mathcal{K}_0 \lfloor u^n \rfloor, \tag{4.5.36}$$

Step 2 – construction of the low-order non-oscillatory scheme

Following the formalism of [Kuzmin, 2009], the low-order non-oscillatory scheme is constructed by *upwinding* the high-order centered FE scheme (4.5.36).

Consider a numerical scheme of the form

$$\mathcal{A}\lfloor u^{n+1}\rfloor = \mathcal{B}\lfloor u^{n}\rfloor, \tag{4.5.37}$$

with $\mathcal{A}$ a non-singular matrix. Following [Kuzmin et al., 2012], such a scheme is positivity-preserving if $\mathcal{A}$ is an *M-matrix* and $\mathcal{B} \geq 0$, i.e. the coefficients $\mathcal{B}_{ij}$ are positive or zero for any (i, j). The usual definition of an M-matrix is the following:

A matrix $\mathcal{A}$ is called an M-matrix *if:*

i. $a_{ij} \leq 0 \quad$ for $j \neq i$,

ii. *All principal minors of $\mathcal{A}$ are positive.*

Among the various characterizations of M-matrices (see [Poole and Boullion, 1974] for an extensive survey), the important one according to the present concern is that $\mathcal{A}$ is a M-matrix if and only if $\mathcal{A}^{-1} \geq 0$.

The low-order scheme is built to satisfy this posivity-preservation condition. The first step in the construction of the low-order scheme consists in the *lumping* of the mass matrix [Kuzmin, 2009]. The lumping operation reads:

$$(\mathcal{M}_L)_{ij} = \begin{cases} 0 & \text{if } i \neq j, \\ \sum_{k=1}^{n_{\text{DoF}}} \mathcal{M}_{ik} & \text{if } i = j. \end{cases} \tag{4.5.38}$$

And obtained lumped mass matrix $\mathcal{M}_L$ reads

$$\mathcal{M}_L = \Delta x \mathcal{M}_{L,0} = \Delta x \mathcal{I}_d, \tag{4.5.39}$$

with $\mathcal{I}_d$ the identity matrix. Physically, using a lumped mass matrix corresponds to assuming a constant time-derivative within each grid element [Lamarque, 2007]. Mathematically, the high-order scheme (4.5.36) can be rewritten as

$$\mathcal{M}_{L,0}\lfloor u^{H}\rfloor = \mathcal{M}_{L,0}\lfloor u^{n}\rfloor + \eta_C \mathcal{T}_0 \lfloor u^{n}\rfloor + \frac{1}{2}\eta_C^2 \mathcal{D}_0 \lfloor u^{n}\rfloor - \left(\mathcal{M}_0 - \mathcal{M}_{L,0}\right)\left(\lfloor u^{H}\rfloor - \lfloor u^{n}\rfloor\right), \tag{4.5.40}$$

showing that substituting the *consistent* mass matrix $\mathcal{M}$ by its lumped version corresponds to adding the diffusive term $\left(\mathcal{M}_0 - \mathcal{M}_{L,0}\right)\left(\lfloor u^{H}\rfloor - \lfloor u^{n}\rfloor\right)$ to the high-order scheme. The obtained lumped mass-matrix is obviously an M-matrix.

The strategy then consists in adding the lowest possible amount of numerical diffusion to recover a non-oscillatory first-order scheme. The stiffness matrix $\mathcal{K}$ given by (4.5.35) is replaced by

$$\mathcal{L} = \mathcal{K} + \mathcal{D}^*, \tag{4.5.41}$$

with $\mathcal{D}^*$ the diffusion matrix defined by:

$$\begin{cases} \mathcal{D}^*_{ij} = \mathcal{D}^*_{ji} = \max\left\{0, -\mathcal{K}_{ij}, -\mathcal{K}_{ji}\right\} \quad \text{for } j \neq i & \text{(4.5.42a)} \\ \mathcal{D}^*_{ii} = -\sum_{j \neq i} \mathcal{D}^*_{ij}, & \text{(4.5.42b)} \end{cases}$$

which guarantees $\mathcal{L} \geq 0$ and preserves discrete conservation.

The low-order scheme finally reads

$$\mathcal{M}_{L,0}\lfloor u^L \rfloor = \left(\mathcal{M}_{L,0} + \eta_C \mathcal{L}\right) \lfloor u^n \rfloor. \tag{4.5.43}$$

In order to ensure positivity preservation, the matrix $\left(\mathcal{M}_{L,0} + \eta_C \mathcal{L}\right)$ must have only non-negative coefficients, which imposes a limitation on the CFL number:

$$\forall i \mid \mathcal{L}_{ii} < 0, \quad \eta_C \leq \min_i \left\{ -\frac{\mathcal{M}_{ii}}{\mathcal{L}_{ii}} \right\} \tag{4.5.44}$$

Step 3 – computation of the anti-diffusive contributions

From (4.5.40) and (4.5.41), the anti-diffusion necessary to recover the high-order update from the low-order one is given by

$$\lfloor \Psi \rfloor = \left(\mathcal{M}_{L,0} - \mathcal{M}_0\right) \left(\lfloor u^H \rfloor - \lfloor u^n \rfloor \right) - \eta_C \mathcal{D}^* \lfloor u^n \rfloor. \tag{4.5.45}$$

This can be written as a sum of skew-symmetric flux contributions between nodes [Kuzmin, 2009], $\Psi = \sum_{j \neq i} \psi_{ij}$, with the contribution of a node j to another node i given by:

$$\psi_{ij} = \left[\mathcal{M}_{ij} - \eta_C \mathcal{D}^*\right] \left(u_j^n - u_i^n\right) - \mathcal{M}_{ij} \left(u_j^H - u_i^H\right). \tag{4.5.46}$$

Step 4 – limitation of the anti-diffusive contributions

In order to ensure monotonicity preservation, the strategy consists in first splitting the anti-diffusive contributions into the positive and negative contributions received by each node i:

$$\mathrm{P}_i^{\oplus} = \frac{1}{\sum_j \mathcal{M}_{ij}} \sum_{j \neq i} \max\left\{0, \psi_{ij}\right\}, \qquad \mathrm{P}_i^{\ominus} = \frac{1}{\sum_j \mathcal{M}_{ij}} \sum_{j \neq i} \min\left\{0, \psi_{ij}\right\}. \tag{4.5.47}$$

The idea is then to limit the positive contributions in order to prevent the creation or increase of a local maximum, and to limit the negative contributions to prevent the creation or increase of a local minimum. This is done separately, assuming a worst-case scenario [Kuzmin, 2009]. The limitation procedure requires to define the distance from the value at node i to the local maximum and to the local minimum, which read respectively:

$$\begin{aligned} \mathrm{Q}_i^{\oplus} &= \max\left\{ \max_{j \in \mathcal{D}_i}\left\{u_j^n\right\}, \max_{j \in \mathcal{D}_i}\left\{u_j^L\right\} \right\} - u_i^n, \\ \mathrm{Q}_i^{\ominus} &= \min\left\{ \min_{j \in \mathcal{D}_i}\left\{u_j^n\right\}, \min_{j \in \mathcal{D}_i}\left\{u_j^L\right\} \right\} - u_i^n. \end{aligned} \tag{4.5.48}$$

The limitation ratios for the positive and negative contributions are then defined as:

$$\mathrm{R}_i^{\oplus} = \begin{cases} \min\left\{1, \mathrm{Q}_i^{\oplus}/\mathrm{P}_i^{\oplus}\right\}, & \text{if } \mathrm{P}_i^{\oplus} > 0, \\ 1, & \text{if } \mathrm{P}_i^{\oplus} = 0, \end{cases} ; \qquad \mathrm{R}_i^{\oplus} = \begin{cases} \min\left\{1, \mathrm{Q}_i^{\ominus}/\mathrm{P}_i^{\ominus}\right\}, & \text{if } \mathrm{P}_i^{\ominus} < 0, \\ 1, & \text{if } \mathrm{P}_i^{\ominus} = 0. \end{cases} \tag{4.5.49}$$

Note that by construction, $\left(\mathrm{R}_i^{\oplus}, \mathrm{R}_i^{\ominus}\right) \in [0,1]^2$.

Step 5 – computation of the update

The global update of the FEM-FCT is computed as

$$\lfloor u^{n+1} \rfloor = \lfloor u^L \rfloor + \mathcal{M}_{L,0}^{-1} \lfloor \bar{\Psi} \rfloor, \tag{4.5.50}$$

where the limited anti-diffusive flux reads

$$\bar{\Psi}_i = \sum_{j \neq i} \alpha_{ij} \psi_{ij}, \tag{4.5.51}$$

with the limitation coefficients

$$\alpha_{ij} = \begin{cases} \min\left\{ \mathrm{R}_i^{\oplus}, \mathrm{R}_j^{\ominus} \right\} & \text{if } \psi_{ij} \geq 0, \\ \min\left\{ \mathrm{R}_i^{\ominus}, \mathrm{R}_j^{\oplus} \right\} & \text{if } \psi_{ij} < 0, \end{cases} \tag{4.5.52}$$

so that if the limitation coefficients α_{ij} are all zero, the low-order update $\lfloor u^{n+1} \rfloor = \lfloor u^L \rfloor$ is obtained, whereas if they are all unity, the high-order unlimited update $\lfloor u^{n+1} \rfloor = \lfloor u^H \rfloor$ is found. The non-linear update $\lfloor u^{n+1} \rfloor$ verifies the capping

$$\forall i \in [\![1, n_{\mathrm{DoF}}]\!], \quad u_i^{n+1} \in \left[\min_{j \in \mathcal{D}i} \{u_j^n\}, \max_{j \in \mathcal{D}i} \{u_j^n\} \right]. \tag{4.5.53}$$

4.5.2.3 Extension to a third-order TTG method

In order to investigate possible higher-order convergence, the association of FCT to a third-order scheme is now developed. In this respect, a third-order TTG method is considered, e.g. TTG4A or TTGC. From equation (4.5.31), for the one-dimensional linear advection on a periodic regular grid, such schemes can be summarized into:

$$\begin{cases} \mathcal{M}_0 \lfloor \tilde{u}^n \rfloor = \mathcal{M}_0 \lfloor u^n \rfloor - \alpha_{\mathrm{TTG}} \eta_C \mathcal{T}_0 \lfloor u^n \rfloor + \beta_{\mathrm{TTG}} \eta_C^2 \mathcal{D}_0 \lfloor u^n \rfloor, & \text{(4.5.54a)} \\ \mathcal{M}_0 \lfloor u^H \rfloor = \mathcal{M}_0 \lfloor u^n \rfloor - \eta_C \left(\theta_{\mathrm{TTG}} \mathcal{T}_0 \lfloor u^n \rfloor + \tilde{\theta}_{\mathrm{TTG}} \mathcal{T}_0 \lfloor \tilde{u}^n \rfloor \right) & \text{(4.5.54b)} \\ \qquad\qquad + \eta_C^2 \left(\varepsilon_{\mathrm{TTG}} \mathcal{D}_0 \lfloor u^n \rfloor + \tilde{\varepsilon}_{\mathrm{TTG}} \mathcal{D}_0 \lfloor \tilde{u}^n \rfloor \right), \end{cases}$$

which is rewritten as

$$\begin{cases} \mathcal{M}_0 \lfloor \tilde{u}^n \rfloor = \mathcal{M}_0 \lfloor u^n \rfloor + \eta_C \mathcal{K}_1 \lfloor u^n \rfloor, & \text{(4.5.55a)} \\ \mathcal{M}_0 \lfloor u^H \rfloor = \mathcal{M}_0 \lfloor u^n \rfloor + \eta_C \mathcal{K}_2 \lfloor u^n \rfloor + \eta_C \tilde{\mathcal{K}} \lfloor \tilde{u}^n \rfloor, & \text{(4.5.55b)} \end{cases}$$

where the following notations are used:

$$\mathcal{K}_1 = -\alpha_{\mathrm{TTG}} \eta_C \mathcal{T}_0 + \beta_{\mathrm{TTG}} \eta_C^2 \mathcal{D}_0, \tag{4.5.56a}$$
$$\mathcal{K}_2 = -\theta_{\mathrm{TTG}} \eta_C \mathcal{T}_0 + \varepsilon_{\mathrm{TTG}} \eta_C^2 \mathcal{D}_0, \tag{4.5.56b}$$
$$\tilde{\mathcal{K}} = -\tilde{\theta}_{\mathrm{TTG}} \eta_C \mathcal{T}_0 + \tilde{\varepsilon}_{\mathrm{TTG}} \eta_C^2 \mathcal{D}_0. \tag{4.5.56c}$$

4.5.2.3.1 A first idea to apply FEM-FCT

In this section, a direct adaptation of the FEM-FCT methodology of [Kuzmin, 2009] and described in section 4.5.2.2 is detailed.

Step 1 – the high-order FE method

The first idea considered consists in defining the high-order scheme as the single-step reformulation of (4.5.55b), which reads:

$$\mathcal{M}_0 \lfloor u^H \rfloor = \mathcal{M}_0 \lfloor u^n \rfloor + \eta_C \left(\mathcal{K}_2 + \tilde{\mathcal{K}} + \eta_C \tilde{\mathcal{K}} \mathcal{M}_0^{-1} \mathcal{K}_1 \right) \lfloor u^n \rfloor. \tag{4.5.57}$$

Step 2 – the low-order scheme

The low-order scheme is then computed as in section 4.5.2.2, by introducing the diffusion matrix $\mathcal{D}^*_{\mathrm{TTG}}$:

$$\begin{cases} \mathcal{D}^*_{ij} = \mathcal{D}^*_{ji} = \max\left\{0, -\mathcal{K}_{\mathrm{TTG}ij}, -\mathcal{K}_{\mathrm{TTG}ji}\right\}, \quad \text{for } j \neq i, & \text{(4.5.58a)} \\ \mathcal{D}^*_{ii} = -\sum_{j \neq i} \mathcal{D}^*_{ij}, & \text{(4.5.58b)} \end{cases}$$

where the global stiffness matrix $\mathcal{K}_{\mathrm{TTG}}$ of the TTG scheme is defined as

$$\mathcal{K}_{\mathrm{TTG}} = \mathcal{K}_2 + \tilde{\mathcal{K}} + \eta_C \tilde{\mathcal{K}} \mathcal{M}_0^{-1} \mathcal{K}_1. \tag{4.5.59}$$

Note that unlike for the one-step formulation considered in section 4.5.2.2, the operator $\mathcal{K}_{\mathrm{TTG}}$ is not tridiagonal because of the last term, which comes from the two-step character of the scheme. This implies that the adequate numerical diffusion $\mathcal{D}^*$, given by equation (4.5.42) and required to build the low-order scheme verifying $\mathcal{K}_{\mathrm{TTG}} + \mathcal{D}^* \geq 0$, is now non-local (because not tridiagonal). This will be shown to have undesired consequences on the FEM-FCT update.

Steps 3, 4 & 5 – computation and limitation of the antidiffusive contributions, and FEM-FCT update computation

These steps are applied following the classic formulation of section 4.5.2.2.

By doing so, the non-local character of the low-order update is observed to jeopardize the monotonicity of the solution. In order to illustrate this observation, the first iteration for the advection of a step function is displayed in figure 4.20, in which an oscillation has been created. It appears that the high-order contributions would tend to increase the value of the rightmost point of the hatched area, while they would tend to decrease the value of the penultimate point.

Applying the limitation then yields the FEM-FCT update displayed in figure 4.21. An oscillation has been created, which can be attributed to the non-local stencil of the low-order method. Indeed, this caused the penultimate point to be decreased by the low-order update, although its direct neighbours were initially constant and equal to its value. In this respect, the FCT procedure tolerates in this case the creation of an oscillation within the hatched area in figure 4.20b. In order to prevent such behaviour, another low-order scheme is now introduced that is *not* obtained using the classic procedure of [Kuzmin, 2009], relying instead on a finite-volume method.

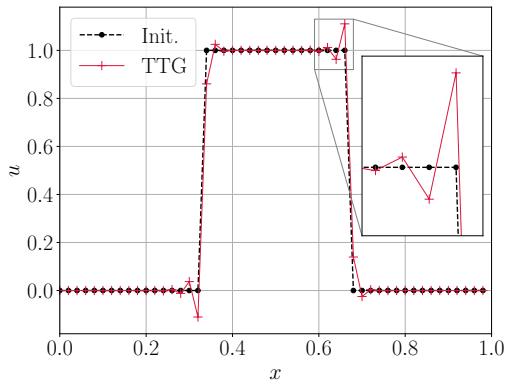

(a) High-order update

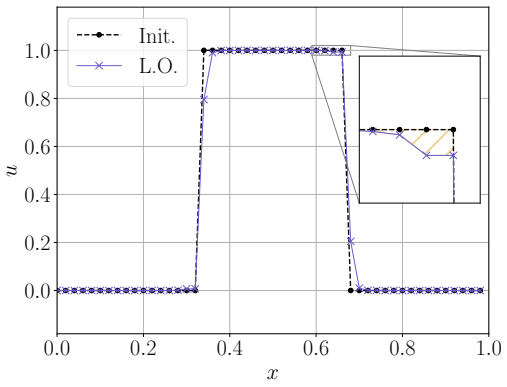

(b) Low-order update. The hatches indicate the area within which the limited solution is allowed to be according to $Q_i^{\oplus}, Q_i^{\ominus}$ in equation (4.5.48)

Figure 4.20: Low- and High-order updates after one iteration for a step function initial profile.

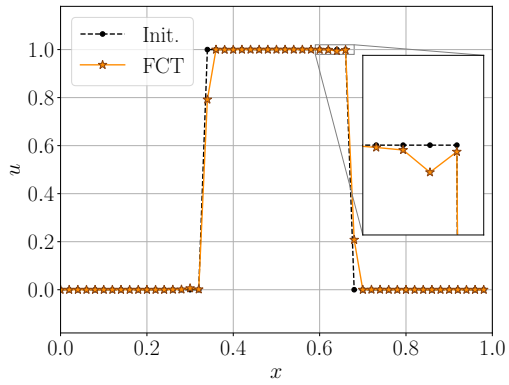

Figure 4.21: FCT update after one iteration for a step function initial profile.

4.5.2.3.2 A solution: setting up a FEM-FCT method using a finite-volume low-order scheme

The idea here is to use a local-stencil low-order FV method, and to write the high-order FEM scheme and the low-order FV method written under a form that allows to evaluate the anti-diffusive node-to-node contributions ψ_{ij} defined in equation (4.5.46).

Step 1 – the high-order FE method

The high-order FE method considered is the TTG method (4.5.55).

In order to be able to decompose the update into node-to-node contributions – which will be necessary to compute the antidiffusive node-to-node contributions ψ_{ij} –, the one-dimensional high-order TTG scheme is split into its *left* and *right* contributions. In this respect, one defines the following operators decomposition:

$$\begin{cases} \mathcal{T}_0 = \mathcal{T}_L + \mathcal{T}_R, & \text{(4.5.60a)} \\ \mathcal{D}_0 = \mathcal{D}_L + \mathcal{D}_R, & \text{(4.5.60b)} \end{cases}$$

with $\mathcal{T}_L, \mathcal{D}_L$ and $\mathcal{T}_R, \mathcal{D}_R$ respectively lower- and upper-triangular matrices, with entries given by:

$$\begin{cases} \mathcal{T}_{Lij} = \displaystyle\int_{x_{i-1}}^{x_i} \hat{\phi}_i \frac{\partial \hat{\phi}_j}{\partial x} \,\mathrm{d}x, \qquad \mathcal{T}_{Rij} = \int_{x_i}^{x_{i+1}} \hat{\phi}_i \frac{\partial \hat{\phi}_j}{\partial x} \,\mathrm{d}x, & (4.5.61a) \\ \mathcal{D}_{Lij} = \displaystyle\int_{x_{i-1}}^{x_i} \frac{\partial \hat{\phi}_i}{\partial x} \frac{\partial \hat{\phi}_j}{\partial x} \,\mathrm{d}x, \qquad \mathcal{D}_{Rij} = \int_{x_i}^{x_{i+1}} \frac{\partial \hat{\phi}_i}{\partial x} \frac{\partial \hat{\phi}_j}{\partial x} \,\mathrm{d}x. & (4.5.61b) \end{cases}$$

The high-order update can then be written as

$$\lfloor u^H \rfloor = \lfloor u^n \rfloor + \lfloor \check{\phi}_R^H \rfloor + \lfloor \check{\phi}_L^H \rfloor, \tag{4.5.62}$$

with

$$\begin{cases} \mathcal{M}_0 \lfloor \check{\phi}_L^H \rfloor = -\eta_C \left(\theta_{\mathrm{TTG}} \mathcal{T}_L \lfloor u^n \rfloor + \tilde{\theta}_{\mathrm{TTG}} \mathcal{T}_L \lfloor \tilde{u}^n \rfloor \right) + \eta_C^2 \left(\varepsilon_{\mathrm{TTG}} \mathcal{D}_L \lfloor u^n \rfloor + \tilde{\varepsilon}_{\mathrm{TTG}} \mathcal{D}_L \lfloor \tilde{u}^n \rfloor \right), & (4.5.63a) \\ \mathcal{M}_0 \lfloor \check{\phi}_R^H \rfloor = -\eta_C \left(\theta_{\mathrm{TTG}} \mathcal{T}_R \lfloor u^n \rfloor + \tilde{\theta}_{\mathrm{TTG}} \mathcal{T}_R \lfloor \tilde{u}^n \rfloor \right) + \eta_C^2 \left(\varepsilon_{\mathrm{TTG}} \mathcal{D}_R \lfloor u^n \rfloor + \tilde{\varepsilon}_{\mathrm{TTG}} \mathcal{D}_R \lfloor \tilde{u}^n \rfloor \right), & (4.5.63b) \\ \mathcal{M}_0 \lfloor \tilde{u}^n \rfloor = \mathcal{M}_0 \lfloor u^n \rfloor - \alpha_{\mathrm{TTG}} \eta_C \mathcal{T}_0 \lfloor u^n \rfloor + \beta_{\mathrm{TTG}} \eta_C^2 \mathcal{D}_0 \lfloor u^n \rfloor. & (4.5.63c) \end{cases}$$

It will be important in the following to note that this TTG method is *globally* conservative, as it verifies (since periodic boundary conditions are used):

$$\check{\phi}_{i,R}^H + \check{\phi}_{i+1,L}^H \neq 0, \qquad \text{but} \qquad \sum_{i=1}^{n_{\mathrm{DoF}}} \check{\phi}_{i,R}^H + \check{\phi}_{i+1,L}^H = 0. \tag{4.5.64}$$

It is also convenient for what follows to define the *total residual* $\Phi_{i,i+1}^H$ for the high-order method over element $\mathcal{E}_i^{i+1}$, as:

$$\Phi_{i,i+1}^H = \check{\phi}_{i,R}^H + \check{\phi}_{i+1,L}^H. \tag{4.5.65}$$

The total residual and the left and right contributions are illustrated in figure 4.22b.

Step 2 – the low-order method

The low-order method considered is the following first-order upwind FV scheme, assuming a positive advection velocity $a > 0$:

$$u_i^L = u_i^n - \eta_C \left(u_i^n - u_{i-1}^n \right). \tag{4.5.66}$$

In the same fashion as for the TTG scheme, the low-order update is split into left and right contributions, as:

$$u_i^L = u_i^n + \check{\phi}_{i,R}^L + \check{\phi}_{i,L}^L, \quad \text{with} \quad \begin{cases} \check{\phi}_{i,R}^L = -\eta_C u_i^n, \\ \check{\phi}_{i,L}^L = \eta_C u_{i-1}^n. \end{cases} \tag{4.5.67}$$

This FV formulation is defined on the dual mesh, as illustrated by figure 4.22a.
It is important to note that unlike the TTG method, the FV formulation is *locally* conservative:

$$\check{\phi}_{i,R}^L + \check{\phi}_{i+1,L}^L = 0. \tag{4.5.68}$$

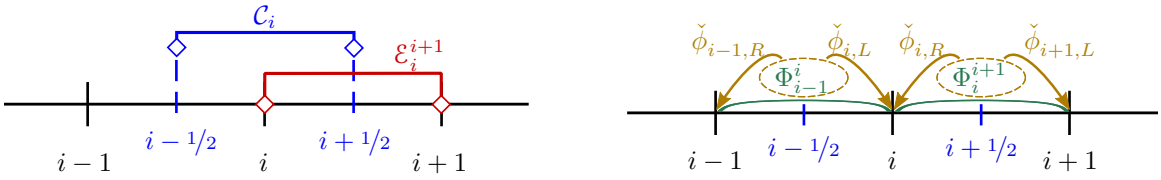

(a) Primal and dual cells, respectively $\mathcal{E}_i^{i+1}$ and $\mathcal{C}_i$.

(b) Contributions of the elements to the nodes.

Figure 4.22: Illustration of the high-order and low-order methods

Steps 3, 4 & 5 – computation and limitation of the antidiffusive contributions, and FEM-FCT update computation

Following the FEM-FCT procedure, the anti-diffusive node-to-node contributions ψ_{ij} are then computed. Considering the left and right splitting formalism introduced in (4.5.62) and (4.5.67), these are the left and right anti-diffusive contributions:

$$\begin{cases} \psi_{i,L} = \psi_{i,i-1} = -\psi_{i-1,i}, & \text{(4.5.69a)} \\ \psi_{i,R} = \psi_{i,i+1} = -\psi_{i+1,i}. & \text{(4.5.69b)} \end{cases}$$

They read:

$$\begin{cases} \psi_{i,L} = \check{\phi}_{i,L}^{H} - \check{\phi}_{i,L}^{L}, & \text{(4.5.70a)} \\ \psi_{i,R} = \check{\phi}_{i,R}^{H} - \check{\phi}_{i,R}^{L}. & \text{(4.5.70b)} \end{cases}$$

For each element, the limiting coefficient $\alpha_{i,i+1} = \alpha_{i+1,i}$ is evaluated as in equation (4.5.52), and the FCT update is

$$u_i^{n+1} = u_i^L + \alpha_{i-1,i}\psi_{i,L} + \alpha_{i,i+1}\psi_{i,R}, \tag{4.5.71}$$

Equivalently, introducing $\check{\phi}_{i,L}^{\text{FCT}} = \check{\phi}_{i,L}^{L} + \alpha_{i-1,i}\psi_{i,L}$ and $\check{\phi}_{i,R}^{\text{FCT}} = \check{\phi}_{i,R}^{L} + \alpha_{i,i+1}\psi_{i,R}$ and using the local conservation property of the FV scheme (4.5.68), the FCT update reads:

$$u_i^{n+1} = u_i^L + \check{\phi}_{i,L}^{\text{FCT}} + \check{\phi}_{i,R}^{\text{FCT}}. \tag{4.5.72}$$

Over an element $\mathcal{E}_i^{i+1}$, the *total residual* $\Phi_{i,i+1}^{\text{FCT}}$ for the FCT scheme, defined as $\Phi_{i,i+1}^{\text{FCT}} = \check{\phi}_{i,R}^{\text{FCT}} + \check{\phi}_{i+1,L}^{\text{FCT}}$, reads:

$$\Phi_{i,i+1}^{\text{FCT}} = \underbrace{\check{\phi}_{i,R}^{L} + \check{\phi}_{i+1,L}^{L}}_{=0} + \alpha_{i,i+1}\Big(\check{\phi}_{i,R}^{H} + \check{\phi}_{i+1,L}^{H} - \big(\underbrace{\check{\phi}_{i,R}^{L} + \check{\phi}_{i+1,L}^{L}}_{=0}\big)\Big) \tag{4.5.73}$$

so that

$$\Phi_{i,i+1}^{\text{FCT}} = \alpha_{i,i+1}\Phi_{i,i+1}^{H}, \tag{4.5.74}$$

where $\Phi_{i,i+1}^{H}$ is the total residual for the high-order method over element $\mathcal{E}_i^{i+1}$, defined in equation (4.5.65).

Here, $\Phi_{i,i+1}^{H} = \left(\check{\phi}_{i,R}^{H} + \check{\phi}_{i+1,L}^{H} - \check{\phi}_{i,R}^{L} - \check{\phi}_{i+1,L}^{L}\right) = \left(\check{\phi}_{i,R}^{H} + \check{\phi}_{i+1,L}^{H}\right)$ is generally non-zero. Thus, if the limitation coefficients are such that $0 < \alpha_{i,i+1} < 1$, the global conservation that was verified for the high-order method (4.5.64) is no longer guaranteed for this FCT update. Indeed, in general, one has

$$\sum_{i=1}^{n_{\text{DoF}}} \check{\phi}_{i,R}^{\text{FCT}} + \check{\phi}_{i+1,L}^{\text{FCT}} = \sum_{i=1}^{n_{\text{DoF}}} \alpha_{i,i+1}\Phi_{i,i+1}^{H} \neq 0. \tag{4.5.75}$$

This comes from the fact that the low-order scheme, if formulated as in (4.5.67), does not distribute the same total residual as the high-order scheme. Hence the necessity to reformulate the low-order scheme so that it verifies:

$$\check{\phi}^H_{i,R} + \check{\phi}^H_{i+1,L} - \check{\phi}^L_{i,R} - \check{\phi}^L_{i+1,L} = 0. \tag{4.5.76}$$

To do this, one can see that the low-order scheme (4.5.67) is equivalent to:

$$u_i^L = u_i^n + \check{\phi}^L_{i,R} + \check{\phi}^L_{i,L}, \quad \text{with} \begin{cases} \check{\phi}^L_{i,R} = -\eta_C u_i^n + \overline{\phi}_i, \\ \check{\phi}^L_{i,L} = \eta_C u_{i-1}^n - \overline{\phi}_i. \end{cases} \tag{4.5.77}$$

This scheme yields the same update as (4.5.67). Nevertheless, when used to limit the high-order scheme, the total residual (4.5.73) of the FCT method becomes:

$$\Phi^{\text{FCT}}_{i,i+1} = \overline{\phi}_i - \overline{\phi}_{i+1} + \alpha_{i,i+1}\left(\check{\phi}^H_{i,R} + \check{\phi}^H_{i+1,L} - \left(\overline{\phi}_i - \overline{\phi}_{i+1}\right)\right) \tag{4.5.78}$$

Additionally, one can show that the total residual of the high-order scheme defined in (4.5.65) boils down, using (4.5.63c), to:

$$\begin{aligned} \Phi^H_{i,i+1} &= \check{\phi}^H_{i,R} + \check{\phi}^H_{i+1,L} \\ &= \eta_C \left(\mathcal{M}_0^{-1}\left(\theta_{\text{TTG}}\lfloor u^n \rfloor + \tilde{\theta}_{\text{TTG}}\lfloor \tilde{u}^n \rfloor\right)\right)_{i+1} - \eta_C \left(\mathcal{M}_0^{-1}\left(\theta_{\text{TTG}}\lfloor u^n \rfloor + \tilde{\theta}_{\text{TTG}}\lfloor \tilde{u}^n \rfloor\right)\right)_{i}. \end{aligned} \tag{4.5.79}$$

Finally, choosing

$$\boxed{\overline{\phi}_i \mathrel{\hat{=}} \eta_C \left(\mathcal{M}_0^{-1}\left(\theta_{\text{TTG}}\lfloor u^n \rfloor + \tilde{\theta}_{\text{TTG}}\lfloor \tilde{u}^n \rfloor\right)\right)_i}, \tag{4.5.80}$$

results in:

$$\Phi^{\text{FCT}}_{i,i+1} = \Phi^H_{i,i+1}, \tag{4.5.81}$$

and the conservation of the FEM-FCT scheme is restored.

4.5.2.4 Results and discussion

The previous developments are now evaluated on two test cases. The first one consists in the transport of the same smooth profile as in paragraph 4.4.2.2, considering the initial profile defined by equation 4.4.29. The second test case consists in the transport of a rectangle function, defined by:

$$u_0^{\text{rect}}(x) = \begin{cases} 1 & \text{if } x \in \left[1/4, 3/4\right], \\ 0 & \text{otherwise.} \end{cases} \tag{4.5.82}$$

The constant advection velocity is taken equal to $c_0 = 1$ m/s. The results after one rotation (final time $t_f = 1$ s) are displayed in figure 4.23. The computations are led with $n_x = 40$ points, and a CFL number $\eta_C = 0.45$.

After one rotation, the differences between the two schemes are slight but noticeable. Regarding the smooth case, depicted in figure 4.23a, the results are very close. The TTGC-FCT solution appears to be more antidiffusive than the LW-FCT scheme, as it tends to sharpen the gradients lightly more than the latter scheme. Also, the TTGC-FCT scheme tends to decrease the global maximum slightly more than the LW-FCT scheme. The discontinuous case, corresponding to figure 4.23b, shows a better resolution of the discontinuity by the TTGC-FCT scheme. The LW-FE scheme is observed to smooth

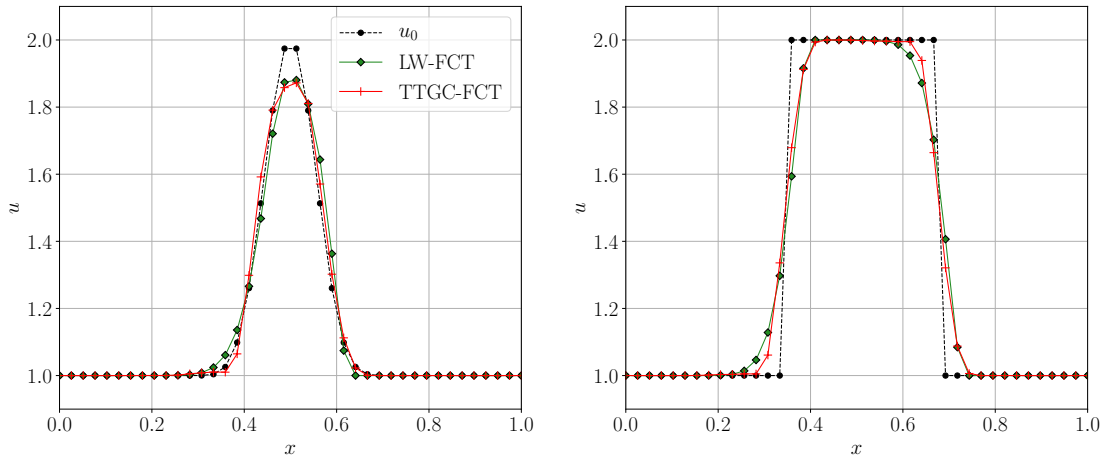

(a) Final solutions for the smooth profile

(b) Final solutions from the rectangular profile

Figure 4.23: Comparative view of the solutions for the LW-FCT and TTGC-FCT, for smooth and sharp initial solutions after one rotation.

the solution before the discontinuities, while the TTGC-FCT preserves better the symmetry of the solution.

In figure 4.24, the solutions for the non-limited TTGC and LW-FE schemes are shown, to give an idea of the differences with their FCT formulations. Naturally, the maximum value of the smooth solution is better conserved, since the limitation procedure introduces numerical diffusion. Yet, the non-limited schemes display strong dispersion errors in the sharp case. Undershoots are also observed in the smooth case, although less noticeable, in particular regarding the TTGC scheme.

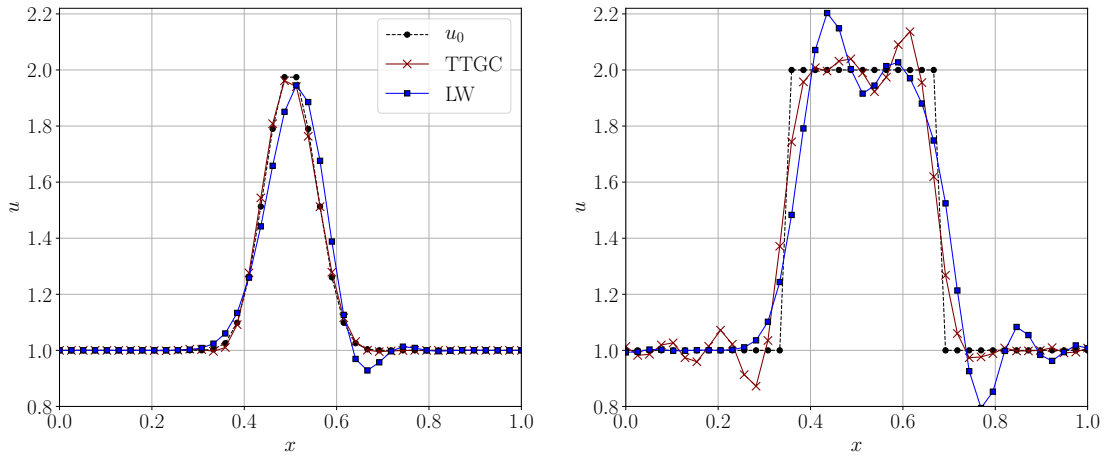

(a) Final solutions for the smooth profile

(b) Final solutions from the rectangular profile

Figure 4.24: Illustration of the solutions for the LW-FE and TTGC, for smooth and sharp initial solutions after one rotation.

In order to emphasize the differences between the two schemes, the solutions of the two cases after 10 rotations (corresponding to a final time $t_f = 10$ s) are given in figure 4.25. For both cases, the TTGC-FCT scheme exhibits more accurate results. The solution has better preserved its symmetry with the TTGC-FCT than with the LW-FCT, although the region upwind of the transported perturbation

presents a small – and relatively flat – increase, that is not observed downwind. Contrarily to the observations of figure 4.23a after 1 rotation, the dissipation of the maximum value is now stronger in the LW-FCT case. All these results are satisfying regarding the proposed TTGC-FCT scheme.

It is now interesting to compare the convergence order of the methods. This is done by processing a mesh refinement experiment for the transport of the smooth solution. The results are shown in figure 4.26.

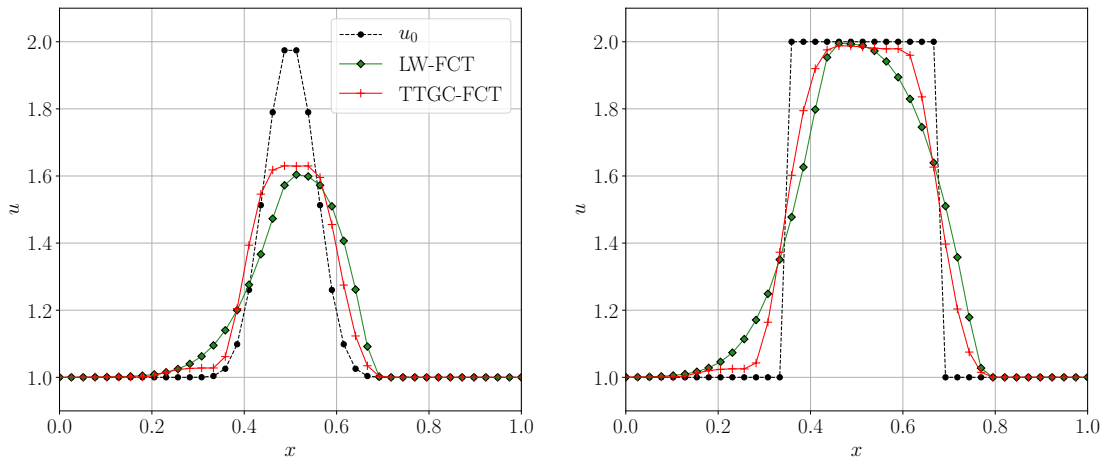

(a) Final solutions for the smooth profile

(b) Final solutions from the rectangular profile

Figure 4.25: Comparative view of the solutions for the LW-FCT and TTGC-FCT, for smooth and sharp initial solutions after 10 rotations.

The error of the TTGC-FCT method for coarse grids is higher than the LW-FCT method. This is mainly due the dissipation of the maximum value that is more pronounced with the TTGC-FCT method than for the LW-FCT method when the resolution is poor. This localized discrepancy strongly affects the L_∞ norm, whereas the L_1 norm is the least impacted. The convergence rate is found to be better for the TTGC-FCT than for the LW-FCT although it is obviously far from the non-limited TTGC scheme.

4.5.2.5 Conclusions

This study allowed to build up a novel numerical method in the FEM-FCT framework, which is based on a third-order two-step Taylor-Galerkin method. The TTGC-FCT method that has been developed shows an very satisfying behaviour for the transport of sharp solutions. Conversely, it tends to plane smooth profiles near local extrema, similarly to the one-step LW-FCT method. The rate of convergence is better than for the LW-FCT, although it is unfortunately closer to second-order than to third-order.

In future works, it would then be interesting to take these developments a step further, by working on a multidimensional implementation of a TTGC-FCT for the Euler equations.

4.6 Conclusion

This chapter presented the numerical methods for hyperbolic conservation laws that have been studied and implemented in the course of this thesis. First, important results regarding hyperbolic conservation laws, and more specifically the Euler equations, have been recalled. In particular, the Riemann problem and different approximate solvers that are extensively used by the community of multifluid methods have been presented. Then, different families of numerical methods have been studied. To begin,

the cell-centered methods, including the finite-volume Godunov-like and MUSCL methods have been presented. Then, the family of Runge-Kutta discontinuous-Galerkin methods have been introduced, which provide a valuable high-order framework to be used in chapter 8. Finally, vertex-centered methods – and more specifically finite-element methods – have been described. In particular, the two-step Taylor-Galerkin schemes to be used in chapter 5 and chapter 6 have been introduced. In addition, an original work was presented, which proposed the development of a FEM-FCT scheme based on a third-order two-step Taylor-Galerkin scheme.

The next chapter is dedicated to the formulation of the multifluid models used in this thesis within the Taylor-Galerkin numerical framework.

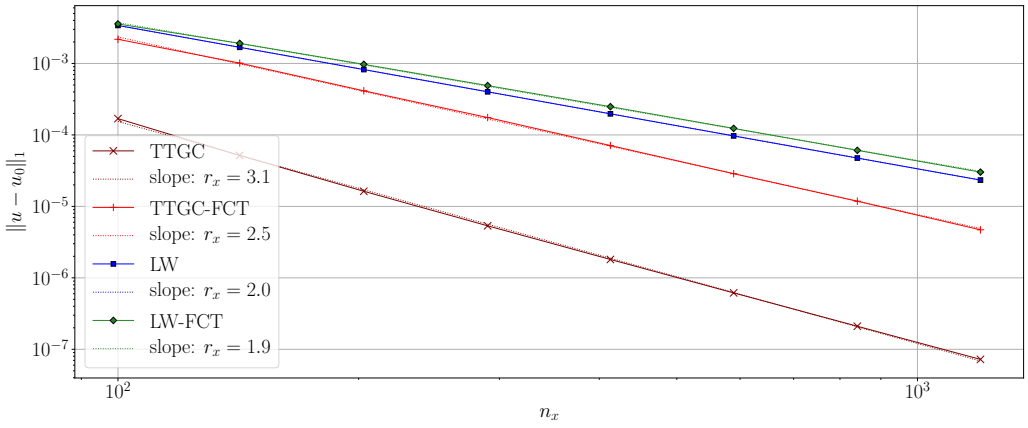

(a) L_1-norm error convergence

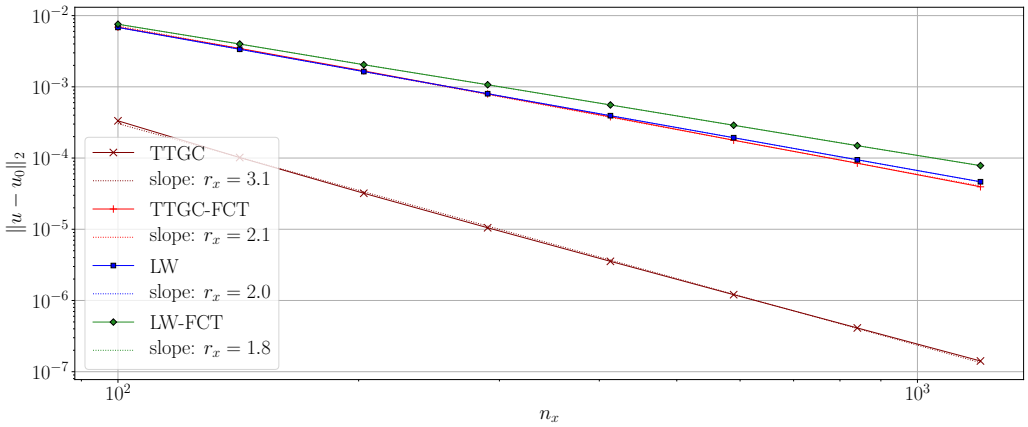

(b) L_2-norm error convergence

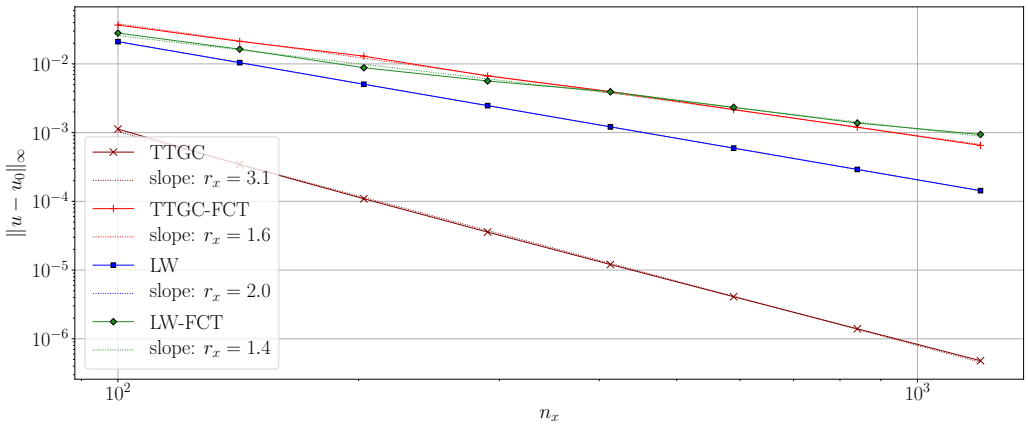

(c) L_∞-norm error convergence

Figure 4.26: Mesh refinement test on the smooth profile for the different numerical methods.

Chapter 5

A unified framework for solving supercritical and subcritical flows

This chapter describes the required developments for the simulation of supercritical flows and subcritical two-phase flows within AVBP, a HPC unstructured solver based on high-order Taylor-Galerkin numerical methods. In particular, the Jacobian matrices of the flux functions are detailed. Characteristic boundary conditions in the different thermodynamic regimes are also provided. Simple test cases are provided to validate the derivation and integration of the model within the numerical framework.

5.1 Introduction

High-pressure flows in supercritical conditions have been and remain widely studied, as they represent a scientific and industrial challenge. In the context of the AVBP solver, used for the multidimensional unstructured computations of this Ph.D work, previous works have been led to implement real-gas thermodynamics [Schmitt, 2009, Ruiz, 2012]. These developments rely on the use of cubic EoS (cf. Chapter **2**). In particular, the integration of such EoS for high-order TTG numerical methods (see section 4.5.1) has been done by [Schmitt, 2009]. Although the accurate simulation of the non-ideal thermodynamic effects and their impact on the flow behaviour are still an active field of research, the present work and, especially, the present chapter, focus on the extension of the real-gas solver to subcritical states.

Such extension is not straightforward, as the cubic EoS become non-convex in the subcritical domain (cf. Chapter **2**). To some limit, this causes the system to lose its hyperbolicity, as the squared speed of sound (5.2.43) becomes negative. This non-convexity is the expression of the thermodynamic instability that causes the fluid to undergo phase separation. Starting from a supercritical flow solver, a natural way to address phase separation is to change the thermodynamic closure from a mere cubic EoS to a two-regime EoS: using a cubic EoS when a stable thermodynamic state is obtained, or switching to a two-phase equilibrium state when an unstable thermodynamic state occurs.

From the point of view of two-phase flow modeling, this strategy actually corresponds to a multifluid *three-equation model*, described in section 3.3.2. This simplified diffuse interface model assumes a homogeneous thermodynamic equilibrium between the phases. It is worth noting that most classically, the multifluid models are closed with stiffened-gas EoS (2.2.57), which are conveniently unconditionally convex, and can be applied even with non stable thermodynamic states. Conversely, the use of a single cubic EoS to model each phase requires to make sure that the fluid remains out of the unstable region in order to prevent the loss of hyperbolicity of the flow model, which is guaranteed by the homogeneous equilibrium assumption.

The integration of this three-equation model within the numerical framework of AVBP (i.e. with TTG

numerical schemes), as described in what follows, requires to compute the Jacobian matrix of the flux function (4.2.6). Its analytical derivation requires to know the variations of the phases properties at equilibrium with respect to temperature and composition variations. Such relations are derived from the Clausius-Clapeyron relation (2.3.23) in the case of a single-component fluid, or from its extended formulation (2.3.3.3) for the simplified multicomponent equilibrium. Otherwise, a numerical estimation can be considered, but inconveniently increases the cost of the procedure as it requires for at least one additional equilibrium computation per grid node.

In order to overcome this difficulty, another strategy has been investigated. It consists in applying a so-called *four-equation model* that assumes pressure, temperature and velocity equilibrium between phases, but relaxes the chemical potential equilibrium condition. This equilibrium is enforced after the transport step by applying an instantaneous relaxation towards the chemical potential equilibrium (cf. section 3.3.2). This operator-splitting strategy allows to formulate a system for which the analytical Jacobian is known for any thermodynamic closure, as it will be shown hereafter.

For each of these closures, the Jacobian matrix of the flux function, together with adapted formulations for the characteristic boundary conditions must be derived.

The present chapter is organized as follows: section 5.2 recalls the main results for the resolution of one-phase flows (typically in the case of supercritical flows) and presents the framework of characteristic boundary conditions. Then, section 5.2.3 presents the necessary derivations for the three-equation model. Section 5.3 presents the corresponding four-equation model and provides comparisons between the two models. Finally, section 5.4 summarizes the resolution strategy.

5.2 Extending the supercritical flow model to subcritical states: the three-equation model

The present section describes the flow model used for the simulation of supercritical flows, with a particular focus on the formulation of characteristic boundary conditions. Generic relations are derived, independent from the thermodynamic closure. Then, the specific results assuming a cubic EoS are given, as the present work mainly focuses on the PR and SRK cubic EoS. After recalling these results obtained in previous works [Schmitt, 2009], the extension to the subcritical multifluid three-equation model is presented. The corresponding Jacobian matrices and differential terms are derived, and validations of the derivation and implementation are finally given.

5.2.1 Euler equations

To describe the advective part of the Navier-Stokes equations used to model the supercritical flows, the Euler equations are studied. The set of Euler equations corresponding to a three-dimension multicomponent flow of N_s species consits in the conservation law (4.2.4), with the conservative variables and associated flux given in equation (4.2.11). These definitions are recalled hereafter in the three-dimensional case:

$$\frac{\partial \mathbf{U}}{\partial t} + \vec{\boldsymbol{\nabla}} \cdot \vec{\mathcal{F}}\left(\mathbf{U}\right) = 0, \quad \text{with} \tag{5.2.1}$$

$$\mathbf{U} = \begin{bmatrix} \rho Y_1 \\ \vdots \\ \rho Y_{N_s} \\ \rho u \\ \rho v \\ \rho w \\ \rho e_\mathrm{t} \end{bmatrix} \quad \text{and} \quad \vec{\mathcal{F}}(\mathbf{U}) = \begin{bmatrix} \rho u Y_1 & \rho v Y_1 & \rho w Y_1 \\ \vdots & \vdots & \vdots \\ \rho u Y_{N_s} & \rho v Y_{N_s} & \rho w Y_{N_s} \\ \rho u^2 + P & \rho v u & \rho w u \\ \rho u v & \rho v^2 + P & \rho w v \\ \rho u w & \rho v w & \rho w^2 + P \\ (\rho e_\mathrm{t} + P) u & (\rho e_\mathrm{t} + P) v & (\rho e_\mathrm{t} + P) w \end{bmatrix}. \tag{5.2.2}$$

The thermodynamic closure used in the context of supercritical flows in order to evaluate the pressure from the transported values of density, sensible energy and mixture composition $P(\rho, e_s, \underline{\boldsymbol{Y}})$ is a cubic EoS, either SRK or PR, described in section 2.2.2.

The characteristic structure of Euler equations is a classic result which has been recalled in section 4.2 of the present manuscript. In particular, the speed of sound is derived and its value can be evaluated using (5.2.43).

5.2.2 Characteristic boundary conditions

5.2.2.1 Formulation of the characteristic boundary conditions

The use of the non-dissipative numerical methods targeted in the present work requires a careful treatment for the boundary terms. As mentioned in [Poinsot and Lele, 1992], the numerical forcing of the boundary conditions may result, for Euler equations, in polluting the wave content of the physical solution by spurious waves of physically plausible wavelength. Such waves cannot be distinguished from the physically relevant waves once they propagate within the fluid domain, hence the need to prevent their generation, or at least minimize their amplitude.

This can be achieved in the context of the Navier-Stokes equations – and, *a fortiori*, for the Euler equations – by means of the *characteristic boundary conditions* [Poinsot and Lele, 1992], for which the characteristic waves of the system are approximated assuming the boundary problem to be *locally one-dimensional inviscid* (LODI). The corresponding procedure is depicted in Figure 5.1, and the notations are introduced.

The change of basis to obtain the residual in characteristic variables from conservative variables can be written as

$$\mathrm{d}\mathbf{W} = \mathcal{T}_{\mathbf{UW}} \mathrm{d}\mathbf{U} = \mathcal{T}_{\boldsymbol{V}\mathbf{W}} \mathcal{T}_{\mathbf{U}\boldsymbol{V}} \mathrm{d}\mathbf{U} \tag{5.2.3}$$

Assuming that the boundary normal is carried by the x direction of the cartesian frame – otherwise, it would be necessary to first rotate the frame to express the momentum conservative variables in the boundary frame – the transformation matrix reads:

$$\mathcal{T}_{\mathbf{UW}} = \begin{bmatrix} 1 - \frac{\zeta(e_c - \xi_1) Y_1}{c^2} & \cdots & -\frac{\zeta(e_c - \xi_{N_s}) Y_1}{c^2} & \frac{\zeta u Y_1}{c^2} & \frac{\zeta v Y_1}{c^2} & \frac{\zeta w Y_1}{c^2} & \frac{-\zeta Y_1}{c^2} \\ \vdots & \ddots & \vdots & \vdots & \vdots & \vdots & \vdots \\ -\frac{\zeta(e_c - \xi_1) Y_{N_s}}{c^2} & \cdots & 1 - \frac{\zeta(e_c - \xi_{N_s}) Y_{N_s}}{c^2} & \frac{\zeta u Y_{N_s}}{c^2} & \frac{\zeta v Y_{N_s}}{c^2} & \frac{\zeta w Y_{N_s}}{c^2} & \frac{-\zeta Y_{N_s}}{c^2} \\ 0 & \cdots & 0 & 0 & 1/\rho & 0 & 0 \\ 0 & \cdots & 0 & 0 & 0 & 1/\rho & 0 \\ \frac{1}{\rho}\left(\zeta \frac{e_c - \xi_1}{c} + u\right) & \cdots & \frac{1}{\rho}\left(\zeta \frac{e_c - \xi_{N_s}}{c} + u\right) & -\frac{\zeta u - c}{\rho c} & -\frac{\zeta v}{\rho c} & -\frac{\zeta w}{\rho c} & \frac{\zeta}{\rho c} \\ \frac{1}{\rho}\left(\zeta \frac{e_c - \xi_1}{c} - u\right) & \cdots & \frac{1}{\rho}\left(\zeta \frac{e_c - \xi_{N_s}}{c} - u\right) & -\frac{\zeta u + c}{\rho c} & -\frac{\zeta v}{\rho c} & -\frac{\zeta w}{\rho c} & \frac{\zeta}{\rho c} \end{bmatrix}, \tag{5.2.4}$$

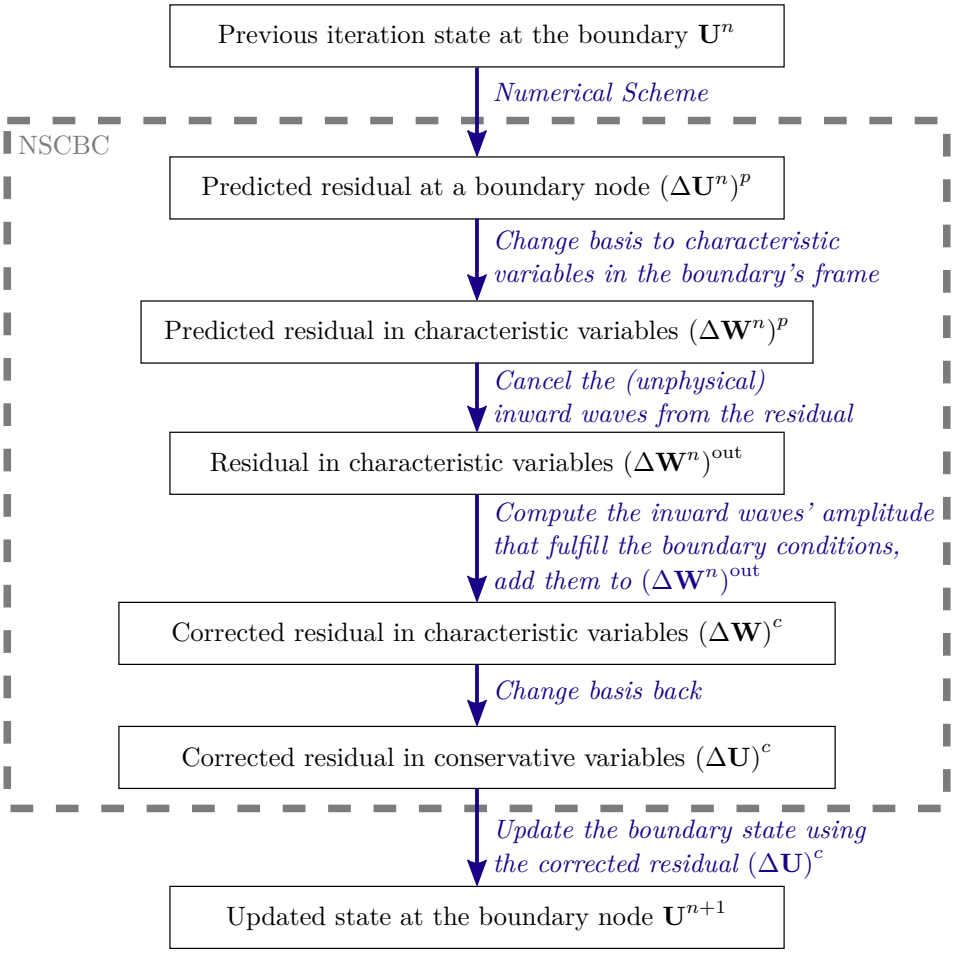

Figure 5.1: Schematic representation of the NSCBC procedure for the boundary treatment.

the inverse transformation matrix being

$$\mathcal{T}_{\mathbf{WU}} = \begin{bmatrix} 1 & \cdots & 0 & 0 & 0 & \frac{\rho Y_1}{2c} & \frac{\rho Y_1}{2c} \\ \vdots & \ddots & \vdots & \vdots & \vdots & \vdots & \vdots \\ 0 & \cdots & 1 & 0 & 0 & \frac{\rho Y_{N_s}}{2c} & \frac{\rho Y_{N_s}}{2c} \\ u & \cdots & u & 0 & 0 & \frac{\rho}{2c}(u-c) & \frac{\rho}{2c}(u+c) \\ v & \cdots & v & \rho & 0 & \frac{\rho}{2c}v & \frac{\rho}{2c}v \\ w & \cdots & w & 0 & \rho & \frac{\rho}{2c}w & \frac{\rho}{2c}w \\ e_c+\xi_1 & \cdots & e_c+\xi_{N_s} & 0 & 0 & \frac{\rho}{2c}\left(e_c - cu + \frac{c^2}{\zeta} + \overline{\xi}\right) & \frac{\rho}{2c}\left(e_c + cu + \frac{c^2}{\zeta} + \overline{\xi}\right) \end{bmatrix}. \quad (5.2.5)$$

5.2.2.2 Information specification

At a boundary node, the characteristic representation of the residual allows to evaluate which part of the updated information comes from inside the fluid domain. Such information is carried by the hyperbolic numerical scheme and corresponds to physical information that reaches the boundary node. The number of inward and outward waves depends on the nature of the boundary (inlet/outlet) and the flow Mach number (subsonic/supersonic), as depicted in Figure 5.2. This determines the number of information to be prescribed by the boundary treatment:

– At a subsonic inlet (Figure 5.2a), there are $(N_s + 3)$ quantities to be imposed. The species waves and the two orthogonal velocity waves carry $(N_s + 2)$ information (linearly degenerate waves), and the forward acoustic wave $u + c$ carries one additional information. Only the backward acoustic wave $(u - c)$ goes outward and must remain unmodified by the boundary treatment.
– At a supersonic inlet (Figure 5.2c), all $(N_s + 4)$ quantities must be prescribed. Indeed, all waves go inward as no information goes back up the flow.
– At a subsonic outlet (Figure 5.2b), there is only 1 quantity to be imposed, as only the backward acoustic wave goes inward. The N_s species waves and the forward acoustic wave carry information from within the domain and must exit the domain without being modified by the boundary treatment.
– At a supersonic outlet (Figure 5.2d), no quantity is prescribed and no specific boundary treatment is done, as all the information goes outward.

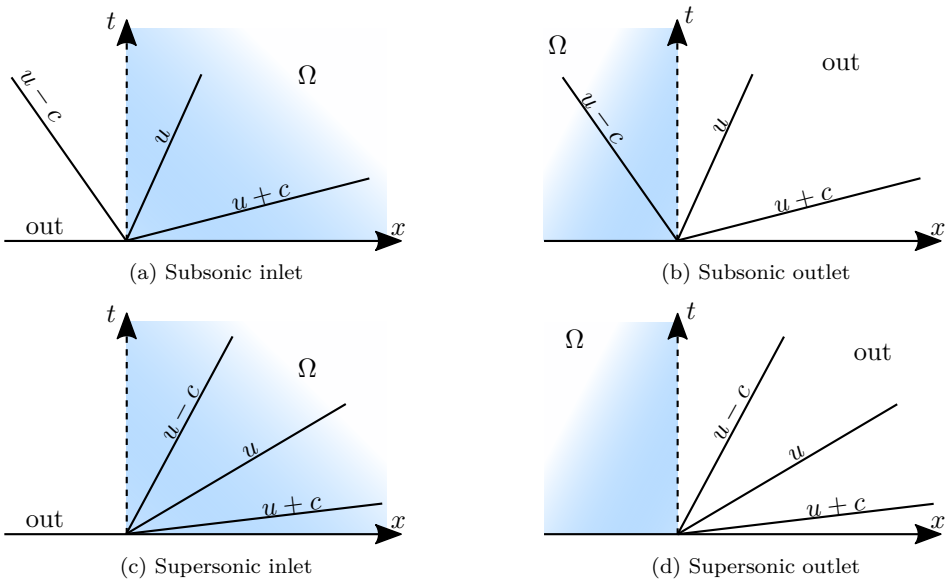

Figure 5.2: Characteristic representation of the different configurations for the LODI flow. The boundary is materialized by the dashed vertical lines. Ω represents the inner fluid domain, filled with blue. Graphically, the waves that enter the blue domain correspond to information that must be prescribed by the boundary conditions. Waves that enter the outer white-filled domain correspond to the information coming from inside the domain which must be unmodified.

5.2.2.3 Fully reflecting boundary conditions

For instance, for a subsonic flow, one can prescribe the quantities $(\rho^{\text{in}}, \underline{\boldsymbol{Y}}^{\text{in}}, u^{\text{in}}, v^{\text{in}}, w^{\text{in}})$ at the inlet, and (P^{out}) at the outlet.

Once the incoming waves residual erroneously predicted by the numerical scheme are cancelled, the corrections can be computed using the transformation matrix (4.2.36). Indeed, variations of the char-

acteristic variables are related to variations of the primitive variables as

$$\begin{cases} \mathrm{d}W_i = -\dfrac{Y_i}{c^2}\,\mathrm{d}P + Y_i\,\mathrm{d}\rho + \rho\,\mathrm{d}Y_i \qquad \text{for } i \in \{1...N_s\} & \text{(5.2.6a)} \\ \mathrm{d}W_{N_s+1} = \mathrm{d}v & \text{(5.2.6b)} \\ \mathrm{d}W_{N_s+2} = \mathrm{d}w & \text{(5.2.6c)} \\ \mathrm{d}W_{u-c} = -\,\mathrm{d}u + \dfrac{1}{\rho c}\,\mathrm{d}P & \text{(5.2.6d)} \\ \mathrm{d}W_{u+c} = \mathrm{d}u + \dfrac{1}{\rho c}\,\mathrm{d}P. & \text{(5.2.6e)} \end{cases}$$

At the inlet, since u is imposed, its variations must be zero, which means that the characteristic variables variations must be such that

$$\mathrm{d}W_{u+c} - \mathrm{d}W_{u-c} = 0 \tag{5.2.7}$$

For the variations of v and w to be zero, one must have

$$\mathrm{d}W_{N_s+1} = 0 \tag{5.2.8}$$
$$\mathrm{d}W_{N_s+2} = 0 \tag{5.2.9}$$

And the species and density being constant, it comes that

$$\mathrm{d}W_i - \frac{Y_i}{\rho c}\,\mathrm{d}W_{u-c} = 0 \qquad \text{for } i \in \{1...N_s\} \tag{5.2.10}$$

In practice, in order to avoid drifts of the imposed quantities, a restoring term, corresponding to the distance to the target value, is added. The corrected characteristic waves at the inlet are then

$$\begin{cases} (\Delta W_i)^c = \dfrac{Y_i}{\rho c}\,(\Delta W_{u-c})^p + Y_i\left(\rho^{\text{in}} - \rho^p\right) + \rho\left(Y_i^{\text{in}} - Y_i^p\right) \qquad \text{for } i \in \{1...N_s\} & \text{(5.2.11a)} \\ (\Delta W_{N_s+1})^c = v^{\text{in}} - v^p & \text{(5.2.11b)} \\ (\Delta W_{N_s+2})^c = w^{\text{in}} - w^p & \text{(5.2.11c)} \\ (\Delta W_{u+c})^c = (\Delta W_{u-c})^p + 2\left(u^{\text{in}} - u^p\right). & \text{(5.2.11d)} \end{cases}$$

Similarly, the corrected characteristic quantity at the outlet corresponds to the backward acoustic wave of celerity $u - c$ and its correction reads:

$$(\Delta W_{u-c})^c = -\,(\Delta W_{u+c})^p + \frac{2}{\rho c}\left(P^{\text{out}} - P^p\right) \tag{5.2.12}$$

Such boundary conditions are referred to as *Fully reflecting Boundary Conditions* as it is clear from equations (5.2.12) and (5.2.11d) that any acoustic wave within the domain that impacts a boundary will cause the boundary treatment to inject an inward wave of equal amplitude.

5.2.2.4 Partially reflecting boundary conditions

The use of fully reflecting boundary conditions as formulated in the previous paragraph leads any noise generated inside the domain to be kept, so that there are risks for the simulation to crash for example when long simulation times are involved, since physical noise and the noise due to numerical errors keeps accumulating.

In this respect, it is relevant to introduce partially reflecting boundary conditions. The strategy for their application is similar to the fully reflecting boundary conditions, except that the corrected characteristic wave now consist only in the restoring terms. Thus, the previously described inlet prescribing $(\rho^{\text{in}}, \underline{\boldsymbol{Y}}^{\text{in}}, u^{\text{in}}, v^{\text{in}}, w^{\text{in}})$ has the following corrected values

$$\begin{cases} (\Delta W_i)^c = \dfrac{1}{\tau_{\text{in}}} \left(Y_i \left(\rho^{\text{in}} - \rho^p \right) + \rho \left(Y_i^{\text{in}} - Y_i^p \right) \right) & \text{for } i \in \{1...N_s\} \quad (5.2.13a) \\ (\Delta W_{N_s+1})^c = \dfrac{1}{\tau_{\text{in}}} \left(v^{\text{in}} - v^p \right) & (5.2.13b) \\ (\Delta W_{N_s+2})^c = \dfrac{1}{\tau_{\text{in}}} \left(w^{\text{in}} - w^p \right) & (5.2.13c) \\ (\Delta W_{u+c})^c = \dfrac{2}{\tau_{\text{in}}} \left(u^{\text{in}} - u^p \right), & (5.2.13d) \end{cases}$$

and the outlet prescribing $\left(P^{\text{out}}\right)$ has

$$(\Delta W_{u-c})^c = \frac{1}{\tau_{\text{out}}} \frac{2}{\rho c} \left(P^{\text{out}} - P^p \right) \tag{5.2.14}$$

where τ_{in} and τ_{out} are characteristic relaxation times. These parameters allow to control the cutoff frequencies characterizing the low-pass filters to which this boundary treatment corresponds.

Note that it is possible in practice to formulate fully non-reflecting boundary conditions, by setting the coefficients $\frac{1}{\tau_{\text{in}}}$ or $\frac{1}{\tau_{\text{out}}}$ to zero. Yet, although this formulation is interesting to validate the derivation and implementation of the boundary treatment, it leads to an ill-posed boundary value problem since no information is ever injected into the flow.

5.2.2.5 One-dimensional validations

In order to validate the formulation and practical implementation of the Jacobian matrices and boundary treatments, the following two test configurations are considered. Both are applied on a uniform mesh of $n_x = 100$ nodes, on a domain $\Omega = [0, L]$ of length $L = 1$ m.

5.2.2.5.1 Fully reflecting boundary conditions

In order to test the behaviour of the characteristic boundary conditions, the first test case considers a gaussian perturbations on the characteristic variables associated to the forward and backward acoustic eigenvalues $\Delta\mathbf{W}^+(x) = \Delta\mathbf{W}^-(x) = \exp\left(-200\left(x - L/2\right)^2\right)$. This perturbation is superimposed over a homogeneous supercritical solution $\mathbf{U}_0$. $\mathbf{U}_0$ is the set of conservative variables corresponding to density $\rho_0 = 100$ kg/m^3, pressure $P_0 = 20$ MPa, velocity $u_0 = 0$ m/s and species mass fractions $Y_{O_2} = 1 - Y_{N_2} = 0.8$. Note that the corresponding temperature is $T_0 = 600$ K. The equation of state used for all the test cases of the present chapter is SRK (2.2.16a). The initial solution is then

$$\mathbf{U}(x, t = 0) = \mathbf{U}_0 + \mathcal{T}_{\mathbf{WU}_0} \cdot \begin{bmatrix} 0 \\ \vdots \\ 0 \\ \Delta\mathbf{W}_{u-c}(x) \\ \Delta\mathbf{W}_{u+c}(x) \end{bmatrix}, \tag{5.2.15}$$

with $\mathcal{T}_{\mathbf{WU}_0}$ defined by (5.2.5). The results are displayed in Figure 5.3.

This test case shows that both acoustic waves are reflected as expected, the amplitude of the waves being conserved. As observed, imposing pressure on the outlet results in reflecting into the domain an acoustic wave of opposite sign. On the contrary, imposing velocity at the inlet results in reflecting into the domain an acoustic wave of same sign.

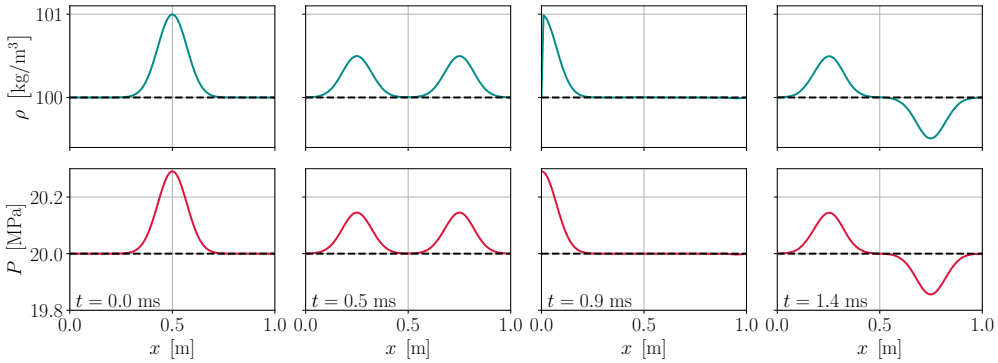

Figure 5.3: Test case 1 – Initially superimposed backward and forward acoustic waves with fully reflecting boundary conditions for a supercritical fluid state. Density and pressure snapshots of the solution. From left to right: initial profile, solution before, during and after interaction with domain boundaries.

5.2.2.5.2 Non-reflecting boundary conditions

For this test case, the considered initial condition is identical to the previous one (5.2.15), with forward and backward acoustic waves. The results are presented in Figure 5.4.

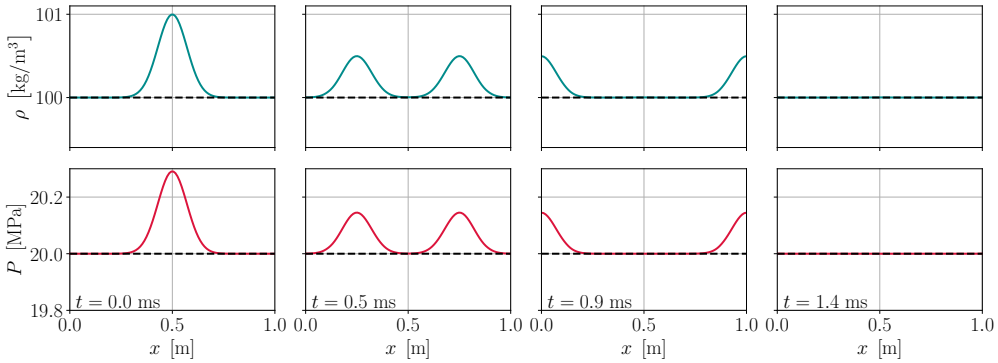

Figure 5.4: Test case 2 – Initially superimposed backward and forward acoustic waves with non-reflecting boundary conditions for a supercritical fluid state. Density and pressure snapshots of the solution. From left to right: initial profile, solution before, during and after interaction with domain boundaries.

This concludes this somehow technical section, which allowed to introduce the concepts and tools that will be useful for the following developments.

5.2.3 Extension to subcritical transport: the 3-equation model

5.2.3.1 Introduction

The basic idea to be explored in the present work for solving subcritical flows is to extend the of the PR or SRK cubic EoS to subcritical states. As these EoS are known lose their convexity as they yield thermodynamically unstable or metastable states (see section 2.3), the proposed strategy is to restore their convexity by considering phase change when such states are reached. Phase changes are then addressed by considering the fluid mixture to be in thermodynamic equilibrium.

This strategy can actually be related to the family of multifluid methods, in which such treatment had been used for liquid-gas simulations in which liquid and gas phases are usually described by two distinct convex EoS, as reviewed in section 3.3.2. The obtained model can then be related to the

so-called 3-equation method studied in 7.4.

This section describes the derivation of the 3-equation model's properties that are requested for its resolution with the high-order numerical methods considered in the context of this work, and the corresponding characteristic boundary conditions. This formulation is mostly dedicated to the simplified equilibrium formulation of section 2.3.3, since its analytical expression requires to know the differential of the pressure or the temperature at equilibrium (corresponding to Clausius-Clapeyron-like relations, e.g. (2.3.23) and (2.3.60)), which are not available for the exact equilibrium. In this respect, the developments will be provided assuming that the simplified equilibrium closure is used (in particular for the derivation of the speed of sound).

5.2.3.2 Model formulation

Formally, the 3-equation model has the same formulation as the Euler equations studied in the previous section.

$$\frac{\partial \mathbf{U}}{\partial t} + \vec{\nabla}\cdot\vec{\mathcal{F}}\left(\mathbf{U}\right) = 0, \tag{5.2.16}$$

$$\mathbf{U} = \begin{bmatrix} \rho Y_1 \\ \vdots \\ \rho Y_{N_s} \\ \rho u \\ \rho v \\ \rho w \\ \rho e_{\mathrm{t}} \end{bmatrix} \quad \text{and} \quad \vec{\mathcal{F}}\left(\mathbf{U}\right) = \begin{bmatrix} \rho Y_1 u & \rho Y_1 v & \rho Y_1 w \\ \vdots & \vdots & \vdots \\ \rho Y_{N_s} u & \rho Y_{N_s} v & \rho Y_{N_s} w \\ \rho u^2 + P & \rho v u & \rho w u \\ \rho u v & \rho v^2 + P & \rho w v \\ \rho u w & \rho v w & \rho w^2 + P \\ (\rho e_{\mathrm{t}} + P)u & (\rho e_{\mathrm{t}} + P)v & (\rho e_{\mathrm{t}} + P)w \end{bmatrix}. \tag{5.2.17}$$

If one single component is present in the mixture, the thermodynamic state is then computed using the strategy described in section 2.3.2. If multiple components are present, the approximate equilibrium hypothesis is used and is computed as explained in section 2.3.3.4.

Two regimes may then be encountered: if the single-phase solution is stable (pure liquid or pure gas), then the thermodynamic closure is simply the cubic EoS and the developments of the previous section are applicable. Otherwise, if the single-phase solution is unstable, the thermodynamic state eventually obtained is a two-phase mixture, so that the transported density and volume-specific sensible energy correspond to a mixture density and a mixture energy, which write

$$\begin{cases} \rho = z_\ell \rho_\ell + (1 - z_\ell)\rho_v & \text{(5.2.18a)} \\ \rho e_s = z_\ell \rho_\ell e_\ell + (1 - z_\ell)\rho_v e_v. & \text{(5.2.18b)} \end{cases}$$

From this point, the present section focuses on the two-phase case.

5.2.3.3 Characteristic structure of the system

5.2.3.3.1 Pseudo-linearized form in conservative variables

As the formulation of the 3-equation model (5.2.16) is similar to the Euler equations previously studied in section 4.2.2, its pseudo-linearized expression in conservative variables involves Jacobian matrices of the same form, provided by equation (4.2.19).

As stated in the previous section, the thermodynamic closure appears through the coefficients two differential coefficients:

$$\begin{cases} \zeta = \left.\dfrac{\partial P}{\partial \rho e_s}\right|_{\rho, Y_j} & \text{(5.2.19a)} \\ \xi_i = \left.\dfrac{\partial \rho e_s}{\partial \rho Y_i}\right|_{P, \rho Y_{j\neq i}}, & \text{(5.2.19b)} \end{cases}$$

Their expression is the same as for the supercritical/one-phase case, though their derivation must take into account the fact that ρe_s and ρ now consist in mixture quantities. Let one first write the differential of the mixture sensible energy (5.2.18b),

$$\mathrm{d}(\rho e_s) = z_\ell \,\mathrm{d}(\rho_\ell e_\ell) + (1 - z_\ell)\,\mathrm{d}(\rho_v e_v) + (\rho_\ell e_\ell - \rho_v e_v)\,\mathrm{d}z_\ell \tag{5.2.20}$$

It is then worth mentioning that the phase-wise quantities at equilibrium $\rho_\ell, \rho_v, e_\ell, e_v$ are function of the pressure and mixture composition only. For phase $\phi \in \{\ell, v\}$, volume-specific energy differential reads:

$$\mathrm{d}\big(\rho_\phi e_\phi\big) = \left.\frac{\partial \rho_\phi e_\phi}{\partial P}\right|_{\mathrm{sat}, Y_j} \mathrm{d}P + \sum_{k=1}^{N_s} \left.\frac{\partial \rho_\phi e_\phi}{\partial Y_k}\right|_{\mathrm{sat}, P, Y_{j\neq k}} \mathrm{d}Y_k \tag{5.2.21}$$

This expression can then be developed as:

$$\begin{aligned} \mathrm{d}\big(\rho_\phi e_\phi\big) = &\left[\rho_\phi \left(c_{p,\phi} - \alpha_\phi h_\phi\right) \left.\frac{\partial T^{\mathrm{sat}}}{\partial P}\right|_{\underline{\boldsymbol{Y}}} + \rho_\phi \beta_\phi h_\phi - \alpha_\phi T\right] \mathrm{d}P \\ &+ \frac{\rho_\phi}{\rho} \sum_{k=1}^{N_s} \left[\left(c_{p,\phi} - \alpha_\phi h_\phi\right) \left.\frac{\partial T^{\mathrm{sat}}}{\partial Y_k}\right|_{Y_{j\neq k}} + e_{\phi,k} - \rho_\phi v_{\phi,k} e_\phi\right] \mathrm{d}(\rho Y_k) \end{aligned} \tag{5.2.22}$$

where $c_{p,\phi}$ is the specific heat capacity of phase ϕ, α_ϕ the thermal expansion coefficient, β_ϕ the isothermal compressibility coefficient, $h_\phi = e_\phi + \frac{P}{\rho_\phi}$ the sensible enthalpy and $v_{\phi,k}$ the partial specific volume of species k in phase ϕ.

Besides, the last term in equation (5.2.20) requires differentiating the liquid volume fraction. This is done using (5.2.18a):

$$\mathrm{d}z_\ell = \mathrm{d}\left(\frac{\rho - \rho_v}{\rho_\ell - \rho_v}\right) = \frac{1}{\rho_\ell - \rho_v}\left[\mathrm{d}\rho - z_\ell\,\mathrm{d}\rho_\ell - (1 - z_\ell)\,\mathrm{d}\rho_v\right]$$

which can be developed into:

$$\mathrm{d}z_\ell = \tfrac{1}{\rho_\ell - \rho_v}\left[(\rho\alpha)_{\mathrm{mix}} \left.\tfrac{\partial T^{\mathrm{sat}}}{\partial P}\right|_{\underline{\boldsymbol{Y}}} - (\rho\beta)_{\mathrm{mix}}\right] \mathrm{d}P + \tfrac{1}{\rho(\rho_\ell - \rho_v)} \sum_{k=1}^{N_s} \left[(\rho\alpha)_{\mathrm{mix}} \left.\tfrac{\partial \rho_\phi e_\phi}{\partial Y_k}\right|_{\mathrm{sat}, P, Y_{j\neq k}} + \left(\rho^2 v_k\right)_{\mathrm{mix}}\right] \mathrm{d}(\rho Y_k) \tag{5.2.23}$$

where the subscript $_{\mathrm{mix}}$ for any quantity ψ denotes the volume-weighted mixture value defined as

$$\psi_{\mathrm{mix}} = z_\ell \psi_\ell + (1 - z_\ell)\psi_v. \tag{5.2.24}$$

Using, at equilibrium, the equality $g_\ell = g_v$, one can write:

$$\frac{\rho_\ell e_\ell - \rho_v e_v}{\rho_\ell - \rho_v} = h_\ell - \frac{1}{\rho_\ell} T \left.\frac{\partial T^{\mathrm{sat}}}{\partial P}\right|_{\underline{\boldsymbol{Y}}}^{-1} = h_v - \frac{1}{\rho_v} T \left.\frac{\partial T^{\mathrm{sat}}}{\partial P}\right|_{\underline{\boldsymbol{Y}}}^{-1}$$

hence

$$\frac{\rho_\ell e_\ell - \rho_v e_v}{\rho_\ell - \rho_v} = z_\ell h_\ell + (1-z_\ell)h_v - z_\ell \frac{1}{\rho_\ell} T \left.\frac{\partial T^{\text{sat}}}{\partial P}\right|_{\underline{\boldsymbol{Y}}}^{-1} - (1-z_\ell)\frac{1}{\rho_v} T \left.\frac{\partial T^{\text{sat}}}{\partial P}\right|_{\underline{\boldsymbol{Y}}}^{-1} \tag{5.2.25}$$

Finally, combining (5.2.25), (5.2.23) and (5.2.22), the mixture volume-specific energy differential reads:

$$\begin{aligned} \mathrm{d}(\rho e_s) = &\left(\left.\frac{\partial T^{\text{sat}}}{\partial P}\right|_{\underline{\boldsymbol{Y}}} \quad C_{p,\text{mix}} - 2T\alpha_{\text{mix}} + T \left.\frac{\partial T^{\text{sat}}}{\partial P}\right|_{\underline{\boldsymbol{Y}}}^{-1} \beta_{\text{mix}} \right) \mathrm{d}P \\ &+ \frac{1}{\rho}\sum_{k=1}^{N_s} \Bigg[\quad \left(C_{p,\text{mix}} - T \left.\frac{\partial T^{\text{sat}}}{\partial P}\right|_{\underline{\boldsymbol{Y}}}^{-1} \alpha_{\text{mix}} \right) \left.\frac{\partial T^{\text{sat}}}{\partial Y_k}\right|_{Y_{j\neq k}} \\ &\qquad + \left(P - T \left.\frac{\partial T^{\text{sat}}}{\partial P}\right|_{\underline{\boldsymbol{Y}}}^{-1} \right) (\rho v_k)_{\text{mix}} + (\rho e_k)_{\text{mix}} \Bigg] \mathrm{d}(\rho Y_k) \end{aligned} \tag{5.2.26}$$

These developments finally lead to:

$$\xi_i = \frac{1}{\rho}\left[\left(C_{p,\text{mix}} - T \left.\frac{\partial T^{\text{sat}}}{\partial P}\right|_{\underline{\boldsymbol{Y}}}^{-1} \alpha_{\text{mix}} \right) \left.\frac{\partial T^{\text{sat}}}{\partial Y_i}\right|_{Y_{j\neq i}} + (\rho h_i)_{\text{mix}} - T \left.\frac{\partial T^{\text{sat}}}{\partial P}\right|_{\underline{\boldsymbol{Y}}}^{-1} (\rho v_i)_{\text{mix}} \right] \tag{5.2.27}$$

and

$$\zeta = \frac{1}{\left.\frac{\partial T^{\text{sat}}}{\partial P}\right|_{\underline{\boldsymbol{Y}}} C_{p,\text{mix}} - 2T\alpha_{\text{mix}} + T \left.\frac{\partial T^{\text{sat}}}{\partial P}\right|_{\underline{\boldsymbol{Y}}}^{-1} \beta_{\text{mix}}} \tag{5.2.28}$$

where $C_p^{\text{mix}} = z_\ell \rho_\ell c_{p,\ell} + (1-z_\ell)\rho_v c_{p,v}$ is the mixture volume-specific isobaric heat capacity, $\alpha^{\text{mix}} = z_\ell \alpha_\ell + (1-z_\ell)\alpha_v$ is a mixture thermal expansion coefficient and $\beta^{\text{mix}} = z_\ell \beta_\ell + (1-z_\ell)\beta_v$ a mixture isothermal compressibility coefficient. In these expressions, for each phase $\phi \in \{\ell, v\}$ appear the thermal expansion and isothermal compressibility coefficients and the specific isobaric heat capacity $c_{p,\phi} = \left.\frac{\partial h_\phi}{\partial T}\right|_P$.

5.2.3.3.2 Speed of sound

The generic form of the speed of sound for the hyperbolic PDE given by equation (4.2.32) is recalled:

$$c_H^2 = c^2 + \left.\frac{\partial P}{\partial e_s}\right|_{\rho,\underline{\boldsymbol{Y}}} \left(\frac{P}{\rho^2} - \left.\frac{\partial e_s}{\partial \rho}\right|_{s,\underline{\boldsymbol{Y}}} \right). \tag{5.2.29}$$

First, it is necessary that the two-phase mixture in simplified equilibrium, considered as a whole, also verifies the mass-specific Gibbs relation valid within each phase, so that $\frac{P}{\rho^2} - \left.\frac{\partial e_s}{\partial \rho}\right|_{s,\underline{\boldsymbol{Y}}} = 0$. Consider the extensive form of the Gibbs-Duhem equation (2.1.11), which is verified within each phase. For $\phi \in \{\ell, v\}$, it reads

$$-\mathcal{S}_\phi \,\mathrm{d}T + \mathcal{V}_\phi \,\mathrm{d}P - \sum_{i=1}^{N_s} m_i^\phi \,\mathrm{d}g_i^\phi = 0. \tag{5.2.30}$$

As the approximate equilibrium hypothesis states that $m_i^\ell = m_\ell Y_i$ and $m_i^v = m_v Y_i$, summing equation (5.2.30) over the two phases writes

$$-\mathcal{S}\,\mathrm{d}T + \mathcal{V}\,\mathrm{d}P - m_\ell \sum_{i=1}^{N_s} Y_i\,\mathrm{d}g_i^\ell - m_v \sum_{i=1}^{N_s} Y_i\,\mathrm{d}g_i^v = 0. \tag{5.2.31}$$

The differentiation of the simplified phase equilibrium condition $g_\ell = g_v$ can be expressed as

$$\sum_{i=1}^{N_s} Y_i\,\mathrm{d}g_{\ell,i} + \sum_{i=1}^{N_s} g_{\ell,i}\,\mathrm{d}Y_i = \sum_{i=1}^{N_s} Y_i\,\mathrm{d}g_{v,i} + \sum_{i=1}^{N_s} g_{v,i}\,\mathrm{d}Y_i. \tag{5.2.32}$$

Injecting (5.2.32) into (5.2.31), one gets

$$\begin{aligned}-\mathcal{S}\,\mathrm{d}T + \mathcal{V}\,\mathrm{d}P - m_\ell \sum_{i=1}^{N_s} Y_i\,\mathrm{d}g_i^\ell - m_v \sum_{i=1}^{N_s} Y_i\,\mathrm{d}g_i^v \\ + m_\ell \sum_{i=1}^{N_s} \left(g_{\ell,i} - g_{v,i}\right)\mathrm{d}Y_i + m_v \sum_{i=1}^{N_s} \left(g_{v,i} - g_{\ell,i}\right)\mathrm{d}Y_i = 0,\end{aligned}$$

so that

$$\begin{aligned}-\mathcal{S}\,\mathrm{d}T + \mathcal{V}\,\mathrm{d}P - m_\ell \sum_{i=1}^{N_s} \left[Y_i\,\mathrm{d}g_i^\ell + g_i^\ell\,\mathrm{d}Y_i\right] - m_v \sum_{i=1}^{N_s} \left[Y_i\,\mathrm{d}g_i^v + g_i^v\,\mathrm{d}Y_i\right] \\ + m_\ell \sum_{i=1}^{N_s} g_i^\ell\,\mathrm{d}Y_i + m_v \sum_{i=1}^{N_s} g_i^v\,\mathrm{d}Y_i = 0,\end{aligned}$$

and

$$-\mathcal{S}\,\mathrm{d}T + \mathcal{V}\,\mathrm{d}P - m_\ell\,\mathrm{d}g_\ell - m_v\,\mathrm{d}g_v + m_\ell \sum_{i=1}^{N_s} g_i^\ell\,\mathrm{d}Y_i + m_v \sum_{i=1}^{N_s} g_i^v\,\mathrm{d}Y_i = 0.$$

Noting that $g_\ell = g_v = g$ and defining $\tilde{g}_i = y_\ell g_i^\ell + (1 - y_\ell) g_i^v$, it comes that

$$-\mathcal{S}\,\mathrm{d}T + \mathcal{V}\,\mathrm{d}P - m\,\mathrm{d}g + m \sum_{i=1}^{N_s} \tilde{g}_i\,\mathrm{d}Y_i = 0.$$

dividing by the mixture's mass, one has

$$-s\,\mathrm{d}T + v\,\mathrm{d}P - \mathrm{d}g + \sum_{i=1}^{N_s} \tilde{g}_i\,\mathrm{d}Y_i = 0 \tag{5.2.33}$$

Also, writing Euler theorem for each phase $\phi \in \{\ell, v\}$ gives

$$\mathcal{E}_\phi = T\mathcal{S}_\phi - P\mathcal{V}_\phi + \sum_{i=1}^{N_s} m_i^\phi g_i^\phi, \tag{5.2.34}$$

the sum of which writes

$$\mathcal{E}_s = T\mathcal{S} - P\mathcal{V} + \sum_{i=1}^{N_s} m_\ell Y_i g_i^\ell + m_v Y_i g_i^v,$$

$$\mathcal{E}_s = T\mathcal{S} - P\mathcal{V} + mg.$$

Dividing this relation by mass m, one gets

$$e_s = Ts - Pv + g,$$

which can be differentiated into

$$\mathrm{d}e_s = T\,\mathrm{d}s + s\,\mathrm{d}T - P\,\mathrm{d}v - v\,\mathrm{d}P + \mathrm{d}g \tag{5.2.35}$$

Summing (5.2.35) with (5.2.33) finally yields the two-phase mixture's mass-specific Gibbs equation:

$$\mathrm{d}e_s = T\,\mathrm{d}s - P\,\mathrm{d}v + \sum_{i=1}^{N_s} \tilde{g}_i\,\mathrm{d}Y_i. \tag{5.2.36}$$

In this respect, one has $\frac{P}{\rho^2} - \left.\frac{\partial e_s}{\partial \rho}\right|_{s,\underline{\boldsymbol{Y}}} = 0$, and the speed of sound reduces to its classic form:

$$c_H^2 = c^2 = \left.\frac{\partial P}{\partial \rho}\right|_s. \tag{5.2.37}$$

Yet, in this formula, the entropy and density now represent two-phase mixture properties. The speed of sound expression can now be derived. The mixture's entropy is defined by

$$\rho s = z_\ell \rho_\ell s_\ell + (1 - z_\ell)\rho_v s_v. \tag{5.2.38}$$

The squared speed of sound c^2 can then be recast into

$$c^2 = \left.\frac{\partial P}{\partial \rho}\right|_{s,\underline{\boldsymbol{Y}}} = -\left.\frac{\partial s}{\partial P}\right|_{\rho,\underline{\boldsymbol{Y}}}^{-1} \left.\frac{\partial s}{\partial \rho}\right|_{P,\underline{\boldsymbol{Y}}}, \tag{5.2.39}$$

it can be expressed by differentiating the mixture entropy definition (5.2.38) with fixed species composition.

$$\left.\frac{\partial s}{\partial P}\right|_{\rho,\underline{\boldsymbol{Y}}} = \frac{1}{\rho}\left(z_\ell \left.\frac{\partial \rho_\ell s_\ell}{\partial P}\right|_{\mathrm{sat},\underline{\boldsymbol{Y}}} + (1 - z_\ell) \left.\frac{\partial \rho_v s_v}{\partial P}\right|_{\mathrm{sat},\underline{\boldsymbol{Y}}} + (\rho_\ell s_\ell - \rho_v s_v) \left.\frac{\partial z_\ell}{\partial P}\right|_{\mathrm{sat},\underline{\boldsymbol{Y}}}\right), \tag{5.2.40}$$

$$\left.\frac{\partial s}{\partial \rho}\right|_{P,\underline{\boldsymbol{Y}}} = \frac{1}{\rho}\left((\rho_\ell s_\ell - \rho_v s_v) \left.\frac{\partial z_\ell}{\partial \rho}\right|_{\mathrm{sat},P,\underline{\boldsymbol{Y}}} - s\right). \tag{5.2.41}$$

This expression involves the following differential relations:

$$\begin{cases} \left.\dfrac{\partial \rho_\phi s_\phi}{\partial P}\right|_{\mathrm{sat},\underline{\boldsymbol{Y}}} = \left.\dfrac{\partial \rho_\phi s_\phi}{\partial P}\right|_T + \left.\dfrac{\partial T^{\mathrm{sat}}}{\partial P}\right|_{\underline{\boldsymbol{Y}}} \left.\dfrac{\partial \rho_\phi s_\phi}{\partial T}\right|_P, & \text{(5.2.42a)} \\ \left.\dfrac{\partial z_\ell}{\partial P}\right|_{\mathrm{sat},\underline{\boldsymbol{Y}}} = \left.\dfrac{\partial z_\ell}{\partial P}\right|_T + \left.\dfrac{\partial T^{\mathrm{sat}}}{\partial P}\right|_{\underline{\boldsymbol{Y}}} \left.\dfrac{\partial z_\ell}{\partial T}\right|_P, & \text{(5.2.42b)} \\ \left.\dfrac{\partial z_\ell}{\partial \rho}\right|_{\mathrm{sat},P,\underline{\boldsymbol{Y}}} = \dfrac{1}{\rho_\ell - \rho_v}. & \text{(5.2.42c)} \end{cases}$$

Finally, the square of the speed of sound is given by

$$c^2 = \frac{1}{\rho\left[\frac{1}{\beta^{\mathrm{mix}}}\left(\beta^{\mathrm{mix}} - \alpha^{\mathrm{mix}} \left.\frac{\partial T^{\mathrm{sat}}}{\partial P}\right|_{\underline{\boldsymbol{Y}}}\right)^2 + \frac{C_v^{\mathrm{mix}}}{T} \left.\frac{\partial T^{\mathrm{sat}}}{\partial P}\right|_{\underline{\boldsymbol{Y}}}^2\right]}, \tag{5.2.43}$$

which is always positive. It is expressed as a function of the thermodynamic quantities of each phase α_ϕ, β_ϕ and $C_{v,\phi}$ through mixing combinations. These quantities represent respectively the isobaric thermal expansion coefficient, the isothermal compressibility coefficient and the volume-specific isochoric heat capacity. For a thermodynamic quantity ψ defined for each phase, the mixing quantity ψ_{mix} is defined as

$$\psi_{\text{mix}} = z_\ell \psi_\ell + (1 - z_\ell)\psi_v. \tag{5.2.44}$$

Using the obtained coefficients ζ, ξ_i and the speed of sound c, the same strategy as for the supercritical case can be used.

5.2.3.4 One-dimensional validations

In order to validate the formulation and practical implementation of the Jacobian matrices and boundary treatments, one-dimensional test setups are considered, similarly to the supercritical case. The validations are run on a uniform 100-node mesh, over a domain $\Omega = [0, L]$ of length $L = 10^{-2}$ m. The numerical scheme used is TTG4A (cf. section 4.5.1.3.4, page 124).

5.2.3.4.1 Fully-Reflecting Boundary Conditions

In order to test the behaviour of the Characteristic Boundary Conditions, the first test case is built by adding gaussian perturbations on the characteristic variables associated to the forward and backward acoustic characteristics $\Delta\mathbf{W}^+(x) = \Delta\mathbf{W}^-(x) = \exp\left(-200\left(x - L/2\right)^2\right)$ to the homogeneous two-phase solution $\mathbf{U}_0$. $\mathbf{U}_0$ is the set of conservative variables corresponding to density $\rho_0 = 100$ kg/m^3, pressure $P_0 = 1$ MPa, velocity $u_0 = 0$ m/s and species mass fractions $Y_{O_2} = 1 - Y_{N_2} = 0.8$. Initial solution is then

$$\mathbf{U}(x, t = 0) = \mathbf{U}_0 + \mathcal{T}_{\mathbf{WU}_0} \cdot \begin{bmatrix} 0 \\ \vdots \\ 0 \\ \Delta\mathbf{W}_{u-c}(x) \\ \Delta\mathbf{W}_{u+c}(x) \end{bmatrix}, \tag{5.2.45}$$

with $\mathcal{T}_{\mathbf{WU}_0}$ defined by (5.2.5). The results are displayed in Figure 5.5.

The results for this test case are in agreement with the expected behaviour.

5.2.3.4.2 Non-Reflecting Boundary Conditions

The same initial condition as in section 5.2.3.4.1 with forward and backward acoustic waves is used here. The results are presented in Figure 5.6.

Once again, the proper behaviour is observed with zero reflection at both boundaries.

5.2.3.5 Conclusion on the subcritical homogeneous equilibrium

This section described the characteristic properties of the subcritical model. The possibility to express analytically the speed of sound and the differential properties of the system were possible because the approximate equilibrium method allows for the formulation of the extended Clausius-Clapeyron relation derived in section 2.3.3.3.

A similar implementation of the exact equilibrium would actually require to know the differential of the flux function and the speed of sound, which is not possible to get analytically. In this respect, one

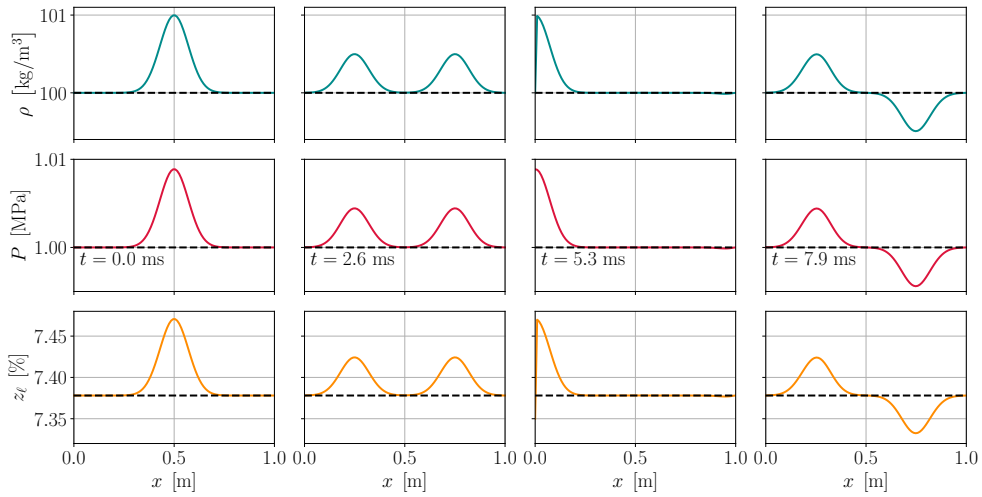

Figure 5.5: Test case 1 – Initially superimposed backward and forward acoustic waves with fully reflecting boundary conditions. Density and pressure snapshots of the solution. From left to right: initial profile, solution before, during and after interaction with domain boundaries.

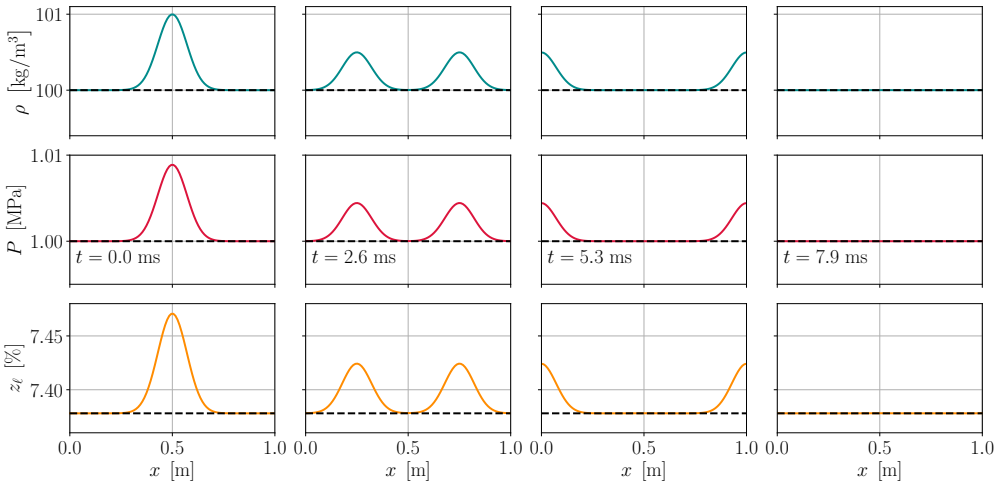

Figure 5.6: Test case 2 – Initially superimposed backward and forward acoustic waves with non-reflecting boundary conditions. Density and pressure snapshots of the solution. From left to right: initial profile, solution before, during and after interaction with domain boundaries.

can consider the numerical computation of such derivatives. Yet, this treatment is computationally expansive.

Another option is to formulate a 4-equation model and use an operator-splitting strategy to compute the true equilibrium. This is described in the next section.

5.3 Formulation with a relaxation method: the 4-equation model

Although the analytical computation of the speed of sound is possible in the case of the simplified multicomponent two-phase equilibrium of section 2.3.3, there is no analytical formulation of the speed of sound nor of the coefficients ξ_i and ζ of the Jacobian matrix of the flux function for the exact two-phase equilibrium. In this respect, the application of the 3-equation model with the exact two-phase equilibrium would require numerical differentiation in order to evaluate the Jacobian matrix and the speed of sound.

An alternative strategy [Le Martelot et al., 2014] consists in transporting the flow variables by means of a 4-equation model – which considers only temperature and pressure equilibrium between phases – and applying a stiff relaxation towards the chemical potential equilibrium by means of an operator splitting. This way, the Jacobian matrix and speed of sound for the 4-equation model can be derived analytically, as described in the present section. Such developments allows to propose a Taylor-Galerkin implementation of the 4-equation model.

5.3.1 Hyperbolic transport

5.3.1.1 Transport equations

This can be done by augmenting the system of Euler equations into

$$\frac{\partial \mathbf{U}}{\partial t} + \nabla \cdot \vec{\boldsymbol{\mathcal{F}}}(\mathbf{U}) = \frac{1}{\tau}\boldsymbol{\mathcal{R}}(\mathbf{U}), \tag{5.3.1}$$

with the conservative variables and flux now defined as

$$\mathbf{U} = \begin{bmatrix} \rho Y_1^\ell \\ \vdots \\ \rho Y_{N_s}^\ell \\ \rho Y_1^v \\ \vdots \\ \rho Y_{N_s}^v \\ \rho u \\ \rho v \\ \rho w \\ \rho e_\mathrm{t} \end{bmatrix} \quad \text{and} \quad \vec{\boldsymbol{\mathcal{F}}}(\mathbf{U}) = \begin{bmatrix} \rho Y_1^\ell u & \rho Y_1^\ell v & \rho Y_1^\ell w \\ \vdots & \vdots & \vdots \\ \rho Y_{N_s}^\ell u & \rho Y_{N_s}^\ell v & \rho Y_{N_s}^\ell w \\ \rho Y_1^v u & \rho Y_1^v v & \rho Y_1^v w \\ \vdots & \vdots & \vdots \\ \rho Y_{N_s}^v u & \rho Y_{N_s}^v v & \rho Y_{N_s}^v w \\ \rho u^2 + P & \rho v u & \rho w u \\ \rho u v & \rho v^2 + P & \rho w v \\ \rho u w & \rho v w & \rho w^2 + P \\ (\rho e_\mathrm{t} + P)u & (\rho e_\mathrm{t} + P)v & (\rho e_\mathrm{t} + P)w \end{bmatrix}, \tag{5.3.2}$$

so that the species mass fractions corresponding to each phase $Y_i^\phi = \frac{m_{i,\phi}}{m}$ are transported separately, and the liquid and gas phases are now considered in temperature and pressure equilibrium only. The

relaxation source terms can be written as

$$\mathcal{R}(\mathbf{U}) = \begin{bmatrix} \rho Y_1^\ell - \rho Y_1^{\ell,\mathrm{eq}} \\ \vdots \\ \rho Y_{N_s}^\ell - \rho Y_{N_s}^{\ell,\mathrm{eq}} \\ \rho Y_1^v - \rho Y_1^{v,\mathrm{eq}} \\ \vdots \\ \rho Y_{N_s}^v - \rho Y_{N_s}^{v,\mathrm{eq}} \\ 0 \\ 0 \\ 0 \\ 0 \end{bmatrix}, \tag{5.3.3}$$

where the superscript $^{\mathrm{eq}}$ denotes the state corresponding to the equilibrium, either simplified (cf. section 2.3.3) or exact (cf. section 2.4). The quantity τ represents the characteristic relaxation time, which is considered to tend to zero. This system is solved by means of an operator-splitting strategy [Strang, 1968], considering sequentially the advective part and the relaxation source terms. The numerical methods require to formulate the Jacobian matrix of this augmented flux function. This is the object of the next section.

5.3.1.2 Jacobian matrix

The Jacobian matrix $\mathcal{A}_x(\mathbf{U})$ of system (5.3.1) along direction x is now considered:

$$\mathcal{A}_x(\mathbf{U})_{ij} = \left.\frac{\partial \mathcal{F}_x(\mathbf{U})_i}{\partial \mathbf{U}_j}\right|_{\mathrm{U}_{k\neq j}} \tag{5.3.4}$$

The sensible energy differential is noted

$$\mathrm{d}(\rho e_s) = \frac{1}{\zeta}\,\mathrm{d}P + \sum_{i=1}^{N_s} \xi_i^\ell\,\mathrm{d}(\rho Y_i^\ell) + \sum_{i=1}^{N_s} \xi_i^v\,\mathrm{d}(\rho Y_i^v), \tag{5.3.5}$$

so that the total energy differential is

$$\mathrm{d}(\rho e_\mathrm{t}) = \frac{1}{\zeta}\,\mathrm{d}P + \sum_{i=1}^{N_s}\left(\xi_i^\ell - e_c\right)\mathrm{d}(\rho Y_i^\ell) + \sum_{i=1}^{N_s}(\xi_i^v - e_c)\,\mathrm{d}(\rho Y_i^v) + u\,\mathrm{d}(\rho u) + v\,\mathrm{d}(\rho v) + w\,\mathrm{d}(\rho w)\,. \tag{5.3.6}$$

Then, the Jacobian matrix reads

$$\mathcal{A}_x(\mathbf{U}) = \begin{bmatrix} (1-Y_1^\ell)u & \cdots & -Y_{N_s}^\ell u & -Y_1^v u & \cdots & -Y_{N_s}^v u & Y_1^\ell & 0 & 0 & 0 \\ \vdots & \ddots & \vdots & \vdots & \ddots & \vdots & \vdots & \vdots & \vdots & \vdots \\ -Y_1^\ell u & \cdots & (1-Y_{N_s}^\ell)u & -Y_1^v u & \cdots & -Y_{N_s}^v u & Y_{N_s}^\ell & 0 & 0 & 0 \\ -Y_1^\ell u & \cdots & -Y_{N_s}^\ell u & (1-Y_1^v)u & \cdots & -Y_{N_s}^v u & Y_1^v & 0 & 0 & 0 \\ \vdots & \ddots & \vdots & \vdots & \ddots & \vdots & \vdots & \vdots & \vdots & \vdots \\ -Y_1^\ell u & \cdots & -Y_{N_s}^\ell u & -Y_1^v u & \cdots & (1-Y_{N_s}^v)u & Y_{N_s}^v & 0 & 0 & 0 \\ -u^2+\zeta\left(e_c-\xi_1^\ell\right) & \cdots & -u^2+\zeta\left(e_c-\xi_{N_s}^\ell\right) & -u^2+\zeta\left(e_c-\xi_1^v\right) & \cdots & -u^2+\zeta\left(e_c-\xi_{N_s}^v\right) & (2-\zeta)u & -\zeta v & -\zeta w & \zeta \\ -uv & \cdots & -uv & -uv & \cdots & -uv & v & u & 0 & 0 \\ -uw & \cdots & -uw & -uw & \cdots & -uw & w & 0 & u & 0 \\ \left[\left(e_c-\xi_1^\ell\right)\zeta-h_\mathrm{t}\right]u & \cdots & \left[\left(e_c-\xi_{N_s}^\ell\right)\zeta-h_\mathrm{t}\right]u & \left[\left(e_c-\xi_1^v\right)\zeta-h_\mathrm{t}\right]u & \cdots & \left[\left(e_c-\xi_{N_s}^v\right)\zeta-h_\mathrm{t}\right]u & h_\mathrm{t}-u^2\zeta & -\zeta v & -\zeta w & (1+\zeta)u \end{bmatrix}, \tag{5.3.7}$$

The coefficients ζ and ξ_i^ℓ, ξ_i^v can be obtained by writing the mixture sensible energy and specific volume differentials:

$$\mathrm{d}e_s = y_\ell\,\mathrm{d}e_\ell + y_v\,\mathrm{d}e_v + e_\ell\,\mathrm{d}y_\ell + e_v\,\mathrm{d}y_v \tag{5.3.8a}$$
$$\mathrm{d}v = y_\ell\,\mathrm{d}v_\ell + y_v\,\mathrm{d}v_v + v_\ell\,\mathrm{d}y_\ell + v_v\,\mathrm{d}y_v, \tag{5.3.8b}$$

where the sensible energy and volume of each phase vary as

$$\mathrm{d}e_\phi = \left(v_\phi\beta_\phi P - v_\phi\alpha_\phi T\right)\mathrm{d}P + \left(c_{p,\phi} - v_\phi\alpha_\phi P\right)\mathrm{d}T + \sum_{i=1}^{N_s} e_{\phi,i}\,\mathrm{d}\left(\frac{Y_i^\phi}{y_\phi}\right) \tag{5.3.9a}$$

$$\mathrm{d}v_\phi = -v_\phi\beta_\phi\,\mathrm{d}P + v_\phi\alpha_\phi\,\mathrm{d}T + \sum_{i=1}^{N_s} v_{\phi,i}\,\mathrm{d}\left(\frac{Y_i^\phi}{y_\phi}\right). \tag{5.3.9b}$$

Noting that

$$y_\phi = \sum_{i=1}^{N_s} Y_i^\phi, \tag{5.3.10}$$

equations (5.3.9) become

$$\mathrm{d}e_\phi = \left(v_\phi\beta_\phi P - v_\phi\alpha_\phi T\right)\mathrm{d}P + \left(v_\phi C_{p,\phi} - v_\phi\alpha_\phi P\right)\mathrm{d}T + \sum_{i=1}^{N_s}\frac{e_{\phi,i}-e_\phi}{y_\phi}\,\mathrm{d}Y_i^\phi \tag{5.3.11a}$$

$$\mathrm{d}v_\phi = -v_\phi\beta_\phi\,\mathrm{d}P + v_\phi\alpha_\phi\,\mathrm{d}T + \sum_{i=1}^{N_s}\frac{v_{\phi,i}-v_\phi}{y_\phi}\,\mathrm{d}Y_i^\phi. \tag{5.3.11b}$$

Recasting this result into (5.3.8), one gets

$$\mathrm{d}e_s = \frac{1}{\rho}\left[\beta_{\mathrm{mix}}P - \alpha_{\mathrm{mix}}T\right]\mathrm{d}P + \frac{1}{\rho}\left[C_{p,\mathrm{mix}} - \alpha_{\mathrm{mix}}P\right]\mathrm{d}T + \sum_{i=1}^{N_s} e_{\ell,i}\,\mathrm{d}Y_i^\ell + \sum_{i=1}^{N_s} e_{v,i}\,\mathrm{d}Y_i^v \tag{5.3.12a}$$

$$\mathrm{d}v = -\frac{1}{\rho}\beta_{\mathrm{mix}}\,\mathrm{d}P + \frac{1}{\rho}\alpha_{\mathrm{mix}}\,\mathrm{d}T + \sum_{i=1}^{N_s} v_{\ell,i}\,\mathrm{d}Y_i^\ell + \sum_{i=1}^{N_s} v_{v,i}\,\mathrm{d}Y_i^v \tag{5.3.12b}$$

Then, from (5.3.12b), since, $\mathrm{d}v = -\frac{1}{\rho^2}\,\mathrm{d}\rho$, the temperature differential can be written as

$$\mathrm{d}T = -\frac{1}{\rho\alpha_{\mathrm{mix}}}\,\mathrm{d}\rho + \frac{\beta_{\mathrm{mix}}}{\alpha_{\mathrm{mix}}}\,\mathrm{d}P - \sum_{i=1}^{N_s}\frac{\rho v_{\ell,i}}{\alpha_{\mathrm{mix}}}\,\mathrm{d}Y_i^\ell - \sum_{i=1}^{N_s}\frac{\rho v_{v,i}}{\alpha_{\mathrm{mix}}}\,\mathrm{d}Y_i^v \tag{5.3.13}$$

Injecting this relation into the sensible energy differential (5.3.12a), it yields

$$\begin{aligned}\mathrm{d}e_s =& \frac{1}{\rho}\left[C_{p,\mathrm{mix}}\frac{\beta_{\mathrm{mix}}}{\alpha_{\mathrm{mix}}} - \alpha_{\mathrm{mix}}T\right]\mathrm{d}P + \frac{1}{\rho^2}\left[P - \frac{C_{p,\mathrm{mix}}}{\alpha_{\mathrm{mix}}}\right]\mathrm{d}\rho \\ &- \frac{C_{p,\mathrm{mix}}}{\alpha_{\mathrm{mix}}}\left[\sum_{i=1}^{N_s} v_{\ell,i}\,\mathrm{d}Y_i^\ell + \sum_{i=1}^{N_s} v_{v,i}\,\mathrm{d}Y_i^v\right] + \sum_{i=1}^{N_s} h_{\ell,i}\,\mathrm{d}Y_i^\ell + \sum_{i=1}^{N_s} h_{v,i}\,\mathrm{d}Y_i^v\end{aligned} \tag{5.3.14}$$

which corresponds to

$$\begin{aligned}\mathrm{d}(\rho e_s) =& \left(C_{p,\mathrm{mix}}\frac{\beta_{\mathrm{mix}}}{\alpha_{\mathrm{mix}}} - \alpha_{\mathrm{mix}}T\right)\mathrm{d}P + \left[h_s - \frac{C_{p,\mathrm{mix}}}{\alpha_{\mathrm{mix}}}\right]\mathrm{d}\rho \\ &- \frac{C_{p,\mathrm{mix}}}{\alpha_{\mathrm{mix}}}\left[\sum_{i=1}^{N_s} v_{\ell,i}\rho\,\mathrm{d}Y_i^\ell + \sum_{i=1}^{N_s} v_{v,i}\rho\,\mathrm{d}Y_i^v\right] + \sum_{i=1}^{N_s} h_{\ell,i}\rho\,\mathrm{d}Y_i^\ell + \sum_{i=1}^{N_s} h_{v,i}\rho\,\mathrm{d}Y_i^v\end{aligned} \tag{5.3.15}$$

and

$$\mathrm{d}(\rho e_s) = \left(C_{p,\mathrm{mix}} \frac{\beta_{\mathrm{mix}}}{\alpha_{\mathrm{mix}}} - \alpha_{\mathrm{mix}} T \right) \mathrm{d}P + \sum_{\phi \in \{\ell, v\}} \sum_{i=1}^{N_s} \left(h_{\phi,i} - \frac{C_{p,\mathrm{mix}}}{\alpha_{\mathrm{mix}}} v_{\phi,i} \right) \mathrm{d}\left(\rho Y_i^{\phi} \right). \tag{5.3.16}$$

Finally, this provides the values of the coefficients:

$$\begin{cases} \zeta = \dfrac{1}{C_{p,\mathrm{mix}} \frac{\beta_{\mathrm{mix}}}{\alpha_{\mathrm{mix}}} - \alpha_{\mathrm{mix}} T} & \text{(5.3.17a)} \\ \xi_i^{\phi} = h_{\phi,i} - \dfrac{C_{p,\mathrm{mix}}}{\alpha_{\mathrm{mix}}} v_{\phi,i} & \text{(5.3.17b)} \end{cases}$$

5.3.1.3 Speed of sound

The Jacobian matrix having the same form as for the previous systems, the speed of sound reads:

$$c^2 = \left. \frac{\partial P}{\partial \rho} \right|_{s, \underline{\boldsymbol{Y}}}, \tag{5.3.18}$$

except that now, the mass fractions $\underline{\boldsymbol{Y}} = \left[Y_1^{\ell}, \cdots, Y_{N_s}^{\ell}, Y_1^{v}, \cdots, Y_{N_s}^{v} \right]^t$ of the components in the liquid and the vapour phases are fixed. Note that the liquid mass fraction y_ℓ is then also constant.
In this respect, one can write the differential of the mixture mass-specific volume at constant composition:

$$\mathrm{d}v = \mathrm{d}\big(y_\ell v_\ell + (1 - y_\ell) v_v \big) = y_\ell \, \mathrm{d}v_\ell + (1 - y_\ell) \, \mathrm{d}v_v. \tag{5.3.19}$$

Expanding the differentials of the liquid and vapour specific volumes, at constant composition, on has

$$\begin{aligned} \mathrm{d}v &= \big(y_\ell v_\ell \alpha_\ell + (1 - y_\ell) v_v \alpha_v \big) \, \mathrm{d}T - \big(y_\ell v_\ell \beta_\ell + (1 - y_\ell) v_v \beta_v \big) \, \mathrm{d}P, & \text{(5.3.20)} \\ &= v \alpha_{\mathrm{mix}} \, \mathrm{d}T - v \beta_{\mathrm{mix}} \, \mathrm{d}P, & \text{(5.3.21)} \end{aligned}$$

so that

$$\mathrm{d}T = -\frac{1}{\rho \alpha_{\mathrm{mix}}} \, \mathrm{d}\rho + \frac{\beta_{\mathrm{mix}}}{\alpha_{\mathrm{mix}}} \, \mathrm{d}P. \tag{5.3.22}$$

Similarly, the mixture entropy differential at constant composition reads

$$\mathrm{d}s = y_\ell \, \mathrm{d}s_\ell + (1 - y_\ell) \, \mathrm{d}s_v, \tag{5.3.23}$$

which expands to

$$\begin{aligned} \mathrm{d}s &= \left[y_\ell \frac{c_{p,\ell}}{T} + (1 - y_\ell) \frac{c_{p,v}}{T} \right] \mathrm{d}T - \left[y_\ell v_\ell \alpha_\ell + (1 - y_\ell) v_v \alpha_v \right] \mathrm{d}P, & \text{(5.3.24)} \\ &= \frac{\bar{c_p}}{T} \, \mathrm{d}T - \frac{\alpha_{\mathrm{mix}}}{\rho} \, \mathrm{d}P, & \text{(5.3.25)} \end{aligned}$$

with $\bar{c_p} = y_\ell c_{p,\ell} + (1 - y_\ell) c_{p,v}$. Casting (5.3.22) into (5.3.25) finally yields:

$$\mathrm{d}s = -\frac{1}{\rho \alpha_{\mathrm{mix}}} \frac{\bar{c_p}}{T} \, \mathrm{d}\rho + \left[-\frac{\alpha_{\mathrm{mix}}}{\rho} + \frac{\bar{c_p}}{T} \frac{\beta_{\mathrm{mix}}}{\alpha_{\mathrm{mix}}} \right] \mathrm{d}P, \tag{5.3.26}$$

hence the speed of sound for the 4-equation system:

$$c^2 = \frac{\bar{c_p}}{\rho \beta_{\mathrm{mix}} \bar{c_p} - \alpha_{\mathrm{mix}}^2 T} \tag{5.3.27}$$

5.3.2 Characteristic boundary conditions

5.3.2.1 Accounting for the stiff relaxation source terms at the boundaries

A particular care must be taken for the proper application of the characteristic boundary conditions, which require to take into account the relaxation source terms.

Figure 5.7 shows the comparison between two simulations of the 4-equation model with fully reflecting boundary conditions: the first one using the characteristic variables of the 4-equation model, and the other one using the characteristic variables of the 3-equation model. This latter computation corresponds to taking into account the infinitely fast relaxation source terms. The simplified equilibrium

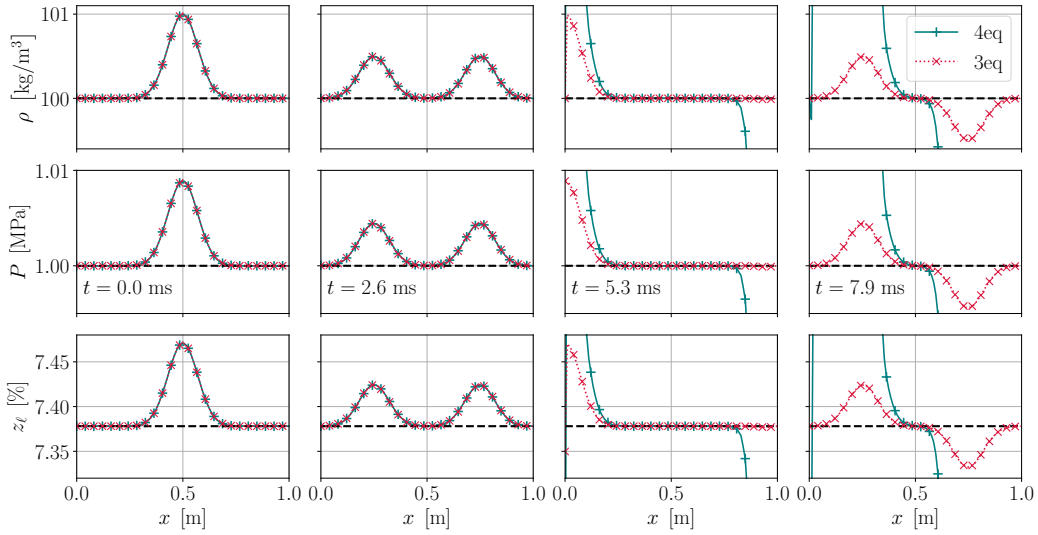

(a) Using the characteristics of the 4-equation model

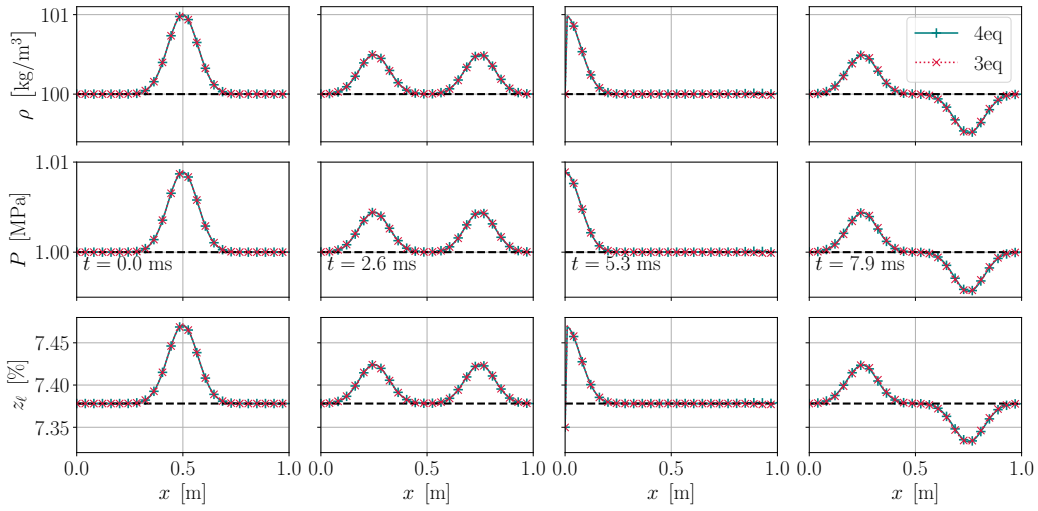

(b) Using the characteristics of the 3-equation model

Figure 5.7: Comparison of the behaviour of characteristic boundary conditions whether the relaxation source terms are accounted for or not. In both cases, the results of the 4-equation model computation (blue solid lines) are compared to the results of the 3-equation model of figure 5.5 (red dotted lines).

formulation is used, in order to allow for comparisons with the simulations of section 5.2.3.4.1. These

results confirm the need for computing the characteristics of the 3-equation model for the boundary conditions, when the 4-equation model with stiff relaxation is used. Indeed, figure 5.7a exhibits a completely wrong behaviour of the boundary conditions, which eventually causes the divergence of the flow values at both the inlet and outlet. Instead, figure 5.7b shows that an appropriate behaviour is retrieved when considering the characteristics of the 3-equation model.

While the characteristics of the 3-equation model can be computed analytically for the simplified equilibrium formulation, numerical differentiation must be used to compute the coefficients ξ_i and ζ. Thus, compared to the 3-equation model, using the 4-equation model with stiff relaxation allows to greatly reduce the number of required numerical differentiation computations, which are only done at the boundary nodes for the latter method.

5.3.2.2 One-dimensional tests with the exact multicomponent equilibrium

Finally, the implementation of the 4-equation model with the multicomponent equilibrium can be validated on a configuration similar to the ones of the previous sections. In order to get the proper wave content, the initial condition is computed using the characteristic variables of the 3-equation system. The procedure is the following:

First, the vector of conservative variables of the 3-equation system is computed as

$$\mathbf{U}^{3\text{eq}}(x, t=0) = \mathbf{U}_0^{3\text{eq}} + \mathcal{T}^{3\text{eq}}_{\mathbf{WU}_0} \cdot \begin{bmatrix} 0 \\ \vdots \\ 0 \\ \Delta\mathbf{W}_{u-c}(x) \\ \Delta\mathbf{W}_{u+c}(x) \end{bmatrix}, \tag{5.3.28}$$

with $\mathbf{U}^{3\text{eq}}$, $\mathcal{T}^{3\text{eq}}_{\mathbf{WU}}$ defined respectively in equations (5.2.17) and (5.2.5). The differential coefficients $(\xi_i)_{i\in[\![1,N_s]\!]}$ and ζ appearing in the definition of $\mathcal{T}^{3\text{eq}}_{\mathbf{WU}}$ are evaluated numerically by a centered second-order differentiation. Then, the calculation of the thermodynamic equilibrium provides the phase-wise species mass fractions Y_i^ℓ and Y_i^v. Finally, these quantities allow to obtain the vector of conservative variables for the 4-equation model defined in (5.3.2).

For this validation case, the pressure is set to $P_0 = 10$ bar, the density to $\rho_0 = 50$ kg/m^3 and the species mass fractions to $Y_{O_2} = 1 - Y_{H_2} = 0.95$.

5.3.2.2.1 Fully reflecting boundary conditions

The results for the case of fully reflecting boundary conditions are displayed in figure 5.8. The expected behaviour is observed, as the acoustic waves are fully reflected.

5.3.2.2.2 Non-reflecting boundary conditions

The results for the case of non-reflecting boundary conditions are displayed in figure 5.9. Again, the results correspond to the expected behaviour. Note that a very small reflexion (about 1% of the initial perturbation) is actually reflected. This small discrepancy is attributed to the numerical evaluation of the differential terms which is naturally not as accurate as an analytical solution would.

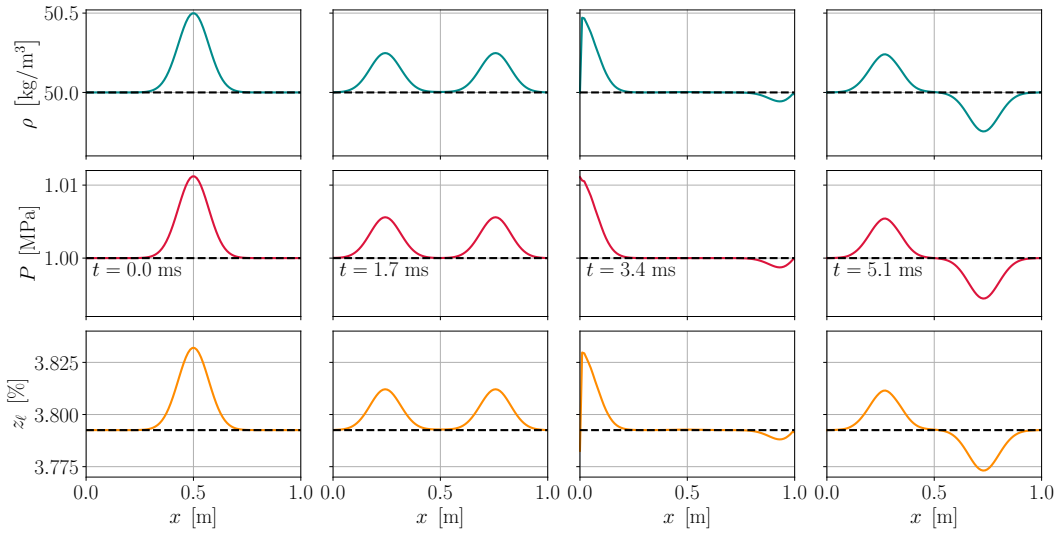

Figure 5.8: Test case 1 – Initially superimposed backward and forward acoustic waves with fully reflecting boundary conditions. Density and pressure snapshots of the solution. From left to right: initial profile, solution before, during and after interaction with domain boundaries.

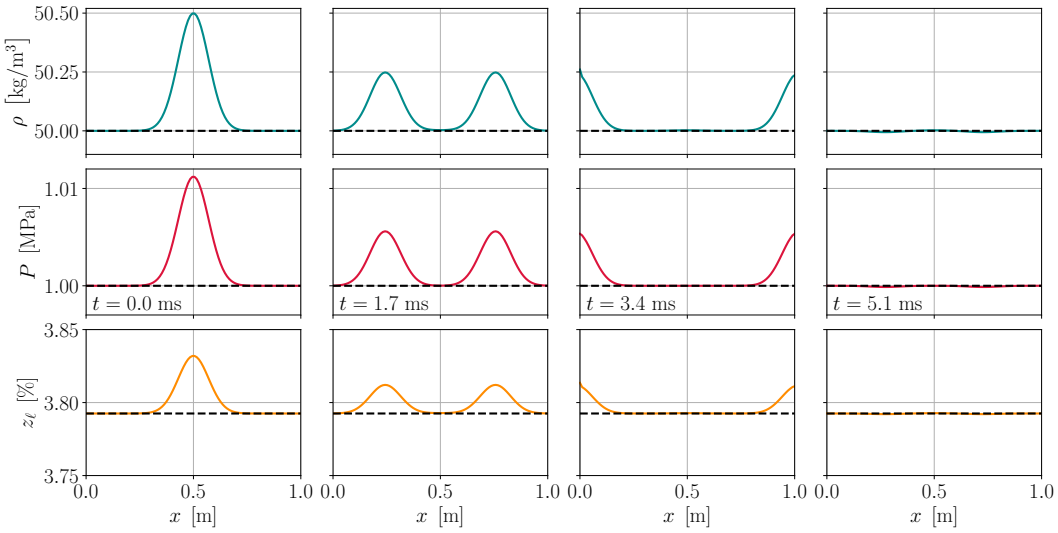

Figure 5.9: Test case 2 – Initially superimposed backward and forward acoustic waves with non-reflecting boundary conditions. Density, pressure and liquid volume fraction snapshots of the solution. From left to right: initial profile, solution before, during and after interaction with domain boundaries.

5.4 Summary of the solver

This section briefly recalls the global strategy for the resolution of the 3-equation model and 4-equation model with stiff relaxation towards equilibrium.

5.4.1 3-equation model

The resolution is processed by means of the following algorithm:

1. From the conservative variables from the previous iteration, compute the 1-phase pressure $P^{\mathrm{m}}(\mathbf{U}^n)$ and temperature $T^{\mathrm{m}}(\mathbf{U}^n)$ using directly the cubic EoS;
2. If the obtained pressure P^{m} is positive, then apply a stability test (cf. chapter 2) for the state $(P^{\mathrm{m}}, T^{\mathrm{m}}, \rho^n)$, otherwise it is unstable;
3. If the 1-phase state is stable, then $P^n := P^{\mathrm{m}}$ and $T^n := T^{\mathrm{m}}$; the thermodynamic properties and Jacobian terms are computed using the 1-phase formulas;
   Else, if the 1-phase state is unstable, then compute the 2-phase equilibrium state (cf. chapter 2); set $P^n := P^{\mathrm{eq}}(\mathbf{U}^n)$ and $T^n := T^{\mathrm{eq}}(\mathbf{U}^n)$; the thermodynamic properties and Jacobian terms are computed by means of the 2-phase formulas;
4. Compute the update using the numerical scheme;
5. Apply the boundary conditions and obtain $\mathbf{U}^{n+1}$;
6. Continue to next time step...

5.4.2 4-equation model

The resolution of the 4-equation model with stiff relaxation towards two-phase equilibrium is processed by means of the following algorithm:

1. From the conservative variables from the previous iteration $\mathbf{U}^n$, compute the overall mixture composition $\underline{\boldsymbol{Y}}^n = (\underline{\boldsymbol{Y}}^\ell)^n + (\underline{\boldsymbol{Y}}^v)^n$, density ρ^n and sensible energy e_s^n;
2. Compute the 1-phase pressure $P^{\mathrm{m}}((\rho\underline{\boldsymbol{Y}})^n, e_s^n)$ and temperature $T^{\mathrm{m}}((\rho\underline{\boldsymbol{Y}})^n, e_s^n)$ using directly the cubic EoS;
3. **If** the obtained pressure P^{m} is positive **then**
   Apply a stability test (cf. chapter 2) for the state $(P^{\mathrm{m}}, T^{\mathrm{m}}, \rho^n)$
   Else, the 1-phase solution is unstable;
4. **If** the 1-phase state is stable **then**
   Set $P^n := P^{\mathrm{m}}$ and $T^n := T^{\mathrm{m}}$;
   Overwrite the species mass fractions so that $\underline{\boldsymbol{Y}}^\ell := \underline{\boldsymbol{Y}}^n$ and $\underline{\boldsymbol{Y}}^v := 0$ if the 1-phase stable state corresponds to a liquid phase, otherwise set $\underline{\boldsymbol{Y}}^\ell := 0$ and $\underline{\boldsymbol{Y}}^v := \underline{\boldsymbol{Y}}^n$;
   Compute the thermodynamic properties of the single phase that is present;
   Compute the Jacobian terms;
   Else, Compute the 2-phase equilibrium state (cf. chapter 2);
   Set $P^n := P^{\mathrm{eq}}((\rho\underline{\boldsymbol{Y}})^n, e_s^n)$ and $T^n := T^{\mathrm{eq}}((\rho\underline{\boldsymbol{Y}})^n, e_s^n)$
   Overwrite the species mass fractions $\underline{\boldsymbol{Y}}^\ell := (\underline{\boldsymbol{Y}}^\ell)^{\mathrm{eq}}$ and $\underline{\boldsymbol{Y}}^v := (\underline{\boldsymbol{Y}}^v)^{\mathrm{eq}}$
   Compute the thermodynamic properties of each phase;
   Compute the Jacobian terms;
5. Compute the update using the numerical scheme;
6. Apply the boundary conditions and obtain $\mathbf{U}^{n+1}$;
7. Continue to next time step...

5.5 Conclusion

The different models that have been investigated and implemented into the solver for unstructured multidimensional simulations have been presented. In particular, the necessary derivations for the application of Taylor-Galerkin numerical methods have been presented. In addition, the characteristic boundary conditions have been formulated for the different models. These developments allow to compute supercritical flows as well as subcritical flows in the context of both simplified or exact multicomponent equilibrium formulations.

Simple test cases were provided for each model. These test configurations involve both the high-order numerical transport within the domain and the characteristic boundary conditions for the different models, allowing for the global validation of the derivations and implementation. The next chapter is dedicated to the application of these models to realistic cases.

Chapter 6

Large-Eddy Simulations of Mascotte A10 and Spray-A configurations

This chapter presents the simulation results obtained with the previously described 3-equation and 4-equation models. In particular, simulations based on the Mascotte experimental bench are led. After a global description of the numerical setup and the models used, a set of two-dimensional simulations is first proposed, using different multifluid models and thermodynamic equilibrium formulations, allowing for comparisons. Then, a three-dimensional case is computed and compared with the available experimental data. Finally, a first set of simulation of the Spray-A configuration of the Engine Combustion Network (ECN) is presented and encouraging results are shown.

6.1 Governing equations, models and numerics

The framework of Large-Eddy Simulation (LES) is adopted in the present section, in order to address the highly turbulent flows involved in the realistic applications considered. This strategy consists in spatially filtering the conservation equations to remove the small scale turbulent structures that cannot be resolved on affordable grids. The effects of these small structures are then accounted for by means of *sub-grid scale* (SGS) models. Classical gaseous SGS closures are used here, even though it is expected that additional sub-grid scale contributions may have to be considered for two-phase flows. This last point is out of the scope of this thesis. It should be pointed out that without SGS models, the numerics being weakly dissipative, calculations are not stable.

Additional simplifications are assumed in this work that will require more investigation in the future. First, surface tension is neglected, which seems reasonable given the high Weber number encountered in the targeted applications. Second, atomisation is neglected so that no droplets are considered at the SGS level. This is a strong hypothesis, as droplets might influence the flame structure, which will need further development to properly couple the liquid / gas interfaces and a dedicated method for the dispersed phase.

6.1.1 The 3-equation model for the LES of reacting flows

The 3-equation models being similar to Euler equations used in gaseous and supercritical flows, similar closure are used here. Thus, the models are those used for the simulation of supercritical reacting flows [Schmitt, 2019]. This is an assumption that needs further investigations or validations against experimental data of realistic cases.

6.1.1.1 Governing equations

The Favre-filtered, fully compressible Navier-Stokes equations for the 3-equation model is given by [Poinsot and Veynante, 2005]:

$$\frac{\partial \overline{\rho}\widetilde{Y}_k}{\partial t} + \frac{\partial \overline{\rho}\widetilde{Y}_k\widetilde{u}_j}{\partial x_j} = -\frac{\partial \overline{J_{k,j}}}{\partial x_j} - \frac{\partial J^t_{k,j}}{\partial x_j} + \overline{\dot{\omega}_k} \tag{6.1.1}$$

$$\frac{\partial \overline{\rho}\widetilde{u}_i}{\partial t} + \frac{\partial \overline{\rho}\widetilde{u}_i\widetilde{u}_j}{\partial x_j} = -\frac{\partial \overline{p}}{\partial x_i} + \frac{\partial \overline{\tau_{i,j}}}{\partial x_j} + \frac{\partial \tau^t_{i,j}}{\partial x_j} \tag{6.1.2}$$

$$\frac{\partial \overline{\rho}\widetilde{E}}{\partial t} + \frac{\partial \overline{\rho}\widetilde{u}_j\widetilde{E}}{\partial x_j} = -\frac{\partial \overline{p}\widetilde{u}_j}{\partial x_j} + \frac{\partial \widetilde{u}_i\overline{\tau_{i,j}}}{\partial x_j} - \frac{\partial \overline{q_j}}{\partial x_j} - \frac{\partial q^t_j}{\partial x_j} + \overline{\dot{\omega}_T} \tag{6.1.3}$$

where $\overline{\phi}$ and $\tilde{\phi}$ denote spatial and mass-weighted (Favre) spatially filtered quantities. P is the pressure, T the temperature, ρ the density, Y_k is the mass fraction of the species k, u_i is the velocity vector, x_i the three spatial coordinates, t the time, E the total sensible energy, $\tau^t_{i,j}$ the sub-grid scale (SGS) stress tensor, q^t_j the SGS energy fluxes, $J^t_{k,j}$ the SGS species fluxes, $\dot{\omega}_k$ the species reaction rate and $\dot{\omega}_T$ the heat release rate. The fluid viscosity and the heat diffusion coefficient are calculated following the Chung *et al.* method [Chung et al., 1988] and mass diffusion coefficients are deduced from heat diffusivity by assuming a unity Lewis number (Le=1). The Soret and Dufour effects are neglected. The heat flux $\vec{q}$ uses a classical gradient approach. The laminar species flux $\vec{J}_k$ should account for non-ideal molecular effects [Gaillard, 2015], in order to guarantee positive entropy production from laminar diffusion. Nonetheless, considering the very slight impact of laminar diffusion in the highly turbulent flows simulated, the simple Fick's law is used instead [Giovangigli, 2012].

6.1.1.2 Models

The sub-grid scale (SGS) energy and species fluxes are modeled using the gradient transport assumption, introducing SGS turbulent viscosity ν_t, turbulent species diffusion D_t and turbulent thermal conductivity coefficients λ^t:

$$\tau^t_{ij} = 2\,\overline{\rho}\,\nu_t\left(\widetilde{S}_{ij} - \frac{1}{3}\delta_{ij}\widetilde{S}_{ll}\right) \quad \text{with} \quad \widetilde{S}_{ij} = \frac{1}{2}\left(\frac{\partial \widetilde{u}_j}{\partial x_i} + \frac{\partial \widetilde{u}_i}{\partial x_j}\right) - \frac{1}{3}\,\frac{\partial \widetilde{u}_k}{\partial x_k}\,\delta_{ij} \tag{6.1.4}$$

$$J^t_{i,k} = -\overline{\rho}\left(D_t\frac{\partial \widetilde{Y}_k}{\partial x_i}\right) \tag{6.1.5}$$

$$q^t_i = -\lambda_t\frac{\partial \widetilde{T}}{\partial x_i} + \sum_{k=1}^{N} J^t_{i,k}\,\widetilde{h}_{s,k} \tag{6.1.6}$$

with:

$$D_t = \frac{\nu^t}{\mathrm{Sc}_t} \quad \text{and} \quad \lambda_t = \frac{\rho\nu_t c_p}{\mathrm{Pr}_t} \tag{6.1.7}$$

where $h_{s,k}$ is the partial-mass sensible enthalpy of species k, and turbulent Prandtl Pr_t and Schmidt Sc_t numbers are both set to 0.7. In three dimensions, the SGS turbulent viscosity ν_t is modeled with the *wall-adapting large eddy* (WALE) model [Nicoud and Ducros, 1999], well-suited for shear flows [Schmitt et al., 2010]. In two dimensions, the *dynamic* Smagorinsky model [Lilly, 1992] is used.

6.1.1.3 Combustion model

Similarly to what is done for supercritical flows [Schmitt, 2019], it is assumed that combustion is fast and operates in a pure diffusion regime. Species equilibrium is assumed in this work. All the species are then deduced from equilibrium calculations as a function of the mixture fraction Z. In

order to properly represent the temperature over the whole mixture fraction domain for the H_2-O_2 case considered in this chapter, four species (H_2O, H_2, O_2 and OH) are considered here for cases involving hydrogen - oxygen combustion. Filtered mass fractions are computed using a β-pdf [Poinsot and Veynante, 2005, Veynante and Vervisch, 2002]:

$$\widetilde{Y_k}(\widetilde{Z}, \widetilde{Z''^2}) = \int_0^1 Y_k(Z^*) P(Z^*, x, t)\, \mathrm{d}Z^* \tag{6.1.8}$$

where P is the β-pdf depending on $\widetilde{Z}$ and $\widetilde{Z''^2}$, the filtered variance of the mixture fraction. Both $\widetilde{Z}$ and $\widetilde{Z''^2}$ are transported in the simulation [Domingo et al., 2008]:

$$\frac{\partial \overline{\rho}\widetilde{Z}}{\partial t} + \nabla \cdot (\overline{\rho}\widetilde{Z}\widetilde{u}) = \nabla \cdot (\overline{\rho}(D + D_t)\nabla \widetilde{Z}) \tag{6.1.9}$$

$$\frac{\partial \overline{\rho}\widetilde{Z''^2}}{\partial t} + \nabla \cdot (\overline{\rho}\widetilde{Z''^2}\widetilde{u}) = \nabla \cdot (\overline{\rho}(D + D_t)\nabla \widetilde{Z''^2}) + 2\overline{\rho}D_t \|\nabla \widetilde{Z}\|^2 - 2\overline{\rho}D_t \frac{\widetilde{Z''^2}}{{\Delta_x}^2} \tag{6.1.10}$$

Finally the filtered reaction rate $\overline{\dot{\omega}_k}$ determined from a relaxation between the tabulated filtered mass fraction $\widetilde{Y_k}(\widetilde{Z}, \widetilde{Z''^2})$ and the one transported assuming pure mixing $\widetilde{Y_k^+}$ [Schmitt et al., 2011, Pera et al., 2009]:

$$\overline{\dot{\omega}_k} = \overline{\rho}\frac{\widetilde{Y_k}(\widetilde{Z}, \widetilde{Z''^2}) - \widetilde{Y_k^+}}{C_r \Delta t} \tag{6.1.11}$$

where Δt is the time step and C_r a constant set to 100 in this work. The filtered heat release rate is then computed from $\overline{\dot{\omega}_k}$:

$$\overline{\dot{\omega}_T} = -\sum_{k=1}^{N} \Delta h^0_{f,k} \overline{\dot{\omega}_k} \tag{6.1.12}$$

where $\Delta h^0_{f,k}$ is the formation enthalpy of species k.

6.1.2 The 4-equation model for the LES of non-reacting flows

Reaction rates are not considered in this formalism which was only used for non-reacting cases at the moment.

6.1.2.1 Governing equations

The Favre-filtered, fully compressible Navier-Stokes equations for the 4-equation model are given by:

$$\frac{\partial \overline{\rho}\widetilde{Y}_k^\phi}{\partial t} + \frac{\partial \overline{\rho}\widetilde{Y}_k^\phi \widetilde{u}_j}{\partial x_j} = -\frac{\partial \overline{J_{k,j}^\phi}}{\partial x_j} - \frac{\partial J_{k,j}^{t,\phi}}{\partial x_j} \tag{6.1.13}$$

$$\frac{\partial \overline{\rho}\widetilde{u}_i}{\partial t} + \frac{\partial \overline{\rho}\widetilde{u}_i\widetilde{u}_j}{\partial x_j} = -\frac{\partial \overline{p}}{\partial x_i} + \frac{\partial \overline{\tau_{i,j}}}{\partial x_j} + \frac{\partial \tau_{i,j}^t}{\partial x_j} \tag{6.1.14}$$

$$\frac{\partial \overline{\rho}\widetilde{E}}{\partial t} + \frac{\partial \overline{\rho}\widetilde{u}_j\widetilde{E}}{\partial x_j} = -\frac{\partial \overline{p}\widetilde{u}_j}{\partial x_j} + \frac{\partial \widetilde{u}_i\overline{\tau_{i,j}}}{\partial x_j} - \frac{\partial \overline{q_j}}{\partial x_j} - \frac{\partial q_j^t}{\partial x_j} \tag{6.1.15}$$

where Y_k^ϕ, $\phi \in \{\ell, v\}$, is the species mass fraction for each phase. As for the 3-equation model, the species $\vec{J}_k^\phi$ and heat fluxes $\vec{q}$ use classical gradient approaches, the species heat flux making use of the phase species mass fraction Y_k^ϕ, instead of the species mass fraction $Y_k = Y_k^v + Y_k^l$ for the 3-equation model. The fluid viscosity and the heat diffusion coefficient are calculated following the Chung *et al.* method [Chung et al., 1988] and mass diffusion coefficients are deduced from heat diffusivity by assuming a unity Lewis number (Le=1). The Soret and Dufour effects are neglected.

6.1.2.2 Models

The same sub-grid scale (SGS) models as for the 3-equation model are used for the 4-equation model. The turbulent species flux is now written in terms of phase species mass fraction Y_k^ϕ:

$$\overline{J_{i,k}}^{t,\phi} = -\overline{\rho}\left(D_t \frac{\partial \widetilde{Y}_k^\phi}{\partial x_i}\right) \tag{6.1.16}$$

In the present work, only two-dimensional computations are led with the 4-equation model. Therefore, as for the 3-equation model, the SGS turbulent viscosity ν_t is modeled with the dynamic Smagorinsky model [Lilly, 1992].

6.1.3 Thermodynamic closures

The Soave-Redlich-Kwong equation of state [Soave, 1972] is used in the simulations of the present chapter (see chapter 2 for details). The multifluid models and thermodynamic closures used to compute the two-phase equilibrium states for the different simulations are summarized in table 6.1.

Section	Configuration	Reactive flow	Multifluid model	Two-phase multicomponent equilibrium formulation
6.2.2.2	2D Mascotte A10	No	3-equation	Simplified
6.2.2.2 & 6.2.2.3	2D Mascotte A10	No	4-equation	Simplified
6.2.2.3	2D Mascotte A10	No	4-equation	Exact
6.2.3	3D Mascotte A10	Yes	3-equation	Simplified
6.3	3D SprayA	no	3-equation	Simplified

Table 6.1: Multifluid models and thermodynamic closures used for the different Mascotte simulations and the SprayA test case.

6.1.4 Numerics and stabilization method

6.1.4.1 Numerical schemes

The TTGC scheme (see chapter 4) is used to compute the hyperbolic transport in all the calculations of the present chapter. The diffusion operators are discretized following the local stencil "2-Δ" finite-element formulation of [Colin, 2003]. More details about this method can be found in chapter 4 of [Lamarque, 2007].

6.1.4.2 Stabilization method

The numerical method is stabilized by applying artificial viscosity to guarantee both accuracy and stability [Schmitt, 2019]. Cells with under-resolved wavelength oscillations are detected by a density sensor S_ρ:

$$S_\rho = \frac{|\vec{u}\cdot\vec{n}|\Delta t}{\Delta x}\left|\frac{\widehat{\overline{\rho}} - \overline{\rho}}{0.01\overline{\rho}}\right| \tag{6.1.17}$$

where Δt is the time step, Δx the characteristic cell size, $\vec{n}$ the normal to the density gradient and $\widehat{\phi} = F * \phi$ denotes a spatial filtering of variable ϕ. The spatial recursive filter F used in this work

follows the strategy depicted in Mathew and al. [Mathew et al., 2003] based on an extension to the deconvolution method of Stolz et al. [Stolz and Adams, 1999]. A species limiter S_{Y_k} is computed to locate regions of negative mass fractions:

$$S_{Y_k} = \begin{cases} \min\left\{\frac{|Y_k|}{\epsilon}, 1\right\}, & \text{if } Y_k < 0. \\ \min\left\{\frac{|Y_k - 1|}{\epsilon}, 1\right\}, & \text{if } Y_k > 1. \end{cases} \tag{6.1.18}$$

with $\epsilon = 0.1$. At the end of the temporal iteration (i.e. after the two sub-steps of the TTGC scheme) and before the application of the boundary conditions, second-order derivatives are used to add artificial diffusion and filter the conservative variables when the sensor is activated to smooth the largest gradient. At node i, artificially diffused conservative variables are obtained from:

$$(\overline{\rho}\widetilde{Y_k})_i^{AV} = (\overline{\rho}\widetilde{Y_k})_i + \frac{1}{\mathcal{V}_i}\sum_{e|i\in\mathcal{E}_e} -\frac{\mathcal{V}_{\mathcal{E}_e}}{n_v^{\mathcal{E}_e}}\left((\overline{\rho}\widetilde{Y_k})_{\mathcal{E}_e} - (\overline{\rho}\widetilde{Y_k})_i\right)(S_{\rho,\mathcal{E}_e} + S_{Y_k,\mathcal{E}_e}) \tag{6.1.19}$$

$$(\overline{\rho}\widetilde{u})_i^{AV} = (\overline{\rho}\widetilde{u})_i + \frac{1}{\mathcal{V}_i}\sum_{e|i\in\mathcal{E}_e} -\frac{\mathcal{V}_{\mathcal{E}_e}}{n_v^{\mathcal{E}_e}}\widetilde{u}_{\mathcal{E}_e}\left(\overline{\rho}_{\mathcal{E}_e} - \overline{\rho}_i\right)S_{\rho,\mathcal{E}_e} \tag{6.1.20}$$

$$(\overline{\rho}\widetilde{E})_i^{AV} = (\overline{\rho}\widetilde{E})_i + \frac{1}{\mathcal{V}_i}\sum_{e|i\in\mathcal{E}_e} -\frac{\mathcal{V}_{\mathcal{E}_e}}{n_v^{\mathcal{E}_e}}\left[(\overline{\rho}\widetilde{e_s})_{\mathcal{E}_e} - (\overline{\rho}\widetilde{e_s})_i + \widetilde{e}_{c,\mathcal{E}_e}\left(\overline{\rho}_{\mathcal{E}_e} - \overline{\rho}_i\right)\right](S_{\rho,\mathcal{E}_e} + S_{Y_k,\mathcal{E}_e}) \tag{6.1.21}$$

where $S_{\rho,\mathcal{E}_e} = 1/n_v^{\mathcal{E}_e}\sum_{k\in\mathcal{E}_e} S_{\rho,k}$ and $S_{Y_k,\mathcal{E}_e} = 1/n_v^{\mathcal{E}_e}\sum_{i\in\mathcal{E}_e} S_{Y_k,i}$. Here, $\mathcal{E}_e$ denote the e^{th} element of the mesh, $\mathcal{V}_{\mathcal{E}_e}$ its volume, $n_v^{\mathcal{E}_e}$ the number of vertices in $\mathcal{E}_e$, i the vertex index, $\mathcal{V}_i$ the volume of the dual cell $\mathcal{C}_i$ associated with the vertex i. The quantity $(\overline{\rho}\widetilde{Y_k})_{\mathcal{E}_e}$ is the mean weighted value of $\overline{\rho}\widetilde{Y_k}$ over the vertices of element $\mathcal{E}_e$.

Cell velocity equilibrium is assumed in equations (6.1.20) and (6.1.21) during the diffusion of the conservative variables. The mixture fraction and its variance are filtered the same way as species density $\overline{\rho}\widetilde{Y_k}$ (equation (6.1.19)).

6.2 Mascotte A-10 configuration

6.2.1 Experimental configuration

The Mascotte experimental configuration of ONERA [Vingert et al., 2000], which has been extensively used for experimental studies of cryogenic combustion in collaboration with Laboratoire EM2C [Habiballah et al., 2006, Candel et al., 2006], is considered here (figure 6.1). The present simulations reproduce case A10 corresponding to subcritical pressure flames [Candel et al., 1998, Candel et al., 2006]. A single coaxial injector produces a liquid oxygen stream at low velocity (less than 10 m/s), surrounded by a high-velocity gaseous hydrogen stream (more than 100 m/s), in a chamber at 10 bar, a pressure lower than the critical pressure for both reactants ($P_{C,\mathrm{O_2}}$=50.4 bar, $P_{C,\mathrm{H_2}}$=12.8 bar). Table 6.2 details the inflow conditions. Oxygen is injected at 80 K, well below its critical value $T_{C,\mathrm{O_2}} = 154$ K and is liquid, while hydrogen, injected at 289 K is gaseous ($T_{C,\mathrm{H_2}} = 33$ K). Under such conditions, the density of oxygen ($\rho_{\mathrm{O_2}} = 1190$ kg.m^{-3}) is much larger than that of hydrogen ($\rho_{\mathrm{H_2}} = 0.84$ kg.m^{-3}). The momentum flux ratio J=$(\rho_f u_f^2)/(\rho_{\mathrm{O_2}} u_{\mathrm{O_2}}^2)$, a critical parameter that drives coaxial flames length and spreading rate [Candel et al., 2006], is close to 14. It should be noticed that mixture is rich so that hydrogen is in excess.

Experimental visualisations of the OH* emission are available [Candel et al., 1998]. The average emission image treated with Abel's transform provides the mean flame position (figure 6.2a) and can be qualitatively compared with numerical OH field. Quantitative temperature measurements based

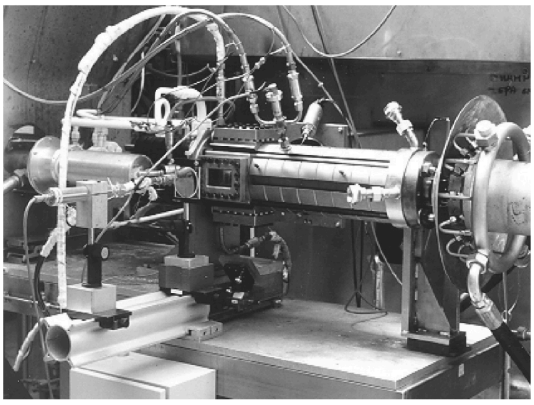

(a) Photography of the Mascotte experimental test bench at ONERA

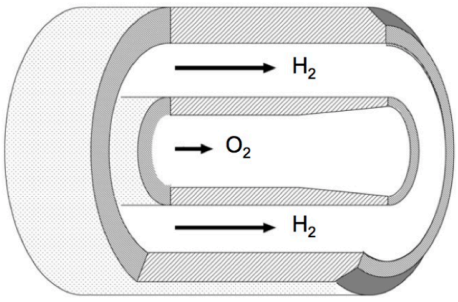

(b) Schematic representation of the coaxial injector with tapered lips

Figure 6.1: The Mascotte experimental setup.

P_{ch} [MPa]	T_{inj,H_2} [K]	T_{inj,O_2} [K]	$\dot{m}_{H_2}$ [g/s]	$\dot{m}_{O_2}$ [g/s]	u_{inj,H_2} [m/s]	u_{inj,O_2} [m/s]
1.0	289	80	23.7	50	308	2.23

Table 6.2: Injection conditions for the Mascotte A10 case simulated in this chapter. P_{ch} is the chamber pressure, T_{inj} is the injection temperature, $\dot{m}$ is the mass flow rate and u_{inj} is the injection bulk velocity.

on coherent anti-Stokes Raman scattering from H_2 are also available for comparison with numerical results (figure 6.2b).

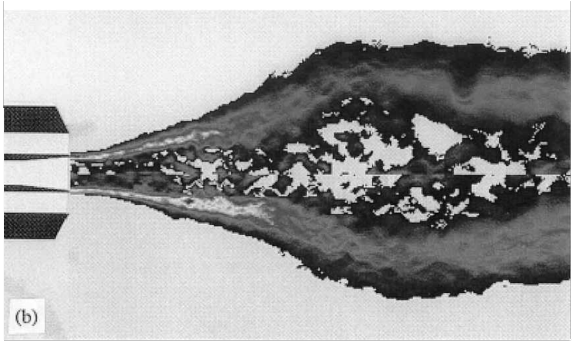

(a) Abel's transform of OH* mean emission for case A10

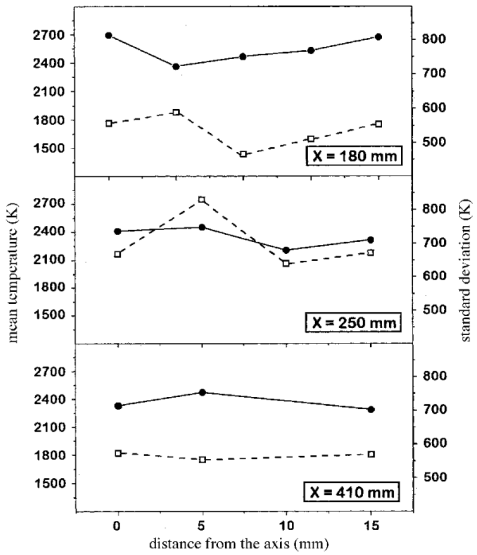

(b) Example of temperature measurements at different distances from the injector

Figure 6.2: Illustrations of experimental results for the Mascotte configuration.

6.2.2 Non reactive two-dimensional simulations

The objective of the two-dimensional simulations is to compare the different thermodynamic closures on a realistic case. After having detailed the numerical setup (section 6.2.2.1), the 3-equation and 4-equation models are compared using the simplified equilibrium model (section 6.2.2.2). Finally, the simplified thermodynamic model is compared with a real equilibrium closure (section 6.2.2.3).

6.2.2.1 Mesh, boundary conditions and numerical setup

The simulation domain and the grid distribution are shown in figure 6.3a. While the injector geometry is the actual one from the experiment, the chamber has been modified and its width is increased to 20d. This was done in order to prevent excessive flapping of the jet due to confinement, which is more pronounced in two-dimensions than in three-dimensions. A view of the mesh in the near injector region is offered in figure 6.3b. The characteristic size of the mesh is constant and set to $\Delta_x = \delta_{lip}/3$, with δ_{lip} the lip thickness, from the inlet up to $x = 10$d, with d the diameter of the oxygen injector. It is then smoothly coarsened, up to a characteristic cell size $\Delta_x = 3\delta_{lip}$. The grid contains 300 000 nodes and 600 000 triangles.

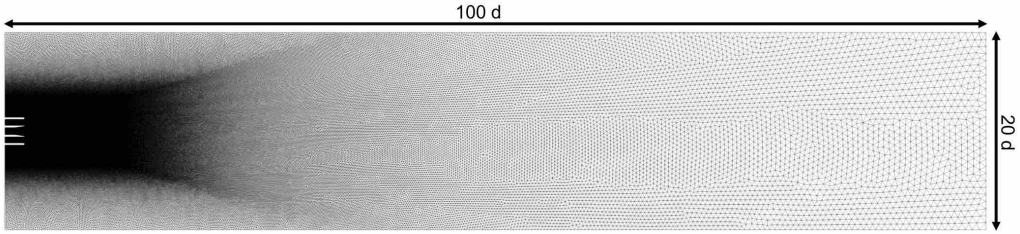

(a) Overview of the mesh

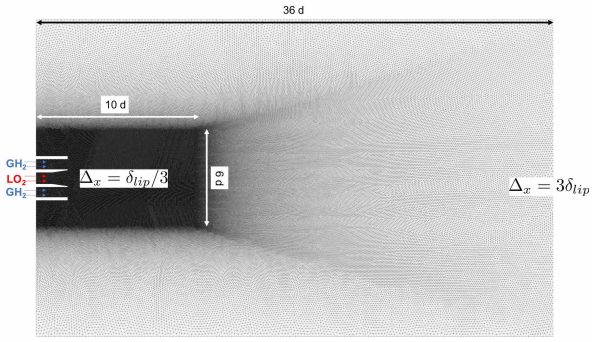

(b) Zoom on the injector

Figure 6.3: Computational domain and grid distribution for the two-dimensional simulations. d refers to the inner injector diameter, δ_{lip} is the inner injector lip thickness and Δ_x is the characteristic cell size.

Walls are treated using adiabatic slip wall-law boundary condition [Schmitt et al., 2007]. The inlet and outlet conditions both use non-reflecting characteristic boundary conditions, with a relaxation on the pressure at the exit boundary condition [Poinsot and Lele, 1992]. Turbulent velocity fluctuations are superimposed to the bulk flow at the injection on both oxygen and fuel streams [Kraichnan, 1970, Smirnov et al., 2001] following turbulent injection profiles from prior pipe flow calculations and a Passot-Pouquet spectrum.

6.2.2.2 3-equation and 4-equation models with simplified equilibrium

Instantaneous fields of the density, temperature, oxygen mass fraction and axial velocity for the 3-equation model assuming simplified equilibrium are shown in figure 6.4. Since the results from the 4-equation model simulation are qualitatively similar, they are not shown here. Because of the strong shear produced by the high velocity outer hydrogen jet, the inner high density jet features a large scale motion, similar to a flag in the wind, and is quickly mixed with the surrounding gas. Despite the high velocity and density difference between the two streams, the simulation remains stable and no numerical crashes have been experienced. However, disabling the sub-grid scale model rapidly stops the simulation after few iterations.

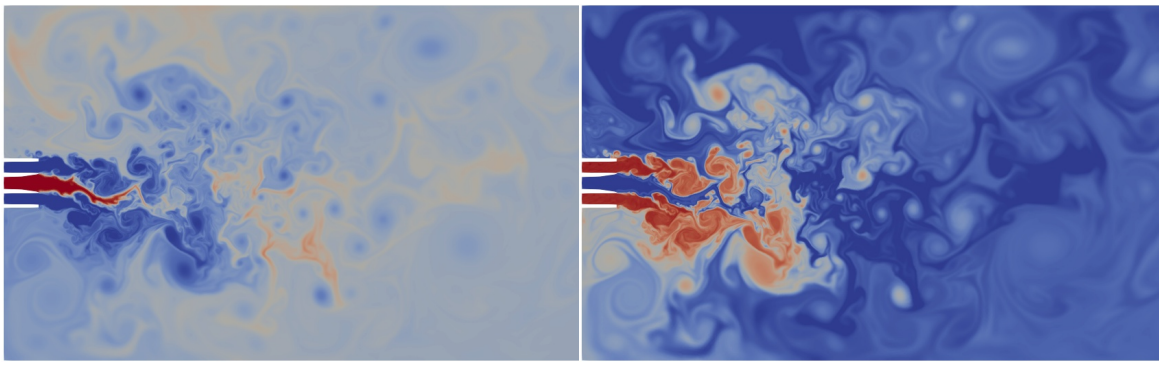

(a) Density (b) Temperature

(c) Oxygen mass fraction (d) Axial velocity

Figure 6.4: Two-dimensional simulation for the 3-equation model. Instantaneous fields of density (blue: 1 kg/m^3, red: 1 200 kg/m^3, log scale), temperature (blue: 80 K, red: 300 K), oxygen mass fraction (blue: 0, red: 1) and axial velocity (blue: -300 m/s, red: 500 m/s).

The thermodynamic behavior of the 3-equation and 4-equation models are now compared performing scatter plots of temperature and species mass fraction in terms of density in figure 6.5. As expected, since the thermodynamic closure is the same for both formulations, results are similar and the equilibrium temperature in the interface is found to be around 95 K. A small amount of hydrogen (0.02 in mass fraction) penetrates the liquid / gas interface. The results for the 4-equation model are less scattered than the ones for the 3-equation model. While the reason for this is not so clear, this behavior is attributed to the slightly noisier nature of the 3-equation model compared with the 4-equation one (see chapter 7). This could be due to the difference in sound speeds in the interface between the two models, which are used for the advection step of the scheme.

The two models however generate non-physical pressure fluctuations of large amplitude, as shown in the pressure scatter plot in figure 6.6. The 3-equation model produces slightly larger pressure

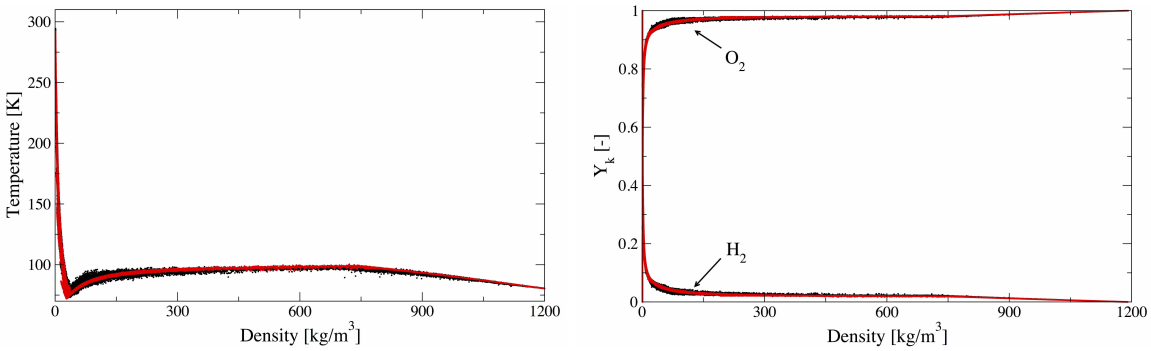

Figure 6.5: Scatter plots of temperature (top) and species mass fraction (bottom) against density. Black: 3-equation model, red: 4-equation model.

perturbations. These perturbations are particularly strong on the liquid side (where the density is larger than 750 kg/m^3) for both models and for density between 50 and 300 kg/m^3 for the 3-equation model. An instantaneous field of pressure for the 3-equation model is shown in figure 6.7. Surprisingly, these oscillations does not seem to strongly affect the jets. This might be due to the very high frequency content of this noise, to which the jet is not sensitive. It should also be noted that this noise remains confined in the high density jet and does not notably pollute the rest of the chamber.

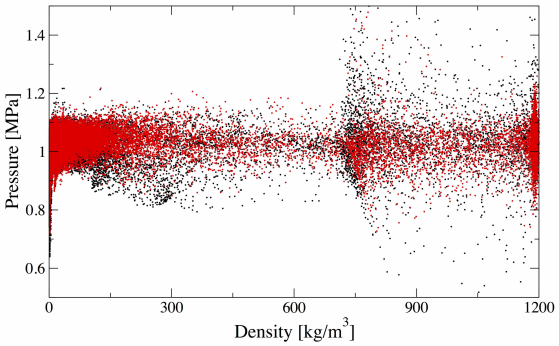

Figure 6.6: Scatter plot of pressure against density. Black: 3-equation model, red: 4-equation model.

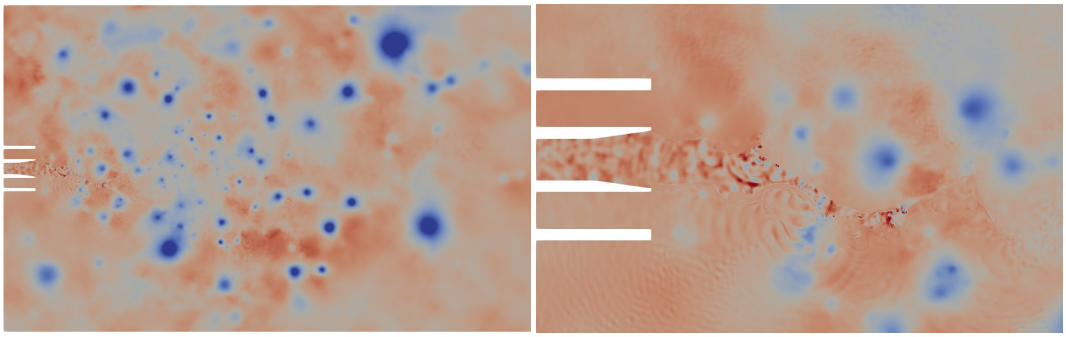

(a) Large scale view.

(b) Zoom in the near injector region, in the high density jet.

Figure 6.7: Two-dimensional simulations for the 3-equation model. Instantaneous pressure fields (blue: 0.8 MPa, red: 1.2 MPa).

Finally, average profiles are plotted in Figs. 6.8 and 6.9. Because of the low frequency motion of the inner jet and flow separation in the injector, a perfect statistical convergence is difficult to reach. However, the longitudinal and radial profiles of density, temperature and axial velocity are similar between the 3-equation and 4-equation models, indicating the methods lead to the same final results.

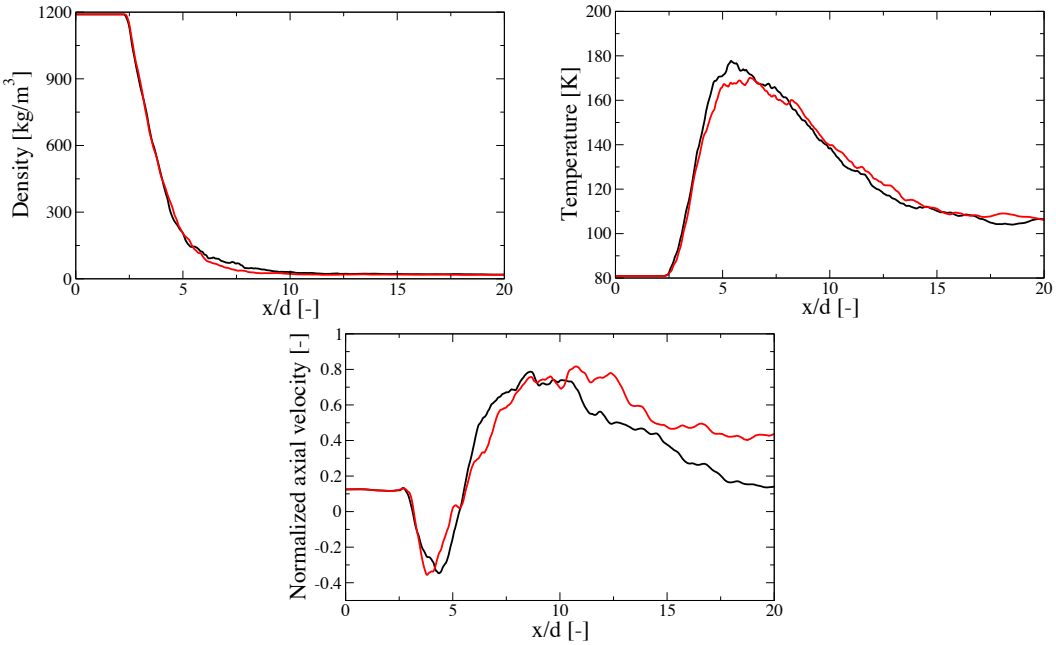

Figure 6.8: Longitudinal profiles of average density and temperature. Black: 3-equation model, red: 4-equation model. x is the axial distance from the inlet.

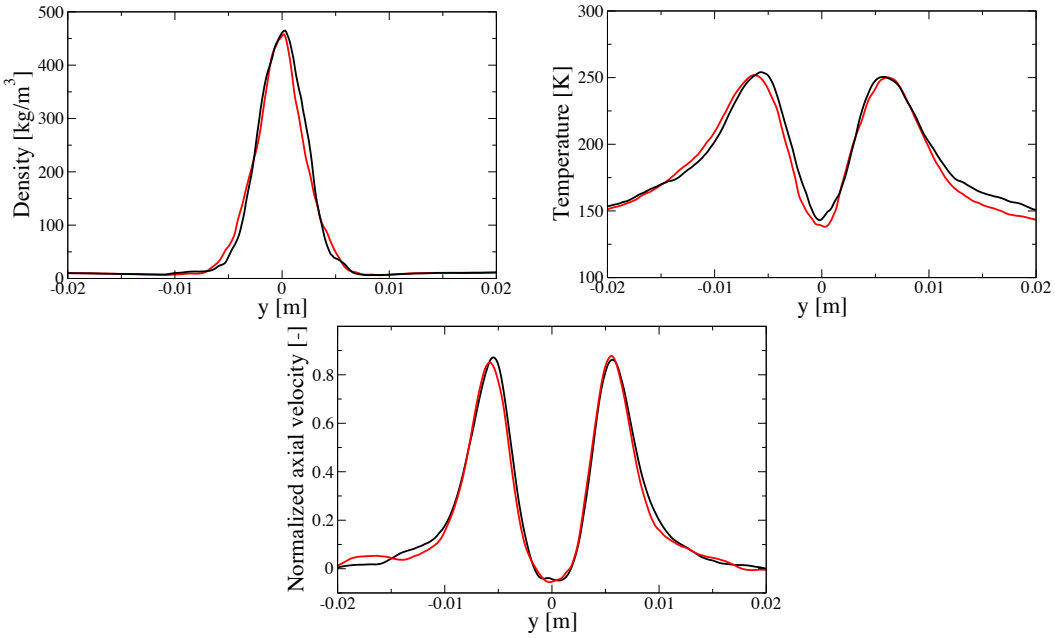

Figure 6.9: Radial profiles of average density and temperature near the injector exit. Black: 3-equation model, red: 4-equation model. y is the radial coordinate.

6.2.2.3 Exact multicomponent equilibrium calculations

The 4-equation model is now used, in order to provide comparisons between the simplified and the exact multicomponent equilibrium formulations. It is worth mentioning that the computations using the exact equilibrium were much more difficult to achieve than the one with the simplified one. First, the total CPU cost of the simulation is increased by a factor 10, even though only 2 species were considered. Although the routine as not been the object of thorough optimization, the complexity of the calculations involved in the exact equilibrium (see chapter 2) is responsible for this high computational cost. It is thus expected that complex cases including dozens of species will be out of reach in realistic configurations. Second, convergence issues have been encountered in the equilibrium loop, which had to be fixed. For these reasons, the calculations presented here are not fully converged so that only qualitative conclusions can be drawn.

Scatter plots of temperature and species mass fraction against density are shown in figures 6.10a and 6.10b, for both the simplified and exact equilibrium formulations. The amount of hydrogen that penetrates the interface is observed to be lower in the simulation with the exact equilibrium than with the simplified formualtion. This behavior only results from the equilibrium closure and not from species diffusion as complex species diffusion is not accounted for in the sub-grid scale model (and is however the same for the two closures). As species diffusion could not be responsible for this behavior, species advection is expected to be the leading contribution, *a priori* because of a modification of the pressure in the interface due to the modified thermodynamic closure. The temperature within the interface is also different (around 90 K for the exact equilibrium), this difference being however limited. The pressure-density scatter plot of figure 6.10c indicates than the exact equilibrium model seems to produce pressure fluctuations that are comparable to those of the simplified equilibrium one.

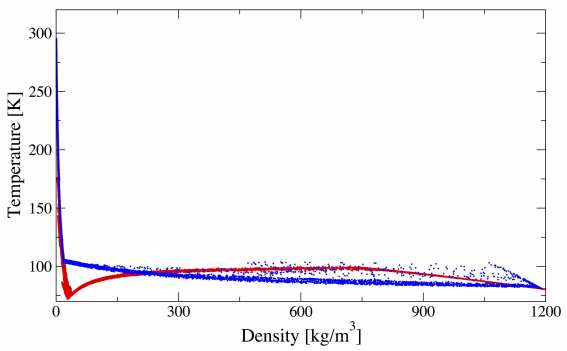

(a) Temperature *vs.* density

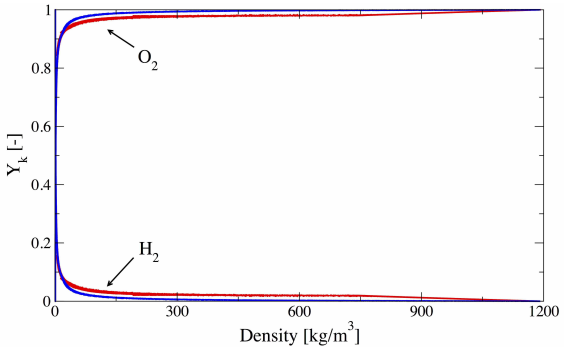

(b) Species mass fraction *vs.* density

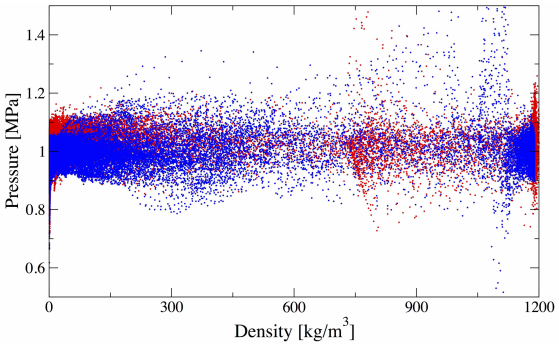

(c) Pressure *vs.* density

Figure 6.10: Scatter plots for the 4 equations model with simplified equilibrium (red) and full equilibrium (blue).

6.2.2.3.1 Conclusions

The simulations allowed to observe that the exact equilibrium provides globally a similar behaviour to the simplified equilibrium, although some differences are found within the interface, in particular regarding the penetration of H_2 within the liquid jet and the temperature within the interface. The simulation using the exact equilibrium formulation is yet much more difficult to compute, especially regarding its very high computational cost.

The approximate equilibrium is finally considered satisfying regarding an application to the Mascotte configuration. It will now be used to carry out a three-dimensional numerical simulations.

6.2.3 Reactive three-dimensional simulation on a coarse grid

The 3-equation model with the simplified equilibrium is now applied to the three-dimensional simulation of the reactive configuration Mascotte A10, using the models presented in section 6.1.2. The main objective of this calculation is to assess the performance of the model on a realistic configuration with experimental data. For this three-dimensional calculation, a coarse grid is considered and the numerical strategy that is typically used for transcritical flows is followed [Schmitt, 2009].

6.2.3.1 Mesh, boundary conditions and numerical setup

The simulation domain and the grid distribution are shown in figure 6.11a. It exactly corresponds to the one from the experiment, except that the outlet nozzle is replaced with an outlet where the pressure is imposed. A view of the mesh in the near injector region is provided in figure 6.11b. The mesh is refined just behind the lip, with 3 cells in the thickness. There are around 15 cells in each injector diameter. The grid contains 700 000 nodes and 3 800 000 triangles.

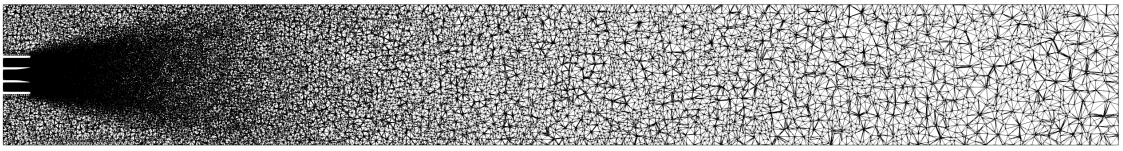

(a)

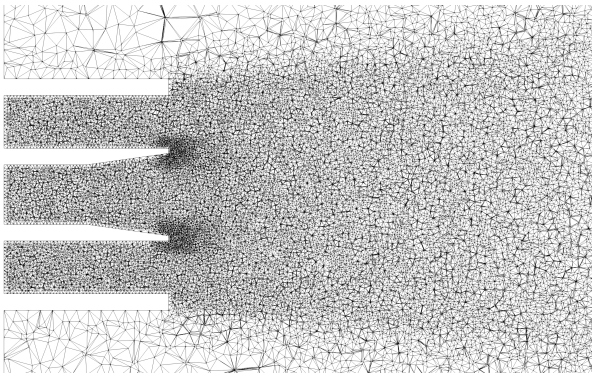

(b)

Figure 6.11: Computational domain and grid distribution for the three-dimensional reactive simulation.

As for the two-dimensional cases, the walls are treated using adiabatic slip wall-law boundary condition [Schmitt et al., 2007]. The inlet and outlet conditions are both set with non-reflecting characteristic boundary conditions, with a relaxation on the pressure at the exit boundary condition [Poinsot and Lele, 1992]. Turbulent velocity fluctuations are superimposed to the bulk flow at the injection on both

oxygen and fuel streams [Kraichnan, 1970, Smirnov et al., 2001] following turbulent injection profiles from prior pipe flow calculations and a Passot-Pouquet spectrum.

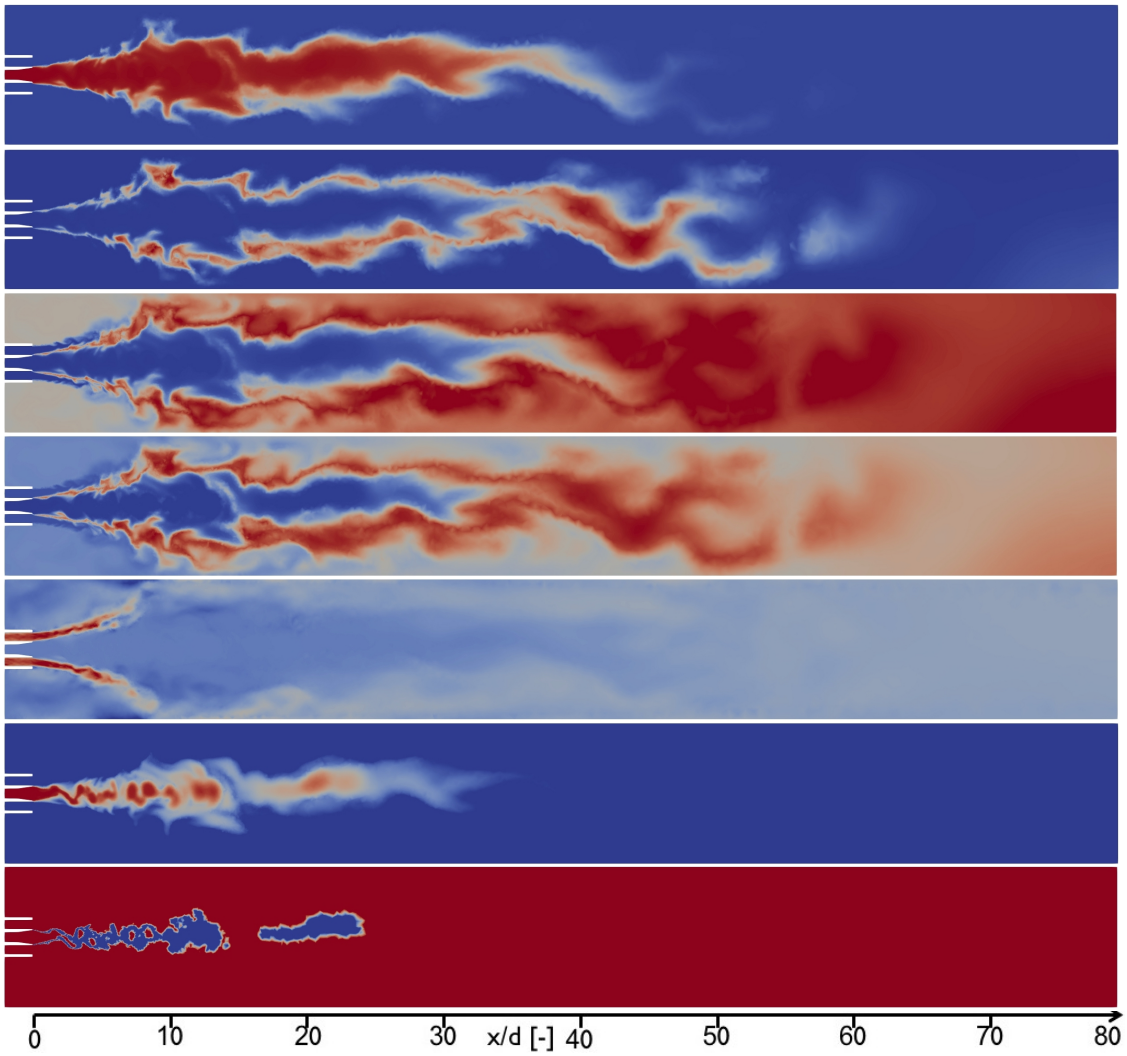

Figure 6.12: Instantaneous fields for the three-dimensional simulation using the 3-equation model with simplified equilibrium. From top to bottom: O_2 mass fraction Y_{O_2} (blue: 0, red: 1); OH mass fraction Y_{OH} (blue: 0, red: 0.05); H_2O mass fraction Y_{H_2O} (blue: 0, red: 0.75); temperature (blue: 80 K, red: 3300 K); axial velocity (blue: -100 m/s, red: 400 m/s). density (blue: 1 kg/m^3, red: 1200 kg/m^3, log scale); stability criterion (blue: unstable, red:stable)

6.2.3.2 Results and discussion

6.2.3.2.1 Flow visualization: snapshots

Instantaneous fields of representative flow variables (temperature, O2, OH and water mass fractions, axial velocity and density) are shown in figure 6.12. They qualitatively show the flame topology and flow dynamics. A turbulent diffusion flame is formed at the exit of the coaxial injector and surrounds the high density inner jet. The confinement of the flow by the walls produces a sudden opening of the flame at 10d (d being the inner injector diameter) and the formation of a recirculation region between the flame and the inner high density jet. Large scale motions are noticeable further downstream. Such a flame topology is similar to the ones computed at supercritical pressure [Schmitt, 2019]. The region

of two-phase coexistance is shown on the bottom field in figure 6.12. As the inner jet is destabilized, large scale regions are thermodynamically unstable. They disappear as the oxygen mixes and burns with the surrounding gases.

6.2.3.2.2 Flow visualization: average fields

The previous observations are confirmed looking at the average fields in figure 6.13. They are computed over a simulation of 70 ms of physical time.

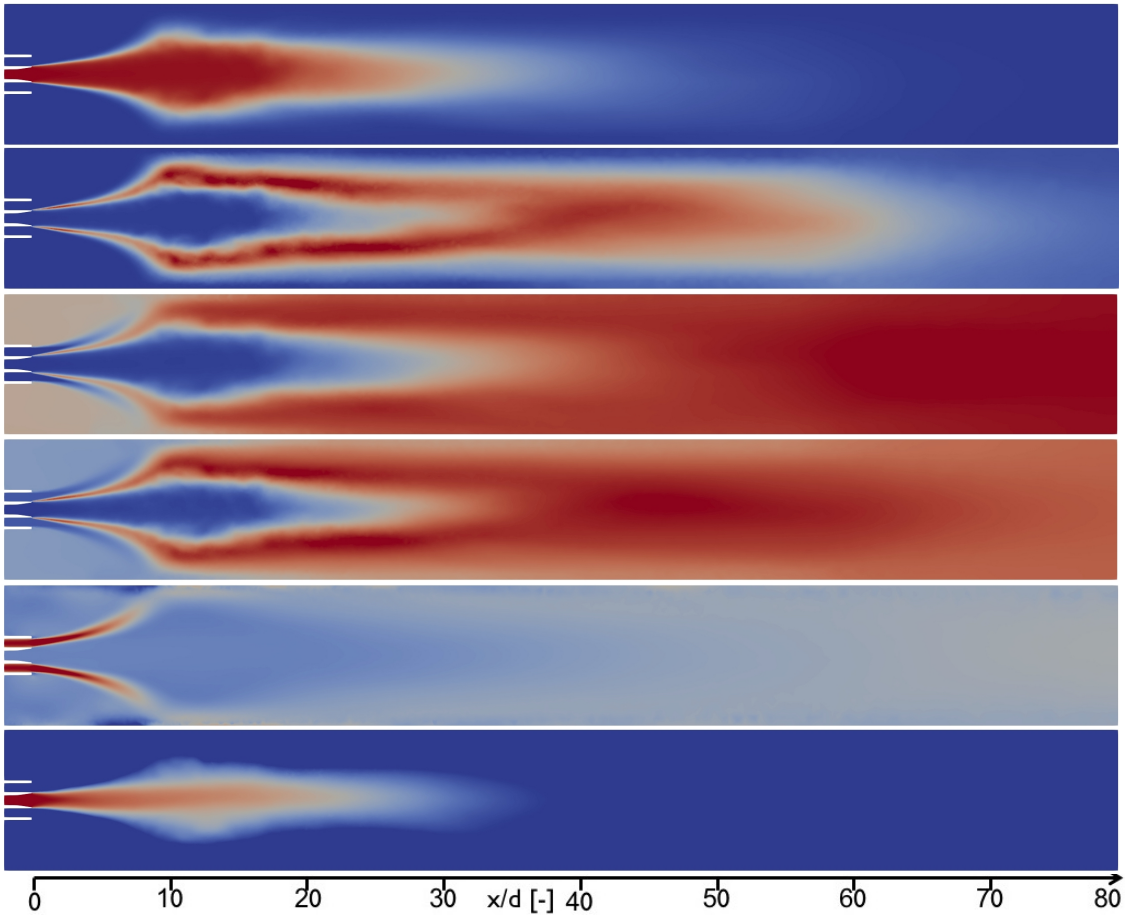

Figure 6.13: Mean fields for the reactive three-dimensional simulation using the 3-equation model with simplified equilibrium. From top to bottom: O_2 mass fraction Y_{O_2} (blue: 0, red: 1); OH mass fraction Y_{OH} (blue: 0, red: 0.05); H_2O mass fraction Y_{H_2O} (blue: 0, red: 0.75); temperature (blue: 80 K, red: 2500 K); axial velocity (blue: -100 m/s, red: 350 m/s). density (blue: 1 kg/m^3, red: 1200 kg/m^3, log scale);

6.2.3.2.3 Thermodynamics

In order to investigate the thermodynamic regime in the flow, scatter plots of temperature and species mass fraction are plotted in terms of density in figure 6.14. The saturation temperature is found to be close to 125 K. A small amount of water is present in the interface. However, the interface is essentially constituted of pure oxygen.

As for the two dimensional simulations, large pressure noise is present in this simulation, in particular in the liquid phase. A scatter plot of pressure is shown in figure 6.15a. Pressure fluctuations are

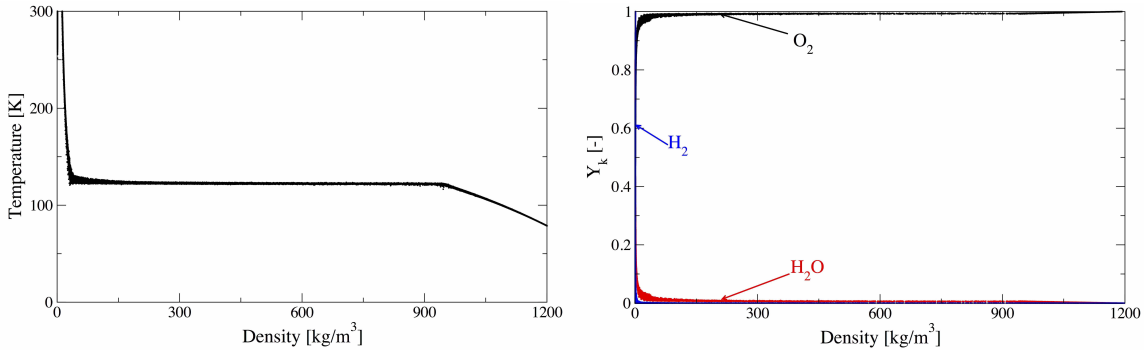

(a) Temperature *vs.* density

(b) Species mass fractions *vs.* density

Figure 6.14: Scatter plots of temperature and species mass fraction against density for the reactive simulation.

strongly increasing at the transition from the interface to the pure liquid phase ($\rho \approx 950$ kg/m^3), and are mostly present within the liquid phase, as also evidenced by figure 6.15b. Again, the fluctuations do not seem to notably impact the inner jet dynamics.

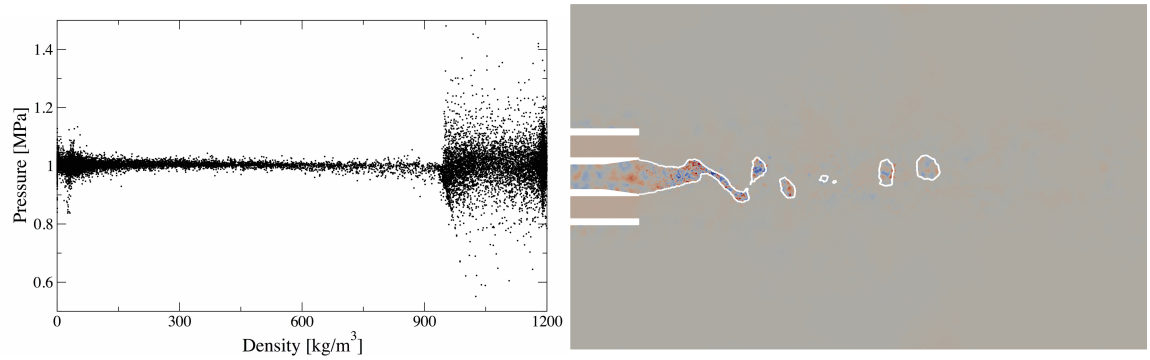

(a) Scatter plot of pressure against density

(b) Instantaneous pressure field. Blue: 0.8 MPa, red: 1.2 MPa

Figure 6.15: Analyses of the pressure field. The instantaneous pressure field is displayed with the isocontour $\rho = 950$ kg/m^3, highlighting the presence of spurious noise within the liquid phase.

6.2.3.2.4 Comparison with experimental results

Results are compared with the available experimental data from [Candel et al., 1998]. Figure 6.16 shows an Abel's transform of experimental OH* mean emission, which qualitatively represent the flame location through the excited OH radical. In order to compare the flame position, OH mass fraction iso-contours are superimposed on the same figure. Good agreements are found. It seems that, despite the strong simplifications made in this simulation (no atomization, no surface tension, fast chemistry), the model can already give reasonable results for reactive liquid rocket engine flows.

Temperature radial profiles are now compared with temperature measurements at different axial positions. Results are in reasonable agreements both in terms of mean and rms profiles. However, the large uncertainties associated with these measurements [Candel et al., 1998] limit the scope of this comparison.

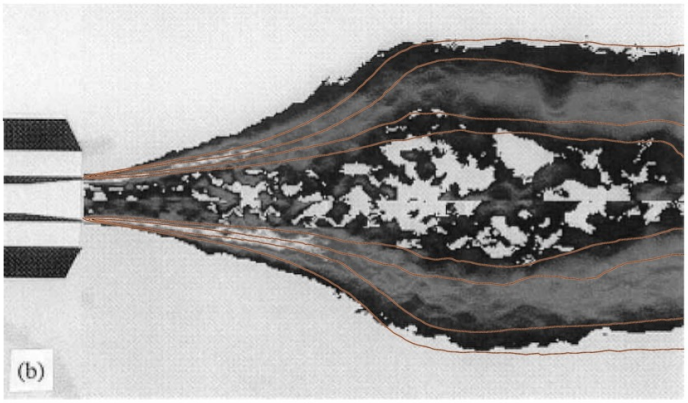

Figure 6.16: Background, in greyscale: Abel's transform of experimental OH* mean emission for the case A10. Red lines: iso-contours of OH mass fraction (0.01 and 0.03) from LES.

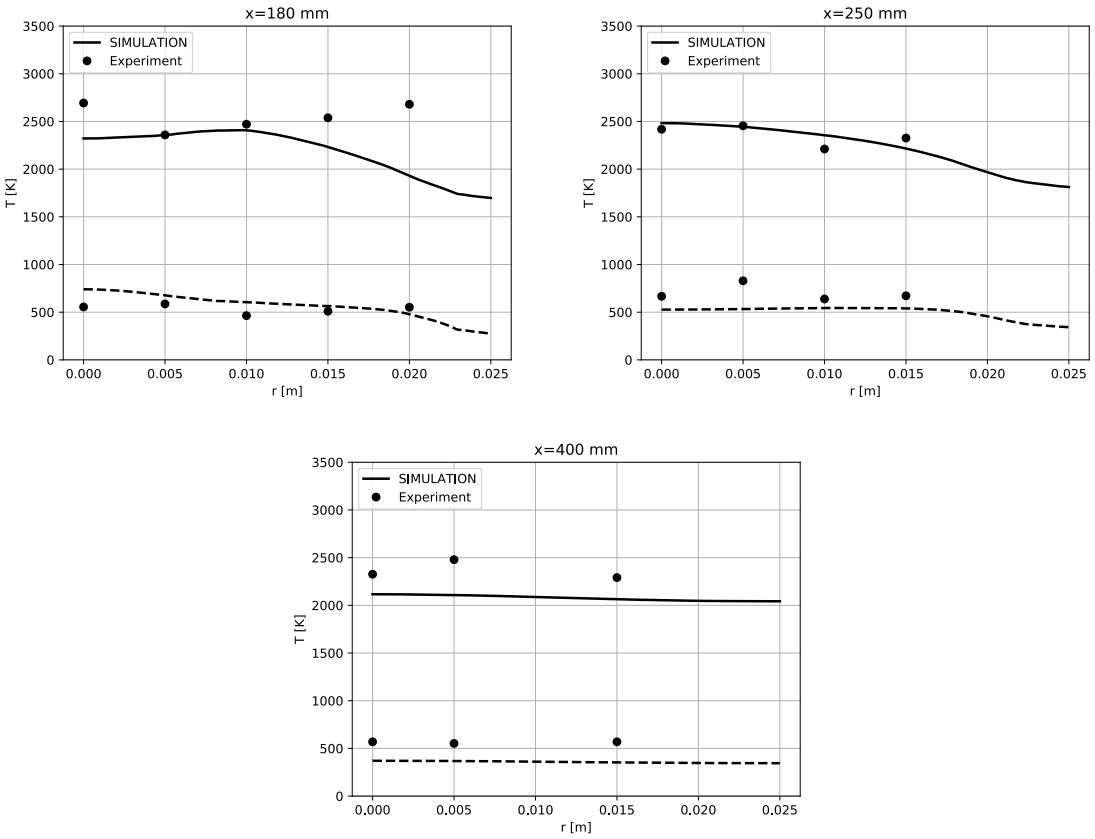

Figure 6.17: Comparison between mean radial temperature profiles from experiments (dots) and LES (continuous lines are Reynolds average temperature and dashed lines are rms temperature).

6.2.3.2.5 Discussion on the model

Modeling the whole process of liquid oxygen jet atomization and vaporization of the droplets in the gaseous mixture of hydrogen and burnt products would require to couple the multifluid model to a

disperse phase model. In the present work, the phase change is directly treated by the 3-equation model, through the phase equilibrium assumption.

The good results obtained by this simplified treatment may be explained by the efficient mixing dynamics of the Mascotte A10 configuration, characterized by its high Weber and Reynolds number values.

The Weber number We is a dimensionless number that compares the drag forces to the surface tension forces, computed as

$$\mathrm{We} = \frac{\rho_{v,0} l_0 (\Delta u)_0^2}{\sigma_0}, \tag{6.2.1}$$

where $\rho_{v,0}$ is the injected gas phase density, l_0 a typical length scale for the liquid jet (chosen here equal to the nozzle diameter), $(\Delta u)_0$ a typical velocity difference responsible for the shear forces and σ_0 the surface tension coefficient. High Weber numbers are observed in flows where the surface tension has negligible effect compared to the drag force, so that the liquid phase cohesion cannot be maintained by the capillary forces. In the Mascotte A10 configuration, the Weber number is $\mathrm{We} \approx 28 \times 10^3$, following [Candel et al., 1998].

The Reynolds number for the liquid jet Re_ℓ is defined as

$$\mathrm{Re}_\ell = \frac{d_0 u_{0,\ell}}{\nu_\ell}, \tag{6.2.2}$$

which for the A10 configuration yields $\mathrm{Re}_\ell \approx 67 \times 10^3$. According to [Chigier and Reitz, 1996, Lasheras and Hopfinger, 2000], the regime associated with this set $(\mathrm{We}, \mathrm{Re}_\ell)$ corresponds to the fiber-typer regime, in which the jet rapidly breaks-up into droplets of diameter several orders of magnitude below the nozzle diameter, see Figure 6.18. The flow topology is thus expected to consist of a thin liquid/gas

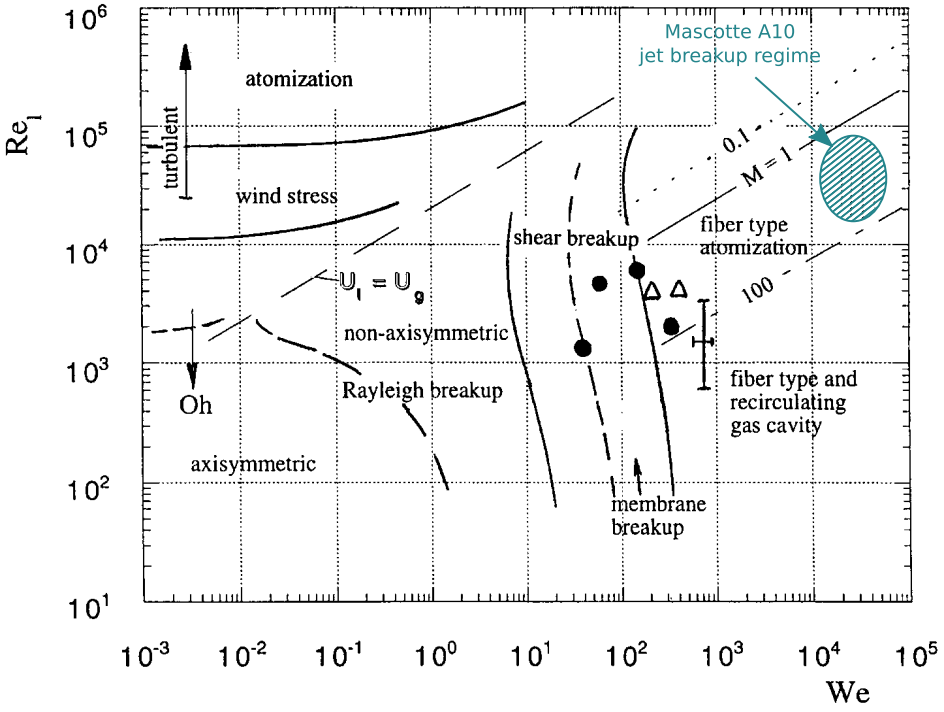

Figure 6.18: Characterization of the different spray regimes in the Re_ℓ-We space. Image taken from [Lasheras and Hopfinger, 2000].

interface that quickly atomizes into very small droplets. Throughout this process, because of the high

Weber number of this configuration, one can expect the intermediate liquid ligaments formed to have a very short lifetime, and quickly break into the small droplets. In this respect, it might be reasonable to neglect the ligament formation and assume that droplets are formed instantaneously.

The obtained spray is then expected to be made up of small (low-inertia) droplets, which can reasonably be assumed to be in mechanical equilibrium with the gas phase. The temperature and thermodynamic equilibrium assumption is more questionable. This hypothesis is expected to have an impact on the vaporization time of the droplets. Yet, this vaporization time is expected to be essentially controlled by the strong heat fluxes induced by the flame, which may lead anyway to a fast evaporation. In the absence of a flame, such assumption should not be acceptable.

Under this simplified modeling, two-phase regions of two different natures are observed in the flow (see Figure 6.12). Near the injector, a thin two-phase region separates liquid and gas phases and corresponds to a diffuse liquid-gas interface representation. Conversely, downstream the liquid core, one may interpret the two-phase *pockets* that are surrounded by gas regions as liquid spray areas. Within such regions, the 3-equation model behaves like a simplified disperse phase model.

Finally, in this simulation, the dynamics are globally dominated by the turbulent fluxes. Although the use of ad-hoc subgrid-scale terms for the two-phase region would improve the accuracy of the simulation, the use of pure-phase turbulent closures even in the "disperse" two-phase regions may be satisfying since the droplets are expected to always remain close to the mechanical equilibrium with the carrier phase.

6.2.3.3 Conclusions

This study, based on the Mascotte configuration of ONERA, allowed to illustrate the behaviour of the multifluid models and their implementation on a realistic case. First, two-dimensional simulations using the simplified two-phase equilibrium formulation allowed to compare the behaviour of the 3-equation model against the 4-equation model with stiff relaxation towards thermodynamic equilibrium. Very similar results have been obtained for these two computations. Then, computations using the exact and simplified multicomponent two-phase equilibrium formulations have been presented. The approximate equilibrium provided satisfying results, close to the exact equilibrium formulation. Subsequently, the computation of a three-dimensional subcritical reactive case was carried out, allowing for comparisons with experimental data. Despite the simplifications made in this computation, the results were in good agreement with the experiments. These results are finally very encouraging regarding the application of the proposed methodology to liquid rocket engine simulations.

6.3 The Spray-A configuration of the Engine Combustion Network (ECN)

The Spray-A configuration is considered in this section (`https://ecn.sandia.gov/`). This setup mimics a Diesel injection in a high pressure chamber, up to 60 bar. The main experimental objectives are to understand the dynamics of Diesel spray injection, its auto-ignition, and eventually to give access to detailed experimental measurements for code validations. The case under consideration in this section is the one operating at 60 bar.

The 3-equation model with the simplified equilibrium is applied here for the non-reacting case using the models presented in section 6.1.2. As for the Mascotte test-case, the main objective of this calculation is to assess the performance of the model on a realistic configuration with experimental data. The thermodynamic regime of Spray-A differs from Mascotte case. The pressure is now larger than the critical pressure of the injected fuel and injection is *transcritical*. However, a two-phase flow transition may occur because of multicomponent mixing [Matheis and Hickel, 2018] and the depressions involved by the strong dynamics encountered in this flows.

The dynamics of this case also strongly departs from the one of the Mascotte configuration. Injection velocity is much larger for Spray-A (600 m/s vs less than 10 m/s for Mascotte) which implies new numerical issues. In particular, the non-linear thermodynamics used here are known to generate spurious pressure oscillations in the presence of density gradients [Pantano et al., 2017, Lacaze et al., 2019]. Such errors may become large when the flow velocity is high, as for the Spray-A case. This noise is augmented in the presence of unstructured grid, since the grid points are not initially aligned with the flow direction at the injector exit. One solution to limit this issue is to use a non conservative formulation [Ma et al., 2019], but at the price of large error on temperature [Lacaze et al., 2019].

For this configuration, a first approach had been considered, using the mere Navier-Stokes equations closed by a cubic EoS (instead of the 3-equation model which addresses the possible two-phase states). Yet, this computation using a fully conservative approach was found to be unstable. Indeed, at the location of the pressure fluctuations generated during the jet destabilization, unstable thermodynamic states lying in the spinodal zone occurred. For these states, the cubic EoS yielded incorrect values for the thermodynamic quantities, leading to a crash of the computation. The idea here is then to stabilize the simulation by computing two-phase equilibrium using the simplified equilibrium formulation, when unstable states are found.

6.3.1 Experimental setup

The chamber consists in a $108 \times 108 \times 108$ mm^3 cubic box at 60 bar. It is initially filled with 87.7% Nitrogen, 10% carbon dioxyde and 2.3% water in mass at 900 K. Fuel (n-dodecane: $C_{12}H_{26}$) is injected at $T_{\text{inj}} = 360$ K through a small injector with a diameter of 0.09 mm displayed in figure 6.20b. The injection mass flow rate versus time is plotted in figure 6.19.

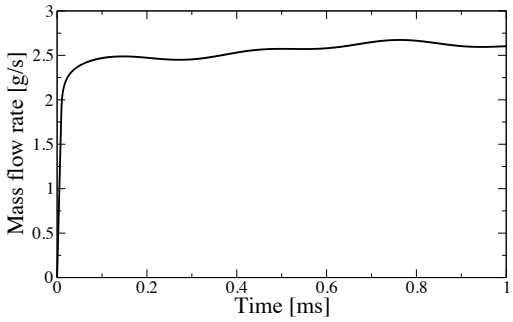

Figure 6.19: Injection mass-flow rate over time.

6.3.2 Mesh, boundary conditions and numerical setup

The simulation domain and the grid distribution are shown in figure 6.20a. The injector diameter and the chamber geometry exactly correspond to those of the experimental setup. A portion of the injector has been included, in order to avoid the issue of defining a proper injection profile (which might not be fully turbulent) at the injector exit. A view of the mesh in the near injector region is provided in figure 6.20b. There are around 15 cells in the injector diameter. The grid contains 4 400 000 nodes and 25 000 000 tetrahedra. 25 000 000 The walls are treated using adiabatic slip wall-law boundary conditions [Schmitt et al., 2007]. The temperature and the mass-flow rate are imposed at the inlet by means of characteristic boundary conditions [Poinsot and Lele, 1992].

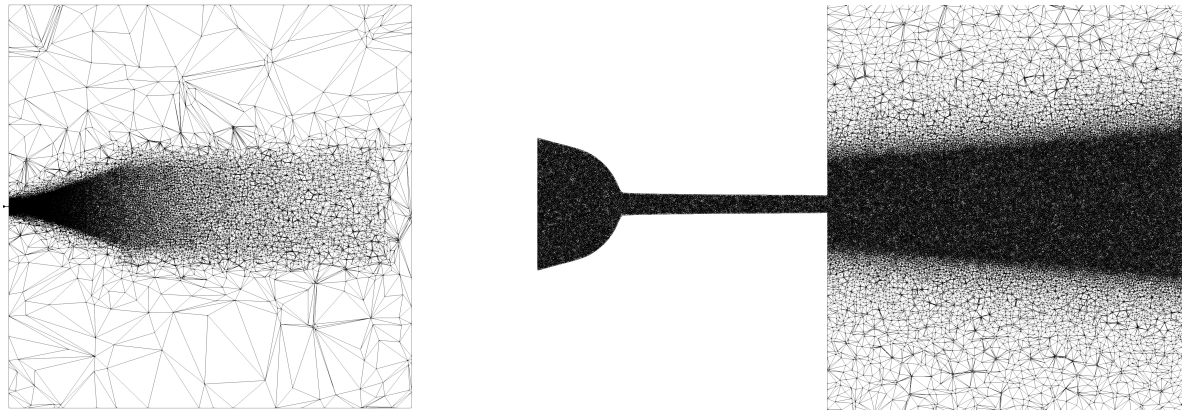

(a) Overview (b) Zoom on the injector

Figure 6.20: Computational domain and grid distribution for the Spray A configuration.

6.3.3 Flow visualizations

Instantaneous flow visualizations at 0.5 ms are shown in figure 6.21. The jet gets quickly destabilized and a fully turbulent stream is observed. Injection velocity is found to be close to 700 m/s and density varies from 650 kg/m^3 at injection to 21 kg/m^3 in the chamber. The pressure field in the vicinity of the injector is displayed in figure 6.22a. Very large amplitude pressure fluctuations are present (more than 50 bar !). Unstable regions are found in the location of these fluctuations. This behavior does not seem physical, and might be caused by numerical errors coupled with the non-linear thermodynamics used here.

6.3.4 Comparison with experimental data

Instantaneous results are now compared with experimental shadowgraphs from Pickett et al. [Pickett et al., 2011] in figure 6.23. Temperature fields are used for the comparison. The jet topology is qualitatively well retrieved, the maximum positions are in good agreement, although the spreading angle seems slightly over-predicted in the simulation.

The jet penetration can then be quantitatively compared with the experimental measurements from Sandia and IFP-EN in figure 6.24. The jet penetration is slightly under-predicted. Finally, the mean longitudinal profiles of $Y_{C_{12}H_{26}}$ and temperature are compared with experimental measurements in figure 6.25. The jet length is under-predicted regarding the experiments. It seems that the initial destabilization is occuring too fast, probably because of the strong pressure activity in the near injector region.

6.3.5 Conclusions on the Spray A simulation

This study allowed to confront the modeling strategy with a configuration involving very strong dynamics. The use of the 3-equation model with simplified equilibrium allowed to stabilize the computation by computing two-phase equilibrium when unstable states were met. The flow topology was found to be qualitatively satisfying regarding the experiments. Nonetheless, very strong pressure fluctuations were encountered, certainly due to numerical errors. These fluctuations are suspected to cause the destabilization of the jet too early, resulting in the underestimation of the jet penetration compared to experimental data.

For this configuration, it would be interesting to investigate the behaviour of the exact multicomponent

(a) $C_{12}H_{26}$ mass fraction $Y_{C_{12}H_{26}}$ (blue: 0, red: 1)

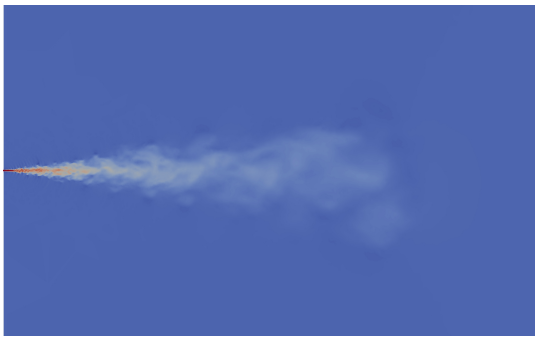

(b) Axial velocity (blue: −100 m/s, red: 700 m/s)

(c) Density (blue: 21 kg/m^3, red: 650 kg/m^3, log scale)

(d) Temperature (blue: 360 K, red: 920 K)

Figure 6.21: Instantaneous fields for the simulation of case Spray-A.

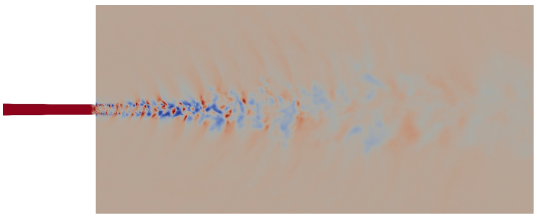

(a) Pressure (blue: 10 bar, red: 100 bar)

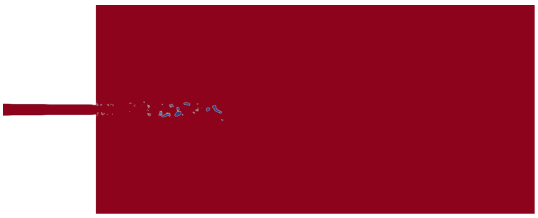

(b) Thermodynamic stability flag (blue: unstable, red: stable)

Figure 6.22: Instantaneous fields for the simulation of case Spray-A in the vicinity of the injector.

equilibrium computation. Yet, given the number of species involved and the high computational cost of this closure, this would require first to thoroughly optimize the equilibrium solver and add thresholds and simplification hypotheses as in [Matheis and Hickel, 2018] to limit the amount of equilibrium computations.

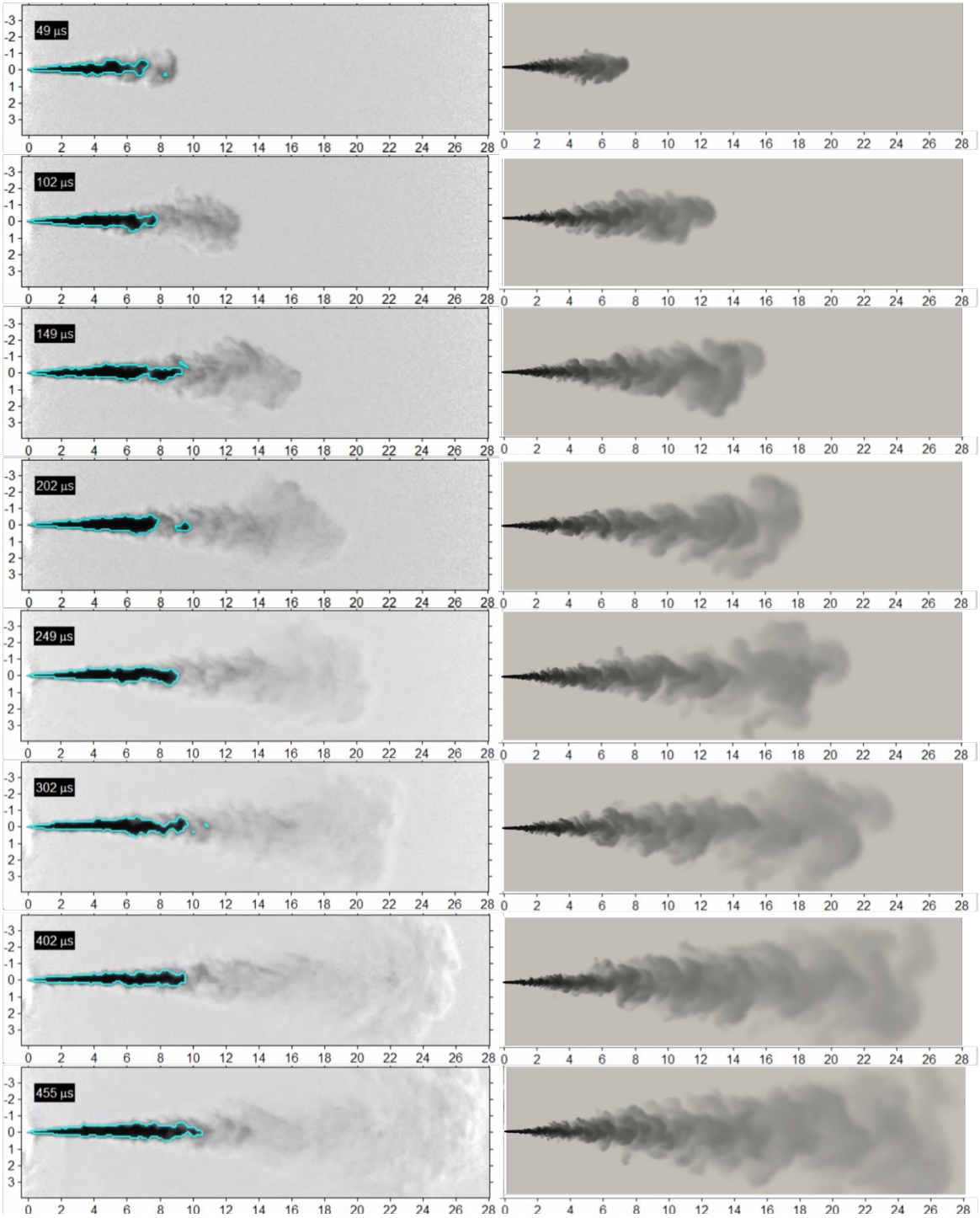

Figure 6.23: Comparison of instantaneous temperature fields (right) with experimental shadowgraphs from [Pickett et al., 2011] (left).

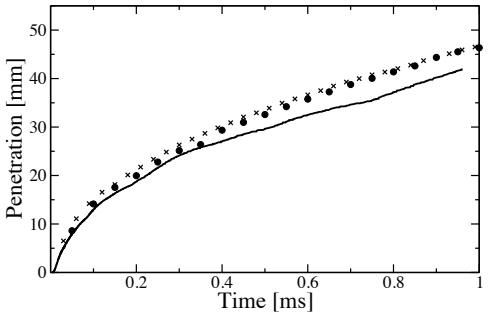

Figure 6.24: Comparison of jet penetration from LES (computed as the maximum position where $Y_{C12H_{26}} > 0.01$) against experimental measurements from (×) Sandia and (•) IFP-EN.

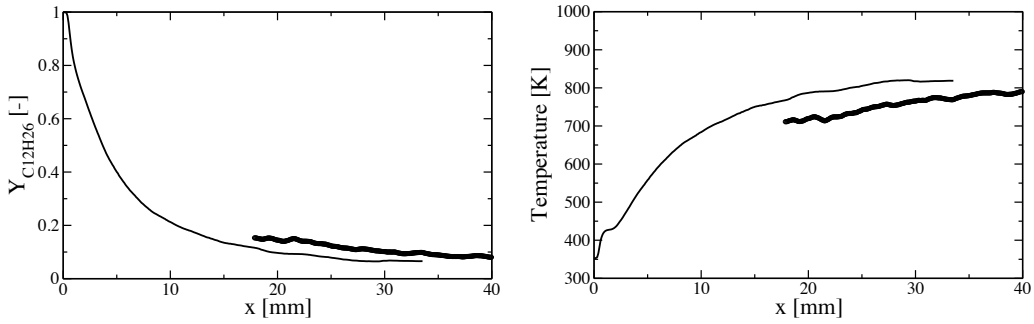

(a) $C_{12}H_{26}$ mass fraction (b) Temperature

Figure 6.25: Longitudinal mean profiles. − LES, ∘ Experiments.

6.4 Conclusion

This chapter presented the global modeling and numerical strategies, and their application to realistic configurations. The first study was led on the Mascotte A10 case. Two-dimensional configuration have been simulated, in order to compare the behaviour of the 3- and 4-equation models, and to provide comparisons between the simplified and exact multicomponent equilibrium formulations. The two models exhibited similar results, and the simplified equilibrium formulation was found to be satisfyingly close to the exact one. Relatively strong pressure oscillations were noticed, in particular in the liquid phase, for both the 3- and 4-equation models, and for both equilibrium formulations. Also, it is worth mentioning that the exact equilibrium formulation was observed to be much more expensive than the simplified equilibrium formulation, increasing the total CPU cost by a factor 10. In this respect, the subsequent three-dimensional reactive calculation has been led using the 3-equation model with the simplified multicomponent equilibrium. The results obtained were in good agreement with the available experimental data, which is very encouraging regarding the strategy adopted. Finally, the ECN *spray A* Diesel injection configuration was studied. A three-dimensional computation was led using the simplified multicomponent equilibrium formulation. The results were qualitatively similar to the experimental snapshots. Yet, the jet penetration was underestimated by the computation. This was attributed to an anticipated destabilization of the jet due to strong pressure oscillations, attributed to a coupling between the strong dynamics and the numerical errors on the pressure field.

The results were found to be globally encouraging. Obviously, a lot of improvements can be brought to the model, but relatively good results were obtained. Yet, the strong pressure noise observed motivated a closer study of the spurious pressure noise in the framework of multifluid models. This is the object of the next chapter.

Chapter 7

Pressure noise and multifluid methods

This chapter is dedicated to the study of the behaviour of different multifluid models when advecting an liquid-gas interface. In particular, the generation of spurious pressure noise is examined. This is motivated by the spurious pressure oscillations observed for the Mascotte and Spray A simulations of the previous chapter. For each of the 5-, 4- and 3-equation models, their formulation and properties are recalled. A common basis of numerical test cases is defined, to evaluate the behaviour of the different models. The tests are made using a similar numerical method in order to provide relevant comparisons.

7.1 Introduction

The present chapter focuses on the effective behaviour of the multifluid models regarding the transport of a contact discontinuity. Such problem is characteristic of the transport of a droplet (or a bubble) within a two-phase flow. The underlying purpose of this chapter is to evaluate the ability of the different reduced multifluid models to fulfill the following physical principle: *"the transport of a contact discontinuity – typically a liquid-vapour interface – within a flow of initially homogeneous pressure and velocity fields should not produce pressure and velocity oscillations."* Such condition has driven various works, see e.g. [Abgrall, 1996, Abgrall and Karni, 2001], which most often resulted in the formulation of a non-conservative resolution of the flow.

For this purpose, the formulation of the reduced multifluid models – from the 5- to the 3-equation models – is briefly recalled. In particular, details of the implementation are highlighted in order to provide the necessary information to perform numerical experiments. For each model, test cases are run considering the transport of an entropy perturbation with initially homogeneous pressure and velocity flows. Additional test cases are run to highlight other specific features of the different models.

The chapter is organized as follows. First, the 5-equation model is presented in section 7.2 and the corresponding numerical experiments are provided. Then, the 4-equation model is studied in section 7.3.1. Section 7.4 presents the 3-equation model and its comparison with the previous models. In particular, the 3-equation model is also compared with the 5-equation and 4-equation models applied in combination with a stiff relaxation towards homogeneous thermodynamic equilibrium.

7.2 The 5-equation model

7.2.1 Brief presentation of the model

Historically, the five-equation model was formulated by [Kapila et al., 2001] as a reduction of the 7-equation model of [Baer and Nunziato, 1986]. This model corresponds to a further simplification of the 7-equation solver with instantaneous relaxation to equilibrium proposed in [Saurel and Abgrall, 1999]. It corresponds to the asymptotic model towards which tends the 7-equation model when assuming the pressure P and velocity u to be equal at all times in both phases. Such simplifications allow to elude the questions regarding the definition of the interface pressure and velocity and their impact on the mathematical structure of the model, as mentioned in section 3.3.2.1.1. This model was initially formulated for applications to granular materials, as was the model of [Baer and Nunziato, 1986].

Subsequently, a similar model has been proposed by [Allaire et al., 2002] in the context of diffuse interface two-phase models. Formally, the only difference between these two models reduces to the source term appearing in the compaction equation given in (3.3.12e). Yet, the major evolution is conceptual in the sense that this model applies to the simulation of separate two-phase flows, similarly as how [Saurel and Abgrall, 1999] extended the use of the 7-equation model of [Baer and Nunziato, 1986]. Following this direction, [Murrone and Guillard, 2005] proposed a detailed derivation of Kapila's Model and appropriate numerical methods to handle the compaction equation. As the compaction equation (3.3.12e) boils down to an equivalent form in the context of a homogeneous pressure and velocity flow, it is simpler to consider here the five-equation model of Allaire, which reads

$$\begin{cases} \dfrac{\partial \rho y_v}{\partial t} + \dfrac{\partial \rho y_v u}{\partial x} = 0, & \text{(7.2.1a)} \\ \dfrac{\partial \rho y_\ell}{\partial t} + \dfrac{\partial \rho y_\ell u}{\partial x} = 0, & \text{(7.2.1b)} \\ \dfrac{\partial \rho u}{\partial t} + \dfrac{\partial \rho u^2 + P}{\partial x} = 0, & \text{(7.2.1c)} \\ \dfrac{\partial \rho e_\mathrm{t}}{\partial t} + \dfrac{\partial \left(\rho e_\mathrm{t} + P\right) u}{\partial x} = 0, & \text{(7.2.1d)} \\ \dfrac{\partial z_\ell}{\partial t} + u \dfrac{\partial z_\ell}{\partial x} = 0. & \text{(7.2.1e)} \end{cases}$$

This system is also referred to as the five-equation *transport* model in [Murrone and Guillard, 2005].

7.2.2 Practical implementation

7.2.2.1 Numerical method

The dedicated first-order numerical method for the 5-equation model (7.2.1), taken from [Allaire et al., 2002], is now briefly described. The reader is referred to this latter paper for more information. As this model features both conservative and non-conservative transport equations, the numerical scheme description is split into two parts. The conservative part is discretized using a finite-volume method, while the compaction equation is described with an ad-hoc upwind scheme.

7.2.2.1.1 Conservative part

The conservative variables are defined as $\mathbf{U}_c = [z_\ell \rho_\ell, z_v \rho_v, \rho u, \rho e_\mathrm{t}]^t$. The update follows a classic Godunov-like scheme formulation:

$$\mathbf{U}_{c_i}^{n+1} = \mathbf{U}_{c_i}^{n} - \frac{\Delta t}{\Delta x} \left(\mathbf{F}_{i+\frac{1}{2}}^{n} - \mathbf{F}_{i-\frac{1}{2}}^{n} \right). \tag{7.2.2}$$

Following [Allaire et al., 2002], the numerical flux $\mathbf{F}^n_{i+\frac{1}{2}}$ is approximated by the Roe numerical flux [Roe, 1986]:

$$\mathbf{F}^n_{i+\frac{1}{2}} = \frac{1}{2}\left[\mathcal{F}_c\left(\mathbf{U}^n_i\right) + \mathcal{F}_c\left(\mathbf{U}^n_{i+1}\right)\right] - \frac{1}{2}\boldsymbol{R}\left(\mathbf{U}^n_i, \mathbf{U}^n_{i+1}\right), \tag{7.2.3}$$

where $\mathcal{F}_c\left(\mathbf{U}^n_i\right)$ is the conservative quantities flux, $\boldsymbol{R}$ is the Roe flux for the 5-equation system, whose derivation is detailed in [Allaire et al., 2002]. Its expression for this two-phase model is an extension of the single-phase one provided in section 4.2.3.3.4. It is given as a function of left and right states of the Riemann problem denoted respectively $\mathbf{U}_L$ and $\mathbf{U}_R$:

$$\boldsymbol{R}\left(\mathbf{U}_L, \mathbf{U}_R\right) = |\bar{u} - c^*|\,\xi_\ominus \begin{bmatrix} \bar{y}_\ell \\ \bar{y}_v \\ \bar{u} - c^* \\ \bar{h}_{\text{tot}} - \bar{u}c^* \end{bmatrix} + |\bar{u}| \begin{bmatrix} \xi_\ell \\ \xi_v \\ \bar{u}\left(\xi_\ell + \xi_v\right) \\ B \end{bmatrix} + |\bar{u} + c^*|\,\xi_\oplus \begin{bmatrix} \bar{y}_\ell \\ \bar{y}_v \\ \bar{u} + c^* \\ \bar{h}_{\text{tot}} + \bar{u}c^* \end{bmatrix}. \tag{7.2.4}$$

In the expression above, the coefficients $(\xi_j)_{j=1..5}$ and B are defined by

$$\xi_\ominus = \frac{1}{2c^{*2}}\left(\Delta P - \underline{\rho} c^* \Delta u\right) \tag{7.2.5a}$$

$$\xi_\ell = \Delta(z_\ell \rho_\ell) - \frac{\overline{y_\ell}}{c^{*2}}\Delta P \tag{7.2.5b}$$

$$\xi_v = \Delta(z_v \rho_v) - \frac{\overline{y_v}}{c^{*2}}\Delta P \tag{7.2.5c}$$

$$\xi_\oplus = \frac{1}{2c^{*2}}\left(\Delta P + \underline{\rho} c^* \Delta u\right) \tag{7.2.5d}$$

$$B = \frac{\overline{u}^2}{2}\Delta\rho + \Delta(\rho e_s) - \frac{\overline{h_{\text{t}}}}{c^{*2}}\Delta P \tag{7.2.5e}$$

For any quantity φ, the jump $\Delta\varphi$ is defined by $\Delta\varphi = \varphi_R - \varphi_L$. The *Roe mean values* are defined in (4.2.71), and the approximate speed of sound reads

$$c^* = \sqrt{\frac{\overline{y_\ell \zeta_\ell c_\ell^2} + \overline{y_v \zeta_v c_v^2}}{\overline{\zeta}}}. \tag{7.2.6}$$

with

$$\zeta_\phi = \left.\frac{\partial\left(\rho_\phi e_\phi\right)}{\partial P_\phi}\right|_{\rho_\phi} \text{ for } \phi \in \{\ell, v\}, \qquad \text{and} \qquad \zeta = z_\ell \zeta_\ell + (1 - z_\ell)\zeta_v \tag{7.2.7}$$

7.2.2.1.2 Compaction Equation

The compaction equation is then solved using an upwind scheme:

$$z_{\ell_i}^{n+1} = z_{\ell_i}^n - \frac{\Delta t}{\Delta x}\left[\bar{u}^-_{i+1/2}\Delta z_{\ell i+1/2} + \bar{u}^+_{i-1/2}\Delta z_{\ell i-1/2}\right], \tag{7.2.8}$$

with $u^\pm = \frac{(u \pm |u|)}{2}$, $\Delta z_{\ell i+1/2} = z_{\ell i+1} - z_{\ell i}$ and $\overline{u}_{i+1/2}$ is the Roe average (4.2.71a) of the velocity between cells i and $i+1$.

7.2.2.2 Thermodynamic closure

This model finally requires thermodynamic closures for both phases. Each phase can have its own EoS, e.g. Ideal Gas for the vapour phase and Stiffened Gas for the liquid phase (see [Allaire et al., 2002] for examples).

7.2.2.2.1 Stiffened gas EoS

In the case of a stiffened gas EoS, the explicit computation of the thermodynamic state from the transported variables is possible. One can use equation (2.2.57) for each phase, which yields

$$\begin{cases} P_\ell(\rho_\ell, e_\ell) = (\gamma_\ell - 1)\left(\rho_\ell e_\ell - \rho_\ell e_{0,\ell}\right) - \gamma_\ell P_{\infty,\ell}, & \text{(7.2.9a)} \\ P_v(\rho_v, e_v) = (\gamma_v - 1)\left(\rho_v e_v - \rho_v e_{0,v}\right) - \gamma_v P_{\infty,v}, & \text{(7.2.9b)} \end{cases}$$

or, equivalently,

$$\begin{cases} \rho_\ell e_\ell = \rho_\ell e_{0,\ell} + \dfrac{P_\ell + \gamma_\ell P_{\infty,\ell}}{\gamma_\ell - 1}, & \text{(7.2.10a)} \\ \rho_v e_v = \rho_v e_{0,v} + \dfrac{P_v + \gamma_v P_{\infty,v}}{\gamma_v - 1}. & \text{(7.2.10b)} \end{cases}$$

Using the isobaric closure $P_\ell = P_v = P$ of the 5-equation model of [Allaire et al., 2002] and computing z_ℓ(7.2.10a) + $(1 - z_\ell)$(7.2.10b) yields

$$\rho e_s = z_\ell \left[\rho_\ell e_{0,\ell} + \frac{\gamma_\ell P_{\infty,\ell}}{\gamma_\ell - 1}\right] + (1 - z_\ell)\left[\rho_v e_{0,v} + \frac{\gamma_v P_{\infty,v}}{\gamma_v - 1}\right] + \left[\frac{z_\ell}{\gamma_\ell - 1} + \frac{1 - z_\ell}{\gamma_v - 1}\right] P \tag{7.2.11}$$

so that

$$P = \left[\frac{z_\ell}{\gamma_\ell - 1} + \frac{1 - z_\ell}{\gamma_v - 1}\right]^{-1} \left(\rho e_s - z_\ell \left[\rho_\ell e_{0,\ell} + \frac{\gamma_\ell P_{\infty,\ell}}{\gamma_\ell - 1}\right] + (1 - z_\ell)\left[\rho_v e_{0,v} + \frac{\gamma_v P_{\infty,v}}{\gamma_v - 1}\right]\right) \tag{7.2.12}$$

Once the pressure is obtained, the state of each phase is completely determined, as the density of each phases is also known.

7.2.2.2.2 General EoS

The analytic computation of the pressure is not always possible, for example when cubic EoS are used. In this case, in order to achieve the computation of the thermodynamic state from the transported set of variables, the equilibrium pressure P is retrieved using a classic Newton-Raphson method. The function to be canceled is:

$$f_{NR} : P \longmapsto \left[(z_\ell)_i^{n+1} \rho_{\ell,i}^{n+1} e_\ell\left(\rho_{\ell,i}^{n+1}, P\right) + \left(1 - (z_\ell)_i^{n+1}\right) \rho_{v,i}^{n+1} e_v\left(\rho_{v,i}^{n+1}, P\right)\right] - (\rho e_s)_i^{n+1}. \tag{7.2.13}$$

In other words, $f(P) = \rho e_s\left(\rho_{\ell,i}^{n+1}, \rho_{v,i}^{n+1}, z_\ell, P\right) - (\rho e_s)_i^{n+1}$. The differential of the mixture sensible energy $\rho e_s\left(\rho_\ell, \rho_v, z_\ell, P\right)$ can be obtained from

$$\mathrm{d}(\rho e_s) = \mathrm{d}\big(z_\ell \rho_\ell e_\ell + (1 - z_\ell)\rho_v e_v\big) = z_\ell\, \mathrm{d}(\rho_\ell e_\ell) + (1 - z_\ell)\, \mathrm{d}(\rho_v e_v) + (\rho_\ell e_\ell - \rho_v e_v)\, \mathrm{d}z_\ell. \tag{7.2.14}$$

The isobaric thermodynamic closure $P_\ell = P_v$ implies

$$\begin{cases} \mathrm{d}P = \mathrm{d}P_\ell = \dfrac{\alpha_\ell}{\rho_\ell \beta_\ell c_{v,\ell}}\, \mathrm{d}(\rho_\ell e_\ell) + \dfrac{\alpha_\ell}{\rho_\ell \beta_\ell c_{v,\ell}} \left(\dfrac{c_{p,\ell}}{\alpha_\ell} - h_\ell\right) \mathrm{d}\rho_\ell, & \text{(7.2.15a)} \\ \mathrm{d}P = \mathrm{d}P_v = \dfrac{\alpha_v}{\rho_v \beta_v c_{v,v}}\, \mathrm{d}(\rho_v e_v) + \dfrac{\alpha_v}{\rho_v \beta_v c_{v,v}} \left(\dfrac{c_{p,v}}{\alpha_v} - h_v\right) \mathrm{d}\rho_v, & \text{(7.2.15b)} \end{cases}$$

which yields

$$\begin{cases} \mathrm{d}(\rho_\ell e_\ell) = \dfrac{\rho_\ell \beta_\ell c_{v,\ell}}{\alpha_\ell}\, \mathrm{d}P - \left(\dfrac{c_{p,\ell}}{\alpha_\ell} - h_\ell\right) \mathrm{d}\rho_\ell, & \text{(7.2.16a)} \\ \mathrm{d}(\rho_v e_v) = \dfrac{\rho_v \beta_v c_{v,v}}{\alpha_v}\, \mathrm{d}P - \left(\dfrac{c_{p,v}}{\alpha_v} - h_v\right) \mathrm{d}\rho_v. & \text{(7.2.16b)} \end{cases}$$

Combining equations (7.2.14) and (7.2.16) provides the following relation:

$$\begin{aligned}\mathrm{d}(\rho e_s) = &\left[z_\ell \frac{\rho_\ell \beta_\ell c_{v,\ell}}{\alpha_\ell} + (1-z_\ell)\frac{\rho_v \beta_v c_{v,v}}{\alpha_v}\right]\mathrm{d}P \\ &- z_\ell \left(\frac{c_{p,\ell}}{\alpha_\ell} - h_\ell\right)\mathrm{d}\rho_\ell - (1-z_\ell)\left(\frac{c_{p,v}}{\alpha_v} - h_v\right)\mathrm{d}\rho_v + \left[\rho_\ell e_\ell - \rho_v e_v\right]\mathrm{d}z_\ell.\end{aligned} \tag{7.2.17}$$

Hence the derivative for the Newton-Raphson algorithm

$$f'_{NR}(P) = \left.\frac{\partial \rho e_s}{\partial P}\right|_{\rho_\ell,\rho_v,z_\ell} = z_\ell \frac{\rho_\ell \beta_\ell c_{v,\ell}}{\alpha_\ell} + (1-z_\ell)\frac{\rho_v \beta_v c_{v,v}}{\alpha_v}. \tag{7.2.18}$$

The pressure is initialized from its previous value $P^{k=0} = P_i^n$ and the following iterations are computed

$$P^{k+1} = P^k - \frac{f_{NR}(P^k)}{f'_{NR}(P^k)}, \tag{7.2.19}$$

until the relative error is under a tolerance threshold $\dfrac{f_{NR}(P^k)}{(\rho e_s)_i^{n+1}} < \varepsilon_{(\rho e_s)}$, e.g. $\varepsilon_{(\rho e_s)} = 10^{-12}$.

7.2.3 Numerical experiments

Numerical experiments are now proposed. All the numerical experiments are led in a one-dimensional periodic context for the sake of simplicity and clarity of the results. The domain length is set to $L = 1$ m, and the mesh contains 100 cells. In order to compare the different multifluid methods, each of them will be identically tested on two benchmark configurations. To avoid non-linear effects of the cubic EoS which may cause spurious pressure oscillations and pollute the readability and interpretation of the results, stiffened-gas equations of states are used to model the liquid and vapour phases in the context of the benchmark configurations. The parameters of these stiffened-gas EoS are set to those of liquid and vapour water, taken from [Chiapolino et al., 2016]. They are summarized in Table 7.1.

Stiffened Gas coefficients	c_v [J/kg/K]	γ	P_∞ [Pa]	q [J/kg]	q' [J/kg/K]
Liquid phase	1816	2.35	10^9	-1667	0
Vapour phase	1040	1.43	0	2030	-23×10^3

Table 7.1: Stiffened Gas coefficients for the numerical experiments on contact discontinuities

The configurations that will be used for the different numerical experiments are now described.

Configuration 1 (Pure phases in equilibrium). The initial solution is a near-pure liquid inclusion within a near-pure vapour environment. Both fluids are in pressure, temperature and chemical potential equilibriums. The velocity and pressure are initially constant in the domain. The initial condition is then given as:

$$\begin{cases} \rho^0(x) = z_\ell(x)\rho_\ell^{\mathrm{sat}}(P_0) + \big(1 - z_\ell(x)\big)\,\rho_v^{\mathrm{sat}}(P_0), & \text{(7.2.20a)} \\ u^0(x) = u_0, & \text{(7.2.20b)} \\ P^0(x) = P_0, & \text{(7.2.20c)} \\ z_\ell(x) = \begin{cases} 1 - \epsilon_{z_\ell} \text{ if } x \in \left[1/4, 3/4\right], \\ 0 + \epsilon_{z_\ell} \text{ otherwise,} \end{cases} & \text{(7.2.20d)} \end{cases}$$

with $\epsilon_{z_\ell} = 10^{-8}$. The initial data for this configuration is graphically represented in Figure 7.1.

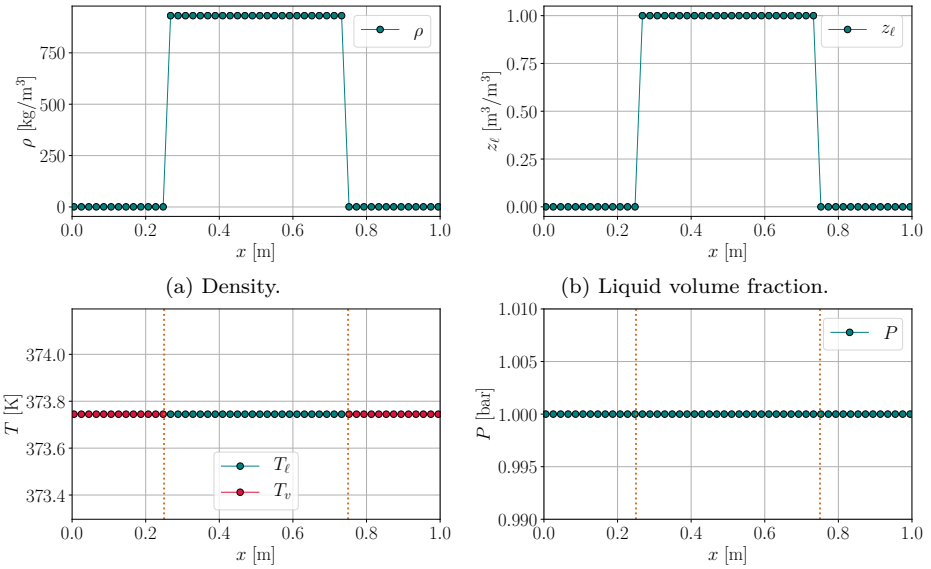

(a) Density. (b) Liquid volume fraction.

(c) Temperature. (d) Pressure.

Figure 7.1: Initial solution for the benchmark test case 1 (phases in equilibrium). The orange dotted lines indicate the position of the interface in the bottom plots.

Note that the temperature field corresponds to the saturation temperature $T_\ell = T_v = T^{\text{sat}}(P_0)$. The initial velocity is arbitrarily set to $u_0 = 100$ m/s, the speed of sound in the liquid phase being $c_\ell = 1597$ m/s.

Configuration 2 (Pure phases in disequilibrium). The initial solution is made of slightly subcooled *pure* liquid and slightly overheated *pure* vapour states, which are in pressure equilibrium. The velocity and pressure are initially constant in the domain. This initial solution corresponds to the following profiles:

$$\begin{cases} \rho^0(x) = z_\ell(x)\left[\rho_\ell^{\text{sat}}(P_0) + \Delta\rho_\ell\right] + \left(1 - z_\ell(x)\right)\left[\rho_v^{\text{sat}}(P_0) - \Delta\rho_v\right], & \text{(7.2.21a)} \\ u^0(x) = u_0, & \text{(7.2.21b)} \\ P^0(x) = P_0, & \text{(7.2.21c)} \\ z_\ell(x) = \begin{cases} 1 \text{ if } x \in \left[1/4, 3/4\right], \\ 0 \text{ otherwise.} \end{cases} & \text{(7.2.21d)} \end{cases}$$

with $\Delta\rho_\ell \ll \rho_\ell^{\text{sat}}$ and $\Delta\rho_v \ll \rho_v^{\text{sat}}$ strictly positive density shifts. Here, the values $\Delta\rho_\ell = \frac{\rho_\ell^{\text{sat}}}{1000}$ and $\Delta\rho_v = \frac{\rho_v^{\text{sat}}}{1000}$ are taken.

The initial data for this configuration is depicted in Figure 7.2.

After testing these configurations, additional configurations are investigated, specifically to each model, in order to highlight particular features.

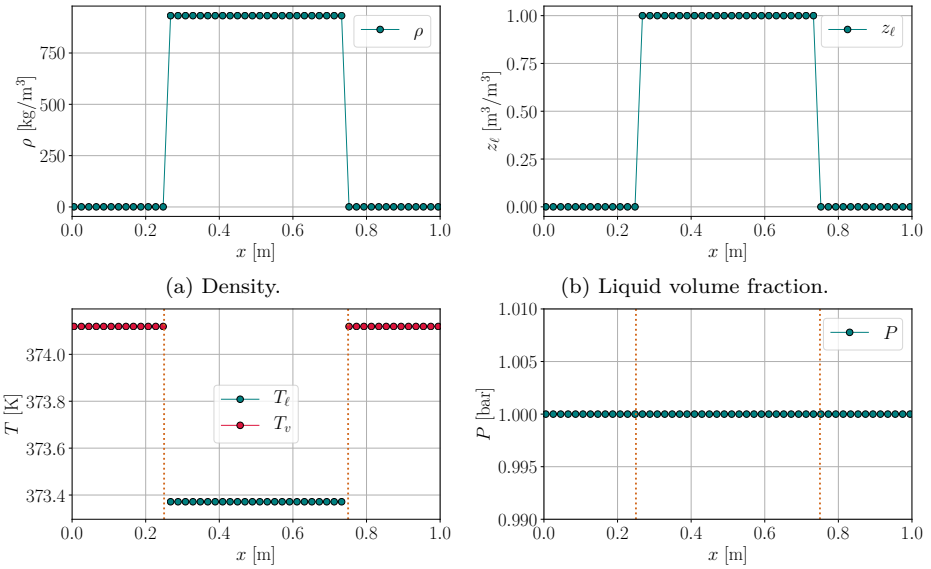

(a) Density. (b) Liquid volume fraction.

(c) Temperature. (d) Pressure.

Figure 7.2: Initial solution for the benchmark test case 2 (phases in disequilibrium).

7.2.3.1 Tests on the benchmark configurations

7.2.3.1.1 Configuration 1 – pure phases in equilibrium

The results of the test case for Configuration 1 is represented in Figure 7.3.

No spurious noise is generated by the diffusion of the interface due to the first-order scheme used. The pressure remains constant throughout the simulation, despite the smearing of the interface.

7.2.3.1.2 Configuration 2 – pure phases in disequilibrium

Applying the 5-equation model to solve the benchmark configuration 2 yields the solution of figure 7.4. One can notice that the simultaneous numerical diffusion of the mixture density, liquid phase volume fraction and mixture sensible energy do not yield pressure noise. Indeed, the initial pressure and velocity being set constant (and positive), the numerical flux for the conservative terms boils down to:

$$\mathbf{F}^n_{i+1/2} = \begin{bmatrix} (z_\ell \rho_\ell)^n_i u_0 \\ (z_v \rho_v)^n_i u_0 \\ \rho^n_i u_0^2 + 2P \\ (\rho e_s)^n_i u_0 + \frac{1}{2}\rho^n_i u_0^3 \end{bmatrix},$$

which yields the update expression

$$\begin{bmatrix} (z_\ell \rho_\ell)_i \\ (z_v \rho_v)_i \\ (\rho u)_i \\ (\rho e_t)_i \end{bmatrix}^{n+1} = \begin{bmatrix} (z_\ell \rho_\ell)_i \\ (z_v \rho_v)_i \\ (\rho u)_i \\ (\rho e_t)_i \end{bmatrix}^{n} - \frac{u_0 \Delta t}{\Delta x} \begin{bmatrix} (z_\ell \rho_\ell)_i - (z_\ell \rho_\ell)_{i-1} \\ (z_v \rho_v)_i - (z_v \rho_v)_{i-1} \\ (\rho_i - \rho_{i-1}) u_0 \\ ((\rho e_t)_i - (\rho e_t)_{i-1}) \end{bmatrix}. \tag{7.2.22a}$$

Whereas the non-conservative term is updated as

$$z_{\ell_i}^{n+1} = z_{\ell_i}^{n} - \frac{u_0 \Delta t}{\Delta x} \left[z_{\ell_i}^{n} - z_{\ell_{i-1}}^{n} \right]. \tag{7.2.22b}$$

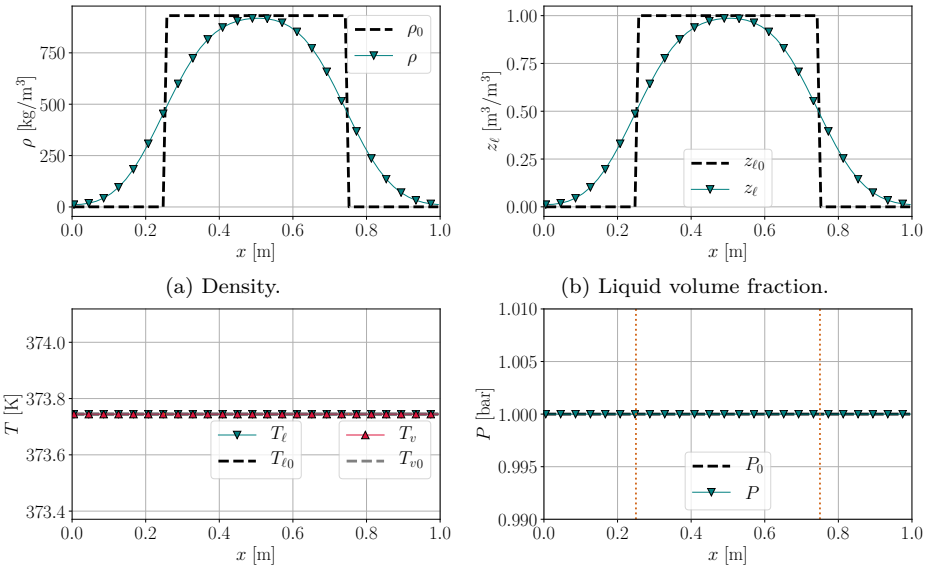

(a) Density.

(b) Liquid volume fraction.

(c) Temperature.

(d) Pressure.

Figure 7.3: Results for the 5-equation model applied to the benchmark test case 1 (phases in equilibrium).

In this test case, $\rho_\ell = \rho_{\ell,0}$ and $\rho_v = \rho_{v,0}$ are uniform. The pressure being uniform, each phase's volume-specific total energy $(\rho_\phi e_\phi)_{\phi\in\{\ell,v\}}$ is uniform. Thereby, the update (7.2.22) reduces to

$$\begin{bmatrix} (z_\ell\rho_\ell)_i \\ (z_v\rho_v)_i \\ (\rho u)_i \\ (\rho e_{\mathrm{t}})_i \\ (z_\ell)_i \end{bmatrix}^{n+1} = \begin{bmatrix} (z_\ell)_i^{n+1}\rho_{\ell,0} \\ (z_v)_i^{n+1}\rho_{v,0} \\ \left((z_\ell)_i^{n+1}\rho_{\ell,0} + (z_v)_i^{n+1}\rho_{v,0}\right) u_0 \\ \left((z_\ell)_i^{n+1}\rho_{\ell,0}e_{\ell,0} + (z_v)_i^{n+1}\rho_{v,0}e_{v,0}\right) + \frac{1}{2}\left((z_\ell)_i^{n+1}\rho_{\ell,0} + (z_v)_i^{n+1}\rho_{v,0}\right) u_0^2 \\ (z_\ell)_i^{n+1} \end{bmatrix} \tag{7.2.23}$$

which finally implies that ${\rho_\ell}_i^{n+1} = \rho_{\ell,0}$; ${\rho_v}_i^{n+1} = \rho_{v,0}$; ${e_\ell}_i^{n+1} = e_{\ell,0}$ and ${e_v}_i^{n+1} = e_{v,0}$. This necessarily guarantees that the pressure remains uniform and equal to P_0, as the uniform velocity u_0 is similarly preserved. Such result is valid for any equation of state. As the actual thermodynamic state of each phase remains constant with time, the EoS of each phase does not actually play a part in the computation.

In addition to this interesting result, the robustness and ability of the method to preserve the pressure within the interface region can be further tested by considering a non-uniform pressure profile in each phase. This is the purpose of the next section.

7.2.3.2 Complementary test cases

7.2.3.2.1 Robustness against pressure oscillations

In the context of single phase flows, the use of a cubic EoS with Euler equations is known to yield pressure noise, see e.g. [Pantano et al., 2017]. Indeed, because of the non-linearity of the EoS, pressure is impacted by the numerical errors and diffusion inherent to the discrete transport of the conservative variables.

In order to further test the ability of this numerical strategy to preserve the pressure in the interface region, a van der Waals EoS is now considered for both the liquid and gas phases. A sinusoidal noise

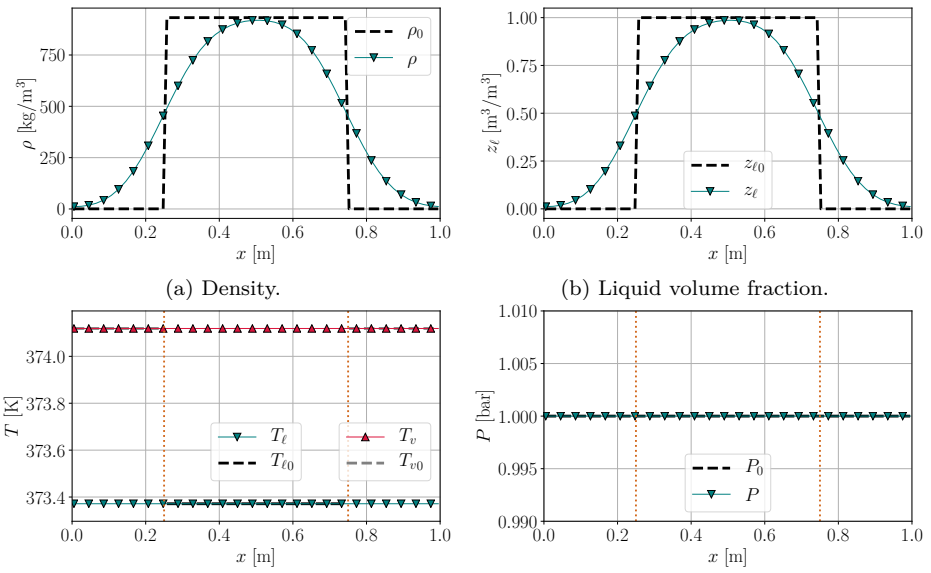

(a) Density.

(b) Liquid volume fraction.

(c) Temperature.

(d) Pressure.

Figure 7.4: Results for the 5-equation model applied to the canonical test case 2 (phases in disequilibrium).

is superimposed to constant liquid and vapour density profiles. The initial conditions are given by:

$$\begin{cases} \rho^0(x) = z_\ell(x)\left[\rho_{\phi,0} + \rho_{\text{noise}}\sin(8\pi x)\right] + \big(1 - z_\ell(x)\big)\left[\rho_{\phi,0} + \rho_{\text{noise}}\sin(8\pi x)\right], & \text{(7.2.24a)} \\ u^0(x) = u_0, & \text{(7.2.24b)} \\ P^0(x) = P_0, & \text{(7.2.24c)} \\ z_\ell(x) = \begin{cases} 1 \text{ if } x \in \left[1/4, 3/4\right], \\ 0 \text{ otherwise.} \end{cases} & \text{(7.2.24d)} \end{cases}$$

with $\rho_{\text{noise}} = 2$ kg/m^3. The solution is then initialized with these phases' density fields and homogeneous pressure P_0 and velocity u_0 as previously.

As for the simple Euler equations (cf. [Pantano et al., 2017]), the use of the five-equation model together with cubic EoS leads to pressure noise generation as the conservative variables get diffused by the first-order transport used here. This noise is already visible after one iteration, with a sinusoidal shape within each phase. Because of the low compressibility of the liquid phase, the noise amplitude is higher there than in the vapour phase.

It is worth underlining that the pressure noise observed in the interface area is actually lower than the amplitude observed in the pure phase regions. This appears even more clearly in Figure 7.6 and further confirms the robust behaviour of the interface transport in terms of pressure, as observed in the previous section.

It can actually be formally demonstrated that the equilibrium pressure retrieved from the isobaric closure is necessarily bounded by the pressures of the pure phases. Indeed, considering a liquid and vapour initial states defined by $\rho_\ell, P_\ell, \rho_v, P_v$ with for instance $P_\ell < P_v$, a mixing of such states with any liquid volume fraction $z_\ell \in]0, 1[$ verifies the following inequalities:

$$z_\ell \rho_\ell e_\ell\left(\rho_\ell, P_v\right) + (1 - z_\ell)\rho_v e_v\left(\rho_v, P_v\right) \;>\; z_\ell \rho_\ell e_\ell\left(\rho_\ell, P_\ell\right) + (1 - z_\ell)\rho_v e_v\left(\rho_v, P_v\right) \quad \text{(7.2.25a)}$$

$$z_\ell \rho_\ell e_\ell\left(\rho_\ell, P_\ell\right) + (1 - z_\ell)\rho_v e_v\left(\rho_v, P_\ell\right) \;>\; z_\ell \rho_\ell e_\ell\left(\rho_\ell, P_\ell\right) + (1 - z_\ell)\rho_v e_v\left(\rho_v, P_\ell\right) \quad \text{(7.2.25b)}$$

as the functions $e_\ell : P \mapsto e_\ell\left(\rho_\ell, P\right)$ and $e_v : P \mapsto e_v\left(\rho_v, P\right)$ are increasing functions. Then, noting

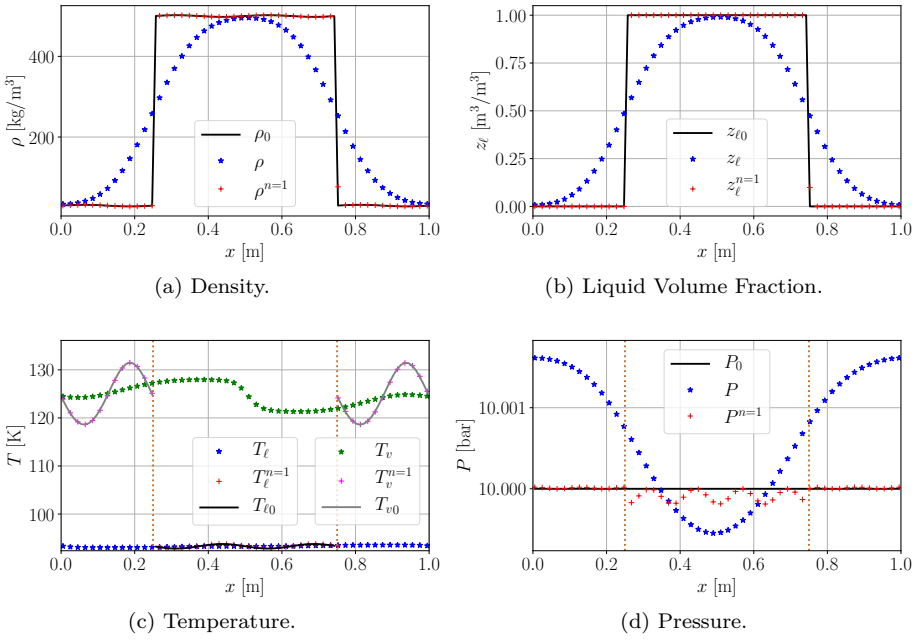

(a) Density. (b) Liquid Volume Fraction.

(c) Temperature. (d) Pressure.

Figure 7.5: Solution of the contact discontinuity test case for a five-equation model (7.2.1). Final time $t = 10^{-2}$ s is such that the solution is back to its initial position. Only one point out of two is displayed for the sake of readability. Solid lines denote the initial profiles. Plus signs denote the solution after one iteration. Stars represent the final solution. Initial profiles for the liquid and vapour temperatures do not span over the entire domain as one phase's temperature is not uniquely defined when this phase is not present.

that $z_\ell \rho_\ell e_\ell(\rho_\ell, P_\ell) + (1 - z_\ell)\rho_v e_v(\rho_v, P_v) = \rho e_s(\rho_\ell, \rho_v, z_\ell, P)$, one gets

$$\rho e_s(\rho_\ell, \rho_v, z_\ell, P_\ell) \;<\; \rho e_s(\rho_\ell, \rho_v, z_\ell, P) \;<\; \rho e_s(\rho_\ell, \rho_v, z_\ell, P_v) \tag{7.2.26}$$

From (7.2.17), it comes that $\left.\frac{\partial \rho e_s}{\partial P}\right|_{\rho_\ell, \rho_v, z_\ell} > 0$, which finally implies

$$P_\ell < P < P_v. \tag{7.2.27}$$

A similar conclusion stands for the case $P_\ell > P_v$.

7.2.3.2.2 Thermodynamic consistency of the predicted states

The 5-equation models [Allaire et al., 2002, Murrone and Guillard, 2005] have been shown able to treat compressible two-phase flows without generating spurious noise in the interface region. Unfortunately, using this model by itself may lead, in some situations, to the apparition of non-physical thermodynamic states, e.g. for flow configurations that produce cavitation. In order to illustrate – in a simplified manner – the consequences that a pressure drop may have, the 1D test case of Figure 7.7 is considered. The initial velocity field is given by

$$u_0(x) = \begin{cases} \dfrac{4\sin(\pi\frac{x-1/2}{d}) + 2\sin(2\pi\frac{x-1/2}{d})}{3\sqrt{3}} & \text{for } x \in \left[\dfrac{1}{2} - d, \dfrac{1}{2} + d\right] u_{\max} \\ 0 & \text{otherwise} \end{cases} \tag{7.2.28}$$

The initial condition and results after a time $t = 0.3$ ms are displayed in figure 7.7. The pressure of the center point ($x = 0.5$ m), corresponding to the middle of the liquid phase region, is monitored. In

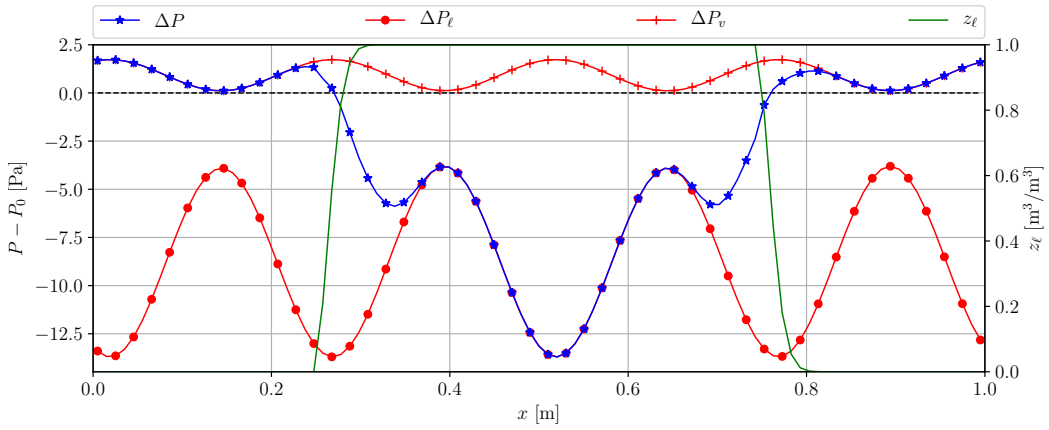

Figure 7.6: Comparison of the pressure errors between Allaire equations for the transport of a liquid-vapour contact discontinuity and Euler equations for the liquid phase only and Euler equations for the vapour phase only. The noise is due to the numerical diffusion of the sinusoidal density perturbation defined in (7.2.24a). Both phases are pure nitrogen $N2$ with the van der Waals EoS. Solution is displayed after 0.15 ms.

figure 7.8, a scatter plot shows its evolution within the Clapeyron Diagram corresponding to the SRK EoS.

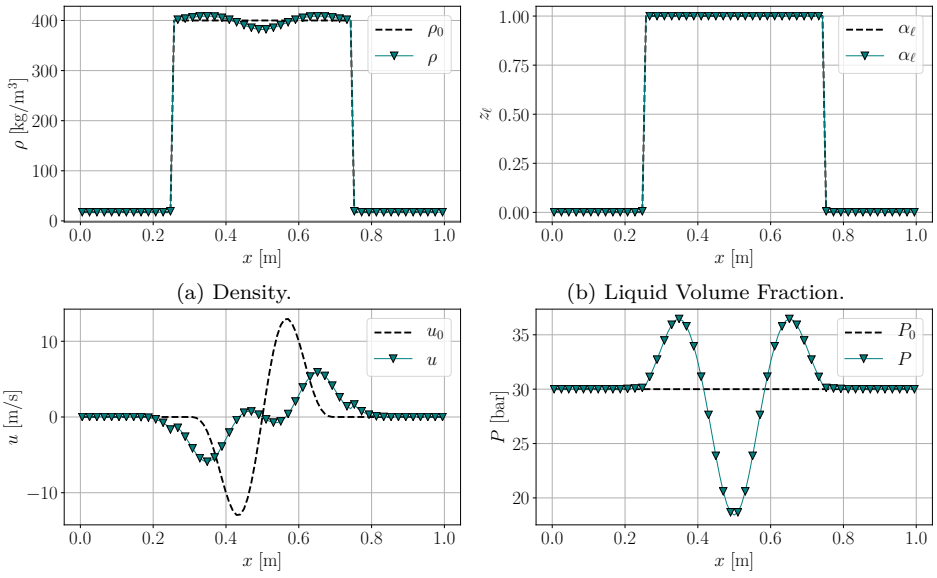

(a) Density.

(b) Liquid Volume Fraction.

(c) Velocity.

(d) Pressure.

Figure 7.7: Test case with a velocity divergence causing a pressure drop. Initial pressure is $P_0 = 30$ [bar]. The initial velocity profile is given in equation (7.2.28). The half-width of the velocity perturbation is set to $d = 0.2$. The vapour and liquid phases densities are in a thermodynamically stable state, as they verify the inequality $\rho_{\ell,0} > \rho_\ell^{\text{sat}}(P_0) > \rho_v^{\text{sat}}(P_0) > \rho_{v,0}$. SRK EoS is used for both phases, which consist in pure N_2.

It appears that the pressure has no reason to remain in the thermodynamically stable region. The thermodynamic state evolves across the metastable region, as there is no phase change model added to the two-phase transport model. This even results in a thermodynamic state that can cross the spinodal line, yielding nonphysical thermodynamically unstable states – as this is the case for the final state displayed in red. This can even result in a loss of hyperbolicity of the system, as the sound speed to the square c^2 is negative in part of the spinodal region.

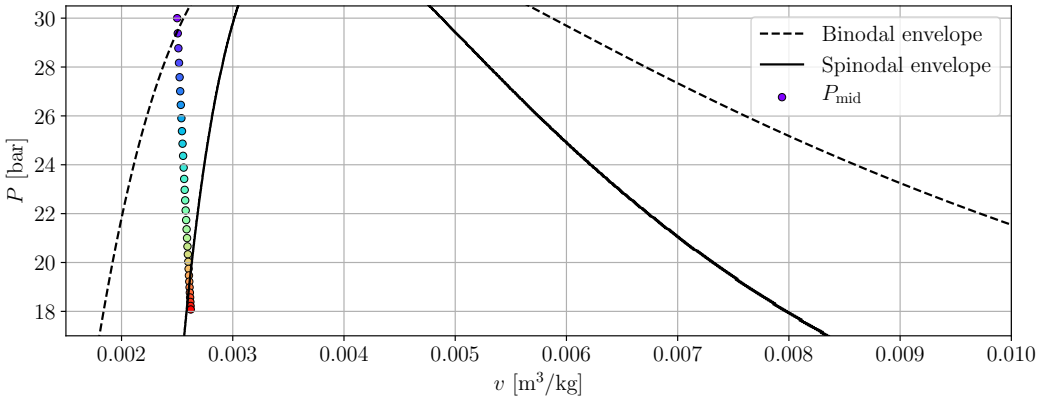

Figure 7.8: Scatter plot of the thermodynamic state at the center point $x_{\text{mid}} = 0.5$ m in a Clapeyron Diagram. The successive iterations are plotted with, the first point at $P = 30$ bar is coloured purple, final point after $t = 300$ ms is coloured red.

7.2.4 Conclusions on the 5-equation models

Finally, the five-equation models [Allaire et al., 2002, Murrone and Guillard, 2005] have been tested, showing that they provide a convenient framework to treat interface problems for fluids in mechanical equilibrium. The resulting model is robust in the sense that it is not a source of spurious pressure oscillations at the interface for contact discontinuity transport cases. Nevertheless, the model used by itself is incomplete for the simulation of two-phase reactive flows, as it requires further modeling in order to take into account phase change phenomena.

7.3 The 4-equation model

7.3.1 Practical implementation

The four-equation model at stake in this section can be found in [Le Martelot et al., 2014, Chiapolino et al., 2016]. It can be derived from the five-equation model by considering that the liquid and vapour phases do not only share a common pressure but also a common temperature. The corresponding PDE can be written in 1D as:

$$\begin{cases} \dfrac{\partial z_\ell \rho_\ell}{\partial t} + \dfrac{\partial z_\ell \rho_\ell u}{\partial x} = 0 & \text{(7.3.1a)} \\ \dfrac{\partial z_v \rho_v}{\partial t} + \dfrac{\partial z_v \rho_v u}{\partial x} = 0 & \text{(7.3.1b)} \\ \dfrac{\partial \rho u}{\partial t} + \dfrac{\partial \rho u^2 + P}{\partial x} = 0 & \text{(7.3.1c)} \\ \dfrac{\partial \rho e_{\text{t}}}{\partial t} + \dfrac{\partial \left(\rho e_{\text{t}} + P\right) u}{\partial x} = 0 & \text{(7.3.1d)} \end{cases}$$

7.3.2 Practical implementation

7.3.2.1 Numerical method

As for the 5-equation model, the numerical method used is a Godunov-like scheme:

$$\mathbf{U}_i^{n+1} = \mathbf{U}_i^n - \frac{\Delta t}{\Delta x}\left(\mathbf{F}_{i+\frac{1}{2}}^n - \mathbf{F}_{i-\frac{1}{2}}^n\right). \tag{7.3.2}$$

Here, all transported variables are conservative and discretized by this equation, unlike for the 5-equation model. The numerical flux is similarly computed using a Roe-like scheme, similar to the one of [Allaire et al., 2002] described in section 7.2. It reads

$$\mathbf{F}_{i+\frac{1}{2}}^n = \frac{1}{2}\left[\mathcal{F}\left(\mathbf{U}_i^n\right) + \mathcal{F}\left(\mathbf{U}_{i+1}^n\right)\right] - \frac{1}{2}\boldsymbol{R}\left(\mathbf{U}_i^n, \mathbf{U}_{i+1}^n\right), \tag{7.3.3}$$

with the roe flux $\boldsymbol{R}$ given by

$$\boldsymbol{R}\left(\mathbf{U}_L, \mathbf{U}_R\right) = |\bar{u} - c^*|\,\xi_{\ominus}\begin{bmatrix}\bar{y}_\ell\\ \bar{y}_v\\ \bar{u}-c^*\\ \bar{h}_{\text{tot}} - \bar{u}c^*\end{bmatrix} + |\bar{u}|\begin{bmatrix}\xi_\ell\\ \xi_v\\ \bar{u}\left(\xi_\ell+\xi_v\right)\\ B\end{bmatrix} + |\bar{u}+c^*|\,\xi_{\oplus}\begin{bmatrix}\bar{y}_\ell\\ \bar{y}_v\\ \bar{u}+c^*\\ \bar{h}_{\text{tot}} + \bar{u}c^*\end{bmatrix}. \tag{7.3.4}$$

With coefficients given in equations (7.2.5) and the approximate speed of sound (7.2.6) Although the formulation is similar to the previous one, the difference stands in the volume fraction computation. Indeed, this quantity is not transported anymore. It is instead computed from the set of transported conservative variables using the thermodynamic closure and assuming temperature and pressure equilibriums. This is described in the next paragraph.

7.3.2.2 Thermodynamic closure

7.3.2.2.1 Stiffened Gas EoS

In the original work, these transport equations are closed by two Stiffened Gas EoS, the formulation of which is detailed in Section 2.2.3.1.

The isobaric and isothermal closure allow in this particular context for an explicit formulation of the pressure from the transported conservative quantities. This expression reads:

$$P = \frac{1}{2}\left(A_\ell + A_v - \left(P_{\infty,\ell} + P_{\infty,v}\right)\right) + \sqrt{\frac{1}{4}\left[A_v - A_\ell - \left(P_{\infty,\ell} - P_{\infty,v}\right)\right]^2 + A_\ell A_v} \tag{7.3.5}$$

with the coefficients A_ϕ defined for $\phi \in \{\ell, v\}$ as

$$A_\phi = \frac{y_\phi\left(\gamma_\phi - 1\right)c_{v,\phi}}{y_\ell c_{v,\ell} + y_v c_{v,v}}\left(\rho\left(e_s - \left(y_\ell q_\ell + y_v q_v\right)\right) - P_{\infty,\phi}\right). \tag{7.3.6}$$

The corresponding temperature is

$$T = \frac{1}{\rho}\left[y_\ell\frac{(\gamma_\ell - 1)c_{v,\ell}}{P + P_{\infty,\ell}} + y_v\frac{(\gamma_v - 1)c_{v,v}}{P + P_{\infty,v}}\right]^{-1} \tag{7.3.7}$$

7.3.2.2.2 General EoS

In general, there is no explicit formulation for computing the temperature and pressure corresponding to the transported conservative variables. Indeed, pressure and temperature are in this case implicitly defined as the solution of

$$\begin{cases} \dfrac{1}{\rho^n} = \dfrac{y_\ell^n}{\rho_\ell\left(T,P\right)} + \dfrac{1-y_\ell^n}{\rho_v\left(T,P\right)} & \text{(7.3.8a)} \\ e_s^n = y_\ell^n e_\ell\left(T,P\right) + (1-y_\ell^n) e_v\left(T,P\right), & \text{(7.3.8b)} \end{cases}$$

where ρ^n, e_s^n and y_ℓ^n are the density, sensible energy and liquid mass fraction obtained after the n^{th} transport step.

This system is solved iteratively using a Newton-Raphson algorithm. The function to be cancelled is

$$f_{\text{NR}} : \begin{bmatrix} P \\ T \end{bmatrix} \longmapsto \begin{bmatrix} \frac{y_\ell^n}{\rho_\ell(T,P)} + \frac{1-y_\ell^n}{\rho_v(T,P)} - \frac{1}{\rho^n} \\ y_\ell^n e_\ell\left(T,P\right) + (1-y_\ell^n) e_v\left(T,P\right) - e_s^n \end{bmatrix}, \tag{7.3.9}$$

whose Jacobian matrix writes:

$$f'_{\text{NR}} = \begin{bmatrix} -\left(\frac{y_\ell}{\rho_\ell}\beta_\ell + \frac{(1-y_\ell)}{\rho_v}\beta_v\right) & \frac{y_\ell}{\rho_\ell}\alpha_\ell + \frac{(1-y_\ell)}{\rho_v}\alpha_v \\ y_\ell \frac{P\beta_\ell - T\alpha_\ell}{\rho_\ell} + (1-y_\ell)\frac{P\beta_v - T\alpha_v}{\rho_v} & y_\ell\left(c_{p,\ell} - \frac{\alpha_\ell P}{\rho_\ell}\right) + (1-y_\ell)\left(c_{p,v} - \frac{\alpha_v P}{\rho_v}\right) \end{bmatrix} \tag{7.3.10}$$

In the case where a single cubic EoS is used for both phases, the subscript ℓ and v denote the thermodynamic quantities computed for densities corresponding to the lower and upper roots of the cubic equation.

7.3.2.3 Tests on the benchmark configurations

7.3.2.3.1 Configuration 1 – pure phases in equilibrium

The results of the test case for Configuration 1 is represented in Figure 7.9.

As for the 5-equation model, no spurious noise is generated by the diffusion of the interface. The pressure remains constant throughout the simulation.

7.3.2.3.2 Configuration 2 – pure phases in disequilibrium

Here, one can note that numerical diffusion creates mixing cells where liquid and vapour coexist. In such cells, the thermodynamic closure of the 4-equation model imposes especially the equality of phases temperature. If this has no consequence in the case of an initially constant temperature field, it causes pressure variations when an initial temperature difference is present. The pressure noise is yet relatively smooth, unlike for the 3-equation model to be presented in the following.

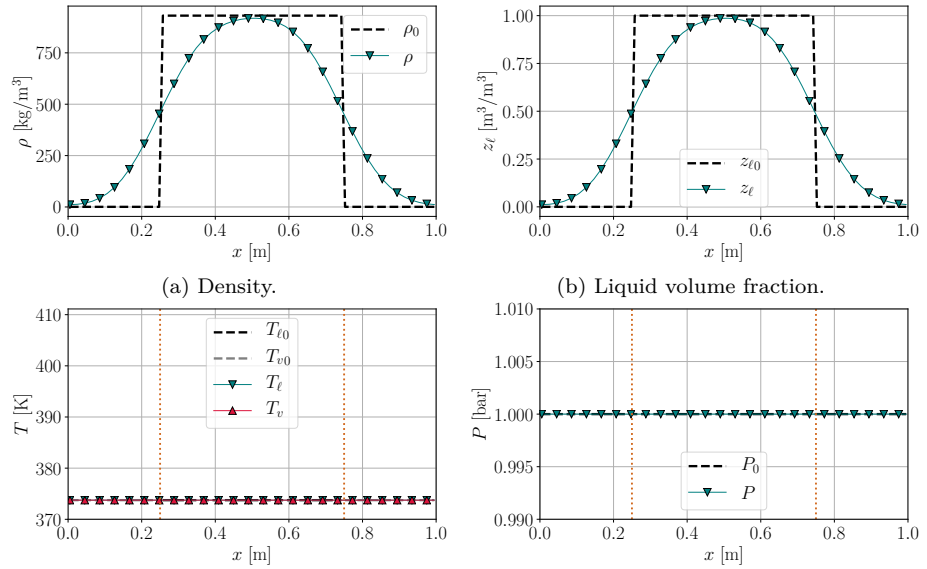

(a) Density. (b) Liquid volume fraction.

(c) Temperature. (d) Pressure.

Figure 7.9: Results for the 4-equation model applied to the benchmark test case 1. For the sake of clarity, only one point out of two is visible.

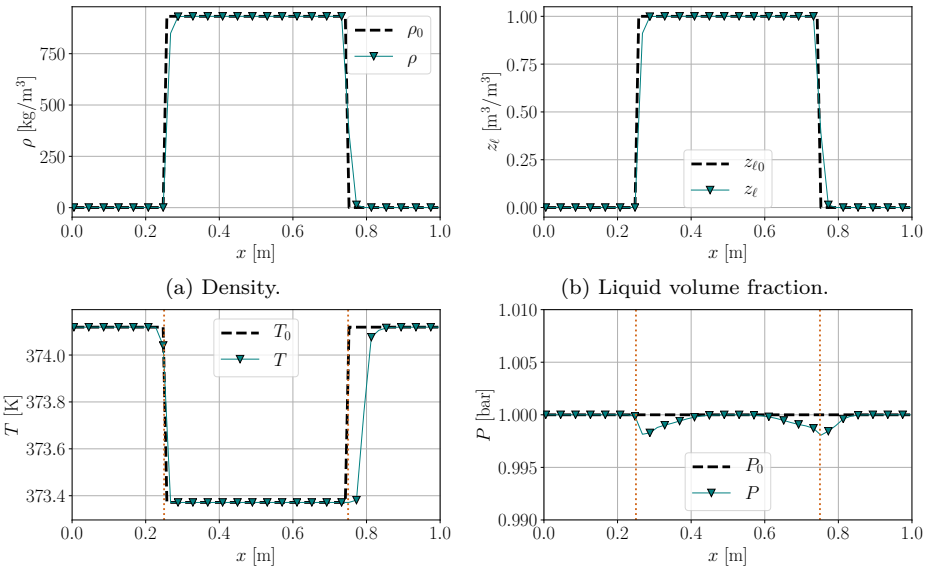

(a) Density. (b) Liquid volume fraction.

(c) Temperature. (d) Pressure.

Figure 7.10: Results for the 4-equation model applied to the benchmark test case 2. For the sake of clarity, only one point out of two is visible. Final time is 0.05 ms

7.4 3-equation model

The 3-equation model is now considered. This model consists in applying an additional chemical potential equilibrium hypothesis to the 4-equation model. As previously mentioned in section 5.2.3,

the 3-equation model formulation is similar to the Euler equations. It simply reads

$$\begin{cases} \dfrac{\partial \rho}{\partial t} + \dfrac{\partial \rho u}{\partial x} = 0 & \text{(7.4.1a)} \\ \dfrac{\partial \rho u}{\partial t} + \dfrac{\partial \rho u^2 + P}{\partial x} = 0 & \text{(7.4.1b)} \\ \dfrac{\partial \rho e_{\mathrm{t}}}{\partial t} + \dfrac{\partial \left(\rho e_{\mathrm{t}} + P\right) u}{\partial x} = 0. & \text{(7.4.1c)} \end{cases}$$

Yet, in this system, the density ρ is defined as a mixture density, as well as the volume-specific total energy ρe_{t}. They can be explicitly split up into

$$\rho = z_\ell \rho_\ell + (1 - z_\ell)\rho_v \quad \text{(7.4.2a)}$$

$$\rho e_{\mathrm{t}} = z_\ell \rho_\ell e_{\mathrm{t},\ell} + (1 - z_\ell)\rho_v e_{\mathrm{t},v}. \quad \text{(7.4.2b)}$$

The reader is referred to Paragraph 2.3.2.2 for the detailed computation of the thermodynamic equilibrium and to Section 5.2.3 the consequences of this equilibrium on the thermo-mechanical properties of the fluid. In a nutshell, system (7.4.1) is closed by evaluating the thermodynamic stability of the transported state ρ, e_s. If the result correspond to a single-phase stable state (pure liquid or pure vapour), then the equation of state of this pure phase is used in order to retrieve the pressure and temperature of the fluid. Otherwise, if the state is unstable, then both z_ℓ and $(1 - z_\ell)$ are non-zero and an equilibrium computation is required to evaluate the pressure and temperature, allowing to evaluate the fluxes that are required for the numerical method.

Noticeably, this 3-equation model has no longer a mass-conservation equation for each phase, since the phases exchange mass through a phase transition process that is modeled by the assumption of thermodynamic equilibrium at all time. In this respect, only the total mass is conserved, through equation (7.4.1a).

7.4.1 Numerical Method

Again, a finite-volume method is used. The Roe solver used for the numerical flux evaluation is formally the one for the Euler equations descibed in section 4.2.3.3.4.

7.4.2 Numerical experiments

7.4.2.1 Benchmark configurations

7.4.2.1.1 Configuration 1 – pure phases in equilibrium

The results for test configuration 1 are displayed in Figure 7.11.

The pressure and temperature remain noticeably homogeneous in the domain, while the numerical diffusion smooths out the density profile.

7.4.2.1.2 Configuration 2 – pure phases out of equilibrium

As for the four-equation model, the pressure profile is no longer preserved. Yet, the amplitude of the pressure noise is much higher. In addition to the fact that the phases temperature homogenize in the mixing cells where the interface is smeared, the mixture's temperature is constrained by the chemical potential equilibrium assumption. This system forces the mixture to be in a saturated state, which results in a stiffer system's behaviour, as one degree of freedom was removed compared to the 4-equation model. Identical time steps and final time were used for this test configuration for the 4-equation and 3-equation models, and the ratio of the pressure noise amplitude is about 10 times higher for the 3-equation model.

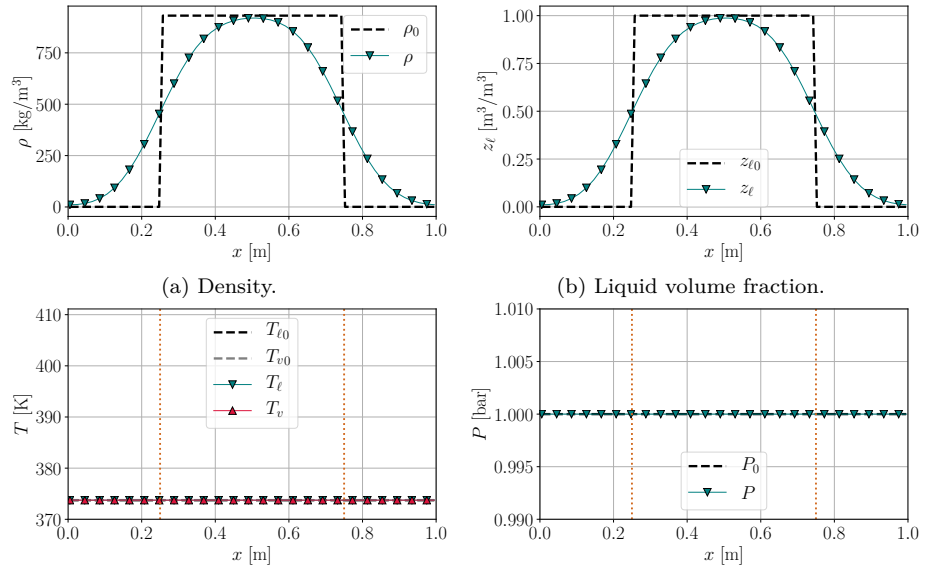

(a) Density. (b) Liquid volume fraction.

(c) Temperature. (d) Pressure.

Figure 7.11: Results for the 3-equation model applied to the benchmark test case 1. For the sake of clarity, only one point out of two is visible.

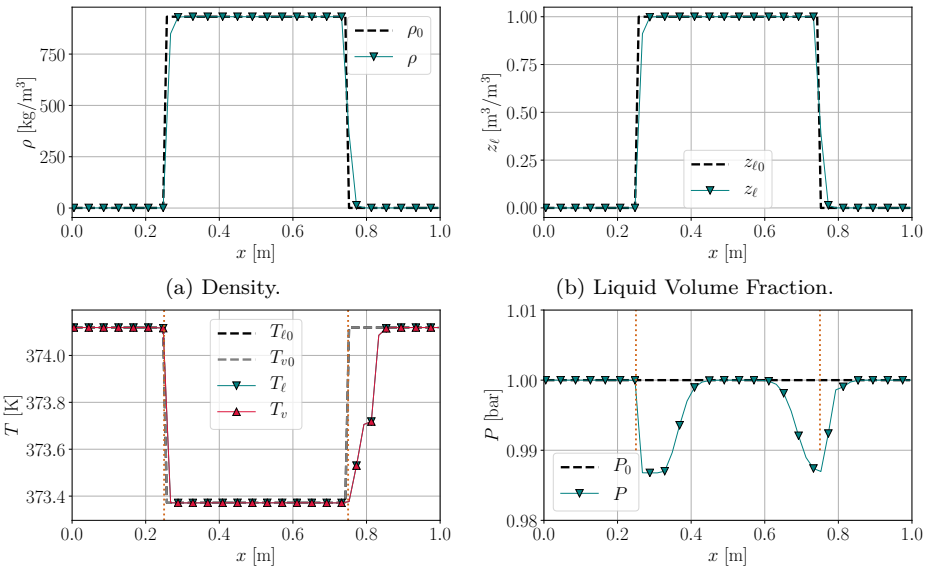

(a) Density. (b) Liquid Volume Fraction.

(c) Temperature. (d) Pressure.

Figure 7.12: Results for the 3-equation model applied to the benchmark test case 1. Final time is $t = 0.05$ ms.

7.4.2.2 Complementary analyses

7.4.2.2.1 Noise at the "interface" between saturated states and a pure phase

A closer look is now taken at the conditions in which the spurious noise appears. In particular, it is shown that the transport of a flow within which a region in a two-phase state and a pure-phase region coexist, the transport with a 3-equation model generates spurious pressure oscillations. To this end

three test cases are considered. In all three cases, the pressure and velocity are constant, while the density varies smoothly from a minimum value $\rho_{\min}$ to a maximum value $\rho_{\max}$. The density profile is defined by:

$$\rho^0(x) = \rho_{\min} + (\rho_{\max} - \rho_{\min}) f(x), \tag{7.4.3}$$

where f is defined as

$$f(x) = \begin{cases} \left[\cos\left(\dfrac{\pi\,(x-0.5)}{2l_0}\right)\right]^2 & \text{when } x \in \left[\dfrac{1-l_0}{2}, \dfrac{1+l_0}{2}\right], \\ 0 & \text{otherwise.} \end{cases} \tag{7.4.4}$$

The different test cases are such that:

(i) $\rho_\ell < \rho_{\min} < \rho_{\max}$,

(ii) $\rho_v < \rho_{\min} < \rho_\ell < \rho_{\max}$,

(iii) $\rho_v < \rho_{\min} < \rho_{\max} < \rho_\ell$.

The initial density profiles are depicted in figure 7.13a. Note that similar test cases can be considered, by setting instead the values of $\rho_{\min}$ and $\rho_{\max}$ around the limit between pure vapour and saturated states, leading to identical observations.

The resulting pressure profiles after 5 iterations are shown in Figure 7.13b. Zero pressure noise is generated for cases (i) and (iii). On the contrary, test case (ii) involves pressure noises, at the precise location where the fluid switches from a pure liquid state to a saturated two-phase state. Further analysis of this phenomenon is proposed in Chapter 8.

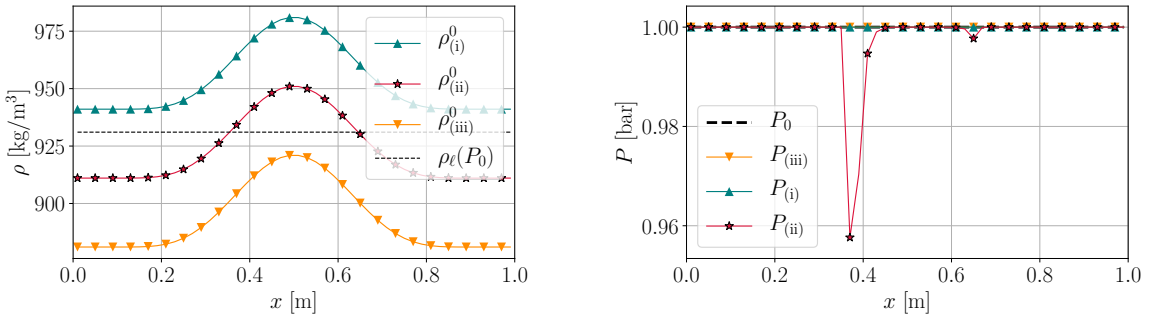

(a) Initial density profiles

(b) Pressure after 5 iterations

Figure 7.13: Test cases with smoothly varying density profiles: (i) density variation within pure liquid, (ii) density variation within two-phase states at saturation, (iii) density variation across the limit between pure liquid and two-phase states at saturation. Pressure profile is shown after 5 iterations for a time step of $\Delta t = 1$ μs

7.4.2.2.2 Comparison with 4-equation and 5-equations models with stiff relaxation to equilibrium

By themselves, the 5-equation and 4-equation models previously studied do not address phase change phenomena. In order to incorporate phase change into multifluid models, a common strategy [Furfaro and Saurel, 2016, Chiapolino et al., 2016] is to use an operator splitting method: the 4- or 5-equation transport is computed, and a stiff relaxation towards thermodynamic equilibrium is computed in a decoupled fashion. This process is illustrated by Figure 7.14.

This strategy is now applied to the 4-equation and 5-equation models on the test configuration of the previous paragraph 7.4.2.2.1. The 3-equation model (Homogeneous Equilibrium Model) already

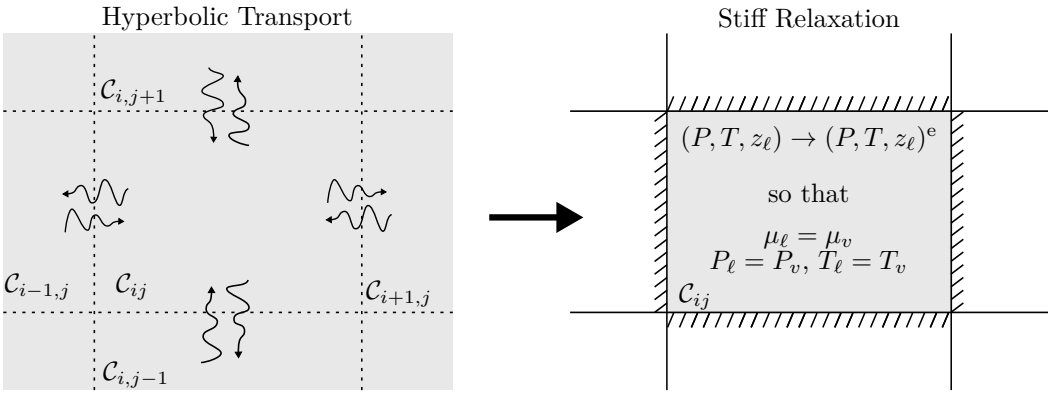

Figure 7.14: Operator-splitting procedure for stiff relaxation towards thermodynamic equilibrium. During the transport step, the cells exchange mass of each phase, momentum and energy following the 4- or 5-equation model. During the relaxation step, mixture total energy, momentum and mass remain constant in the cell, and the pressure, temperature and the volume and mass fractions of the phases are relaxed to their values at thermodynamic equilibrium.

addresses phase change, hence the absence of need for operator splitting and stiff relaxation for this model. All three models are compared in figures 7.15 and 7.16.

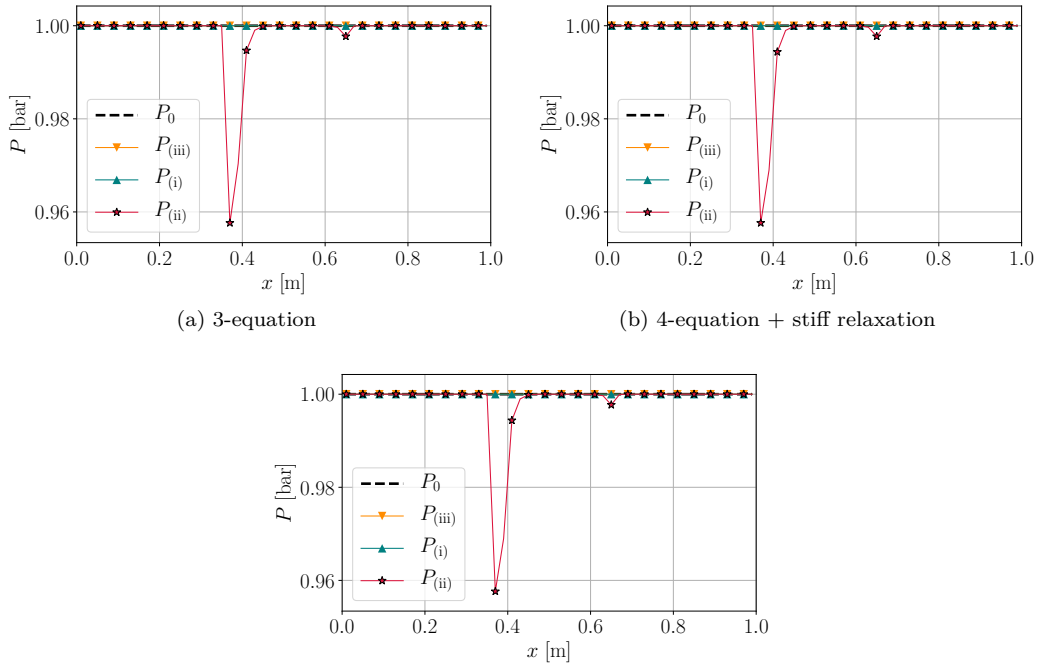

(a) 3-equation

(b) 4-equation + stiff relaxation

(c) 5-equation + stiff relaxation

Figure 7.15: Pressure fields for test cases of paragraph 7.4.2.2.1, with phase change. Snapshots taken after 5 iterations (0.005 ms)

The results are very similar, and the spurious noise is present for all the models, for test case (ii) where the pure-phase/saturation limit is crossed. The only difference that can be perceived is due to the difference of the speed of sound between the different models. These different speeds of sound used in the respective hyperbolic solver of each model results in slightly different noise generations at the pure-phase/saturation limit. For this reason, slight differences are observed after 400 iterations,

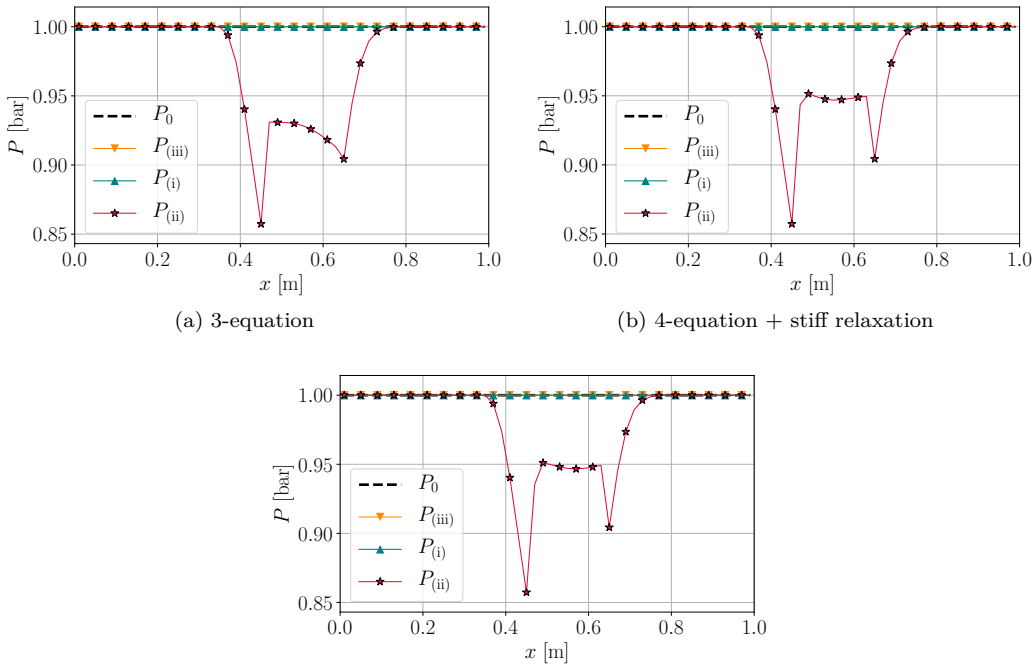

(a) 3-equation

(b) 4-equation + stiff relaxation

(c) 5-equation + stiff relaxation

Figure 7.16: Pressure fields for test cases of paragraph 7.4.2.2.1, with phase change. Snapshots taken after 400 iterations (0.4 ms)

especially for the 3-equation model for which the speed of sound is much lower than the ones of the other models (see figure 3.15).

In particular, solving the 3-equation model while imposing artificially $c^2_{3-\text{eq}} = c^2_{4-\text{eq}}$ in the solver provides formally the same results as the 4-equation model with stiff relaxation. The same solution can thus be obtained with less effort, by transporting less information. A similar conclusion stands with the 5-equation model.

7.5 Conclusion

Four multifluid methods have been presented. In particular, the 5-equation model of [Allaire et al., 2002], the 4-equation model used by [Chiapolino et al., 2016] and the 3-equation model studied by [Clerc, 2000] have been described. The physical hypotheses on which they rely have been recalled, and their implementation with Finite-Volume Godunov-like methods has been summarized.

Their behaviour has been tested separately on test cases involving the transport of a contact discontinuity, allowing to highlight interesting properties for each model:

- the ability to transport pure-phase contact discontinuities for the 5-equation model without yielding pressure oscillations;
- the fully conservative form of the 4-equation model and its ability to preserve homogeneous pressure when transporting an isothermal flow;
- the fully conservative form of the 3-equation model and its ability to introduce mass exchange between phases.

Finally, in agreement with the scope of this work and targeted applications, the use of these differ-

ent models with phase change has been considered, showing close results despite the difference of formulation of the models.

Chapter 8

Regularized thermodynamics

The present chapter proposes an analysis of the spurious pressure noise observed in the previous chapter for the 3-equation system. The impact of the pressure noise on the convergence order of the numerical transport is evidenced. A local modification of the thermodynamics is proposed, aiming to reduce the noise. Finally, a discussion on the results is provided.

8.1 Introduction

The pressure variations observed in a numerical simulation may have different nature. Naturally, physically meaningful pressure variations can occur, e.g. the pressure drop within the vortices or the propagation of acoustic waves. Conversely, spurious pressure variations can be encountered. Such phenomenon appears when a conservative transport is computed for a fluid with a variable heat capacity ratio $\gamma = \frac{c_p}{c_v}$. This is the case of an ideal gas mixture with a heterogeneous composition, as analyzed by [Abgrall, 1996]. It is also observed when a fluid of heterogeneous density is modeled by a real gas EoS, as depicted in Figure 7.5 and studied by [Pantano et al., 2017]. Such spurious oscillations are smoothly distributed along the variations of, respectively, the mixture composition or the fluid density.

Unlike this smoothly distributed pressure error, it is obvious that the pressure noise observed in Figure 7.15 is located at the specific point where the fluid state transitions between pure-fluid state and a two-phase mixture state. In particular, this numerical error may impair the convergence order of the numerical methods (cf. section 8.2). In order to address the noise related with this particular point, different ideas can be proposed.

A first idea consists in avoiding to cross the pure phase limit. Unfortunately, even with a bounded numerical scheme and initial conditions that verify $z_\ell \in]0,1[$ in the whole domain, physical evolutions of the flow can lead the fluid to cross the limit between stable one-phase states and saturated two-phase states, so that there is no explicit condition on the physical data to necessarily guarantee that the fluid remains within the two-phase mixture bounds. Also, if one could somehow constrain the mixture state to remain in the two-phase region, it would not be satisfactory to represent the pure phases by near-pure phases, since the speed of sound in such approximate pure phases is significantly lower than its actual pure phases value, as depicted in Figure 3.15. Similarly, one could consider setting a threshold value for the liquid ${z_\ell}^{\text{liquid}} = (1-\epsilon)$ and ${z_\ell}^{\text{vapour}} = \epsilon$ with $0 < \epsilon \ll 1$. Actually, such treatment does not overcome the pressure issue.

A second idea would be to track the spatial position of the point at which the pure phase limit is crossed, to properly compute the pressure by taking into account the difference of thermodynamic regimes on each side of the pure phase limit. Yet, this idea is contrary to the principle of diffuse interface models: it would require to use treatments similar to the sharp interface methods to track this pure phase limit position, leading to a greatly increased complexity, especially in multiple dimensions.

Another idea, similar to [Abgrall, 1996], would consist in giving up the discrete conservation of the numerical transport and propose a non-conservative transport. Yet, doing so can lead to temperature errors, especially in the context of reactive flows.

A last idea, which is investigated along the present chapter, is to propose a local modification of the thermodynamics, in order to smooth the equation of state, and observe if this improves the transport behaviour. In section 8.2, an analysis of the spurious noise is proposed. Then, section 8.3 introduces the modification of the equation of state and its consequences on the different thermodynamic quantities. Finally, in section 8.4 the strategy is tested and the results are analyzed.

8.2 Analysis of the problem

As observed in the previous chapter, the homogeneous equilibrium model tends to generate pressure noise when the fluid state crosses the pure-phase/saturation limit. The impact of such spurious behaviour on the quality of the numerical transport can be highlighted by evaluating the effective convergence order of the numerical method. In this respect, different RKDG methods of respective convergence orders 1, 2 and 3 are used. Details of their implementation have been provided in section 4.4.2. The test case consists in a solution at constant pressure P_0 and velocity u_0, with an initial density profile given by

$$\rho^0(x) = \rho_{\min} + (\rho_{\max} - \rho_{\min}) f(x), \tag{8.2.1}$$

where f is defined as

$$f(x) = \begin{cases} \left[\cos\left(\dfrac{\pi\,(x - 0.5)}{2 l_0} \right) \right]^8 & \text{when } |x - 0.5| < l_0, \\ 0 & \text{otherwise,} \end{cases} \tag{8.2.2}$$

so that $\rho_{\min}$ is a pure-vapour state $\rho_{\min} < \rho_v^{\text{sat}}(P_0)$ and $\rho_{\max}$ is a saturated state $\rho_{\max} > \rho_v^{\text{sat}}(P_0)$. For the tests of the present chapter, the pure phases are described using an ideal gas law for the vapour and a stiffened gas for the liquid. As for the tests of chapter 7, the parameters of these EoS are taken from [Chiapolino et al., 2016]. They are given in table 7.1. The initial pressure used is $P_0 = 3$ bar, so that $\rho_v(P_0) = 12.84$ kg/m^3. The densities are $\rho_{\min} = 8$ kg/m^3 and $\rho_{\max} = 18$ kg/m^3. The value considered for the perturbation width is $l_0 = 0.4$ m

A mesh refinement study is led in order to observe the effective rate of convergence of the solution when the switch between thermodynamic regimes is involved. Figures 8.1 and 8.2 display respectively the results for RKDG2 and RKDG3. One can see that the results are much more noisy than when the density variation does not involve the thermodynamic regime switch point. In addition, the global rate of convergence of the error is penalized by the noise generated by the switch of thermodynamics: all methods accuracies are reduced to first order.

The hypothesis explored here is that this noise would be due to the non-regularity of the thermodynamic functions at the switch point. This non-regularity appears in the change of slope of the isothermal lines in the Clapeyron diagram, as well as in the discontinuity of the speed of sound, both depicted in figure 8.3. The following sections investigate if the discontinuity of the speed of sound is responsible for the noise. In this respect, the following section proposes a modification of the thermodynamics in order to artificially restore the continuity of the speed of sound.

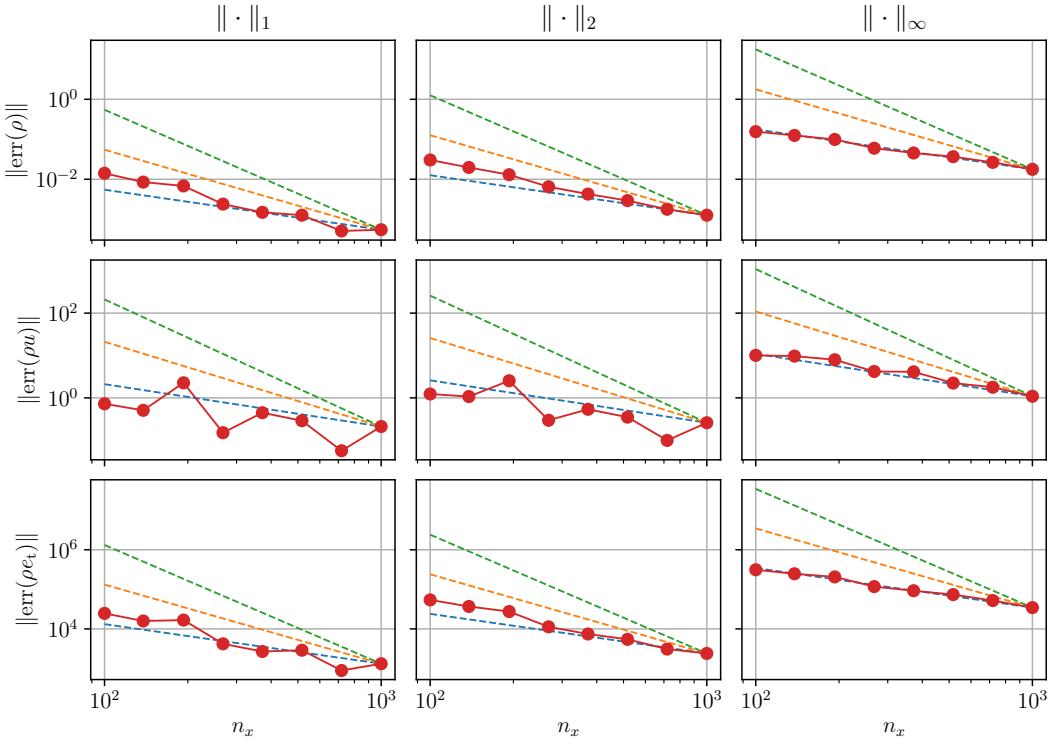

Figure 8.1: RKDG2 convergence experiment around the vapour density. The blue, orange and green dashed lines represent the first-order, second-order and third-order slopes.

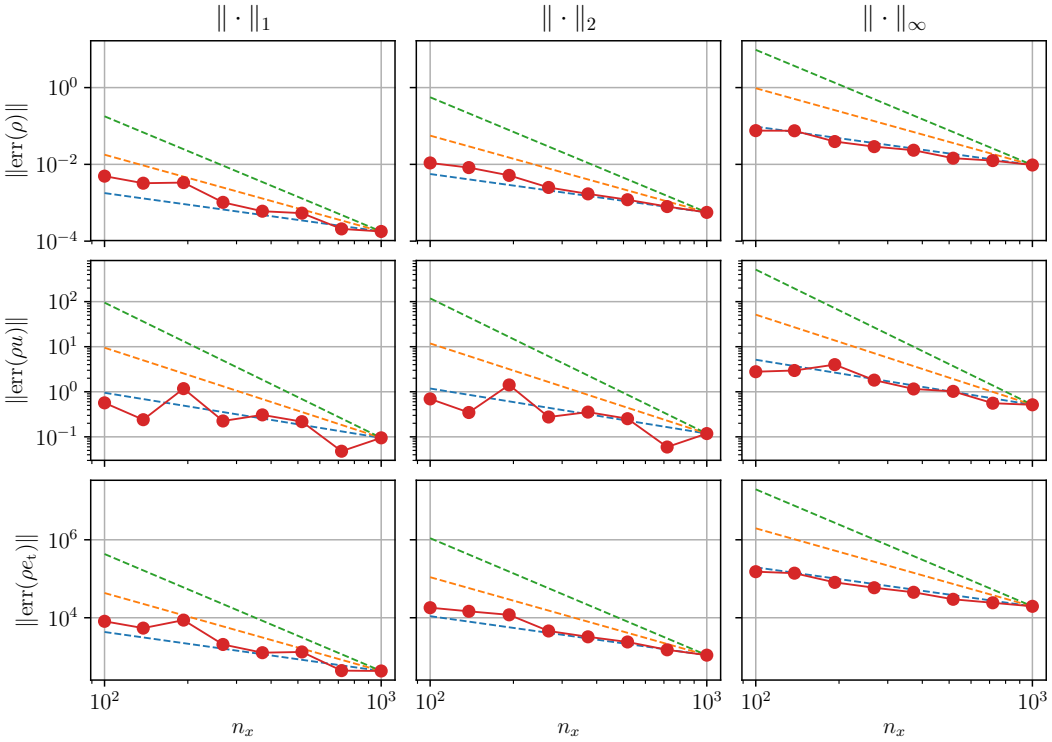

Figure 8.2: RKDG3 convergence experiment around the vapour density. The blue, orange and green dashed lines represent the first-order, second-order and third-order slopes.

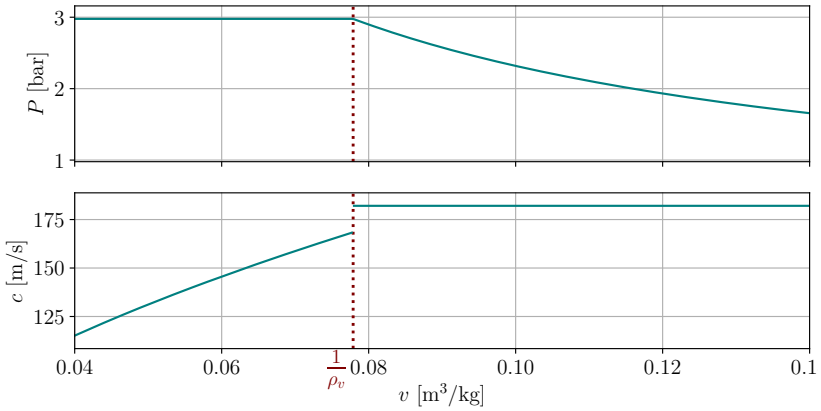

Figure 8.3: Clapeyron diagram showing a non-regular equation of state. The corresponding sound speed is discontinuous.

8.3 Development of a more regular equation of state

In this chapter, the 3-equation model is interpreted as the Euler equations for which the thermodynamic closure is given by the *equilibrium* EoS, which can be written as

$$P^{\mathrm{eq}}(\rho,T)=\begin{cases}P_v(\rho,T)=\rho\,(\gamma-1)\,c_{v,v}T & \text{if } \rho\leq\rho_v(T),\\ P^{\mathrm{sat}}(T) & \text{if } \rho\in\left]\rho_v(T),\rho_\ell(T)\right[,\\ P_\ell(\rho,T)=\rho\,(\gamma-1)\,c_{v,\ell}T+P_{\infty,\ell} & \text{if } \rho\geq\rho_\ell(T),\end{cases}\tag{8.3.1}$$

where P_v and P_ℓ are the pressures given by the EoS of the pure phases. For the sake of simplicity, the vapour and liquid are assumed to follow respectively an ideal gas law and a stiffened gas law in the current context, although they could naturally be modeled with a cubic EoS. The isochoric heat capacity is assumed constant in each phase.

8.3.1 Formulation of a regularized equation of state

The idea explored in the present section consists in formulating an equation of state that would be close to the two-phase homogeneous equilibrium EoS (eq-EoS), while restoring the continuity of the speed of sound. This is done here by allowing the regular EoS to deviate from the eq-EoS within a thin *connexion zone*. This way, instead of having a sharp switch of thermodynamic regime between the pure-phase and the saturated states, a smooth evolution is obtained.

For a given temperature T, the connexion zones on the vapour and liquid sides are defined as $\left[\rho_v^{\ominus}(T),\rho_v^{\oplus}(T)\right]$ and $\left[\rho_\ell^{\ominus}(T),\rho_\ell^{\oplus}(T)\right]$, with

$$\begin{cases}\rho_v^{\ominus}(T)=\rho_v(T)-\sigma_v, & \rho_\ell^{\ominus}(T)=\rho_\ell(T)-\sigma_\ell, \qquad (8.3.2a)\\ \rho_v^{\oplus}(T)=\rho_v(T)+\sigma_v, & \rho_\ell^{\oplus}(T)=\rho_\ell(T)+\sigma_\ell, \qquad (8.3.2b)\end{cases}$$

where σ_v and σ_ℓ are constant parameters, half-width of the connexion zone. Within this interval, the pressure is defined by a cubic spline interpolation between its pure-vapour value $P(\rho_v(T)-\sigma_v,T)$ and its saturated value $P^{\mathrm{sat}}(T)$. The use of a cubic spline allows to reach a $\mathcal{C}^1$-regularity of the equation of state, as both the values and derivatives of the pressure are equal at the connexion points. The regularized EoS then reads

$$P(\rho,T)=\begin{cases}P_v(\rho,T) & \text{if } \rho\leq\rho_v^{\ominus}(T),\\ P_v^{\mathrm{co}}(\rho,T) & \text{if } \rho\in\left]\rho_v^{\ominus}(T),\rho_v^{\oplus}(T)\right[,\\ P^{\mathrm{sat}}(T) & \text{if } \rho\in\left[\rho_v^{\oplus}(T),\rho_\ell^{\ominus}(T)\right],\\ P_\ell^{\mathrm{co}}(\rho,T) & \text{if } \rho\in\left]\rho_\ell^{\ominus}(T),\rho_\ell^{\oplus}(T)\right[,\\ P_\ell(\rho,T) & \text{if } \rho\geq\rho_\ell^{\oplus}(T),\end{cases}\tag{8.3.3}$$

with $P_v^{\mathrm{co}}(\rho,T)$ defined as

$$P_v^{\mathrm{co}}(\rho,T)=p_v^{\mathrm{co}}\left(\xi_v(\rho,T)\right),\tag{8.3.4}$$

where $\xi_v(\rho,T)$ is the change of variable defined by

$$\xi_v(\rho,T)=\frac{\rho-\rho_v^{\ominus}(T)}{\rho_v^{\oplus}(T)-\rho_v^{\ominus}(T)}=\frac{\rho-\rho_v^{\ominus}(T)}{2\sigma_v},\tag{8.3.5}$$

and the cubic spline reads

$$p_v^{\mathrm{co}}(\xi_v,T)=A_3(T)\xi_v^3+A_2(T)\xi_v^2+A_1(T)\xi_v+A_0(T),\tag{8.3.6}$$

with the following coefficients:

$$\begin{cases} A_3(T) = 2\sigma_v \left.\dfrac{\partial P_v}{\partial \rho}\right|_T^{\ominus} + 2\left(P_v^{\ominus}(T) - P^{\rm sat}(T)\right), & \text{(8.3.7a)} \\ A_2(T) = -\left[4\sigma_v \left.\dfrac{\partial P_v}{\partial \rho}\right|_T^{\ominus} + 3\left(P_v^{\ominus}(T) - P^{\rm sat}(T)\right)\right], & \text{(8.3.7b)} \\ A_1(T) = 2\sigma_v \left.\dfrac{\partial P_v}{\partial \rho}\right|_T^{\ominus}, & \text{(8.3.7c)} \\ A_0(T) = P_v^{\ominus}(T), & \text{(8.3.7d)} \end{cases}$$

where the superscript $^{\ominus}$ denotes quantities evaluated at the connection point $(\rho_v^{\ominus}(T), T)$.
As an ideal gas law is considered in the pure vapour phase, one has

$$P_v^{\ominus}(T) = \rho_v^{\ominus}\,(\gamma_v - 1)\,c_{v,v}T \qquad \text{and} \qquad \left.\frac{\partial P_v}{\partial \rho}\right|_T^{\ominus} = (\gamma_v - 1)\,c_{v,v}T. \tag{8.3.8}$$

For the sake of conciseness, the liquid connexion zone is not described, as it is similar to the connexion on the vapour side. Also, the connexion on the vapour side is sufficient for the developments and numerical tests presented in this chapter. Indeed, since the numerical simulations will be performed for $\rho < \rho_\ell^{\ominus}$, we investigate only the connexion between P_v and $P^{\rm sat}$, namely:

- vapour states $\rho \leq \rho_v^{\ominus}$
- connexion states $\rho \in \left]\rho_v^{\ominus}, \rho_v^{\oplus}\right[$
- saturated states $\rho \in \left[\rho_v^{\oplus}, \rho_\ell^{\ominus}\right]$

Starting from the pressure definition, the set of the corresponding thermodynamic quantities can be derived.

8.3.2 Derivation of important thermodynamic quantities

The EoS being defined, the different thermodynamic quantities required for a numerical simulation are derived. More precisely, the isothermal compressibility coefficient β, the isobaric thermal expansion coefficient α, the sensible energy, the isochoric heat capacity and the speed of sound are derived.

8.3.2.1 Isothermal compressibility coefficient

The isothermal compressibility coefficient is defined as

$$\beta = \frac{1}{\rho}\left.\frac{\partial \rho}{\partial P}\right|_T. \tag{8.3.9}$$

In the connexion zone, one has

$$\left.\frac{\partial P_v^{\rm co}}{\partial \rho}\right|_T = \left(3A_3(T)\xi_v^2 + 2A_2(T)\xi_v + A_1(T)\right)\left.\frac{\partial \xi_v}{\partial \rho}\right|_T = \frac{3A_3(T)\xi_v^2 + 2A_2(T)\xi_v + A_1(T)}{2\sigma_v}, \tag{8.3.10}$$

so that for $\rho \in \left]\rho_v^{\ominus}, \rho_v^{\oplus}\right[$,

$$\beta = \beta_v^{\rm co} = \frac{1}{\rho}\frac{2\sigma_v}{3A_3(T)\xi_v^2 + 2A_2(T)\xi_v + A_1(T)}. \tag{8.3.11}$$

8.3.2.2 Isobaric thermal expansion coefficient

Similarly, one can compute the isobaric thermal expansion coefficient defined by

$$\alpha = -\frac{1}{\rho}\left.\frac{\partial \rho}{\partial T}\right|_P = \frac{1}{\rho}\left.\frac{\partial \rho}{\partial P}\right|_T \left.\frac{\partial P}{\partial T}\right|_\rho = \beta \left.\frac{\partial P}{\partial T}\right|_\rho . \tag{8.3.12}$$

In order to obtain the value of α within the connexion zone, is then interesting to evaluate $\left.\frac{\partial P}{\partial T}\right|_\rho$. One has

$$\left.\frac{\partial \xi_v}{\partial T}\right|_\rho = \frac{-1}{2\sigma_v}\frac{\mathrm{d}\rho_v^{\ominus}}{\mathrm{d}T} = -\frac{\rho_v'}{2\sigma_v}, \tag{8.3.13}$$

with

$$\rho_v' = \left.\frac{\mathrm{d}\rho_v}{\mathrm{d}T}\right|_{\mathrm{sat}} = -\rho_v\alpha_v + \rho_v\beta_v\frac{\mathrm{d}P^{\mathrm{sat}}}{\mathrm{d}T} = -\frac{\rho_v}{T} + \frac{\rho_v}{P}\frac{\mathrm{d}P^{\mathrm{sat}}}{\mathrm{d}T}. \tag{8.3.14}$$

The differential of the pressure with respect to temperature can then be written under the form

$$\left.\frac{\partial P_v^{\mathrm{co}}}{\partial T}\right|_\rho = B_3(T)\xi_v^3 + B_2(T)\xi_v^2 + B_1(T)\xi_v + B_0(T), \tag{8.3.15}$$

with the coefficients

$$\begin{cases} B_3(T) = A_3'(T), & \text{(8.3.16a)} \\ B_2(T) = A_2'(T) - 3A_3(T)\dfrac{\rho_v'(T)}{2\sigma_v}, & \text{(8.3.16b)} \\ B_1(T) = A_1'(T) - 2A_2(T)\dfrac{\rho_v'(T)}{2\sigma_v}, & \text{(8.3.16c)} \\ B_0(T) = A_0'(T) - A_1(T)\dfrac{\rho_v'(T)}{2\sigma_v}. & \text{(8.3.16d)} \end{cases}$$

The derivatives $A_k'(T)$ of the coefficients $A_k(T)$ defined in equation (8.3.7) can be obtained using

$$\frac{\mathrm{d}}{\mathrm{d}T}\left(2\sigma_v\left.\frac{\partial P_v}{\partial \rho}\right|_T^{\ominus}\right) = 2\sigma_v\left(\gamma_v - 1\right)c_{v,v}, \tag{8.3.17a}$$

$$P_v^{\ominus\prime} = \frac{\mathrm{d}P_v^{\ominus}}{\mathrm{d}T} = \left(\gamma_v - 1\right)c_{v,v}\left(\rho_v^{\ominus}(T) + T\rho_v'(T)\right), \tag{8.3.17b}$$

and using the Clausius-Clapeyron relation (2.3.23) for $\dfrac{\mathrm{d}P^{\mathrm{sat}}}{\mathrm{d}T}$. It finally reads

$$\begin{cases} A_3'(T) = 2\sigma_v\left(\gamma_v - 1\right)c_{v,v} + 2\left(P_v^{\ominus\prime} - \dfrac{\mathrm{d}P^{\mathrm{sat}}}{\mathrm{d}T}\right), & \text{(8.3.18a)} \\ A_2'(T) = -\left[4\sigma_v\left(\gamma_v - 1\right)c_{v,v} + 3\left(P_v^{\ominus\prime} - \dfrac{\mathrm{d}P^{\mathrm{sat}}}{\mathrm{d}T}\right)\right], & \text{(8.3.18b)} \\ A_1'(T) = 2\sigma_v\left(\gamma_v - 1\right)c_{v,v}, & \text{(8.3.18c)} \\ A_0'(T) = P_v^{\ominus\prime}, & \text{(8.3.18d)} \end{cases}$$

8.3.2.3 Sensible energy

Introducing the *residual value* $\underset{\rho}{\Delta} e_s(\rho,T)$, presented in section 2.2.2.2, the sensible energy can be obtained. It reads

$$e_s(\rho,T) = e_s^{\mathrm{IG}}(T) + \underset{\rho}{\Delta} e_s(\rho,T). \tag{8.3.19}$$

Since the pure vapour is modeled by an ideal gas law, one has:

$$\forall \rho < \rho_v^{\ominus}, \quad \underset{\rho}{\Delta} e_s(\rho,T) = \int_0^{\rho} \frac{1}{\varrho^2}\left(P(\varrho,T) - T\left.\frac{\partial P}{\partial T}\right|_{\rho}\right)\mathrm{d}\varrho = 0, \tag{8.3.20}$$

and

$$\boxed{\forall \rho < \rho_v^{\ominus}, \quad e_s(\rho,T) = e_s^{\mathrm{IG}}(T).} \tag{8.3.21}$$

The residual value of the sensible energy in the connexion zone (i.e. for $\rho \in \left[\rho_v^{\ominus}, \rho_v^{\oplus}\right]$) is then:

$$\underset{\rho}{\Delta} e_s^{\mathrm{co}}(\rho,T) = \int_{\rho_v^{\ominus}}^{\rho} \frac{1}{\varrho^2}\left(P_v^{\mathrm{co}}(\varrho,T) - T\left.\frac{\partial P_v^{\mathrm{co}}}{\partial T}\right|_{\rho}\right)\mathrm{d}\varrho, \tag{8.3.22}$$

which can be recast into

$$\underset{\rho}{\Delta} e_s^{\mathrm{co}}(\rho,T) = \sum_{k=0}^{3}\left(A_k(T) - TB_k(T)\right) I_k(\rho,T), \tag{8.3.23}$$

with the terms A_k and B_k defined in equations (8.3.7) and (8.3.16), and introducing the integral terms $I_k(\rho,T)$ defined by

$$\begin{cases} I_0(\rho,T) = \displaystyle\int_{\rho_v^{\ominus}}^{\rho} \frac{1}{\varrho^2} = \frac{1}{\rho_v^{\ominus}} - \frac{1}{\rho}, & \text{(8.3.24a)} \\ I_1(\rho,T) = \displaystyle\int_{\rho_v^{\ominus}}^{\rho} \frac{\xi_v(\rho,T)}{\varrho^2} = \frac{1}{2\sigma_v r_\rho}\left[r_\rho \ln\left(r_\rho\right) + 1 - r_\rho\right], & \text{(8.3.24b)} \\ I_2(\rho,T) = \displaystyle\int_{\rho_v^{\ominus}}^{\rho} \frac{\xi_v^2(\rho,T)}{\varrho^2} = \frac{\rho_v^{\ominus}}{4\sigma_v^2 r_\rho}\left[-2r_\rho \ln\left(r_\rho\right) - 1 + r_\rho^2\right], & \text{(8.3.24c)} \\ I_3(\rho,T) = \displaystyle\int_{\rho_v^{\ominus}}^{\rho} \frac{\xi_v^3(\rho,T)}{\varrho^2} = \frac{\rho_v^{\ominus 2}}{8\sigma_v^3 r_\rho}\left[6r_\rho \ln\left(r_\rho\right) + 2 + 3r_\rho - 6r_\rho^2 + r_\rho^3\right], & \text{(8.3.24d)} \end{cases}$$

with

$$r_\rho = \frac{\rho}{\rho_v^{\ominus}}. \tag{8.3.25}$$

In the connexion zone, the sensible energy finally reads:

$$\boxed{\forall \rho \in \left[\rho_v^{\ominus}, \rho_v^{\oplus}\right], \quad e_s(\rho,T) = e_s^{\mathrm{IG}}(\rho,T) + \sum_{k=0}^{3}\left(A_k(T) - TB_k(T)\right) I_k(\rho,T).} \tag{8.3.26}$$

Note that the sensible energy in the saturated two-phase regime (i.e. $\rho \in \left[\rho_v^{\oplus}, \rho_\ell^{\ominus}\right]$) has been slightly

modified by the regularization. In this interval, computing the residual value yields:

$$\begin{aligned} e_s(\rho,T) &= e_s^{\mathrm{IG}}(\rho,T) + \int_{\rho_v^{\ominus}}^{\rho_v^{\oplus}} \frac{1}{\varrho^2}\left(P_v^{\mathrm{co}}(\varrho,T) - T\left.\frac{\partial P_v^{\mathrm{co}}}{\partial T}\right|_{\rho}\right)\mathrm{d}\varrho + \int_{\rho_v^{\oplus}}^{\rho} \frac{1}{\varrho^2}\left(P^{\mathrm{sat}}(T) - T\frac{\mathrm{d}P^{\mathrm{sat}}}{\mathrm{d}T}\right)\mathrm{d}\varrho, \\ &= e_s^{\mathrm{co}}(\rho_v^{\oplus},T) + \int_{\rho_v^{\oplus}}^{\rho} \frac{1}{\varrho^2}\left(P^{\mathrm{sat}}(T) - T\frac{\mathrm{d}P^{\mathrm{sat}}}{\mathrm{d}T}\right)\mathrm{d}\varrho, \\ &= e_s^{\mathrm{co}}(\rho_v^{\oplus},T) + \int_{\rho_v}^{\rho} \frac{1}{\varrho^2}\left(P^{\mathrm{sat}}(T) - T\frac{\mathrm{d}P^{\mathrm{sat}}}{\mathrm{d}T}\right)\mathrm{d}\varrho - \int_{\rho_v}^{\rho_v^{\oplus}} \frac{1}{\varrho^2}\left(P^{\mathrm{sat}}(T) - T\frac{\mathrm{d}P^{\mathrm{sat}}}{\mathrm{d}T}\right)\mathrm{d}\varrho, \end{aligned}$$

which can be rewritten as

$$\boxed{\forall \rho \in \left[\rho_v^{\oplus}, \rho_\ell^{\ominus}\right], \quad e_s(\rho,T) = e_s^{\mathrm{eq}}(\rho,T) + \left(e_s^{\mathrm{co}}(\rho_v^{\oplus},T) - e_s^{\mathrm{eq}}(\rho_v^{\oplus},T)\right),} \tag{8.3.27}$$

with e_s^{eq} the sensible energy corresponding to the eq-EoS.

8.3.2.4 Isochoric heat capacity

8.3.2.4.1 Pure vapour

Since the pure vapour is modeled by a constant-c_v ideal gas law, one has

$$\boxed{\forall \rho \leq \rho_v^{\ominus}, \quad c_v(\rho,T) = c_{v,v}.} \tag{8.3.28}$$

8.3.2.4.2 Connexion zone

The heat capacity in the connexion zone $\rho \in \left[\rho_v^{\ominus}, \rho_v^{\oplus}\right]$ is written as:

$$c_v(\rho,T) = c_{v,v} + \underset{\rho}{\Delta} c_v^{\mathrm{co}}(\rho,T) = c_{v,v} - \int_{\rho_v^{\ominus}}^{\rho} \frac{T}{\varrho^2}\left.\frac{\partial^2 P}{\partial T^2}\right|_{\rho} \mathrm{d}\varrho, \tag{8.3.29}$$

One can introduce the notation

$$\left.\frac{\partial^2 P}{\partial T^2}\right|_{\rho} = C_3(T)\xi_v^3 + C_2(T)\xi_v^2 + C_1(T)\xi_v + C_0(T), \tag{8.3.30}$$

so that

$$\boxed{\forall \rho \in \left[\rho_v^{\ominus}, \rho_v^{\oplus}\right], \quad c_v(\rho,T) = c_{v,v} - \sum_{k=0}^{3} TC_k(T)I_k(\rho,T).} \tag{8.3.31}$$

The coefficients C_k have the following expression:

$$\begin{cases} C_3(T) = B_3'(T) & = A_3''(T), & \text{(8.3.32a)} \\ C_2(T) = B_2'(T) - 3B_3(T)\dfrac{\rho_v'(T)}{2\sigma_v} & = A_2''(T) - 3\left(A_3'(T) + B_3(T)\right)\dfrac{\rho_v'(T)}{2\sigma_v} - 3A_3(T)\dfrac{\rho_v''(T)}{2\sigma_v}, & \text{(8.3.32b)} \\ C_1(T) = B_1'(T) - 2B_2(T)\dfrac{\rho_v'(T)}{2\sigma_v} & = A_1''(T) - 2\left(A_2'(T) + B_2(T)\right)\dfrac{\rho_v'(T)}{2\sigma_v} - 2A_2(T)\dfrac{\rho_v''(T)}{2\sigma_v}, & \text{(8.3.32c)} \\ C_0(T) = B_0'(T) - B_1(T)\dfrac{\rho_v'(T)}{2\sigma_v} & = A_0''(T) - \left(A_1'(T) + B_1(T)\right)\dfrac{\rho_v'(T)}{2\sigma_v} - A_1(T)\dfrac{\rho_v''(T)}{2\sigma_v}. & \text{(8.3.32d)} \end{cases}$$

In order to compute the second-order derivatives $A_k''(T)$ of the coefficients $A_k(T)$ defined in equation (8.3.7), one has,

$$\frac{\mathrm{d}^2}{\mathrm{d}T^2}\left(2\sigma_v \left.\frac{\partial P_v}{\partial \rho}\right|_T^{\ominus}\right) = 0, \tag{8.3.33a}$$

$$P_v^{\ominus\prime\prime} = \frac{\mathrm{d}^2 P_v^{\ominus}}{\mathrm{d}T^2} = (\gamma_v - 1)\, c_{v,v}\left(2\rho_v'(T) + T\rho_v''(T)\right), \tag{8.3.33b}$$

so that

$$\begin{cases} A_3''(T) = 2\left(P_v^{\ominus\prime\prime} - \dfrac{\mathrm{d}^2 P^{\mathrm{sat}}}{\mathrm{d}T^2}\right), & (8.3.34a)\\ A_2''(T) = -\left[4\sigma_v(\gamma_v - 1)\, c_{v,v} + 3\left(P_v^{\ominus\prime\prime} - \dfrac{\mathrm{d}^2 P^{\mathrm{sat}}}{\mathrm{d}T^2}\right)\right], & (8.3.34b)\\ A_1''(T) = 0, & (8.3.34c)\\ A_0''(T) = P_v^{\ominus\prime\prime}. & (8.3.34d) \end{cases}$$

The quantity $\rho_v''(T)$ is obtained by differentiating equation (8.3.14), which yields

$$\rho_v''(T) = \rho_v'\left(\frac{1}{P}\frac{\mathrm{d}P^{\mathrm{sat}}}{\mathrm{d}T} - \frac{1}{T}\right) + \rho_v\left[\frac{1}{P}\frac{\mathrm{d}^2 P^{\mathrm{sat}}}{\mathrm{d}T^2} - \frac{1}{P^2}\left(\frac{\mathrm{d}P^{\mathrm{sat}}}{\mathrm{d}T}\right) + \frac{1}{T^2}\right], \tag{8.3.35}$$

and

$$\frac{\mathrm{d}^2 P^{\mathrm{sat}}}{\mathrm{d}T^2} = \frac{\mathrm{d}}{\mathrm{d}T}\left(\frac{\rho_v\rho_\ell\,(h_v - h_\ell)}{T\,(\rho_\ell - \rho_v)}\right) \tag{8.3.36}$$

$$= \left(\frac{\rho_v'}{\rho_v} + \frac{\rho_\ell'}{\rho_\ell} - \frac{1}{T} + \frac{\gamma_v c_{v,v} - \gamma_\ell c_{v,\ell}}{h_v - h_\ell} - \frac{\rho_v' - \rho_\ell'}{\rho_v - \rho_\ell}\right)\frac{\mathrm{d}P^{\mathrm{sat}}}{\mathrm{d}T}, \tag{8.3.37}$$

with

$$\rho_\ell' = \left.\frac{\mathrm{d}\rho_\ell}{\mathrm{d}T}\right|_{\mathrm{sat}} = -\rho_\ell\alpha_\ell + \rho_\ell\beta_\ell\frac{\mathrm{d}P^{\mathrm{sat}}}{\mathrm{d}T} = -\frac{\rho_\ell}{T} + \frac{\rho_\ell}{P + P_{\infty,\ell}}\frac{\mathrm{d}P^{\mathrm{sat}}}{\mathrm{d}T}. \tag{8.3.38}$$

8.3.2.4.3 Saturation zone

In the saturation interval, the isochoric heat capacity is obtained similarly to the sensible energy,

$$\boxed{\forall \rho \in \left[\rho_v^{\oplus}, \rho_\ell^{\ominus}\right], \quad c_v(\rho, T) = c_v^{\mathrm{eq}}(\rho, T) + \left(c_v^{\mathrm{co}}(\rho_v^{\oplus}, T) - c_v^{\mathrm{eq}}(\rho_v^{\oplus}, T)\right),,} \tag{8.3.39}$$

where the heat capacity of the eq-EoS in the saturation reads

$$c_v^{\mathrm{eq}}(\rho, T) = c_{v,v} - T\frac{\mathrm{d}^2 P^{\mathrm{sat}}}{\mathrm{d}T^2}\left(\frac{1}{\rho} - \frac{1}{\rho_v}\right), \tag{8.3.40}$$

see appendix B.1 for its derivation.

8.3.2.5 Speed of sound

Using the previous derivations, the speed of sound in the connexion zone is obtained using equations (2.2.54) and (2.2.53) page 27, which yield

$$c^2 = \frac{c_p}{\rho\beta c_v} = \frac{1}{\rho\beta} + \frac{\alpha^2 T}{\rho^2\beta^2 c_v} = \frac{1}{\rho\beta} + \frac{T}{\rho^2 c_v}\left(\left.\frac{\partial P}{\partial T}\right|_\rho\right)^2, \tag{8.3.41}$$

the terms in this expression being calculated in the previous paragraphs of the present section.

The speed of sound in the saturation zone is also modified by the regularization. Its derivation being rather long, it is provided in appendix B.1. Its final expression is:

$$\frac{1}{\rho^2 c^2(\rho,T)} = \frac{1}{\rho^2 c_{\text{eq}}^2(\rho,T)} + \frac{1}{{\rho_v^\oplus}^2 c_{\text{co}}^2(\rho_v^\oplus,T)} - \frac{1}{{\rho_v^\oplus}^2 c_{\text{eq}}^2(\rho_v^\oplus,T)}. \tag{8.3.42}$$

From these expressions, it is clear that the speed of sound is now continous at both ends of the connexion zone.

8.3.3 Illustration of the regularized quantities

The pressure, sensible energy, isochoric heat capacity and the speed of sound are displayed in figure 8.4. These quantities are plotted with respect to the mass-specific volume along an isothermal line. They are compared to the results of the eq-EoS. This naturally confirms that the regularization of the pressure along isothermal lines restores in particular the continuity of the speed of sound.

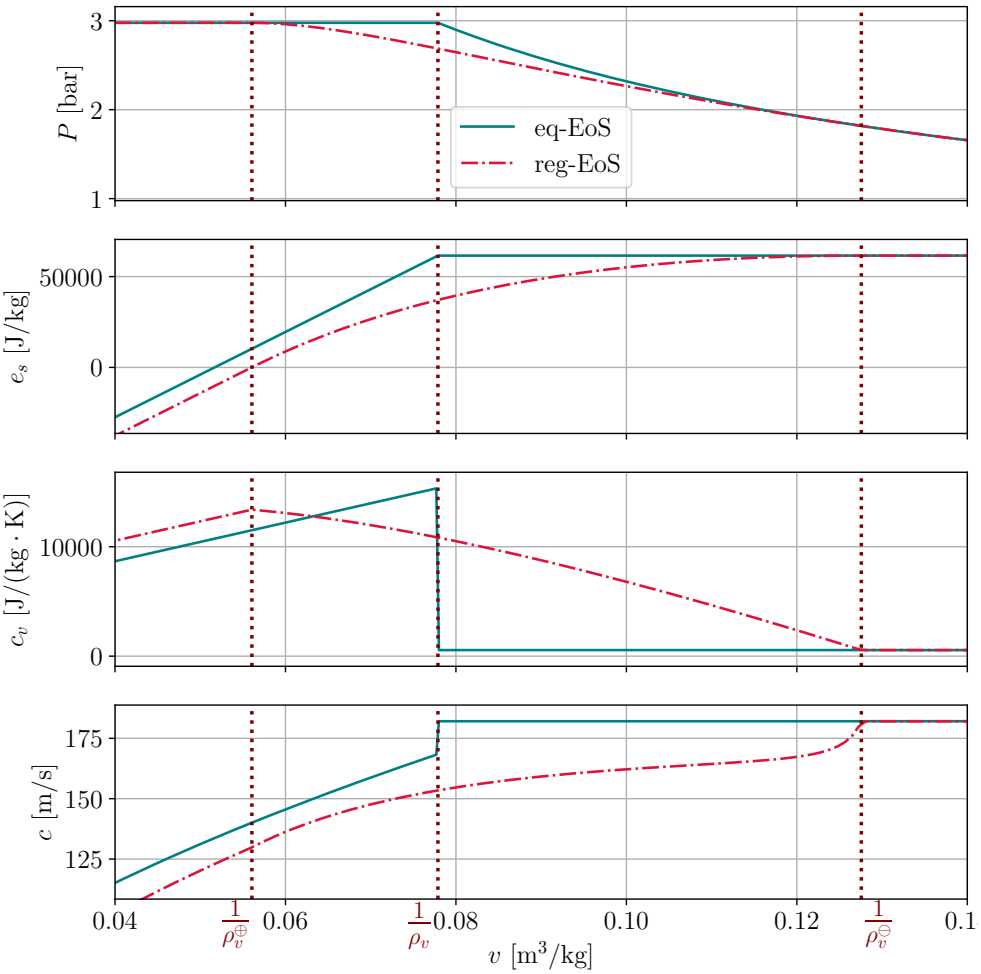

Figure 8.4: Illustration of the thermodynamic properties of the regularized EoS. The pressure, sensible energy, isochoric heat capacity and speed of sound along an isothermal line are respectively displayed against the non-regularized equilibrium EoS.

8.4 Results and discussion

8.4.1 Behaviour of the regularized EoS

In order to evaluate the behaviour of the regularized EoS, snapshots of the solution are compared to a transport using the non-regularized EoS. The initial fields are given in figure 8.5. The half-width of the connexion zone used is the same as in figure 8.4 $\sigma_v = \dfrac{\rho_v^{\oplus} - \rho_v^{\ominus}}{2} = 5$ kg/m^3. One can note that

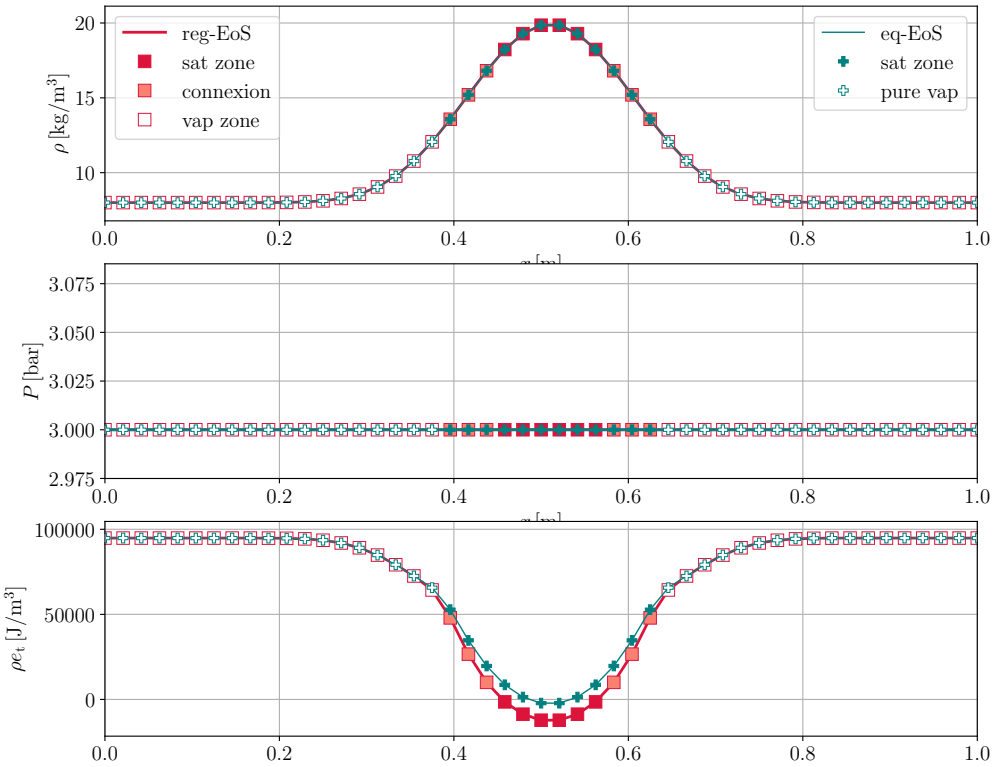

Figure 8.5: Initial solution for the tests with the regularized EoS and the equilibrium EoS. The red lines denotes the solution for the regularized EoS, while the blue lines denote the solution for the equilibrium EoS. For each EoS, the symbols are filled with different colors regarding the interval in which the thermodynamic state is. For the reg-EoS, pure vapour states are in white, while the connexion zone is in orange and the saturation zone are in red. For the equilibrium EoS, the pure vapour states are in white and the two-phase states are in blue.

the total energy field is different between the two solutions. This comes from the modification of the sensible energy by the regularization of the equation of state.

For all the test cases, a second-order RKDG method is employed (i.e. $\mathbb{P}^1$-polynomials are used). The CFL number is taken as $\eta_C = 0.2$.

First, a discretization with 50 elements is considered. A snapshot of the density and pressure fields is displayed in figure 8.6. The results are very close. It appears that the noise, in the regularized case, seems to be generated at the switch between the connexion zone and the pure vapour zone. One can see in figure 8.4 that this zone corresponds to the zone with the strongest variations of the speed of sound. In this respect, it may be interesting to refine the mesh in order to see if a better resolution in this thermodynamic zone allows to reduce the height of the spurious peaks.

Figure 8.7 displays the solution obtained on refined meshes, of respectively 100 and 1000 elements.

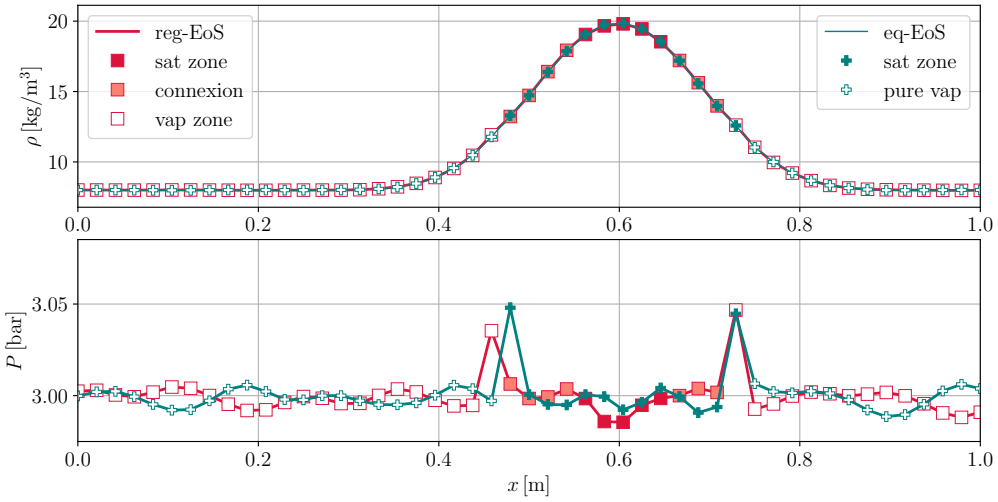

Figure 8.6: Snapshot of the solution after 4.3 ms. The mesh contains 50 elements. density and pressure fields are given.

Yet, there is unfortunately no noticeable improvement in the behaviour of the regularized solution. Restoring the continuity of the speed of sound does not seem to be sufficient to effectively reduce the spurious noise. It would thus be interesting to investigate smoother regularizations, by setting up higher-order connexions, in order to check if higher regularity allows for a better behaviour of the pressure field at the connexion between the pure vapour and the saturated zone.

8.5 Conclusion

This chapter provided an exploratory study that aimed at testing the conjecture stating that, for the equilibrium EoS, the noise observed at the switch between pure phase and two-phase states was due to the discontinuity of the speed of sound. In order to do this, a regularized formulation of the equilibrium EoS was proposed, and all the subsequent derivations were provided in order to formulate a consistent set of thermodynamic quantities that are necessary for the flow solver.

Unfortunately, the regularized EoS displayed no noticeable improvement compared to the equilibrium EoS. Indeed, despite the continuity of the speed of sound, the amount of spurious noise is actually comparable to the one of the equilibrium EoS. Higher-order regularization may then be necessary to improve effectively the solution.

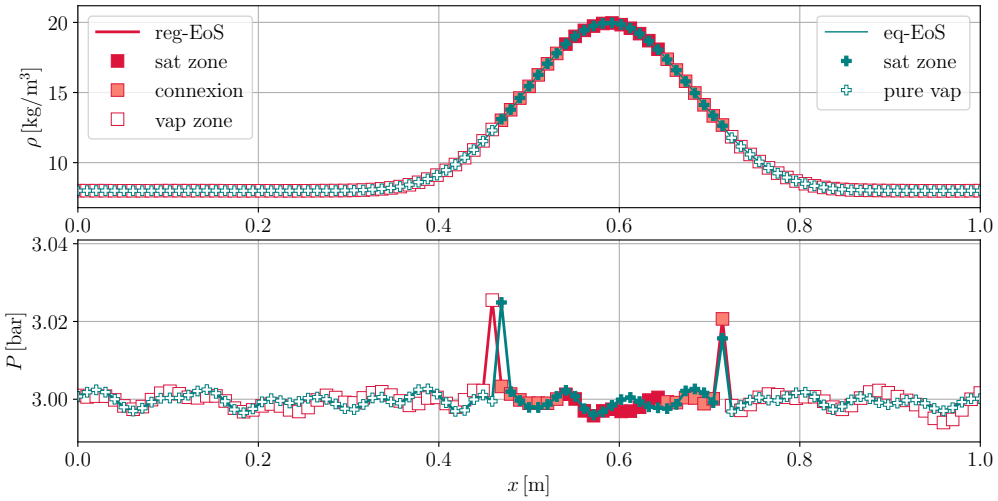

(a) 100-element mesh

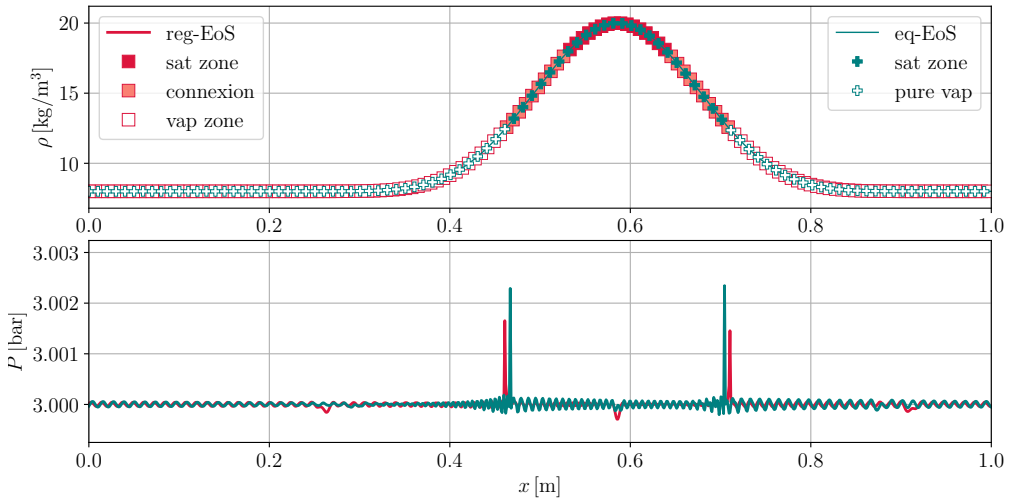

(b) 1000-element mesh

Figure 8.7: Snapshot of the solution after 4.3 ms, for two mesh resolutions. Density and pressure fields are given. For the 1000-element mesh, symbols were removed from the pressure plot in order to enhance the readability.

General conclusion and perspectives

Conclusions

This thesis was dedicated to the development of a unified framework to model subcritical and supercritical flows in a HPC unstructured multicomponent solver, which is well suited for LES computations on complex geometries. In order to achieve this goal, a variety of questions has been addressed.

First, the real gas thermodynamics have been studied, in order to account for the non-ideal molecular interactions that characterize high-pressure flows. As they represent a satisfying compromise between efficiency and accuracy, the choice was made to use cubic equations of state, typically the *Peng-Robinson* or the *Soave-Redlich-Kwong* equations of state. From this choice of thermodynamics, the practical computation of two-phase equilibrium was provided. In addition, a computationally efficient simplified equilibrium formulation was proposed and compared to the actual equilibrium computation, on a liquid-gas interface representative of the configuration encountered in a liquid rocket engine.

Then, a global study of interface modeling techniques has been led to identify the most relevant interface representation for subcritical flows, regarding the current objectives. The natural choice that emerged was to use multifluid methods. The target applications require the model to handle phase change phenomena. In the context of multifluid methods, this can be achieved by considering stiff relaxation towards thermodynamic equilibrium, either by considering directly the homogeneous equilibrium 3-equation model or by using a 4-equation model with an operator splitting technique to treat the instantaneous relaxation towards equilibrium. The required developments for the integration of both the 3-equation and the 4-equation models into the solver AVBP have been provided and validated. In particular, the Jacobian matrix of the flux function for both models has been described and the corresponding formulations for the characteristic boundary conditions have been derived.

This allowed to perform numerical simulations in order to demonstrate the ability of the implemented model to solve subcritical flows. The Mascotte configuration was simulated in subcritical pressure operating conditions. Two-dimensional simulations were led to compare the different formulations, using either the 3-equation or the 4-equation models, and applying the exact or approximate equilibrium computations. Even if these models are relatively simple, and even if physical phenomena, such as atomization and non-ideal multicomponent diffusion have been neglected, the three-dimensional reactive computation provides satisfying results, that are encouraging regarding the approach developed in this Ph.D thesis. In addition, the 3-equation model was applied to the ECN[1] *spray A* case. For this configuration involving transcritical chamber pressure regarding the critical pressure of the pure components, the use of the 3-equation model allowed to stabilize the computation, for which fully conservative Navier-Stokes simulations had led to numerical crashes. Despite these interesting results, the simulation results were found to feature strong pressure oscillations, leading to anticipated jet destabilization compared to the experimental results. On this case, further investigation would be necessary to go towards more predictive simulations.

[1] Engine Combustion Network (https://ecn.sandia.gov/)

Nevertheless, the computations exhibited relatively large spurious pressure noise at points where the thermodynamic regime enters the two-phase region. This motivated to take a step back, in order to compare the multifluid models on elementary academic configurations, and study their behaviour in terms of pressure noise. It has been observed that this spurious noise generation was closely related to the homogeneous thermodynamic equilibrium assumption, whether when imposed by solving directly the homogeneous equilibrium 3-equation model, or by applying stiff relaxation towards this equilibrium on the 4-equation or 5-equations models by an operator splitting technique. This undesired behaviour has been shown to deteriorate the convergence order of the numerical method. Finally, an investigation has been led in order to see if such noise could be reduced by fixing the speed of sound discontinuity at the limit between two-phase and single phase states for the 3-equation model. This was done by introducing a novel thermodynamic closure consisting in the regularization of the homogeneous equilibrium equation of state. It appeared that the mere continuity of the speed of sound, as restored by this regularization, was not sufficient to effectively improve the global behaviour of the numerical resolution of the flow.

Multiple contributions to the research effort have been carried out in throughout the present Ph.D thesis. Concerning the numerical methods, a new formulation of finite-element method with flux-corrected transport based on a third-order two-step Taylor-Galerkin method was proposed, providing a positivity preserving scheme with a slightly better convergence rate than the previously existing FEM-FCT schemes based on one-step methods.

Regarding the flow model, the present work proposed a formulation of the 3-equation and 4-equation compressible multifluid methods, classicaly used with finite-volume Godunov-like transport, to a Taylor-Galerkin numerical framework. For this, the general expression for the Jacobian matrices of the flux function and for the characteristic boundary conditions were provided for both models, valid for any choice of thermodynamic closure for each phase. These models have been implemented into the HPC unstructured solver AVBP and applied to realistic (liquid rocket engine injection and Diesel engine injection) configurations, for which they provided encouraging results.

A study of the generation of spurious pressure noise for the different multifluid models, based on elementary numerical experiments, was proposed. In particular, the pressure noise encountered when using the 3-equation model was further studied in order to open a discussion on the consequences of a non-regular equation of state on the numerical transport. Finally, regarding the equilibrium thermodynamics, a simplified version of the multicomponent two-phase equilibrium formulation was proposed, which allowed for a very valuable speedup (about 10 times faster on a 2D simulation), while providing an acceptable approximation for the considered cases.

Perspectives

This Ph.D thesis has paved the way for further developments towards the accurate simulation of subcritical to supercritical flows. There remain a lot of ways to improve the model and go towards more predictive results.

Regarding the developments provided in chapter 2, the exact multicomponent equilibrium computation may be further optimized – although its complexity makes it naturally very expensive to compute, especially when more than two chemical components are involved.

Concerning the results of chapter 6, the excessive interface smearing observed in the simulations, due to the numerical diffusion of the interface, should be prevented. Developments in this direction have been led by [Shukla et al., 2010, Chiapolino et al., 2017], but the first one is non-conservative and the second one applies to the 5-equation model in which the liquid volume fraction z_ℓ is transported. It would be interesting to work on the adaptation of one of these methods to a conservative compressible

3-equation or 4-equation formulation. In terms of physical models, it would be necessary to integrate surface tension. Also, finer representation of multicomponent diffusion, both in the pure phases and in the interface region, should be provided. This would allow for example to investigate the ability of the solver to address laminar counter-flow flames. Another very important point to address is the coupling of the separate two-phase flow multifluid solver with a disperse flow solver, in order for the model to be able to handle atomization, enhancing the representation of the flow when the inclusions (droplets, bubbles) become unresolved on the computational grid. In this context of large-eddy simulations, it would be interesting to work on subgrid-scale models for the interface region, which have not been studied at the present time.

Finally, according to the discussions of chapters 7 and 8 the issue of the spurious noise at the interface deserves further studies, in order to limit the numerical error and allow to effectively reach higher order convergence for the numerical methods.

Appendix A

Thermodynamic Developments

This appendix summarizes complementary thermodynamic developments.

A.1 Thermodynamic potential values for Ideal gases

For an single-component ideal gas, the sensible energy and enthalpy can be shown to depend only on the temperature and mixture composition. They write respectively

$$e_s^{\mathrm{IG}}(\rho,T) = e_s^{\mathrm{IG}}(T) = \int_{T_0}^{T} c_v^0(T')\,\mathrm{d}T' + e_0, \tag{A.1.1}$$

and

$$h_s^{\mathrm{IG}}(\rho,T) = h_s^{\mathrm{IG}}(T) = \int_{T_0}^{T} c_p^0(T')\,\mathrm{d}T' + h_0 = \int_{T_0}^{T} c_v^0(T')\,\mathrm{d}T' + r(T-T_0) + h_0, \tag{A.1.2}$$

with the mass-specific reference isochoric heat capacity of pure components c_v^0 obtained, as a function of temperature, from experimental data (by tabulation or polynomial fits such as the NASA polynomials) [McBride et al., 2002]. The reference isobaric heat capacity c_p^0 is obtained from $c_p^0 = c_v^0 + r$. e_0 is the reference energy for the thermodynamic point (P_0, T_0), and $h_0 = e_0 + \frac{P_0}{\rho_0}$ with $\rho_0 = \frac{P_0}{rT_0}$.
Entropy is given as

$$s^{\mathrm{IG}}(\rho,T) = \int_{T_0}^{T} \frac{c_v^0(T')}{T'}\,\mathrm{d}T' + r\left[\ln\left(\frac{T}{T_0}\right) - \ln\left(\frac{P}{P_0}\right)\right] + s_0, \tag{A.1.3}$$

where $s_0 = s^{\mathrm{IG}}(T_0, P_0)$ is the entropy of the reference state (T_0, P_0).
From these values, the Helmoltz energy is easily obtained:

$$f_s^{\mathrm{IG}}(\rho,T) = \int_{T_0}^{T} c_v^0(T')\left(1-\frac{T}{T'}\right)\mathrm{d}T' + rT\left[\ln\left(\frac{P}{P_0}\right) - \ln\left(\frac{T}{T_0}\right)\right] + (T-T_0)s_0 + f_0, \tag{A.1.4}$$

and the Gibbs energy reads:

$$g^{\mathrm{IG}}(\rho,T) = \int_{T_0}^{T} c_v^0(T')\left(1-\frac{T}{T'}\right)\mathrm{d}T' + rT\left[\ln\left(\frac{P}{P_0}\right) - \ln\left(\frac{T}{T_0}\right)\right] + (T-T_0)(s_0+r) + g_0. \tag{A.1.5}$$

Their reference values are defined by $f_0 = e_0 - T_0 s_0$ and $g_0 = h_0 - T_0 s_0$.

A.2 Practical calculations for the cubic equations of states

A.2.1 Solving the cubic density equation

The different cubic EoS (2.2.17) are defined as pressure-explicit relations. Computing the density for a given couple of pressure and temperature yields the following cubic polynomial equation:

$$\left(1+\varepsilon_1\bar{b}\rho-\varepsilon_2\bar{b}^2\rho^2\right)\left(1-\bar{b}\rho\right)P+\left(1-\bar{b}\rho\right)\bar{a}\rho^2-\left(1+\varepsilon_1\bar{b}\rho-\varepsilon_2\bar{b}^2\rho^2\right)\rho\bar{r}T=0 \tag{A.2.1}$$

i.e.

$$A_{[P,T,\underline{\boldsymbol{Y}}]}\rho^3+B_{[P,T,\underline{\boldsymbol{Y}}]}\rho^2+C_{[P,T,\underline{\boldsymbol{Y}}]}\rho+D_{[P,T,\underline{\boldsymbol{Y}}]}=0 \tag{A.2.2}$$

with

$$\begin{cases} A_{[P,T,\underline{\boldsymbol{Y}}]}=\varepsilon_2\bar{b}^3P-\bar{a}\bar{b}+\varepsilon_2\bar{b}^2\bar{r}T & \text{(A.2.3a)}\\ B_{[P,T,\underline{\boldsymbol{Y}}]}=-P\left(\varepsilon_1+\varepsilon_2\right)\bar{b}^2+\bar{a}-\varepsilon_1\bar{b}\bar{r}T & \text{(A.2.3b)}\\ C_{[P,T,\underline{\boldsymbol{Y}}]}=P\left(\varepsilon_1-1\right)\bar{b}-\bar{r}T & \text{(A.2.3c)}\\ D_{[P,T,\underline{\boldsymbol{Y}}]}=P & \text{(A.2.3d)} \end{cases}$$

Equation (A.2.2) is then solved using Cardano's method [Cardano, 1662], briefly described hereafter.

A.2.2 Cardano's method

A third-degree polynomial equation of the form

$$Ax^3+Bx^2+Cx+D=0 \tag{A.2.4}$$

can be solved by eliminating the square term Bx^2 by substituting $x=t-\frac{B}{3A}$, which reads

$$t^3+\left(\frac{C}{A}-\frac{B^2}{3A^2}\right)t+\frac{D}{A}+\frac{2B^3-9ABC}{27A^3}=0 \tag{A.2.5}$$

Defining

$$\begin{cases} p=\dfrac{C}{A}-\dfrac{B^2}{3A^2} & \text{(A.2.6a)}\\ q=\dfrac{D}{A}+\dfrac{2B^3-9ABC}{27A^3}, & \text{(A.2.6b)} \end{cases}$$

equation (A.2.4) reduces to

$$t^3+pt+q=0. \tag{A.2.7}$$

Three cases are then possible.

Case $4p^3+27q^2>0$. The equation has two complex conjugate roots and one real solution. Note that in this case, the latter solution is then the only admissible density value, which writes

$$x=\sqrt[3]{-\frac{q}{2}+\sqrt{\frac{q^2}{4}+\frac{p^3}{27}}} \tag{A.2.8}$$

Case $4p^3 + 27q^2 = 0$. The equation has one double real root and one simple real root, which read respectively:

$$x_0 = -\frac{3q}{2p} \tag{A.2.9a}$$

$$x_1 = \frac{3q}{p} \tag{A.2.9b}$$

Case $4p^3 + 27q^2 < 0$. The equation has three real roots:

$$x_1 = 2\sqrt[3]{-\frac{p}{3}}\cos(\theta) \tag{A.2.10a}$$

$$x_2 = 2\sqrt[3]{-\frac{p}{3}}\cos\left(\theta + \frac{2\pi}{3}\right) \tag{A.2.10b}$$

$$x_3 = 2\sqrt[3]{-\frac{p}{3}}\cos\left(\theta + \frac{4\pi}{3}\right) \tag{A.2.10c}$$

where θ is defined by

$$\theta = \arccos\left(\frac{3q}{2p}\sqrt{-\frac{3}{p}}\right) \tag{A.2.11}$$

A.2.3 Finding the stable density solution

Once the cubic polynomial equation is solved, only the solutions within the interval $\left[0, \bar{b}^{-1}\right]$ are plausible.

When more than one solution are found, the thermodynamic stability of the roots must be evaluated. The solution of minimal fugacity is the stable solution. The particular case where two solutions minimize the fugacity happens when the couple (P, T) is such that $T = T^{\text{sat}}(P)$, and the two solutions correspond to the saturated liquid and vapour densities.

A.3 Reduced Cubic Equations of State and their properties

In this appendix, the main properties of the reduced cubic EoS as defined by Equation (2.3.30) are described.

A.3.1 General relations

It is first important to note that the reduced cubic EoS are defined for $\nu \in]1, +\infty[$, as the reduced covolume is unity. The reduced temperature θ being inverse proportional to the actual temperature T, subcritical temperatures correspond to $\theta > \theta_c$ and supercritical ones to $\theta < \theta_c$.

A.3.1.1 Critical point

In a similar way as the cubic EoS, the critical point of the reduced equation is the point (π_c, θ_c, ν_c) defined by:

$$\begin{cases} \left.\dfrac{\partial \pi}{\partial \nu}\right|_{\theta} (\nu_c, \theta_c) = 0 & \text{(A.3.1a)} \\ \left.\dfrac{\partial^2 \pi}{\partial \nu^2}\right|_{\theta} (\nu_c, \theta_c) = 0 & \text{(A.3.1b)} \\ \pi_c = \pi(\nu_c, \theta_c) & \text{(A.3.1c)} \end{cases}$$

A.3.1.2 Clausius-Clapeyron relation in the reduced form

A reduced form of the Clausius-Clapeyron relation can be derived, allowing to compute *saturation derivatives* in the context of reduced EoS. To this end, it is first interesting to write the actual *one-fluid* equlibrium condition, as:

$$g(v_\ell, T) = g(v_v, T). \tag{A.3.2}$$

Substracting the perfect-gas reference to both sides yields the following equality on the departure values

$$\underset{P}{\Delta} g(v_\ell, T) = \underset{P}{\Delta} g(v_v, T) \tag{A.3.3}$$

One may now define a reduced Gibbs energy γ as

$$\gamma(v, T) = \frac{\underset{P}{\Delta} g(v, T)}{\bar{r} T} + 1. \tag{A.3.4}$$

Changing parameters to the reduced ones yields:

$$\gamma(\nu, \theta) = \frac{\theta}{\varepsilon_{12}} \ln\left(\frac{2\nu + \varepsilon_1 - \varepsilon_{12}}{2\nu + \varepsilon_1 + \varepsilon_{12}}\right) - \ln\big(\pi(\nu - 1)\big) + \pi\nu \tag{A.3.5}$$

which again does not any longer rely on species-dependent quantities. The equilibrium A.3.2 writes then equivalently:

$$\gamma(\nu_\ell, \theta) = \gamma(\nu_v, \theta), \tag{A.3.6}$$

which can be differentiated into

$$\mathrm{d}\gamma(\nu_\ell, \theta) = \mathrm{d}\gamma(\nu_v, \theta). \tag{A.3.7}$$

After some algebraic manipulations, one can show that

$$\mathrm{d}\gamma(v, T) = -\left(\frac{1}{\bar{r}} \underset{P}{\Delta} s + \gamma\right) \frac{\mathrm{d}T}{T} + \frac{v}{\bar{r} T} P \tag{A.3.8}$$

One may then define a reduced departure entropy as

$$\sigma = \frac{1}{\bar{r}} \left(\underset{P}{\Delta} s\right) = \frac{-\theta}{\varepsilon_{12}} \ln\left(\frac{2\nu + \varepsilon_1 - \varepsilon_{12}}{2\nu + \varepsilon_1 + \varepsilon_{12}}\right) \frac{\theta \bar{a}'(\theta)}{\theta \bar{a}'(\theta) - \bar{a}} + \ln\big(\pi(\nu - 1)\big) \tag{A.3.9}$$

which allows finally to reduce A.3.8 into

$$\mathrm{d}\gamma(v,T) = \left[\frac{1}{\varepsilon_{12}}\ln\left(\frac{2\nu+\varepsilon_1-\varepsilon_{12}}{2\nu+\varepsilon_1+\varepsilon_{12}}\right)\right]\mathrm{d}\theta + \nu\,\mathrm{d}\pi. \tag{A.3.10}$$

Substituting A.3.10 into A.3.7 gives finally

$$\left.\frac{\mathrm{d}\pi}{\mathrm{d}\theta}\right|_{\mathrm{sat}} = \frac{1}{\varepsilon_{12}}\frac{1}{\nu_v-\nu_\ell}\left[\ln\left(\frac{2\nu_\ell+\varepsilon_1-\varepsilon_{12}}{2\nu_\ell+\varepsilon_1+\varepsilon_{12}}\right) - \ln\left(\frac{2\nu_v+\varepsilon_1-\varepsilon_{12}}{2\nu_v+\varepsilon_1+\varepsilon_{12}}\right)\right] \tag{A.3.11}$$

or, using A.3.5,

$$\left.\frac{\mathrm{d}\pi}{\mathrm{d}\theta}\right|_{\mathrm{sat}} = \frac{\pi^{\mathrm{sat}}}{\theta} - \frac{\ln(\nu_v-1)-\ln(\nu_\ell-1)}{\theta(\nu_v-\nu_\ell)} \tag{A.3.12}$$

This relation is the Clausius-Clapeyron relation for the reduced EoS. In particular, at the critical point, one may find

$$\left.\frac{\mathrm{d}\pi}{\mathrm{d}\theta}\right|_{\mathrm{sat}}(\theta_c) = \pi_c - \frac{1}{\nu_c-1} = -\frac{\theta_c}{\nu_c^2+\varepsilon_1\nu_c-\varepsilon_2} \tag{A.3.13}$$

It is then possible to derive the derivatives of both phases $\phi\in\{\ell,v\}$ reduced volumes using the chain rule:

$$\left.\frac{\mathrm{d}\nu_\phi}{\mathrm{d}\theta}\right|_{\mathrm{sat}}(\theta) = \left.\frac{\partial\nu_\phi}{\partial\theta}\right|_\pi(\pi^{\mathrm{sat}},\theta) + \left.\frac{\partial\nu_\phi}{\partial\pi}\right|_\theta(\pi^{\mathrm{sat}},\theta)\left.\frac{\mathrm{d}\pi}{\mathrm{d}\theta}\right|_{\mathrm{sat}}(\theta) \tag{A.3.14}$$

with reduced thermal expansion and compressibility coefficients α^ν and β^ν defined through

$$\mathrm{d}\nu = \nu\alpha^\nu\,\mathrm{d}\theta - \nu\beta^\nu\,\mathrm{d}\pi \tag{A.3.15}$$

with

$$\begin{cases} \beta^\nu = -\dfrac{1}{\nu}\left.\dfrac{\partial\nu}{\partial\pi}\right|_\theta = \dfrac{(\nu-1)^2\left(\nu^2+\varepsilon_1\nu-\varepsilon_2\right)^2}{\nu\left[\left(\nu^2+\varepsilon_1\nu-\varepsilon_2\right)^2-\theta\left(2\nu+\varepsilon_1\right)(\nu-1)^2\right]} & \text{(A.3.16a)} \\ \alpha^\nu = \dfrac{1}{\nu}\left.\dfrac{\partial\nu}{\partial\theta}\right|_\pi = \dfrac{\beta^\nu}{\nu\left(\nu^2+\varepsilon_1\nu-\varepsilon_2\right)} & \text{(A.3.16b)} \end{cases}$$

Finally,

$$\begin{cases} \left.\dfrac{\mathrm{d}\nu_\ell}{\mathrm{d}\theta}\right|_{\mathrm{sat}}(\theta) = \nu_\ell\alpha_\ell^\nu - \nu_\ell\beta_\ell^\nu\left.\dfrac{\mathrm{d}\pi}{\mathrm{d}\theta}\right|_{\mathrm{sat}} & \text{(A.3.17a)} \\ \left.\dfrac{\mathrm{d}\nu_v}{\mathrm{d}\theta}\right|_{\mathrm{sat}}(\theta) = \nu_v\alpha_v^\nu - \nu_v\beta_v^\nu\left.\dfrac{\mathrm{d}\pi}{\mathrm{d}\theta}\right|_{\mathrm{sat}} & \text{(A.3.17b)} \end{cases}$$

A.3.2 Reduced van der Waals EoS

The reduced form of VDW EoS is:

$$\pi(\nu,\theta) = \frac{1}{\nu-1} - \frac{\theta}{\nu^2}. \tag{A.3.18}$$

Corresponding fugacity coefficient is then:

$$\varphi(\nu,\theta) = \frac{1}{\pi(\nu-1)}\exp\left(\frac{1}{\nu-1} - \frac{2\theta}{\nu}\right) \tag{A.3.19}$$

Critical Point: From (A.3.1a) and (A.3.1b), one gets:

$$\begin{cases} \theta_c(\nu_c) = \dfrac{\nu_c^3}{2(\nu_c - 1)^2} & \text{(A.3.20a)} \\ -2\nu_c^6(\nu_c - 3) = 0, & \text{(A.3.20b)} \end{cases}$$

hence the critical values for the reduced VDW EoS:

$$\theta_c = 3.375 \quad \text{(A.3.21a)}$$
$$\pi_c = 0.125 \quad \text{(A.3.21b)}$$
$$\nu_c = 3 \quad \text{(A.3.21c)}$$

The corresponding reduced saturation values are displayed in Figure A.1

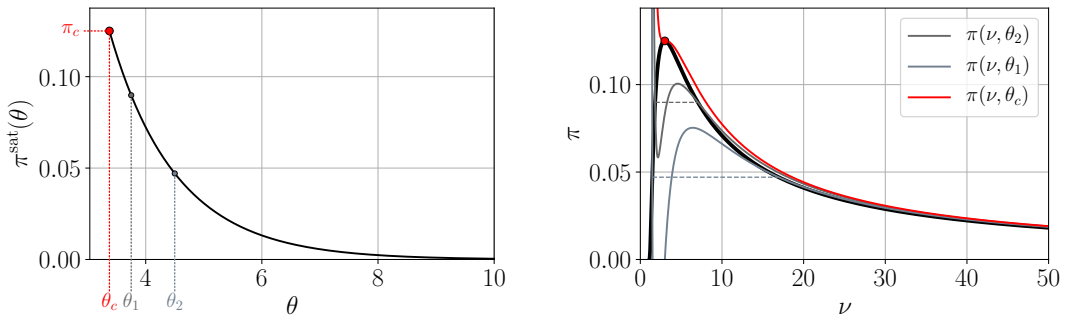

(a) Saturation curve

(b) Clapeyron diagram

Figure A.1: Saturation properties of the VDW reduced EoS.

A.3.3 Reduced Soave-Redlich-Kwong EoS

In its reduced form, SRK EoS reads:

$$\pi(\nu, \theta) = \frac{1}{\nu - 1} - \frac{\theta}{\nu(\nu + 1)} \quad \text{(A.3.22)}$$

Critical Point: Equations (A.3.1a) and (A.3.1b) yield the following system:

$$\begin{cases} \theta_c = \dfrac{\nu_c}{2} + 1 + \dfrac{1}{2\nu_c} & \text{(A.3.23a)} \\ -2\nu_c^5 + 2\nu_c^4 + 16\nu_c^3 + 20\nu_c^2 + 10\nu_c + 2 = 0 & \text{(A.3.23b)} \end{cases}$$

Equation (A.3.23b) admits a double negative root, two conjugate complex roots and only one real positive solution (above unity) which therefore corresponds to the critical reduced volume:

$$\nu_c = 1 + \sqrt[3]{2} + 2^{\frac{2}{3}}. \quad \text{(A.3.24)}$$

Substituting (A.3.24) into Equations (A.3.1b) and (A.3.1c) finally yields:

$$\theta_c = 4.93396245182803 \quad \text{(A.3.25a)}$$
$$\pi_c = 0.0866403499649577 \quad \text{(A.3.25b)}$$
$$\nu_c = 3.84732210186307 \quad \text{(A.3.25c)}$$

The corresponding reduced saturation values are displayed in Figure A.2

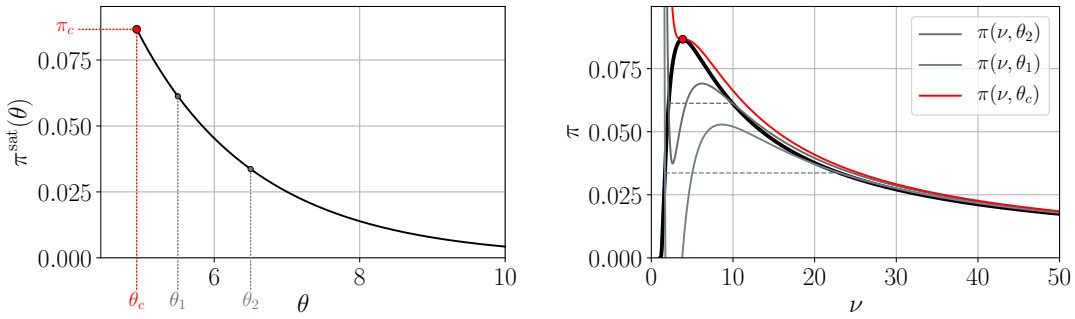

(a) Saturation curve

(b) Clapeyron diagram

Figure A.2: Saturation properties of the SRK reduced EoS.

A.3.4 Reduced Peng-Robinson EoS

The reduced form of PR EoS can be expressed as:

$$\pi(\nu, \theta) = \frac{1}{\nu - 1} - \frac{\theta}{\nu^2 + 2\nu - 1} \tag{A.3.26}$$

Critical Point: Equations (A.3.1a) and (A.3.1b) applied to PR EoS correspond to the following system:

$$\begin{cases} \theta_c = \dfrac{\nu_c^2 + 4\nu_c + 4}{2\nu_c + 1} & \text{(A.3.27a)} \\ -2\nu_c^7 - 2\nu_c^6 + 26\nu_c^5 + 50\nu_c^4 + 10\nu_c^3 - 6\nu_c^2 - 18\nu_c + 6 = 0 & \text{(A.3.27b)} \end{cases}$$

Among the solutions of Equation (A.3.27b), there are two different double roots which are under unity, two conjugate complex roots and only one real solution above unity which therefore corresponds to the critical reduced volume:

$$\nu_c = 1 + \frac{2}{\sqrt[3]{2\sqrt{2} + 4}} + \sqrt[3]{2\sqrt{2} + 4}. \tag{A.3.28}$$

Substituting (A.3.28) into Equations (A.3.1b) and (A.3.1c) finally yields:

$$\theta_c = 5.87735994860440 \tag{A.3.29a}$$
$$\pi_c = 0.0777960739038884 \tag{A.3.29b}$$
$$\nu_c = 3.95137303559144 \tag{A.3.29c}$$

An insight on the saturation curves is given on Figure A.3

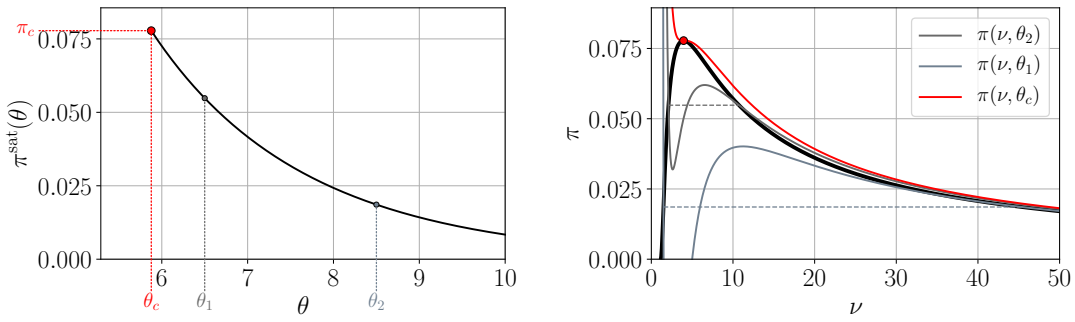

(a) Saturation curve

(b) Clapeyron diagram

Figure A.3: Saturation properties of the PR reduced EoS.

A.4 Fitting Stiffened Gas EoS parameters on thermodynamic data

Provided two thermodynamic saturated states data points Θ_1 and Θ_2, with

$$\Theta_i = \left\{ T_i, P_i^{\mathrm{sat}}, \rho_{\ell i}, \rho_{v i}, h_{\ell i}, h_{v i} \right\}, \tag{A.4.1}$$

parameters of a Stiffened Gas EoS can be derived, following the work of [Le Métayer et al., 2004]. The method is briefly recalled hereafter. In the first place, the isobaric heat capacity of each phase is obtained as:

$$c_{p,\ell} = \frac{h_{\ell 1} - h_{\ell 0}}{T_1 - T_0} \tag{A.4.2a}$$

$$c_{p,v} = \frac{h_{v1} - h_{v0}}{T_1 - T_0}. \tag{A.4.2b}$$

Then, one has

$$q_\ell = h_{\ell 0} - c_{p,\ell} T_0 \tag{A.4.3a}$$

$$q_v = h_{v0} - c_{p,v} T_0. \tag{A.4.3b}$$

The pressure coefficients $P_{\infty,\ell}, P_{\infty,v}$ can be evaluated from

$$P_{\infty,\ell} = \frac{\rho_{\ell 1} T_1 P_0^{\mathrm{sat}} - \rho_{\ell 0} T_0 P_1^{\mathrm{sat}}}{\rho_{\ell 0} T_0 - \rho_{\ell 1} T_1} \tag{A.4.4a}$$

$$P_{\infty,v} = \frac{\rho_{v1} T_1 P_0^{\mathrm{sat}} - \rho_{v0} T_0 P_1^{\mathrm{sat}}}{\rho_{v0} T_0 - \rho_{v1} T_1}. \tag{A.4.4b}$$

Finally, the isochoric heat capacities are obtained as

$$c_{v,\ell} = c_{p,\ell} - \frac{P_0^{\mathrm{sat}} + P_{\infty,\ell}}{\rho_{\ell 0} T_0} \tag{A.4.5a}$$

$$c_{v,v} = c_{p,v} - \frac{P_0^{\mathrm{sat}} + P_{\infty,v}}{\rho_{v0} T_0}. \tag{A.4.5b}$$

and the corresponding heat capacity ratio

$$\gamma_\ell = \frac{c_{p,\ell}}{c_{v,\ell}} \tag{A.4.6a}$$

$$\gamma_v = \frac{c_{p,v}}{c_{v,v}}. \tag{A.4.6b}$$

Appendix B

Complements on the regularized thermodynamics

This appendix describes complementary derivations for the regularized equation of state of chapter 8.

B.1 Complementary calculations for regularized thermodynamics

This section provides useful calculations for the developments of chapter 8. As in this latter chapter, in all the following, the vapour and liquid phases are assumed to follow respectively an ideal gas law and a stiffened gas EoS.

B.1.1 Additional properties of the homogeneous equilibrium EoS

As in chapter 8, the homogeneous equilibrium EoS is considered, here, consisting in the following definition:

$$P^{\mathrm{eq}}(\rho,T)=\begin{cases}P_v(\rho,T)=\rho\,(\gamma-1)\,c_{v,v}T & \text{if } \rho\leq\rho_v(T),\\ P^{\mathrm{sat}}(T) & \text{if } \rho\in\left]\rho_v(T),\rho_\ell(T)\right[,\\ P_\ell(\rho,T)=\rho\,(\gamma-1)\,c_{v,\ell}T+P_{\infty,\ell} & \text{if } \rho\geq\rho_\ell(T),\end{cases} \tag{B.1.1}$$

B.1.1.1 Heat capacity of the equilibrium EoS in the saturation zone

The derivation of the heat capacity of the equilibrium EoS (eq-EoS) in the saturation zone (i.e. for $\rho\in\left[\rho_v(T),\rho_\ell(T)\right]$) is provided. Using the heat capacity residual value presented in section 2.2.2.2, one has

$$c_v^{\mathrm{eq}}(\rho,T)=c_{v,v}(\rho_v,T)+\underset{\rho}{\Delta}c_v^{\mathrm{eq}}(\rho,T)=c_{v,v}(\rho_v,T)-\int_{\rho_v}^{\rho}\frac{T}{\varrho^2}\left.\frac{\partial^2 P}{\partial T^2}\right|_{\rho}\mathrm{d}\varrho, \tag{B.1.2}$$

which yields

$$c_v^{\mathrm{eq}}(\rho,T)=c_{v,v}(\rho_v,T)-\int_{\rho_v}^{\rho}\frac{T}{\varrho^2}\frac{\mathrm{d}^2 P^{\mathrm{sat}}}{\mathrm{d}T^2}\,\mathrm{d}\varrho, \tag{B.1.3}$$

so that

$$c_v^{\text{eq}}(\rho,T) = c_{v,v}(\rho_v,T) - T\frac{\mathrm{d}^2 P^{\text{sat}}}{\mathrm{d}T^2}\int_{\rho_v}^{\rho}\frac{1}{\varrho^2}\,\mathrm{d}\varrho. \tag{B.1.4}$$

Finally, one finds

$$c_v^{\text{eq}}(\rho,T) = c_{v,v}(\rho_v,T) - T\frac{\mathrm{d}^2 P^{\text{sat}}}{\mathrm{d}T^2}\left(\frac{1}{\rho}-\frac{1}{\rho_v}\right). \tag{B.1.5}$$

B.1.1.2 Alternative form of the speed of sound for the equilibrium EoS in the saturation zone

A derivation of the speed of sound within the saturated two-phase regime was proposed in paragraph 5.2.3.3.2. Here, an alternative derivation is proposed for the speed of sound within the saturated two-phase regime, that will be useful for the determination of the speed of sound of the regularized EoS within the saturation zone.

B.1.1.2.1 Entropy

First, the entropy value for $\rho \in [\rho_v(T), \rho_\ell(T)]$ is obtained using the two-phase mixture entropy:

$$s^{\text{eq}}(\rho,T) = y_\ell s_\ell(\rho_\ell,T) + (1-y_\ell)s_v(\rho_v,T), \tag{B.1.6}$$

with the liquid mass fraction is defined as $y_\ell = \dfrac{\frac{1}{\rho}-\frac{1}{\rho_v}}{\frac{1}{\rho_\ell}-\frac{1}{\rho_v}}$. One has

$$\begin{aligned} s^{\text{eq}}(\rho,T) &= s_v(\rho_v,T) + y_\ell\left(s_\ell(\rho_\ell,T) - s_v(\rho_v,T)\right), \\ &= s_v(\rho_v,T) + \left(\frac{1}{\rho}-\frac{1}{\rho_v}\right)\frac{s_\ell(\rho_\ell,T)-s_v(\rho_v,T)}{\frac{1}{\rho_\ell}-\frac{1}{\rho_v}}. \end{aligned}$$

Using the Clausius-Clapeyron relation (2.3.22) on page 33, one gets

$$s^{\text{eq}}(\rho,T) = s_v(\rho_v,T) + \frac{\mathrm{d}P^{\text{sat}}}{\mathrm{d}T}\left(\frac{1}{\rho}-\frac{1}{\rho_v}\right). \tag{B.1.7}$$

Note that this relation can equivalently be obtained by computing the residual value of the entropy for the eq-EoS, instead of writing the mixture entropy (B.1.6).

B.1.1.2.2 Speed of sound

One can obtain the isentropic speed of sound at saturation (i.e. for $\rho \in [\rho_v(T), \rho_\ell(T)]$) by writing

$$c_{\text{eq}}^2 = \left.\frac{\partial P}{\partial \rho}\right|_s = -\left.\frac{\partial P}{\partial s}\right|_\rho \left.\frac{\partial s}{\partial \rho}\right|_P, \tag{B.1.8}$$

so that

$$c_{\text{eq}}^2 = -\left.\frac{\partial s}{\partial \rho}\right|_P \left(\left.\frac{\partial s}{\partial P}\right|_\rho\right)^{-1}. \tag{B.1.9}$$

At saturation, one has $P^{\text{eq}}(\rho,T) = P^{\text{sat}}(T)$, so that

$$\left.\frac{\partial s}{\partial \rho}\right|_P = \left.\frac{\partial s}{\partial \rho}\right|_T + \underbrace{\left.\frac{\partial s}{\partial T}\right|_\rho \left.\frac{\partial T}{\partial \rho}\right|_P}_{=0}, \tag{B.1.10}$$

and

$$\left.\frac{\partial s}{\partial P}\right|_{\rho} = \left.\frac{\partial s}{\partial T}\right|_{\rho} \left.\frac{\partial T}{\partial P}\right|_{\rho} = \left.\frac{\partial s}{\partial T}\right|_{\rho} \left(\frac{\mathrm{d}P^{\mathrm{sat}}}{\mathrm{d}T}\right)^{-1}, \tag{B.1.11}$$

Using equation (B.1.7), yields

$$\left.\frac{\partial s}{\partial \rho}\right|_{T} = -\frac{1}{\rho^2}\frac{\mathrm{d}P^{\mathrm{sat}}}{\mathrm{d}T}, \tag{B.1.12}$$

and the speed of sound can be expressed as

$$c_{\mathrm{eq}}^2 = \frac{1}{\rho^2}\left(\frac{\mathrm{d}P^{\mathrm{sat}}}{\mathrm{d}T}\right)^2 \left(\left.\frac{\partial s}{\partial T}\right|_{\rho}\right)^{-1}. \tag{B.1.13}$$

This formula will be useful to derive the speed of sound for the regularized EoS within the saturation zone, which is done in the next section.

B.1.2 Speed of Sound for the regularized EoS at saturation

Here, the regularized EoS (8.3.3), page 213 is considered. The objective of this section is to show that the speed of sound within the saturation zone $\rho \in [\rho_v^{\oplus}(T), \rho_\ell^{\ominus}(T)]$ can be written as:

$$\frac{1}{\rho^2 c^2(\rho,T)} = \frac{1}{\rho^2 c_{\mathrm{eq}}^2(\rho,T)} + \frac{1}{{\rho_v^{\oplus}}^2 c_{\mathrm{co}}^2(\rho_v^{\oplus},T)} - \frac{1}{{\rho_v^{\oplus}}^2 c_{\mathrm{eq}}^2(\rho_v^{\oplus},T)}. \tag{B.1.14}$$

First, the entropy is expressed. Then the speed of sound is computed by differentiating the entropy expression.

B.1.2.1 Within the connexion zone $\rho \in [\rho_v^{\ominus}(T), \rho_v^{\oplus}(T)]$

B.1.2.1.1 Entropy

The entropy of the regularized EoS within the connexion zone can be written thanks to the residual value, as

$$s^{\mathrm{co}}(\rho,T) = s_v(\rho,T) + \underset{\rho}{\Delta} s^{\mathrm{co}}(\rho,T) \tag{B.1.15}$$

$$= s_v(\rho,T) - \int_0^{\rho} \frac{1}{\varrho^2}\left.\frac{\partial P}{\partial T}\right|_{\rho} \mathrm{d}\varrho + r\ln\left(\frac{P^{\mathrm{co}}}{\rho r T}\right) \tag{B.1.16}$$

$$= s_v(\rho,T) - \int_{\rho_v^{\ominus}}^{\rho} \frac{1}{\varrho^2}\left.\frac{\partial P}{\partial T}\right|_{\rho} \mathrm{d}\varrho + r\ln\left(\frac{P^{\mathrm{co}}}{\rho r T}\right), \tag{B.1.17}$$

with $r = (\gamma_v - 1)c_{v,v}$, and with the entropy of the ideal gas

$$s_v(\rho,T) = s_0 + c_{v,v}\ln(T) + r\ln(\rho). \tag{B.1.18}$$

B.1.2.1.2 Speed of sound

An expression for the speed of sound has been provided in chapter 8. Yet, an alternative derivation is now proposed, which will be useful to obtain the expression of the speed of sound within the saturation zone. The speed of sound in the connexion zone can be written as

$$c_{\mathrm{co}}^2 = \left.\frac{\partial P}{\partial \rho}\right|_{s} = -\left.\frac{\partial P}{\partial s}\right|_{\rho}\left.\frac{\partial s}{\partial \rho}\right|_{P}, \tag{B.1.19}$$

so that

$$c_{\text{co}}^2 = -\left.\frac{\partial s}{\partial \rho}\right|_P \left(\left.\frac{\partial s}{\partial P}\right|_\rho\right)^{-1}. \tag{B.1.20}$$

Focusing on the endpoint of the connection zone $\rho_v^\oplus(T)$, one has $P^{\text{co}}(\rho_v^\oplus, T) = P^{\text{sat}}(T)$, so that at this point,

$$\left.\frac{\partial s}{\partial \rho}\right|_P (\rho_v^\oplus, T) = \left.\frac{\partial s}{\partial \rho}\right|_T (\rho_v^\oplus, T) + \underbrace{\left(\left.\frac{\partial s}{\partial T}\right|_\rho (\rho_v^\oplus, T)\right)\left(\left.\frac{\partial T}{\partial \rho}\right|_P (\rho_v^\oplus, T)\right)}_{=0}, \tag{B.1.21}$$

and

$$\left.\frac{\partial s}{\partial P}\right|_\rho (\rho_v^\oplus, T) = \left.\frac{\partial s}{\partial T}\right|_\rho (\rho_v^\oplus, T)\left.\frac{\partial T}{\partial P}\right|_\rho (\rho_v^\oplus, T) = \left.\frac{\partial s}{\partial T}\right|_\rho (\rho_v^\oplus, T)\left(\frac{\mathrm{d}P^{\text{sat}}}{\mathrm{d}T}\right)^{-1}. \tag{B.1.22}$$

One can then differentiate (B.1.17) to write:

$$\left.\frac{\partial s^{\text{co}}}{\partial \rho}\right|_T (\rho_v^\oplus, T) = -\frac{1}{{\rho_v^\oplus}^2}\frac{\mathrm{d}P^{\text{sat}}}{\mathrm{d}T} \tag{B.1.23}$$

And speed of sound can be written as:

$$c_{\text{co}}^2(\rho_v^\oplus, T) = \frac{1}{{\rho_v^\oplus}^2}\left(\frac{\mathrm{d}P^{\text{sat}}}{\mathrm{d}T}\right)\left(\left.\frac{\partial s}{\partial T}\right|_\rho\right)^{-1}. \tag{B.1.24}$$

B.1.2.2 Within the saturation zone $\rho \in [\rho_v^\oplus(T), \rho_\ell^\ominus(T)]$

B.1.2.2.1 Entropy

Similarly as for the sensible energy in paragraph 8.3.2.3, one can show that the entropy, for $\rho \in [\rho_v^\oplus, \rho_\ell^\ominus]$, can be written as

$$s(\rho, T) = s^{\text{co}}(\rho_v^\oplus, T) + \left(s^{\text{eq}}(\rho, T) - s^{\text{eq}}(\rho_v^\oplus, T)\right). \tag{B.1.25}$$

B.1.2.2.2 Speed of sound

Similarly as in the previous paragraphs, it is possible to derive the following form for the speed of sound:

$$c_{\text{eq}}^2 = \frac{1}{\rho^2}\left(\frac{\mathrm{d}P^{\text{sat}}}{\mathrm{d}T}\right)^2\left(\left.\frac{\partial s}{\partial T}\right|_\rho\right)^{-1}. \tag{B.1.26}$$

The partial derivative of equation (B.1.25) with respect to the temperature reads

$$\left.\frac{\partial s}{\partial T}\right|_\rho = \left.\frac{\partial s^{\text{co}}}{\partial T}\right|_\rho (\rho_v^\oplus, T) + \left.\frac{\partial s^{\text{eq}}}{\partial T}\right|_\rho (\rho, T) - \left.\frac{\partial s^{\text{eq}}}{\partial T}\right|_\rho (\rho_v^\oplus, T) + \rho_v'\left(\left.\frac{\partial s^{\text{co}}}{\partial \rho}\right|_T (\rho_v^\oplus, T) - \left.\frac{\partial s^{\text{eq}}}{\partial \rho}\right|_T (\rho_v^\oplus, T)\right). \tag{B.1.27}$$

Using equations (B.1.12) and (B.1.23), one has

$$\left.\frac{\partial s^{\mathrm{co}}}{\partial \rho}\right|_T (\rho_v^{\oplus}, T) - \left.\frac{\partial s^{\mathrm{eq}}}{\partial \rho}\right|_T (\rho_v^{\oplus}, T) = 0, \tag{B.1.28}$$

and

$$c_{\mathrm{eq}}^2 = \frac{1}{\rho^2}\left(\frac{\mathrm{d}P^{\mathrm{sat}}}{\mathrm{d}T}\right)^2 \left(\left.\frac{\partial s^{\mathrm{co}}}{\partial T}\right|_\rho (\rho_v^{\oplus}, T) + \left.\frac{\partial s^{\mathrm{eq}}}{\partial T}\right|_\rho (\rho, T) - \left.\frac{\partial s^{\mathrm{eq}}}{\partial T}\right|_\rho (\rho_v^{\oplus}, T)\right)^{-1}, \tag{B.1.29}$$

which, using equations (B.1.13) and (B.1.13) finally yields

$$\boxed{\frac{1}{\rho^2 c^2(\rho, T)} = \frac{1}{\rho^2 c_{\mathrm{eq}}^2(\rho, T)} + \frac{1}{{\rho_v^{\oplus}}^2 c_{\mathrm{co}}^2(\rho_v^{\oplus}, T)} - \frac{1}{{\rho_v^{\oplus}}^2 c_{\mathrm{eq}}^2(\rho_v^{\oplus}, T)}.} \tag{B.1.30}$$

Appendix C

Numerical Tools

C.1 Numerical integration of ordinary differential equations (ODE)

In the present appendix, the following ODE is considered:

$$\frac{\mathrm{d}\boldsymbol{U}}{\mathrm{d}t} = \boldsymbol{H}(t, \boldsymbol{U}) \tag{C.1.1}$$

C.1.1 The family of Runge-Kutta methods

C.1.1.1 General formulation

The Runge-Kutta methods are a family of explicit multi-stage [1] time-integration methods that achieve high-order accuracy using intermediate evaluations of the function and its derivative. The general form is given for a m-stage Runge-Kutta method writes [Hairer et al., 2008]:

$$\begin{cases} \boldsymbol{U}^{(1)} = \boldsymbol{U}^n & \text{(C.1.2a)} \\ \boldsymbol{U}^{(i)} = \boldsymbol{U}^n + \Delta t \sum_{j=1}^{i-1} a_{ji}^{\mathrm{RK}} \boldsymbol{H}^{(i)} \quad \text{for } j \in \{2, m\} & \text{(C.1.2b)} \\ \boldsymbol{U}^{n+1} = \boldsymbol{U}^n + \Delta t \sum_{i=1}^{m} b_i^{\mathrm{RK}} \boldsymbol{H}^{(i)} & \text{(C.1.2c)} \end{cases}$$

with the notation $\boldsymbol{H}^{(i)} = \boldsymbol{H}\left(t^n + c_i^{\mathrm{RK}} \Delta t, \boldsymbol{U}^{(i)}\right)$.

The different Runge-Kutta methods can then be summarized by means of the *Butcher tableau*. Its general form is provided in Table C.1. In particular, the one-stage RK method, with $b_1 = 1$, corresponds to the forward-Euler method.

The RK framework allows to define an complete zoology of explicit time-marching schemes. Some specifically designed RK methods have noteworthy additional properties, that are presented hereafter.

[1] Semantically, the term *stage* must be distinguished from *step*. Indeed, there exist *multi-step* methods which achieve high-order accuracy using the values of multiple consecutive time-steps. The *stages* refer to additional computations "between" the time-steps.

c_2	a_{21}				
c_3	a_{31}	a_{32}			
$\vdots$	$\vdots$	$\vdots$	$\ddots$		
c_m	a_{m1}	a_{m2}	$\cdots$	$a_{m,m-1}$	
	b_1	b_2	$\cdots$	b_{m-1}	b_m

Table C.1: General representation of RK methods using a Butcher tableau

C.1.1.2 Low-storage RK methods

It is naturally interesting to avoid storing the solution at multiple stages of the RK method, to reduce memory consumption and data communications. A RK method is said to be low-storage if:

$$\begin{cases} \forall j < (i-1), & a_{ij} = 0, & \text{(C.1.3a)} \\ \forall i < m, & b_i = 0, & \text{(C.1.3b)} \\ & b_m = 1. & \text{(C.1.3c)} \end{cases}$$

Note that some authors such as [Hairer et al., 2008] relax conditions (C.1.3b)-(C.1.3c) in the definition of low-storage RK schemes.

A low-storage method in the sense of (C.1.3) can then be summarized by its coefficients $\left(a_{i,i-1}\right)_{i\in[\![1,m]\!]}$. The low-storage Runge-Kutta schemes implemented into the solver AVBP [Lamarque, 2007] are summarized in Table C.2

m	a_{21}^{RK}	a_{32}^{RK}	a_{43}^{RK}	a_{54}^{RK}	b_m^{RK}
1 (forward-Euler)	0	0	0	0	1
2 (Heun scheme)	1/2	0	0	0	1
3	1/3	1/2	0	0	1
4	1/4	1/3	1/2	0	1
5	1/5	1/4	1/3	1/2	1

Table C.2: Low-storage RK methods implemented into AVBP

C.2 Gaussian quadrature rules

A brief description of Gaussian quadrature rules is provided here. The interested reader will find further information in section 25.4 of the reference book [Abramowitz and Stegun, 1965].

C.2.1 General principle

Gaussian quadratures are a tool that allows to approximate integrals of a function from its values taken at a limited number of points. Considering the integral of a function f over the interval $[-1, 1]$, the approximation using a Gaussian quadrature reads

$$\int_{-1}^{1} f(x)\,\mathrm{d}x \approx \sum_{q=1}^{n^Q} \omega_q f(x_q), \tag{C.2.1}$$

where x_q and ω_q are respectively the n^Q quadrature points $x_q \in [-1, 1]$ and their associated weights. Their values are detailed in the next sections, for the Gauss-Legendre and the Gauss-Lobatto quadrature rules.

Note that if the function f is a polynomial function, it is possible to compute *exactly* its integral from formula (C.2.1) if enough quadrature points are used. The number of required quadrature points depends on the chosen quadrature rule.

C.2.2 The Gauss-Legendre quadrature rule

The Gauss-Legendre quadrature rule is based on the family of Legendre polynomials. The n^Q quadrature points correspond to the roots of the Legendre polynomial p_{n^Q} of degree n^Q. The Legendre polynomial p_{n^Q} reads

$$p_{n^Q}(x) = \frac{1}{2^{n^Q}} \sum_{j=0}^{n^Q} \binom{n}{k}^2 (x-1)^{n-k} (x+1)^k . \tag{C.2.2}$$

The weigths are then computed as:

$$\omega_q = \frac{2}{(1-x_q^2)\left[p'_{n^Q}(x_q)\right]^2}. \tag{C.2.3}$$

The values of the quadrature points and the weight functions up to $n^Q = 3$ are recalled in table C.3.

n^Q	quadrature points $\{x_q\}_{q\in[\![1,n^Q]\!]}$	quadrature weights $\{\omega_q\}_{q\in[\![1,n^Q]\!]}$
1	$\{0\}$	$\{2\}$
2	$\left\{-\frac{\sqrt{3}}{3}, \frac{\sqrt{3}}{3}\right\}$	$\{1,1\}$
3	$\left\{-\frac{\sqrt{15}}{5}, 0, \frac{\sqrt{15}}{5}\right\}$	$\left\{\frac{5}{9}, \frac{8}{9}, \frac{5}{9}\right\}$

Table C.3: Quadrature points and weights for the Gauss-Legendre quadrature rule

The *degree of exactness*, representing the highest polynomial degree of a polynomial function f for which the Gauss-Legendre quadrature rule provides exact integration, is equal to $2n^Q - 1$. In other words, for any polynomial function f of degree less or equal to $2n^Q - 1$, the Gauss-Legendre quadrature rule will yield the exact value of the integral.

C.2.3 The Gauss-Lobatto quadrature rule

The Gauss-Lobatto quadrature rule is similar to the Gauss-Legendre rule, but includes the boundary points $[-1, 1]$ into the quadrature points. This decreases the degree of exactness of the method to $2n^Q - 3$. For a polynomial of degree less or equal to $2n^Q - 3$, the Gauss-Lobatto quadrature formula reads

$$\int_{-1}^{1} f(x)\,\mathrm{d}x = \sum_{q=1}^{n^Q} \omega_q f(x_q), \tag{C.2.4}$$

The values of the quadrature points and the weight functions up to $n^Q = 3$ are given in table C.4

n^Q	quadrature points $\left\{x_q\right\}_{q\in[\![1,n^Q]\!]}$	quadrature weights $\left\{\omega_q\right\}_{q\in[\![1,n^Q]\!]}$
2	$\{-1,1\}$	$\{1,1\}$
3	$\{-1,0,1\}$	$\left\{\frac{1}{3},\frac{4}{3},\frac{1}{3}\right\}$

Table C.4: Quadrature points and weights for the Gauss-Lobatto quadrature rule

Appendix D

Résumé en Français

Au cours de l'utilisation de certains systèmes propulsifs, tels que les moteurs fusées cryotechniques ou les moteurs Diesel, le point de fonctionnement peut varier sur une large plage de pressions. Ces variations de pression peuvent conduire à un changement de régime thermodynamique si la pression critique du fluide est franchie, l'injection initialement diphasique devenant alors transcritique. Ce changement modifie la topologie de l'écoulement, ainsi que la dynamique du mélange, ce qui impacte le comportement de la flamme. L'objectif de cette thèse est de développer une méthodologie originale capable de traiter au sein du même solveur des écoulements sous-critiques ainsi que supercritiques.

Ce manuscrit de thèse propose tout d'abord une description de la modélisation thermodynamique nécessaire à la prise en compte des effets gaz-réel propres aux écoulements à haute densité, ainsi qu'à la description des équilibres liquide-gaz rencontrés au niveaux des interfaces entre deux phases. Une formulation simplifiée de l'équilibre est également proposée afin de simplifier les procédures de calcul dans le cadre des mélanges multi-espèces.

Ensuite, une revue des approches existantes pour représenter et modéliser l'évolution des interfaces entre fluides est proposée. Les méthodes d'interface raide telles que la méthode *level-set*, la méthode *volume-of-fluid* ou encore la méthode *front-tracking* sont présentées. Ensuite, les méthodes d'interface diffuse sont introduites. Après avoir décrit les méthodes de *champ de phase*, les méthodes *multifluides* sont détaillées et la pertinence de leur application dans le cadre de cette étude est argumentée.

Par la suite, les différentes stratégies numériques envisagées au cours de ce travail sont présentées en détail. En particulier, les méthodes volumes-finis classiques – de type solveur de Godunov –, les méthodes Runge-Kutta Galerkin discontinu, et enfin les méthodes d'éléments finis de type Taylor-Galerkin, sont décrites.

Tous ces développements préliminaires permettent alors d'introduire la méthodologie globale pour la simulation numérique d'écoulements aussi bien diphasiques que supercritiques, reposant sur une formulation Taylor-Galerkin des méthodes multifluides à 3 et 4 équations. Cela permet d'intégrer ces développements au solveur supercritique AVBP-RG, de manière d'étendre l'utilisation de ce dernier aux écoulements diphasiques sous-critiques. Dans ce cadre, une formulation des conditions aux limites caractéristiques associées aux modèles multifluides à 3 et 4 équations est également proposée.

Des simulations numériques multidimensionnelles sont ensuite proposées de manière à confronter le modèle à des données expérimentales. Dans cette optique, les modèles à 3 et 4 équations sont agrémentés de modèles de turbulence (dans le cadre de la *simulation aux grandes échelles*), de diffusion et de combustion. Les écoulements correspondants aux configurations du banc d'essai *Mascotte* de l'ONERA, à injection cryogénique coaxiale, ainsi que le banc d'essai *Spray A* de l'Engine Combustion Network, à injection Diesel, sont simulés. Les résultats permettent d'observer un accord satisfaisant avec les données expérimentales, ce qui offre des perspectives encourageantes vers de futures améliorations du modèle et des applications à des configurations industrielles complexes.

Les résultats de ces calculs mettent également en évidence la génération d'oscillations de pression d'origine numérique. Celles-ci font alors l'objet d'une étude approfondie, plus académique, portant sur les modèles multifluides à 5, 4 et 3 équations. Enfin, une interprétation de ces oscillations de pression est proposée et étudiée numériquement.

En conclusion, ces travaux auront permis de proposer une nouvelle stratégie de modélisation et de résolution numérique permettant la simulation d'écoulements sous-critiques à supercritiques. Les résultats obtenus sont très encourageants, et mettent en évidence l'intérêt de la stratégie retenue dans ces travaux pour aller vers des simulations plus complexes et plus réalistes.

Bibliography

Abgrall, R. (1996). How to prevent pressure oscillations in multicomponent flow calculations: a quasi conservative approach. *Journal of Computational Physics 125*(1), 150–160. *(p. 28, 187, 209, 210)*

Abgrall, R. and S. Karni (2001). Computations of compressible multifluids. *Journal of computational physics 169*(2), 594–623. *(p. 61, 187)*

Abgrall, R. and R. Saurel (2003). Discrete equations for physical and numerical compressible multiphase mixtures. *Journal of Computational Physics 186*(2), 361–396. *(p. 74)*

Abramowitz, M. and I. A. Stegun (1965). *Handbook of mathematical functions: with formulas, graphs, and mathematical tables*, Volume 55. Courier Corporation. *(p. 246)*

Abramzon, B. and W. Sirignano (1989). Droplet vaporization model for spray combustion calculations. *International journal of heat and mass transfer 32*(9), 1605–1618. *(p. 79)*

Allaire, G., S. Clerc, and S. Kokh (2002). A five-equation model for the simulation of interfaces between compressible fluids. *Journal of Computational Physics 181*(2), 577–616. *(p. 3, 4, 75, 81, 99, 100, 188, 189, 190, 196, 198, 199, 206)*

Atkins, P., J. De Paula, and J. Keeler (2018). *Atkins' physical chemistry*. Oxford university press. *(p. 14, 18)*

Augonnet, C., S. Thibault, R. Namyst, and P.-A. Wacrenier (2011). StarPU: A Unified Platform for Task Scheduling on Heterogeneous Multicore Architectures. *CCPE - Concurrency and Computation: Practice and Experience, Special Issue: Euro-Par 2009 23*, 187–198. *(p. 117)*

Baer, M. and J. Nunziato (1986). A two-phase mixture theory for the deflagration-to-detonation transition (ddt) in reactive granular materials. *International journal of multiphase flow 12*(6), 861–889. *(p. 3, 73, 80, 188)*

Bellan, J. (2006). Theory, modeling and analysis of turbulent supercritical mixing. *Combustion Science and Technology 178*(1-3), 253–281. *(p. 2)*

Boris, J. P. and D. L. Book (1973). Flux-corrected transport. I. SHASTA, a fluid transport algorithm that works. *Journal of computational physics 11*(1), 38–69. *(p. 5, 125)*

Brackbill, J., D. Kothe, and C. Zemach (1992). A continuum method for modeling surface tension. *Journal of Computational Physics 100*(2), 335 – 354. *(p. 79)*

Cahn, J. W. and J. E. Hilliard (1958). Free energy of a nonuniform system. I. Interfacial free energy. *The Journal of chemical physics 28*(2), 258–267. *(p. 72)*

Candel, S., G. Herding, R. Synder, P. Scouflaire, C. Rolon, L. Vingert, M. Habiballah, F. Grisch, M. Péalat, P. Bouchardy, D. Stepowski, A. Cessou, and P. Colin (1998). Experimental investigation of shear coaxial cryogenic jet flames. *Journal of Propulsion and Power 14*(5), 826–834. *(p. 167, 177, 179)*

Candel, S., M. Juniper, G. Singla, P. Scouflaire, and C. Rolon (2006). Structure and dynamics of cryogenic flames at supercritical pressure. *Combustion Science and Technology 178*(1-3), 161–192. *(p. 2, 167)*

Cardano, G. (1662). Artis magnae, sive de regulis algebraicis. In *Opera Omnia*. Leiden. *(p. 230)*

Charalampous, G., Y. Hardalupas, and A. KP Taylor (2009). Novel technique for measurements of continuous liquid jet core in an atomizer. *AIAA journal 47*(11), 2605–2615. *(p. 57)*

Chiapolino, A., P. Boivin, and R. Saurel (2016). A simple phase transition relaxation solver for liquid-vapor flows. *International Journal for Numerical Methods in Fluids 83*(7), 583–605. *(p. 3, 27, 28, 78, 191, 198, 204, 206, 210)*

Chiapolino, A., P. Boivin, and R. Saurel (2017). A simple and fast phase transition relaxation solver for compressible multicomponent two-phase flows. *Computers & Fluids 150*, 31–45. *(p. 3, 78)*

Chiapolino, A., R. Saurel, and B. Nkonga (2017). Sharpening diffuse interfaces with compressible fluids on unstructured meshes. *Journal of Computational Physics 340*, 389–417. *(p. 81, 83, 109, 226)*

Chigier, N. and R. D. Reitz (1996). Regimes of jet breakup and breakup mechanisms- physical aspects. *Recent advances in spray combustion: Spray atomization and drop burning phenomena. 1*, 109–135. *(p. 179)*

Chung, T. H., M. Ajlan, L. L. Lee, and K. E. Starling (1988). Generalized multiparameter correlation for nonpolar and polar fluid transport properties. *Industrial & engineering chemistry research 27*(4), 671–679. *(p. 164, 165)*

Clain, S., S. Diot, and R. Loubère (2011). A high-order finite volume method for systems of conservation laws – Multi-dimensional Optimal Order Detection (MOOD). *Journal of computational Physics 230*(10), 4028–4050. *(p. 109)*

Clerc, S. (2000). Numerical simulation of the homogeneous equilibrium model for two-phase flows. *Journal of Computational Physics 161*(1), 354–375. *(p. 206)*

Cockburn, B., G. E. Karniadakis, and C.-W. Shu (2000). The development of discontinuous Galerkin methods. In *Discontinuous Galerkin Methods*, pp. 3–50. Springer. *(p. 113)*

Cockburn, B. and C.-W. Shu (1998). The Runge–Kutta discontinuous Galerkin method for conservation laws V: multidimensional systems. *Journal of Computational Physics 141*(2), 199–224. *(p. 110)*

Colella, P. and P. R. Woodward (1984). The piecewise parabolic method (PPM) for gas-dynamical simulations. *Journal of computational physics 54*(1), 174–201. *(p. 109)*

Colin, O. (2003). A finite element operator for diffusion terms in AVBP. Technical report, IFP. *(p. 166)*

Colin, O. and M. Rudgyard (2000). Development of high-order Taylor–Galerkin schemes for LES. *Journal of Computational Physics 162*(2), 338–371. *(p. 5, 119, 120, 122, 124, 125)*

Davis, S. (1988). Simplified second-order Godunov-type methods. *SIAM Journal on Scientific and Statistical Computing 9*(3), 445–473. *(p. 97)*

DeBar, R. (1974). Fundamentals of the KRAKEN code. [Eulerian hydrodynamics code for compressible nonviscous flow of several fluids in two-dimensional (axially symmetric) region]. Technical report, California Univ., Livermore (USA). Lawrence Livermore Lab. *(p. 63)*

Desjardins, O., V. Moureau, and H. Pitsch (2008). An accurate conservative level-set/ghost-fluid method for simulating turbulent atomization. *Journal of Computational Physics 227*(18), 8395–8416. *(p. 59, 60, 61, 82)*

Domingo, P., L. Vervisch, and D. Veynante (2008). Large-eddy simulation of a lifted methane jet flame in a vitiated coflow. *Combustion and Flame 152*(3), 415–432. *(p. 165)*

Donea, J. (1984). A Taylor–Galerkin method for convective transport problems. *International Journal for Numerical Methods in Engineering 20*(1), 101–119. *(p. 119)*

Donea, J. and A. Huerta (2003). *Finite element methods for flow problems*. John Wiley & Sons. *(p. 5, 101, 120, 121, 123)*

Drew, D. A. (1983). Mathematical modeling of two-phase flow. *Annual review of fluid mechanics 15*(1), 261–291. *(p. 73)*

Dyadechko, V. and M. Shashkov (2005). Moment-of-fluid interface reconstruction. Technical report, Los Alamos Report LA-UR-05-7571. *(p. 64)*

Essadki, M., J. Jung, A. Larat, M. Pelletier, and V. Perrier (2018). A task-driven implementation of a simple numerical solver for hyperbolic conservation laws. *ESAIM: Proceedings and Surveys 63*, 228–247. *(p. 117)*

Fedkiw, R. P., T. Aslam, B. Merriman, and S. Osher (1999). A non-oscillatory Eulerian approach to interfaces in multimaterial flows (the ghost fluid method). *Journal of computational physics 152*(2), 457–492. *(p. 61, 62)*

Fletcher, C. A. (1996). *Computational techniques for fluid dynamics 1: Fundamental and General Techniques*, Volume 1. Springer-Verlag. *(p. 120)*

Fouillet, C. (2003). *Généralisation à des mélanges binaires de la méthode du second gradient et application à la simulation numérique directe de l'ébullition nucléée*. Ph. D. thesis, Paris 6. *(p. 71)*

Furfaro, D. and R. Saurel (2016). Modeling droplet phase change in the presence of a multi-component gas mixture. *Applied Mathematics and Computation 272*, 518–541. *(p. 3, 79, 204)*

Gaillard, P. (2015, Dec). *Diffuse interfaces and LOx/H2 transcritical flames*. Ph. D. thesis, Université Pierre et Marie Curie - Paris VI. *(p. 71, 164)*

Giovangigli, V. (2012). Multicomponent flow modeling. *Science China Mathematics 55*(2), 285–308. *(p. 164)*

Giovangigli, V. and L. Matuszewski (2012). Numerical simulation of transcritical strained laminar flames. *Combustion and Flame 159*(9), 2829–2840. *(p. 2)*

Giovangigli, V., L. Matuszewski, and F. Dupoirieux (2011). Detailed modeling of planar transcritical H2–O2–N2 flames. *Combustion Theory and Modelling 15*(2), 141–182. *(p. 2)*

Glimm, J., E. Isaacson, D. Marchesin, and O. McBryan (1981). Front tracking for hyperbolic systems. *Advances in Applied Mathematics 2*(1), 91–119. *(p. 66)*

Godunov, S. K. (1959). A difference method for numerical calculation of discontinuous solutions of the equations of hydrodynamics. *Matematicheskii Sbornik 89*(3), 271–306. *(p. 96, 107)*

Gueyffier, D., J. Li, A. Nadim, R. Scardovelli, and S. Zaleski (1999). Volume-of-fluid interface tracking with smoothed surface stress methods for three-dimensional flows. *Journal of Computational Physics 152*(2), 423 – 456. *(p. 80)*

Habiballah, M., M. Orain, F. Grisch, L. Vingert, and P. Gicquel (2006). Experimental studies of high-pressure cryogenic flames on the Mascotte facility. *Combustion Science and Technology 178*(1-3), 101–128. *(p. 2, 167)*

Hairer, E., S. P. Nørsett, and G. Wanner (2008). *Solving ordinary differential equations I: nonstiff problems*, Volume 8. Springer Science & Business Media. *(p. 245, 246)*

Harten, A., B. Engquist, S. Osher, and S. R. Chakravarthy (1987). Uniformly high order accurate essentially non-oscillatory schemes, III. In *Upwind and high-resolution schemes*, pp. 218–290. Springer. *(p. 109)*

Harten, A., P. D. Lax, and B. v. Leer (1983). On upstream differencing and Godunov-type schemes for hyperbolic conservation laws. *SIAM review 25*(1), 35–61. *(p. 81, 96)*

Hernández, J., J. López, P. Gómez, C. Zanzi, and F. Faura (2008). A new volume of fluid method in three dimensions – Part I: Multidimensional advection method with face-matched flux polyhedra. *International Journal for Numerical Methods in Fluids 58*(8), 897–921. *(p. 65)*

Hirsch, C. (1997). *Numerical computation of internal and external flows: Computational methods for inviscid and viscous flows*, Volume 2. Wiley. *(p. 105, 106)*

Hirschfelder, J. O., C. F. Curtiss, R. B. Bird, and M. G. Mayer (1954). *Molecular theory of gases and liquids*, Volume 26. Wiley New York. *(p. 8, 14)*

Hirt, C. W. and B. D. Nichols (1981). Volume of fluid (VOF) method for the dynamics of free

boundaries. *Journal of computational physics 39*(1), 201–225. *(p. 63, 65)*

Ivey, C. B. and P. Moin (2015). Accurate interface normal and curvature estimates on three-dimensional unstructured non-convex polyhedral meshes. *Journal of Computational Physics 300*, 365–386. *(p. 64)*

Ivey, C. B. and P. Moin (2017). Conservative and bounded volume-of-fluid advection on unstructured grids. *Journal of Computational Physics 350*, 387–419. *(p. 65)*

Jacqmin, D. (1999). Calculation of two-phase Navier–Stokes flows using phase-field modeling. *Journal of Computational Physics 155*(1), 96–127. *(p. 72)*

Jamet, D. (1998). *Etude des potentialités de la théorie du second gradient pour la simulation numérique directe des écoulements liquide-vapeur avec changement de phase*. Ph. D. thesis, Châtenay-Malabry, Ecole centrale de Paris. *(p. 71)*

Jamet, D., O. Lebaigue, N. Coutris, and J. Delhaye (2001). The second gradient method for the direct numerical simulation of liquid–vapor flows with phase change. *Journal of Computational Physics 169*(2), 624–651. *(p. 71)*

Juniper, M., A. Tripathi, P. Scouflaire, J.-C. Rolon, and S. Candel (2000). Structure of cryogenic flames at elevated pressures. *Proceedings of the Combustion Institute 28*(1), 1103–1109. *(p. 3)*

Kapila, A., R. Menikoff, J. Bdzil, S. Son, and D. S. Stewart (2001). Two-phase modeling of deflagration-to-detonation transition in granular materials: reduced equations. *Physics of fluids 13*(10), 3002–3024. *(p. 3, 74, 188)*

Kim, J., S. Lee, Y. Choi, S.-M. Lee, and D. Jeong (2016). Basic principles and practical applications of the Cahn–Hilliard equation. *Mathematical Problems in Engineering 2016*, 1–11. *(p. 73)*

Kinzel, M. P., J. W. Lindau, and R. F. Kunz (2018). A multiphase level-set approach for all-Mach numbers. *Computers & Fluids 167*, 1–16. *(p. 61)*

Korteweg, D. J. (1901). Sur la forme que prennent les équations du mouvements des fluides si l'on tient compte des forces capillaires causées par des variations de densité considérables mais connues et sur la théorie de la capillarité dans l'hypothèse d'une variation continue de la densité. *Archives Néerlandaises des Sciences Exactes et Naturelles 6*, 1–24. *(p. 71)*

Kraichnan, R. H. (1970). Diffusion by a random velocity field. *The physics of fluids 13*(1), 22–31. *(p. 169, 175)*

Kuzmin, D. (2009). Explicit and implicit FEM-FCT algorithms with flux linearization. *Journal of Computational Physics 228*(7), 2517–2534. *(p. 126, 127, 128, 129, 130)*

Kuzmin, D., R. Löhner, and S. Turek (2012). *Flux-corrected transport: principles, algorithms, and applications*. Springer. *(p. 5, 127)*

Kuzmin, D., M. Möller, and S. Turek (2004). High-resolution FEM–FCT schemes for multidimensional conservation laws. *Computer Methods in Applied Mechanics and Engineering 193*(45-47), 4915–4946. *(p. 5)*

Kuzmin, D. and S. Turek (2002). Flux correction tools for finite elements. *Journal of Computational Physics 175*(2), 525–558. *(p. 126)*

Lacaze, G., T. Schmitt, A. Ruiz, and J. C. Oefelein (2019). Comparison of energy-, pressure- and enthalpy-based approaches for modeling supercritical flows. *Computers & Fluids 181*, 35–56. *(p. 2, 28, 181)*

Lamarque, N. (2007). *Schémas numériques et conditions limites pour la simulation aux grandes échelles de la combustion diphasique dans les foyers d'hélicoptère*. Ph. D. thesis, Institut National Polytechnique de Toulouse-INPT. *(p. 123, 127, 166, 246)*

Landau, L. and E. Lifshitz (1987). Fluid mechanics (second edition). In *Course of Theoretical Physics*, Volume 6. Pergamon. *(p. 79)*

Lasheras, J. C. and E. Hopfinger (2000). Liquid jet instability and atomization in a coaxial gas

stream. *Annual review of fluid mechanics 32*(1), 275–308. *(p. 179)*

Le Chenadec, V. and H. Pitsch (2013). A monotonicity preserving conservative sharp interface flow solver for high density ratio two-phase flows. *Journal of Computational Physics 249*, 185–203. *(p. 66)*

Le Martelot, S., R. Saurel, and B. Nkonga (2014). Towards the direct numerical simulation of nucleate boiling flows. *International Journal of Multiphase Flow 66*, 62–78. *(p. 3, 4, 27, 28, 29, 77, 78, 81, 154, 198)*

Le Métayer, O., J. Massoni, and R. Saurel (2004, 03). Élaboration des lois d'état d'un liquide et de sa vapeur pour les modèles d'écoulements diphasiques. *International Journal of Thermal Sciences 43*, 265–276. *(p. 4, 27, 28, 236)*

Le Métayer, O. and R. Saurel (2016). The Noble-Abel stiffened-gas equation of state. *Physics of Fluids 28*(4), 046102. *(p. 4, 28, 116)*

LeVeque, R. J. (1992). *Numerical methods for conservation laws*, Volume 132. Springer. *(p. 86, 93)*

Lilly, D. K. (1992). A proposed modification of the Germano subgrid-scale closure method. *Physics of Fluids A: Fluid Dynamics 4*(3), 633–635. *(p. 164, 166)*

Liu, T.-P. (1987). Hyperbolic conservation laws with relaxation. *Communications in Mathematical Physics 108*(1), 153–175. *(p. 76)*

Liu, X.-D., S. Osher, and T. Chan (1994). Weighted essentially non-oscillatory schemes. *Journal of computational physics 115*(1), 200–212. *(p. 61)*

Löhner, R., K. Morgan, M. Vahdati, J. P. Boris, and D. Book (1988). FEM-FCT: combining unstructured grids with high resolution. *Communications in Applied Numerical Methods 4*(6), 717–729. *(p. 5, 126)*

Löhner, R., K. Morgan, and O. C. Zienkiewicz (1984). The solution of non-linear hyperbolic equation systems by the finite element method. *International Journal for Numerical Methods in Fluids 4*(11), 1043–1063. *(p. 119)*

Lund, H. (2012). A hierarchy of relaxation models for two-phase flow. *SIAM Journal on Applied Mathematics 72*(6), 1713–1741. *(p. 76, 77)*

Ma, P. C., H. Wu, T. Jaravel, L. Bravo, and M. Ihme (2019). Large-eddy simulations of transcritical injection and auto-ignition using diffuse-interface method and finite-rate chemistry. *Proceedings of the Combustion Institute 37*(3), 3303–3310. *(p. 4, 181)*

Matheis, J. and S. Hickel (2018). Multi-component vapor-liquid equilibrium model for LES of high-pressure fuel injection and application to ECN spray A. *International Journal of Multiphase Flow 99*, 294–311. *(p. 4, 45, 48, 79, 180, 183)*

Mathew, J., R. Lechner, H. Foysi, J. Sesterhenn, and R. Friedrich (2003). An explicit filtering method for large eddy simulation of compressible flows. *Physics of fluids 15*(8), 2279–2289. *(p. 167)*

Matuszewski, L. (2011). *Modélisation et simulation numérique des phénomènes de combustion en régime supercritique*. Ph. D. thesis, Paris 6. Thèse de doctorat dirigée par Giovangigli, Vincent. Mécanique des fluides. *(p. 45)*

Mavriplis, D. J. and A. Jameson (1990). Multigrid solution of the Navier-Stokes equations on triangular meshes. *AIAA journal 28*(8), 1415–1425. *(p. 102, 119)*

Mayer, W., A. Schik, B. Vielle, C. Chauveau, I. Gokalp, D. Talley, and R. Woodward (1998). Theoretical and experimental approaches – Atomization and breakup of cryogenic propellants under high-pressure subcritical and supercritical conditions. *Journal of Propulsion and Power 14*(5), 835–842. *(p. 17)*

McBride, B. J., M. J. Zehe, and S. Gordon (2002). NASA Glenn coefficients for calculating thermodynamic properties of individual species. Technical report, NASA. *(p. 229)*

Michelsen, M. L. and J. Mollerup (2004). *Thermodynamic Modelling: Fundamentals and Computational Aspects*. Tie-Line Publications. *(p. 4, 38, 40, 42, 45, 47, 48)*

Mosso, S., B. Swartz, D. Kothe, and S. Clancy (1996). Recent enhancements of volume tracking algorithms for irregular grids. Technical report, Los Alamos National Laboratory, Los Alamos, NM, LA-cp-96-227. *(p. 64)*

Mulder, W., S. Osher, and J. A. Sethian (1992). Computing interface motion in compressible gas dynamics. *Journal of Computational Physics 100*(2), 209–228. *(p. 59)*

Muldoon, F. and S. Acharya (2008). A divergence-free interpolation scheme for the immersed boundary method. *International journal for numerical methods in fluids 56*(10), 1845–1884. *(p. 67)*

Murrone, A. and H. Guillard (2005). A five equation reduced model for compressible two phase flow problems. *Journal of Computational Physics 202*(2), 664–698. *(p. 3, 4, 74, 75, 80, 81, 188, 196, 198)*

Nayigizente, D., S. Thomas, and S. Ducruix (2018). Unsteady simulations of liquid/gas interfaces using the second gradient theory. In *ICLASS 2018*. *(p. 71, 72)*

Nicoud, F. and F. Ducros (1999). Subgrid-scale stress modelling based on the square of the velocity gradient tensor. *Flow, turbulence and Combustion 62*(3), 183–200. *(p. 164)*

Noh, W. F. and P. Woodward (1976). SLIC (Simple Line Interface Calculation). In A. I. van de Vooren and P. J. Zandbergen (Eds.), *Proceedings of the Fifth International Conference on Numerical Methods in Fluid Dynamics June 28 – July 2, 1976 Twente University, Enschede*, Berlin, Heidelberg, pp. 330–340. Springer Berlin Heidelberg. *(p. 63)*

Nourgaliev, R. R. and T. G. Theofanous (2007). High-fidelity interface tracking in compressible flows: unlimited anchored adaptive level set. *Journal of Computational Physics 224*(2), 836–866. *(p. 61)*

Oefelein, J. C. (2005). Thermophysical characteristics of shear-coaxial LOx–H2 flames at supercritical pressure. *Proceedings of the Combustion Institute 30*(2), 2929–2937. *(p. 2)*

Olsson, E. and G. Kreiss (2005). A conservative level set method for two phase flow. *Journal of computational physics 210*(1), 225–246. *(p. 59, 60)*

Olsson, E., G. Kreiss, and S. Zahedi (2007). A conservative level set method for two phase flow II. *Journal of Computational Physics 225*(1), 785–807. *(p. 60, 61)*

Oschwald, M., J. Smith, R. Branam, J. Hussong, A. Schik, B. Chehroudi, and D. Talley (2006). Injection of fluids into supercritical environments. *Combustion Science and Technology 178*(1-3), 49–100. *(p. 2)*

Osher, S. and J. A. Sethian (1988). Fronts propagating with curvature-dependent speed: algorithms based on Hamilton-Jacobi formulations. *Journal of computational physics 79*(1), 12–49. *(p. 59)*

Owkes, M. and O. Desjardins (2014). A computational framework for conservative, three-dimensional, unsplit, geometric transport with application to the volume-of-fluid (VOF) method. *Journal of Computational Physics 270*, 587–612. *(p. 64, 65)*

Pantano, C., R. Saurel, and T. Schmitt (2017). An oscillation free shock-capturing method for compressible van der Waals supercritical fluid flows. *Journal of Computational Physics 335*, 780–811. *(p. 2, 28, 181, 194, 195, 209)*

Parker, B. and D. Youngs (1992). *Two and three dimensional Eulerian simulation of fluid flow with material interfaces*. Atomic Weapons Establishment. *(p. 63)*

Peng, D.-Y. and D. B. Robinson (1976). A new two-constant equation of state. *Industrial & Engineering Chemistry Fundamentals 15*(1), 59–64. *(p. 2, 20)*

Pera, C., O. Colin, and S. Jay (2009). Development of a FPI detailed chemistry tabulation methodology for internal combustion engines. *Oil & Gas Science and Technology-Revue de l'IFP 64*(3), 243–258. *(p. 165)*

Perigaud, G. and R. Saurel (2005, October). A compressible flow model with capillary effects. *J. Comput. Phys. 209*(1), 139–178. *(p. 80)*

Peskin, C. S. and B. F. Printz (1993). Improved volume conservation in the computation of flows

with immersed elastic boundaries. *Journal of computational physics 105*(1), 33–46. *(p. 67)*

Pickett, L. M., C. L. Genzale, G. Bruneaux, L.-M. Malbec, L. Hermant, C. Christiansen, and J. Schramm (2010). Comparison of Diesel spray combustion in different high-temperature, high-pressure facilities. *SAE International Journal of Engines 3*(2), 156–181. *(p. 4, 79)*

Pickett, L. M., C. L. Genzale, J. Manin, L.-M. Malbec, and L. Hermant (2011). Measurement uncertainty of liquid penetration in evaporating Diesel sprays. In *Institute for Liquid Atomization and Spray Systems (ILASS)*. *(p. 182, 184)*

Pilliod Jr, J. E. and E. G. Puckett (2004). Second-order accurate volume-of-fluid algorithms for tracking material interfaces. *Journal of Computational Physics 199*(2), 465–502. *(p. 63, 64, 65)*

Poinsot, T. and D. Veynante (2005). *Theoretical and numerical combustion*. RT Edwards, Inc. *(p. 164, 165)*

Poinsot, T. J. and S. Lele (1992). Boundary conditions for direct simulations of compressible viscous flows. *Journal of computational physics 101*(1), 104–129. *(p. 141, 169, 174, 181)*

Poling, B. E., J. M. Prausnitz, O. John Paul, and R. C. Reid (2001). *The properties of gases and liquids*, Volume 5. Mcgraw-hill New York. *(p. 2, 9, 15, 19, 20, 21, 22, 29)*

Poole, G. and T. Boullion (1974). A survey on M-matrices. *SIAM Review 16*(4), 419–427. *(p. 127)*

Popinet, S. and S. Zaleski (1999). A front-tracking algorithm for accurate representation of surface tension. *International Journal for Numerical Methods in Fluids 30*(6), 775–793. *(p. 67)*

Prausnitz, J. M., R. N. Lichtenthaler, and E. G. de Azevedo (1998). *Molecular thermodynamics of fluid-phase equilibria*. Pearson Education. *(p. 46)*

Qiu, L., Y. Wang, Q. Jiao, H. Wang, and R. D. Reitz (2014). Development of a thermodynamically consistent, robust and efficient phase equilibrium solver and its validations. *Fuel 115*, 1–16. *(p. 79)*

Rayleigh, L. (1892). On the theory of surface forces.–II. Compressible fluids. *The London, Edinburgh, and Dublin Philosophical Magazine and Journal of Science 33*(201), 209–220. *(p. 70)*

Ribert, G., N. Zong, V. Yang, L. Pons, N. Darabiha, and S. Candel (2008). Counterflow diffusion flames of general fluids: Oxygen/hydrogen mixtures. *Combustion and Flame 154*(3), 319–330. *(p. 2)*

Rocard, Y. (1967). Thermodynamique. *(p. 71)*

Roe, P. L. (1986). Characteristic-based schemes for the Euler equations. *Annual review of fluid mechanics 18*(1), 337–365. *(p. 81, 99, 189)*

Ruiz, A. (2012). *Unsteady Numerical Simulations of Transcritical Turbulent Combustion in Liquid Rocket Engines*. Ph. D. thesis, INP Toulouse. Thèse de doctorat dirigée par Cuenot, Bénédicte et Selle, Laurent Energétique et transferts Toulouse. *(p. 139)*

Saurel, R. and R. Abgrall (1999). A multiphase Godunov method for compressible multifluid and multiphase flows. *Journal of Computational Physics 150*(2), 425–467. *(p. 3, 4, 73, 74, 81, 188)*

Saurel, R. and C. Pantano (2018). Diffuse-interface capturing methods for compressible two-phase flows. *Annual Review of Fluid Mechanics 50*, 105–130. *(p. 80)*

Saurel, R., F. Petitpas, and R. Abgrall (2008). Modelling phase transition in metastable liquids: application to cavitating and flashing flows. *Journal of Fluid Mechanics 607*, 313–350. *(p. 29, 77, 78)*

Saurel, R., F. Petitpas, and R. A. Berry (2009). Simple and efficient relaxation methods for interfaces separating compressible fluids, cavitating flows and shocks in multiphase mixtures. *Journal of Computational Physics 228*(5), 1678–1712. *(p. 75)*

Schmitt, P., T. Poinsot, B. Schuermans, and K. Geigle (2007). Large-eddy simulation and experimental study of heat transfer, nitric oxide emissions and combustion instability in a swirled turbulent high-pressure burner. *Journal of Fluid Mechanics 570*, 17–46. *(p. 169, 174, 181)*

Schmitt, T. (2009). *Simulation des grandes échelles de la combustion turbulente à pression supercritique*. Ph. D. thesis, INP Toulouse. Thèse de doctorat dirigée par Cuenot, Bénédicte et Selle, Laurent

Dynamique des fluides Toulouse, INPT 2009. *(p. 139, 140, 174)*

Schmitt, T. (2019). Large-eddy simulations of the Mascotte test cases operating at supercritical pressure (submitted). *Journal of Flow, Turbulence and Combustion*. *(p. 2, 3, 163, 164, 166, 175)*

Schmitt, T., Y. Méry, M. Boileau, and S. Candel (2011). Large-eddy simulation of oxygen/methane flames under transcritical conditions. *Proceedings of the Combustion Institute 33*(1), 1383–1390. *(p. 2, 165)*

Schmitt, T., L. Selle, A. Ruiz, and B. Cuenot (2010). Large-eddy simulation of supercritical-pressure round jets. *AIAA journal 48*(9), 2133–2144. *(p. 164)*

Segal, C. and S. Polikhov (2008). Subcritical to supercritical mixing. *Physics of Fluids 20*(5), 052101. *(p. 2)*

Selmin, V. (1987). *Third-order finite element schemes for the solution of hyperbolic problems*. Ph. D. thesis, INRIA. *(p. 124)*

Seppecher, P. (1987). *Etude d'une modelisation des zones capillaires fluides: interfaces et lignes de contact*. Ph. D. thesis, Ecole Nationale Superieure de Techniques Avancees. *(p. 71)*

Shin, S. and D. Juric (2002). Modeling three-dimensional multiphase flow using a level contour reconstruction method for front tracking without connectivity. *Journal of Computational Physics 180*(2), 427–470. *(p. 67, 68)*

Shukla, R. K., C. Pantano, and J. B. Freund (2010). An interface capturing method for the simulation of multi-phase compressible flows. *Journal of Computational Physics 229*(19), 7411–7439. *(p. 82, 83, 226)*

Singla, G., P. Scouflaire, C. Rolon, and S. Candel (2005). Transcritical oxygen/transcritical or supercritical methane combustion. *Proceedings of the combustion institute 30*(2), 2921–2928. *(p. 3)*

Smirnov, A., S. Shi, and I. Celik (2001). Random flow generation technique for large eddy simulations and particle-dynamics modeling. *Journal of fluids engineering 123*(2), 359–371. *(p. 169, 175)*

Soave, G. (1972). Equilibrium constants from a modified Redlich-Kwong equation of state. *Chemical Engineering Science 27*(6), 1197 – 1203. *(p. 2, 20, 166)*

Stolz, S. and N. A. Adams (1999). An approximate deconvolution procedure for large-eddy simulation. *Physics of Fluids 11*(7), 1699–1701. *(p. 167)*

Strang, G. (1968). On the construction and comparison of difference schemes. *SIAM Journal on Numerical Analysis 5*(3), 506–517. *(p. 81, 155)*

Sussman, M. and E. G. Puckett (2000). A coupled level-set and volume-of-fluid method for computing 3D and axisymmetric incompressible two-phase flows. *Journal of Computational Physics 162*(2), 301 – 337. *(p. 64)*

Sussman, M., P. Smereka, and S. Osher (1994). A level set approach for computing solutions to incompressible two-phase flow. *Journal of Computational physics 114*(1), 146–159. *(p. 59)*

Sweby, P. K. (1984). High resolution schemes using flux limiters for hyperbolic conservation laws. *SIAM journal on numerical analysis 21*(5), 995–1011. *(p. 61, 81, 82, 109)*

Terashima, H. and G. Tryggvason (2009). A front-tracking/ghost-fluid method for fluid interfaces in compressible flows. *Journal of Computational Physics 228*(11), 4012–4037. *(p. 67, 69)*

Toro, E. F. (2013). *Riemann solvers and numerical methods for fluid dynamics: a practical introduction*. Springer Science & Business Media. *(p. 4, 93, 97, 100, 107)*

Toro, E. F., M. Spruce, and W. Speares (1994). Restoration of the contact surface in the HLL-Riemann solver. *Shock waves 4*(1), 25–34. *(p. 81, 98, 116)*

Urbano, A., L. Selle, G. Staffelbach, B. Cuenot, T. Schmitt, S. Ducruix, and S. Candel (2016). Exploration of combustion instability triggering using large eddy simulation of a multiple injector liquid rocket engine. *Combustion and Flame 169*, 129–140. *(p. 2)*

van der Waals, J. D. (1873). *Over de Continuiteit van den Gas-en Vloeistoftoestand*, Volume 1.

Sijthoff. *(p. 17)*

van der Waals, J. D. (1893, Feb). The thermodynamic theory of capillarity under the hypothesis of a continuous variation of density. Transl. J. S. Rowlinson, 1979. *Journal of Statistical Physics 20*(2), 200–244. *(p. 70)*

Van Konynenburg, P. and R. Scott (1980). Critical lines and phase equilibria in binary van der waals mixtures. *Philosophical Transactions of the Royal Society of London. Series A, Mathematical and Physical Sciences 298*(1442), 495–540. *(p. 46)*

van Leer, B. (1979). Towards the ultimate conservative difference scheme. V. A second-order sequel to Godunov's method. *Journal of computational Physics 32*(1), 101–136. *(p. 61, 81, 107)*

Veynante, D. and L. Vervisch (2002). Turbulent combustion modeling. *Progress in energy and combustion science 28*(3), 193–266. *(p. 165)*

Vingert, L., M. Habiballah, P. Vuillermoz, and S. Zurbach (2000). Mascotte, a test facility for cryogenic combustion research at high pressure. In *IAF, International Astronautical Congress, 51 st, Rio de Janeiro, Brazil*. *(p. 167)*

Weymouth, G. D. and D. K.-P. Yue (2010). Conservative volume-of-fluid method for free-surface simulations on cartesian-grids. *Journal of Computational Physics 229*(8), 2853–2865. *(p. 65)*

Yi, P., S. Yang, C. Habchi, and R. Lugo (2019). A multicomponent real-fluid fully compressible four-equation model for two-phase flow with phase change. *Physics of Fluids 31*(2), 026102. *(p. 4)*

Youngs, D. L. (1982). Time-dependent multi-material flow with large fluid distortion. *Numerical methods for fluid dynamics*, 273–285. *(p. 63)*

Zalesak, S. T. (1979). Fully multidimensional flux-corrected transport algorithms for fluids. *Journal of computational physics 31*(3), 335–362. *(p. 125, 126)*

Zhang, X. and C.-W. Shu (2010a). On maximum-principle-satisfying high order schemes for scalar conservation laws. *Journal of Computational Physics 229*(9), 3091–3120. *(p. 116)*

Zhang, X. and C.-W. Shu (2010b). On positivity-preserving high order discontinuous Galerkin schemes for compressible Euler equations on rectangular meshes. *Journal of Computational Physics 229*(23), 8918–8934. *(p. 117)*

Zhang, Y., X. Zhang, and C.-W. Shu (2013). Maximum-principle-satisfying second order discontinuous Galerkin schemes for convection–diffusion equations on triangular meshes. *Journal of Computational Physics 234*, 295–316. *(p. 117)*

université PARIS-SACLAY

ÉCOLE DOCTORALE
Sciences mécaniques et énergétiques, matériaux et géosciences (SMEMAG)

Titre : Étude des modèles d'interface diffuse et des schémas numériques adaptés pour la simulation d'écoulements sous-critiques à supercritiques

Mots clés : *écoulements diphasiques, écoulements supercritiques, thermodynamique gaz réel, méthodes numériques, combustion*

Résumé : Au cours de l'utilisation de certains systèmes propulsifs, tels que les moteurs fusées cryotechniques ou les moteurs Diesel, le point de fonctionnement peut varier sur une large plage de pressions. Ces variations de pression peuvent conduire à un changement de régime thermodynamique si la pression critique du fluide est franchie, l'injection initialement diphasique devenant alors transcritique. Ce changement modifie la topologie de l'écoulement, ainsi que la dynamique du mélange, ce qui impacte le comportement de la flamme. L'objectif de cette thèse est de développer une méthodologie originale capable de traiter au sein du même solveur des écoulements sous-critiques ainsi que supercritiques. Pour cela, une extension du solveur AVBP-RG aux écoulements diphasiques sous-critiques est proposée, basée sur des modèles d'interface diffuse. Les développements nécessaires à l'intégration de ces modèles dans le cadre du solveur aux éléments finis sont effectués. Des simulations numériques multidimensionnelles sont ensuite proposées de manière à confronter le modèle à des données exprérimentales, vis-à-vis desquelles un bon accord est observé. Ces résultats offrent des perspectives encourageantes vers de futures améliorations du modèle et des applications à des configurations industrielles complexes.

Title : Diffuse interface models and adapted numerical schemes for the simulation of subcritical to supercritical flows

Keywords : *two-phase flows, supercritical flows, real gas thermodynamics, numerical methods, combustion*

Abstract : In various industrial combustion devices, such as liquid rocket engines at ignition or Diesel engines during the compression stage, the operating point varies over a wide range of pressures. These pressure variations can lead to a change of thermodynamic regime when the critical pressure is exceeded, switching from two-phase injection to transcritical injection. This change modifies the topology of the flow and the mixing, thereby impacting the flame dynamics. The objective of the present Ph.D thesis is to develop an original methodology able to address both subcritical and supercritical flows within the same solver. To achieve this, an extension of the real gas solver AVBP-RG to subcritical two-phase flows is provided, based on diffuse interface models. The required developments for the integration of such models into the finite-element framework of the solver are provided. Multidimensional numerical simulations are led in order to confront the model with experimental data, with which good agreement is observed. These results offer encouraging perspectives regarding further enhancements of the model and applications to complex industrial cases.

Université Paris-Saclay
Espace Technologique / Immeuble Discovery
Route de l'Orme aux Merisiers RD 128 / 91190 Saint-Aubin, France